

**MECHANISM OF FRETTING CORROSION AT THE MODULAR  
TAPER INTERFACE OF HIP PROSTHESIS**

By

**Abimbola Oluwawemimo Oladokun**

Submitted in accordance with the requirements for the degree of  
Doctor of philosophy

The University of Leeds  
School of Mechanical Engineering  
Leeds, UK

September, 2017

The candidate confirms that the work submitted is his own, except where work which has formed part of jointly authored publications has been included. The contribution of the candidate and other co-authors in published work from this thesis has been clearly indicated. The candidate confirms that appropriate credit has been given within the thesis where reference has been made to the work of others.

In the papers contributing to this thesis, the candidate (first author) carried out all the experiments, analysis and preparation of the manuscripts. All other authors contributed by proof reading and providing insight for the discussions.

This copy has been supplied on the understanding that it is copyright material and that no quotation from this thesis may be published without proper acknowledgement.

© 2017 The University of Leeds and Abimbola Oluwawemimo Oladokun

## Papers and Conference proceedings contributing to this thesis

- A. Oladokun, M. Pettersson, M. Bryant, H. Engqvist, C. Persson, R. Hall & A. Neville (2015) Fretting of CoCrMo and Ti6Al4V alloys in modular prostheses, *Tribology - Materials, Surfaces & Interfaces*, 9:4, 165-173, DOI: [10.1179/1751584X15Y.0000000014](https://doi.org/10.1179/1751584X15Y.0000000014)
- Oladokun, A., M. Pettersson, M. Bryant, R. Hall, and A. Neville. "SUB-SURFACE INVESTIGATION OF FRETTED CO28CR6MO AND TI6AL4V ALLOYS." *Bone Joint J* 98, no. SUPP 9 (2016): 99-99.
- Oladokun, A., M. Bryant, R. Hall, and A. Neville. "The effect of cyclic load on the evolution of fretting current at the interface of Metal-on-Metal and Ceramic-on-Metal taper junction of hip prostheses." *Bone Joint J* 99, no. SUPP 5 (2017): 68-68.

## **Acknowledgements**

Firstly, I thank Christ Jesus for walking with me throughout this journey. I have experienced grace, strength, specific guidance and tenacity. And therefore, I am increasingly realising that with God, nothing shall be impossible!

I would like to appreciate my core supervisors: Prof. Anne Neville and Dr. Mike Bryant for their support towards my development in this journey. Special thanks to Anne for granting me the opportunity to do this PhD and to Mike for always being available to talk about oxides and amorphous transformations. Thanks to Prof. Richard Hall for making my experience even richer by supporting my attendance to ISTA 2015 and 2016 conference – they served as defining moments in my PhD journey, rekindling my passion for the research.

Special thanks to Dr. Todd Stewart who supervised my bachelors' research project on Spider silk; his encouraging words inspired me to consider a PhD without a Masters' degree. A big 'thank you' to Dr. Saurabh Lal and Dr. Nilanjan for inspiring me with their academic excellence and words of advice.

I am truly grateful to the iFS technicians that supported my research work: Ron, Mick, Andrew, Paul and Jordan. Special appreciation to Tony Weise and Adrian Eagles who were great support of my work from my undergraduate days until now. I am also grateful to Mike Ward and Zabeada of LEMAS; Maria, Ligia, Bianca, Corentin and Ogbemi for their support of this research.

I would like to appreciate all my office mates in Room 332a and Cemetery lodge as well as the entire PhD Eindhoven football team (I claim credit for the name). I have had 4 wonderful years spent with Andrew Barber, Joseph Norton, William Stokes, Benjamin Pickles and Joshua Owen.

Special thanks to my Pastors: Paul and Natasha Okhuoya who supported me throughout the 7 years I've been in Leeds. I am sincerely grateful to the entire Cloverleaf family for being my family in Leeds. I would specifically like to

appreciate John Ojukwu my dearest brother who also contributed to my desire to doing a PhD.

I am so grateful to my parents who sacrificed their jobs and settlement in Nigeria so that I and all my siblings can have a better education. My grand-parents, aunties, uncles and in-laws, I love you all so much. Thank you for the endless prayers; none of them fell to the ground.

And to my wife, Fiona Oladokun, who married me during this PhD journey and supported both of us for over 1 year on her meagre salary when I had no income; I am beyond grateful for your faith, strength and support. By the way, these dots tends to infinity..... → ∞

And to all others whose names I have not mentioned. I am sincerely grateful.

## Abstract

Modularity of total hip arthroplasty (THA) has been linked to various forms of adverse local tissue reaction (ALTR). ALTR is often a result of metallic particles and ions released from corroding implant materials to the peri-prosthetic tissues and blood stream of the human body. More so, it is a consequence of several fretting and crevice-induced corrosion mechanisms occurring simultaneously. Fretting corrosion and fatigue damage of the modular taper is initiated and sustained by micromotions at the taper interface through the multi-directional loads applied onto the prosthesis during daily living activities.

Subsequent to the failure of the implant, analysis of retrieved explants generally offer information regarding the mode of wear and to an extent, the types of corrosion damage. However, retrieval studies are limited in that, they do not provide a holistic insight into the *in-vivo* degradation mechanisms which ultimately led to the early failure of the implant. On the other hand, controlled *in-vitro* studies proves useful for replicating the evolution of wear and corrosion *in-situ*. In addition, the role of multiple individual factors which contribute to fretting corrosion can be elucidated through *in-vitro* methods.

In this study, metal – metal and ceramic – metal fretting interfaces were investigated. Advance microscopy and spectroscopy techniques were employed in the characterisation of passive films, corrosion products and metallurgical transformations of CoCrMo and Ti6Al4V alloys. Both mechanical and electrochemical data consisting of interfacial energy, open circuit potential (OCP) and fretting corrosion currents were measured using an *in-situ* tribocorrosion cell. Other surface analytical techniques were used to quantify wear and obtain surface topography.

The results showed that CoCrMo and Ti6Al4V display independent characteristic behaviours when in a metal – metal or ceramic – metal fretting contact. For example, fretting contacts involving Ti6Al4V experienced higher contact compliance than those of CoCrMo. The higher interfacial compliance

thus led to a significant proportion of wear being redistributed at the contacts involving Ti6Al4V alloys. It was subsequently observed that the redistributed wear at the interface leads to a mixed fretting regime whereby, the contact appear to be 'cold-welded' during a partial-slip regime and subsequently transitions to a gross slip fretting regime when the 'welded' interfacial material fractures. The phenomena was evident in both metal – metal and ceramic – metal interfaces involving Ti6Al4V.

The subsurface transformation in CoCrMo alloy when subjected to fretting was observed to be typically strain-induced twinning and loss of nano-crystalline region. On the other hand, Ti6Al4V alloy was observed to be strain-induced recrystallization, mechanical mixing, crack initiation and propagation.

It was also observed that the chemical composition of fretting corrosion products at the metal – metal interfaces were dependent on the contact condition and the specific area within the contact that the wear product is located. For example, metal-oxides and chlorides were prominent within creviced regions whilst precipitation of metal-phosphates and metal-oxides were present in well aerated regions. Evidence of Cr<sup>6+</sup> and pitting corrosion products were also identified at the most severe creviced environment of the CoCrMo – Ti6Al4V fretting contact.

This research also showed that the evolution of fretting corrosion current (specifically in self-mated CoCrMo contact) can be linked to the surface history of wear and corrosion. Furthermore, studies conducted on realistic taper components revealed that the use of ceramic bearings in order to eliminate one of two conductive components only resulted in the reduction of static corrosion currents but not fretting corrosion currents. Rather, it was deduced that interference fit at the ceramic – metal interface (relative to metal – metal) increases the surface area that is susceptible to passive oxide abrasion under fretting conditions. Therefore, the use of a ceramic bearing did not reduce fretting current at the modular taper interface.





## Table of Contents

<b>Acknowledgements</b> .....	<b>iv</b>
<b>Abstract</b> .....	<b>vi</b>
<b>List of Figures</b> .....	<b>xviii</b>
<b>List of Tables</b> .....	<b>xxxiii</b>
<b>Nomenclature</b> .....	<b>xxxiv</b>
<b>Chapter 1 Introduction</b> .....	<b>1</b>
1.1 Research objectives .....	2
1.2 Thesis outline .....	3
<b>Chapter 2 Background to biomaterials, corrosion and tribology</b> .....	<b>5</b>
2.1 Introduction .....	5
2.2 Metallic biomaterials.....	5
2.2.1 Cobalt based Alloys.....	5
2.2.2 Titanium and Titanium based alloys .....	7
2.2.3 Stainless steel .....	9
2.3 Ceramic biomaterials .....	10
2.3.1 Alumina ( $\text{Al}_2\text{O}_3$ ) and alumina composite .....	11
2.3.2 Silicon Nitride ( $\text{Si}_3\text{N}_4$ ) .....	13
2.4 Corrosion.....	14
2.4.1 Electrochemistry of corrosion .....	14
2.4.2 Types of corrosion effective at the modular junction of THA.....	16
2.4.3 Passivity of biomaterials.....	20
2.4.4 Faraday's law .....	21
2.5 Tribology .....	22
2.5.1 Wear.....	22

2.5.2 Adhesive wear .....	22
2.5.3 Abrasive wear .....	23
2.5.4 Fatigue Wear .....	24
2.5.5 Corrosive wear .....	25
2.6 Fretting .....	26
2.6.1 Fretting regimes .....	27
2.6.2 Fretting corrosion, wear and fatigue .....	31
<b>Chapter 3 Literature review .....</b>	<b>33</b>
3.1 Total hip arthroplasty .....	33
3.1.1 Rationale for modularity in THA.....	34
3.1.2 The Morse taper (head-neck taper).....	36
3.1.3 The neck–stem taper.....	37
3.1.4 Assembly of modular tapers .....	37
3.2 Challenges with modularity .....	38
3.2.1 Fretting and corrosion scores in retrieval studies .....	39
3.2.2 Review of retrieval studies – head-neck interface .....	40
3.2.3 Review of retrieval studies – the neck-stem interface .....	43
3.2.4 Corrosion products and metal ion releases .....	46
3.2.5 Metallurgical transformations in explants .....	49
3.3 In-vitro studies of fretting corrosion .....	50
3.3.1 Common <i>in-vitro</i> methods for assessing fretting corrosion in THA .....	50
3.3.2 Review of tribometer studies .....	52
3.3.3 Review of <i>in-vitro</i> studies using realistic taper components.....	55
3.4 Effect of proteins on corrosion of biomaterials .....	58
3.5 Tribocorrosion .....	59

3.5.1 Tribocorrosion in fretting.....	62
3.5.2 Mechanically assisted crevice corrosion .....	63
3.5.3 Repassivation characteristics of CoCrMo and Ti6Al4V .....	64
3.6 Summary.....	65
3.6.1 Gaps in literature .....	65

<b>Chapter 4 Experimental methodology and surface analytical techniques .....</b>	<b>67</b>
4.1 Introduction .....	67
4.2 Experimental materials.....	67
4.2.1 Metallic and ceramic sample preparation .....	67
4.2.2 Test environments and lubricants .....	68
4.3 Electrochemical technique .....	68
4.3.1 Open circuit potential measurement.....	69
4.3.2 Potentio-static polarisation .....	69
4.4 Experimental set-up .....	71
4.4.1 Fretting tribometer with in-situ electrochemistry .....	71
4.4.2 Tribometer fretting corrosion studies (test protocol) .....	73
4.4.3 Fatigue loading set – up with in-situ electrochemistry .....	78
4.5 Surface, sub-surface and chemical analysis .....	83
4.5.1 Optical light microscopy .....	83
4.5.2 White light interferometry .....	83
4.5.3 Scanning electron microscopy (SEM) .....	84
4.5.4 Focused Ion Beam (FIB) .....	85
4.5.5 Transmission Electron Microscope (TEM).....	87
4.5.6 X-Ray Powder Diffraction (XRD) Analysis.....	88
4.5.7 Energy Dispersed X-Ray Spectroscopy (EDS) .....	89
4.5.8 X-Ray Photoelectron Spectroscopy (XPS) .....	89

4.5.9 Nano-indentation hardness .....	91
4.5.10 Coordinate Measurement Machine (CMM).....	91

**Chapter 5 Metallurgy and surface chemistry of CoCrMo and Ti6Al4V**

.....	<b>92</b>
5.1 Introduction .....	92
5.2 Crystalline structure of CoCrMo and Ti6Al4V .....	93
5.3 Subsurface microscopy and spectroscopy .....	94
5.3.1 TEM and SAED of polished CoCrMo and Ti6Al4V .....	94
5.3.2 TEM – EDS of polished CoCrMo and Ti6Al4V .....	97
5.4 Surface chemistry.....	100
5.4.1 XPS assessment of CoCrMo passive film .....	100
5.4.2 XPS assessment of Ti6Al4V passive film .....	103
5.5 Nano-indentation hardness of polished surface .....	105
5.6 Discussion and summary .....	106

**Chapter 6 Fretting wear mechanism of metal – metal material combinations .....**

.....	<b>109</b>
6.1 Introduction .....	109
6.2 Tribological assessment of metal – metal fretting contacts .....	111
6.2.1 Fretting loop analysis .....	112
6.3 Open circuit potential measurement.....	115
6.4 Wear volume .....	118
6.5 Surface Analysis.....	120
6.5.1 3D and 2D surface profilometry of fretted contacts .....	120
6.5.2 Back scatter SEM of CoCrMo and Ti6Al4V surface .....	125
6.6 Spectroscopy of CoCrMo and Ti6Al4V surface from the metal – metal interface.....	127

6.6.1 EDS analysis of CoCrMo and Ti6Al4V surfaces (metal – metal) .....	128
6.6.2 XPS analysis of CoCrMo and Ti6Al4V surfaces (metal – metal) .....	131
6.7 Characterisation of metallurgical transformations (metal – metal) .....	138
6.7.1 TEM of Fretted CoCrMo and Ti6Al4V alloy .....	138
6.7.2 TEM-EDS and SAED analysis .....	143
6.8 Nano-indentation .....	157
6.9 Discussion and summary .....	158
<b>Chapter 7 Fretting wear mechanism of ceramic – metal material combinations .....</b>	<b>165</b>
7.1 Introduction .....	165
7.2 Tribological assessment of Ceramic – Metal and Ceramic – Ceramic Fretting Contacts .....	167
7.2.1 Fretting loop analysis .....	168
7.3 Open circuit potential measurement .....	173
7.4 Wear volume .....	177
7.5 Surface analysis .....	179
7.5.1 3D and 2D surface profilometry of fretted wear surface ...	179
7.5.2 BS-SEM analysis .....	186
7.6 Spectroscopy of CoCrMo and Ti6Al4V surface from the ceramic – metal interface .....	188
7.6.1 EDS analysis of CoCrMo and Ti6Al4V surfaces (ceramic – metal) .....	188
7.6.2 XPS analysis of CoCrMo and Ti6Al4V surface (ceramic – metal) .....	190

7.7	Characterisation of metallurgical transformations (ceramic – metal) .....	196
7.8	Nano-indentation .....	204
7.9	Fretting of Biolox Ceramic on CoCrMo and Ti6Al4V alloy .....	205
7.9.1	Fretting wear mechanism of Biolox – CoCrMo .....	206
7.9.2	Fretting wear mechanism of Biolox – Ti6Al4V (mixed regime) .....	210
7.9.3	Fretting wear mechanism of Biolox – Ti6Al4V (gross slip regime) .....	214
7.10	Discussion and summary .....	218
<b>Chapter 8 Quantification of fretting corrosion current using self-mated CoCrMo material combination .....</b>		<b>224</b>
8.1	Introduction .....	224
8.2	Anodic current in static condition.....	226
8.3	Method 1 .....	227
8.3.1	Fretting loop analysis .....	227
8.3.2	Electrochemical results .....	229
8.3.3	Surface analysis .....	230
8.3.4	Tribocorrosion mass loss.....	231
8.4	Method 2 .....	234
8.4.1	Fretting loop analysis .....	234
8.4.2	Electrochemical results .....	236
8.4.3	Surface analysis .....	237
8.4.4	Tribocorrosion mass loss.....	238
8.5	Method 3 .....	239
8.5.1	Fretting loop analysis .....	239
8.5.2	Electrochemical results .....	240

8.5.3 Surface analysis .....	242
8.5.4 Tribocorrosion mass loss .....	242
8.6 Discussion and summary .....	243
<b>Chapter 9 Assessment of fretting current from the head-neck metal-metal and ceramic-metal taper interface.....</b>	<b>248</b>
9.1 Introduction .....	248
9.2 Electrochemical results .....	253
9.2.1 Open Circuit Potential .....	253
9.2.2 Static Anodic Current Transient .....	255
9.2.3 Frequency variation.....	256
9.2.4 Mean load variation.....	258
9.2.5 Cyclic load variation .....	260
9.2.6 Systemic checks .....	261
9.3 Mechanical results .....	263
9.4 Surface Analysis .....	266
9.4.1 CoCrMo – CoCrMo.....	266
9.4.2 CoCrMo – Ti6Al4V .....	267
9.4.3 Biolox – CoCrMo .....	268
9.4.4 Biolox – Ti6Al4V.....	270
9.5 The case of misalignment .....	271
9.6 Discussion and summary .....	273
<b>Chapter 10 Overall discussion.....</b>	<b>276</b>
10.1 Introduction .....	276
10.2 Linking fretting loops with the fretting interface .....	276
10.2.1 Fretting loop deviations at the self-mated CoCrMo interface .....	278
10.2.2 Fretting loop deviations at ceramic – metal interface .....	280

10.2.3 Fretting loop deviations at CoCrMo – Ti6Al4V interface	282
10.2.4 Summary	284
10.3 Aspects of fretting and corrosion mechanisms	284
10.3.1 Mechanism of cold-welding and pseudo-amorphous structures at CoCrMo – Ti6Al4V interface	284
10.3.2 Mechanism of stiction at the Si <sub>3</sub> N <sub>4</sub> – Ti6Al4V interface	290
10.4 Characteristics of biomedical materials at the modular taper junction of hip implants	293
10.4.1 CoCrMo at the modular taper interface	293
10.4.2 Ti6Al4V at the modular taper interface	295
10.4.3 Si <sub>3</sub> N <sub>4</sub> at the modular taper interface	295
10.4.4 Biolox at the modular taper interface	297
10.5 Relevance to clinical application	298
<b>Chapter 11 Conclusions and Future work</b>	<b>301</b>
11.1 Conclusions	301
11.1.1 Material characterisation, metal – metal and ceramic – metal systems (Chapters 5 – 7)	301
11.1.2 Quantification of fretting corrosion current on self-mated CoCrMo (Chapter 8)	303
11.1.3 Component testing of metal – metal and ceramic – metal tapers (Chapter 9)	304
11.2 Future work	305



<b>References.....</b>	<b>306</b>
<b>Appendix A– Composition of FBS and PBS .....</b>	<b>334</b>
<b>Appendix B– Determination of contact compliance.....</b>	<b>336</b>
<b>Appendix C – Interactions between energy, wear and oxidation.....</b>	<b>340</b>
<b>Appendix D – List of oral presentations.....</b>	<b>341</b>

## List of Figures

Figure 2-1 – Generations of alumina ceramic [13].....	12
Figure 2-2 Mechanism of improved toughness in composite alumina ceramic [15].....	12
Figure 2-3 – Electrical interactions at the metallic surface a) Schematic diagram of electric double layer [23] b) Anodic and Cathodic sites during corrosion [21].....	16
Figure 2-4 – Intergranular attack on CoCrMo alloy [27].....	17
Figure 2-5 – Pitting corrosion attack on CoCrMo alloy [27]. ....	18
Figure 2-6 – A simplified 3 stage depiction of crevice corrosion: a) conducting electrolyte in contact with crevice. b) cathodic and anodic sites are formed, c) corrosion products create a severer crevice [21].....	19
Figure 2-7 – Theoretical plot of a potentiodynamic scan in the anodic direction for a passive alloy [32] .....	21
Figure 2-8 – Adhesive wear mechanism [35] .....	23
Figure 2-9 – Abrasive wear mechanism [35] .....	24
Figure 2-10 – Fatigue wear mechanism [35] .....	24
Figure 2-11 – Corrosive wear mechanism [35].....	25
Figure 2-12 – Difference between a fretting contact (left) and a reciprocating sliding contact (right). Adapted from [39] .....	27
Figure 2-13 – Fretting hysteresis loops from a plot of tangential force and fretting displacement amplitude [41], beneath the fretting regimes are the characteristic surface damage profiles [38]......	28
Figure 2-14 – Fretting regimes: a) characterisation of the fretting contact of a partial-slip regime in terms of tangential force ( $F_t$ ) and traction force ( $q_x$ ) [42].....	29
Figure 2-15 – Schematic representation of Mindlin’s hypothesis.....	30

Figure 2-16 – Fretting damage modes: a) wear and fatigue modes as a function of displacement, b) wear and fatigue modes as a function of load [38].	32
Figure 3-1 – Percentage of bearing combinations a) cemented b) uncemented [1].	34
Figure 3-2 – Evolution of modularity in THA.	35
Figure 3-3 – Increasing bearing sizes from left to right and decreasing taper sizes in the same direction [57].	37
Figure 3-4 – Fixation of both head–neck and neck–stem [62].	38
Figure 3-5 – Fretting corrosion at the head-neck interface: a) evidence of Ti-Cr-Mo interfacial layer [27] b) evidence of corrosion products on the trunnion surface [67].	41
Figure 3-6 – Fracture of the Ti6Al4V trunnion resulting from corrosion [74].	42
Figure 3-7 – Wear pattern commonly observed at the head-neck taper interface: Assymmetric and Axisymmetric [75].	43
Figure 3-8 – Neck components of bi-modular tapers a) distribution of stresses across the neck component at the head-neck and neck-stem interfaces [77] b) Corrosion at the neck-stem interface of a circular neck design [79].	44
Figure 3-9 – Fracture of the neck component at the neck-stem interface [81].	46
Figure 3-10 – Solid corrosion products in retrieval. The region ‘A’ is typically mixed metal-oxides and chlorides while the region ‘B’ is typically metal-phosphates [87].	47
Figure 3-11 – Subsurface transformation in the partial-slip region of a) CoCrMo and b) TMZF [98].	50
Figure 3-12 – Fretting tribometer instrumented with <i>in-situ</i> electrochemistry for the assessment of fretting corrosion [99].	51

Figure 3-13 – Fatigue assembly of the Morse taper interface instrumented with <i>in-situ</i> electrochemistry [101].	52
Figure 3-14 – Considerations of a tribocorrosion systems [137].	60
Figure 3-15 – A model of tribocorrosion system in a sliding contact	61
Figure 3-16 – Stack and Chi’s criteria of degradation mechanism in a tribocorrosion system [136].	62
Figure 4-1 – Schematic representation of a tribocorrosion current – time plot.	70
Figure 4-2 – Schematic diagram of the fretting tribometer	71
Figure 4-3 – Image of the fretting corrosion tribometer set-up	72
Figure 4-4 – Schematic diagram of fretting corrosion protocol under OCP conditions	75
Figure 4-5 – Schematic diagram of potentiostatic fretting corrosion protocol	77
Figure 4-6 – Taper assembly: a) Dimension of spigot and surface profile of the grooved taper, b) assembly and pull-off method, c) an example of the taper separation force.	79
Figure 4-7 – 3D representation of the fatigue set-up for assessing fretting corrosion of realistic taper geometry.	80
Figure 4-8 – Protocol for fatigue loading tests on realistic taper components.	82
Figure 4-9 – Schematic for determining wear volume	84
Figure 4-10 – Elastic contact stress pattern for a ball-on- flat contact [42]	86
Figure 4-11 – FIB SEM micrographs of TEM sample preparation stages (a) Pt deposited on area of interest (b) removal of material from either side of Pt deposit (c) removal of lamella from bulk material (d) attachment of lamella to TEM post (e) final thinning of sample to electron transparency	87

Figure 4-12 – Schematic diagram of atoms in planes separated by a space 'd' as incident X-ray of wavelength $\lambda$ diffracts at angle ' $\theta$ '.....	88
Figure 5-1 – Outline of analyses performed in chapter 5.....	92
Figure 5-2 – Crystalline structure of polished CoCrMo alloy .....	93
Figure 5-3 Crystalline structure of polished Ti6Al4V alloy .....	94
Figure 5-4 – TEM and SAED of polished CoCrMo: a) Bright-field micrograph. b) Dark-field micrograph c) SAED of nano-crystalline region 'A' d) SAED of single crystal 'B'.....	96
Figure 5-5 – TEM and SAED of Polished Ti6Al4V: a) Bright-field micrograph. b) Dark-field micrograph c) SAED of nano-crystalline region 'A' d) SAED of single crystal 'B'.....	97
Figure 5-6 – TEM–EDS map of polished CoCrMo showing Co, Cr, Mo, O.....	98
Figure 5-7 – TEM–EDS map of polished Ti6Al4V showing Ti, Al, V, O.....	98
Figure 5-8 – XPS Depth profile analysis of CoCrMo passive film.....	101
Figure 5-9 – Proportion of species in CoCrMo protective layer: a) O species, b) Cr species, c) Mo species.....	102
Figure 5-10 – XPS Depth profile analysis of Ti6Al4V passive film .....	103
Figure 5-11 – Proportion of species in Ti6Al4V protective layer: a) O species, b) Ti species, c) Al species, d) V species.....	104
Figure 5-12 – Nano-indentation hardness of CoCrMo and Ti6Al4V a) P vs. h plot for CoCrMo b) P vs. h plot for Ti6Al4V c) calculated hardness of CoCrMo and Ti6Al4V.....	106
Figure 5-13 – Schematic diagram of a three-layer surface structure of CoCrMo and Ti6Al4V. Surface contaminants are not included in the three layers. ....	108
Figure 6-1 – Outline of the fretting experiments and analyses performed in chapter 6. C and T represents CoCrMo and Ti6Al4V respectively. The letters that appear in red represent the samples analysed. ....	110

Figure 6-2 – Slip ratio of CoCrMo – CoCrMo and CoCrMo – Ti6Al4V under OCP conditions from $\pm 10$ to $\pm 150$ $\mu\text{m}$ displacement.....	111
Figure 6-3 – Fretting of CoCrMo – CoCrMo: a) Fretting loop b) Energy dissipated per unit cycle.....	113
Figure 6-4 – Fretting of CoCrMo – Ti6Al4V: a) Fretting loop b) Energy dissipated per unit cycle.....	114
Figure 6-5 – Open circuit potential of CoCrMo – CoCrMo: a) OCP plot for $\pm 10$ $\mu\text{m}$ , $\pm 25$ $\mu\text{m}$ , $\pm 50$ $\mu\text{m}$ and $\pm 150$ $\mu\text{m}$ . b) Max. cathodic shift of all displacements.....	116
Figure 6-6 – Open circuit potential of CoCrMo – Ti6Al4V: a) OCP plot for $\pm 10$ $\mu\text{m}$ , $\pm 25$ $\mu\text{m}$ , $\pm 50$ $\mu\text{m}$ and $\pm 150$ $\mu\text{m}$ . b) Max. cathodic shift of all displacements. ....	118
Figure 6-7 – Sum of ball and flat wear volume and redistributed volume for CoCrMo – CoCrMo fretting contact.....	119
Figure 6-8 – Sum of ball and flat wear volume and redistributed volume for CoCrMo – Ti6Al4V fretting contact.....	120
Figure 6-9 – Surface profilometry of CoCrMo ball and CoCrMo flat for all four displacements under OCP conditions: a) 3D surface profile, b) 2D cross-section of the vertical axis of the wear surface.....	122
Figure 6-10 – Surface profilometry of CoCrMo ball and Ti6Al4V flat for all four displacements under OCP conditions: a) 3D surface profile, b) 2D cross-section of the vertical axis of the wear surface .....	124
Figure 6-11 – Back scatter-SEM of CoCrMo flat from the CoCrMo – CoCrMo interface at $\pm 50$ $\mu\text{m}$ under OCP conditions. ....	126
Figure 6-12 – Back scatter-SEM of Ti6Al4V flat from the CoCrMo – Ti6Al4V interface at $\pm 50$ $\mu\text{m}$ under OCP conditions. ....	127
Figure 6-13 – SEM-EDS of CoCrMo flat at $\pm 50$ $\mu\text{m}$ from CoCrMo – CoCrMo interface under OCP conditions. The inset table outlines the composition of a specific third-body region. ....	129

Figure 6-14 – SEM-EDS of Ti6Al4V flat at $\pm 50 \mu\text{m}$ from CoCrMo – Ti6Al4V interface under OCP conditions.....	130
Figure 6-15 – XPS analysis of wear and corrosion product from the wear surface of CoCrMo – CoCrMo combination at $\pm 50 \mu\text{m}$ under OCP conditions.....	132
Figure 6-16 – XPS analysis of wear and corrosion product from the wear surface of CoCrMo – Ti6Al4V combination at $\pm 50 \mu\text{m}$ . Creviced region – Region ‘C’.....	135
Figure 6-17 – XPS analysis of wear and corrosion product from the wear surface of CoCrMo – Ti6Al4V combination at $\pm 50 \mu\text{m}$ under OCP conditions. Region of mechanically induced crack – region ‘D’.....	137
Figure 6-18 – TEM bright and dark field micrographs of CoCrMo flat from CoCrMo – CoCrMo interface at $\pm 10 \mu\text{m}$ (a & b), $\pm 25 \mu\text{m}$ (c & d), $\pm 50 \mu\text{m}$ (e & f), $\pm 150 \mu\text{m}$ (g & h).....	141
Figure 6-19 – TEM bright and dark field micrographs of Ti6Al4V flat component from CoCrMo – Ti6Al4V interface at $\pm 10 \mu\text{m}$ (a & b), $\pm 25 \mu\text{m}$ (c & d), $\pm 50 \mu\text{m}$ (e & f), $\pm 150 \mu\text{m}$ (g & h). ....	143
Figure 6-20 – TEM and SAED of CoCrMo – CoCrMo at $\pm 150 \mu\text{m}$ : a) Bright field TEM micrograph of CoCrMo subsurface b) Close-up image of tribochemical products on surface c) SAED of structure 1 d) SAED of structure 2 e) SAED of CoCrMo bulk.....	145
Figure 6-21 – TEM-EDS map of CoCrMo – CoCrMo flat surface at $\pm 150 \mu\text{m}$ .....	146
Figure 6-22 – TEM and EDS analysis of the transferred third-body at the interface of CoCrMo – CoCrMo, $\pm 150 \mu\text{m}$ .....	148
Figure 6-23 – TEM and SAED of mechanically mixed layers on Ti6Al4V alloy: a) TEM micrograph of Ti6Al4V subsurface b) high-resolution micrographs of the subsurface structures c) SAED of the mechanically mixed layer d) SAED of mechanically mixed Ti6Al4V structures e) SEAD of Ti6Al4V nano-crystalline structure. ....	150

Figure 6-24 – TEM-EDS map of the mechanically mixed layer and transformed Ti6Al4V alloy from CoCrMo – Ti6Al4V interface.....	151
Figure 6-25 – TEM and SAED of Ti6Al4V surface (mechanically cracked region): a) TEM micrograph of Ti6Al4V subsurface b) high resolution image of the region in red dotted square c) SAED of the nano-crystalline mesh d) SAED of a single large particle.....	153
Figure 6-26 – TEM-EDS map of the Ti6Al4V flat at the mechanically induced crack region of the CoCrMo – Ti6Al4V interface.....	154
Figure 6-27 – TEM and SAED of CoCrMo ball surface: a) Dark field TEM micrograph of CoCrMo subsurface b) Bright field image c) SAED of the transferred material d) SAED of near-surface CoCrMo bulk. ....	156
Figure 6-28 – TEM-EDS analysis of the CoCrMo ball surface from the CoCrMo – Ti6Al4V interface.....	156
Figure 6-29 – Nano-indentation of layer formed at the CoCrMo – Ti6Al4V interface: a) image of the indented cross-section b) P vs. h graph of indentations c) average hardness of the layer.....	157
Figure 6-30 – Comparing Max. cathodic shift of the two metal – metal material combinations. ....	159
Figure 6-31 – Schematic diagram of fretting corrosion products and SEM micrographs of CoCrMo and Ti6Al4V from the CoCrMo – Ti6Al4V interface at $\pm 50 \mu\text{m}$ displacement.....	164
Figure 7-1 – Outline of the fretting experiments and analyses performed in chapter 7 for $\text{Si}_3\text{N}_4$ ceramic. C and T represents CoCrMo and Ti6Al4V respectively. The letters that appear in red represent the samples analysed. The green ticks represent the analysis performed on self-mated $\text{Si}_3\text{N}_4$ .....	166
Figure 7-2 – Outline of the fretting experiments and analyses performed in chapter 7 for Biolox ceramic. ....	167
Figure 7-3 – Slip ratio of $\text{Si}_3\text{N}_4$ – CoCrMo, $\text{Si}_3\text{N}_4$ – Ti6Al4V and $\text{Si}_3\text{N}_4$ – $\text{Si}_3\text{N}_4$ under OCP conditions for $\pm 10$ , $\pm 25$ $\pm 50 \mu\text{m}$ displacements. ...	168



Figure 7-4 – Fretting contact analysis for Si <sub>3</sub> N <sub>4</sub> – CoCrMo: a) Fretting loop b) Energy dissipated per cycle. ....	169
Figure 7-5 – Fretting contact analysis for Si <sub>3</sub> N <sub>4</sub> – Ti6Al4V: a) Fretting loop b) Energy dissipated per cycle. ....	171
Figure 7-6 – Fretting contact analysis for Si <sub>3</sub> N <sub>4</sub> – Si <sub>3</sub> N <sub>4</sub> : a) Fretting loop b) Energy dissipated per cycle. ....	173
Figure 7-7 – Open circuit potential of Si <sub>3</sub> N <sub>4</sub> – CoCrMo: a) OCP plot for ±10 µm, ±25 µm, ±50 µm. b) Max. cathodic shift for all displacements. ....	175
Figure 7-8 – Open circuit potential of Si <sub>3</sub> N <sub>4</sub> – Ti6Al4V: a) OCP plot for ±10 µm, ±25 µm, ±50 µm. b) Max. cathodic shift for all displacements. ....	176
Figure 7-9 – Wear and redistributed volume from the Si <sub>3</sub> N <sub>4</sub> – CoCrMo fretting contact. A summation of both ball and flat components. ....	177
Figure 7-10 – Wear and redistributed volume from the Si <sub>3</sub> N <sub>4</sub> – Ti6Al4V fretting contact. A summation of both ball and flat components. ....	178
Figure 7-11 – Wear and redistributed volume from the Si <sub>3</sub> N <sub>4</sub> – Si <sub>3</sub> N <sub>4</sub> fretting contact. A summation of both ball and flat components. ....	178
Figure 7-12 – Surface profilometry of Si <sub>3</sub> N <sub>4</sub> ball and CoCrMo flat surfaces: a) 3D surface profile of all displacements, b) 2D cross-section of the vertical axis of the wear surface. ....	181
Figure 7-13 – Surface profilometry of Si <sub>3</sub> N <sub>4</sub> ball and Ti6Al4V flat surfaces: a) 3D surface profile of all displacements, b) 2D cross-section of the vertical axis of the wear surface. ....	183
Figure 7-14 – Surface profilometry of Si <sub>3</sub> N <sub>4</sub> ball and Si <sub>3</sub> N <sub>4</sub> flat surfaces: a) 3D surface profile of all displacements, b) 2D cross-section of the vertical axis of the wear surface. ....	185
Figure 7-15 – Back scatter-SEM micrograph of CoCrMo flat from the fretting against Si <sub>3</sub> N <sub>4</sub> ball at ±50 µm. ....	186

Figure 7-16 – Back scatter-SEM micrograph of Ti6Al4V flat fretted against Si <sub>3</sub> N <sub>4</sub> ball at ±50 μm. ....	187
Figure 7-17 – SEM-EDS of CoCrMo flat fretted against Si <sub>3</sub> N <sub>4</sub> ball at ±50 μm. ....	188
Figure 7-18 – SEM-EDS of Ti6Al4V flat fretted against Si <sub>3</sub> N <sub>4</sub> ball at ±50 μm. ....	189
Figure 7-19 – XPS analysis of wear and corrosion product from the wear surface of Si <sub>3</sub> N <sub>4</sub> – CoCrMo combination at ±50 μm. Si&O-rich third-body product on CoCrMo. ....	191
Figure 7-20 – XPS analysis of wear and corrosion product from the wear surface of Si <sub>3</sub> N <sub>4</sub> – Ti6Al4V combination at ±50 μm. Mechanically mixed layer on Ti6Al4V – Region ‘C’ .....	193
Figure 7-21 – XPS analysis of wear and corrosion product from the wear surface of Si <sub>3</sub> N <sub>4</sub> – Ti6Al4V combination at ±50 μm. Ti6Al4V surface which was once covered by the mechanically mixed layer – Region ‘D’ .....	195
Figure 7-22 – TEM and SAED of CoCrMo from the Si <sub>3</sub> N <sub>4</sub> – CoCrMo combination: a) TEM micrograph of CoCrMo subsurface b) high resolution image of the uppermost subsurface c) SAED of Si and O-rich material d) SAED of CoCrMo single-crystal.....	197
Figure 7-23 – TEM-EDS map of the CoCrMo subsurface from the Si <sub>3</sub> N <sub>4</sub> – CoCrMo material combination. Above the white-line are deposited Pt and empty space. ....	198
Figure 7-24 – TEM and SAED of Ti6Al4V from the Si <sub>3</sub> N <sub>4</sub> – Ti6Al4V combination (region of mechanically mixed layer): a) TEM micrograph of the Ti6Al4V subsurface b) high resolution image of the mechanically mixed layer c) high resolution image of the transformed amorphous Ti6Al4V structure d) SAED of the mechanically mixed layer e) SAED of the suspending large particle f) SAED of fractured region. ....	200

Figure 7-25 – TEM-EDS map of the Ti6Al4V subsurface from the Si <sub>3</sub> N <sub>4</sub> – Ti6Al4V material combination – region of mechanically mixed layer. ....	201
Figure 7-26 – TEM and SAED of Ti6Al4V from the Si <sub>3</sub> N <sub>4</sub> – Ti6Al4V combination (region absent of mechanically mixed layer): a) TEM micrograph of CoCrMo subsurface b) high resolution image of the nano-crystalline region c) SAED of the uppermost region d) SAED of the totally transformed region e) SAED of nano-crystalline area...	203
Figure 7-27 – TEM-EDS map of the Ti6Al4V subsurface from the Si <sub>3</sub> N <sub>4</sub> – Ti6Al4V material combination – region absent of mechanically mixed layer.....	204
Figure 7-28 – Nano-indentation of layer formed at the CoCrMo – Ti6Al4V interface: a) P vs. h graph of indentations b) average hardness of the layer. ....	205
Figure 7-29 – Fretting of Biolox – CoCrMo material combination at ±50 µm, P <sub>max</sub> = 1 GPa: a) 2D fretting loop b) Energy dissipated per cycle c) OCP measurement. ....	207
Figure 7-30 – 3D and 2D surface profilometry of Biolox – CoCrMo at ±50 µm displacement.....	208
Figure 7-31 – SEM-EDS map of Biolox – CoCrMo flat surface at ±50 µm a) BS-SEM micrograph b) SEM – EDS .....	209
Figure 7-32 – Fretting of Biolox – Ti6Al4V material combination at ±50 µm (P <sub>max</sub> = 1 GPa): a) 2D fretting loop b) Energy dissipated per cycle c) OCP measurement. ....	211
Figure 7-33 – 3D and 2D surface profilometry of Biolox – Ti6Al4V at ±50 µm displacement (P <sub>max</sub> = 1 GPa). ....	212
Figure 7-34 – SEM-EDS map of Biolox – Ti6Al4V flat surface at ±50 µm (1 GPa) a) BS-SEM micrograph b) SEM – EDS.....	214
Figure 7-35 – Fretting of Biolox – Ti6Al4V material combination at ±50 µm (0.77 GPa): a) 2D fretting loop b) Energy dissipated per cycle c) OCP measurement. ....	215

Figure 7-36 – 3D and 2D surface profilometry of BioloX – Ti6Al4V at $\pm 50$ $\mu\text{m}$ displacement ( $P_{\text{max}} = 0.77$ GPa). .....	216
Figure 7-37 – SEM-EDS map of BioloX – Ti6Al4V flat surface at $\pm 50$ $\mu\text{m}$ ( $0.77$ GPa) a) BS-SEM micrograph b) SEM – EDS.....	218
Figure 7-38 – Comparing Max. cathodic shift in ceramic – metal combinations.....	223
Figure 8-1 – Outline of the fretting experiments performed in chapter 8 ...	225
Figure 8-2 – Slip ratio of CoCrMo – CoCrMo under potentiostatic conditions for $\pm 10$ – $\pm 150$ $\mu\text{m}$ in ‘Methods 1 – 3’. .....	226
Figure 8-3 – Anodic current transient of loaded CoCrMo – CoCrMo contact subjected to $0\text{V}$ vs. Ag/AgCl of potentiostatic polarisation for 4000 seconds in static conditions. ....	227
Figure 8-4 – Method 1: fretting loop analysis of CoCrMo – CoCrMo at $\pm 10$ $\mu\text{m}$ , $\pm 25$ $\mu\text{m}$ , $\pm 50$ $\mu\text{m}$ , $\pm 150$ $\mu\text{m}$ displacement in potentiostatic conditions. a) Fretting loop b) Energy dissipated per cycle. ....	228
Figure 8-5 – Method 1: fretting current from CoCrMo – CoCrMo contact at $\pm 10$ $\mu\text{m}$ , $\pm 25$ $\mu\text{m}$ , $50$ $\mu\text{m}$ , $\pm 150$ $\mu\text{m}$ displacement, a) Fretting current transient b) Cumulative charge .....	230
Figure 8-6 – Method 1: 3D surface profilometry of CoCrMo ball and flat fretting interface assessed under potentiostatic conditions.....	231
Figure 8-7 – Method 1: the sum of tribocorrosion mass loss from ball and flat components; a) Wear volume (blue) and Re-distributed volume (orange); b) Mass loss as a proportion of $M_{\text{mech}}$ and $M_{\text{chem}}$ , c) Total mass loss vs. Cumulative energy.....	233
Figure 8-8 – Method 2: fretting loop analysis of CoCrMo – CoCrMo at $\pm 10$ $\mu\text{m}$ , $\pm 25$ $\mu\text{m}$ , $\pm 50$ $\mu\text{m}$ , $\pm 150$ $\mu\text{m}$ displacement in potentiostatic conditions. a) Fretting loop b) Energy dissipated per cycle. ....	235
Figure 8-9 – Method 2: fretting current from CoCrMo – CoCrMo contact at $\pm 10$ $\mu\text{m}$ , $\pm 25$ $\mu\text{m}$ , $50$ $\mu\text{m}$ , $\pm 150$ $\mu\text{m}$ displacement; a) Fretting current transient b) Cumulative charge .....	237

Figure 8-10 – Method 2: 3D surface profilometry of CoCrMo ball and flat fretting contacts tested in potentio-static conditions.....	238
Figure 8-11 – Method 2: tribocorrosion mass loss; a) Wear volume; b) Mass loss as a proportion of $M_{\text{mech}}$ and $M_{\text{chem}}$ .....	238
Figure 8-12 – Method 3: fretting loop analysis of CoCrMo – CoCrMo at $\pm 150 \mu\text{m}$ , $\pm 50 \mu\text{m}$ , $\pm 25 \mu\text{m}$ , $\pm 10 \mu\text{m}$ displacement in potentio-static conditions. a) Fretting loop b) Energy dissipated per cycle. ....	240
Figure 8-13 – Method 3: fretting current from CoCrMo – CoCrMo contact at $\pm 150 \mu\text{m}$ , $\pm 50 \mu\text{m}$ , $\pm 25 \mu\text{m}$ , $\pm 10 \mu\text{m}$ displacement, a) Fretting current transient b) Cumulative charge .....	241
Figure 8-14 – Method 3: 3D surface profilometry of CoCrMo ball and flat fretting contacts tested in potentio-static conditions.....	242
Figure 8-15 – Method 3: tribocorrosion mass loss; a) Wear volume; b) Mass loss as a proportion of $M_{\text{mech}}$ and $M_{\text{chem}}$ .....	243
Figure 8-16 – The sum of $M_{\text{mech}}$ and $M_{\text{chem}}$ for all displacements in the three methods of assessment. The $M_{\text{chem}}/M_{\text{mech}}$ ratio for each method is also shown above.....	247
Figure 9-1 – Outline of the fatigue experiments and analyses performed in chapter 9. B, C and T represents BioloX, CoCrMo and Ti6Al4V respectively. ....	249
Figure 9-2 – Fretting current vs. time plot for a complete fatigue loading test. ....	252
Figure 9-3 – OCP of all combinations prior to potentio-static polarisation of 0V vs. Ag/AgCl, a) OCP vs. Time plot b) average OCP and applied over-potential.....	254
Figure 9-4 – Anodic current transient of all material combinations under static conditions: a) CoCrMo – CoCrMo; b) CoCrMo – Ti6Al4V; c) BioloX – CoCrMo; d) BioloX – Ti6Al4V; e) average current at the time $t = 7500 \text{ Sec}$ and f) current at the time $t = 0 \text{ Sec}$ ( $I_{\text{max}}$ ). ....	256

Figure 9-5 – Fretting current (a, b, c, d) and Cumulative charge per 10000 cycles (e, f, g, h) of the material combinations; these were subjected to  $\pm 1.5$  kN cyclic load and mean load of 1.8 kN with varied frequencies of 1, 2 and 5 Hz. .... 258

Figure 9-6 – Fretting current (a, b, c, d) and Cumulative charge (e, f, g, h) of the material combinations; these were subjected to a cyclic load of  $\pm 0.5$  kN at 1 Hz with varied mean load of 0.8, 1.8 and 2.8 kN..... 259

Figure 9-7 – Fretting current (a, b, c, d) and Cumulative charge (e, f, g, h) of the material combinations; these were subjected to mean load of 2.8 kN at 1 Hz with varied cyclic load of  $\pm 0.5$ ,  $\pm 1.5$  and  $\pm 2.5$  kN. .. 261

Figure 9-8 – Fretting current (a, b, c, d) and Cumulative charge (e, f, g, h) of the material combinations; these were subjected to cyclic load of  $\pm 1.5$  kN and mean load of 1.8 kN for 5000 seconds at 1 Hz. .... 263

Figure 9-9 – Cross-head displacement vs. Time graph. Each data point for all material combinations during the dynamic stages represents a point every 1000 seconds of the cross-head position. At the top right corner, a schematic of the cross-head displacement is shown. .... 265

Figure 9-10 – Taper separation force for all material combinations..... 266

Figure 9-11 – 3D reconstruction of CoCrMo – CoCrMo taper interface:  
a) CoCrMo female taper, b) CoCrMo male taper. .... 267

Figure 9-12 – 3D reconstruction of CoCrMo – Ti6Al4V taper interface: a) CoCrMo female taper, b) Ti6Al4V male taper. .... 268

Figure 9-13 – 3D reconstruction of BioloX – CoCrMo taper interface: a) BioloX female taper, b) Image of the BioloX female taper, c) *Full* 3D reconstruction of CoCrMo male taper d) *Customised* reconstruction of CoCrMo male taper..... 269

Figure 9-14 – 3D reconstruction of Biolox – Ti6Al4V taper: a) Biolox female taper, b) Image of the Biolox taper c) <i>Full</i> 3D reconstruction of Ti6Al4V male taper, d) <i>Customised</i> reconstruction of Ti6Al4V male taper. ....	270
Figure 9-15 – Fretting currents of Biolox – Ti6Al4V three repeats, a) frequency variation, b) mean load variation c) cyclic load variation...	272
Figure 9-16 – 3D reconstruction of Biolox – Ti6Al4V taper – the case of misalignment: a) BIOLOX female taper, b) Ti6Al4V male taper. ....	272
Figure 10-1 – Fretting loop of gross slip regime; a) labelled fretting loop b) de-convoluted fretting loop – displacement (solid-line) and tangential force (dashed-line).....	278
Figure 10-2 – Non-symmetrical fretting contact a) CoCrMo – CoCrMo $\pm 50 \mu\text{m}$ fretting loop b) ball and flat wear surface.....	279
Figure 10-3 – Third-body grooving a) CoCrMo – CoCrMo, $\pm 150 \mu\text{m}$ fretting loop b) ball and flat wear surface .....	280
Figure 10-4 – Influence of third-body a) $\text{Si}_3\text{N}_4$ – CoCrMo, $\pm 50 \mu\text{m}$ fretting loop b) BIOLOX – Ti6Al4V, $\pm 50 \mu\text{m}$ fretting loop c) $\text{Si}_3\text{N}_4$ – CoCrMo ball and flat wear surface d) BIOLOX – Ti6Al4V ball and flat wear surface. ....	282
Figure 10-5 – The plunging effect (prior to fracture of cold-welded interface): a) CoCrMo – Ti6Al4V, $\pm 50 \mu\text{m}$ fretting loop, b) schematics of the plunging effect [221]. ....	283
Figure 10-6 – Slip within localised fretting grooves (after the fracture of cold-welded interface): a) CoCrMo – Ti6Al4V, $\pm 50 \mu\text{m}$ fretting loop, b) 3D surface of the ruptured welded interface. ....	284
Figure 10-7 – Mechanism of cold-welding at the CoCrMo – Ti6Al4V interface .....	288
Figure 10-8 – Mechanism of pseudo-amorphous structure of CoCrMo and amorphisation of Ti6Al4V alloys. ....	289
Figure 10-9 – Mechanism of stiction at the $\text{Si}_3\text{N}_4$ – Ti6Al4V interface .....	292

Figure 10-10 – Schematic diagram of different fretting corrosion products at specific regions within the composite contact of self-mated CoCrMo, $\pm 50 \mu\text{m}$ .....	294
Figures 11-1 – Composition of FBS [231] .....	334
Figures 11-2 – Composition of PBS .....	335
Figures 11-3 – Quasi-stick fretting loop of (a) CoCrMo – CoCrMo and (b) CoCrMo – Ti6Al4V tribo-couples.....	337



## List of Tables

Table 2-1 – Chemical composition (in wt%) and recommendation of mechanical properties for wrought CoCrMo alloys according to the American Society for Testing and Materials (ASTM).....	7
Table 2-2 – Chemical composition (in wt%) and recommendation of mechanical properties for unalloyed Titanium and Extra Low Interstitial (ELI) Ti6Al4V alloy according to the ASTM.....	9
Table 2-3 – Chemical composition (in wt%) and recommendation of mechanical properties for 316L stainless steel according to ASTM. .....	10
Table 3-1 – Criteria for corrosion and fretting scores [67] .....	39
Table 4-1 Fretting contact parameters .....	74
Table 5-1 – TEM – EDS chemical composition of CoCrMo.....	99
Table 5-2 – TEM – EDS chemical composition of Ti6Al4V.....	99
Table 6-1 – Attribution of Cr and O species from CoCrMo – CoCrMo interface at $\pm 50 \mu\text{m}$ .....	133
Table 6-2 – Attribution of Cr, Co and O species from CoCrMo – Ti6Al4V interface at $\pm 50 \mu\text{m}$ . Creviced region – Region ‘C’ .....	135
Table 6-3 – Attribution of Ti and O species from CoCrMo – Ti6Al4V interface at $\pm 50 \mu\text{m}$ . Region of mechanically induced crack – region ‘D’ .....	138
Table 7-1 – Attribution of Si, N and O species from $\text{Si}_3\text{N}_4$ – CoCrMo at $\pm 50 \mu\text{m}$ . Si&O-rich third-body product on CoCrMo.....	191
Table 7-2 – Attribution of Si, Ti, Al, N and O species from $\text{Si}_3\text{N}_4$ – Ti6Al4V at $\pm 50 \mu\text{m}$ . Mechanically mixed layer on Ti6Al4V – Region ‘C’ .....	194
Table 8-1 – Breakdown of static current, Faradaic mass loss for both the entire surface sample surface and the fretting surface.....	234
Table 10-1 – Electrode potentials of Si, Cr, Ti and Al vs. SHE [2, 21, 230]. The electrons transferred in the half-cell reaction are omitted from the left column for illustrative purposes. ....	297

## Nomenclature

Terms	Definition	Units
$\alpha C_w$ and $\beta C_w$	Unknown proportions of corrosion enhanced wear	C
<b>a</b>	Hertzian contact width	$\mu\text{m}$
$\alpha$	Head – Neck angle	°
<b>A</b>	Sliding – Displacement ratio	
$\beta$	Adduction angle	°
<b>C</b>	Pure corrosion	C
$\delta_s$	Interfacial slip	$\mu\text{m}$
$\delta_x$	Displacement amplitude	$\mu\text{m}$
$\delta_e$	Elastic displacement	$\mu\text{m}$
<b>e</b>	Fretting/reciprocating criteria	
$E_{pp}$	Passivating potential	V
$\epsilon\text{-Co}$	HCP Co phase	
$\gamma\text{-Co}$	FCC Co phase	
<b>F</b>	Faraday	$\text{CMol}^{-1}$
$F_t/F_x$	Tangential force	N
<b>h</b>	depth	nm
$I_a$	Anodic current	Amps
$I_c$	Cathodic current	Amps
$I_{pass}$	Passivating current	Amps
$I_{base}$	Baseline current	Amps
$I_{peak}$	Peak current	Amps
$I_{crit}$	Critical current	Amps
$I_{max}$	Maximum current	Amps
<b>M</b>	Molar mass	$\text{gmol}^{-1}$
$M_{total}$	Total mass loss	$\mu\text{g}$
$M_{chem}$	Chemical mass loss	$\mu\text{g}$
$M_{mech}$	Mechanical mass loss	$\mu\text{g}$
<b>n</b>	Number of electrons	
<b>P</b>	load	N
$P_{max}$	Maximum contact pressure	GPa
$q_x$	Traction	N
<b>Q</b>	Charge	C
$R_a$	Roughness profile	$\text{nm}/\mu\text{m}$
$R_p$	Profile peak	$\text{nm}/\mu\text{m}$
$R_v$	Profile valley	$\text{nm}/\mu\text{m}$
$R_z$	Average maximum height	$\text{nm}/\mu\text{m}$
<b>t</b>	time	s
<b>At%</b>	Atomic percent	
<b>Wt%</b>	Weight percent	

## Chapter 1 Introduction

Total hip arthroplasty (THA) is known to be one of the most successful surgical interventions of the 21<sup>st</sup> century. In most cases, the prosthetic device has restored function to the elderly and young by alleviating pain and discomfort brought about by arthritis and other diseases. Across a time period of 12 years, there has been over 800 000 primary hip operations performed in the UK alone; and this is expected to increase on a yearly basis due to an aging population [1].

The hip prosthesis has undergone several stages of evolution since the 1950s; one of which is the incorporation of modularity. The feature comes with tremendous advantages to both patients and surgeons as it offers a broad range of design and material options. For example, a broader range of head and taper sizes, neck extensions, several material combinations can be all explored. A number of these benefits contribute to ensuring the patient's specific anatomy can be matched as closely as possible thus achieving the satisfaction of both patient and surgeon.

On the flip side of this intervention, the consequence of introducing modularity is realised. It is widely known amongst 'tribologists' and surface engineers that with every additional interface introduced into a tribological system, the risk of wear and corrosion is largely increased. This is specifically the case in hip prosthesis; micromotions (fretting) at the modular taper interface, in the physiological media of the human body result in wear and corrosion of the implant *in-vivo*. This has been the nemesis of modularity in THA since its inception in the 1970s. Of over 77,000 records of revision procedures held by the National Joint Registry (NJR), over 15% were due to implant wear, fracture and adverse local tissue reactions (ALTR). Therefore, it is of utmost importance to understand the *in-vivo* degradation mechanisms that leads to wear particles and ion release [1].

So far, it is known that corrosion, wear and the synergistic interaction of both are the overarching degradation mechanisms leading to the failure of these implants. Therefore, the motive of this research is to better understand the various damage modes and the mechanisms manifested at the interface of metallic and ceramic biomaterials used in modular hip prosthesis. This research was therefore conducted within the remits of fretting corrosion of the modular taper interface.

## **1.1 Research objectives**

The aim of this research is to develop a better understanding of the mechanisms involved at the fretting interfaces of metal – metal and ceramic – metal systems. This covers a wide scope of experimental and analytical techniques such as: assessment of tribological parameters such as interfacial energy and wear; monitoring of electrochemical activities during *in-situ* tribocorrosion; surface topography; assessment of subsurface metallurgical transformations; and characterisation of tribochemical products. The objectives of this study are as follows:

### **1. Characterisation of CoCrMo and Ti6Al4V alloys (Chapter 5)**

- Employ the use of spectroscopy techniques to characterise passive films on both alloys.
- Utilise advance microscopy techniques to characterise metallurgical structures of a polished sample
- Perform nano-indentation hardness on a polished sample

### **2. Assessment of fretting corrosion in metal – metal and ceramic – metal systems (Tribometer based study – Chapters 6 and 7)**

- Assess various material combinations for varied displacement amplitudes
- Determine the wear volume and conduct surface profilometry
- Utilise advance microscopy and spectroscopy techniques to characterise emanating fretting corrosion products and the resultant metallurgical transformations

**3. Investigate the effect of surface history due to wear and oxidation on the evolution of fretting corrosion current and the tribocorrosion degradation mechanism (Tribometer based study – Chapter 8)**

- Conduct fretting tribometer study under potentiostatic conditions; modify surface history by imposing fretting displacement amplitudes in series (both increasing and decreasing order).

**4. Assessment of metal – metal and ceramic – metal systems using realistic taper geometry (Chapter 9)**

- Conduct fatigue loading experiments of the material combinations under various loading conditions and with *in-situ* corrosion measurements.

## **1.2 Thesis outline**

- Chapter Two: Relevant background and fundamental theories related to this research
- Chapter Three: Literature review of implant retrieval studies, *in-vitro* studies and tribocorrosion
- Chapter Four: Experimental methodology and analytical techniques
- Chapter Five: Results obtain from material characterisation of CoCrMo and Ti6Al4V alloys
- Chapter Six: Fretting corrosion assessment of metal – metal systems (Tribometer based study)

- Chapter Seven: Fretting corrosion assessment of ceramic – metal systems (Tribometer based study)
- Chapter Eight: Quantification of fretting corrosion current using self-mated CoCrMo systems (Tribometer based study)
- Chapter Nine: Comparison of fretting corrosion current from metal – metal and ceramic – metal systems (Realistic components study)
- Chapter Ten: An overall discussion of all five result chapters
- Chapter Eleven: Main conclusions and recommendation for future work

It is worth the mention that each of the result chapters end with a brief 'Discussion and summary' section. This allows the reader to appreciate the findings of each chapter distinctively due to most of the result chapters being quite extensive. Subsequently, the 'Overall discussion' chapter (Chapter 10) is where the overarching themes and mechanisms observed across the whole thesis are discussed in detail.

## **Chapter 2 Background to biomaterials, corrosion and tribology**

### **2.1 Introduction**

In this chapter, the background to metallic and ceramic biomaterials used in THA are explored. And also, the fundamental sciences of tribology, fretting and electrochemistry of corrosion are reviewed.

### **2.2 Metallic biomaterials**

Metallic alloys such as Cobalt (Co) based, Titanium (Ti) based and Iron (Fe) based alloys are commonly used as biomaterials in biomedical applications. This is due to their desirable mechanical properties, corrosion resistance and biocompatibility [2]. The main metallic content are generally alloyed with various other elements such as: Chromium (Cr), Nickel (Ni), Tantalum (Ta), Niobium (Nb), Molybdenum (Mo) and Tungsten (W). Each of these alloying elements play a key role in the optimisation of the material in order to achieve the required properties specific to the material's application[3].

#### **2.2.1 Cobalt-based alloys**

Co-based alloys have been used in the medical industry since the 1940s [4]. They fall into two basic categories namely: that castable Cobalt-Chrome-Molybdenum (CoCrMo) alloy and the wrought Co-based alloy composed mainly of Co, Cr, Ni, W and Mo. The castable and wrought CoCrMo alloys are known to have subtle differences in their mechanical properties, however, both are commonly used as a bearing component in hip prosthesis due to their high abrasion resistant property [5].

CoCrMo alloys forms a solid solution of up to 60% Co which materializes into a Co-rich matrix of Face Centred Cubic (FCC) structure that is stable at room temperature. Its high stiffness arises from the precipitation of carbides at the grain boundaries and can be modified by altering the concentration of the

carbon content. The approved wrought CoCrMo alloy for prosthetic implant applications are commercially available as wrought low carbon CoCrMo (ASTM F 1537 – 08 type 1) and high carbon CoCrMo (ASTM F 1537 – 08 type 2). The former contains less than 0.14 wt% carbon max. and the latter, 0.15 – 0.35 wt% max. [6]. Their full chemical composition and mechanical properties are outlined in Table 2-1. Furthermore, due to the low stacking fault energy of CoCrMo alloys, the FCC structure is susceptible to a strain-induced transformation to a Hexagonal Close Packed (HCP) structure. This is also evidenced by subsurface twinning through which the alloy work-hardens [6].

The role of Cr and Mo in the alloy is mainly for surface passivation. In this process, surface oxides are formed spontaneously on the surface of the alloy thus protecting it from corrosion – hence the corrosion resistant property of CoCrMo alloys. It is also known that the inclusion of Mo aids the formation of finer grains in the alloy matrix, thus further improves the strength of the alloy [3]. More recently, the bio-compatibility of CoCr alloys are in question due to the possible release of Cr (VI) (a supposedly carcinogenic specie) which forms bio-complex molecules in the physiological media of the human body [7, 8].



**Table 2-1 – Chemical composition (in wt%) and recommendation of mechanical properties for wrought CoCrMo alloys according to the American Society for Testing and Materials (ASTM)**

Wrought CoCrMo	Specification	Co	Cr	Mo	Si	Fe	Ni	Mn	C	N
Low Carbon	F1537 – 08	Bal.	26.0	5.0	1.0	0.75	1.0	1.0	0.14	0.25
			30.0	7.0	max	max	max	max	max	max
High Carbon	F1537 – 08	Bal.	26.0	5.0	1.0	0.75	1.0	1.0	0.15	0.25
			30.0	7.0	max	max	max	max	0.35	max

Wrought CoCrMo	Ultimate tensile strength (MPa)	Yield strength (MPa)	% Elongation (per min)	Hardness (HRC)
Low Carbon	897 – 1172	517 – 827	12 – 20	25 – 30
High Carbon	897 – 1172	517 – 827	12 – 20	25 – 30

## 2.2.2 Titanium and titanium-based alloys

Commercially pure titanium (CP Ti) and extra low interstitial Titanium-Aluminium-Vanadium (ELI – Ti6Al4V) are the two most common Ti-based biomaterials used for biomedical applications. They are known to be highly biocompatible and do not promote adverse reactions (within considerable volume of wear) in the human body. This is due to a ~10 nm thick TiO<sub>2</sub> surface oxide film which spontaneously formed on both surfaces [3, 9]. CP Ti is very light with a density of 4.5 g/cm<sup>3</sup> and it is regarded as pure within the range 98.9 – 99.6 wt% Ti. The remainder of the wt% are interstitial elements such as O, C and N. Nitrogen specifically, is known to have a greater influence on Ti as it has double the hardening effect (per atom) than C or O. Table 2-2 shows the elemental constituents of both unalloyed and alloyed Ti as well as specific mechanical properties.

Regarding phases and structure, Ti has a HCP  $\alpha$ -phase structure below 882°C and a  $\beta$ -phase structure above this temperature. In Titanium-Aluminium-Vanadium (Ti6Al4V) alloy, the Al plays the role of stabilizing the  $\alpha$ -phase which forms an HCP structure by heightening the temperature required for the transformation from  $\alpha$  to  $\beta$  phase. On the other hand, the V is included to stabilize the  $\beta$ -phase which has a Body Centred Cubic (BCC) structure by lowering the temperature required for the same transformation thus forming a two-phase system [9]. The  $\alpha$ -phase has excellent strength characteristics and is capable of producing localised strain field that can absorb deformation energy. CP Ti and Ti6Al4V have a relatively low stiffness of 110 GPa compared to CoCrMo (240 GPa). A lower stiffness is desirable for a 'cementless' hip prosthetic procedure in order to reduce the effect of stress shielding. An even lower modulus (80 GPa) alloy called Titanium-12Molybdenum-6Zirconium-2Iron (TMZF), also known as the beta-Titanium was developed to further improve osteo-integration at the Ti-Bone interface [10]. On a less desirable note, Ti alloys are known to having poor shear strength and hence low wear resistance relative to CoCrMo alloy. Therefore, Ti alloys are typically not suitable for bearing applications in hip prosthesis [3, 9].

**Table 2-2 – Chemical composition (in wt%) and recommendation of mechanical properties for unalloyed Titanium and Extra Low Interstitial (ELI) Ti6Al4V alloy according to the ASTM**

Titanium	Specification	Ti	Al	V	Fe	Ni	C	N	O	H
Unalloyed	F67 – 06	Bal.	-	-	0.5 max	0.05 max	0.08 Max	-	0.4 max	0.015 max
ELI Ti6Al4V	F136 – 08	Bal.	5.5 6.5	3.5 4.5	0.25 max	-	0.08 max	0.05 max	0.13 max	0.012 max

Titanium	Ultimate tensile strength (MPa)	Yield strength (MPa)	% Elongation (per min)	Hardness (HRC)
Unalloyed	500	483	15	-
ELI Ti6Al4V	825 – 860	760 – 795	8 – 10	-

### 2.2.3 Stainless steel

Type 302 was the first stainless steel to be fabricated for medical implants. Shortly after, a relatively small amount of Mo (2 – 4 wt%) was introduced into the matrix to further improve its corrosion resistance for *in-vivo* biomedical applications. Thus the type 302 became the common type: 316 stainless steel. The inclusion of Mo specifically plays the role of enhancing resistance to pitting corrosion in salt water. The type 316 was later modified in the 1950s and became known as 316L when the carbon content was reduced from 0.08 wt% to a maximum of 0.03 wt%. The aim of this was to minimize the effect of sensitization whereby specific alloying elements such as Cr is preferentially precipitated from the bulk to the grain boundary as Metal Carbide. Ni is also largely present in both commercial 316 and 316L alloys with a content range of 12 – 14 wt%; its role in the alloy is mainly to stabilize the FCC phase at room temperature.

As for Cr content, the minimum composition of Cr to effectively impart corrosion resistance through passivation in these alloys is said to be 11 wt%

however as its wt% composition also affects the stability of the FCC austenitic phase, the ASTM F138 prescription falls between 17 – 19 wt% as outlined in Table 2-3. On the negative side, 316L alloy is known to be susceptible to crevice corrosion in the harsh crevice environment of the human body where limited access to oxygen inhibits its ability to adequately restore its protective surface oxides [3].

**Table 2-3 – Chemical composition (in wt%) and recommendation of mechanical properties for 316L stainless steel according to ASTM.**

Stainless Steel	Spec.	Fe	Cr	Ni	Mo	Mn	Si	Cu	C	N
316L	F138 – 08	Bal.	17.0	13.0	2.25	2.0	0.75	0.5	0.03	0.25
			19.0	15.0	3.0	max	max	max	max	max

Stainless Steel	Ultimate tensile strength (MPa)	Yield strength (MPa)	% Elongation (min)	Hardness (HRC)
316L	490 – 1350	190 – 690	12 – 40	25

### 2.3 Ceramic biomaterials

The use of ceramics have been incorporated into various prostheses for application in hip, knee, shoulder and spine. Ceramics used in biomedical applications possess desirable properties like: high hardness and strength, electrochemical inertness, excellent biocompatibility and wear resistance [11]. The following are the commonly used ceramics in various prosthetic applications today: alumina, zirconia, zirconia-toughened alumina (ZTA), alumina matrix composites (AMC), alumina-toughened zirconia (ATZ), Silicon Nitride ( $\text{Si}_3\text{N}_4$ ) and hydroxyapatite (HAp) [10]. Further details on ZTA and  $\text{Si}_3\text{N}_4$  ceramics (the two relevant ceramics to this study) are provided in the subsequent sections.

### 2.3.1 Alumina ( $\text{Al}_2\text{O}_3$ ) and alumina composite

Alumina has been the most widely used structural ceramic for about 5 decades now. Pierre Boutin in 1970 implanted the first hip prosthesis with Alumina ceramic bearings and its success led to the current hard-on-hard and hard-on-soft bearing combinations such as the: Ceramic – on – Ceramic (CoC), Ceramic – on – Metal (CoM) and Ceramic – on – Polymer (CoP). It has good biocompatibility, high hardness, low coefficient of friction and hence excellent wear resistance. However, its inadequate fracture strength and toughness led to numerous cases of *in-vivo* fracture; thus leading to failure rates of up to 13.4% being reported in the 1970s [11, 12].

Optimisation of manufacturing processes has led to generations of improved alumina ceramic with excellent mechanical properties as shown in Figure 2-1 [13, 14]. For example, the third generation alumina ceramic (still commercialised today) benefitted from the use of hot-isostatic pressing (HIP) leading to a significant reduction in grain size from  $\sim 3.2 \mu\text{m}$  to  $\sim 1.8 \mu\text{m}$ . The most recent generation of alumina ceramics used specifically in orthopaedic applications is the ZTA ceramic commercially known as BioloX®Delta. It's a composite ceramic of 82% alumina and 17% zirconia nano-particles by volume. In Figure 2-1 it is observable that the strength of the composite is almost double that of the third generation Alumina. Figure 2-2 depicts the two mechanisms attributed for its excellent toughness. The first is the presence of zirconia nano-particles that are used to for arresting propagating cracks. The second are large platelets of elongated oxide crystals that form *in-situ*. To compensate for the lower hardness of the Zirconia particles in the matrix, hardness is restored to the material by adding chromium oxide ( $\text{Cr}_2\text{O}_3$ ) as a solid solution in the alumina matrix [13, 15]. The recent failure rates of these toughened ceramics now range from 0.004 – 0.05% which is a significant improvement [11].

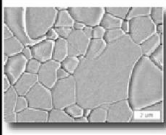
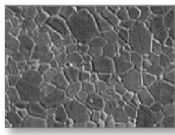
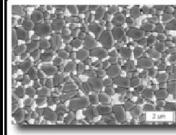
Properties of Ceramics	Alumina Ceramic ISO 6474 1994	1st and 2nd generation Alumina	3rd generation Alumina (Hipped)	Alumina Ceramic Composite
4-point bending strength	400Mpa	500Mpa	580 Mpa	>1000 Mpa
Average Grain Size	< 4.5µm	< 3.2µm	< 1.8µm	< 1,5 µm
Density	3.94g/cm3	3.96g/cm3	3.98g/cm3	4,37g/cm3
Microstructure				

Figure 2-1 – Generations of alumina ceramic [13]

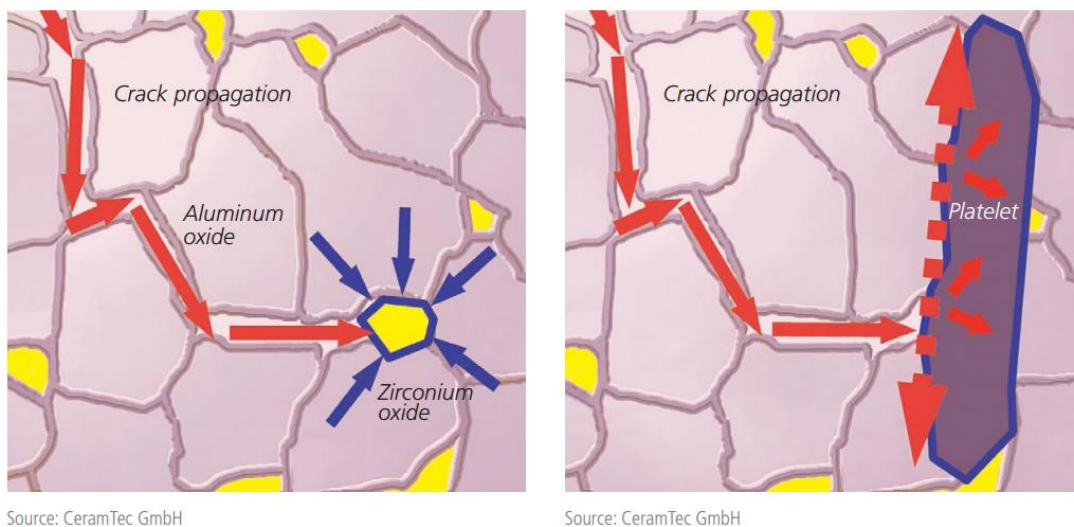


Figure 2-2 Mechanism of improved toughness in composite alumina ceramic [15]

### 2.3.2 Silicon Nitride (Si<sub>3</sub>N<sub>4</sub>)

Silicon nitride is used in a wide range of applications including: automotive, aerospace and more recently biomedical applications [14]. The material had been synthetically developed as early as 1859 however, commercial interest in the material was not until the 1950s when the properties of the material was better understood. The material is known for its high fracture toughness, strength and desirable wear properties. With respect to its biomedical applications, silicon nitride is known for its biocompatibility and ability to dissolve in physiological media thus reducing the effect of particle induced osteolysis [16, 17]. However, it wasn't until 2006 that silicon nitride was officially approved by the food and drug administration (FDA) as a biomaterial [18]. Since 2008, it is being used as spinal fusion cage implants which has proven to be a successful venture with ~25000 implants with only few adverse reported events [14].

The two typical processing methods for manufacturing silicon nitride are: reaction-bonding and HIP. The reaction-bonded silicon nitride produces a relatively low density, high porosity and low strength material. On the other hand, while the HIP method incurs higher manufacturing cost, it was developed to address the listed poor properties of the reaction-bonded method [19]. However, the two technologies can be combined by manufacturing the silicon nitride through an initial stage of sintering and subsequently reaction-bonding. This results in a higher strength material for the manufacturing cost that is lower than the HIPed system. Silicon nitride has a composition of up to 10 wt% Ytria (Y<sub>2</sub>O<sub>3</sub>) and alumina as an additive [19]. Its typical mechanical properties are listed as follows:

- Bending strength – 600 MPa
- Vicker's Hardness ~ 12 – 13 GPa
- Youngs Modulus – 299 GPa
- Poisson ratio – 0.27
- Typical grain size ~ 0.59 μm

Silicon nitride forms a solid-solution of two phase structure: equixed αSi<sub>3</sub>N<sub>4</sub> and acicular βSi<sub>3</sub>N<sub>4</sub>. The toughness of the ceramic can be controlled by the

engineering both the grain size and the transformation of the equiaxed  $\alpha\text{Si}_3\text{N}_4$  to the acicular  $\beta\text{Si}_3\text{N}_4$  phases [14]. Quite importantly,  $\text{Si}_3\text{N}_4$  also has a strong network of  $\text{SiO}_2$  in its grain boundaries which has been shown to play a significant role in the formation of thin oxidised-Si tribofilms and the corrosion of the ceramic [20].

## 2.4 Corrosion

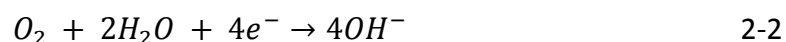
This section covers fundamental principles of corrosion while also drawing on specific electrochemical behaviour of CoCrMo and Ti6Al4V alloys. The synovial fluid in the joint capsule consist of Cl and phosphate ions and other electro-active species (EAS) that contributes to creating an aggressive physiological media for the metallic components used in hip prosthesis. The metallic implants are susceptible to various forms of corrosion mechanisms, namely: fretting corrosion, pitting, crevice corrosion, galvanic corrosion, intergranular corrosion and others.

### 2.4.1 Electrochemistry of corrosion

Corrosion of metals is mostly electrochemical in nature as well as underpinned on thermodynamic principles. Electrochemical reactions is simply characterised by two half-cell reactions in aqueous solution: Anodic (Oxidation) reaction and Cathodic (Reduction) reaction. The anodic reaction releases electrons while the cathodic reaction receives the electrons. Equation 2-1 shows a standard anodic half-cell equation of a metal 'M' with charge valence 'n' which corresponds to 'n' number of electrons.



An example of a cathodic half-cell reaction is one of oxygen reduction within a base or alkali solution shown in Equation 2-2 [21].



A metal within an electrolyte is an array of structured positive cations with a shroud of free electrons, each of which belongs to the valence of an atom in



the structure. The free electrons is the main determinant of the metal's conductivity [22]. In an aqueous solution, water gets adsorbed onto the metallic surface creating an interface between the metallic substrate and hydrated metallic cations ions, which migrated from the surface of the metallic substrate. This leaves the metallic substrate negatively charged and the hydrated layer, populous of positive ion. The two parallel layers can be described as two planes of separate charges hence forming an electrochemical capacitance with a potential difference across the plane, this is known as the electrical double layer (EDL), a model initially introduced by Helmholtz in 1850 [23]. Figure 2-3a shows a schematic of the surface as well as the linear increase in potential (left of the outer Helmholtz plane (OHP)) and the non-linear increase in potential (right of the OHP).

The rate of electrochemical half-cell reactions that occurs on a metallic surface is highly depended on the anodic/cathodic surface area ratio. As a metal corrodes, electrons released at the anodic site flows through the metal to react at the anodic site as depicted in Figure 2-3b for Zinc metal in acidic solution. The flow of electron is the measure of current, therefore, the current due to the anodic reactions at the anodic site can be expressed as a function of the cathodic current and area as shown in Equation **2-3**.  $I_{anodic/cathodic}$  are both the total anodic and cathodic currents measured over the respective surface areas  $S_a$  and  $S_c$  while  $i_a$  and  $i_c$  represents the currents measured at the local sites [21].

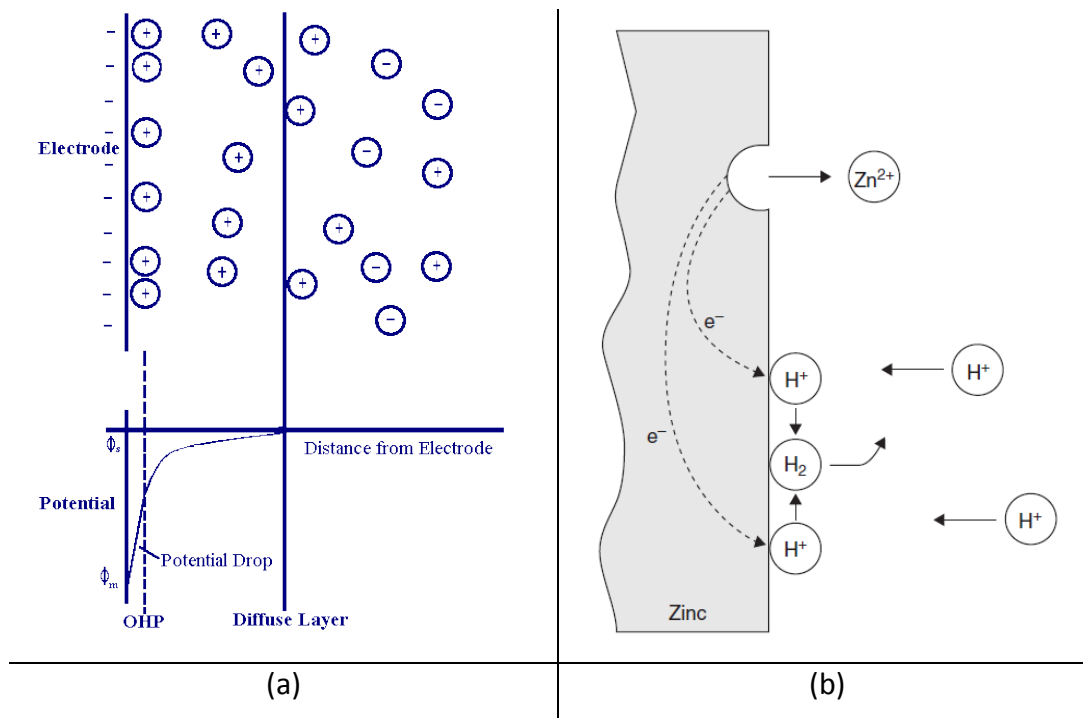


**Figure 2-3 – Electrical interactions at the metallic surface a) Schematic diagram of electric double layer [23] b) Anodic and Cathodic sites during corrosion [21].**

$$I_{anodic} = i_a \times S_a = I_{cathodic} = i_c \times S_c$$

$$\therefore \text{rearranging, } i_a = i_c \left( \frac{S_a}{S_c} \right)$$

2-3

## 2.4.2 Types of corrosion effective at the modular junction of THA

### 2.4.2.1 General corrosion

General corrosion, also known as uniform corrosion acts uniformly over the entire surface area of a metal when exposed to an electrolyte. Air can also be an electrolyte for corrosion if the critical relative humidity of the material is reached or surpassed. This form of corrosion is specifically characterised by numerous individual electrochemical reactions occurring simultaneously over a metallic surface. It is the most common form of corrosion and can be prevented through the use of coating or by solution controls i.e. modifying the pH, temperature etc. [24, 25].

### 2.4.2.2 Intergranular corrosion

Intergranular corrosion occurs in metals and alloys where there is a different electrochemical interaction between the grain boundaries and the grains. In such cases, the grain boundary is prone to localized attack while the remaining parts of the metal remain unaffected. This eventually damages the mechanical integrity of the material. Figure 2-4 shows a micrograph of intergranular corrosion attack on CoCrMo alloy. Causes of this form of corrosion are as follows: impurities at the grain boundary, enrichment or depletion of a particular element in an alloy – like in the case of sensitisation. It has been found that in a Cl rich media, precipitate phases of the alloy can induce intergranular corrosion and so does the precipitation of carbides at the boundaries [24]. CoCrMo alloy is known to be more susceptible to this form of corrosion than Ti6Al4V [26, 27].

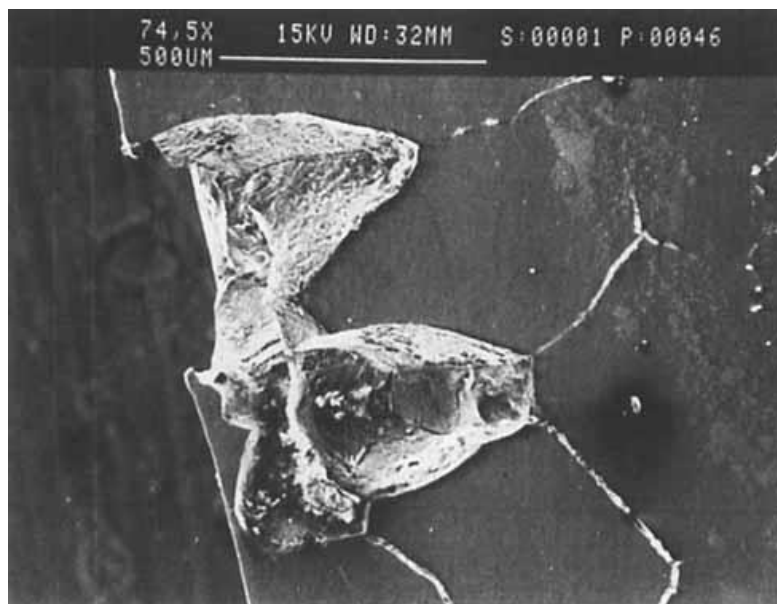


**Figure 2-4 – Intergranular attack on CoCrMo alloy [27]**

### 2.4.2.3 Pitting corrosion

Pitting corrosion is a highly localised corrosion mechanism that proves to be highly destructive to mechanical systems. The process can be very rapid with no appreciable mass loss from the surface under attack. For this reason,

pitting can be very difficult to predict or even detect on a surface. For passive metals and alloys, pitting occurs by locally destroying the oxide layer which leaves the metal or alloy exposed; hence encouraging further pitting of the surface. Titanium and CoCr based alloys used in orthopaedic implants can release metallic ions during an anodic reaction that causes metal dissolution [24, 25]. Release of the metal ions in the presence of EAS and oxygen can make the pitting more aggressive. Pitting corrosion has been detected as a degradation mechanism for CoCrMo in both like and similar material combinations [27].

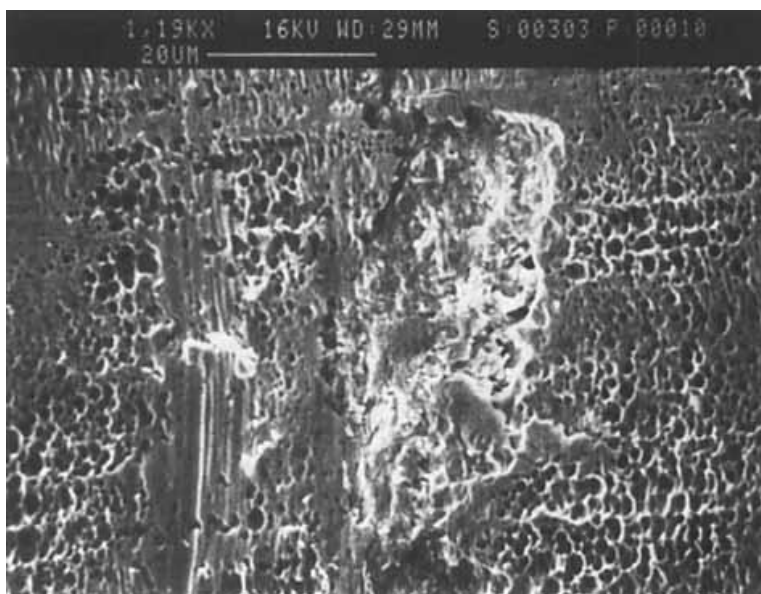


**Figure 2-5 – Pitting corrosion attack on CoCrMo alloy [27].**

#### **2.4.2.4 Crevice corrosion**

Crevice corrosion occurs in cracks and crevices of materials that are either similar or dissimilar. This form of corrosion usually occurs in passive metals and is influenced by the following conditions: geometry of crevice, alloy composition, passive film characteristics, bulk solution composition and temperature. Fontana and Greene [28] explains three conditions required to be met in order for crevice corrosion to be initiated. Firstly, there has to be an electrical connection between the crevice and the external surfaces. Secondly, the fluid in the crevice should be trapped such that the dissolved oxygen in the solution is used up in a reaction with the metal surface to form

oxides within the crevice. The stagnancy of the fluid also means that diffusion of oxygen into trapped fluid is restricted resulting in depleted oxygen.

The third condition is satisfied if the material outside the crevice remains passive. This causes a differential aeration cell between the external material and the microenvironment inside the crevice. The lack of oxygen as well as the migration of Cl ions in the environment also inhibits the normal repassivation that would occur on the metallic surface. Therefore, a permanent breakdown of the passive film also occurs at the crevice [29]. One other key implication of crevice corrosion is that the products of corrosion often result in a tighter crevice as depicted in Figure 2-6. Reactions from the anodic site releases  $H^+$  ions thus creating a highly acidic environment where pH could drop to as low as 0, thus resulting in faster metallic dissolution [29].

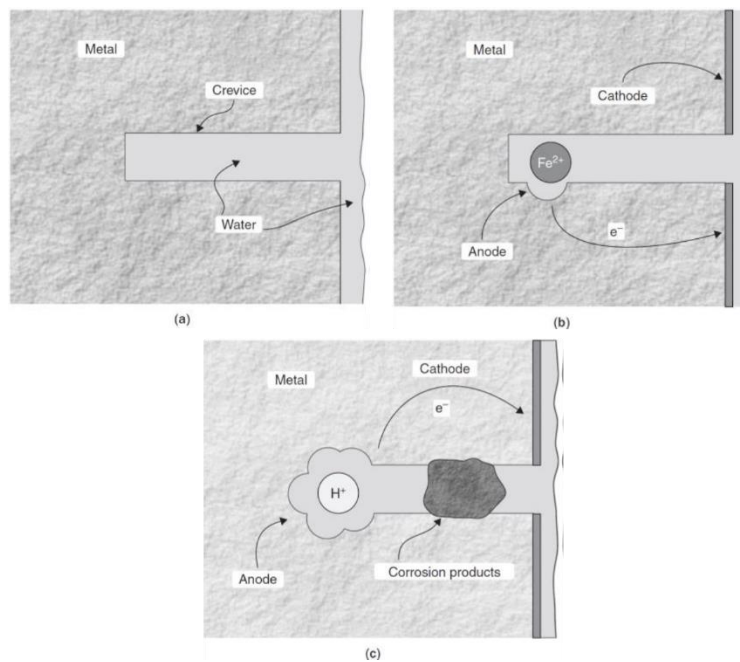


**Figure 2-6 – A simplified 3 stage depiction of crevice corrosion: a) conducting electrolyte in contact with crevice. b) cathodic and anodic sites are formed, c) corrosion products create a severer crevice [21].**

#### 2.4.2.5 Galvanic corrosion

Galvanic corrosion in its simplest manifestation occurs as a result of differences in the standard potential of two metals or alloys that are in a conductive corrosive environment. The factors that significantly affect galvanic

corrosion are: potential difference between two coupled materials; the electrolyte both are exposed to, the area, distance and geometry of the materials when in close proximity of one another or in contact. Furthermore, in galvanic coupling, the surface area is a very important consideration because one of the metals may act as the cathode while the other behaves as the anode. This behaviour is a function of the standard potential of each metal and the electrolyte composition [24, 25]. In the context of modularity in THA, the coupling of CoCrMo alloy against Ti6Al4V is one that had sparked a debate as to whether galvanic corrosion plays a relevant role in the degradation mechanism [27, 30].

### 2.4.3 Passivity of biomaterials

Metallic biomaterials are generally described as passive alloys due to the thin (nano-scale) oxide layer that spontaneously form on the surface of the metal. The corrosion resistance of metallic biomaterials are largely due to their protective oxide layer. This layer limits the rate of corrosion by becoming a physical barrier against metallic ionic dissolution. The absence of such protective layer would make the metal surface prone corrosion attack by EAS in the body [2]. However, metallic biomaterials can behave like active metals in the absence of the passive layer or while the passive film is unstable.

Figure 2-7 shows a theoretical plot of a potentiodynamic scan for a passive alloy. The scan begins in an anodic direction from a potential where the corresponding current is minimum i.e. zero. This potential is known as the open circuit potential (OCP); it is the point where the rate of anodic reaction equals the rate of cathodic reaction thus yielding zero net current. From this point, the metal behaves like an active metal as the corrosion rate rapidly rises up to a critical point termed  $i_{crit}$ . This critical point occurs at the passivation potential  $E_{pp}$  subsequent to which the current falls to a constant rate termed  $i_{pass}$ . This current  $i_{pass}$  remains theoretically constant as potential increases; it is the current required (net anodic reaction current) to form the oxide layer. This region of constant current  $i_{pass}$  is known as the passive region and the larger the potential at this region is, the more stable the oxide layer is. Beyond the passive region is the transpassive region; the region is characterised by

an accelerated corrosion current caused by break down in the oxide layer. The metal's ability to repassivate as well as its resistivity to pitting and crevice corrosion are assessed at this potential [31].

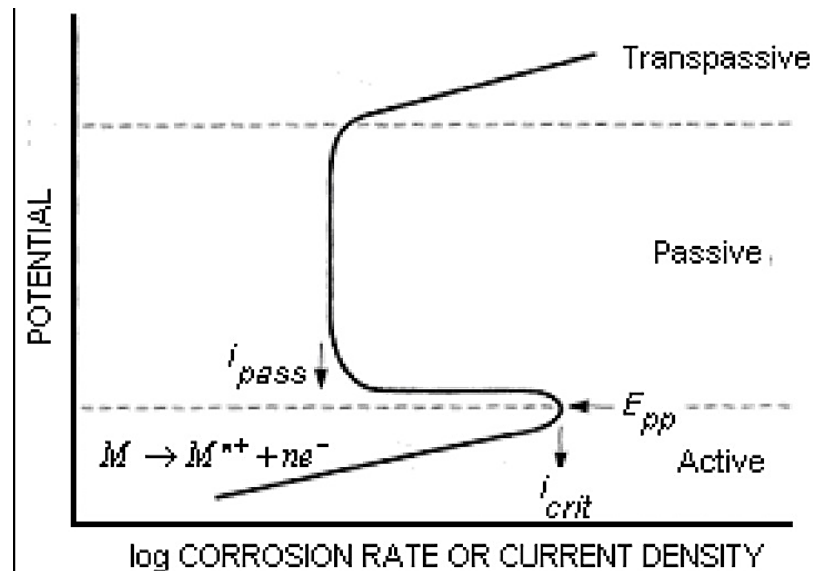


**Figure 2-7 – Theoretical plot of a potentiodynamic scan in the anodic direction for a passive alloy [32]**

#### 2.4.4 Faraday's law

Faraday's law on electrolysis converts the current generated from an anodic reaction into an equivalent mass loss. This law relates the current measured and the number of moles of electrons involved in the reaction by the conversion of 1mol of electrons i.e. 1 Avogadro's number of electrons ( $6.022 \times 10^{23}$ ) into charge. The product of the number of electrons and the charge of a single electron ( $1.6 \times 10^{-19}$ ) gives 1 F which equals to  $96485 \text{ Cmol}^{-1}$  of electrons [21].

The mass loss (m) from the electrochemical reaction is therefore calculated using Faraday's equation in Equation 2-4. The electrical charge (Q) with unit C is determined as the sum of the anodic current generated across a time period (t) as shown in Equation 2-5. 'M' with unit  $\text{gmol}^{-1}$  is the molar mass of the reacting species and 'n' is the number of electrons in the electrochemical reaction.

$$m = \left( \frac{QM}{Fn} \right) \quad 2-4$$

$$Q = \int_0^t I dt \quad 2-5$$

## 2.5 Tribology

Tribology is the study of friction, lubrication and wear between two contacting surfaces in relative motion. Friction is the main route through which energy is dissipated between two contacting materials. The energy may be dissipated through wear, structural transformation of the material, heat etc. Therefore, improved control of friction can prove beneficial while poor management can prove costly. Lubrication is one of such ways in which friction between two moving surfaces can be controlled thus minimising interfacial damage [33]. The following subsections focuses mainly on wear and the most commonly observed wear mechanisms.

### 2.5.1 Wear

Wear generally occurs as a result of mechanical action between two or more solid bodies in contact. A mechanical wear process undergoes two stages: the running-in stage and the steady-state wear rate. After a long period of time, the steady-state wear rate could transition into fatigue behaviour which further reduces the wear rate [34]. Wear is manifested through different mechanisms namely: adhesive wear, corrosive wear, fatigue wear, abrasive wear and others. The subsequent sections address four main wear mechanisms that are effective in biomaterials. Fretting wear and fatigue mechanisms are addressed in Section 2.6.

### 2.5.2 Adhesive wear

Adhesive wear is also known as scoring, galling or seizing together of two contacting surfaces. Materials are prone to this mechanism during relative



motion of two contacting surfaces that are subjected to high contact pressures. The process can also be described as the welding together of the two surface, in which case, the asperities at the contact are plastically deformed and during strong adhesion of metallic surfaces, electrons can be transferred between the bodies in contact. Figure 2-8 provides a depiction of adhesive wear mechanism. Increasing the hardness of surfaces may prevent against this wear mechanism [33].

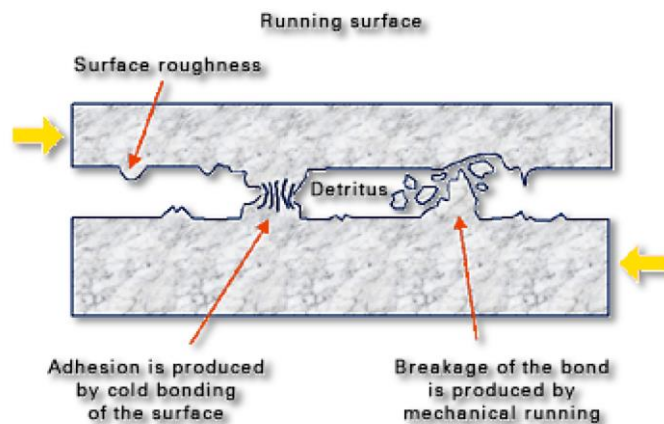


**Figure 2-8 – Adhesive wear mechanism [35]**

### 2.5.3 Abrasive wear

Removal of material due to abrasive wear mechanism is the process where particles or hard asperities are indented into a softer surface with subsequent relative motion. This mechanism, in some cases, is preceded by the adhesive wear in which case, the material detachment came from the welded interface thus creating a much harder particle. This mechanism can also lead to micro-cutting, fracture, as well as ploughing of a surface and hence may contribute to both the initiation and propagation stages of cracks in a contact subject to fatigue stresses. The bearing surface of CoM is one interface susceptible to this mechanism as the hard particulate debris of the ceramic component may abrade the softer metallic surface as depicted in Figure 2-9.

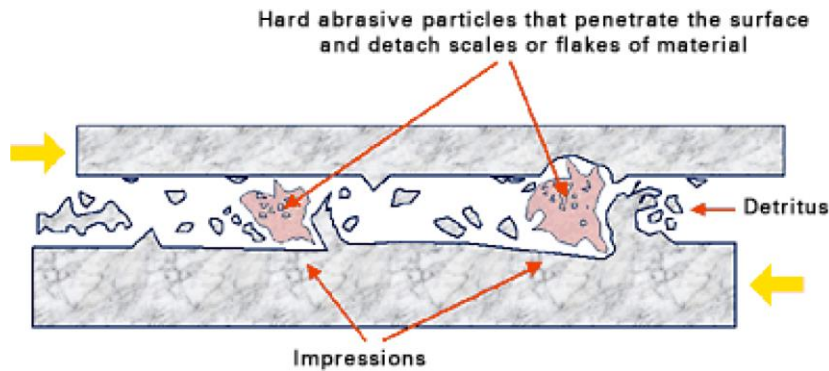


**Figure 2-9 – Abrasive wear mechanism [35]**

### 2.5.4 Fatigue Wear

Cyclic application of stress at the surface of a solid body relative to another, results in fatigue wear. Fatigue wear mechanism generates much less wear compared to other wear mechanisms. The pre-requisite for crack initiation on one of both of the bodies are high normal load and/or high surface compliance of one or both of the bodies. From Figure 2-10, it can be seen that two surfaces that are in contact are loaded against each other and if the tangential forces are insufficient to overcome the static frictional force, the surface elastically deforms repetitively leading to a cyclic fatigue motion. The partial slip regime of a fretting contact often create such contact condition [36].

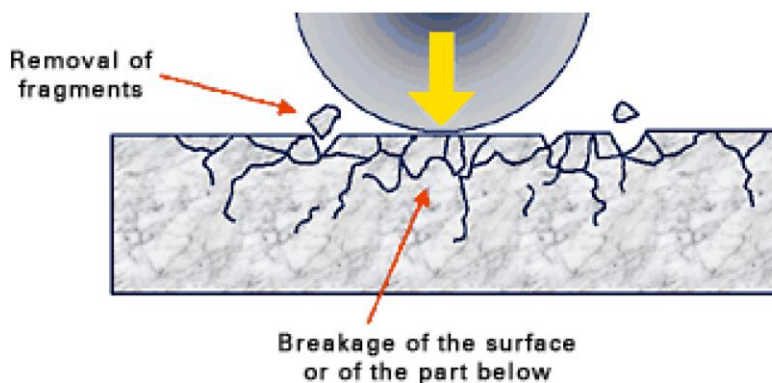


**Figure 2-10 – Fatigue wear mechanism [35]**

### 2.5.5 Corrosive wear

This wear mechanism occurs in a corrosive environment and the interactions between tribology and oxidation reactions occurring at the interface of the contacting materials results in the formation of wear and oxidised products (corrosion). Air at room temperature contains humidity and may also contain other industrial vapors, therefore, oxides and hydroxides of metals are common products formed during corrosive wear [37]. Oxides from the metal surface has the ability to reduce the rate of corrosion given that it satisfies desirable mechanical properties such as wear resistivity, low friction and relatively thick for corrosion resistivity. In some other cases the film formed on the surface is too thin and therefore the film might be too weak to withstand sliding hence the film has a short life span which results in an overall increase in wear rate.

The described process also corresponds to the corrosion enhanced wear ( $C_w$ ) synergy factor in a tribocorrosion system as discussed in Section 3.5. Corrosive wear product can be both beneficial and adversely effectual on biomaterials and this is dependent on the characteristics of the oxide film that is formed on the material surface [33]. Figure 2-11 shows a depiction of corrosion and wear products on the wearing surface.

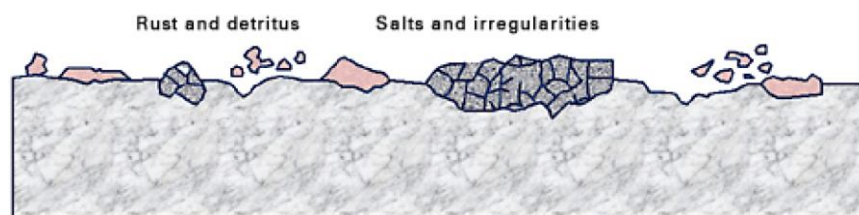


**Figure 2-11 – Corrosive wear mechanism [35]**

## 2.6 Fretting

Fretting is defined as an oscillatory displacement at low amplitude between two contacting surfaces. Although the phrase 'low amplitude' has no formally defined boundary, the generally accepted upper limit is 300  $\mu\text{m}$  above which the contact transitions into reciprocating sliding [38]. However, Fouvry et al [39] expressed fretting independently of an upper limit by expressing it as a characteristic of the Hertzian contact radius 'a' as shown in Figure 2-12. Figure 2-12a shows a schematic representation of a gross slip fretting contact on the left and the representation of a reciprocating sliding contact on the right.

The parameter 'e' is the ratio between the displacement amplitude ' $\delta_x$ ' and the hertzian contact radius 'a'. Through the ratio 'e', a contact can be distinguished as to whether it is in fretting ( $e < 1$ ) or reciprocating sliding contact ( $e > 1$ ). For the fretting contact, an unexposed region exist at the point where the two hertzian contacts overlap. The damage manifested on the contacting surfaces during fretting are generally: minimal; fatigue dominant or wear dominant as characterised by Vingsbo and Soderberg [38]. Furthermore, these three damage modes are generally linked with three fretting regimes which were first described by Mindlin in 1949 [40]. These are outlined in detail in the subsequent sections.

Experimental efforts to characterise fretting damage in realistic systems are often conducted using tribometers where various contact configurations namely: flat-on-flat, cylinder-on-flat, sphere-on-flat and others are established with selectively chosen contact pressures and displacements to represent the realistic conditions as close as possible.

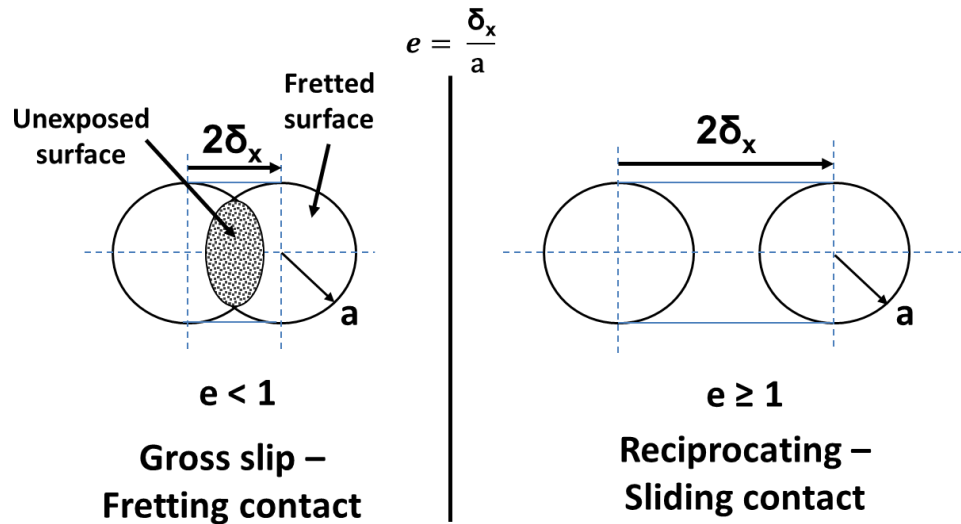


**Figure 2-12 – Difference between a fretting contact (left) and a reciprocating sliding contact (right). Adapted from [39]**

### 2.6.1 Fretting regimes

The fretting regimes described by Mindlin are namely: Stick, Partial-slip (or mixed stick-slip) and gross slip. These were represented by a tangential force ( $F_t$ ) – Displacement ( $\delta_x$ ) plots also known as fretting loops, using a cross cylinder configuration by Vingsbo and Soderberg [38]. Figure 2-13 shows the schematic representation for each fretting regime. In the same figure, the ratio of interfacial slip ( $\delta_s$ ) to the displacement amplitude ( $\delta_x$ ) is denoted 'A' and the area encompassed by the fretting loop corresponds to the dissipated energy ( $E_d$ ).

#### 2.6.1.1 Stick regime

The stick regime is characterised by a tightly closed fretting loop. Wear generated at its interface and fretting damage are minimal as only surface asperities undergo plastic deformation [38]. The damage mechanism is fatigue dominant due to continuous cyclic elastic deformation of the contacting surfaces.

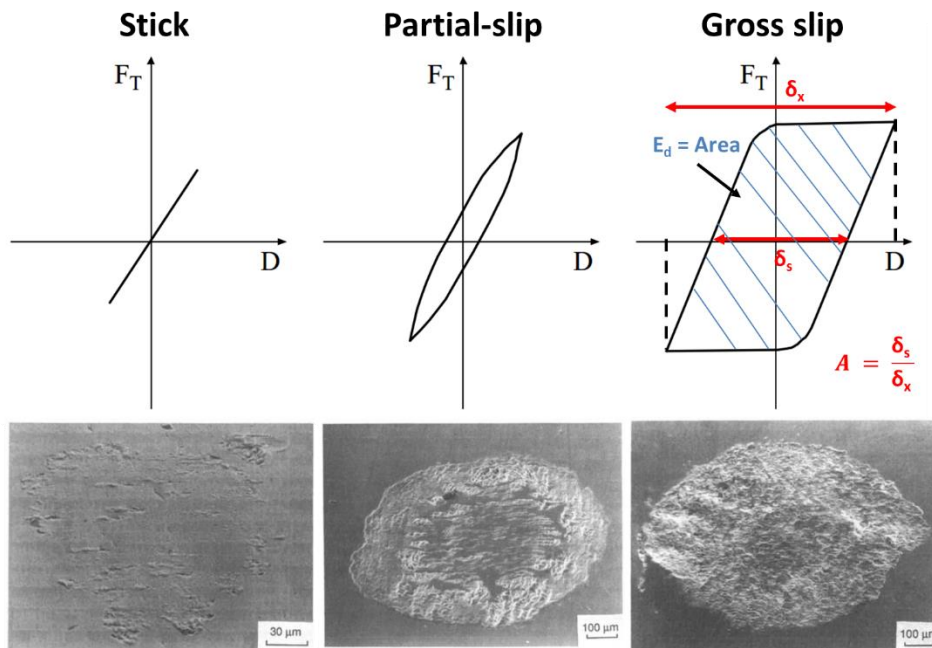


**Figure 2-13 – Fretting hysteresis loops from a plot of tangential force and fretting displacement amplitude [41], beneath the fretting regimes are the characteristic surface damage profiles [38].**

### 2.6.1.2 Partial-slip regime

The Partial-slip regime is characterised by an elliptical shape signifying the introduction of slip at the interface which corresponds to a transition from a dominant elastic shear to plastic shearing of the surface. The surface damage identified in Figure 2-13 (above) shows a central stick region surrounded by an annular of slip area [39, 41]. The damage in the central region is indicative of plastic deformation of the asperity-asperity contacts which contributes little to the overall wear of the interface. The stresses effective at the worn annulus of this regime is more dominant in fatigue crack formation especially at the boundary between the central stick region and the worn region [38, 39]. However, the further away from the boundary and the closer towards the edge of the Hertzian contact, the regime becomes increasingly wear dominated. This is illustrated in Figure 2-14a where a yield annulus is introduced.

The yield annulus corresponds to the point of maximum tangential force prior to the transition from static friction to kinetic (or dynamic) friction; it can also

be referred to as the traction forces ( $q_x$ ) [42]. Intersecting horizontal cracks formed in both yield and slip annular often result in the removal of larger delamination wear product, especially in the case where the contact had been oxidised making the surface harder and brittle compared to rest of the bulk [38].

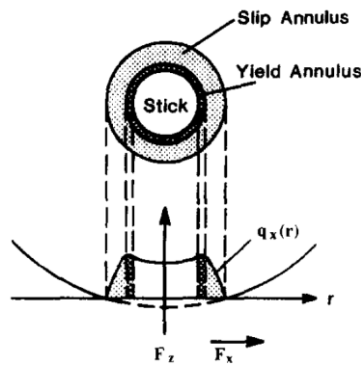


**Figure 2-14 – Fretting regimes: a) characterisation of the fretting contact of a partial-slip regime in terms of tangential force ( $F_t$ ) and traction force ( $q_x$ ) [42].**

### 2.6.1.3 Gross slip regime

The gross slip regime is generally characterised by a parallelogram shape as shown in Figure 2-13 (above). The levelling off of the tangential force in the fretting loop is indicative of a complete transition from static friction to dynamic friction from the micrograph displayed in Figure 2-13 (above), it can be seen that majority of the central region had undergone a plastic shear and across the entire contact, all asperity contacts are broken off [38]. In general, the regime is characterised by extensive wear through delamination and shear of adhesive junctions (especially from the central region) [38, 39, 43]. Wear and oxidation products are usually trapped between the contacting surfaces, resulting in possible shift in wear mechanism to an abrasive dominated mechanism. It is also common for the two bodies subjected to fretting wear to form layers of wear debris and oxidised surfaces that thickens over time and accelerates degradation of the two surfaces through abrasion [44].

#### 2.6.1.4 Mixed regime

The term 'Mixed regime' is often used to describe the partial-slip regime, however, Fouvry et al [39] introduced the 'mixed slip regime' which represents the case whereby the contact condition changes during a fretting experiment. This may be manifested in fretting regime transition from any of the three other regimes to each other. For example, the partial-slip may transition to gross slip during an on-going test and vice-versa. Such fretting behaviour is prominent at a contact characterised with high loads where the imposed displacement exceed the threshold for transition from the partial-slip regime [39].

#### 2.6.1.5 Mindlin's hypothesis

Mindlin's hypothesis as described in the reference [45] predicts that for two materials subject to a single point contact in a purely elastic condition, interfacial slip will always begin at the outer annular as depicted in Figure 2-15. This description becomes relevant at the end of a fretting test when the contact is reviewed. The presence of a central stick region or in the case of gross slip regime, central partial-stick region gives an indication that the wearing mechanism at the fretting interface is still affected by elastic contact compliance. The alternative, which is the more common case, is the influence of third-body product at the fretting contact.

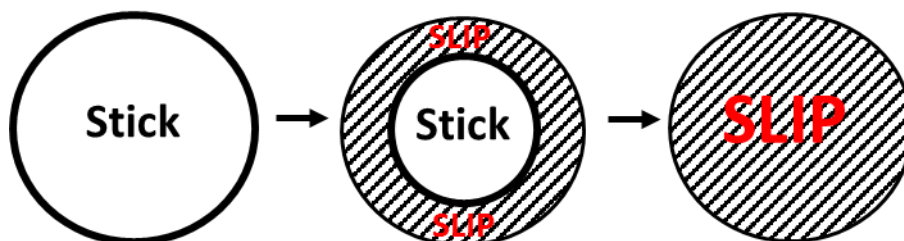


Figure 2-15 – Schematic representation of Mindlin's hypothesis



## 2.6.2 Fretting corrosion, wear and fatigue

The term fretting wear was initially described as fretting corrosion because oxidation plays a large role in its wear mechanism [46] and fretting wear is also often referred to as fretting fatigue due to the delamination processes in its wear mechanism [38]. However, fretting corrosion is more commonly known today as a specific process in a tribocorrosion system [47]. On the other hand, fretting wear and fretting fatigue modes of damage in their right definitions have been compiled from a number of fretting experiments by Vingsbo and Soderberg [38] as a factor of displacement amplitude (Figure 2-16a) and load (Figure 2-16b).

With respect to the wear and fatigue modes of damage in (Figure 2-16a) it is observable that the wear rate rises sharply with a small increase in displacement during the stick regime and the fatigue life is highest at this point whereas as the contact transitions into partial/mixed slip regime, wear rate remains almost constant for a relative large range of displacement while fatigue life drops drastically. On transition into gross slip, a direct proportionality exist between displacement and wear rate. However, a sharp rise in the fatigue life plateaus before reciprocating sliding is reached.

From Figure 2-16b it is observable that at low loads, fatigue life is high and wear rate also but the fatigue life drops sharply at still relatively low loads. At much higher loads, fatigue life drops significantly along with wear rate. And at very high loads, the contact is in a stick regime, fatigue life rises and wear rate drops, providing the least damaging condition.

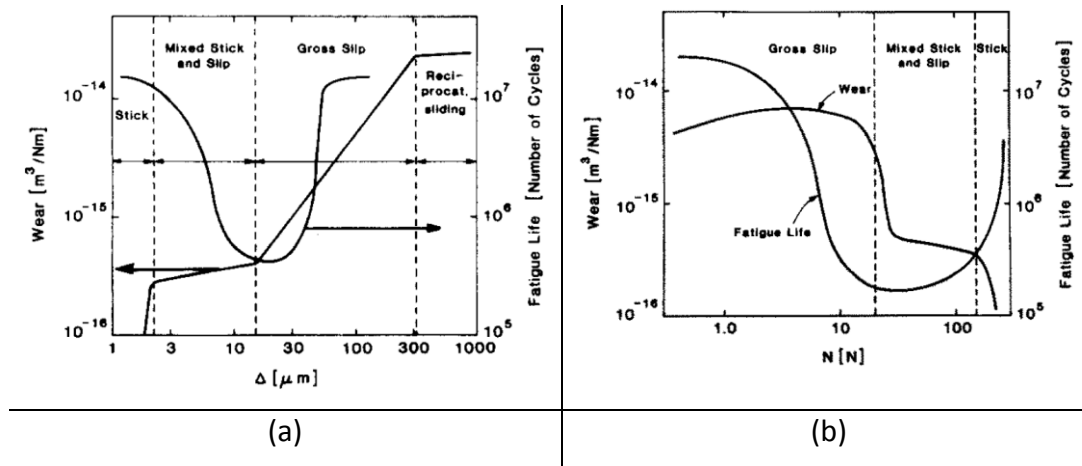


Figure 2-16 – Fretting damage modes: a) wear and fatigue modes as a function of displacement, b) wear and fatigue modes as a function of load [38].

## Chapter 3 Literature review

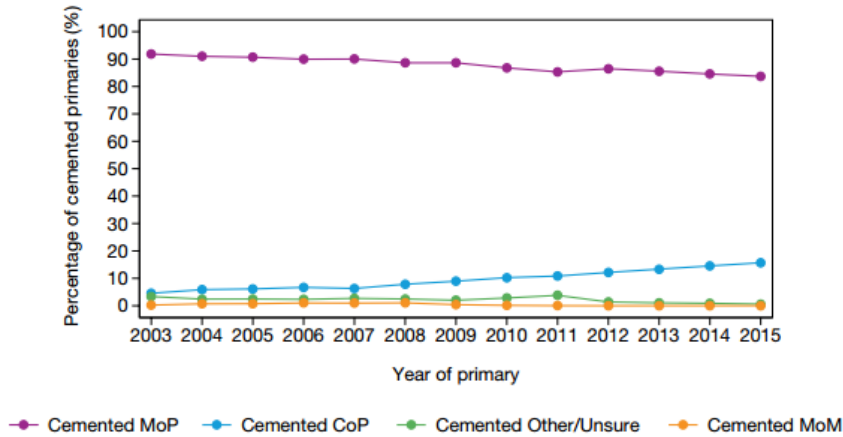
### 3.1 Total hip arthroplasty

The earliest record of THA was by Glück in 1891; although it was not until the 1950s that THA became a long term solution for arthritis and diseases of the joints through Sir John Charnley's low friction arthroplasty [48]. His design consisted of three main parts; a mono-block metallic femoral stem, a polyethylene acetabular component and acrylic bone cement [49]. Presently, advances in the design of polyethylene through the development of crosslinked ultra-high-molecular-weight-polyethylene (UHMWPE) in the late 1990s has kept Metal-on-Polymer (MoP) bearing the most widely used combination in cemented primary THA (see Figure 3-1a) [1, 49, 50].

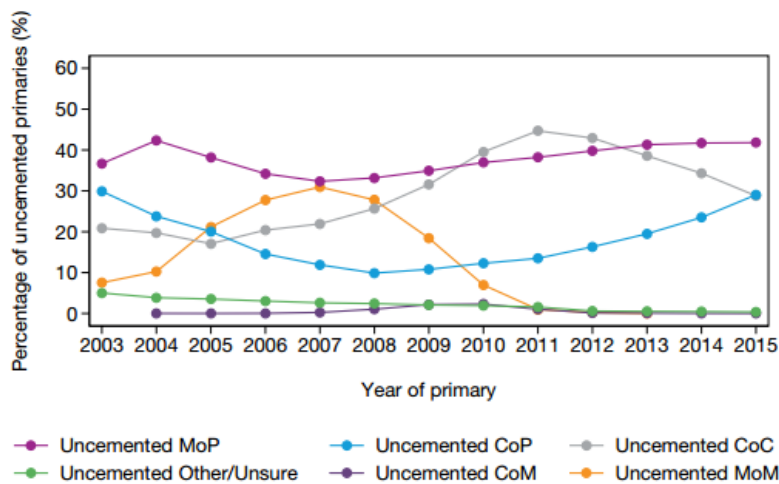
On the contrary, excessive metal ion release into the body led to the down fall of the thriving Metal-on-Metal (MoM) articulating bearings. Consequentially, the excessive metal ion release into the body led to inflammatory responses, pseudo-tumours and other adverse reactions. This resulted in a significant increase of revision rates which led to the recall of some implant designs like the DePuy articular surface replacement (ASR) as well as the Zimmer Durom hip resurfacing system. The impact of this action is reflected in the sharp decline of MoM THA use since 2007 as represented in Figure 3-1b [1].

As aforementioned, alternative bearing combinations became an option in the early 1970s when stem modularity was introduced to the design of THA. This introduced the use of alumina ceramics as a femoral head component. The idea of CoC bearing was first introduced by Pierre Boutin in 1970. And as shown in Figure 3-1b, the use of CoC gained ample attention in uncemented primary THA procedures in the early 2010s. Nevertheless, the hard-on-soft alternative (CoP) is seen as a more popular option in recent times than CoC as shown in the same (Figure 3-1b). CoC bearing combination is today prescribed the best bearing combination for young active patients [51] while the CoP combination is consistently reported as the material combination with the lowest revision risk among all the other bearing combinations [1]. In

general, the number of registered primary procedures in the UK had increased steadily to over 80,000 in 2014 and 2015 and the value is expected to rise due to an aging population [1].



(a)



(b)

**Figure 3-1 – Percentage of bearing combinations a) cemented b) uncemented [1].**

### 3.1.1 Rationale for modularity in THA

The head-neck modularity also known as the Morse taper was introduced to THR in the early 1970s with the purpose of achieving a durable fixation between ceramic femoral ball and a metal stem hence creating an alternative bearing to Cobalt-Chromium-Molybdenum (CoCrMo) alloys [52]. Other advantages of modularity in THA design are: increasing option of intra-

operative customisation of the implant device thus the natural biomechanics of a patient's hip can be better reproduced after surgery; complications in revision surgery and costly inventory can be greatly reduced [53]. Furthermore, modularity allows titanium alloy to be used for the stem component of THA whilst a more wear resistant alloy is used as the bearing component thus the effect of stress shielding is reduced [54].

In the early 1990s, a second modularity was introduced to the femoral stem component of hip prosthesis. This is commonly known as the bi-modular design; it is depicted in Figure 3-2. Subsequently, other forms of modularity were introduced such as the tri-modular design – a design particularly used in the treatment of peri-prosthetic femoral fracture. The proximal shoulder, anterior/posterior pads, modular pads and stem-sleeve junction are also examples of other forms of modularity in THA [55]. Figure 3-2 shows a collage of various implant designs depicting the evolution of the modularity in THA from Charnley's monobloc design in the 1960s to the more recent bi-modular and tri-modular THA design.

It is noteworthy that with every new interface introduced to the hip prosthesis, new challenges related to wear and corrosion arises inevitably. More so, one study has estimated that modular femoral stem components can cost between 15% to 25% more than standard femoral stem components for primary or revision THA thus, the extra cost is also worth considering [54].

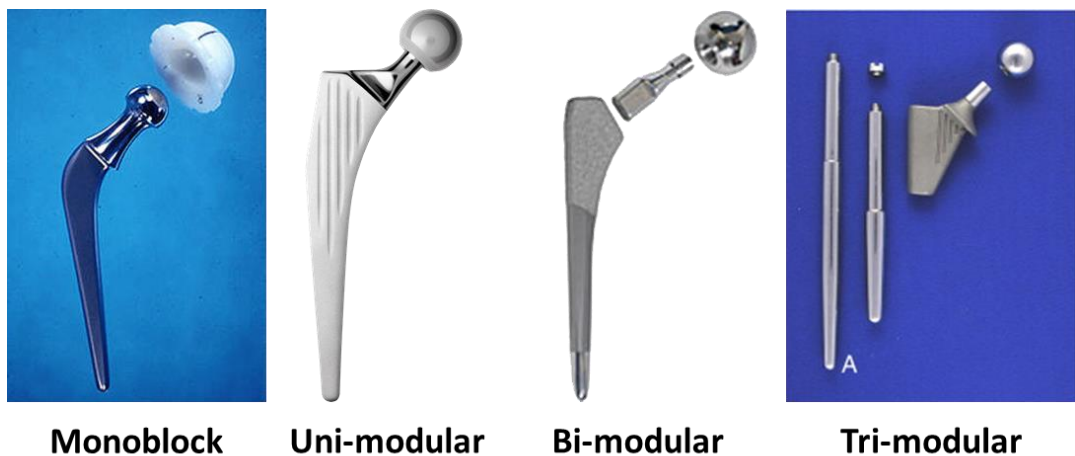


**Figure 3-2 – Evolution of modularity in THA**

### 3.1.2 The Morse taper (head-neck taper)

The Morse taper is ubiquitous in the design of THA devices as a means of securing the male taper onto the female taper throughout the *in-vivo* lifetime of the implant. Impaction force by the surgeon provides frictional resistance against moment or axial forces incurred at the taper interface during daily living activities. Nevertheless, this doesn't eradicate micro-motions at the modular interface hence fretting and corrosion damage are always found at these interfaces after some time *in-vivo*. There are three main taper designs commonly used today namely: 12/14 'Euro'-taper, the V-40 and the 'Type 1' taper. Other taper designs exist such as the: C-taper, 14/16 taper, and the 11/13 taper although these have become less common in the orthopaedic market. For example, the larger 14/16 taper was replaced to reduce the risk of dislocation and the narrower trunnion (also known as male taper) of the 11/13 provides less surface area for interference fit thus increasing fretting damage [56].

Figure 3-3 is a depiction of increasing head sizes from left to right and decreasing taper sizes in the same direction. The Euro – 12/14 is the most widely used amongst various companies while the other two are specific to a company; its dimensions are 12 mm proximal diameter and 14 mm distal diameter. The tolerance and taper surface morphology of these taper differs between companies; some models have smooth finish while others have grooves of varying pitches and depths. For this reason, mixing and matching of components from different manufacturers is generally advised against [57, 58]. A recent study [59], found that the choice between smooth or grooved male taper affects the taper strength as their study reported a higher taper strength when smooth tapers are used compared to grooved tapers. Although, the grooved tapers are necessary for securing ceramic bearings onto the male taper as the grooves deform against the ceramic when the taper is assembled with an impaction force thus creating an interference fit. The multifactorial challenges encountered at the head-neck modular interface are discussed in greater detail later in this chapter.



**Figure 3-3 – Increasing bearing sizes from left to right and decreasing taper sizes in the same direction [57].**

### **3.1.3 The neck–stem taper**

Most femoral stem taper designs are elliptical in shape although few have a circular profile as later shown in Figure 3-8 and Figure 3-9 [54]. The neck trunnion and stem bore both have a tapered profile with a smooth surface finish so that the neck engages with the bore and forms a tight fit with the necessary surgical impaction force through the head component. This modular interface is subject to both axial and bending load possibly leading to micromotions. However, modularity at the neck-stem has the advantage of allowing adjustable leg length independently of both horizontal and femoral offsets. In addition, this extra modularity is said to have improved the range of movement in several patients with complex anatomies [55].

### **3.1.4 Assembly of modular tapers**

In the uni-modular system, the Morse taper at the head-neck interface is simply assembled, firstly by twisting the femoral head onto the male taper (for grooved trunnions) or simply seating the head bore onto the trunnion (for smooth trunnions), subsequently, the taper is secured by applying an impaction force unto the femoral head using a head impactor and a mallet as shown in Figure 3-4. Larger heads (>28 mm) are said to require larger impaction forces to ensure tight fit due to the larger friction forces they transmit to the modular interface [54, 60]. Furthermore, during assembly it is essential that the tapered surfaces are dry and free from contamination before

impaction as this may lead to accelerated fretting and possibly reduce the fracture toughness of ceramic bearings [11, 61].

Bi-modular tapers such as the Zimmer M/L Taper with Kinetiv® Technology prescribes only a single strike using the head impactor to secure both head-neck and neck-stem tapers [62] however multiple impaction may be necessary to ensure the tapers are well fixed. Indeed, a number of studies are advocating the need for larger impaction forces to reduce fretting at the taper interface [59, 63, 64]. In a study by Rehmer et al [65] which focused on the Morse taper connection, it was demonstrated that the taper strength increases linearly with increase in assembly force while multiple impaction force had no effect. However, the ability to separate the tapers by the application of turn-off moments varied correspondingly to material combination and assembly force [59, 65]. In the case of the tri-modular tapers, Figure 3-2 shows how the design allows for various lengths of the stem to be fastened using a screw and once secure, the femoral head is subsequently impacted onto the neck component.



**Figure 3-4 – Fixation of both head–neck and neck–stem [62]**

### **3.2 Challenges with modularity**

The challenges with modularity ultimately culminates in patient discomfort. Examples of these are *in-vivo* fracture, excessive wear and voluminous metal ion release and others. Retrieval analysis of the modular taper interface dates back as far as the early 1970s when modularity was initially introduced [66]. Through the use of electron microscopy, energy dispersed x-ray spectroscopy



(EDS), x-ray powder diffraction (XRD) as well as analysis of urine and serum samples, the extent and effect of fretting corrosion can be quantified and qualitatively characterised. Insight into the various mechanisms that are effective in the degradation processes of the modular interfaces can prove useful in creating hypothesis that shapes the design of *in-vitro* experiments. This section reviews the failure mechanisms of retrieved explants as well as trends in the nature of metal ions released into the body.

### 3.2.1 Fretting and corrosion scores in retrieval studies

In the early 1990s, Gilbert et al [27] introduced a qualitative system for characterising corrosion at the modular taper junction. It worked by categorising explants into 4 groups: no visible corrosion, mild corrosion, moderate corrosion and severe corrosion. In the study by Goldberg et al [67] numbers were allocated to the listed categories as well as a criteria through which the specific categories are qualified hence becoming an official scoring system commonly known as the ‘Goldberg score’ (see Table 3-1). The same scoring system was adopted and modified to charactering the extent of fretting in other components within hip implants [68, 69]. It had also been adopted for characterising corrosion products transferred unto ceramic heads [70].

**Table 3-1 – Criteria for corrosion and fretting scores [67]**

Severity of Corrosion and Fretting	Score	Criteria
None	1	No visible corrosion observed No visible signs of fretting observed
Mild	2	< 30% of taper surface discolored or dull Single band or bands of fretting scars involving three or fewer machine lines on taper surface
Moderate	3	> 30% of taper surface discolored or dull, or < 10% of taper surface containing black debris, pits, or etch marks Several bands of fretting scars or single band involving more than three machine lines
Severe	4	> 10% of taper surface containing black debris, pits, or etch marks Several bands of fretting scars involving several adjacent machine lines, or flattened areas with nearby fretting scars

### 3.2.2 Review of retrieval studies – head-neck interface

Studies conducted on retrieved implants have led to the identification of various fretting and corrosion mechanisms at the head-neck interface. The large retrieval analyses of 148 modular prosthesis conducted by Gilbert et al [27] identified mechanisms such as: preferential dissolution of Co from the CoCrMo alloy, fretting, pitting, formation of an interfacial phases (shown in Figure 3-5a), interdendritic corrosion and intergranular corrosion. Figure 3-5b depicts wear and corrosion products trapped within the taper interface which would influence both the wearing mechanism and the local chemistry at the modular interface.

The modular prostheses analysed in their study were from similar (CoCrMo – CoCrMo) and mixed (CoCrMo – Ti6Al4V) material combinations. Their results reveal that a higher percentage of CoCrMo head taper in the mixed category experienced significant corrosion damage compared to the similar category. This agrees with the observation of Goldberg et al [67] in whose study, 231 cases were analysed. Further observations from these studies [27, 67] and another [71] also shows that the CoCrMo head taper is generally measured with a higher corrosion score than the trunnion taper.

In cases where ceramic bearings were used instead of CoCrMo bearings, the trunnion tapers coupled with CoCrMo heads were observed with a higher degree of fretting corrosion damage than the ceramic – metal trunnion tapers [72]. The study by Kurtz et al [72] also identified that fretting corrosion scores were lower when the ceramic bearings were coupled against titanium alloys (Ti6Al4V and TMZF) compared to CoCr heads. More recently, a study solely comparing the material losses of a single CoCrMo stem design of 48 retrieved explants from CoCrMo heads and ceramic heads concluded that there were no significant difference in the material losses from both male tapers [73].

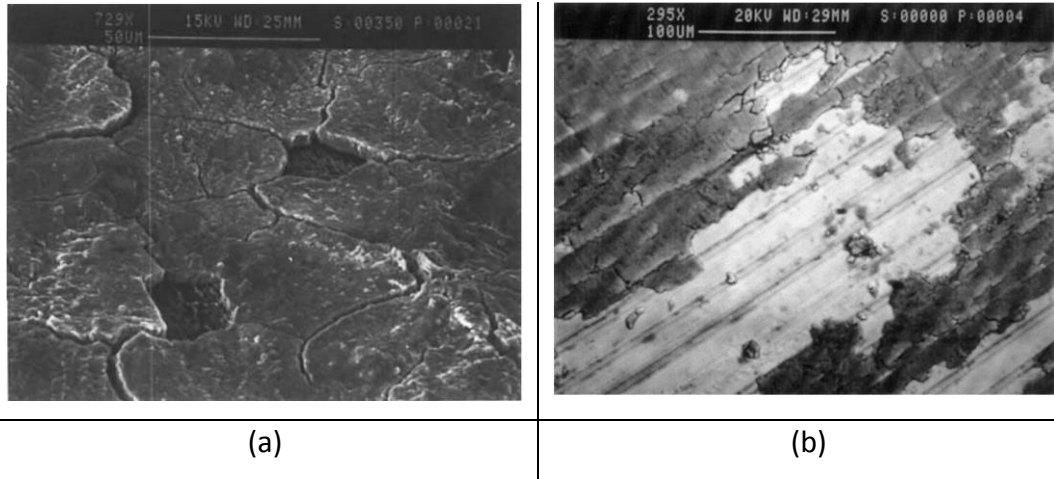


**Figure 3-5 – Fretting corrosion at the head-neck interface: a) evidence of Ti-Cr-Mo interfacial layer [27] b) evidence of corrosion products on the trunnion surface [67].**

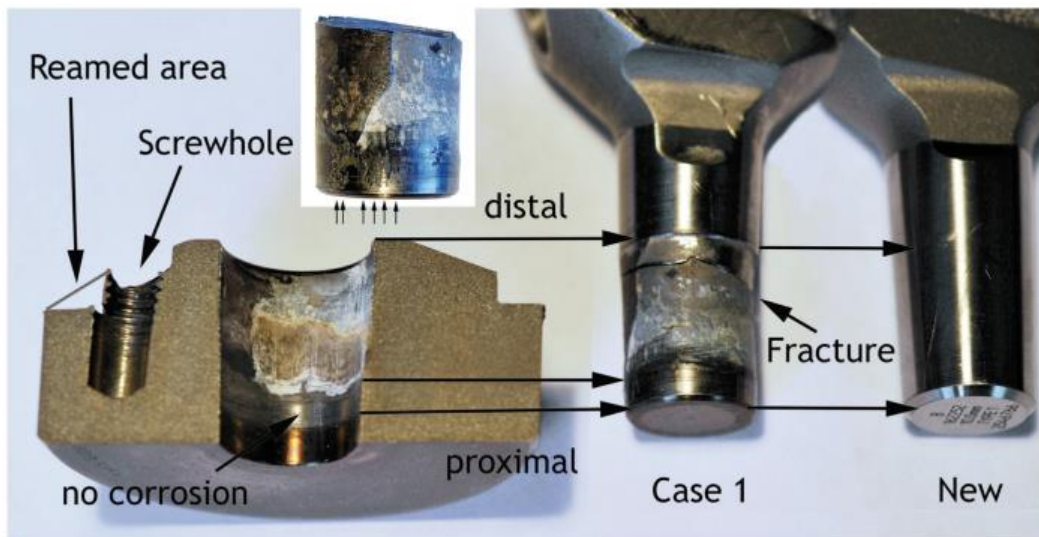
### **3.2.2.1 Factors influencing fretting corrosion at the head-neck interface**

Other trends related to fretting corrosion of the head-neck interface have been explored for example, Goldberg et al [67] assessed the effect of implantation time, metallurgy and stiffness. Their study observed a higher degree of corrosion at the head and neck tapers with longer implantation time while fretting alone was found to be unaffected by implantation time. With respect to metallurgy, corrosion scores for both wrought CoCrMo and wrought Ti6Al4V necks were not different however, their fretting scores differ with Ti6Al4V alloy scoring higher. The cast CoCrMo heads measured slightly higher corrosion scores than the wrought CoCrMo heads while the vice versa was the case (even more significantly) when considering their fretting scores. In addition, it was also observed that the stiffer the neck i.e. using CoCrMo instead of Ti6Al4V, the lower the probability of corrosion of both head and neck components.

### **3.2.2.2 Rare cases of trunnion fracture at the head-neck interface**

Fracture of the neck at the head-neck interface of THA is rarely observed and hence rarely reported in literature however in a rare case of poorly

manufactured CoCrMo alloy, intergranular corrosion led to the fracture of two CoCrMo stem components [26]. More recently, in a specific case of 3 patients, Morlock et al [74] analysed a M2A Magnum CoCr head with a Ti6Al4V ball head insert and a Ti6Al4V stem which cracked at the head-neck interface due to corrosion initiated at the interface as shown in Figure 3-6. This describes a corrosion fatigue failure mechanism in Ti6Al4V.



(c)

**Figure 3-6 – Fracture of the Ti6Al4V trunnion resulting from corrosion [74]**

### 3.2.2.3 Wear pattern

Wear at the modular head-neck taper interface often follow a particular pattern which is influenced by the contact area, micro-motion, load, taper angle difference etc. Bishop et al [75] identified two distinctive wear pattern commonly observed at the interface namely: asymmetric and axisymmetric. These are depicted in Figure 3-7; the asymmetric wear pattern was described to have resulted from a toggling effect due to turning-moments generated *in-vivo*. Radial separation at the head-neck taper interface may result in uneven stress distribution and thus manifested as toggling. This generally leads to significant wearing of a local region at the proximal and/or the distal ends of the taper. On the other hand, a form of uniform wearing of the tapers occur

with the axisymmetric wear pattern. In one example it was observed that the softer titanium alloy trunnion taper wore the harder CoCrMo head bore and migrated up to 1 mm into the CoCrMo alloy further raising interest in the postulation that hard oxides of the titanium alloy causes the wearing of the CoCrMo alloy [76].

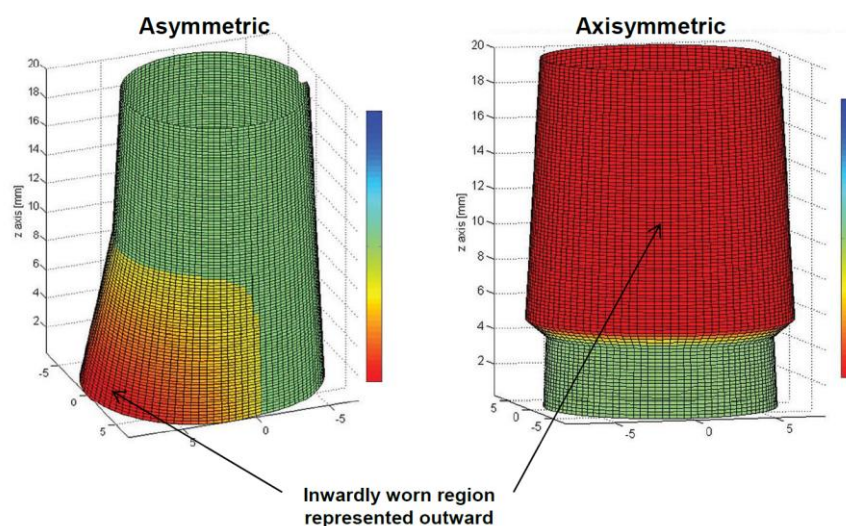


**Figure 3-7 – Wear pattern commonly observed at the head-neck taper interface: Assymmetric and Axisymmetric [75].**

### 3.2.3 Review of retrieval studies – the neck-stem interface

The neck-stem taper interface is generally regarded a more severe contact in comparison to the head-neck interface. This is partly due to higher contact stresses experienced at the neck-stem interface as demonstrated in the finite element (FE) diagram shown in Figure 3-8a [77]. In addition to wear and corrosion mechanisms experienced at this interface, *in-vivo* fracture and cold welding is also prevalent at these contacts causing higher levels of failure rates [55]. From a retrieval analysis of 27 failed *Rejuvenate® modular hip arthroplasties* (Stryker) by Buente et al [78], an observed characteristic wear pattern at the region of material loss on the neck component is said to be indicative of the failure mechanism. The failure was attributed to two main factors: the implant design and the combination of materials used thus

highlighting the possible contribution of engineers and manufacturers to the failure of modular implants.

Figure 3-8b shows an image of corrosion at the neck surface of the *Adaptor GHE/s Short Stem Modular femoral component* (Eska Implants AG) which were said to be experiencing much *in-vivo* corrosion due to high stresses at the modular junction [79]. Grupp et al [80] also reported a 1.4% failure rate in the *Metha® short stem* necks in a time period of 2 years from implantation time. Other assessments in the same study showed that an improvement in the device was observed when the material used was changed from Ti6Al4V to CoCrMo. Thus it is observable that the stiffness of alloy (CoCrMo in this case) plays a significant role in reducing fretting whilst enhancing the fatigue strength of the neck-stem modular interface [55].

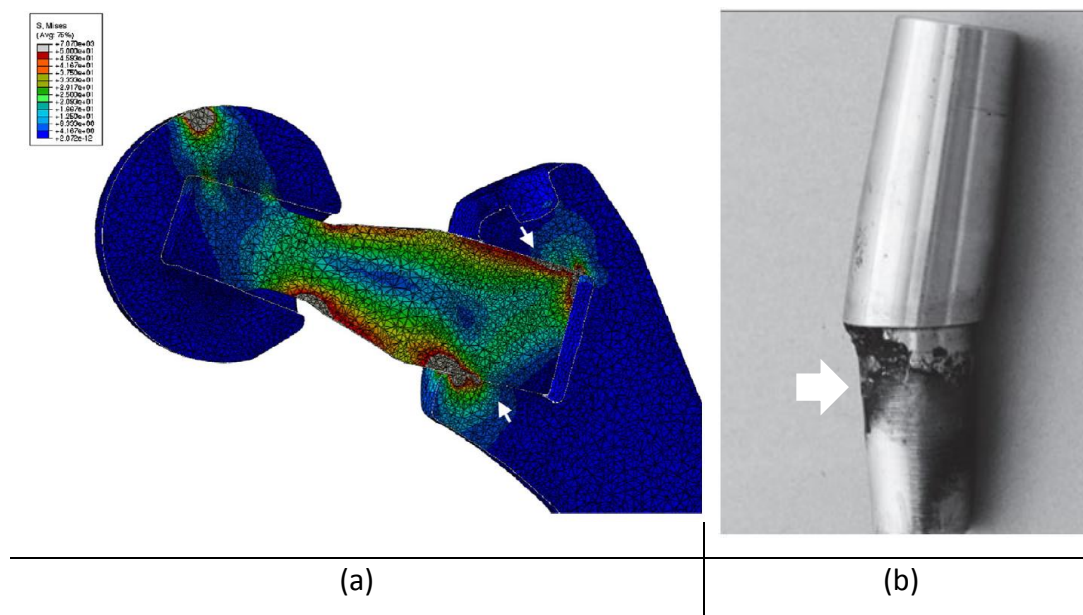


**Figure 3-8 – Neck components of bi-modular tapers a) distribution of stresses across the neck component at the head-neck and neck-stem interfaces [77] b) Corrosion at the neck-stem interface of a circular neck design [79].**

### 3.2.3.1 In-vivo cases of fracture at the neck-stem interface

*In-vivo* fracture of the neck component had been a serious problem observed in at neck-stem interface. This is due to various causes but the most important is the use of titanium alloy as neck component [54]. Dangles and Altstetter [81] reported a fracture of the modular neck in an obese middle-aged man, Figure 3-9 shows the fractured neck with the other half still fixed within the stem bore. In their study, the cause of fracture was proposed to be a result of increase in offset and crevice corrosion, other fractures reported by Skendzel [82] were suggested to be related to the use of long varus style modular neck which is said to increase bending moment by 32.7% compared to short varus stems. The study also concluded that the stem design played a significant role in fracture of the neck. Ti6Al4V alloy necks have been shown to be more prone to fracture than CoCrMo alloy and a study by Nganbe et al [83] gives a good reason through their result which shows that CoCrMo alloy has a 38% higher load-bearing capacity and 1000 times longer fatigue life than Ti6Al4V. This explains why CoCrMo is a better material choice for the neck component.

However, considering the deleterious consequence of adding another CoCrMo component to the hip prosthesis i.e. the risk of increased Co and Cr ions release into the peri-prosthetic tissues; such compromise is a rather difficult one to justify. Nevertheless, it proves a better decision than risking *in-vivo* fracture. In addition, it has been reported that Ti6Al4V alloy is more susceptible to a cold welding phenomena – a solid state joining process occurring without heat at the interface. This has led to several reported cases of damage of the neck component and difficulty in disengaging the neck from the stem component [55, 84].



**Figure 3-9 – Fracture of the neck component at the neck-stem interface  
[81]**

### **3.2.4 Corrosion products and metal ion releases**

#### **3.2.4.1 Solid corrosion product**

The key implication of corrosion at modular taper interfaces are the metal ion and corrosion products released into the peri-prosthetic tissues and blood stream. Consequentially, this causes adverse local tissue reactions (ALTR) that ultimately results in tissue necrosis, bone resorption, inflammation and pain at the joint [8, 54, 85]. High levels of circulating metallic ions have been linked to other serious health problems such as thyroiditis, auditory disturbance, and granulomatous lesions [86]. Various form of solid corrosion products have been found at different regions of the modular taper interface which highlights the transportability of corrosion products *in-vivo*.

For example, studies conducted in the 1990s, by Jacobs et al [85, 87], revealed that solid corrosion products observed within the taper interface were a mixed crystalline metal-oxides of Cr, Mo and Ti (when titanium alloy is a stem component). In addition, Co, Cr and Mo chlorides were also observed in the same region – this is identified as region ‘A’ in Figure 3-10. However, outside the interface, at the rim of the CoCrMo head were crystals of



chromium-orthophosphate hydrate-rich and in 2 unusual cases of the 10 explants assessed, a cobalt-phosphorus oxygen-rich compound was identified – this is signified as region 'B' in Figure 3-10. These products have been categorically linked with the modular interface through peri-prosthetic tissue isolation in both mixed and similar material combinations [54].

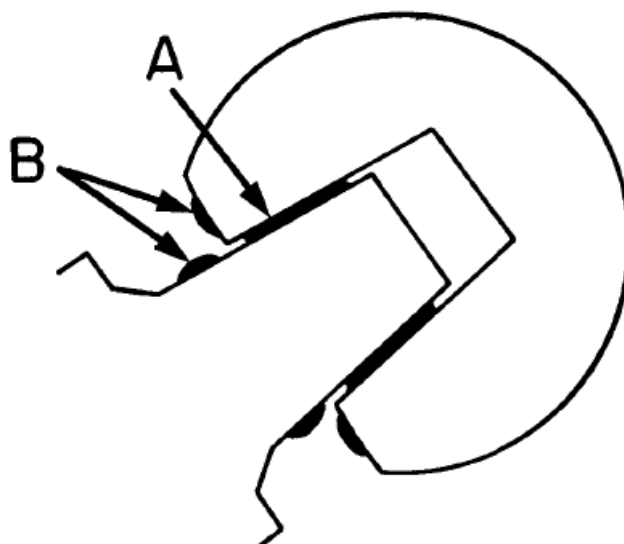


**Figure 3-10 – Solid corrosion products in retrieval. The region 'A' is typically mixed metal-oxides and chlorides while the region 'B' is typically metal-phosphates [87].**

Studies have shown that the dominant corrosion product emanating from the modular taper interface involving CoCrMo alloy is the trivalent Cr (3+) in the form of Chromium-orthophosphate although it is still unclear if the hexavalent Cr (6+) compound also forms *in-vivo* as a result of corrosion [8, 77, 85, 88]. Particles of corrosion products observed were as large as 500  $\mu\text{m}$  in size and it has been found that these corrosion products can migrate to the bearing interface as a third-body, causing increase wear of the softer Poly-Ethylene in a MoP combination [87, 88].

Several studies have also shown that the products obtained from the titanium based alloys are not precipitates of corrosion products as observed in CoCrMo and Stainless steel, but rather, examinations of tissues around the stem reveal that titanium, aluminium and vanadium were measured in similar ratios to their

alloy constituents thereby suggesting that the products are wear particles of the titanium based alloy [89-91]. Nevertheless, it is worth noting that subsequent oxidation of the particles are possible due to increased surface area which encourages further oxidation thus forming oxides and other corrosion products. Physical and histological inspection of the peri-prosthetic tissue have revealed discolouration and titanium particles within macrophages and fibrocytes of densely collagenous membranes but these have not be correlated to the presence of inflammatory cell or necrotic debris at tissue-implant interface [90, 91]. These findings all point to CoCrMo alloy as the focal problem at the modular taper interface.

#### **3.2.4.2 Metal ion release**

Metal ion release from implant corrosion are generally measured by analysing urine and serum samples. It has been shown that even in well-functioning hips metal ion levels in serum can be upto 3-folds higher of titanium and 5-folds higher of CoCr than in control samples [92]. An elevated measure of Co ions beyond the range expected to be found naturally in the body serves as one of the first indications of a failing implant. In the study by Jacob et al [85] urine and serum analysis showed that Co ions were elevated in the serum while Cr in the urine samples from patients with moderate and severe corrosion in comparison to those with 'none' or mild corrosion. Comparison between patients with implants and those without revealed significantly higher urine concentration of Co and Cr for those with implants. A recent study by Scharf et al [8] characterising the extent of Cr and Co-related toxicity concluded that Cr (3+) and Co (2+) were responsible for damages to proteins via an oxidation mechanism and Fenton reaction and they observed a positive correlation between tissue oxidative damage and the concentration of Cr (3+) and Co (2+) ions present in the tissue. Co toxicity has also being linked to damage in the skin and respiratory systems [93].

### 3.2.5 Metallurgical transformations in explants

Although metallurgical transformation of CoCrMo alloy have been well studied at the bearing interface [94, 95]. Only very few studies have examined the subsurface metallurgy of CoCrMo and titanium alloy explants from the modular taper interface. Zeng et al [96] focused their study on the oxide film at the surfaces of CoCrMo head and male tapers but no detailed discussion on metallurgical transformations were made. Gilbert et al [97] examined the fracture of a Ti6Al4V neck and described the corrosion mechanism as an “oxide induced stress corrosion cracking” (OISCC) mechanism but the discussion on metallurgical transformation was also insufficient. However, the study by Bryant et al [98] examined both female and male taper of CoCrMo and TMZF respectively. Their study provided a good insight into how worn and unworn regions within the taper explant translate to subsurface transformations. In the CoCrMo alloy, loss of nano-crystalline layers were observed at regions that had experienced mostly gross sliding regime whereas, an unworn patch which had experienced a partial slip regime was observed with grain refinement ~300 nm in its subsurface from the top surface as well as evidence of directionality 1  $\mu\text{m}$  deep into the alloy. This is shown in Figure 3-11a. On the other hand, the subsurface of the TMZF at a region which had experienced gross sliding revealed mechanical mixing and material flow 5 – 10  $\mu\text{m}$  deep into the alloy while the retained unworn patch was observed with over 2  $\mu\text{m}$  deep of polycrystalline structure. Precipitation and oxidation of elemental species were seen from the surface migrating into the subsurface through a near-surface crack. This is also depicted in Figure 3-11b.

This study therefore strongly highlights the importance of assessing metallurgical transformations of explants and subsequently attempting to replicate the same under *in-vitro* fretting study.

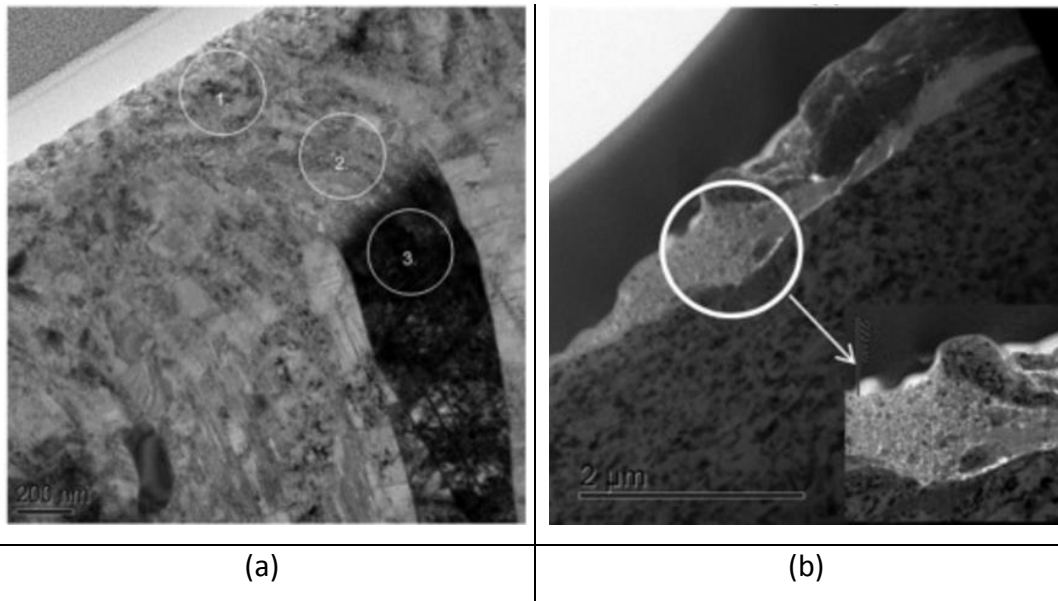


**Figure 3-11 – Subsurface transformation in the partial-slip region of a) CoCrMo and b) TMZF [98]**

### **3.3 In-vitro studies of fretting corrosion**

As aforementioned, retrieval studies are pre-requisites for a well-designed *in-vitro* experiment. The challenge of fretting corrosion at the modular taper interface has so far been shown to be multi-factorial in nature. Some examples are: patient weight, implant design, material combination, surgical impaction force, taper sizes and morphology, minor and major misalignment, contamination of the interface during surgical procedures, bearing size etc. This section reports on the two main *in-vitro* methods used for assessing fretting corrosion at the modular junction of THA.

#### **3.3.1 Common *in-vitro* methods for assessing fretting corrosion in THA**

Several *in-vitro* studies were purposed to assess the metallurgy and electrochemical characteristics of CoCrMo and Ti6Al4V alloys in different physiological solutions and electrochemical potentials. Subsequently, *in-vitro* studies of these alloys under fretting conditions in similar, mixed-metal and ceramic-metal material combinations are undertaken. Examples of

controllable parameters in these studies are: physiological solution, pH, load, displacement, electrochemical potential etc. Elucidating the effect of each individual parameter or their combined effect is achievable using a tribometer. This is a cost effective way of understanding relevant biomedical materials in different environments. For this approach, the relevant material combinations are set-up either in a flat-on-flat, pin-on-plate or ball-on-flat configuration. The tribometer can be instrumented with a 3 – electrode cell set-up so as to monitor *in-situ* electrochemistry as shown in Figure 3-12. Post-test analysis of the interface typically include surface and chemical analytical techniques such as electron microscopy, interferometry and spectroscopy. These are expected to yield the following results: wear volume, wear mechanisms, corrosion current, ion release, corrosion products etc.

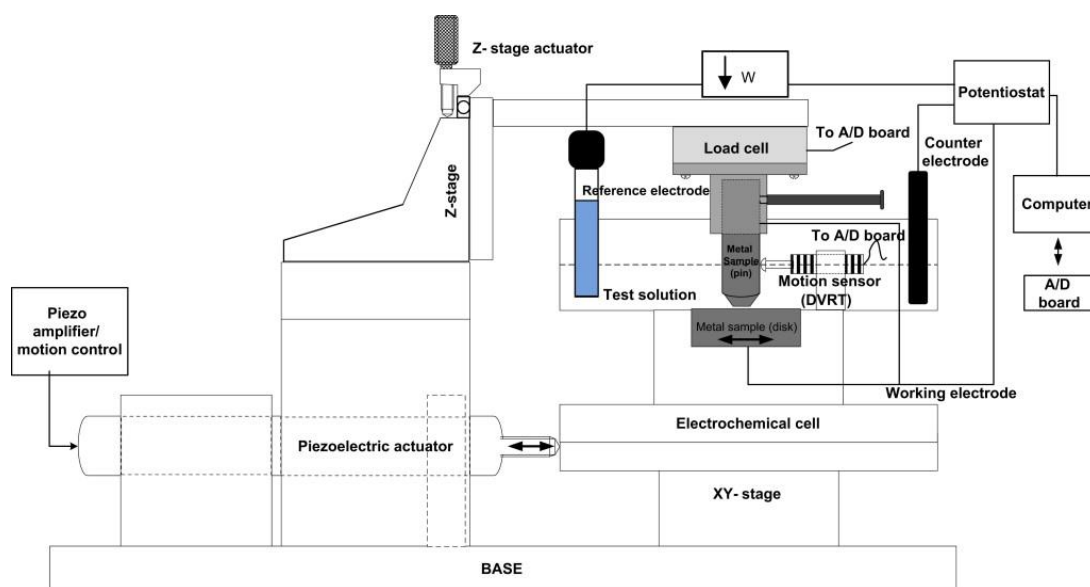


**Figure 3-12 – Fretting tribometer instrumented with *in-situ* electrochemistry for the assessment of fretting corrosion [99]**

However, a more realistic level of assessing fretting corrosion is one whereby implant materials are assessed using geometrical and biomechanically relevant taper interfaces. ASTM F 1875 – 98 [100] is the specific standard that prescribes the loading condition and test set-up for fretting corrosion assessment. Studies can either test material combinations to this standard in its entirety or partly in accordance to it. *In-vitro* assessment of fretting corrosion at this level offers a more relevant quantitative information regarding wear and corrosion than the tribometer studies. However, this comes at a

higher financial cost than the tribometer studies. For this configuration, fatigue loading cycles are imposed onto the femoral head in a physiological media and factors such as: surgical impaction force, frequency, taper size and morphology, misalignments, head size etc. can be investigated either in isolation or in combination. Figure 3-13 shows an example of the set-up with incorporated 3-electrode cell for *in-situ* electrochemistry.

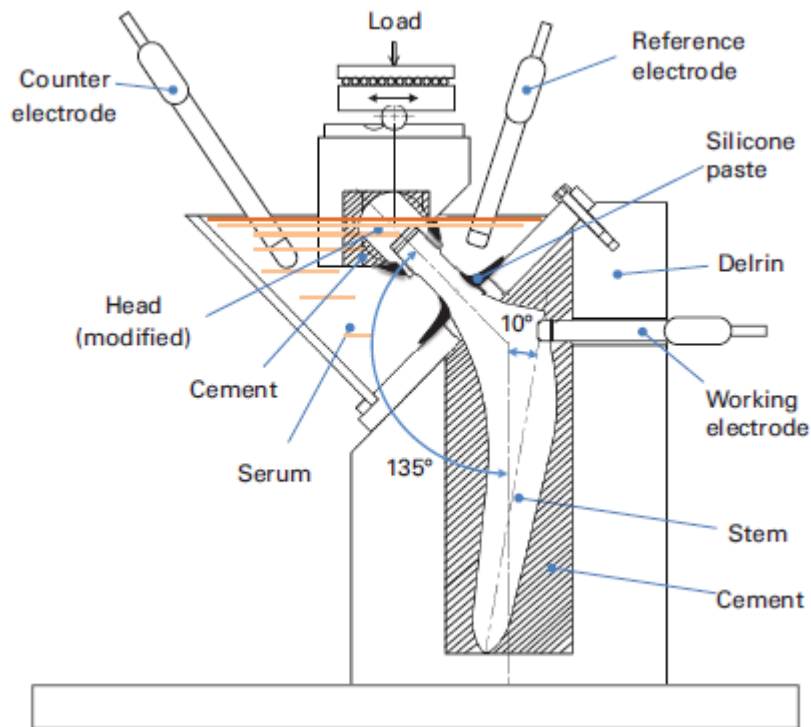


**Figure 3-13 – Fatigue assembly of the Morse taper interface instrumented with *in-situ* electrochemistry [101].**

### 3.3.2 Review of tribometer studies

#### 3.3.2.1 Contact conditions

Studies conducted using a fretting tribometer are generally assessed under a broad range of load and fretting parameters. The contact pressures used in several studies ranges between 10 MPa to 4.2 GPa while for fretting displacement amplitudes, the range varies between 1 to 200  $\mu\text{m}$  [99, 102-105]. Such a broad range is partly due to various studies attempting to understand fretting corrosion in the context of fretting regimes – the realised

fretting regimes at an interface is determined by the combination of load and fretting displacement imposed onto the contact. Although contact pressures and fretting displacements is not known to ever reach as high as 4.2 GPa and 200  $\mu\text{m}$  respectively *in-vivo*, diverse daily living activities (DLA) ranging from running, to stumbling do occur *in-vivo* thus manifested as varying contact pressures and fretting regimes at the real modular taper contact *in-vivo*.

Furthermore, a study by Donaldson et al [106] using FE analysis had shown that contact pressures at the modular taper may increase by 85 MPa for every  $0.1^\circ$  of angular misalignment. This highlights the impact of surgical errors on interfacial contact pressures. Their study also showed that, fretting at the interface may increase by 1  $\mu\text{m}$  for every extra 10 kg of patient weight. Lanting et al [77], using FE analysis showed that the contact stresses experienced by the titanium stem can be as high as 1.6 GPa on average at the neck-stem interface of the modular taper junction while in another study, Zhang et al [107] simulated peak contact pressures of 65 MPa at the head-neck interface. Thus the contact pressures and fretting displacements varies with different taper contacts and under different contact conditions.

### **3.3.2.2 Fretting corrosion of various material combination**

The fretting contact of three main material combinations namely CoCrMo – CoCrMo, CoCrMo – Ti6Al4V and Ti6Al4V – Ti6Al4V were assessed by Swaminathan and Gilbert [99, 108]. Their study examined the effect of electrochemical potential, frequency and load. It was observed in both studies that the Ti6Al4V – Ti6Al4V combination was more susceptible to fretting corrosion than CoCrMo – CoCrMo and CoCrMo – Ti6Al4V. The two contacts involving CoCrMo, was found to have similar coefficient of friction (cof) of 0.3 and Ti6Al4V – Ti6Al4V had friction of  $\sim 0.7$  during gross slip sliding at a contact pressures of  $\sim 73$  MPa.

The fretting current measured for Ti6Al4V – Ti6Al4V contact (3 mA/cm<sup>2</sup>), superseded that of CoCrMo – CoCrMo contact (1.2 mA/cm<sup>2</sup>) which was found to generate double the fretting current of CoCrMo – Ti6Al4V (0.6 mA/cm<sup>2</sup>) for the same contact pressures. The lesser currents measured at the CoCrMo –

Ti6Al4V contact was due to higher interfacial compliance which reduces the overall amount of fretting displacement incurred at the interface in comparison to the CoCrMo – CoCrMo contact [99, 109]. It was also observed that the  $i_{\text{fret}}$  varied with potential for all three combinations however, the Ti6Al4V – Ti6Al4V was the most influenced. With respect to effects of frequency, this was observed to increase linearly with fretting current density only at regions of stable passive film [108].

### **3.3.2.3 Effect of solution chemistry on fretting corrosion**

From fundamental basics of crevice corrosion, the crevice at the modular taper junction ultimately becomes de-aerated and pH drops to acidic levels [27]. Studies have therefore investigated the effect of pH on fretting corrosion and in one study by Royhman et al [103], increased fretting corrosion currents were measured at all displacements amplitudes ranging from 25 - 200  $\mu\text{m}$  and all at the pH of 3.0 and pH of 7.6. Another study which focused on the effect of Molybdate ions identified that Molybdate ions promoted the formation of tribofilm on CoCrMo surface at low pH (4.5) compared to pH 7.6 – both studies were conducted on CoCrMo – Ti6Al4V combination [110].

The role of proteins at the tribological interface of metal have been well documented. Studies by Wimmer et al [111, 112], Martin et al [113] and Matthew et al [95], all of whom are from the same group, have demonstrated that tribofilms consisting predominantly of denatured proteins form at a metal-on-metal sliding interface contributing to low wear, friction and corrosion resistance. However, as it was understood in their findings that the Molybdate ion  $\text{Mo(VI)}$  enhances the formation of these tribofilms by interacting with proteins in physiological solution, a recent study [110] from the group applied this to the fretting contact of CoCrMo – Ti6Al4V and observed that addition of Molybdate ions decreased the release of Co ions by 32% whilst increasing the release of Ti ions. This can be regarded as a more favourable exchange.



### **3.3.3 Review of *in-vitro* studies using realistic taper components**

One of the earliest *in-vitro* studies aimed at assessing parameters such as the effect of material combination on fretting corrosion was conducted by Cook et al [114] in the early 1990s. Their study found that all material combinations which included: wrought CoCrMo – Ti6Al4V (smooth, rough and nitrogen implanted tapers); CoCrMo (10mm neck length increase) – Ti6Al4V (smooth) and Zirconia – Ti6Al4V (smooth and rough tapers) generated wear debris in saline solution at a uniform range of 0.255 – 2.306  $\mu\text{m}$ . The volume of particles were found to be greatest in the first 1 million cycles and it was only the roughened and nitrogen-implanted surfaces that had lesser number of particles than the rest. In the study by Gilbert et al [115], Cook et al [114] and others [101, 116, 117], higher offsets and increase in neck length showed greater fretting and corrosion damage as well as increased particle generation compared to components with 0 mm offset. This indicates the role of increased moment arm in the increase of wear. In addition, dimensional mismatch especially at the metal – metal interface were found to be a factor which led to significant rise in particle generation [114].

In the same study by Gilbert et al [115] Stainless steel (SS) – CoCrMo couple were observed to be more susceptible to fretting corrosion than CoCrMo – CoCrMo combination as the corrosion currents were much larger in SS – CoCrMo than for CoCrMo – CoCrMo at the end of 1 Million cycles of fatigue loading. The rationale for the SS – CoCrMo material combination is mostly aligned with economic reasons because the combination is widely used outside the United States in the interest of cost reduction – an approximate cost of manufacturing high-nitrogen SS stem is 50% less than the CoCrMo alloy equivalent [54].

#### **3.3.3.1 ASTM F 1875 – 98 (2014)**

For the assessment of fretting corrosion mechanisms in THA, fretting corrosion tests are conducted in part reference to ASTM F 1875 – 98 [100]. The following are the relevant prescription from the standard:

- Assembly load – Apply a single static load to 2000 N under dry conditions.
- Cyclic load – Apply a cyclic load of 3 kN with minimum load of 0.3 kN and a maximum of 3.3 kN.
- Frequency – For the 10 million cycles fretting corrosion damage assessment, 5 Hz should be used. For other studies involving electrochemical assessment, 1 Hz is recommended. To assess peak to peak current, 2 Hz is suitable.
- Solution – Volume of solution can range between 5 and 100 mL. Electrolyte solution can be 0.9% NaCl in distilled water. Proteinaceous solution should consist of 10% solution of calf serum.

### 3.3.3.2 Effect of impaction and fretting load

It had been hypothesised that impaction force and dynamic loading at the modular interface has an effect on the degree of corrosion observed. Witt et al [63] examined the effect of assembly load on contact area and observed that at 500 N ~9% of the titanium alloy stem taper surface ridges were in contact with the CoCrMo head and by 8000 N of assembly load, 100% of the ridges were in contact. This corresponded to an overall surface area increase of ~0.6% and ~16% respectively. Mroczkowski et al [118] in their short-term study of 18,900 cycles showed that increasing the magnitude of fretting load led to an increase in fretting current during dynamic loading for both CoCrMo – CoCrMo and CoCrMo – Ti6Al4V combinations. The study, which uses realistic components with realistic taper geometry observed higher fretting corrosion current from the mixed material combination compared to the similar material combination thus agreeing with observations from *in-vivo* explant analysis [27, 67] but disagreeing with tribometer observations [99]. This highlights the relevance of tribocorrosion assessment using realistic components and configurations for quantitative assessment of corrosion. A recent study, featuring a long-term 5 million cycles test of the same CoCrMo – CoCrMo and CoCrMo – Ti6Al4V combinations demonstrated that greater impaction force resulted in less fretting corrosion currents regardless of engagement length, surface roughness or material combination [119].

### **3.3.3.3 Effect of frictional torque and bending moments**

Poor lubrication of large femoral heads may result in increased frictional forces that are transmitted to the modular taper junction. *In-vivo* edge loading and misalignment have also been linked to high torque generated at the bearing interface [120, 121]. The study by Bergmann et al [122] has shown through *in-vivo* load measurement of DLA that average torsional moments acting on the hip may reach up to 17.1 Nm for activities such as stair climbing and as high as 70.5 Nm in extreme cases of stumbling. *In-silico* approach by Farhoudi et al [123] has shown that maximum torque acting at the head-neck interface ranges from 2.3 – 5.7 Nm and bending moment ranges from 7 – 21.6 Nm.

Subsequently, *in-vitro* studies evaluating how changes in torque level and bending moment may effect fretting and corrosion at the modular taper have been a recent focus. Jauch et al [124] identified for CoCrMo – Ti6Al4V combination that torques as low as 3.9 Nm was enough to remove the passive layer at the modular interface for an impaction force of 4.5 kN. However, at a higher impaction force of 6 kN, the torque required was almost double at 7.2 Nm. Furthermore, the study by Panagiotidou et al [101] showed that for CoCrMo – CoCrMo, CoCrMo – Ti6Al4V, and BIOLOX – CoCrMo combinations, increase of bending moment through increase in offsets was found to increase fretting corrosion currents at the taper interface [101]. These studies highlight the effect of torsional and bending loads on fretting corrosion however, the degree of this contribution to fretting and corrosion relative to the axial load is unclear.

### **3.3.3.4 Effect of contact area and topography**

The use of shorter male tapers were one of the solutions introduced to increase range of motion and hence prevent impingement in hip prosthesis. The result of this was a smaller surface area of engagement at the head-neck taper interface. Panagiotidou et al [125, 126] found that the reduction in surface area led to higher fretting corrosion currents due to concentrated bending loads at the reduced contact region. It was also observed in their

study that the roughened surface finish also enhanced fretting corrosion at the interface through significant increase in surface roughness.

### **3.3.3.5 Micromotions**

Micromotions at the modular taper interface of head-neck and neck-stem taper junctions is a pre-requisite for mechanically assisted crevice corrosion (MACC – discussed in section 3.5.2 ). Several *in-vitro* studies have identified factors that influences micromotions at the modular interface. An *in-silico* study by Dyrkacz et al [127] has demonstrated that micromotions at the head-neck interface may vary significantly depending on: head size, material combination, assembly load, taper size, offsets and angle of loading. They measured the highest micromotion of 49  $\mu\text{m}$  when a 500 N assembly load was applied. It was observed that *in-vitro* measurements of micromotion at the head-neck interface is scarce amongst studies assessing realistic components whereas, the contrary is the case for the neck-stem interface.

In the study by Jauch et al [128] micromotion at the neck-stem is shown to be variable for Ti6Al4V – Ti6Al4V combination depending on the taper design. However, independent of the design, the study also revealed that stems made of titanium alloy resulted in higher interface micromotion (fretting) than those made of CoCrMo alloy. Similar observations were made by the same author in a separate study where loads were varied from 2.3 kN (walking contact forces) to 5.3 kN (stumbling loads) [129]. Micromotions has also been shown to be directly influenced by the seating distances of the modular taper which in itself is directly influenced by the magnitude of the assembly load [64, 128] and micromotion decreases with larger negative taper angle difference between male and female tapers [64].

## **3.4 Effect of proteins on corrosion of biomaterials**

The synovial fluid in the human joint consists of an ultra-filtrate of blood plasma, hyaluronic acid and glycol-proteins. The composition of albumin in the synovial fluid can be as high as 70% for arthritic patient whereas this can

be up to 20% lower when bovine calf serum (BCS) is used to represent the synovial fluid [130]. It is important to highlight such a significant difference because several studies have shown that protein concentration has a big influence on both tribological and electrochemical behaviour of biomaterials *in-vivo* [94, 111-113, 131, 132]. One of the most influential mechanism through which protein effect the surface of the biomaterial is adsorption. This interaction is generally governed by chemical composition, surface energy, roughness and the topography of the surface in contact with the proteinaceous fluid. In general, the role of protein on the corrosion of biomaterials is one that is dependent on pH, the bulk alloy material and the concentration of EAS in the solution [132-134].

### 3.5 Tribocorrosion

Tribocorrosion at the interface of two materials in relatively motion is a degradative process involving the tribology; electrochemistry and the synergistic effect of both processes. The damages inflicted by tribocorrosion processes in hip prostheses are more commonly studied at the sliding interface of the bearing components; the fretting interfaces of the head-neck, neck-stem and stem-cement contacts. The conductive physiological solution in the joint space is the electrolyte that completes the electrochemical system.

Tribocorrosion of conductive biomedical materials in relative motion can generally be characterised by assessing the total mass loss 'T' of the materials in contact. Equation 3-1 expresses 'T' as the sum of: 'W' – the pure wearing process in the absence of oxidational effects; 'C' – the pure corrosion process or dissolution of the metal in an electrolyte in the absence of mechanical wear effects; and 'S' – the synergies of both oxidation and mechanical processes.

The synergy can be further expressed as the sum of two components namely: 'W<sub>c</sub>' that is, wear enhanced corrosion – oxidational processes enhanced as a result of wear at the contact and 'C<sub>w</sub>' that is, corrosion enhanced wear – wear processes enhanced as a result of oxidation at the interface [135]. Equation 3-2 shows another general denotation of the expression in Equation 3-1. In this denotation, total mass loss 'T' is denoted ' $M_{total}$ ' and both wear and

oxidational processes are categorised as ' $M_{chem}$ ' the sum of C and  $W_c$  and ' $M_{mech}$ ' the sum of W and  $C_w$  [136].

$$T = W + C + S \tag{3-1}$$

$$S = W_c + C_w$$

$$M_{total} = M_{chem} + M_{mech} \tag{3-2}$$

$$M_{chem} = C + W_c$$

$$M_{mech} = W + C_w$$

Mathew et al [137] identified four key areas that is to be considered and monitored when addressing a tribocorrosion system (see Figure 3-14). The four areas are namely: 1.) Mechanical factors such as normal force, velocity etc.; 2.) Electrochemical factors such as potential, repassivation kinetics etc.; 3.) Material properties such as hardness, microstructure etc. and 4.) Solution chemistry such as pH, conductivity and so on. In this vein, it is deducible that tribocorrosion is a complex and multifactorial subject to which several factors are to be controlled in order to obtain any meaningful information from a single factor.

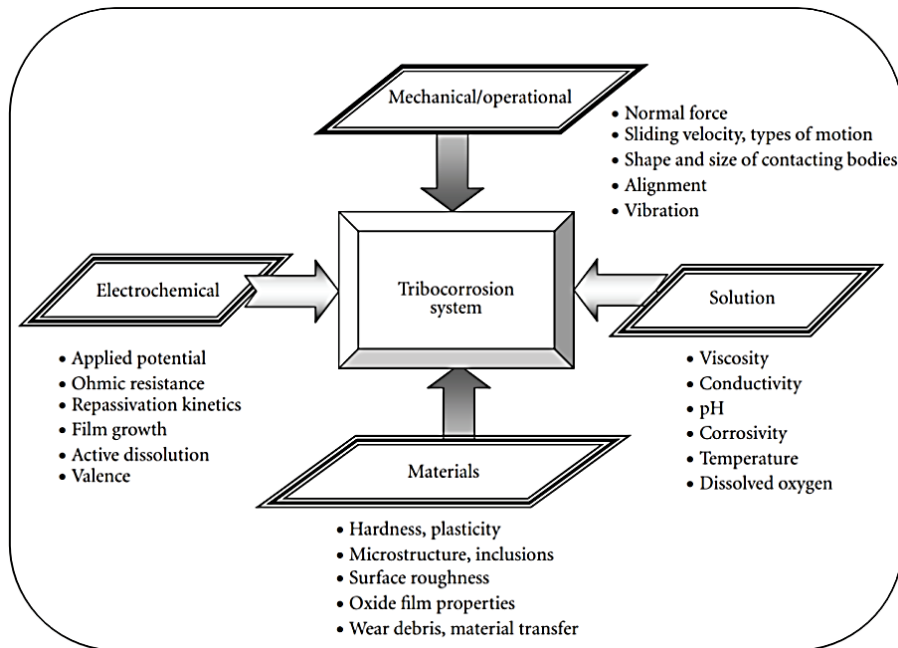


**Figure 3-14 – Considerations of a tribocorrosion systems [137]**

Mischler et al [138] described a model tribocorrosion system in which three distinctive zones experience different degradation mechanisms. Figure 3-15 shows a model wear surface representing a sphere-on-flat reciprocating sliding contact. Zone 'I' is characterised by deformation wear of the contact area – both elastic and plastic deformation of the material occurs in that region leading to the depassivation of the oxide layer. Zone 'II' is a worn region whereby the oxide layer is removed and exposure of the unprotected bulk metal encourages anodic dissolution of the region. The two main damage mechanisms at this region are: detachment of metallic wear particles instigated by crack of oxide layers and accelerated wear enhanced corrosion. Zone 'III' is the mechanically unaffected region. Pure corrosion is the dominant damage mechanism at this region. It is postulated that this region accelerates the pure corrosion occurring in zone II as a result of a galvanic coupling established between the noble zone III and worn zone II. A specific case of tribocorrosion i.e. fretting corrosion in which third-body products have a great effect on the corrosion currents and wear mechanism is discussed in the following sub-section.

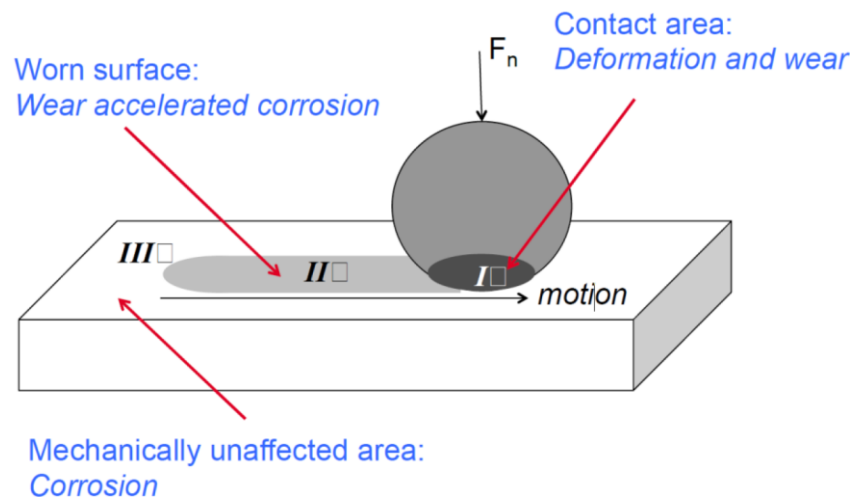


**Figure 3-15 – A model of tribocorrosion system in a sliding contact**  
**[138]**

Stack and Chi [136] developed a criteria by which the degradation mode of a tribocouple in a tribocorrosion system can be predicted based on the ratio of  $M_{chem}$  to  $M_{mech}$  (see Figure 3-16). Although this criteria was developed using a sliding contact, a recent study by Bryant and Neville [139] adopted the

criteria for a fretting interface using a self-mated CoCrMo contact. The study further highlighted the importance of breaking down the contribution of corrosive damage  $C_w$  which is generally attributed to  $M_{mech}$  only into both its mechanical and oxidation components.

Ratio of $M_{chem}/M_{wear}$	Degradation mechanism
$M_{chem}/M_{wear} \leq 0.1$	Wear
$0.1 < M_{chem}/M_{wear} < 1$	Wear–corrosion
$1 < M_{chem}/M_{wear} \leq 10$	Corrosion–wear
$M_{chem}/M_{wear} \geq 10$	Corrosion

**Figure 3-16 – Stack and Chi’s criteria of degradation mechanism in a tribocorrosion system [136].**

### 3.5.1 Tribocorrosion in fretting

Third-body wear and corrosion products form at the interface of material couples in a tribocorrosion system. Often times in a fretting contact, these remain within the interface and thus influence the subsequent tribocorrosion characteristics of interface. In the specific case of fretting corrosion, the influence of third-body products are significant. For example, a material couple in a gross slip fretting regime with relatively large displacement amplitudes can behave quite similar to a reciprocating sliding contact. Therefore, its tribocorrosion characteristics may agree in part with the model shown in Figure 3-15 [104]. However, for a fretting contact, ‘zone I’ in Figure 3-15 would cover a significant proportion of the entire wear scar as depicted earlier in Figure 2-12. Therefore, accumulation of third-body products within the wear scar may significantly reduce the exposed areas (anodic sites) which would have undergone oxidational processes.

The material generated at the fretting contact that are detained at the interface has been found in some studies to influence the electrochemical activity at the interface by reducing fretting corrosion current [110, 140]. In another study which employed electrochemical impedance spectroscopy (EIS), their result showed that polarisation resistance of the fretting interface upon fretting



ceasing was increased thus indicating that the fretting contact is more corrosion resistance after fretting than prior [103].

On the contrary, the formation of third-body objects at the fretting interface may also result in accelerated corrosion current as observed in the study by Landolt and Mischler et al [47]. The study highlighted that the third-body product formed at the interface of their contact was a large particle that was removed from one of the metal surface through an adhesive wear mechanism. This created the exposure of a large anodic site in which oxidation reactions were accelerated. Furthermore, the study highlighted that the accumulation of third-body wear (if unejected) may modify the pressure distribution at the fretting contact thus reducing the rate of mechanical wear as well as reducing the area of unprotected bare metallic surface corresponding to lesser corrosion currents. This shows that the role of third-body products at the fretting interface may be both beneficial and adverse within a tribocorrosion system.

### **3.5.2 Mechanically assisted crevice corrosion**

Mechanically assisted crevice corrosion is the widely accepted mechanism that accelerates the degradation of the modular device in THA. The mechanism was officially named by Gilbert et al [27] although the process had been previously described in part by Collier et al [30]; it agrees with the fundamental processes of crevice corrosion described in section 2.4.2.4. MACC in the context of modular taper junctions of hip prosthesis is initiated by micromotions at the taper interface. The process is described as follows:

- At the initiation of fretting within the modular interface, shear stresses cause the protective oxide films to fracture.
- Oxygen-rich solution migrated into the interface interacts with the freshly exposed bulk metal (which is highly reactive) to restore the oxide layer at the site.
- The repetition of the above process ultimately result in the depletion of oxygen within the crevice while increasing the concentration of free positive metal ions. Depleted oxygen also mean that the region is

unable to repassivate thus metallic dissolution in the region is accelerated.

- Excess of positive metal ions attract EAS such as  $\text{Cl}^-$  to the crevice thus forming metal-chlorides etc.
- Subsequently, the metal-chlorides react with water to form metal-hydroxide and hydrochloric acids thus lowering the pH significantly in the crevice.

### **3.5.3 Repassivation characteristics of CoCrMo and Ti6Al4V**

Studies by Gilbert et al [141], Goldberg and Gilbert [142] characterised the passive layer on Ti6Al4V and CoCrMo alloys respectively, using a scratch test method. Their study observe that for the Ti6Al4V alloy, aeration had little effect on the repassivation mechanism of passive layer once scratched and that higher peak currents were associated with low pH and higher electrochemical potential. The time taken for passive film restoration were also observed to vary with pH and potential. In a similar manner to Ti6Al4V, aeration was found to have no significant effect on the repassivation process of the CoCrMo alloy and this was said to be due to the availability of oxygen through the hydrolysis of water. It was observed for CoCrMo that above a certain potential (300 mV); high peak currents and lower time constants were measured for lower pH of 2 compared to pH 7 thus highlighting the joint effects of lower pH and potential on the repassivation behaviour of CoCrMo.

A general assessment to determine which oxide is restored faster was conducted in 0.9% saline for both Ti6Al4V and CoCrMo and their finding revealed that Ti6Al4V had a ~35% faster surface oxide regeneration time compared to CoCrMo [143, 144]. Two crucial observations from both Gilbert and Goldberg studies highlighted key differences in the passivation behaviour of both alloys in phosphate buffered saline (PBS): a) CoCrMo displayed a transpassive behaviour at 500 mV while no transpassive behaviour was observed for Ti6Al4V b) peak currents were measured for the Ti6Al4V alloy from as early as -700 mV while for CoCrMo this only began between -400 mV and -300mV. The authors concluded that this suggests that corrosion current

is generated from the point of oxide-substrate shear failure for Ti6Al4V whereas, permanent deformation (abrasion) of the oxide from the substrate is required for corrosion current generation in CoCrMo.

### **3.6 Summary**

This chapter has briefly reviewed, from the inception of modularity in THA, the design and challenges associated with the modular taper junction. Analysis of implant retrieval have proven to be a suitable approach for semi-quantitative assessment of the extent of fretting corrosion damage at the modular taper interface. The approach had been useful for identifying several factors and trends related to fretting corrosion i.e. material combinations, implantation time, stiffness and so on. However, retrieval studies are limited, as the insight it offers into the outcomes of several mechanical and electrochemical processes occurring *in-vivo* may be regarded inadequate. Thus, it is from this point that *in-vitro* studies may prove necessary for identifying *in-situ* wear and corrosion mechanisms. The studies would be specifically designed to elucidate the role of individual factors that contribute to the multi-factorial problem of fretting corrosion. Although the review of both tribometer and realistic taper component assessment of fretting corrosion had highlighted the following: effect of pH, contact loads, surface topography, impaction force and many more, there are yet still several gaps to be filled through an *in-vitro* approach. The subsequent section details the gaps that are still present in literature.

#### **3.6.1 Gaps in literature**

- A study conducted using a fretting tribometer will prove much cheaper than those conducted at component level. However, to the best of this review, no study using a tribometer has been able to replicate the composite contact condition of the modular taper in order to generate the diverse forms of corrosion products seen on explants. Successfully

achieving this may prove economically beneficial for assessing THA wear and corrosion mechanism.

- Retrieval studies have highlighted (to an extent), mechanical and corrosion contributions that may lead to the *in-vivo* fracture of titanium alloys. However, a mechanistic *in-vitro* study assessing various fretting regimes and contact conditions of materials couples involving titanium alloy are not well studied. Such study will help to better understand the mechanical contributions and the corresponding electrochemical response to localised corrosion which may be contributing to titanium fracture.
- No study has been found that has correlated fretting regime and interfacial wear mechanisms to the metallurgical transformations occurring in the subsurface of CoCrMo and Ti6Al4V. Moreso, only a few studies have assessed the subsurface degradation of both alloys from a retrieval studies.
- The principle of tribocorrosion and the mechanisms associated such as the effect of third-body have been studied for several materials. However these are commonly in sliding conditions. Exploring the synergistic effect of wear and corrosion as well as understanding the contact conditions that optimises synergistic behaviour or antagonistic effects within a fretting interface is very much lacking in literature.
- Several studies have applied the Goldberg fretting score to semi-quantitatively characterise the degree of fretting corrosion damage in metal – metal and ceramic – metal systems. Other techniques such as volumetric loss have also used for comparison purposes. However, there is still a need for an *in-vitro* assessment of the tribocorrosion characteristics of these two systems under various loading conditions which represent DLA. Perhaps, the effect of replacing a metallic bearing with a ceramic one on fretting corrosion can be elucidated.

## **Chapter 4 Experimental methodology and surface analytical techniques**

### **4.1 Introduction**

This chapter outlines the experimental methods and analytical techniques employed in this research. It provides detailed protocol and rationale for the tribocorrosion experiments, surface and subsurface analyses undertaken in this study. The fundamental theories pertaining to each technique are also summarised in this section.

### **4.2 Experimental materials**

The two metallic alloys studied in this thesis are namely: wrought low carbon Co28Cr6Mo and Ti6Al4V. These are abbreviated to CoCrMo and Ti6Al4V respectively. The ceramic materials are namely: BioloX<sup>®</sup> (BioloX) and Si<sub>3</sub>N<sub>4</sub>. All tests were conducted in protein containing physiological solution as outlined in the sub-section below.

#### **4.2.1 Metallic and ceramic sample preparation**

CoCrMo and Ti6Al4V alloys used for ball and flat components were wrought manufactured according to the specifications in ASTM F 1537 and ASTM F 136 outlined in Table 2-1 and Table 2-2 respectively. The materials were supplied as a 25 mm diameter bar which were cut into plates (flats) of 6 mm thickness and the CoCrMo femoral heads were 28 and 36 mm diameter. For the assessments involving realistic taper components, the alloys were supplied as 12/14 taper spigots with 0 mm offset by *Aesculap, Germany*. The manufactured CoCrMo heads were highly polished to a roughness ( $R_a$ ) < 0.02  $\mu\text{m}$ . The surface of the 6 mm flats after being cut were firstly grounded using Silicon carbide grinding paper then polished to a mirror finish ( $R_a$  < 0.02  $\mu\text{m}$ ) using a 3  $\mu\text{m}$  diamond paste and polishing paper by *Bruker Corporations, UK*.

Commercially available G28 Si<sub>3</sub>N<sub>4</sub> ball bearing with a maximum R<sub>a</sub> of 0.05 μm and diameter of 25.4 mm (1 inch) was purchased from *R&M bearings, UK*. The polished Si<sub>3</sub>N<sub>4</sub> plate had a maximum R<sub>a</sub> of 0.08 μm and was purchased from *Keranova AB, Sweden*. Femoral Biolox heads of 28 and 36 mm diameter, manufactured to an ultra-smooth R<sub>a</sub> of 0.002 μm were purchased from *Aesculap, Germany*. The 28 mm diameter CoCrMo and Biolox heads were only used for the tribometer studies and the 36 mm heads for the taper cyclic loading tests.

#### **4.2.2 Test environments and lubricants**

All tests were conducted in 25% (v/v) diluted Foetal Bovine Serum (FBS), *Seralab, UK*, in part reference to BS ISO 14243-3:2004. 0.03% (v/v) Sodium Azide, *G-Biosciences, USA*, was added to the solution in order to slow down the growth of bacteria during the long-term cyclic fatigue tests. The solution was balanced with isotonic phosphate buffer saline (PBS), *Sigma Aldrich, UK* to represent the osmolality and ion concentration of the human joint fluid. The pH of the solution was 7.6. A list of ionic and protein contents can be found Appendix A.

### **4.3 Electrochemical technique**

Throughout this study, *in-situ* electrochemical measurements were utilised to characterise the corrosion mechanisms of fretting interfaces in both metal – metal and ceramic – metal fretting contacts. The *Autolab PGSTAT101, Metrohm, Switzerland* and the *CompactStat, Ivium technologies, Netherlands* potentiostats were used in two separate studies. The potentiostat connects to a 3-electrode cell which comprises of: the working electrode (WE) – where connections were taken from the metallic alloys (CoCrMo and Ti6Al4V) in the experimental set-up; the reference electrode (RE) – Ag/AgCl (+ 0.196V vs. Standard Hydrogen Electrode (SHE)); and the counter electrode (CE) – platinum plate. In this study, the RE and CE exist as a single device – the *Thermo Fisher Scientific Sureflow REDOX* electrode. Experiments performed

under OCP conditions require the WE and RE only whereas, all three electrodes are required for the potentiostatic tests. The *Autolab* potentiostat was controlled using the licensed software *Nova 10.1* and the licensed *Ivium soft* was used for the *CompactStat*.

#### **4.3.1 Open circuit potential measurement**

The value of OCP is often used as a qualitative indication of the corrosion regime that a metal is in that is, either it is in an active state or a passive state. In the context of tribocorrosion, the value of OCP is indicative of the galvanic coupling between the passive (unworn) site and the depassivated (worn) site of the metallic interfaces involved in the contact [145]. The passive region is mainly dominated by cathodic reactions while the depassivated region is dominantly anodic reactions. Furthermore, the value of OCP for a mixed-metal contact i.e. CoCrMo and Ti6Al4V alloys rubbing against each other represents the sum of galvanic coupling occurring between the worn and unworn regions of both alloys. As each alloy has a different electrode potential, the OCP is a composite of several galvanic interactions. The OCP as an electrochemical technique does not provide information regarding the reaction kinetics. However, the following are theoretical parameters that affect the OCP measured in a tribocorrosion system [146].

- Characteristic corrosion potential of worn and unworn surfaces
- Ratio and position of the worn area relative to the unworn
- Kinetics of electrochemical reactions

#### **4.3.2 Potentiostatic polarisation**

In a potentiostatic test, a fixed potential (anodic or cathodic) is imposed onto a material using the 3-electrode cell. The tribocorrosion characteristics of a material can be assessed under anodic or cathodic conditions. For the anodic condition, an anodic current is generated by applying an over-potential (positive potential above the OCP) to the metallic sample prior to rubbing. On the other hand, a cathodic current is generated by applying a negative

potential below the OCP. At very high cathodic potentials, the material's ability to repassivate is suppressed thus allowing the wear characteristics of the material to be assessed. In this study, fretting tribometer and cyclic fatigue loading tests were conducted under anodic polarisation of 0V vs Ag/AgCl. Potentio-dynamic studies [147, 148] have shown that both CoCrMo and Ti6Al4V may exist in their passive region in serum containing solutions at 0V. Thus, the potential was deemed suitable for the assessment of fretting corrosion currents in this study.

Anodic current measured as a function of time was used to monitor the mechanical depassivation and repassivation characteristics of the various material combinations. Figure 4-1 shows a typical Current vs. Time plot during a tribocorrosion test. At the point of potentio-static polarisation, the current rapidly rises before decreasing exponentially. The peak of the anodic current is the ' $I_{max}$ '. Subsequently, the current tends to zero ( $I \rightarrow 0$ ) as the time tend to infinity ( $t \rightarrow \infty$ ). The area shaded in blue corresponds to the 'Pure corrosion' C. At the initiation of fretting, anodic reactions become dominant for as long as fretting persists. The area encapsulated between the pure corrosion current and the fretting current is cumulative charge representing the wear enhanced corrosion ( $W_c$ ) + an unknown proportion of corrosion enhanced wear denoted ' $\alpha C_w$ ' (see section 8.6 for detailed discussion).

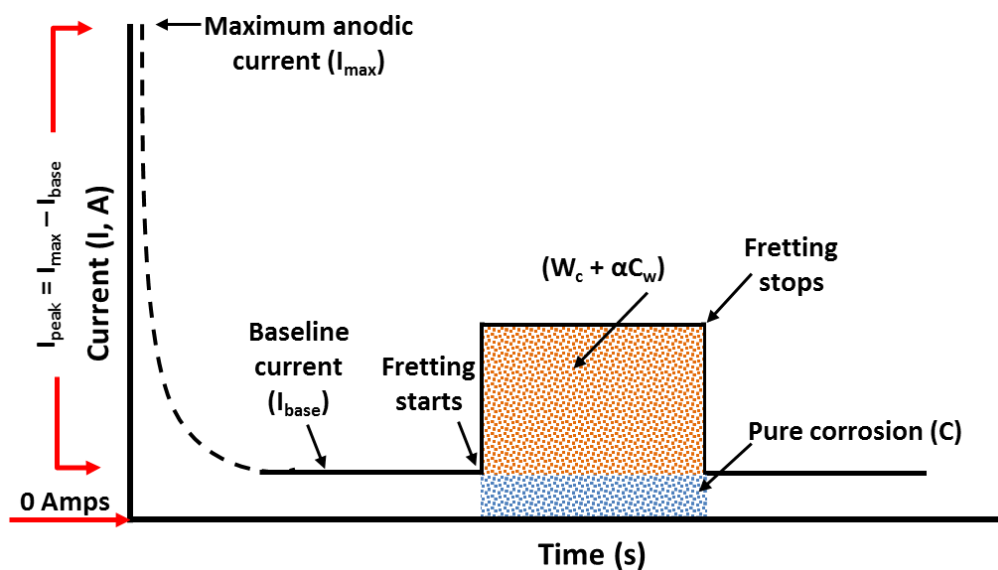


Figure 4-1 – Schematic representation of a tribocorrosion current – time plot.



## 4.4 Experimental set-up

This section details the tribocorrosion tests set-up for both tribometer studies and assessment of realistic taper component. A sample size of  $n = 3$  was conducted across all studies except otherwise stated. Error bars where used, represent standard error of the mean.

### 4.4.1 Fretting tribometer with in-situ electrochemistry

The tribometer used in this study was a custom built fretting rig based in the *School of Mechanical Engineering, University of Leeds, UK*. A schematic representation of the tribometer is shown in Figure 4-2; the rig is controlled using *LabView* programming software, *National Instruments, UK*. The required displacement is manually entered into the program and so also, the normal load is applied manually. Fitted electro-mechanical actuator from *Data Physics Corporations, UK*, applies the desired displacement and the axial displacement of the cantilever is measured through a metal plate positioned in front of the fibre optic displacement sensor which is directly connected to the load cell and shaft of the actuator. The displacement sensor is located on a linear stage and the information collected through it is fed back to ensure the actuator reaches a steady state at the desired displacement. The actuator is capable of applying reciprocal motion at frequencies ranging from 1 – 30 Hz. The load cell by *Kistler, USA* was used to monitor the horizontal tangential forces ( $F_t$ ) during reciprocal fretting.

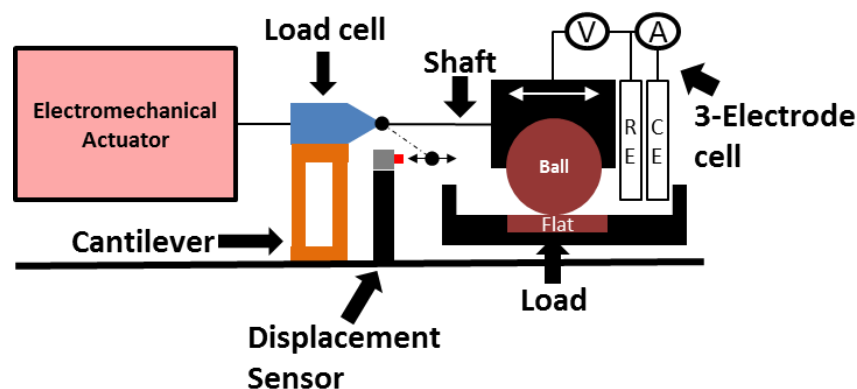
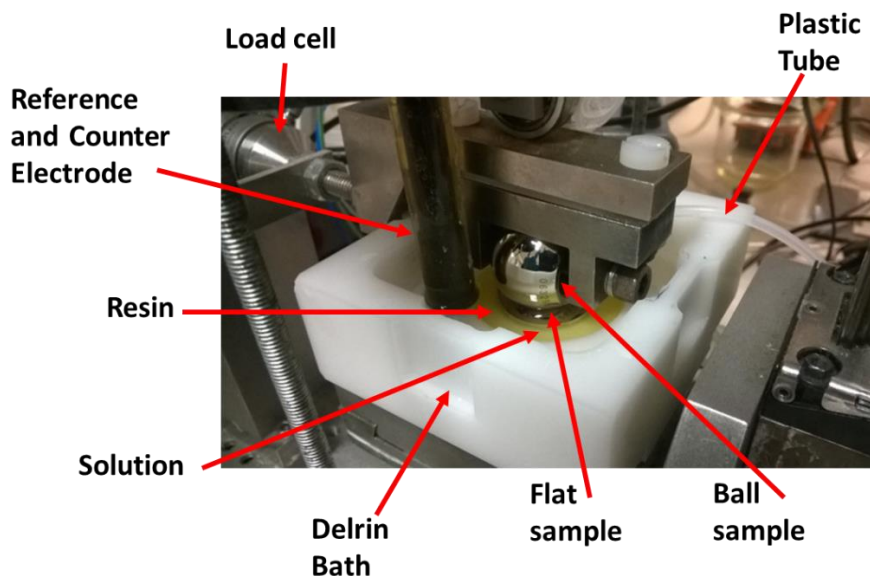


Figure 4-2 – Schematic diagram of the fretting tribometer

Figure 4-3 shows an image of the tribocorrosion test set-up. A delrin bath holds the physiological solution – a volume of 12 – 14 ml which ensures the ball and flat point contact is totally immersed in the solution. The solution is kept at a temperature of  $37 \pm 2^\circ\text{C}$  throughout all tribometer studies. A peristaltic pump is used to circulate hot water from the beaker of water on a thermocouple controlled hotplate. The thermocouple is positioned inside the solution to ensure the solution is constantly at the desired temperature.

The flat metallic/ceramic sample is centred into the bath; flatness is then verified using a spirit level. Due to the unpolished sides of the sample, and in order to ensure that there are no electrochemical activities between the unpolished sides of the sample and the polished surface, a *VariDur 10, Buehler, UK* acrylic resin was allowed to firmly set around the sides of the sample leaving only the flat surface of the sample exposed. Moreover, the hard resin formed a circumferentially secured fixation of the flat component, thus eliminating relative motion of the flat component during fretting. Once the resin is fully set, the surface of the flat components were wiped with acetone; this was to ensure that part of the polished metallic surface was not stained with dried acrylic resin.



**Figure 4-3 – Image of the fretting corrosion tribometer set-up**

#### 4.4.2 Tribometer fretting corrosion studies (test protocol)

The two electrochemical techniques employed for the tribometer studies are OCP and potentiostatic. In both conditions, a ball-on-flat configuration was used to model a point contact. A maximum contact pressure ( $P_{max}$ ) of 1 GPa was used across all tribometer studies except in one instance where  $P_{max}$  of 0.77 GPa was used specifically to attain a gross slip fretting regime. The use of a relatively high  $P_{max}$  to model the modular taper were for the following reasons: a) to establish a large asperity-asperity contact which would generate to a reasonable volume of wear in the short-term 6000 cycles test; b) to ensure sufficient pressures which will facilitate a crevice environment by trapping cumulated wear and oxidised products. The crevice environment is expected to establish a subsequent chemical transformation of metal-oxides. c) encourage *in-vitro* subsurface transformations in the metallic alloy that may take years of fatigue loading *in-vivo*. Other studies have taken a similar approach for a ball-on-flat configuration and applied pressures up to 4.2 GPa [105]. The contact half-width 'a' established from the least compliant material combinations to the most compliant combinations ranged between 120 – 250  $\mu\text{m}$ .

The displacement amplitudes assessed were:  $\pm 10 \mu\text{m}$ ,  $\pm 25 \mu\text{m}$ ,  $\pm 50 \mu\text{m}$  and in the case of CoCrMo – CoCrMo and CoCrMo – Ti6Al4V, an extra displacement ( $\pm 150 \mu\text{m}$ ) was tested. Through the diverse displacement amplitude, all material combinations were assessed under various fretting regimes, including transitional regimes such as the 'mixed regime'. The largest displacement amplitude ( $\pm 150 \mu\text{m}$ ) was specifically tested in order to understand the fretting corrosion behaviour of the metal – metal couple at very large displacements. In the case of CoCrMo – CoCrMo,  $\pm 150 \mu\text{m}$  was very close to the limits of its Hertzian contact half-width 'a'; in other words, it was on the verge of transitioning into a reciprocal sliding contact where the value of 'e' is close to 1. Table 4-1 presents an outline of the fretting contact parameters used in all the tribometer studies. Determination of cumulative energy, slip ratio and transition criteria are based on fundamental work by Fouvry et al [149].

**Table 4-1 Fretting contact parameters**

	Fretting contact parameters		
<b>P<sub>max</sub> for all combinations</b>	1 GPa ( <i>except for the case of BIOLOX – Ti6Al4V where 0.77 GPa was used to attain a gross slip regime</i> )		
<b>Corresponding loads and contact half-width for each material combination</b>		Load (N)	'a' (µm)
	<b>CoCrMo – CoCrMo</b>	50	160
	<b>CoCrMo – Ti6Al4V</b>	120	250
	<b>Si<sub>3</sub>N<sub>4</sub> – CoCrMo</b>	35	130
	<b>Si<sub>3</sub>N<sub>4</sub> – Ti6Al4V</b>	85	200
	<b>Si<sub>3</sub>N<sub>4</sub> – Si<sub>3</sub>N<sub>4</sub></b>	30	120
	<b>Biolox – CoCrMo</b>	40	140
	<b>Biolox – Ti6Al4V (1 GPa / 0.77 GPa)</b>	110 / 50	230 / 180
<b>Fretting displacements</b>	±10 µm, ±25 µm, ±50 µm and ±150 µm ( <i>±150 µm was only tested for CoCrMo – CoCrMo and CoCrMo – Ti6Al4V</i> )		
<b>Frequency</b>	1 Hz		
<b>No. of Cycles</b>	6000 (OCP) and 2000 (potentio-static)		
<b>Repetitions</b>	n = 3 ( <i>except for Biolox fretting contacts which had n = 1</i> )		

#### 4.4.2.1 Fretting corrosion protocol (OCP conditions)

The tribocorrosion experiments reported in chapters 6 and 7 of this thesis were carried out under OCP conditions. Figure 4-4 shows the schematic of a typical OCP trend for a large displacement tribocorrosion system. The protocol used for this study is incorporated in the schematic diagram and is represented as stages. OCP was monitored throughout the three stages of the test at an acquisition rate of 1 point per second. In 'stage 1' the 'Initial Surface Potential' may rise (ennoblement) or decline. However the direction, the purpose of this stage is to permit the loaded contact to equilibrate.

Once fretting has started, a sharp potential shift in the negative direction (cathodic shift) may or may not occur. This depends on the amplitude of the displacement and the applied load. The cathodic shift shown in Figure 4-4 is given the term '*Depassivation potential*'. The potential measured subsequent to the depassivation potential is termed the '*Fretting potential*' i.e. '*Stage 2*'. This may behave either of four ways: rise (ennoble), remain constant, decline or a consecutive occurrence of the previous three. As soon as fretting ceases in '*Stage 3*', the recovery stage may be manifested in two ways: a sharp rise in the '*Repassivation potential*' followed by a slower surface ennoblement termed the '*Final surface potential*' or depending on the rate of the '*Repassivation potential*', the two parts of the recovery stage may occur as one whole recovery stage. The pattern observed in the OCP across the three stages is often indicative of the corrosion regime of the material couple. The maximum (Max.) cathodic shift is determined as the magnitude of the most negative potential during fretting relative to the noblest potential from the initiation of fretting.

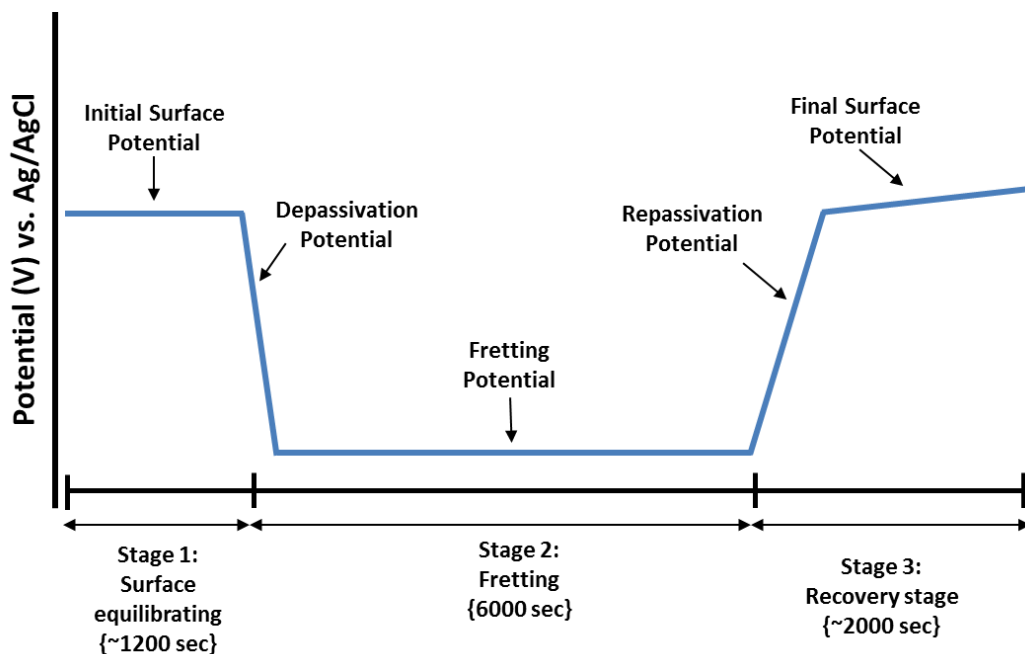


**Figure 4-4 – Schematic diagram of fretting corrosion protocol under OCP conditions**

#### 4.4.2.2 Fretting corrosion protocol (potentio-static conditions)

Tribocorrosion tests under potentio-static conditions were conducted for better understanding of the effect of surface history on the fretting corrosion behaviour of THA *in-vivo*. The tests were conducted on self-mated CoCrMo combination only and the results are presented in Chapter 8 of this thesis. An anodic polarisation potential of 0V vs. Ag/AgCl was applied and the data acquisition rate for the fretting current was 1 current point per second.

Figure 4-5 shows a schematic diagram of the fretting corrosion experiments conducted. The same contact conditions for CoCrMo – CoCrMo outlined in Table 4-1 were also applied in this test. However, the overall protocol were carried out using three methods:

- In 'Method 1' 2000 cycles of fretting (1 Hz) were carried out for each displacement amplitude ( $\pm 10 \mu\text{m}$ ,  $\pm 25 \mu\text{m}$ ,  $\pm 50 \mu\text{m}$  and  $\pm 150 \mu\text{m}$ ). Prior to each test, 4000 seconds of equilibrating period was permitted in order to allow the current transient to be as close to '0 amps' as possible.
- In 'Method 2', the tests were conducted for the same displacements as in method 1. However, in this case, the tests were performed in series, in the increasing order of  $\pm 10$ ,  $\pm 25 \mu\text{m}$ ,  $\pm 50 \mu\text{m}$ ,  $\pm 150 \mu\text{m}$  with an incorporated rest period of 500 seconds after each displacement amplitude.
- 'Method 3' follows the same process as method 2, however, in this case the tests were conducted in a decreasing order ( $\pm 150$ ,  $\pm 50 \mu\text{m}$ ,  $\pm 25 \mu\text{m}$ ,  $\pm 10 \mu\text{m}$ ).

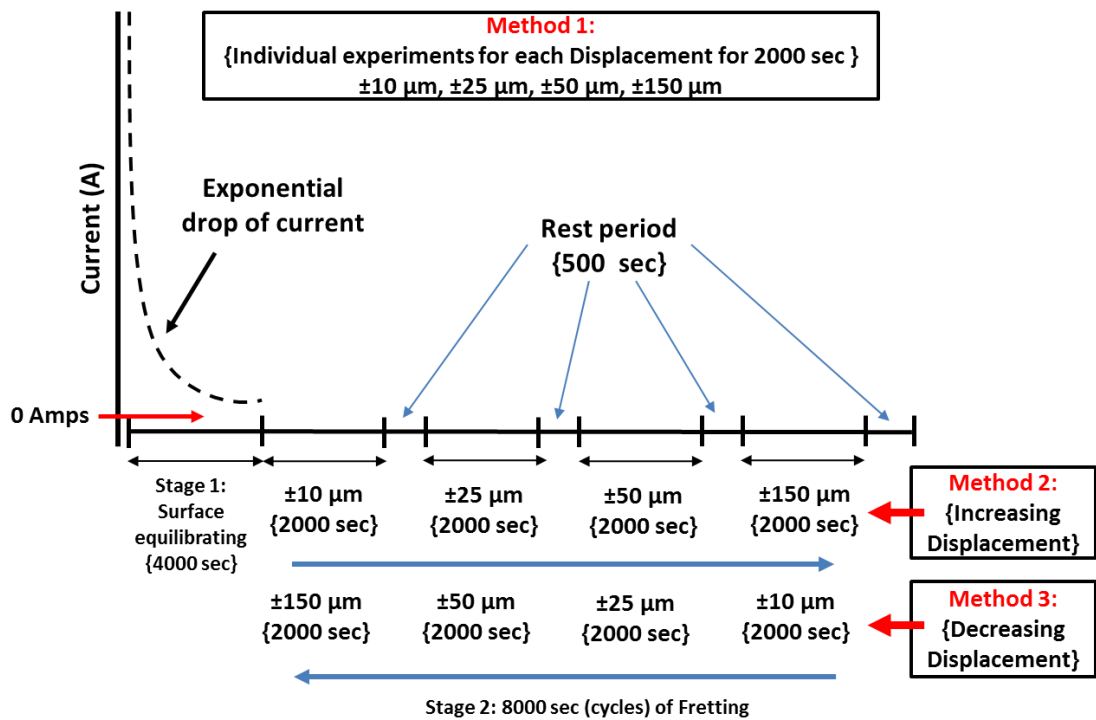


**Figure 4-5 – Schematic diagram of potentiostatic fretting corrosion protocol**

#### 4.4.2.3 Calculations

Tribocorrosion mass loss was determined using Faradays equation expressed in Equation 2-4. The charge 'Q' was determined by integrating the area underneath the fretting current transient as depicted in Figure 4-1. The molar mass 'M' was determined as the stoichiometric average wt% composition for CoCrMo alloy and the valence 'n', thus giving a value of 55.7 gmol<sup>-1</sup> for M and 2.4 for n respectively. These values are similar to those used in others studies for CoCrMo [108, 150].

The contribution of mass loss due to pure corrosion 'C' was determined by firstly establishing an estimated total area of the ball and flat components that were in contact with the solution, thus contributing to the pure corrosion. The estimated area was 11.9 cm<sup>2</sup>. However, as the total mass loss was only measured from the fretting wear scar, the largest fretted area from both ball and flat components was for the largest displacement amplitude which was ±150 μm; this was estimated to 7 x 10<sup>-3</sup> cm<sup>2</sup>. Note, the pure corrosion

contribution to the total mass loss is estimated using the fretted area rather than the total exposed metallic surface area. The result of this calculation are tabulated in Chapter 8.

### 4.4.3 Fatigue loading set – up with in-situ electrochemistry

#### 4.4.3.1 Component assembly

For this study, the *ElectroPuls™ E10000*, Instron, UK was used to apply static assembly force and fatigue cyclic load unto a geometrically relevant head-neck taper material combination. The machine is capable of applying  $\pm 7$  kN of static force and  $\pm 10$  kN of dynamic force at a frequency up to 100 Hz. A *Dynacell™* load cell is connected to the crosshead of the machine and is capable of measuring load of  $\pm 10$  kN and  $\pm 100$  Nm.

In this set-up, spigots of CoCrMo and Ti6Al4V alloys (see Figure 4-6a) were used to represent the neck of the femoral stem component in hip prosthesis. The spigot has a 12/14 micro-grooved taper whereby  $R_z$  ( $R_p + R_v$ ) is  $\sim 12 \mu\text{m}$ . The femoral heads were 36 mm sized ceramic and metal head namely: Biolox and CoCrMo respectively. The tapers were assembled with a quasi-static assembly load of 2 kN according to ASTM F 1875 – 98, at a rate of 1 kN per second. An image of the static loading procedure is shown in Figure 4-6b. In order to minimise the possibility of misalignment, a spirit level is used to ensure flatness of the spigot prior to a 50 N preload. The purpose of the preload was to further ensure an aligned engagement of the taper is established before the 2 kN load is applied. The heads were also pulled off using the same set up; the dowel (shown in the picture) was used to fasten the spigot down while the pull-off force is being applied. Figure 4-6c shows an example of how the taper separation force (pull-off force) is determined.



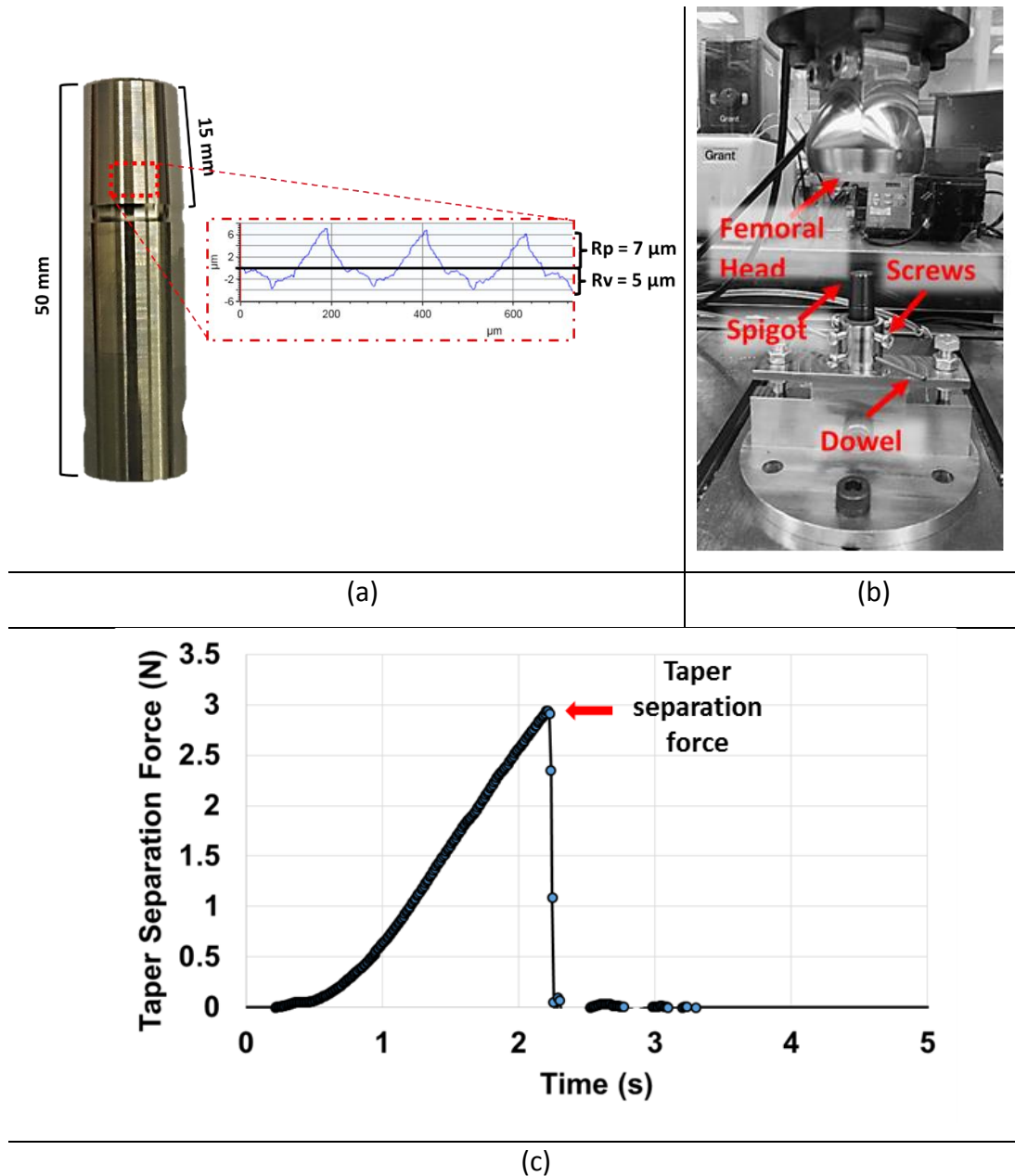


**Figure 4-6 – Taper assembly: a) Dimension of spigot and surface profile of the grooved taper, b) assembly and pull-off method, c) an example of the taper separation force.**

#### 4.4.3.2 Component tribocorrosion cell

Figure 4-7 shows the set-up used for the fatigue study. The orientation of the spigot holder was designed according to ISO 7206-4:2010 which prescribes a  $10^\circ$  adduction and  $9^\circ$  flexion ( $\beta$ ). The head – neck angle ( $\alpha$ ) used was  $135^\circ$  based on other tribocorrosion studies with similar fatigue set-up [101, 119].

The assembled taper interface was exposed to 85 mL solution which covered the femoral head up to the line denoted 'J'. The plastic-metal interface identified as 'E' was isolated from the physiological solution by the use of silicon sealant. The test was conducted at room temperature ( $20\pm 2^\circ\text{C}$ ) which minimised the amount of solution evaporated over the 2.5 days of dynamic loading. The WE for the electrochemical connection was taken from the bottom of the male spigot 'C' and both RE and CE were suspended in the solution in close proximity to the taper interface 'B' thus ensuring accurate electrochemical measurements.

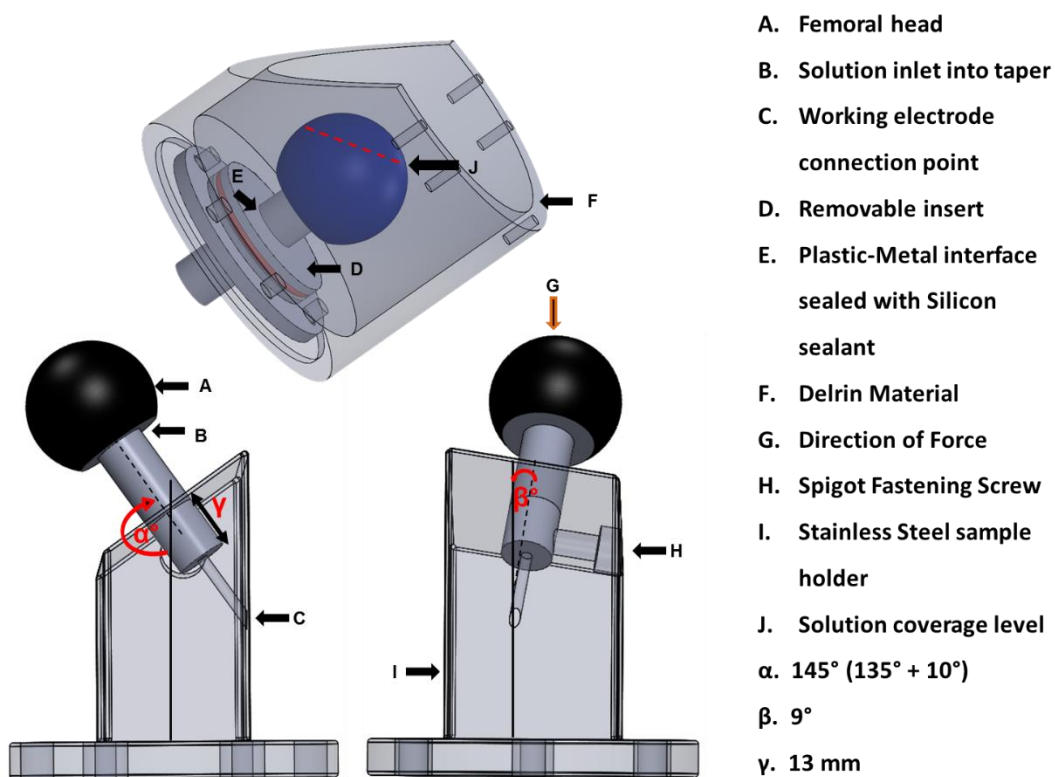


**Figure 4-7 – 3D representation of the fatigue set-up for assessing fretting corrosion of realistic taper geometry.**

#### 4.4.3.3 Fatigue loading (test protocol)

The fatigue loading tests were performed under potentiostatic conditions for four material combinations namely: CoCrMo – CoCrMo, CoCrMo – Ti6Al4V, Biolox – CoCrMo and Biolox – Ti6Al4V. Thus, both metal – metal and ceramic

– metal realistic taper interfaces are studied. Various loading conditions were performed in a series of stages as shown in the schematic diagram of Figure 4-8. In ‘Stage 1’ the system was allowed to equilibrate for 1500 seconds whilst under a static load of 0.3 kN and during which OCP was monitored. Subsequently, anodic potential of 0V vs. Ag/AgCl was imposed onto the system and allowed to equilibrate for at least, another 7500 seconds. In this time, the current drops exponentially and theoretically reaches zero at time  $(t) = \infty$ . ‘Stage 2’ is the beginning of the dynamic loading; three frequencies (1, 2 and 5 Hz) were evaluated consecutively at a constant compressive load of 1.8 kN and cyclic load of 3 kN (standard ASTM F 1875 – 98 profile). However, as the loading condition changes from one profile to the next, 2000 seconds of rest period is permitted in order to ensure adequate repassivation before the next loading profile is actuated.

In-between the stages, a standard ASTM F 1875 – 98 loading profile is applied for 5000 cycles at a frequency of 1 Hz in order to monitor possible systemic effects at the taper interface. Such effects may influence the measured fretting current for the subsequent loading profiles within the series. Nevertheless, the systemic effects were minimised by testing the highest cyclic loads (which is expected to inflict the greatest fretting micromotion) last in ‘Stage 4’. In ‘Stage 3’ fretting corrosion current for an increasing mean compressive load (0.8, 1.8, 2.8 kN) with minimal effect of cyclic loads is assessed –  $\pm 0.5$  kN cyclic load was used for this stage of assessment. In ‘Stage 4’ the effect of cyclic loading ( $\pm 0.5$ ,  $\pm 1.5$  and  $\pm 2.5$  kN) at a mean compressive load of 2.8 kN at 1 Hz was assessed. Fretting current sampling rate were 1 point per 5 seconds for  $n = 2$  test and a higher resolution of 10 points per second for  $n = 1$  of the tests.

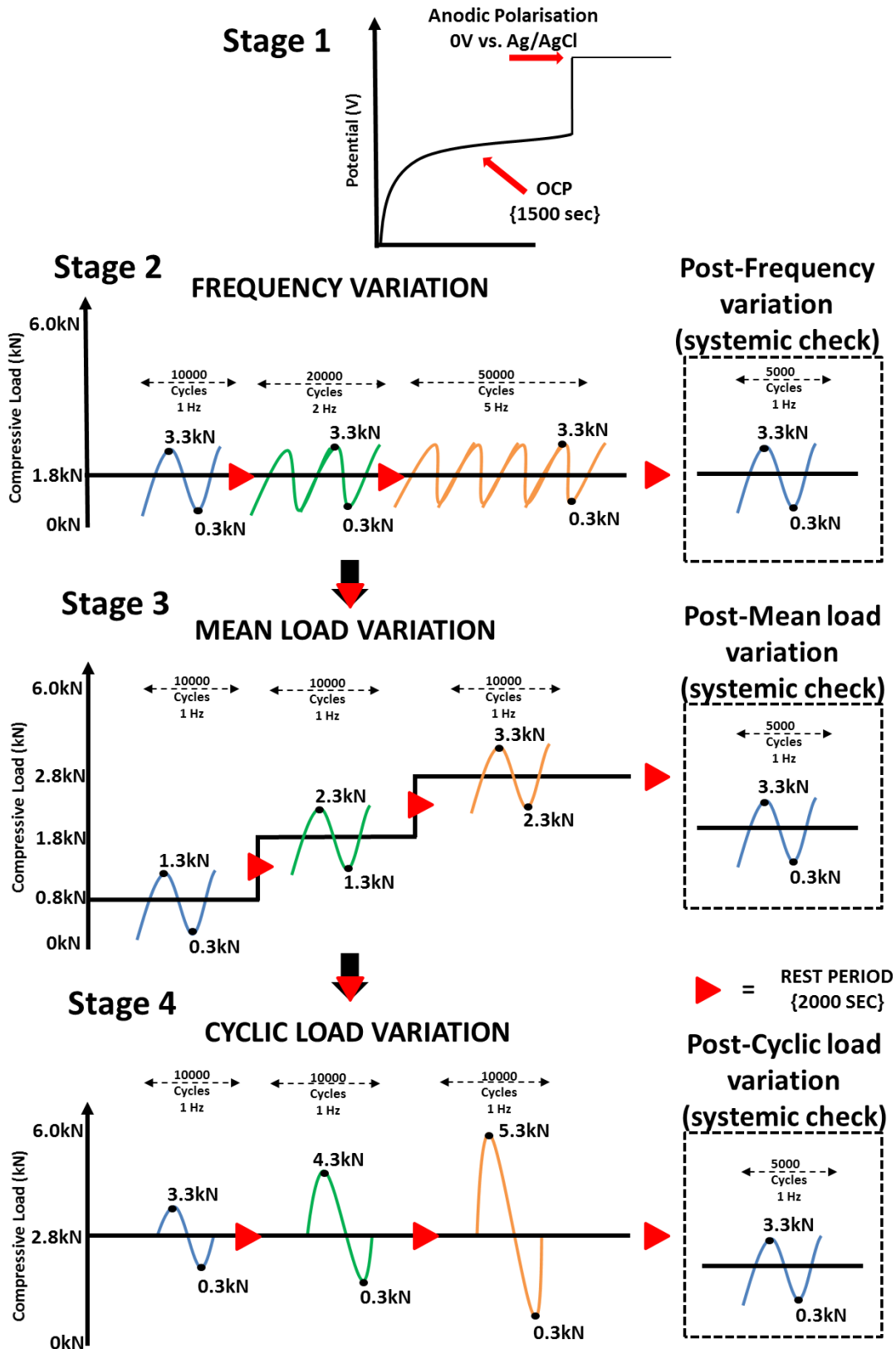


Figure 4-8 – Protocol for fatigue loading tests on realistic taper components

## **4.5 Surface, sub-surface and chemical analysis**

### **4.5.1 Optical light microscopy**

The Leica DM6000 M optical light microscope was used to capture a cross-sectional image of the Resin-Redistributed wear-Ti6Al4V interface prior to nano-indentation tests of the redistributed wear piled-up in the wear surface. The 2D image stacking feature was used to obtain a good contrast for depressed regions within the surfaces of the interfacial structure.

### **4.5.2 White light interferometry (WLI)**

3D optical profiler *NPFLEX* by *Bruker Corporations UK* is a non-contact surface measurement technique which uses white light interferometry technology. The white light is split into two beams; the beam splitter directs one beam towards the reference mirror while the other beam is directed towards the sample being visualised. Subsequently, the beams are recombined to form an interference pattern which are analysed to examine the optical path difference (in length) of the two beams. The technique was used in this study to obtain 2D quantitative measure of wear scar depth, 3D surface topography and the quantitative measure of volume losses. Analysis were carried out using the licenced *Vision 64* software by Bruker.

The wear volume from the fretting contact of the ball and flat components were determined according to the methods outlined by Fouvry et al [151]. Two procedures (outlined below) were used for the estimation of volume loss in this study. Procedure 1 considers 'wear' as the loss of matter from the wear surface and thus, this procedure was used for all the material combinations whereby redistributed wear is minimal. All material combinations tested in this study are aligned with this description except for the material couples involving Ti6Al4V. For these, wear volume was estimated using Procedure 2. In most cases, wear at the interface of material couples involving Ti6Al4V are redistributed within the contact thus giving a near-zero 'loss of matter'. Therefore, for these interfaces, the sum of the negative volume ( $V^-$ ) is the

estimated wear. This assumes that the material redistributed ( $V^+$ ) in the contact originated from the wear depths i.e. the volume below the zero-axis ( $V^-$ ) as depicted in Figure 4-9. However, the limitation of Procedure 2 is that, the redistributed volume below the zero-line is not accounted for as shown in Figure 4-9.

Procedure 1: Wear volume =  $(V^- - V^+)_{ball} + (V^- - V^+)_{flat}$

Procedure 2: Wear volume =  $(V^-)_{ball} + (V^-)_{flat}$

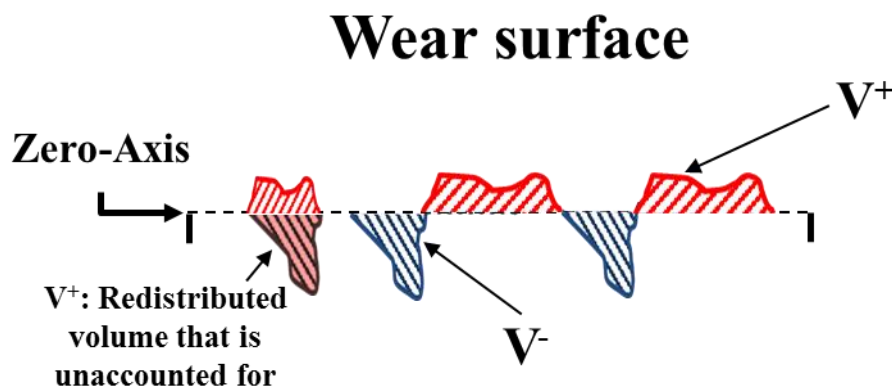


Figure 4-9 – Schematic for determining wear volume

### 4.5.3 Scanning electron microscopy (SEM)

The *Carl Zeiss EVO MA15* scanning electron microscope (SEM) was used for surface analysis in this study. High resolution micrographs and surface characteristics to the nano-meter (nm) scale of worn metallic surfaces were obtained. SEM offers a higher resolution than conventional light microscopes because the wavelengths of electrons bombarded at the sample can be several orders of magnitude smaller in SEM. Images may be obtained in secondary electron (SE) mode where electrons fired at atoms on the specimen surface knocks out an electron in the atom which is then scanned to create an image. The other mode is the back scattered electron (BSE) mode, in this technique, the fired electrons that experienced elastic collision with atoms on the sample surface are scanned to obtain a back scattered image. The BSE technique is also capable of producing a contrasted image

which gives an indication of the relative molecular weight of compounds present on surfaces. For example, on a BSE micrograph image, objects on a surface that have a lower molecular weight appear much darker than those with larger molecular weight. All SEM images in this study were captured in BSE mode at 20 k eV.

#### **4.5.4 Focused ion beam (FIB)**

Focused ion beam (FIB) is a sample preparation technique used in this study for further electron microscope characterisation using the transmission electron microscope (TEM). Tribocorrosion products and metallurgical transformations of the metallic samples were characterised using the TEM. It was anticipated that subsurface metallurgical transformation of the alloys would be site-specific considering that while certain regions of a fretting contact may experience a stick behaviour, another region may experience gross sliding. Thus, considering the composite contact phenomenon in fretting, it is important to obtain samples from a consistent region across all material combinations and displacement amplitudes as much as possible.

Figure 4-10 shows the stress distribution for an elastic contact of a ball-on-flat configuration plotted by Vingsbo and Schon [42]. The material used to generate the plot in their study was Copper and it is observable Max. traction force is ~63% away from the centre of the Hertzian contact. While the region of Max. traction force is expected to vary across various material combinations, 3D surface profilometry of the flat component may be used to estimate the region. The region of Max. traction force is expected to be the deepest region in the worn annulus of a fretting contact. Therefore, in this study, 3D profilometry was used as a guide for selecting the region FIB samples were obtained from, thus allowing for consistency. In some special cases, samples were directly obtained from regions of interests. These are: areas covered in redistributed tribocorrosion wear products and areas with surface cracks.

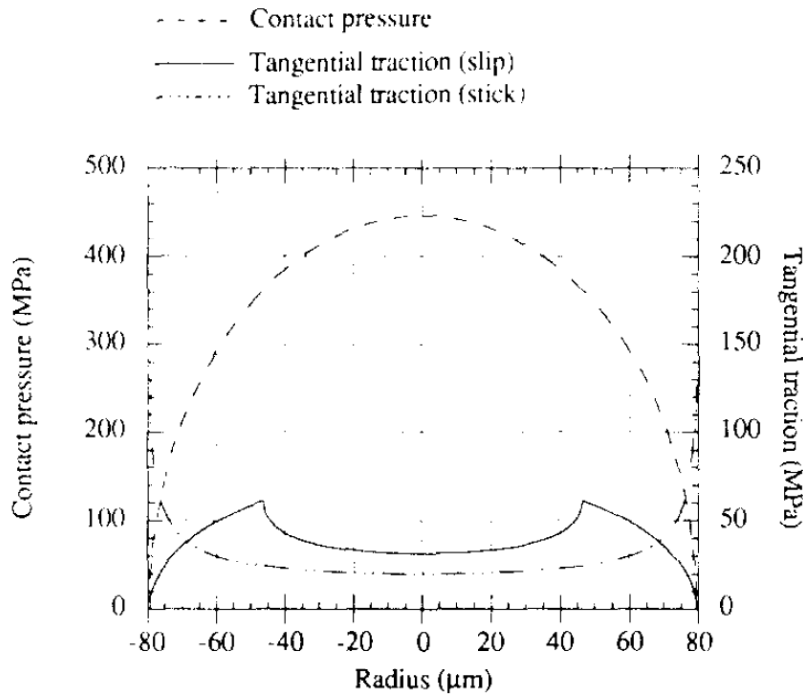


**Figure 4-10 – Elastic contact stress pattern for a ball-on- flat contact**  
**[42]**

An *FEI Nova200 Nanolab dual beam FIBSEM* equipped with a Kleindiek micromanipulator was used for the sample preparation. The key steps taken in the process are outlined as follows:

1. The area of interest of dimension  $\sim 15 \times 2 \mu\text{m}$  is coated with 300 nm of electron beam deposited Pt so as to protect the interested area from ion beam damage. A further 1.5  $\mu\text{m}$  thick ion beam deposited Pt follows. This stage is depicted in Figure 4-11a. All FIB samples were obtained across the wear scar i.e. orthogonal to the direction of fretting.
2. Trenches were removed from either side of the coated region using the ion beam at 30kV, leaving a lamella as shown in Figure 4-11b.
3. The lamella was thinned to 1  $\mu\text{m}$  thickness, cut free and removed *in-situ* using a Kleindiek micromanipulator, shown in Figure 4-11c.
4. The sample was then attached via Pt deposition to a standard 3 post Cu TEM support (Ominprobe), shown in Figure 4-11d.
5. The sample was thereby finally thinned to electron transparency of about 10 nm using  $\text{Ga}^+$  ions at 5kV, shown in Figure 4-11e



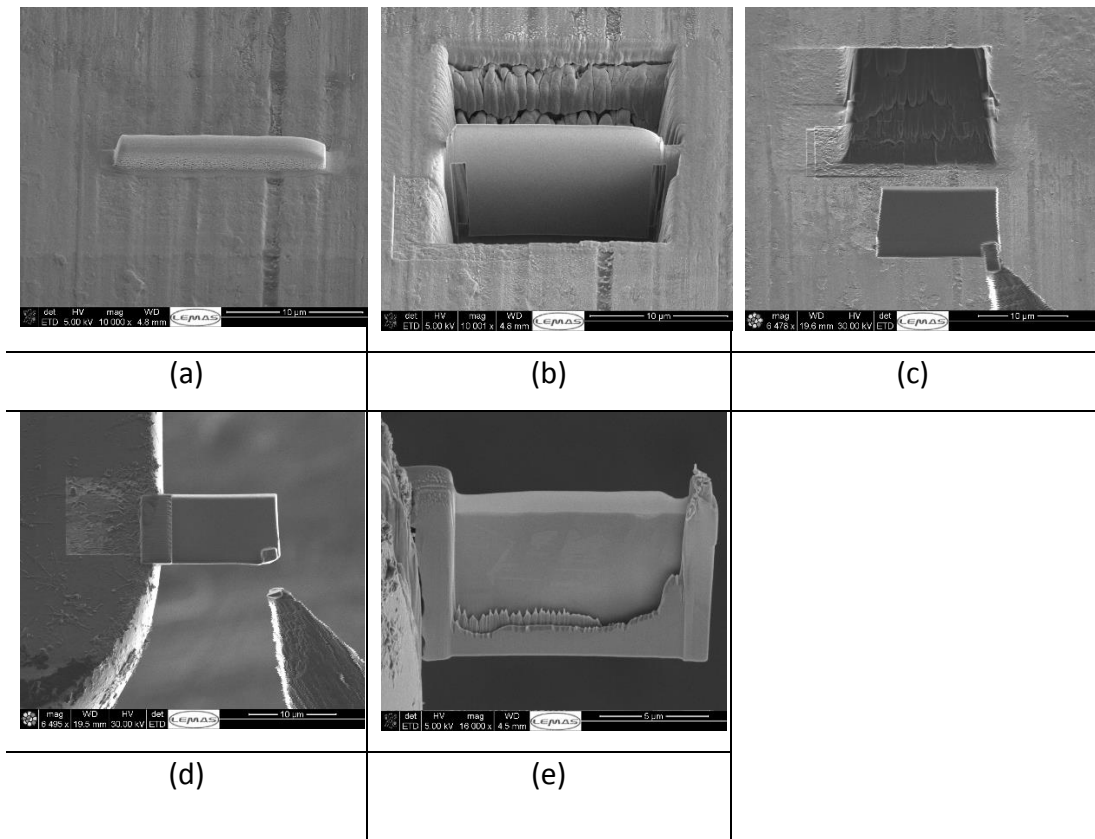


**Figure 4-11 – FIB SEM micrographs of TEM sample preparation stages (a) Pt deposited on area of interest (b) removal of material from either side of Pt deposit (c) removal of lamella from bulk material (d) attachment of lamella to TEM post (e) final thinning of sample to electron transparency**

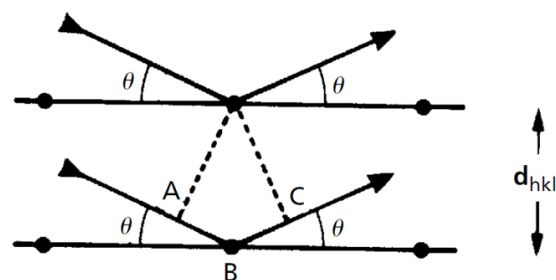
#### **4.5.5 Transmission electron microscope (TEM)**

In TEM, electron beams are transmitted through an electron transparent sample prepared using a FIB. Digital micrographs are obtained as the electron passes through the specimen. When compared to the light microscope, the TEM is capable of imaging at resolutions up to a x1000 higher. This is due to wavelength of  $\sim 0.2$  nm for electron compared to wavelengths of  $\sim 200$  nm in light microscopes. In this study, samples were analysed using a FEI Tecnai F20 FEGTEM (200kV) fitted with a Gatan Orius SC600 CCD camera. Bright-field and dark-field images were captured using the digital camera, the former is generated by passing a single direct beam through an objective aperture and for the dark field, a diffracted beam is imaged instead of the direct beam.

The TEM is also capable of generating selective area electron diffraction (SAED) images which holds information about the orientation of atomic planes within a solid crystal. When electrons beams are fired at voltages as high as 200 kV, they begin to behave like waves hence travelling at de Broglie's wavelengths of  $\sim 2.96$  pm. This is 100x smaller than the lattice parameters of crystals which is about  $\sim 0.3$  nm, thus allowing the electrons to be diffracted between the 'gratings' created by atoms. Electrons undergo an elastic scattering process when they hit the atom that is, they lose no energy and its wavelength remains unchanged [152]. Therefore, 'Spot' electron patterns and ringed patterns are generated which represents single-crystals and nano-crystalline structures respectively.

#### 4.5.6 X-Ray powder diffraction (XRD) analysis

X-ray diffraction provides crystallographic information of a single crystal by providing information related to the 'd-spacing' between atomic planes. A schematic diagram of the atomic planes, incidence and diffraction of beams is shown Figure 4-12. The expression relating the d-spacing to the wavelength of X-ray ' $\lambda$ ' and the angle of incidence theta ( $\theta$ ) is known as Bragg's Law of diffraction as shown in Figure 4-12. In this study, XRD analysis of polished CoCrMo and Ti6Al4V surfaces were conducted using the *Cu K $\alpha$*  radiation over an area of 15 x 15 mm across a  $2\theta$  scan between  $30^\circ$  and  $60^\circ$ .



$$n\lambda = 2d_{hkl} \sin \theta$$

**Figure 4-12 – Schematic diagram of atoms in planes separated by a space 'd' as incident X-ray of wavelength  $\lambda$  diffracts at angle ' $\theta$ '.**

#### **4.5.7 Energy disperse X-Ray spectroscopy (EDS)**

The SEM and TEM used in this study were both equipped with EDS. This technique was used mostly as a post-analysis method to accurately determine the elements present at the worn surfaces of the fretting contact. It was also used with the TEM to identify the distribution of elements in the subsurface of the metallic alloys. The technique works by detecting characteristic X-rays released; thus elements whose characteristic X-rays were detected can be easily identified. When the surface of a specimen is bombarded by electrons during electron microscopy, the incident electrons often displace another electron from within an atomic shell of the specimen. In order to preserve equilibrium, one of the electrons from a higher energy orbital drops to a lower orbital. Through this process, the characteristic X-rays of the specific element is released.

It is worth noting that certain elements have energies that overlap such as Mo and S; P and Pt depending on the characteristic X-ray energy used. Therefore, when generating a map using the licensed software, *Aztec, Oxford Instruments, UK*, the 'TruMap' function was used; which gives a more accurate quantification. The intensity of the EDS maps depicted in the various chapters of this thesis is indicative of the relative abundance of the element. However, there are other limitations associated with the EDS technique: inaccurate quantification of light elements such as N, C etc. Therefore these may appear as background noise in the map and are generally deemed absent unless they are observed to be more concentrated in a specific region relative to another within a single map.

#### **4.5.8 X-Ray photoelectron spectroscopy (XPS)**

X-Ray Photoelectron Spectroscopy (XPS) data was obtained in this study using the *K-Alpha<sup>TM</sup> + XPS, Thermo Fisher Scientific, USA*. This is a surface technique which was employed to further characterise the tribocorrosion products identified using EDS. In XPS, atoms within compounds or bulk materials when exposed to X-ray photons ( $h\nu$ ) become ionised as electrons

from their inner core is ejected. Thus, the binding energy (BE) of the electron is equivalent to the energy required to remove it from its shell.

Elements identified on the surface of a sample, either through EDS or XPS survey scans can be better quantified using high resolution scanning. X-rays can penetrate the specimen surface to a depth of several micro-meters, however, the photoelectrons analysed are generally from several nano-meters of the immediate subsurface of the material. This makes the characterisation of the passive film (generally few nano-meters thick) and the bulk alloy possible. For this study, to assess the variation in atomic composition of high resolution scanned elements as a function of depth, the surfaces were exposed to Argon-ion monoatomic beam at 4 keV across an area of 1 mm x 2 mm (when characterising passive films on CoCrMo and Ti6Al4V polished surface) and 200  $\mu\text{m}$  x 400  $\mu\text{m}$  (when analysing post – fretting surfaces). Licensed *CasaXPS* software was used to fit the XPS peaks obtained for each element. A *Shirley* background remove feature were used in fitting the peaks and the Aliphatic C 1s at 284.8 eV were used for the charge correction of the peaks. The fitting parameters namely: full width half maximum (FWHM), BE and peak shapes were obtained from various sources in literature and respectable webpage repositories [153-165].

#### **4.5.8.1 Estimations of etching rate**

A very rough estimation of the etching rate for CoCrMo and Ti6Al4V protective layer was calculated using the average measured thickness (obtained from TEM micrograph) of the protective film. The average known thickness of the protective layer from each alloy is then divided by the maximum etching time (400 sec) analysed before the bulk metal is reached. These rates were estimated to 0.0094 nm/sec and 0.019 nm/sec for CoCrMo and Ti6Al4V respectively.

#### **4.5.9 Nano-indentation hardness**

Hardness is a key consideration of the mechanical properties of a material in the context of tribological interactions. In this study, nano-indentation hardness of polished CoCrMo and Ti6Al4V and tribocorrosion products were characterised within the top 40 – 60 nm of the metallic surfaces. The *Nano-Indenter – NanoTest NTX, Micromaterials, UK* was used for the study. A calibrated Berkovich diamond indenter with tip-end radius of ~200 nm radius was used. Hardness is automatically determined by the device using the Oliver and Pharr [166] method. The apparatus obtain hardness measurements by measuring penetration depth as a function of load during a load-unload cycle – hardness is the peak load divided by the projected area at peak load. A minimum of 20 indentations from different sites of the sample surfaces were conducted for statistical reliability. Further details are provided in the result chapter for each case.

#### **4.5.10 Coordinate measurement machine (CMM)**

A 3D reconstruction of the male and female taper surfaces were generated by mapping the surface using the coordinate measurement machine (*CMM*), *Legex 322, Mitutoyo, Japan*. The *Redlux sphere profiler, UK* is a commercially available software used to generate the 3D reconstruction. Deviations from a cone reference in the software gives an indication of preferentially worn region thus, the wear pattern from the tapers can be identified. This method was employed mainly to obtain a qualitative assessment of wear pattern on the taper surface for each material combination.

The samples were wiped with acetone then wiped thoroughly with de-ionised water to ensure the stylus is not in contact with acetone. Subsequently, the samples were dried with Nitrogen air-gun. The samples were positioned in a fixture and flatness was ensured using a spirit level. A calibrated M3, 1.5 mm diameter ruby ball, 30 mm length styli was used to generate points 0.2 mm apart (horizontally and vertically). In every case, the measurement begins from the uppermost surface of the taper, to the lowest point.

# Chapter 5 Metallurgy and surface chemistry of CoCrMo and Ti6Al4V

## 5.1 Introduction

In the subsequent chapters of this thesis, results from fretting experiments will be presented. This purpose of this chapter is therefore to characterise a polished CoCrMo and Ti6Al4V sample: examining the crystallinity of the alloy, surface chemistry and hardness in a dry condition. The subsurface characterisation of the polished alloys in this chapter will thus act as a reference for the subsurface transformations observed in the subsequent chapters. An outline of the analysis carried out in this chapter is shown in Figure 5-1.

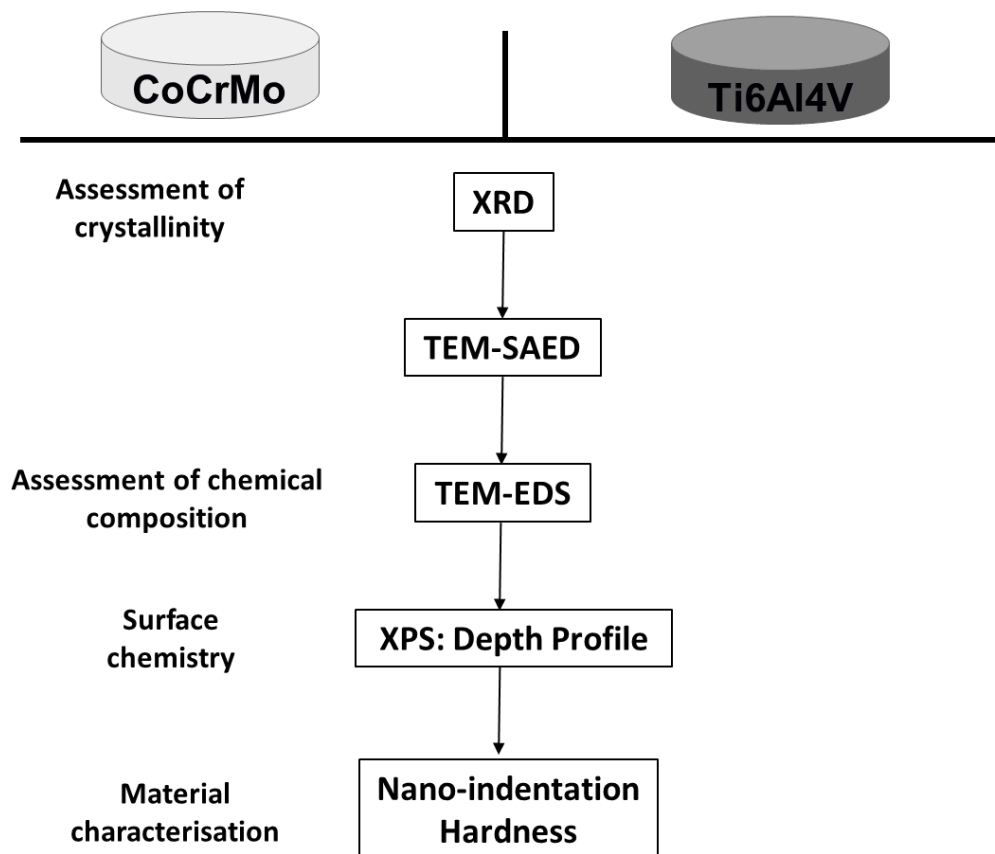
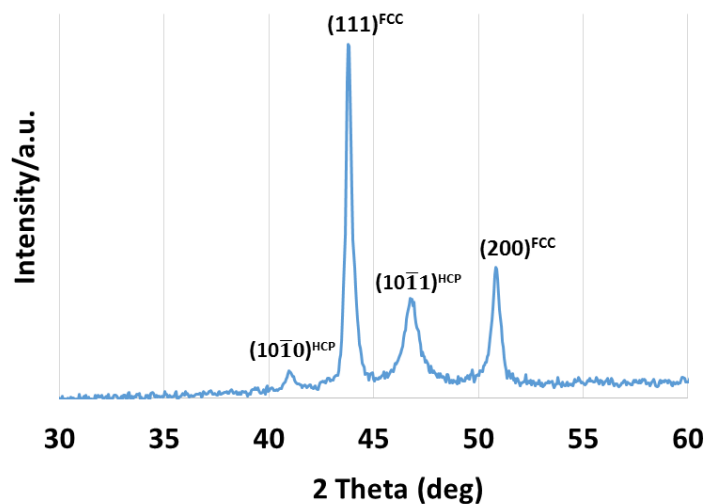


Figure 5-1 – Outline of analyses performed in chapter 5

## 5.2 Crystalline structure of CoCrMo and Ti6Al4V

XRD was used to characterise the crystalline structure of both CoCrMo and Ti6Al4V using the Cu K $\alpha$  radiation. The 2 $\theta$  scans between 30° and 60° shown in Figure 5-2 and Figure 5-3 distinctively identified the HCP and FCC phases of CoCrMo alloy as well as the HCP, BCC ( $\alpha$ ,  $\beta$ ) phases of the Ti6Al4V alloy.

Figure 5-2 shows the co-existing HCP and FCC phases. The FCC (111) peak is the most prominent and is indicative of a metal (M) carbide ( $M_{23}C_6$ ). The FCC (200) peak is the  $\gamma$ -Co phase. The peaks at  $(10\bar{1}0)$  and  $(10\bar{1}1)$  represent the HCP  $\epsilon$ -Co phases as confirmed in other studies [167-169].



**Figure 5-2 – Crystalline structure of polished CoCrMo alloy**

The 2 $\theta$  plot for polished Ti6Al4V alloy in Figure 5-3 shows two prominent HCP  $(10\bar{1}1)$  and  $(10\bar{1}1)$  peaks and two other less prominent HCP peaks  $(0002)$  and  $(10\bar{1}2)$ . Two BCC  $(110)$  and  $(200)$  peaks are also evident in Figure 5-3 thus confirming the co-existing HCP and BCC phases. The XRD peak agrees with reference [170]. Ti and Ti–Al are both  $\alpha$  phases with an HCP structure as identified from the XRD database [171, 172]. The BCC peaks corresponds to the Ti–V  $\beta$  phase [173].

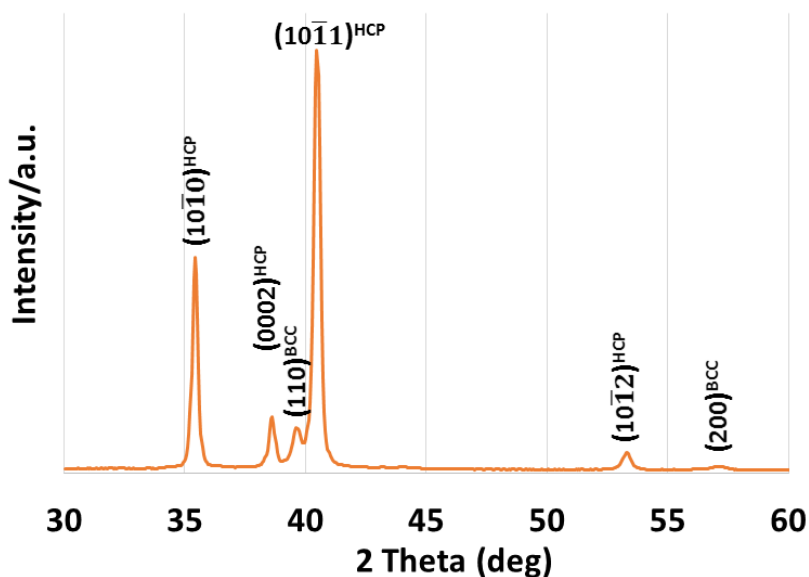


Figure 5-3 – Crystalline structure of polished Ti6Al4V alloy

### 5.3 Subsurface microscopy and spectroscopy

TEM samples of the polished alloys were obtained using the FIB preparation method outlined in section 4.5.4. High resolution micrographs of the subsurface metallurgy in both alloys was thereby acquired. Incorporated with the TEM was SAED through which the crystallinity of a localised region in the subsurface structure was identified. In addition, EDS incorporated with the TEM was used to map the distribution of elements in the grain structure within a selected subsurface region.

#### 5.3.1 TEM and SAED of polished CoCrMo and Ti6Al4V

Figure 5-4a shows the bright-field micrograph of the polished CoCrMo alloy. Directly beneath the two layers of platinum, a protective layer of thickness ranging from 2.5 to 5 nm is observed on the CoCrMo alloy. This is within the expected thickness for CoCrMo alloy [174-176]. The dark-field micrograph of the same region is presented in Figure 5-4b. The micrograph offers a better contrast between the different crystalline structures thus making it possible to distinguish between the nano-crystalline region and the single crystal beneath



it. The nano-crystalline structure has a depth of 130 nm from the uppermost surface. The single crystal structure is seen directly beneath the nano-crystalline structure. It can be seen that the single crystal has experienced some degree of twinning which may have been a result of strain-induced transformations during mechanical polishing of the surface[177].

For further clarification, SAED was conducted at regions A and B. The ringed pattern in Figure 5-4c is an indication of a nano-crystalline structure and Figure 5-4d shows evidence of crystal planes as expected in a single crystal structure [98, 150] thus confirming the observations from the micrographs.

Figure 5-5 shows the TEM and SAED micrographs of Ti6Al4V. The protective layer on the Ti6Al4V is seen more distinctively in the bright-field image of Figure 5-5a and its thickness ranges from 5 to 10 nm as others have also observed [174, 178]. However, thicker surface oxide layer (~15 nm) have been reported for a mechanically polished surface [179]. From both Figure 5-5a and b, the nano-crystalline structure beneath the protective layer does not appear to be of a consistent depth unlike in CoCrMo, although the depth is equally less than 200 nm. SAED pattern in Figure 5-5c confirms the structure in region A to be nano-crystalline and the diffraction pattern of region B in Figure 5-5d confirms the structure to be a single crystal.

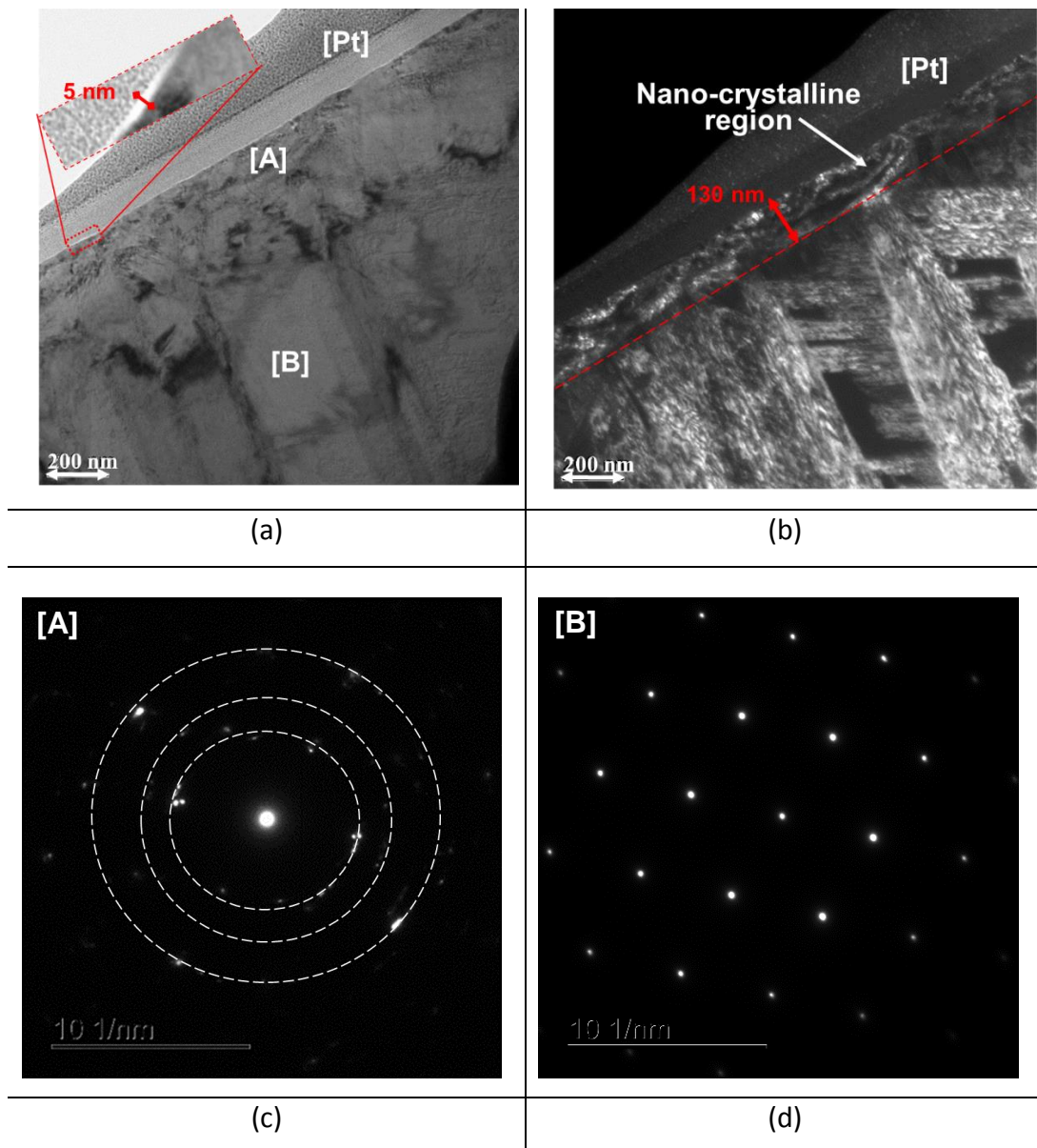


**Figure 5-4 – TEM and SAED of polished CoCrMo: a) Bright-field micrograph. b) Dark-field micrograph c) SAED of nano-crystalline region 'A' d) SAED of single crystal 'B'**

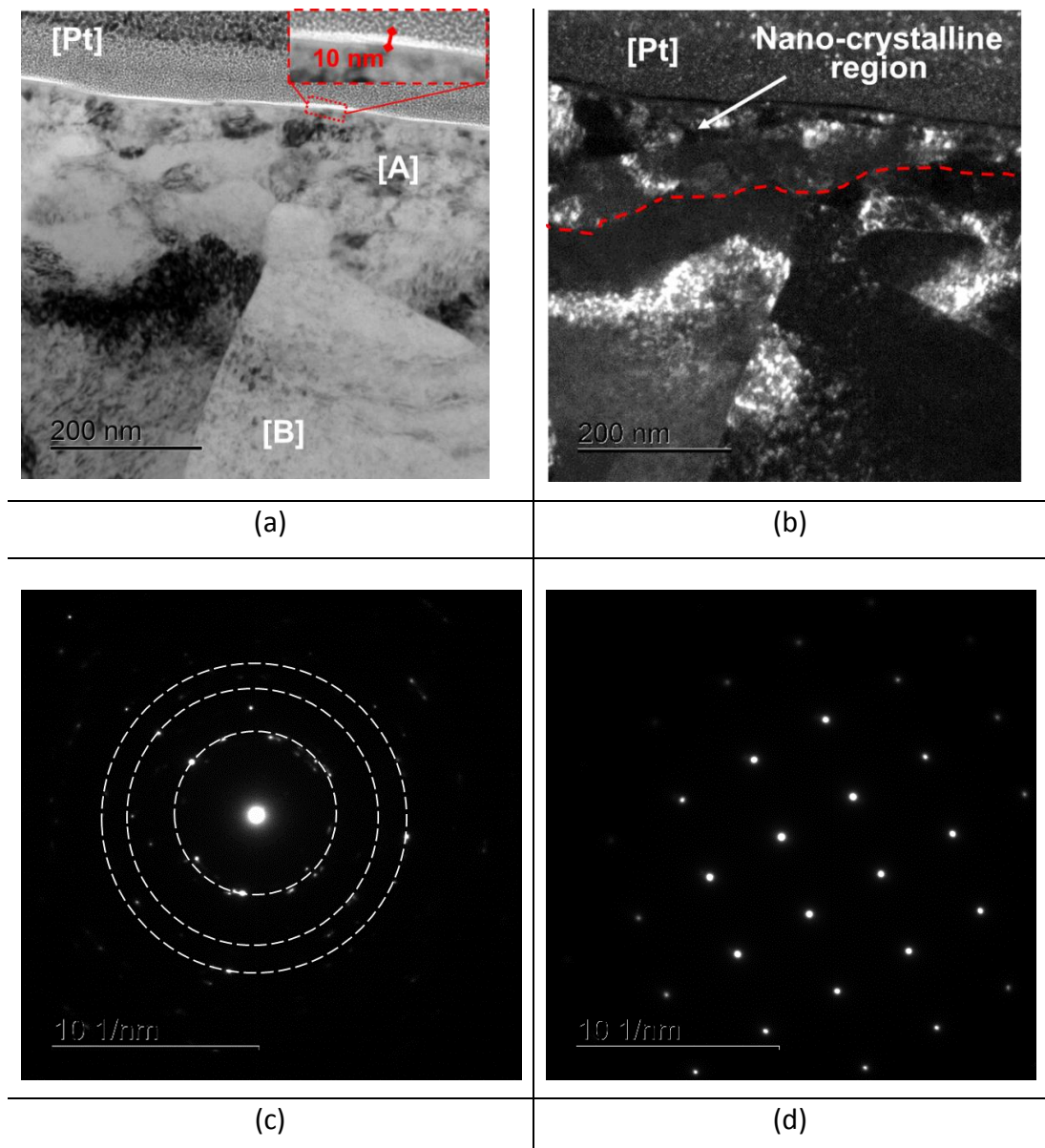


**Figure 5-5 – TEM and SAED of Polished Ti6Al4V: a) Bright-field micrograph. b) Dark-field micrograph c) SAED of nano-crystalline region 'A' d) SAED of single crystal 'B'**

### 5.3.2 TEM – EDS of polished CoCrMo and Ti6Al4V

TEM-EDS maps of CoCrMo and Ti6Al4V are shown in Figure 5-6 and Figure 5-7 respectively. The most abundant elements for both alloys Co, Cr, Mo and Ti, Al, V and O (enriched in the protective layer although not clearly visible) are visible. It is observable that in CoCrMo alloy the three elements are equally distributed at varying intensities across the material subsurface as expected.

On the other hand, distinctive grains corresponding to the  $\alpha$  and  $\beta$  phases of Ti6Al4V is seen Figure 5-7. The  $\beta$  phase is distinguished by the higher intensity of V and lesser Al content.

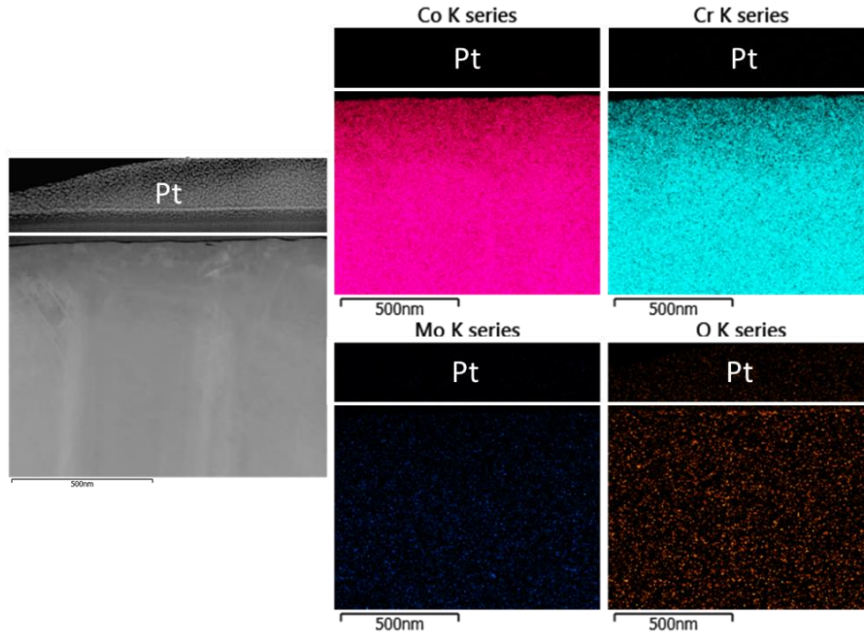


Figure 5-6 – TEM-EDS map of polished CoCrMo showing Co, Cr, Mo, O.

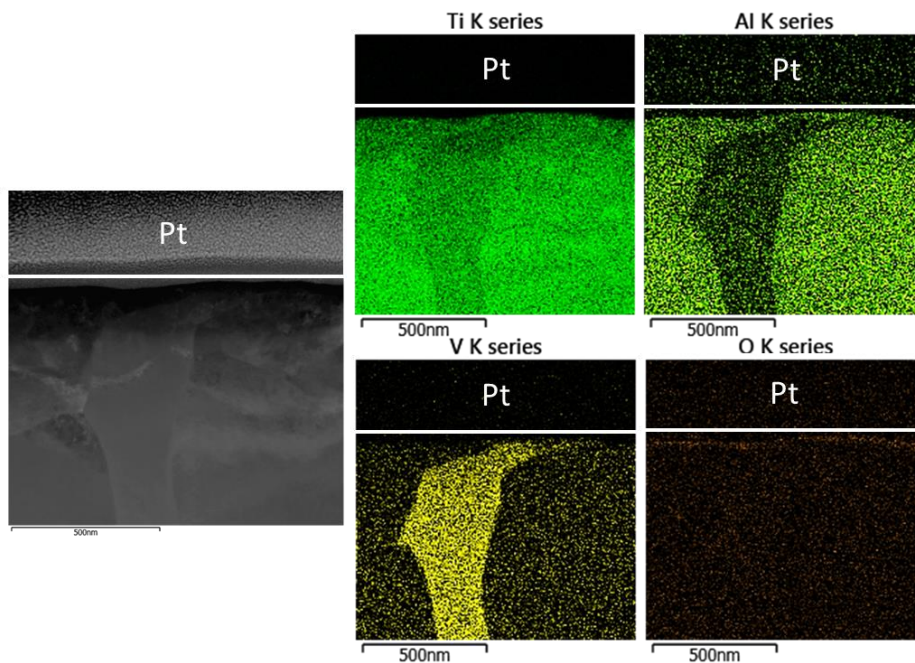


Figure 5-7 – TEM-EDS map of polished Ti6Al4V showing Ti, Al, V, O.

The chemical composition of the alloys were quantified using TEM-EDS. Selected regions from Figure 5-6 and Figure 5-7 were a minimum area of 500 by 200 nm. The results outlined in Table 5-1 for CoCrMo and Table 5-2 for Ti6Al4V are presented in wt% and at%. The proportion of all the heavier elements from CoCrMo observed were within the range presented in the ASTM standard. However in the Ti6Al4V, the V content in the  $\alpha$  phase was 4x higher than the ASTM prescription and 10x the V content in the  $\beta$  phase. This simply highlights the difference in the chemical composition of the two phases whereas ASTM represents an overall  $\alpha - \beta$  phase alloy. The C, O and N content appear exaggerated in both alloys due to the known limitation of EDS technique – light elements are not accurately quantified by EDS.

**Table 5-1 – TEM – EDS chemical composition of CoCrMo**

ASTM F 1537-08 – Chemical Composition (%wt)								
LC CoCrMo	Co	Cr	Mo	Mn	C	N	O	Si
<b>Wt%</b>	Bal.	26.0	5.0	1.0	0.14	0.25	-	1.0
		30.0	7.0	max	max	max		max
EDS – Chemical composition								
LC CoCrMo	Co	Cr	Mo	Mn	C	N	O	Si
<b>Wt%</b>	64.2	27.6	6.0	0.9	0.4	0.2	0.1	0.5
<b>At%</b>	61.4	30.0	3.5	0.9	1.8	0.8	0.5	1.1

**Table 5-2 – TEM – EDS chemical composition of Ti6Al4V**

ASTM F 136-08 – Chemical composition (%wt)								
	Ti	Al	V	Fe	C	N	O	
<b>Ti6Al4V</b>	Bal.	5.5	3.5	0.25	0.08	0.05	0.13	-
		6.5	4.5	max	max	max	max	
EDS – Chemical composition								
<b>α Ti6Al4V</b>	<b>Ti</b>	<b>Al</b>	<b>V</b>	<b>Fe</b>	<b>C</b>	<b>N</b>	<b>O</b>	-
<b>Wt%</b>	88.3	6.3	2.3	0.0	0.4	0.3	2.3	
<b>At%</b>	79.4	10.1	2.0	0.0	1.4	1.0	6.2	
<b>β Ti6Al4V</b>	<b>Ti</b>	<b>Al</b>	<b>V</b>	<b>Fe</b>	<b>C</b>	<b>N</b>	<b>O</b>	-
<b>Wt%</b>	71.2	2.2	21.8	2.1	0.1	0.0	2.6	
<b>At%</b>	67.5	3.7	19.4	1.7	0.3	0.0	7.4	

## 5.4 Surface chemistry

The corrosion resistance of CoCrMo and Ti6Al4V alloys are mainly due to the protective layer that spontaneously form on their surfaces. In this section, XPS is employed to characterise the layer that are identified on both alloys. High resolution scans of C, O, N, Co, Cr Mo were carried out for the CoCrMo and C, O, N, Ti, Al, V for the Ti6Al4V. The elements were examined through a depth profile of five levels (100 s per level). An estimated average etching rate were determined to be 0.0094 nm/sec and 0.019 nm/sec for CoCrMo and Ti6Al4V respectively as outlined in section 4.5.8.

### 5.4.1 XPS assessment of CoCrMo passive film

The concentration in at% of the elements assessed for CoCrMo are shown in Figure 5-8. It is observable that the uppermost surface is mainly organic contaminants composing of C, O and N as described in other references [178,

179]. A sharp increase in the O content between the first and second levels corresponds to the increase in Cr and Mo, this is indicative of the two main metallic elements that contribute to the protective layer. However, the abundance of Cr compared to Mo was seen to be roughly 8:1 ratio across the depths beyond the first level confirming that Cr is the dominant metallic element in the protective layer [180]. Furthermore, no evidence of Co was observed throughout the 5 levels of the depth profile analysis which suggests that the bulk surface of the alloy was not reached. More so, the absence of any oxides of Co is likely due to an observation made in the study referenced already [180] where it is noted that Co-oxide exist deeper within the protective layer – interfacing with the bulk metal.

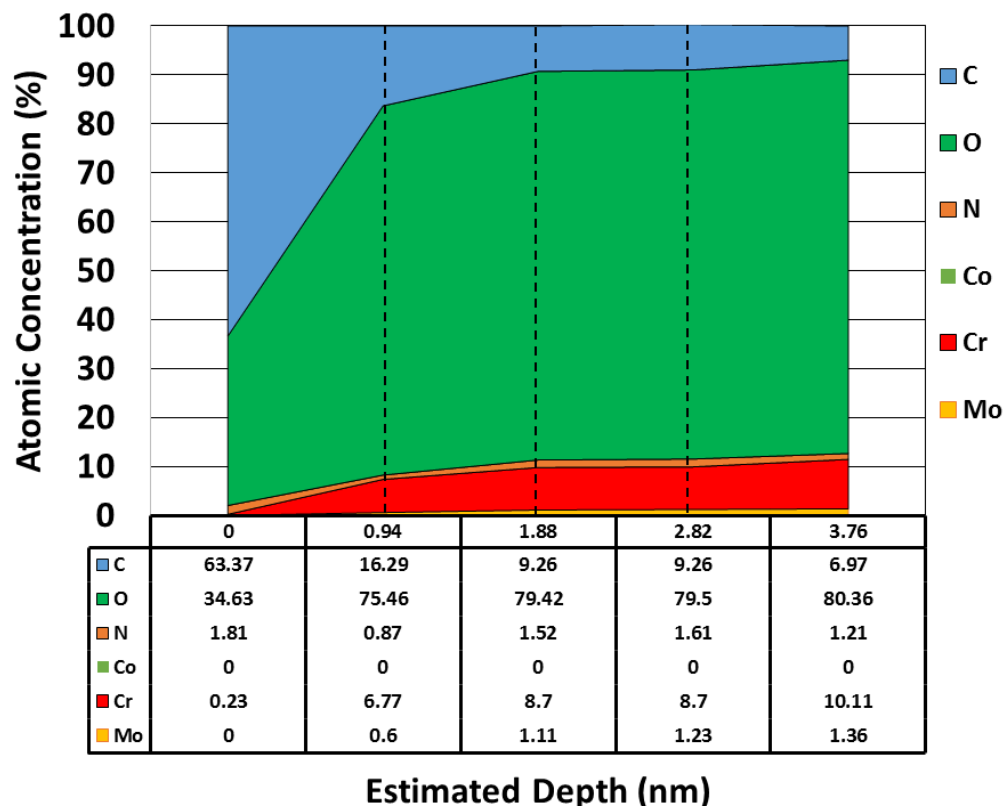
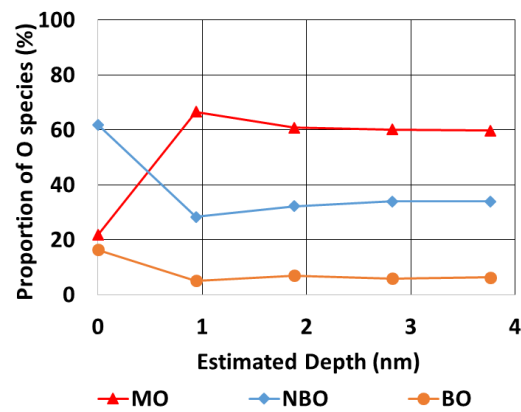


**Figure 5-8 – XPS Depth profile analysis of CoCrMo passive film**

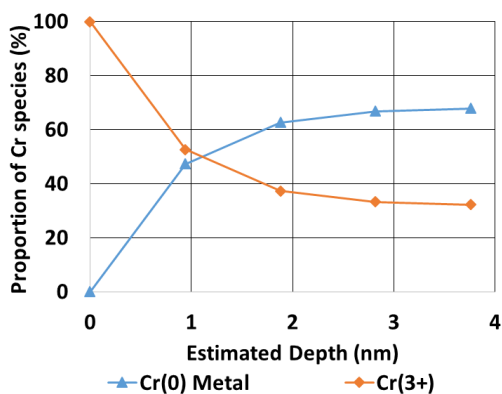
In Figure 5-9, Cr, Mo and O are presented in the percentage proportion of their species as observed through the high resolution scans. Three typical O peaks were identified as shown in Figure 5-9a. These are broadly termed: MO (Metal-oxide) which mainly represents the  $O^{2-}$  at binding energy (BE)  $\sim 529.7$  eV; NBO (non-bridging oxygen) which represents the  $OH^-$  at BE  $\sim 531.4$  eV

and the BO (bridging oxygen) which mainly represents surface adsorbed water (H<sub>2</sub>O) at BE ~533.3 eV [158, 180].

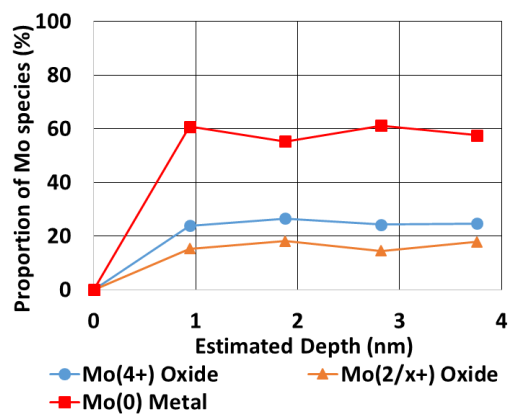
From Figure 5-9b it is observable that the Cr (3+) which generally exist within the protective layer in the form of Cr<sub>2</sub>O<sub>3</sub> and Cr<sub>2</sub>(OH)<sub>3</sub> [181] decreases rapidly in proportion to Cr (0) metal from the uppermost surface towards a constant proportion at the last examined depth. On the other hand, a fairly constant proportion of all Mo species were observed in Figure 5-9d beyond the uppermost surface. The peak at BE 228.1 eV corresponds to Molybdenum sub-oxide (Mo(2+/x) – oxide) which had been identified previously in literature as a peak of Mo (2+)/non-stoichiometric Mo – oxide [182].



(a)



(b)



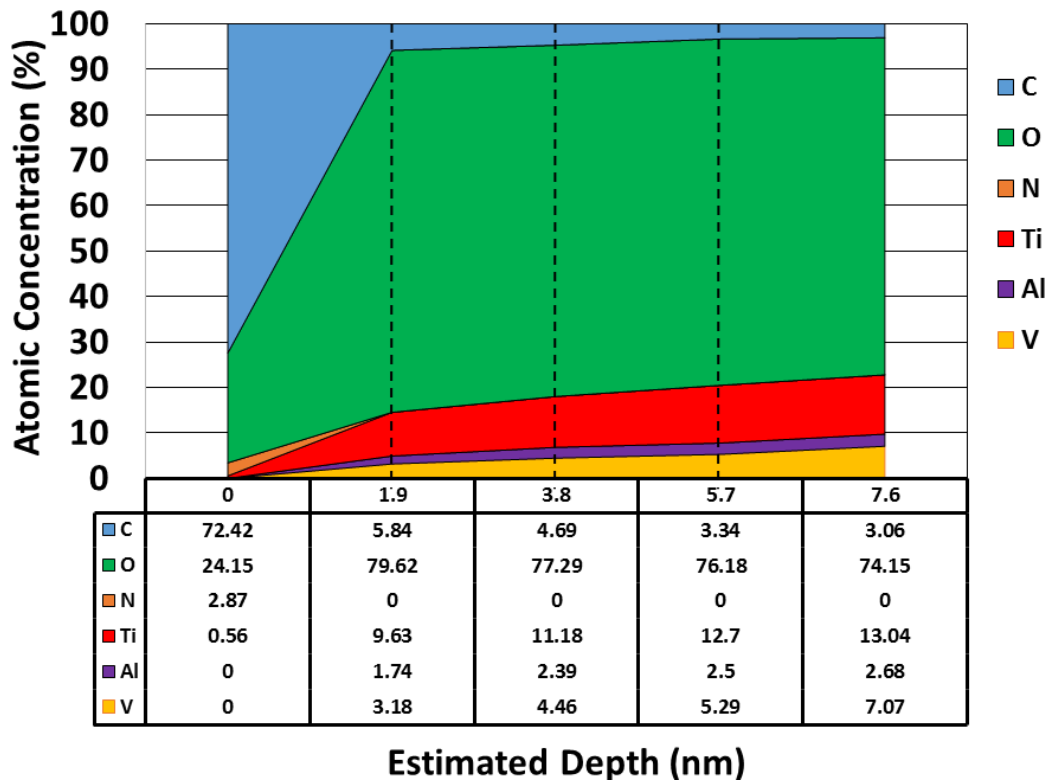
(c)

**Figure 5-9 – Proportion of species in CoCrMo protective layer: a) O species, b) Cr species, c) Mo species**



### 5.4.2 XPS assessment of Ti6Al4V passive film

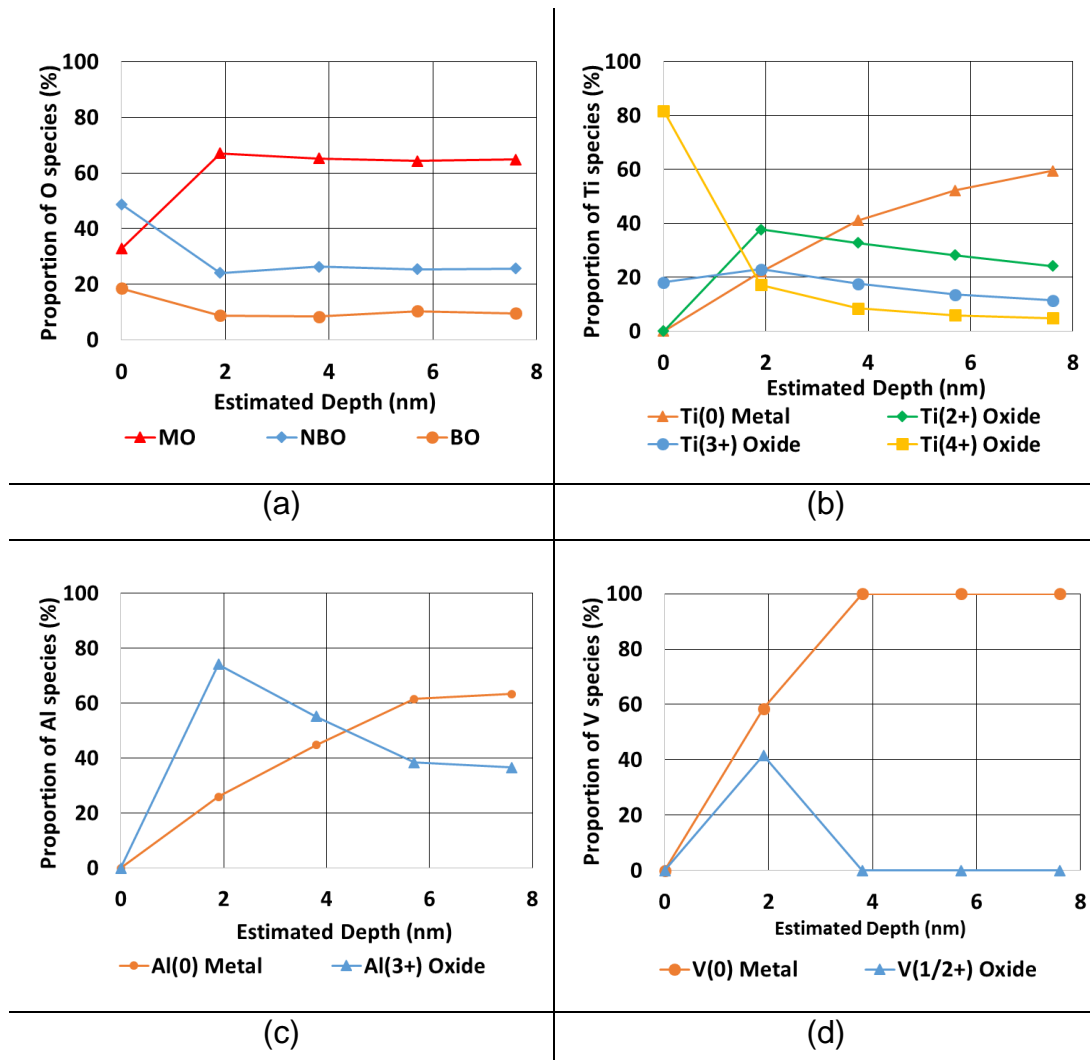
Figure 5-10 shows the concentration of the elements assessed on the Ti6Al4V surface. Similar to the CoCrMo surface, the uppermost surface of the Ti6Al4V alloy also composed of C, O and N and a small proportion of the most reactive metal in the alloy – Cr in the case of CoCrMo and Ti in Ti6Al4V alloy. The proportion of O, C and Ti on the Ti6Al4V follow a similar pattern with O, C and Cr contents as described for the CoCrMo. However, the proportion of Ti in the Ti6Al4V protective layer is seen to be higher than that of Cr in the CoCrMo layer for all levels. Interestingly, the concentration of V was higher in proportion to Al for all levels beyond the uppermost surface.



**Figure 5-10 – XPS Depth profile analysis of Ti6Al4V passive film**

The proportion of species for key elements in Ti6Al4V such as Ti, V, Al and O are shown in Figure 5-11. The O species in Figure 5-11a are observed in a similar proportion compared to the CoCrMo alloy and in Figure 5-11b, it is found that Ti exist in the protective layer in multiple oxidation states. Ti (4+) which generally forms TiO<sub>2</sub> was the most abundant at the uppermost layer as similarly described by Hanawa et al [143]. Interestingly, although Ti (2+) was

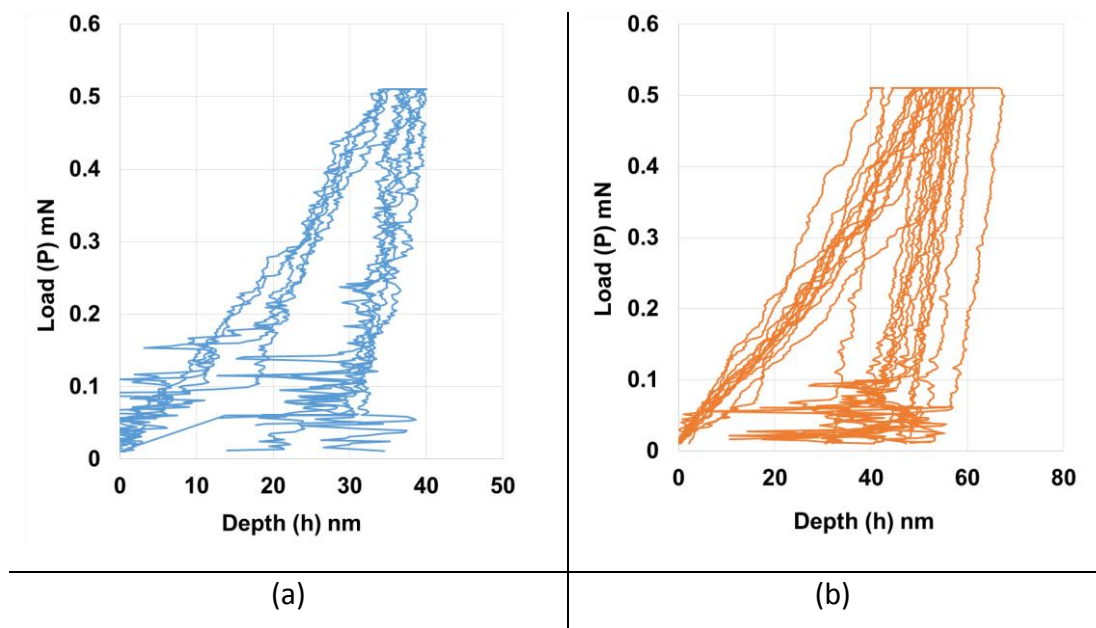
the most abundant specie across the depths beyond the uppermost surface, it is known to be thermodynamically less favourable at the uppermost surface which explains why only Ti (4+) and Ti (3+) were found at the uppermost surface [183]. Oxidised Al (3+) and its metallic component both contributed to the layer beyond the uppermost surface as shown in Figure 5-11c. At the second level where Al (3+) was highest, a non-stoichiometric oxide, V (1/2+) at BE ~513.4 eV was also present. Whereas V doesn't structurally exist in its 1+ oxidation state, it is said that the V (3+) specie commonly exist in the form of V (1+) and V (2+) hence the notation V (1/2+) [157]. Beyond the second level, only metallic specie of V was detected.

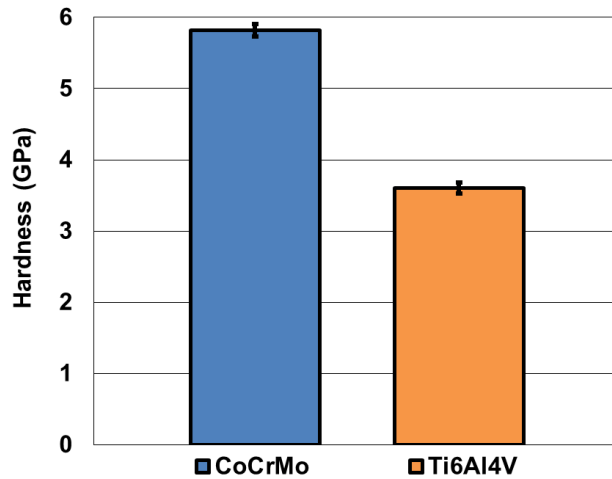


**Figure 5-11 – Proportion of species in Ti6Al4V protective layer: a) O species, b) Ti species, c) Al species, d) V species**

## 5.5 Nano-indentation hardness of polished surface

CoCrMo alloy is the main metallic material used for the bearing component of hip prosthesis; this is partly due to its relatively high bulk hardness. On the other hand, titanium alloys are preferred to CoCrMo for the design of stem components due to its much lower stiffness (~50% that of CoCrMo). Nano-indentation hardness of the polished surfaces of both alloys were performed to further characterise the hardness of the two materials. These are shown in Figure 5-12a and b for CoCrMo and Ti6Al4V respectively. In Figure 5-12c an average of  $n = 40$  indentations at a maximum depth of 40 nm in CoCrMo and 67 nm in Ti6Al4V yielded hardness values of 5.8 GPa and 3.6 GPa respectively. The values measured for Ti6Al4V agrees well with values reported in another study [184]. However, values quoted for CoCrMo in other studies range from 4.5 – 8 GPa [17, 67, 150, 185].





(c)

**Figure 5-12 – Nano-indentation hardness of CoCrMo and Ti6Al4V a) P vs. h plot for CoCrMo b) P vs. h plot for Ti6Al4V c) calculated hardness of CoCrMo and Ti6Al4V.**

## 5.6 Discussion and summary

This chapter has briefly characterised both CoCrMo and Ti6Al4V alloys – the two main materials of interest in this research. XRD analysis of the crystalline structure for both alloys agree with the findings from other studies in literature. However, while only the polished surface of the alloys were analysed in this study, there are other factors such as: surface treatment and roughness that may influence the intensities and/or the existence of a peak observed through XRD that other studies have shown [150, 170].

The key differences identified between CoCrMo and Ti6Al4V alloys are the following: a prominent metal-carbide peak in CoCrMo; segregated  $\alpha - \beta$  microstructure in Ti6Al4V; at least 60% higher hardness in CoCrMo and a less uniform subsurface nano-crystalline structure in the Ti6Al4V alloy.

TEM analysis of CoCrMo and Ti6Al4V surfaces reveal the common feature of a protective thin layer. Both layers had a non-uniform thickness ranging from 2.5 to 5 nm and 5 to 10 nm respectively. Further, depth profile analysis identified metallic species as a contributing constituent of the protective thin

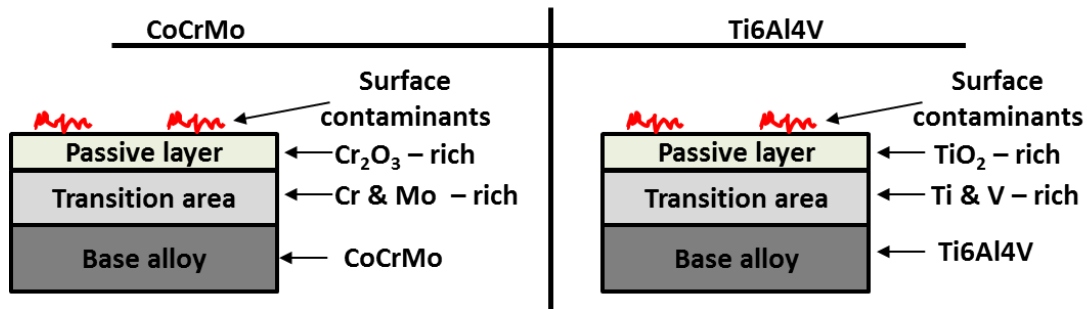
layer. In addition, in both alloys, the depth profile analysis did not reach the bulk material. Therefore, the existence of metallic species in the layer before the bulk is reached suggests that the metallic surface can be represented in three layers, similar to the description offered in a technical report on passivation [186].

Figure 5-13 shows a schematic diagram of the three layers with the chemical compositions that represents the surface of the two alloys. The three layers are namely: passive layer; transition area and base alloy (bulk material). The levels assessed during the depth profile analysis in this study can be apportioned to the three layers. The passive layer corresponds to level 1 although surface contaminants from the topmost surface dwarfs the concentration of the most reactive metals i.e. Cr in the case of CoCrMo and Ti in the case of Ti6Al4V. This is due to the concentrations being normalised to 100%. The transition area consist of both oxides and metallic species and thus, it corresponds to levels 2 – 5. The bulk, which was not reached in this study is expected to be dominantly metallic constituents with only a small concentration of oxygen.

For the CoCrMo surface, the transition area was enriched in Cr and Mo metallic species. Mo is typically added to Cobalt-based alloys for a similar reason as it is for Iron-based alloys. Mo has a role in the improvement of passivation; it is said to facilitate passivation by encouraging Cr enrichment in the passive layer thus protecting against pitting corrosion and general forms of corrosion [3, 186, 187]. Other studies have also demonstrated that Mo at the surface plays a key role in protein adsorption. This may encourage the formation of a proteinaceous tribofilm layer above the passive layer thus may influence friction at the tribological interface of CoCrMo [113].

On the other hand, the transition area on the Ti6Al4V surface was observed to be enriched in Ti and V. Contrary to the case of CoCrMo where the Mo had a specific role to play in the passivation of the alloy, it is not clear in literature if V has such role in Ti6Al4V. Nevertheless, it is clear that its oxides also contribute to the TiO<sub>2</sub>– rich passive layer as observed in other studies [179]. However, what proves to be more common in literature about V are concerns

about its toxicity in the human body. Several research effort have been dedicated to search out other options to replace V. So far, studies have been conducted on other alloying elements such as Mo, Zr and Nb [188-191]. It is therefore highlighted through the findings of this study that the enrichment of V at the nearest surface of Ti6Al4V alloy, may prove more of a negative attribute of its protective layer than a positive one.



**Figure 5-13 – Schematic diagram of a three-layer surface structure of CoCrMo and Ti6Al4V. Surface contaminants are not included in the three layers.**

## Chapter 6 Fretting wear mechanism of metal – metal material combinations

### 6.1 Introduction

The two most commonly used metal – metal combinations at the modular taper junction are: CoCrMo – CoCrMo and CoCrMo – Ti6Al4V. The two combinations are established at the head-neck and neck-stem modular taper interface. During the active life of the implant *in-vivo*, the material combinations are susceptible to fretting corrosion. This is manifested through various mechanisms of fretting wear and fatigue, substantiated by the penetration of corrosive body fluids into the taper junction as the modular taper experiences micromotions at the interface.

The purpose of this chapter is to experimentally simulate and systematically investigate fretting corrosion mechanisms at the modular taper interface. This is achieved by establishing a point contact using a ball-on-flat configuration; the fretting displacement amplitude is varied whilst keeping the initial contact pressure the same (see section 4.4.1). This allows for several material combinations to be assessed under different fretting regimes and contact conditions. *In-situ* OCP was monitored throughout the static and fretting stages of the test for each combination. Post-test surface analytical techniques such as: WLI, SEM-EDS, XPS and TEM-EDS were utilised for the characterisation of the tribocorrosion products and subsurface metallurgical transformations. Nano-indentation was also conducted on the product formed at the interface of CoCrMo – Ti6Al4V in order to quantify the hardness of the material. A schematic outline of the experiments and analysis performed in this chapter are shown in Figure 6-1.

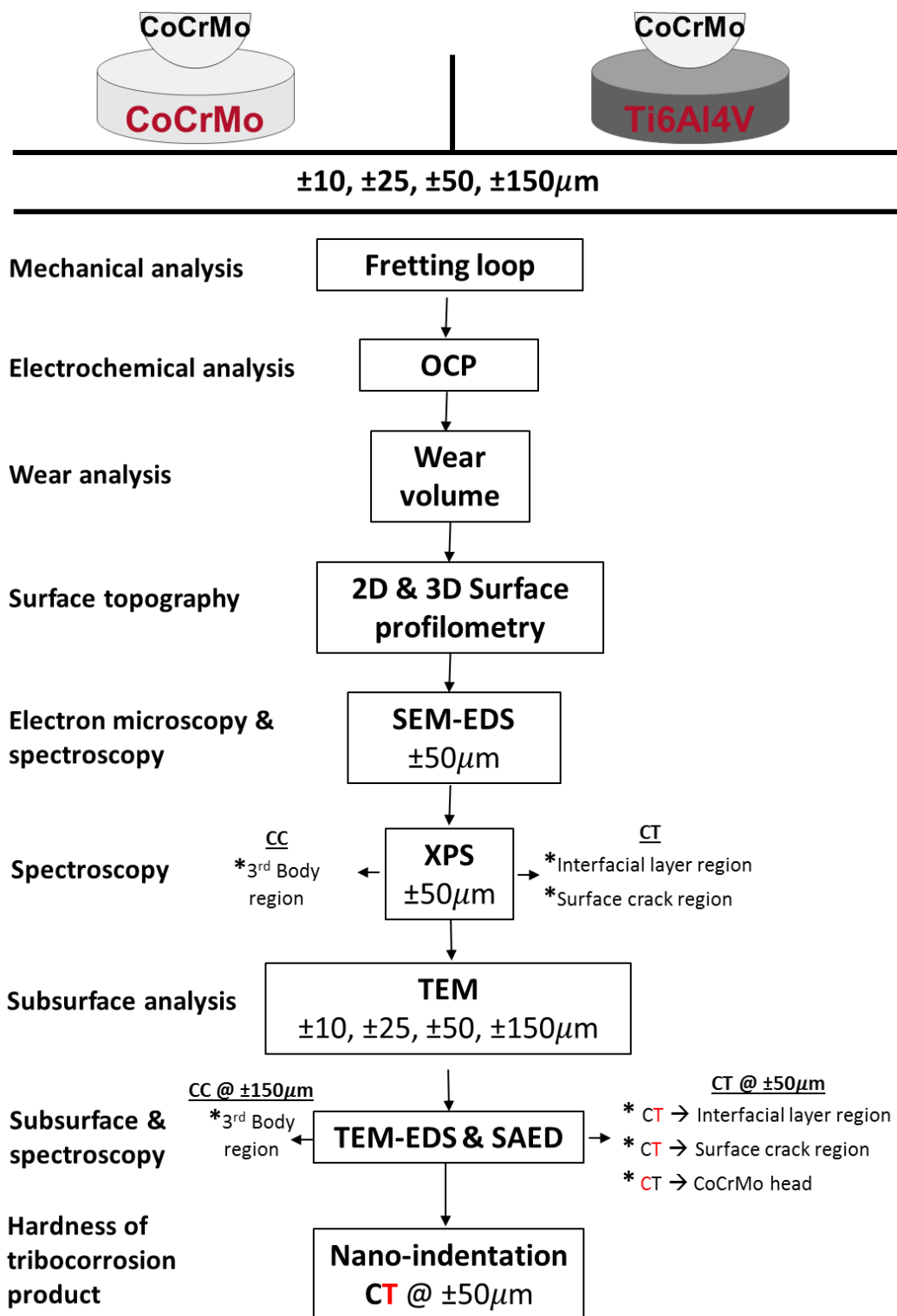


Figure 6-1 – Outline of the fretting experiments and analyses performed in chapter 6. C and T represents CoCrMo and Ti6Al4V respectively. The letters that appear in red represent the samples analysed.



## 6.2 Tribological assessment of metal – metal fretting contacts

The two metal – metal combinations were subjected to fretting displacement amplitudes ' $\delta_x$ ' of  $\pm 10 \mu\text{m}$ ,  $\pm 25 \mu\text{m}$ ,  $\pm 50 \mu\text{m}$  and  $\pm 150 \mu\text{m}$ . an additional displacement of  $\pm 150 \mu\text{m}$ . Figure 6-2 shows the slip ratio for both material combinations at their individual fretting displacements assessed. It is observable that CoCrMo – CoCrMo falls within the gross slip regime for all displacements except at  $\pm 10 \mu\text{m}$  which is in a partial-slip regime according to the gross slip criteria defined in reference [149]. On the other hand, the contact exists in a stick fretting regime for both  $\pm 10 \mu\text{m}$  and  $\pm 25 \mu\text{m}$  displacements for the CoCrMo – Ti6Al4V material combination. There is no specific slip ratio criteria that makes a distinction between the stick and partial-slip regime, instead, these are generally distinguished through the degree of surface damage at the end of the experiment. The fretting regime at  $\pm 50 \mu\text{m}$  displacement for CoCrMo – Ti6Al4V is better described as a mixed regime as later shown in Figure 6-4b through the transitions in the dissipated energy. A full gross slip regime is realised at  $\pm 150 \mu\text{m}$  displacement.

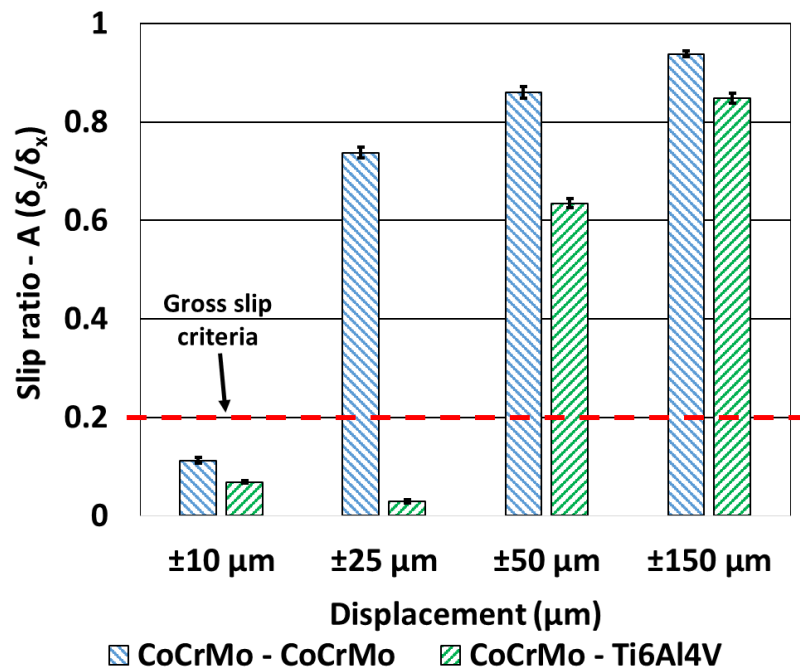
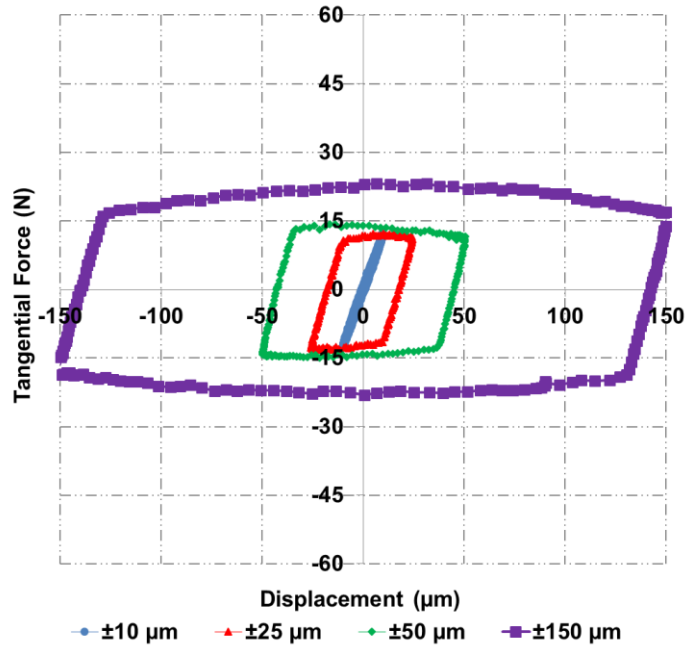


Figure 6-2 – Slip ratio of CoCrMo – CoCrMo and CoCrMo – Ti6Al4V under OCP conditions from  $\pm 10$  to  $\pm 150 \mu\text{m}$  displacement.

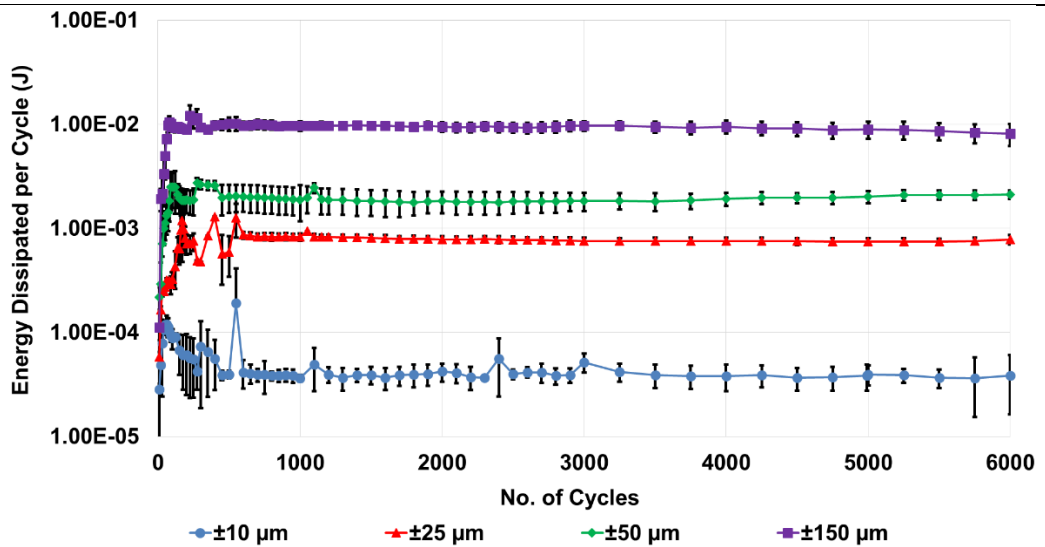
### 6.2.1 Fretting loop analysis

Figure 6-3a shows a graphical representation of the fretting regimes of the CoCrMo – CoCrMo combination. These appear as expected for each regime, the partial-slip regime is represented as a quasi-stick profile while the gross slip regime at  $\pm 25 \mu\text{m}$  appear in a parallelogram-like shape as expected for a gross slip contact. However, for  $\pm 50 \mu\text{m}$  and  $\pm 150 \mu\text{m}$  displacement, subtle deviations from the standard gross slip shape are indicative of the wear mechanisms effective at the interface.

The energy dissipated ( $E_d$ ), is a function of the tangential force ( $F_t$ ) and relative slip at the fretting interface ( $\delta_s$ ) by the expression  $E_d = f(F_t, \delta_s)$ . The tangential force is also known as the ‘frictional force’ at the gross slip regime. Also, the energy dissipated per cycle in a gross slip regime is a representation of the interfacial friction as derived in the reference [192]. Thus in this study, energy dissipated is interchangeably used with the terms ‘frictional energy’ and ‘interfacial friction’ while the term ‘frictional force’ is also interchangeably used with the tangential force. The energy dissipated per cycle is presented in a log plot in Figure 6-3b due to the significant difference in the magnitude of energy from the transition between partial-slip regime to gross slip regime and also among the gross slip regimes.



(a)

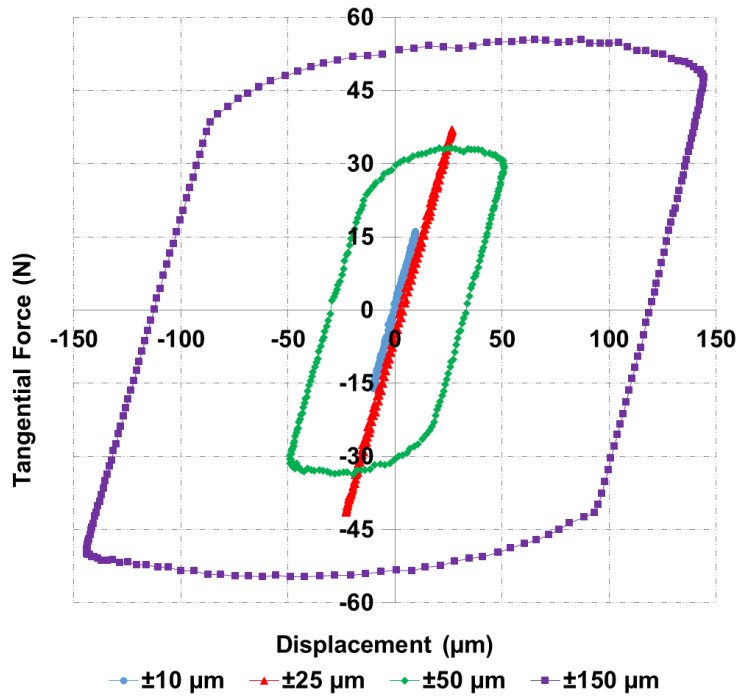


(b)

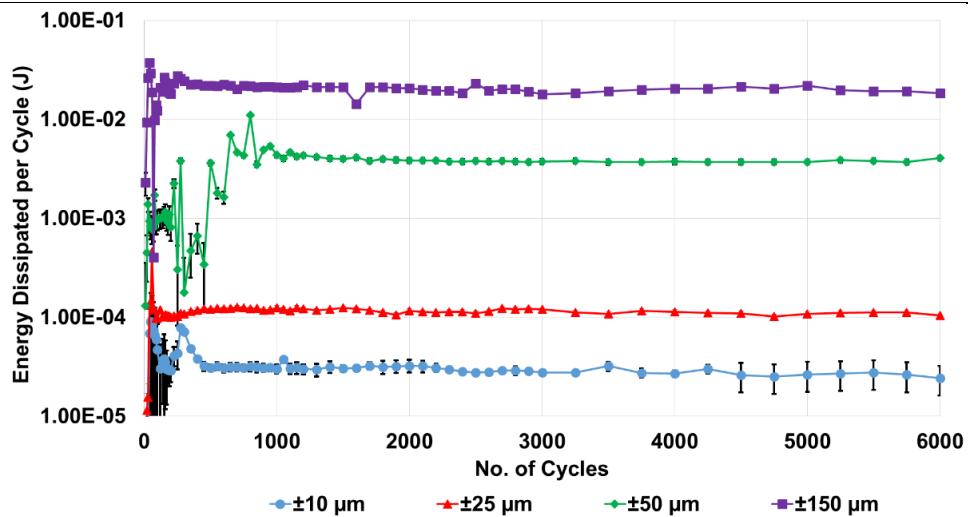
**Figure 6-3 – Fretting of CoCrMo – CoCrMo: a) Fretting loop b) Energy dissipated per unit cycle.**

The 2D fretting loop for CoCrMo – Ti6Al4V in Figure 6-4a confirms the fretting contacts at  $\pm 10 \mu\text{m}$  and  $\pm 25 \mu\text{m}$  are in a stick regime. While only the gross slip fretting loop is shown for  $\pm 50 \mu\text{m}$ , the graph of energy dissipated in Figure 6-4b shows that the contact was in a lower energy regime for few hundred cycles before it gradually transitioned to a gross slip regime at  $\sim 1000$  cycles. The

fretting loop also shows that the gross slip regime at  $\pm 150 \mu\text{m}$  occurred at a much higher frictional force than that of the CoCrMo – CoCrMo combination in Figure 6-3a.



(a)



(b)

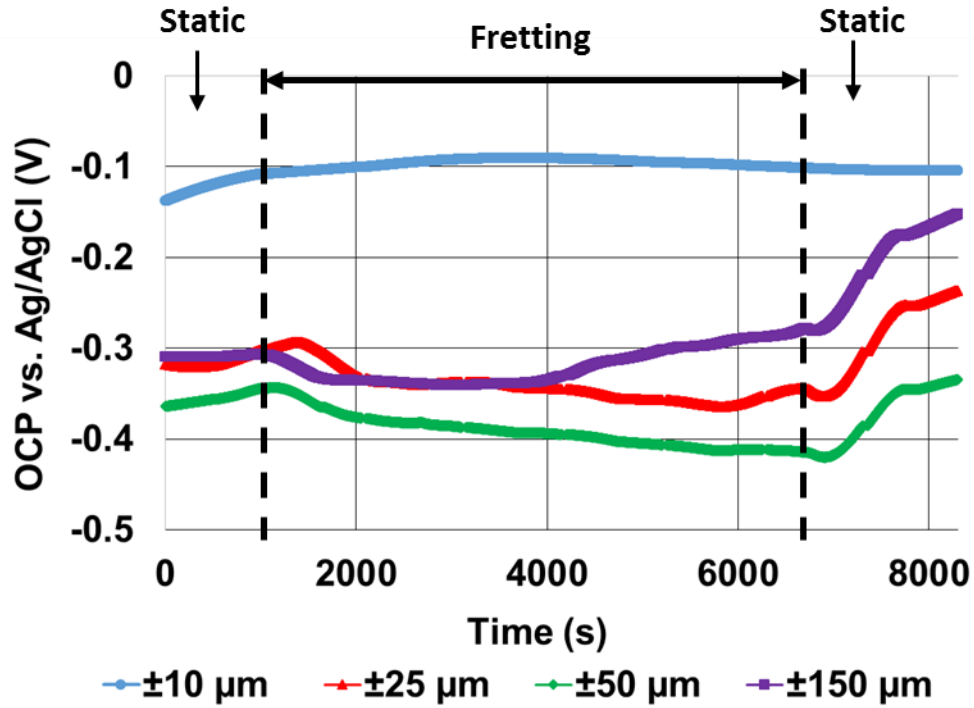
Figure 6-4 – Fretting of CoCrMo – Ti6Al4V: a) Fretting loop b) Energy dissipated per unit cycle.

### 6.3 Open circuit potential measurement

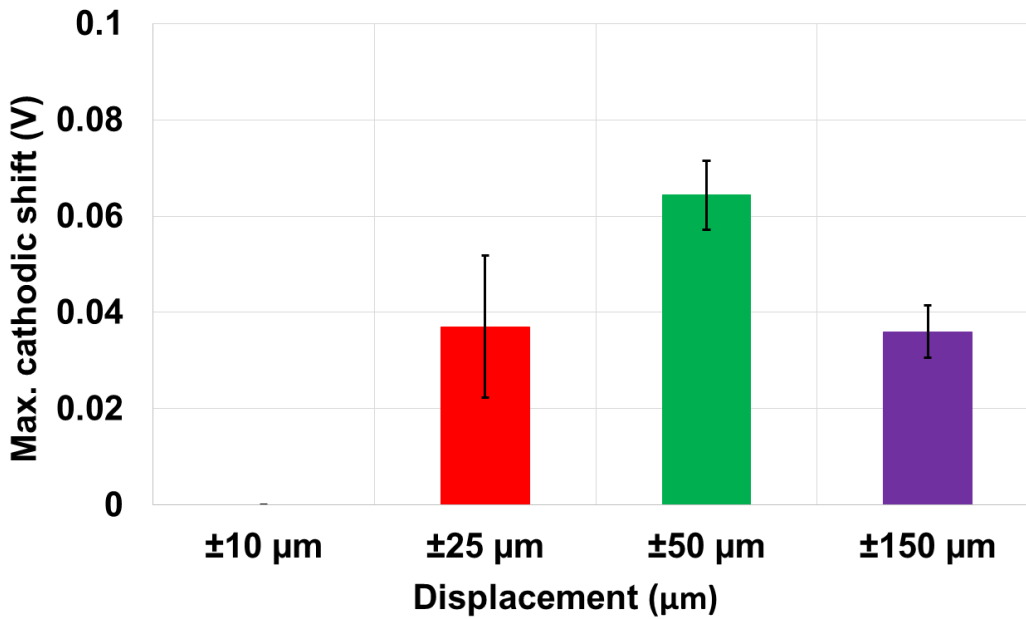
A representation of the OCP measurement for the CoCrMo – CoCrMo combination is shown in Figure 6-5a. During the pre-fretting (static) stage, most of the contact experienced ennoblement which is generally attributed to a build of protective oxide at the interface [193].

At the initiation of fretting, no cathodic shift was measured at  $\pm 10 \mu\text{m}$  which was similarly observed in reference [139]. However, for all the gross slip displacements i.e.  $\pm 25 \mu\text{m}$ ,  $\pm 50 \mu\text{m}$  and  $\pm 150 \mu\text{m}$ , a cathodic shift was observed. Interestingly, during the fretting cycles of  $\pm 150 \mu\text{m}$ , a gradual positive rise in potential which lasted until the end of the fretting cycles was observed. At the end of the fretting cycles for the gross slip regime, a two-stage potential recovery was observed; the repassivation stage and ennoblement stage. The former occurred at a faster rate than the latter. For all gross slip regime, the final OCP recovered to a more noble potential than at the start of the fretting.

The maximum cathodic shift was determined by obtaining the potential difference from the point immediately prior to the initiation of fretting and the most negative point during the fretting potential. Although, for partial-slip contacts where a general ennobling behaviour is observed, maximum cathodic shift is determined by the potential difference between the potential before and after the transient cathodic shift. Figure 6-5b shows no negative potential was observed at  $\pm 10 \mu\text{m}$ , however, the maximum cathodic shift increased from  $\pm 25 \mu\text{m}$  to  $\pm 50 \mu\text{m}$  and dropped for  $\pm 150 \mu\text{m}$  to similar values with that of  $\pm 25 \mu\text{m}$ .



(a)



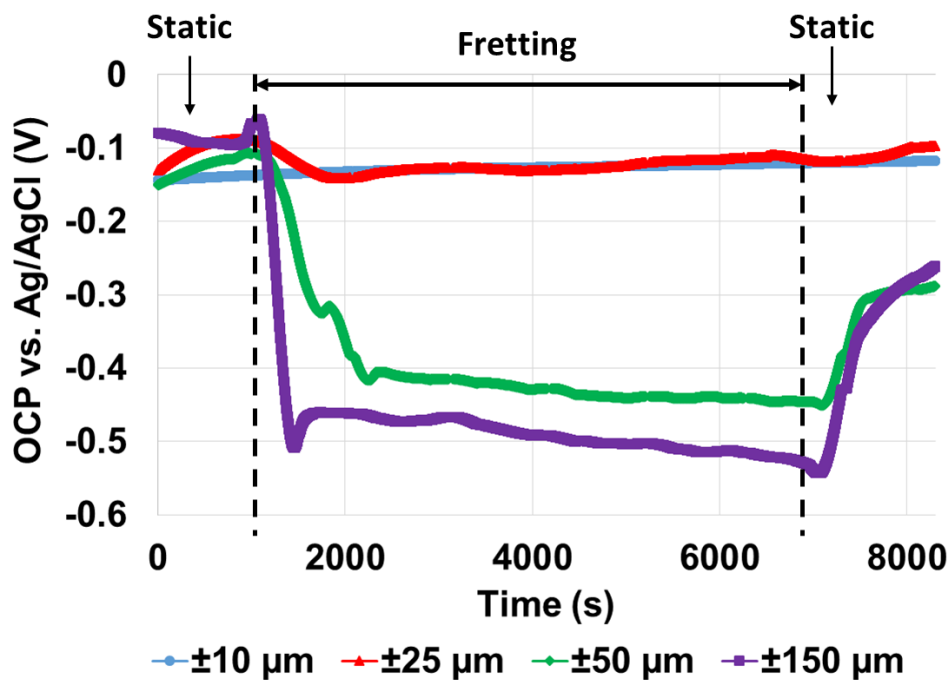
(b)

**Figure 6-5 – Open circuit potential of CoCrMo – CoCrMo: a) OCP plot for  $\pm 10 \mu\text{m}$ ,  $\pm 25 \mu\text{m}$ ,  $\pm 50 \mu\text{m}$  and  $\pm 150 \mu\text{m}$ . b) Max. cathodic shift of all displacements.**

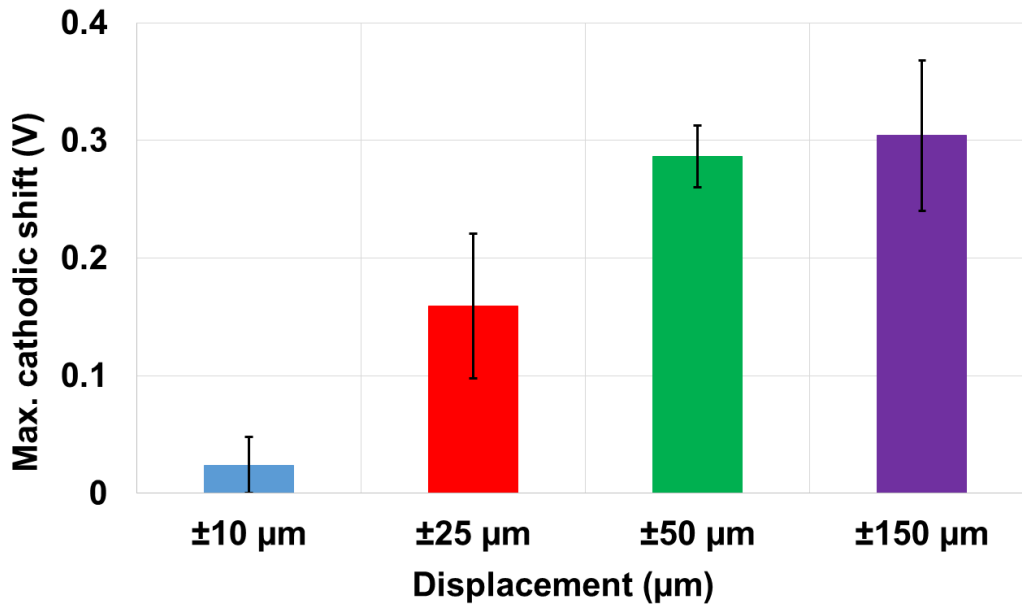
The OCP curves for CoCrMo – Ti6Al4V displacements are shown in Figure 6-6a. The results show a gradual rise in potential throughout the fretting cycles

for both  $\pm 10 \mu\text{m}$  and  $\pm 25 \mu\text{m}$ . Although, at  $\pm 25 \mu\text{m}$  a slower rate and minimal cathodic shift is observed at the initiation of fretting. A much larger drop in potential was observed for the two gross slip displacements i.e.  $\pm 50 \mu\text{m}$  and  $\pm 150 \mu\text{m}$ . The rate and magnitude of the potential drop was seen to be higher for the larger of the two gross slip contacts. Once fretting ceased, no potential recovery was observed for the two sticking contacts, a two-stage recovery process was observed for both gross-slip displacements. The first stage was a rapid repassivation process followed by a much slower ennoblement process in the second stage. It is notable that the total potential recovery after fretting ceased were  $\sim 150 \text{ mV}$  lesser than the potential before fretting started.

Figure 6-6b shows the maximum cathodic shift for the four displacements. It is observable that the potential shift increased with increasing displacement. However, on average, the maximum cathodic shift for  $\pm 50 \mu\text{m}$  and  $\pm 150 \mu\text{m}$  were observed to be similar.



(a)



(b)

**Figure 6-6 – Open circuit potential of CoCrMo – Ti6Al4V: a) OCP plot for  $\pm 10 \mu\text{m}$ ,  $\pm 25 \mu\text{m}$ ,  $\pm 50 \mu\text{m}$  and  $\pm 150 \mu\text{m}$ . b) Max. cathodic shift of all displacements.**

## 6.4 Wear volume

Figure 6-7 shows the total wear volume and redistributed volume of all four displacements for CoCrMo – CoCrMo fretting contact. The column chart represent the sum of both ball and flat components. The redistributed volume (defined in section 4.5.2) were only measurable at the gross slip displacements and were all of similar magnitude. On the other hand, the wear volume was similar for both  $\pm 10 \mu\text{m}$  and  $\pm 25 \mu\text{m}$  and much higher at  $\pm 50 \mu\text{m}$  and  $\pm 150 \mu\text{m}$  displacement as would be expected. However, the proportion of the wear volume between  $\pm 50 \mu\text{m}$  and  $\pm 150 \mu\text{m}$  were not proportional to the three-times multiple of the displacement amplitude thus indicating a transition in wearing mode.



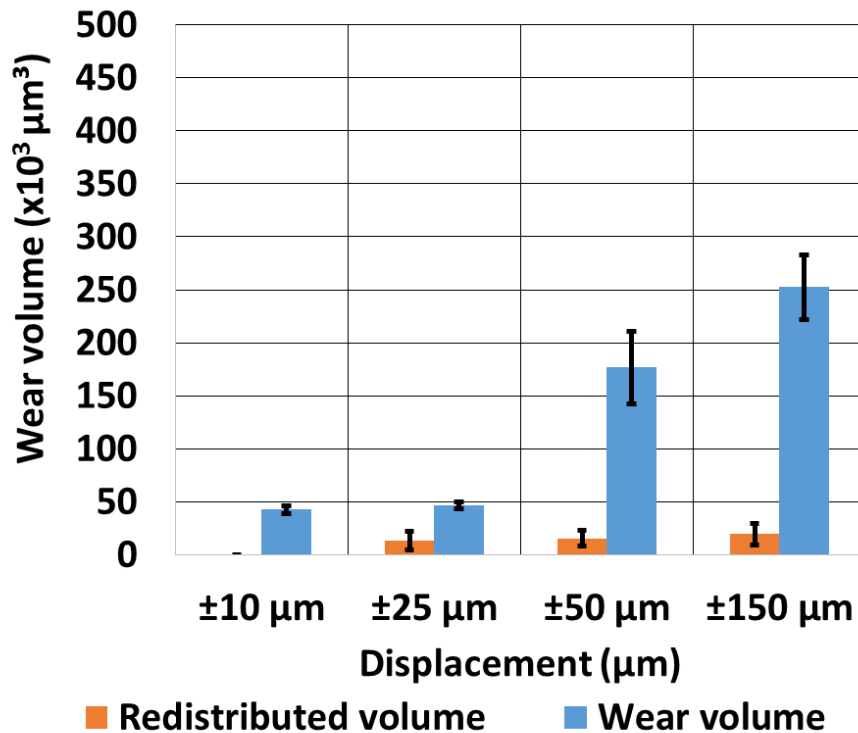


**Figure 6-7 – Sum of ball and flat wear volume and redistributed volume for CoCrMo – CoCrMo fretting contact.**

The total wear volume for CoCrMo – Ti6Al4V material combination is shown in Figure 6-8. The result shows a general increase in the redistributed volume for all displacements. The wear volume for  $\pm 10 \mu\text{m}$  and  $\pm 25 \mu\text{m}$  (stick regime contacts) were near zero as expected. Interestingly, at  $\pm 50 \mu\text{m}$ , the wear volume and redistributed volume were very similar thus describing the case whereby the worn material is almost entirely redistributed within the interface. The wear volume at  $\pm 150 \mu\text{m}$  was significantly larger than at  $\pm 50 \mu\text{m}$  and the error bar was also much higher at this displacement. This is attributed to erratic contact behaviour involving ejection and detainment of third-body product – this is later confirmed through surface analysis in Figure 6-10. In comparison to the CoCrMo – CoCrMo contact, wear volume and redistributed volume for CoCrMo – Ti6Al4V are at least double at the gross slip regimes.

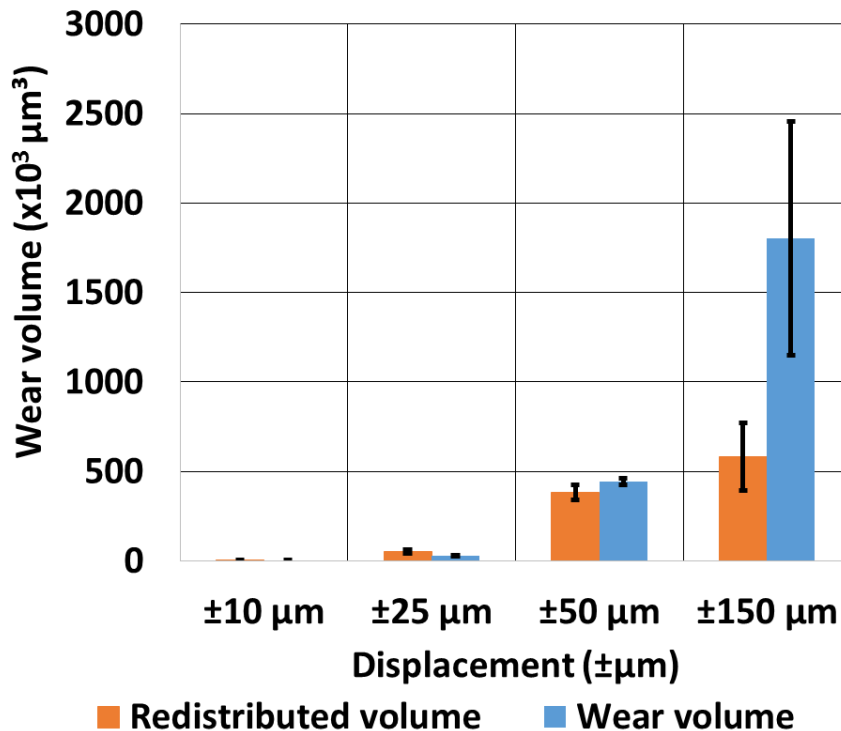


**Figure 6-8 – Sum of ball and flat wear volume and redistributed volume for CoCrMo – Ti6Al4V fretting contact.**

## 6.5 Surface Analysis

In this section, post-test surface analysis using the WLI was used to obtain 3D and 2D surface profilometry for both ball and flat components at all displacements. Subsequently, BS-SEM was used to obtain high resolution surface micrographs for CoCrMo and Ti6Al4V (flat components) at ±50 μm displacement for characterisation of third-body products generated at the fretting interface.

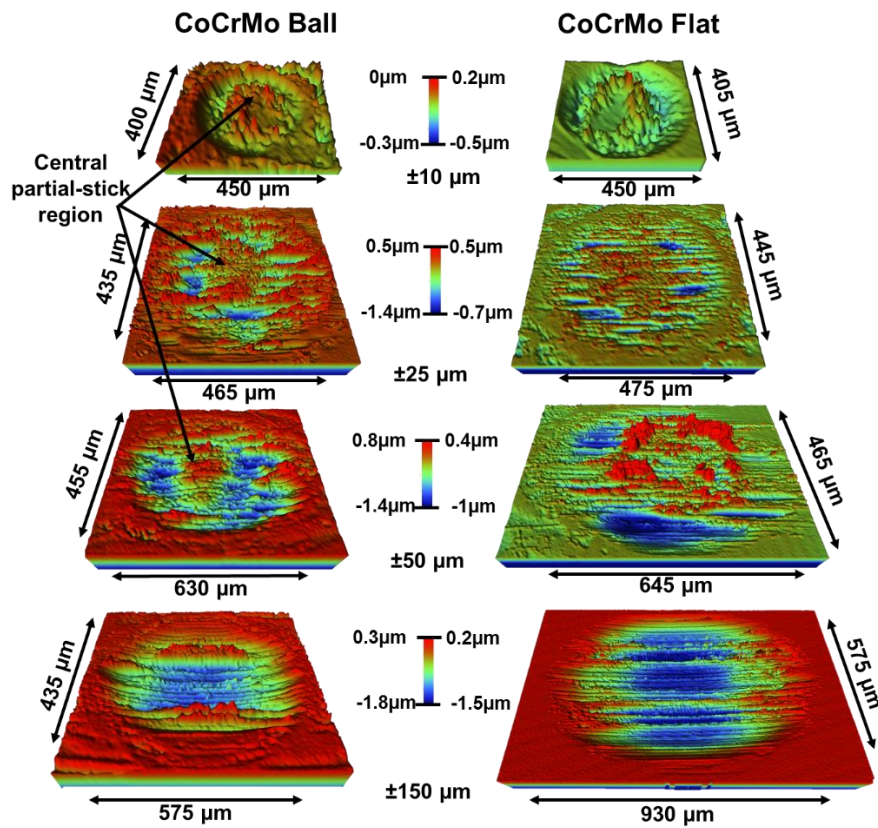
### 6.5.1 3D and 2D surface profilometry of fretted contacts

The 3D and 2D surface profilometry of CoCrMo – CoCrMo ball and flat surfaces are shown in Figure 6-9a and Figure 6-9b. The 2D cross-sections were taken from the vertical y-axis across the centre in most cases. However in some other cases, the 2D cross section that most describes the wear

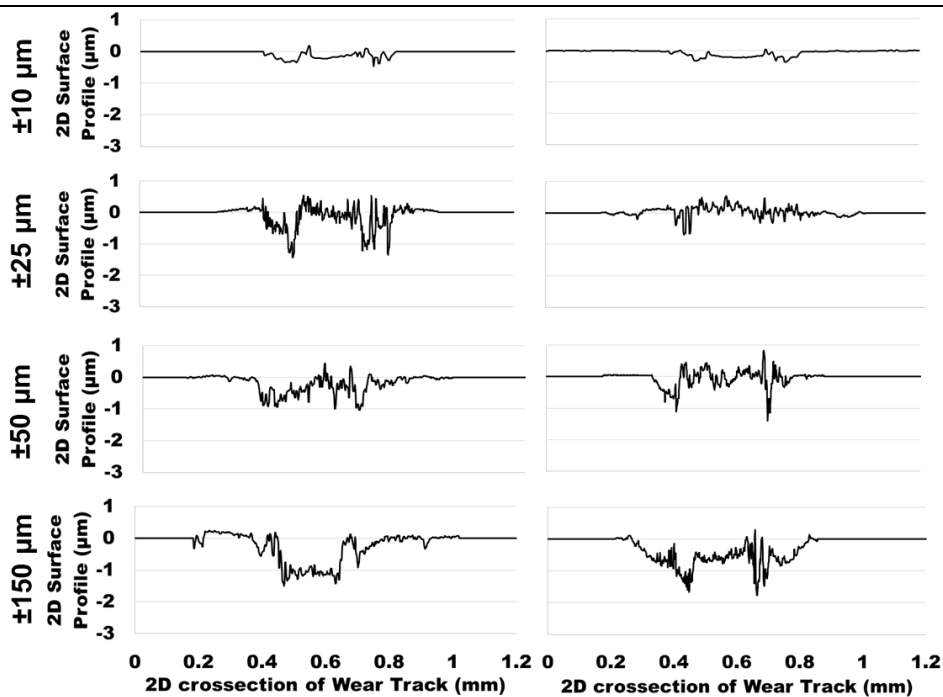
surface based on the 3D surface profile is used instead. The wear depth is estimated using the 2D cross sectional profile. The key observations from each displacement are outlined below:

- $\pm 10 \mu\text{m}$  – Both ball and flat components have a worn annulus with wear depth  $\sim 350 \text{ nm}$  and a partially worn central partial-stick region.
- $\pm 25 \mu\text{m}$  – The central partial-stick region on the ball is still present, however, the worn annulus is relatively wider as expected, due to the transition into gross slip regime. The wear depth is  $\sim 1 \mu\text{m}$  on the ball component and the wear product are redistributed across the surfaces.
- $\pm 50 \mu\text{m}$  – The proportion of the central partial-stick region on the ball decreased further with increase in displacement whilst the wear depth remains  $\sim 1 \mu\text{m}$ . On the flat component, an increased worn annulus is observed however, around the lightly abraded central region are third-body product.
- $\pm 150 \mu\text{m}$  – The central region at this displacement is seen to be totally worn for the ball component resulting in a wear depth of  $\sim 1 \mu\text{m}$ . Interestingly, it appears as though third-body products are redistributed within the ball wear surface which inflicted a deeper groove (wear depth of  $\sim 1.4 \mu\text{m}$ ) into the flat surface. The final length of the flat component is more than double the initial Hertzian contact width ( $2a = 320 \mu\text{m}$ ) thus suggesting a transition to reciprocating sliding.

In general, the presence of the central partial-stick region from  $\pm 10$  to  $\pm 50 \mu\text{m}$  shows that the fretting contacts are still influenced by elastic contact compliance whilst the absence of the central partial-stick region at  $\pm 150 \mu\text{m}$ , is further indication of a third-body controlled wear mechanism at this displacement [39].



(a)



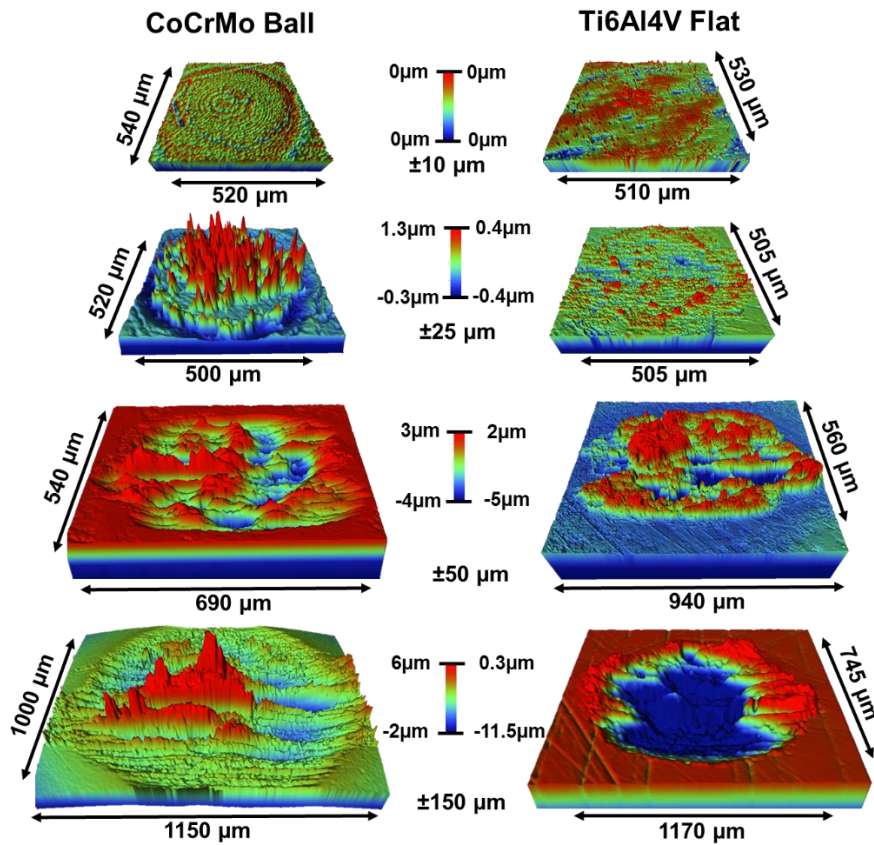
(b)

Figure 6-9 – Surface profilometry of CoCrMo ball and CoCrMo flat for all four displacements under OCP conditions: a) 3D surface profile, b) 2D cross-section of the vertical axis of the wear surface.

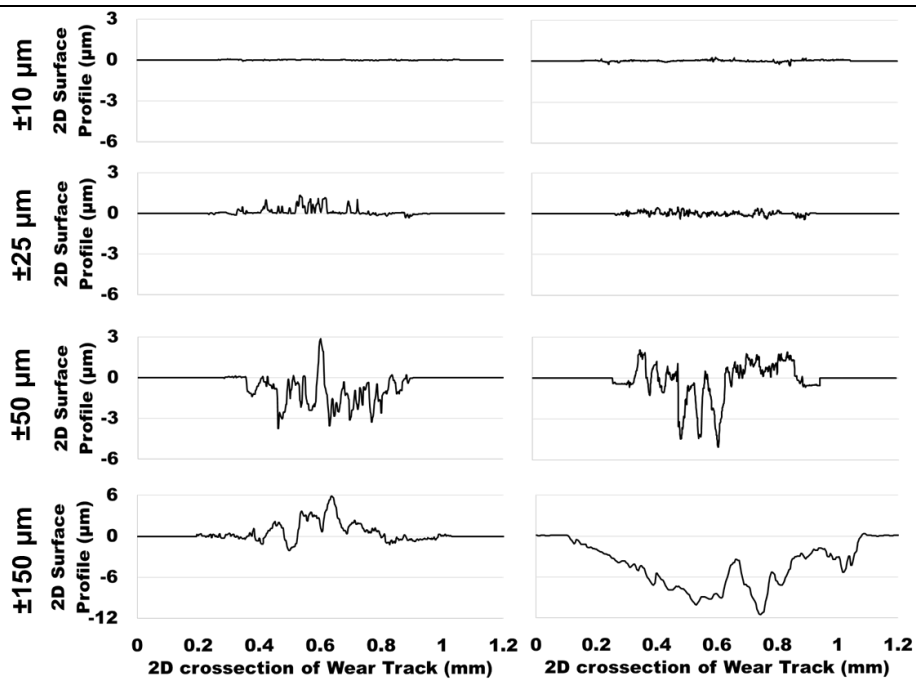
The 3D and 2D surface profiles of the CoCrMo – Ti6Al4V combination are shown in Figure 6-10a and Figure 6-10b. The key observations are outlined below:

- $\pm 10 \mu\text{m}$  – The stick regime fretting contact at this displacement shows no visible signs of wear on either CoCrMo or Ti6Al4V.
- $\pm 25 \mu\text{m}$  – Although this fretting contact is also in a stick regime, a relatively thin worn annulus developed on the CoCrMo ball. The maximum wear depth of the annulus is  $\sim 300 \text{ nm}$  and across the entire central partial-stick region, third-body materials likely transferred from the worn annulus were observed. The third-body materials appear in needle-like peaks of height  $\sim 1 \mu\text{m}$ . On the Ti6Al4V flat however, there is no evidence of wear other than material transferred onto the flat.
- $\pm 50 \mu\text{m}$  – The fretting contact at this displacement experienced a gross-slip regime for most of the fretting cycles. The CoCrMo ball appears to have experienced surface ruptures whereby heaps of fragments with heights up to  $3 \mu\text{m}$  above the unworn surface are visible. A layer of third-body material up to  $2 \mu\text{m}$  thick can be observed on the Ti6Al4V surface. Areas within the layer where cracks of maximum depth  $\sim 5 \mu\text{m}$  exist can be seen to fit well with the area where fragmented heaps of material exist on the CoCrMo. This therefore suggests that the layer fractured from the CoCrMo surface.
- $\pm 150 \mu\text{m}$  – The surface profile shows a much larger wear surface for both the ball and flat components compared with the surfaces at  $\pm 50 \mu\text{m}$ ; heaps of third-body material with height  $\sim 6 \mu\text{m}$  were observed on the CoCrMo surface. The Ti6Al4V surface is mainly characterised with large wear depths with maximum depths reaching up to  $\sim 11 \mu\text{m}$ .

In general, the size of the wear contact surface for both ball and flat components of the stick regimes were similar to the initial Hertzian contact width ( $2a = 500 \mu\text{m}$ ) and wear began at the edge of the Hertzian contact boundaries as expected. Furthermore, the CoCrMo ball is shown to have worn more than the Ti6Al4V for both  $\pm 25 \mu\text{m}$  and  $\pm 50 \mu\text{m}$  displacements.



(a)



(b)

**Figure 6-10 – Surface profilometry of CoCrMo ball and Ti6Al4V flat for all four displacements under OCP conditions: a) 3D surface profile, b) 2D cross-section of the vertical axis of the wear surface**

### **6.5.2 Back scatter SEM of CoCrMo and Ti6Al4V surface**

The surface and chemical analysis in this section is focused on characterising the interfacial wear and corrosion products generated at the fretting contacts of CoCrMo – CoCrMo and CoCrMo – Ti6Al4V. The flat components of  $\pm 50 \mu\text{m}$  in both material combinations withhold a substantial amount of these products hence, surface analysis were conducted only on the flat components.

BS-SEM micrograph of the CoCrMo flat from the CoCrMo – CoCrMo interface is shown in Figure 6-11. There are three regions of interest: Region 'A' identifies the worn annulus with evidence of third-body products present in the region. Region 'B' shows the boundary between the worn annulus and the lightly worn central region as also observed in the 3D surface profilometry of Figure 6-9a,  $\pm 50 \mu\text{m}$ . Region 'C' illustrates evidence of the third-body products generated at the interface. The back scatter technique provides an additional information which helps distinguish third-body products from the base material in the wear surface. Often times, the third-body products are oxidised products of the alloying elements therefore have a lower atomic mass than the bulk alloy hence they appear darker than the base alloy in BS-SEM. Interestingly, the micrograph also shows that majority of the third-body product are located near the boundary between the worn annulus and the central partial-stick region.

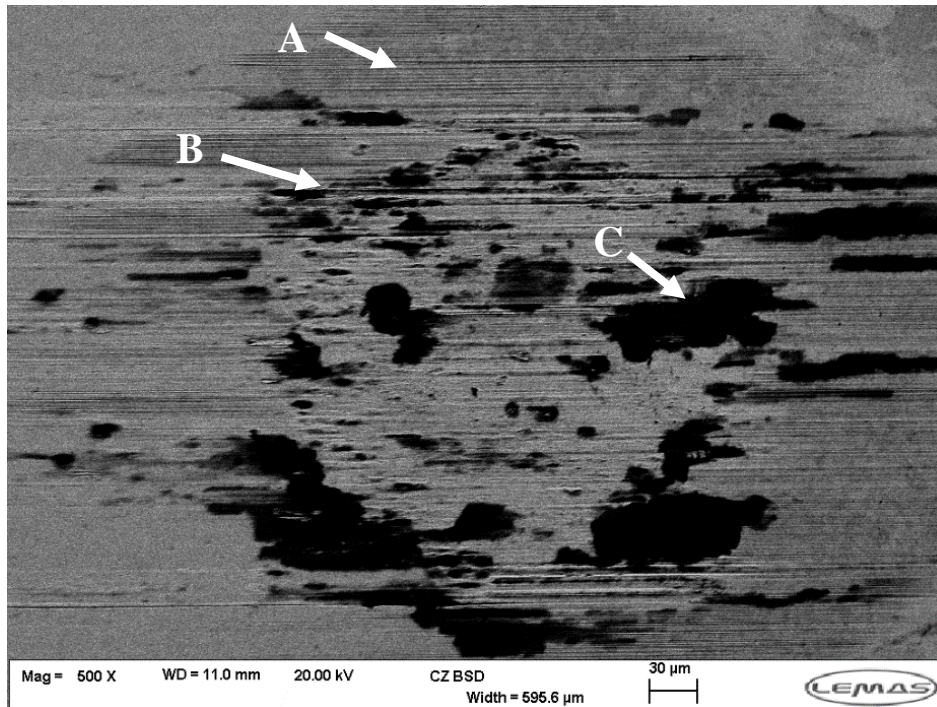


**Figure 6-11 – Back scatter-SEM of CoCrMo flat from the CoCrMo – CoCrMo interface at  $\pm 50 \mu\text{m}$  under OCP conditions.**

The BS-SEM micrograph of Ti6Al4V surface in Figure 6-12 reveal a rather complicated wear surface. Four main region of interests were labelled 'A – D'. Region 'A' is the Ti6Al4V surface external to the fretting contact, the visible scratches observed in the region is a result of the jerking effect from the fretting machine as it returns to zero position at the end of a test. Region 'B' points out the thick layer that ruptured from the CoCrMo surface as described in Figure 6-10a,  $\pm 50 \mu\text{m}$ . Evidence of wear tracks seen across the surface of region B is an indication that the CoCrMo alloy was fretting against this layer instead of Ti6Al4V.

Region 'C' is seen to be almost entirely surrounded by the layer of region B. The height of the material above the plain surface is measured in Figure 6-10b is up to  $2 \mu\text{m}$ . This indicates that region C exists at a lower surface level than region B and thus a likely creviced region. Within region C and all the other regions like it, were found extensive cracks to the Ti6Al4V surface. Furthermore, lighter appearing materials of various shapes and sizes were seen within the region. Considering that the material with the heaviest atomic mass appears the brightest with BS-SEM, the material is likely CoCrMo bulk alloy which has a higher atomic mass than Ti6Al4V (as spectroscopy



techniques later confirms). Region 'D' is seen with surface cracks inflicted unto the Ti6Al4V surface which appear different from those observed in region 'C'. While the cracks in region 'C' appear like cracks formed through surface tension between the elevated layer and the enclosed Ti6Al4V surface, the crack in region D appears to be mechanically induced, that is, due to direct contact with the fragments of material rupture from the CoCrMo as previously shown in Figure 6-10a,  $\pm 50 \mu\text{m}$ .

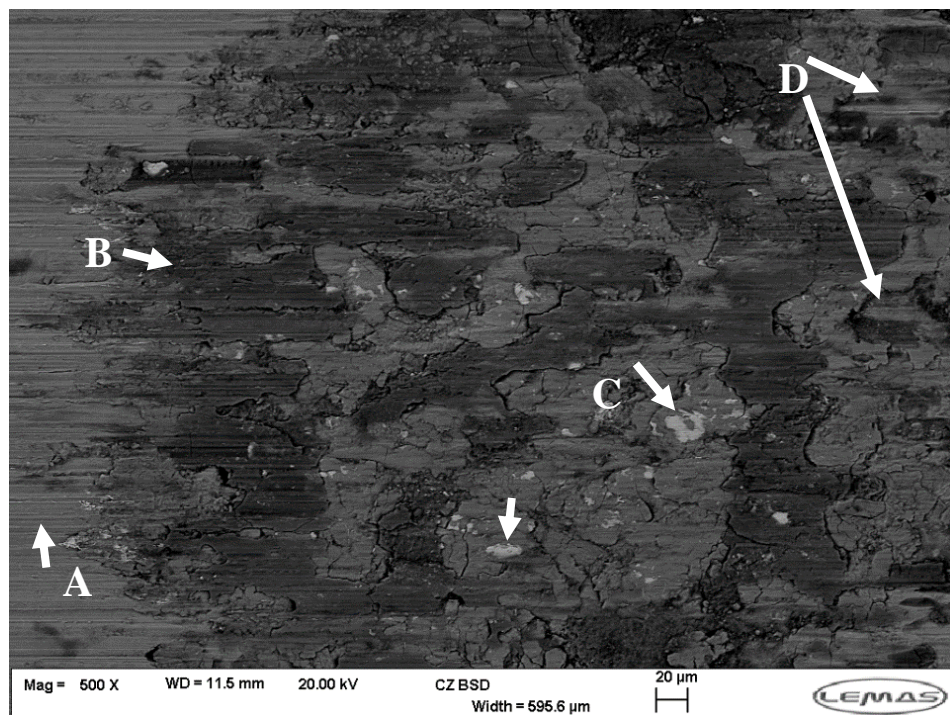


**Figure 6-12 – Back scatter-SEM of Ti6Al4V flat from the CoCrMo – Ti6Al4V interface at  $\pm 50 \mu\text{m}$  under OCP conditions.**

## **6.6 Spectroscopy of CoCrMo and Ti6Al4V surface from the metal – metal interface**

In this section, SEM-EDS and XPS techniques were used to characterise the chemical composition of the third-body products at the interfaces of CoCrMo – CoCrMo and CoCrMo – Ti6Al4V material combinations. SEM-EDS maps are presented to highlight the key elements of interest on the surface. The elements that are not present on the EDS maps are either absent or their concentration is too low to be detected.

The flat surfaces characterised in the previous sections are the same surfaces analysed here. For the high resolution XPS scan, the tribocorrosion products in region 'C' of the CoCrMo flat (Figure 6-11) was scanned for the following key elements: C, O, Co, Cr, Mo, P, S and Si. As for the Ti6Al4V flat, regions C and D of Figure 6-12 were scanned for C, O, Ti, Al, V, Co Cr, Mo, P, S and Si. S was also scanned at high resolution but no peak was detected for all three analysed areas on the CoCrMo and Ti6Al4V flats.

### **6.6.1 EDS analysis of CoCrMo and Ti6Al4V surfaces (metal – metal)**

EDS map of the CoCrMo flat shown in Figure 6-13 identified the presence of Co, Cr and Mo across the entire surface of the alloy as expected. However, Co appears with a lower concentration across regions covered in third-body products. The table inset in Figure 6-13 shows that Co has a concentration about three-times less than its usual bulk concentration which is ~60 at%. O on the other hand, is seen to be mostly abundant across the third-body product. C and N are both identified but have are relatively weak.

Interestingly, Cl is observed to be most abundant within the third-body products that surrounds the boundary between the worn annulus and the central region whereas, P is seen to be concentrated within the product that is present in the worn annulus. The inset table which analysed the P-rich region shows evidence of P however no evidence of Ca. The presence of P in a tribocorrosion region is generally in the form of Ca-phosphate or as Cr-phosphate. Thus the absence of Ca may suggest the presence of Cr-phosphate (as confirmed through XPS). Si and Mo were also detected in the background as would be expected, considering that they are also constituents of the bulk alloy (see section 5.3.2).

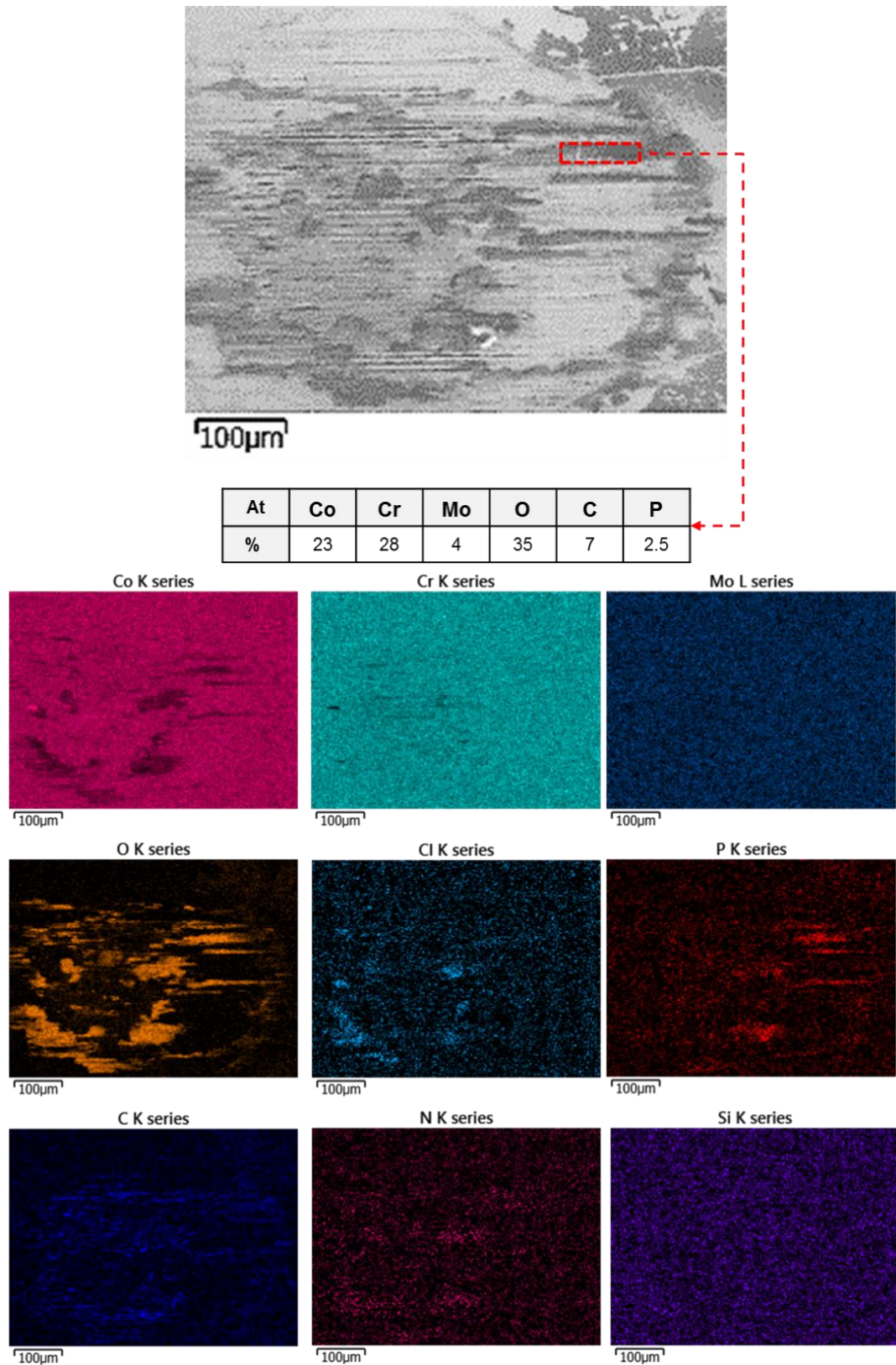
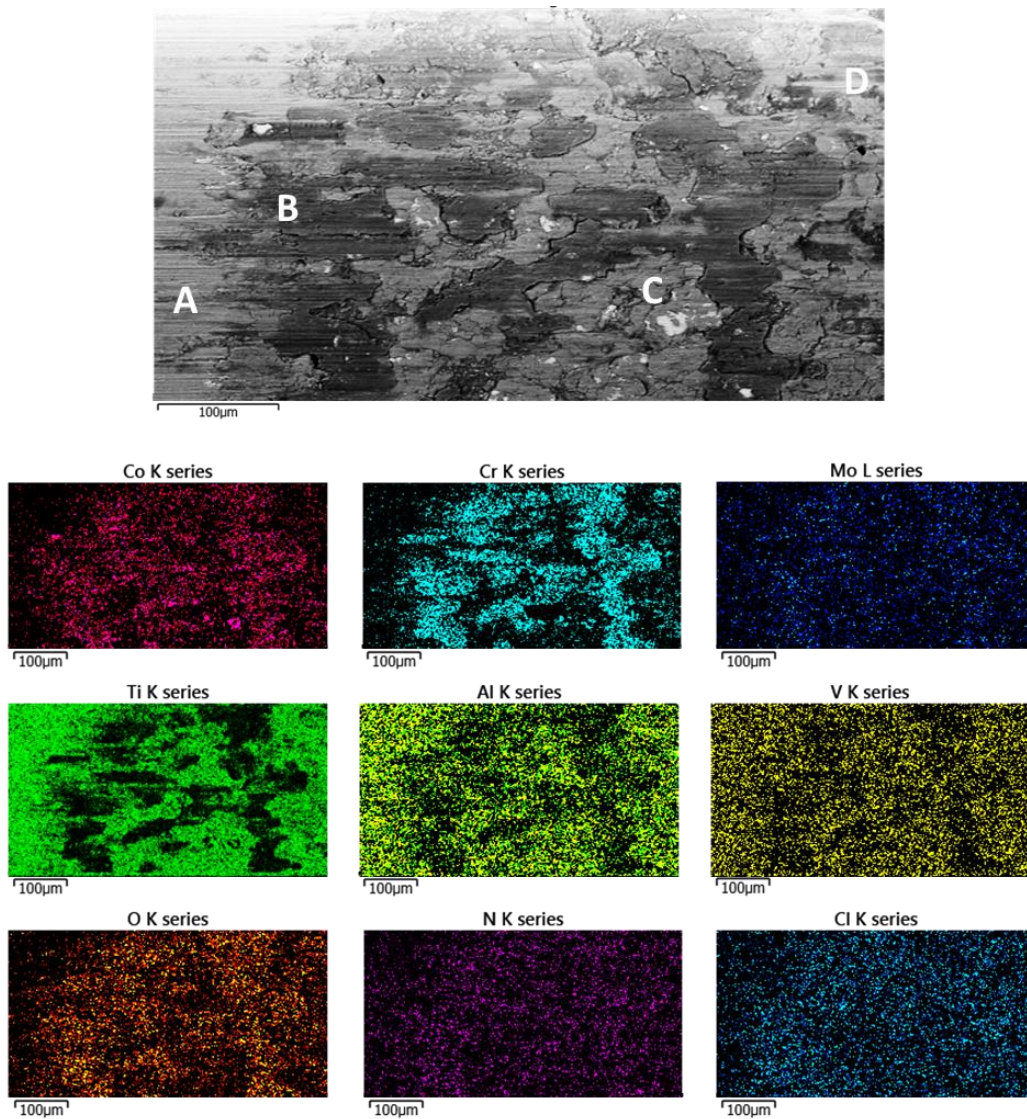


Figure 6-13 – SEM-EDS of CoCrMo flat at  $\pm 50 \mu\text{m}$  from CoCrMo – CoCrMo interface under OCP conditions. The inset table outlines the composition of a specific third-body region.

The EDS map of Ti6Al4V flat shown in Figure 6-14 shows evidence of Co, Cr and Mo – the main chemical composition of CoCrMo alloy across the wear surface. These were most concentrated in region B (the areas covered by the fractured layer) as indicated in Figure 6-12 and illustrated in Figure 6-14. It is observable that O was also more concentrated across the areas covered by the layer, thus indicating the material composes mainly of mixed metal-oxides of CoCrMo. The regions identified as regions, A, C and D in Figure 6-12 appear with relatively higher concentrations of Ti, Al and V – the main chemical composition of Ti6Al4V. N and Cl appear to be more prominent in region B although at relatively low concentrations.



**Figure 6-14 – SEM-EDS of Ti6Al4V flat at  $\pm 50 \mu\text{m}$  from CoCrMo – Ti6Al4V interface under OCP conditions.**

### 6.6.2 XPS analysis of CoCrMo and Ti6Al4V surfaces (metal – metal)

The analysis of the CoCrMo – CoCrMo interface is shown in Figure 6-15(a – g). The specific region scanned is the third-body product illustrated in Figure 6-11 as region 'C'. In this region, a typical adventitious C peak and others generally attributed to contamination and denatured protein is seen in Figure 6-15a. Also, the three typical O peaks namely MO, NBO and BO can be seen in Figure 6-15b. The peak from Co2p in Figure 6-15c indicates the presence of oxidised/metal species of Co as EDS identified in Figure 6-13, however, the intensity of the peak is too weak relative to the background to reliably compute. A similar case is seen for the Mo3d peak in Figure 6-15g. Figure 6-15d shows both metallic and oxidised species of Cr2p. In Figure 6-15e, evidence of the phosphate P (5+) peak is seen as well as Si2p in variable oxidation states in Figure 6-15f.

In Table 6-1 the Cr and O species are attributed mainly to Cr<sub>2</sub>O<sub>3</sub> and CrPO<sub>4</sub>. The significant proportion of the high energy Cr (3+) relative to the lower energy is an indication that CrPO<sub>4</sub> is more abundant in the third-body product than Cr<sub>2</sub>O<sub>3</sub>. The presence of other metallic species (although at much lower intensities) suggests the presence of mixed hydroxide species of Cr, Co and Mo. Although high resolution scanning of Cl was not conducted using XPS, EDS confirms it is present within the analysed third-body product (see Figure 6-13). Thus, it is expected that an unknown proportion of the lower binding energy of Cr (3+) would contribute to the formation of CrCl<sub>3</sub>.

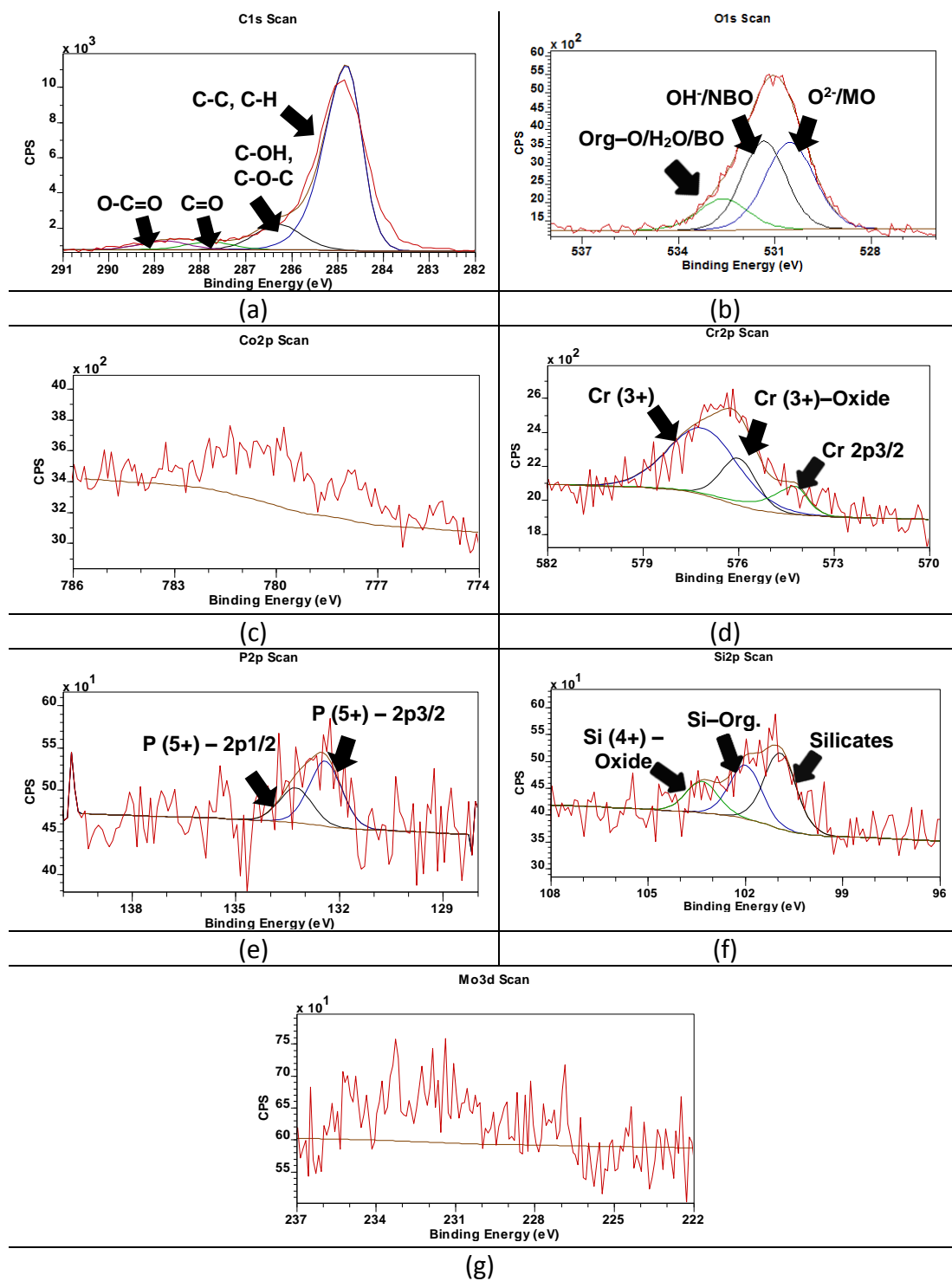


**Figure 6-15 – XPS analysis of wear and corrosion product from the wear surface of CoCrMo – CoCrMo combination at  $\pm 50 \mu\text{m}$  under OCP conditions.**

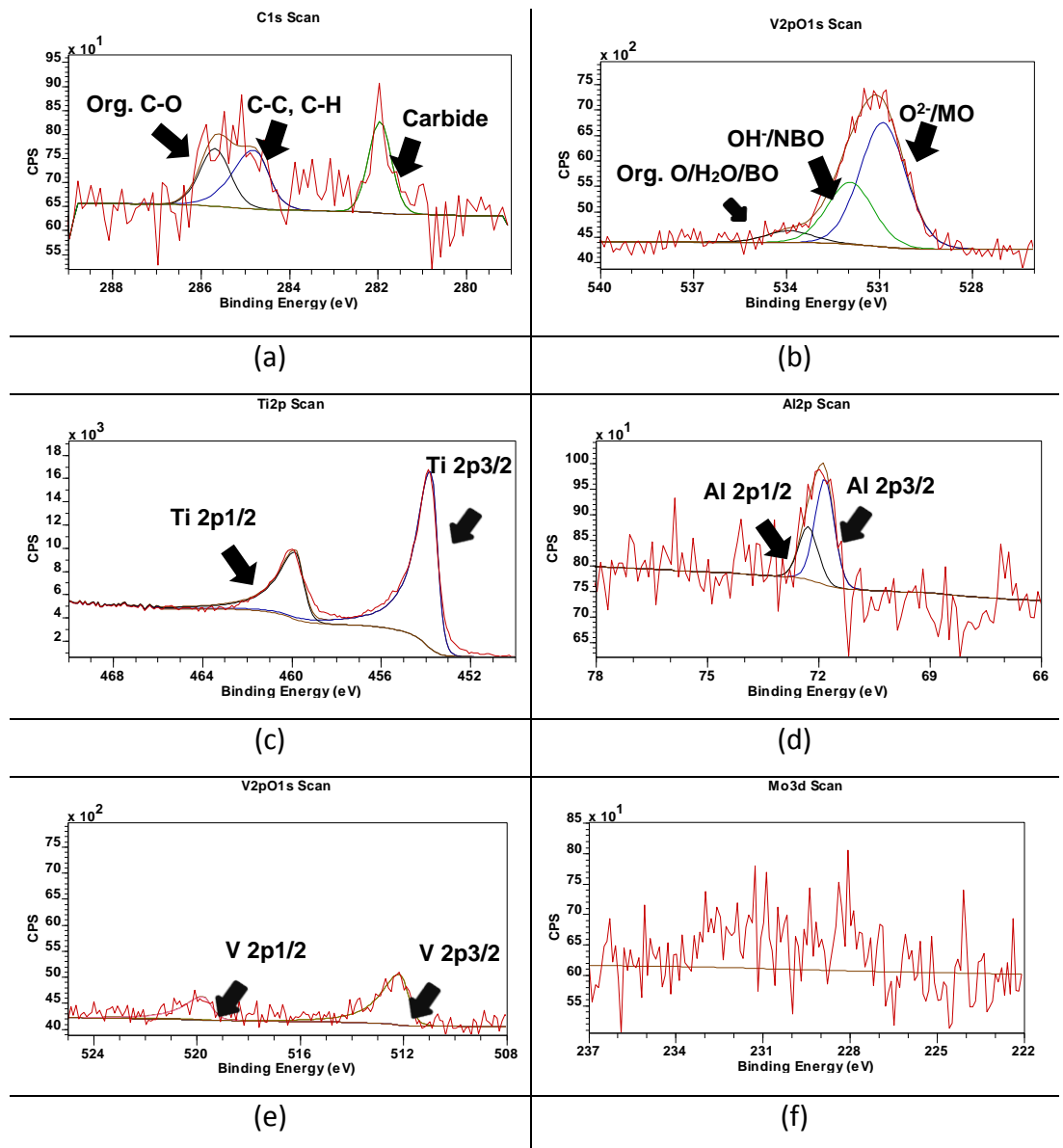
**Table 6-1 – Attribution of Cr and O species from CoCrMo – CoCrMo interface at  $\pm 50 \mu\text{m}$**

Peak	Position (eV)	Attributions [154, 158]		(%)
Cr 2p	574.2	Cr(0) – Metal		16
	576.0	Cr(3+) – Oxide/Chloride		22
	577.1	Cr(3+) – Hydroxide & Phosphate		62
O 1s	530.5	MO	O <sup>2-</sup>	44
	531.3	NBO	OH <sup>-</sup> /PO <sup>4-</sup>	40
	532.6	BO	H <sub>2</sub> O/Si-O/C-O	16

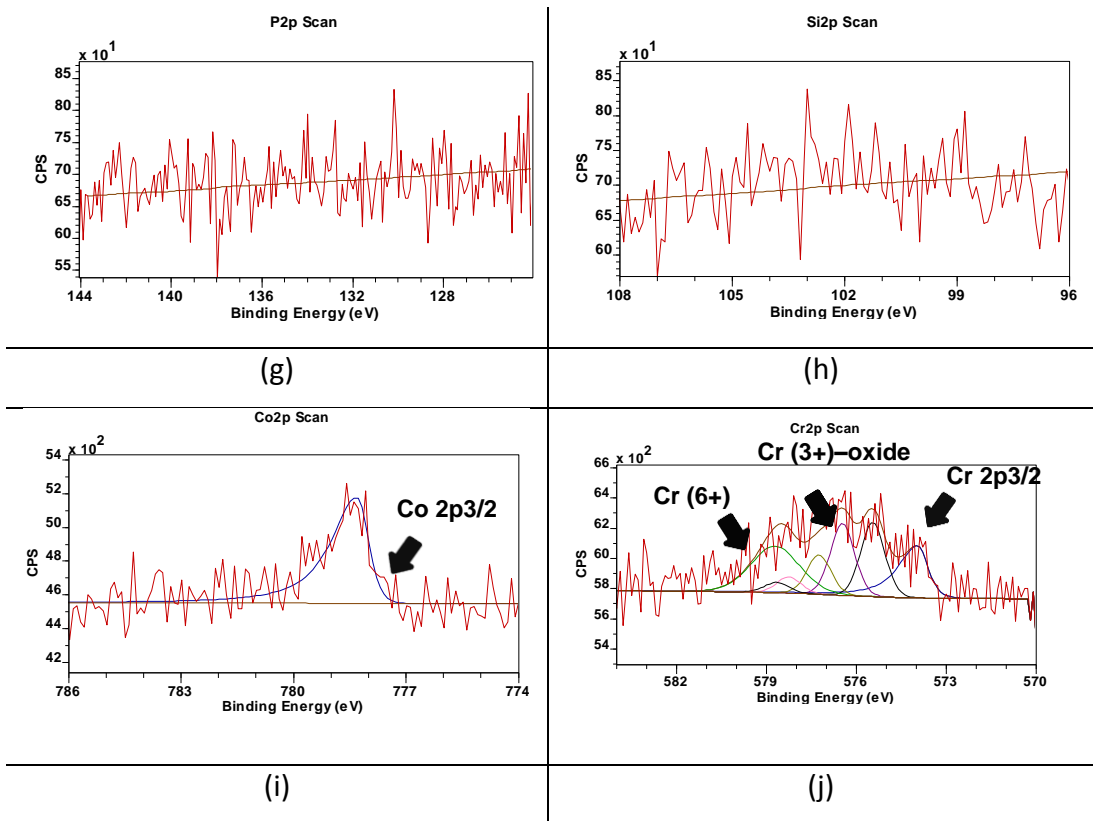
As previously mentioned, two regions of the Ti6Al4V flat from the CoCrMo – Ti6Al4V material combinations were analysed. Analysis of region C (the creviced area) of Figure 6-12 are shown in Figure 6-16(a – j). Figure 6-16a shows the C 1s scan. The typical adventitious C peaks were not present on this surface, but three distinctive C species were identified: 281.9 eV – which corresponds to metal-carbide peak; the Aliphatic C specie at ~284.8 eV and an organic C-O specie at ~285.7 eV. The absence of the adventitious C species is likely because the part of the surface analysed in this region is located below the uppermost surface of the wear scar which is where adventitious C is typically found.

Figure 6-16b shows the three standard O peaks. Figure 6-16c – e shows evidence of bulk metal, non-oxidised Ti, Al and V species respectively. Mo, P and Si species were not detected on this surface as shown in Figure 6-16f – h respectively. Interestingly, in Figure 6-16i, only the metallic specie of Co at 778.3 eV was detected and in Figure 6-16j, three distinctive peaks of Cr were observed including the metallic specie of Cr at ~ 574.0 eV. Cr (3+) – oxide on this surface was fitted with five peaks starting from ~575.5 eV. This is a detailed way of fitting Cr (3+)-oxide as documented in reference [154] although the single peak approach (used in Figure 6-15) is also commonly used [174]. The third Cr specie observed in this creviced region was the highly debated

Cr (6+) peak at 578.7 eV. Considering that the proportion of the MO specie is double the NBO specie as shown in Table 6-2, the Cr (6+) specie is likely in its oxide form of  $\text{CrO}_3$ . It is worth noting that, a proposed rule for ensuring the peak being fitted is actually Cr (6+) as supposed to multi-plets of Cr (3+) oxide is that the peak should encompass an area greater than 15% of the Cr2p scan [154, 159]. The area enclosed by the Cr (6+) in this analysis was up to 25% and all five multi-plet peaks of the Cr (3+) oxide are also fitted.







**Figure 6-16 – XPS analysis of wear and corrosion product from the wear surface of CoCrMo – Ti6Al4V combination at  $\pm 50 \mu\text{m}$ . Creviced region – Region ‘C’**

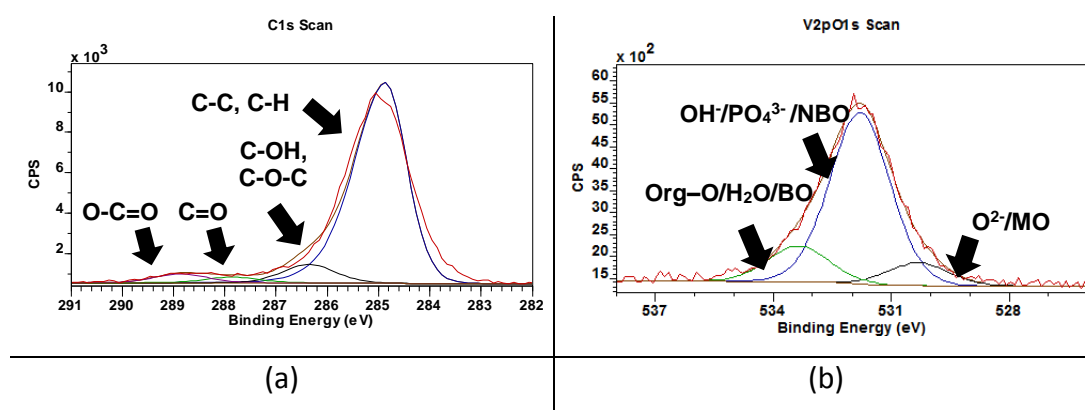
**Table 6-2 – Attribution of Cr, Co and O species from CoCrMo – Ti6Al4V interface at  $\pm 50 \mu\text{m}$ . Creviced region – Region ‘C’**

Peak	Position (eV)	Attributions [154, 158]		(%)
Cr 2p	574.0	Cr(0) – Metal		20
	575.5	Cr(3+) – oxide		55
	578.7	Cr(6+) – oxide		25
Co 2p	778.3	Co(0) – Metal		100
O 1s	530.5	MO	O <sup>2-</sup>	63
	531.3	NBO	OH <sup>-</sup>	31
	532.6	BO	C-O	6

Analysis of the second region on the Ti6Al4V surface of the CoCrMo – Ti6Al4V interface is shown in Figure 6-17(a – j). This corresponds to region D from the BS-SEM micrograph of Figure 6-12; cracks within this region was described to have been mechanically inflicted by the CoCrMo counterpart. In addition, unlike region C, this region is not locally enclosed and is further away from the centre of wear surface. In Figure 6-17a, it can be seen that the adventitious C is present on this surface and so are the three O peaks in Figure 6-17b. shows

No metallic species of Ti were found on this surface as shown in Figure 6-17c however, two oxidised species of Ti (4+) at 459.1 eV and Ti (3+) at 457.6 eV were present. The abundance ratio of Ti (4+) to Ti (3+) are about 8:2 as shown in Table 6-3. Figure 6-17d – f shows that neither oxidised nor the metallic species of Al, V and Mo respectively were detected on the surface and the Si, Co and Cr species in Figure 6-17h – j respectively may either be absent or too weak to compute.

Evidence of a prominent phosphate P (5+) specie was also found in Figure 6-17g. This explains the significant proportion of the NBO specie compared to the MO specie. Further analysis of this region using TEM-EDS in section 6.7.2 may explain the absence of the species pertaining to the CoCrMo.



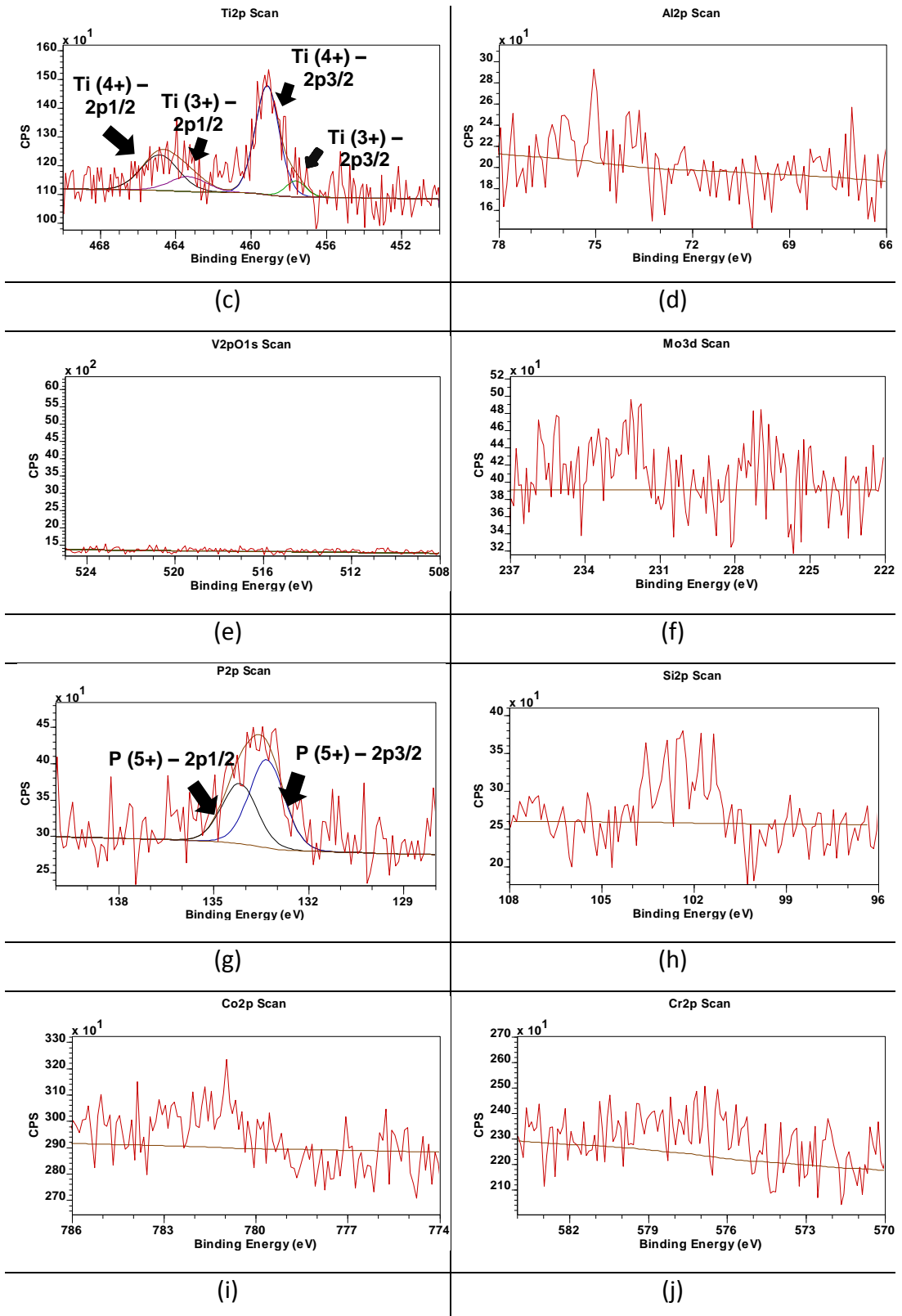


**Figure 6-17 – XPS analysis of wear and corrosion product from the wear surface of CoCrMo – Ti6Al4V combination at  $\pm 50 \mu\text{m}$  under OCP conditions. Region of mechanically induced crack – region 'D'.**

**Table 6-3 – Attribution of Ti and O species from CoCrMo – Ti6Al4V interface at ±50 µm. Region of mechanically induced crack – region ‘D’**

Peak	Position (eV)	Attributions [153, 159]		At (%)
Ti 2p	459.2	Ti(4+) – Oxide		84
	457.7	Ti(3+)		16
O 1s	530.3	MO	O <sup>2-</sup>	10
	531.8	NBO	OH <sup>-</sup> /PO <sup>4-</sup>	74.5
	533.3	BO	H <sub>2</sub> O/C-O	15.5

## 6.7 Characterisation of metallurgical transformations (metal – metal)

It is well understood that the fretting regime of a material combination influences the form of surface and subsurface transformations the energy (work done) expended at the interface would yield [39]. Furthermore, it is expected that increasing energy input by increasing fretting displacements would yield different forms of subsurface transformation in CoCrMo and Ti6Al4V alloys due to their different mechanical properties. For this reason, a cross-section from the CoCrMo flat of the CoCrMo – CoCrMo combination and the Ti6Al4V flat of the CoCrMo – Ti6Al4V combination was prepared with the FIB. Samples were obtained from the worn region of each individual displacement amplitude. From the 3D surface profile of Figure 6-9 and Figure 6-10, it can be seen that the fretting wear surface is highly varied and therefore it is expected that transformation in the metallurgical structures would be site-specific in most cases (see section 4.5.4 for further detail on how specific region for analysis were selected).

### 6.7.1 TEM of Fretted CoCrMo and Ti6Al4V alloy

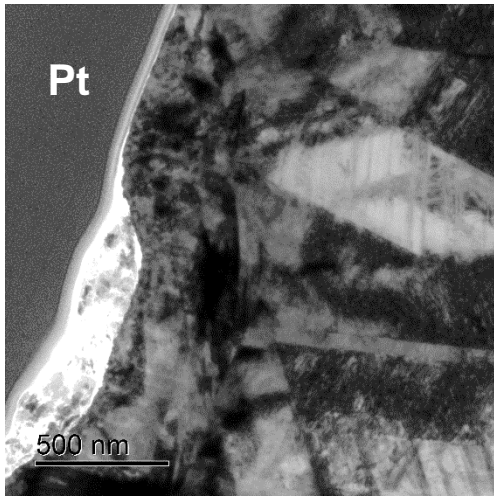
The following at the key observations made from the cross section of CoCrMo flat components:

$\pm 10 \mu\text{m}$  – The bright and dark field images are shown in Figure 6-18a and b respectively. A non-uniform  $\sim 500 \text{ nm}$  deep nano-crystalline region is seen in the subsurface. A worn groove is observed at the uppermost surface to be filled with tribochemical products and numerous wear particles.

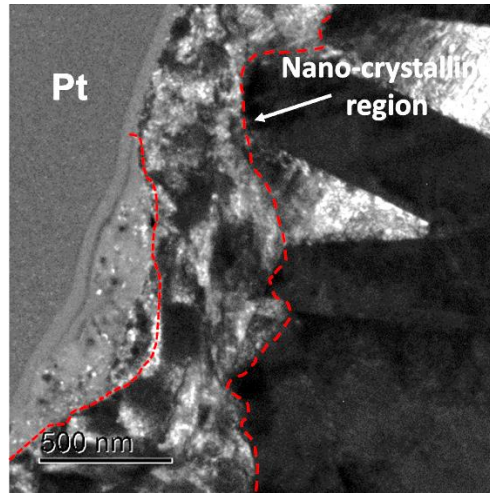
$\pm 25 \mu\text{m}$  – The micrographs of Figure 6-18c and d, shows a surface with tribochemical deposits of  $\sim 200 \text{ nm}$  thick. There were no nano-crystalline structure observed beneath the tribochemical material. However, from the dark field images, strain-induced subsurface twinning of width  $\sim 500 \text{ nm}$  as indicated with red-dotted lines is visible in the material.

$\pm 50 \mu\text{m}$  – Figure 6-18e and f reveal no nano-crystalline structures however a higher degree of strain-induced twinning, beyond those seen at  $\pm 25 \mu\text{m}$  is observed. The smaller sized twins are indicated with red dotted lines.

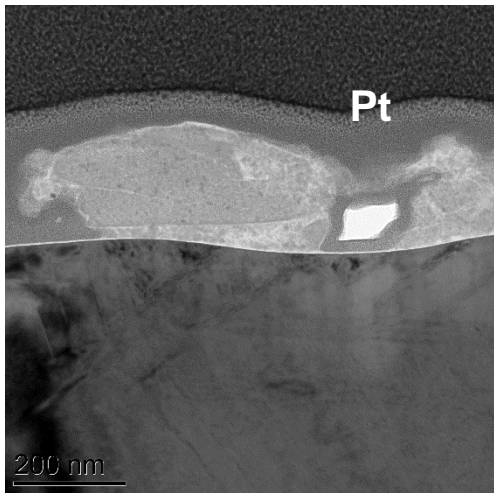
$\pm 150 \mu\text{m}$  – A broad view of the subsurface structure at this displacement is shown in Figure 6-18g and h. It is evident that the strain-induced twinning at this interface is less severe compared to the two previous gross slip displacements. Interestingly, a material deposit on the surface appears with various tribochemical structures as illustrated in the dark field micrograph. Further analysis of this structure and the characterisation of the tribochemical materials on the surface are evaluated in section 6.7.2.



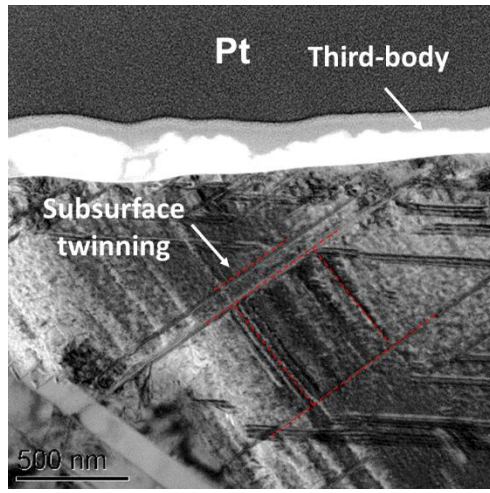
(a)



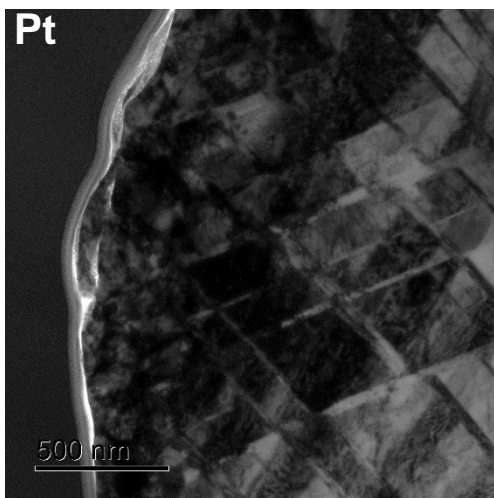
(b)



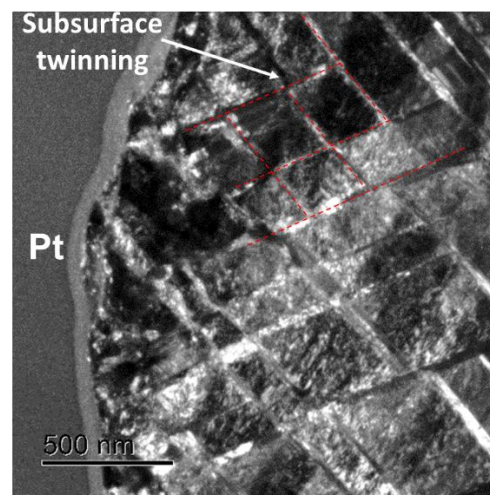
(c)



(d)



(e)



(f)

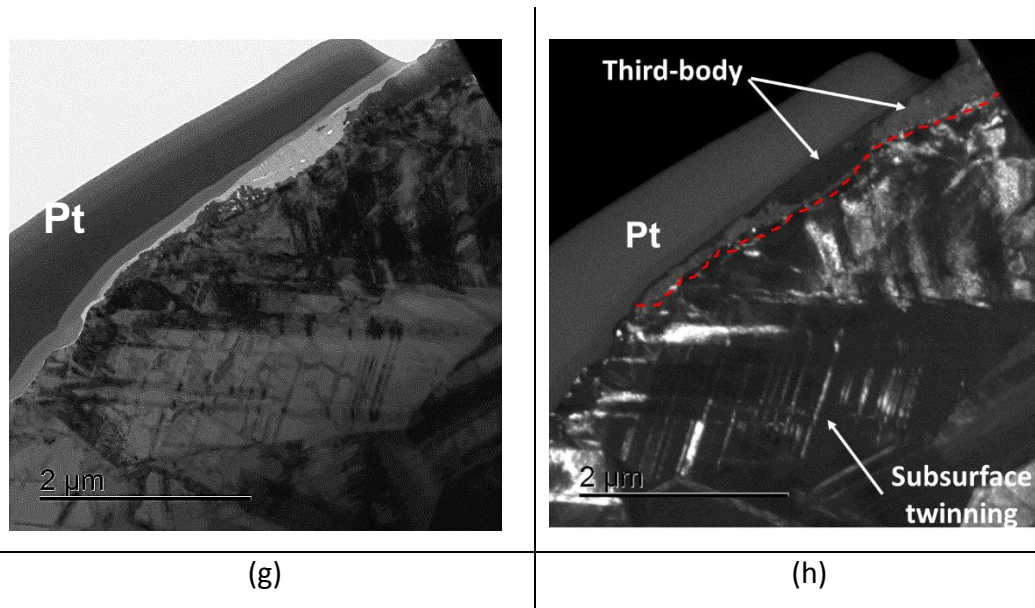


**Figure 6-18 – TEM bright and dark field micrographs of CoCrMo flat from CoCrMo – CoCrMo interface at  $\pm 10 \mu\text{m}$  (a & b),  $\pm 25 \mu\text{m}$  (c & d),  $\pm 50 \mu\text{m}$  (e & f),  $\pm 150 \mu\text{m}$  (g & h).**

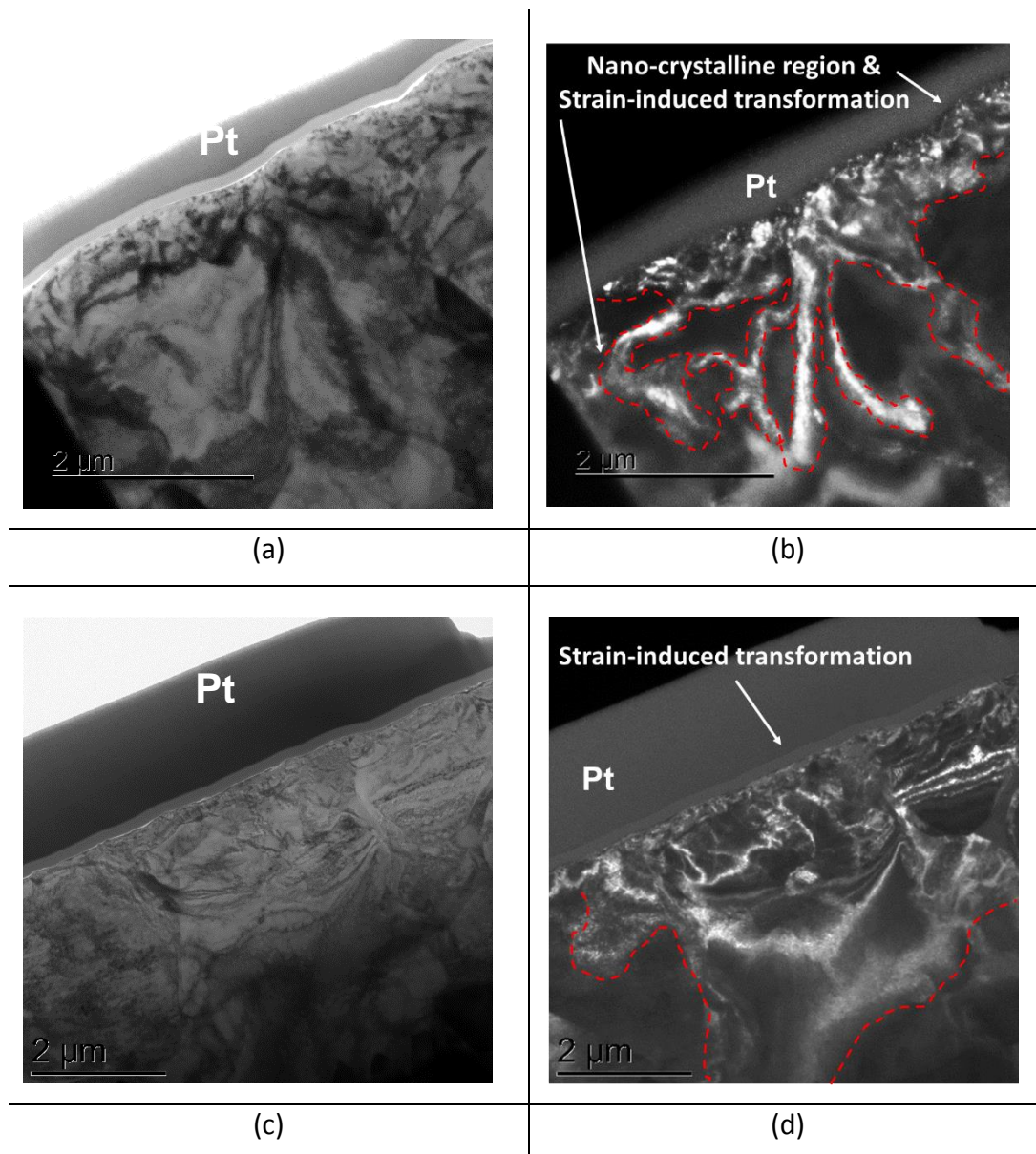
The following are the key observations made from the TEM cross-section of the Ti6Al4V flat component:

$\pm 10 \mu\text{m}$  – The regime at this displacement was a stick fretting regime. Figure 6-19a and b covers a subsurface area of over  $4 \mu\text{m} \times 4 \mu\text{m}$  however, a typical grain structure was not found within this area. Rather, nano-crystalline structures of  $\sim 500 \text{ nm}$  deep from the uppermost surface were seen. The contrasts provided by the dark field image of Figure 6-19b corresponds to the different orientations of crystals within alloy. The absence of a grain-like structure like one observed in the polished reference for Ti6Al4V in section 5.3.1 is a strong indication that a strain-induced subsurface transformation is effective at this displacement. Evidence of directionality downward into the alloy is further illustrated with red-dotted lines. Discretely located passive layers are also visible at the uppermost surface.

$\pm 25 \mu\text{m}$  – The fretting regime at this displacement also experienced a stick regime. Figure 6-19c and d shows a larger cross-sectional area of the subsurface with dimension of  $\sim 6 \mu\text{m} \times 8 \mu\text{m}$ . Similarly, no distinctive grain-like structure were observed. The subsurface transformations in this displacement were very similar to the transformations at  $\pm 10 \mu\text{m}$ .

$\pm 50 \mu\text{m}$  – Transitioning into a gross slip regime, Figure 6-19e and f captures both the Co, Cr and O – rich layer that ruptured from the CoCrMo alloy. The transformed structure of the underlying Ti6Al4V alloy is observed to be nano-crystalline. Detailed analysis of this structure is provided in section 6.7.2.

$\pm 150 \mu\text{m}$  – Figure 6-19g and h, shows at least  $4 \mu\text{m}$  deep Ti6Al4V structure that has been transformed into a nano-crystalline structure from the uppermost downward. In the bright field image, the white arrows are illustrating regions of subsurface cracks which have propagated up to  $500 \text{ nm}$  downwards from the uppermost surface. The dark field image aided the visual identification of mechanical mixing up to  $1 \mu\text{m}$  deep into the subsurface.





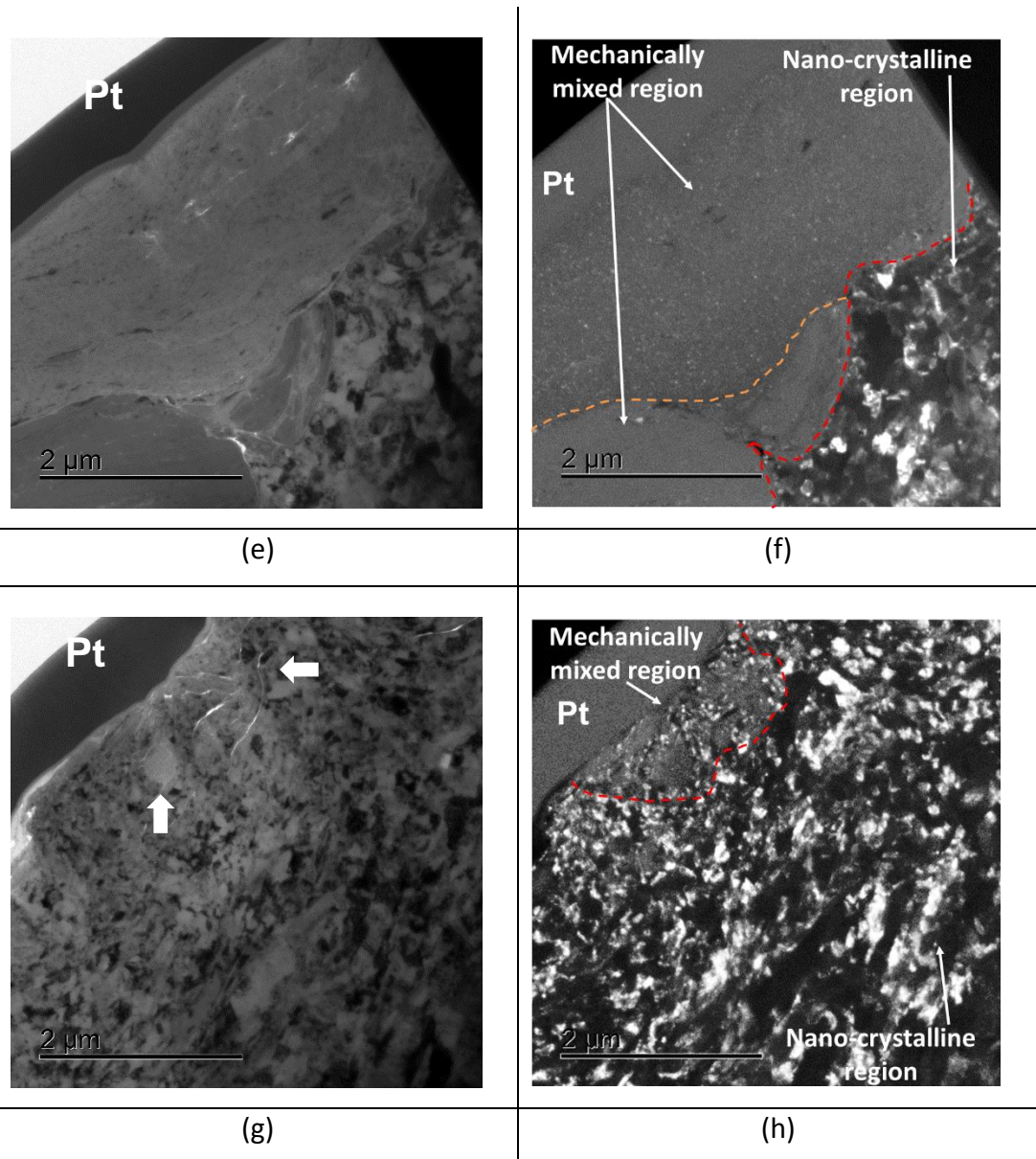


**Figure 6-19 – TEM bright and dark field micrographs of Ti6Al4V flat component from CoCrMo – Ti6Al4V interface at  $\pm 10 \mu\text{m}$  (a & b),  $\pm 25 \mu\text{m}$  (c & d),  $\pm 50 \mu\text{m}$  (e & f),  $\pm 150 \mu\text{m}$  (g & h).**

### 6.7.2 TEM-EDS and SAED analysis

In this section, subsurface TEM, EDS spectroscopy and SAED are combined together in order to in-depthly characterise the third-body wear and corrosion products. The specific samples analysed in this section are outlined below:

- CoCrMo flat from the CoCrMo – CoCrMo combination at  $\pm 150 \mu\text{m}$ :  
Third-body product deposited on the flat component under

reciprocating sliding conduction following a transition from a gross slip regime.

- Ti6Al4V flat from the CoCrMo – Ti6A4V combination at  $\pm 50 \mu\text{m}$ : The region analysed in this section is 'B' from Figure 6-12; the ruptured material which appear as a layer on the Ti6Al4V flat.
- Ti6Al4V flat from the CoCrMo – Ti6A4V combination at  $\pm 50 \mu\text{m}$ : The region analysed in this section is 'D' from Figure 6-12; the mechanically induced cracked region within the Ti6Al4V flat.
- CoCrMo ball from the CoCrMo – Ti6A4V combination at  $\pm 50 \mu\text{m}$ : the CoCrMo ball component is analysed.

#### **6.7.2.1 Analysis of third-body deposit at the CoCrMo – CoCrMo interface**

TEM and SAED analysis of CoCrMo flat component from the fretting displacement at  $\pm 150 \mu\text{m}$  is shown in Figure 6-20a. Three distinctive structures are visible: the first structure is denoted '1'; it is a tribochemical third-body material (~300 nm thick) located within the wear track. The second structure, denoted '2', is better observed in the higher resolution micrograph of Figure 6-20b. It has a honeycomb appearance with a nano-crystalline structure. The bulk alloy, directly beneath both structures 1 and 2 is denoted '3'. In this region, the structure visually appear to be a single crystal.

SAED of structure 1 in Figure 6-20c appears with a shroud of bright spots as well as distinctive spots, thus an indication of an amalgamated amorphous and nano-crystalline structures. The diffraction pattern for structure 2 in Figure 6-20d and structure 3 in Figure 6-20e both agrees with the TEM micrograph observations that both are nano-crystalline and single crystal structures respectively.

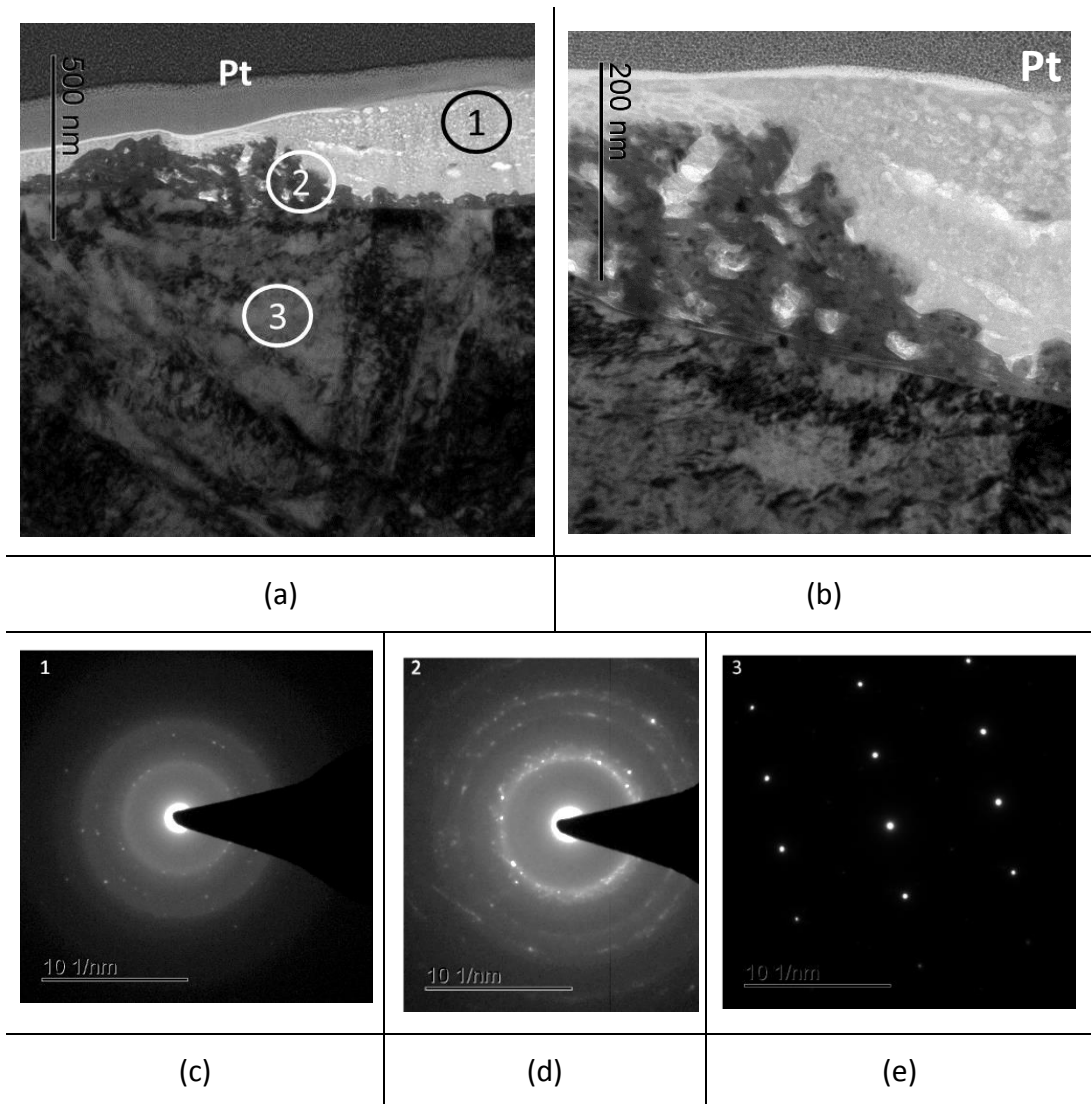


**Figure 6-20 – TEM and SAED of CoCrMo – CoCrMo at  $\pm 150 \mu\text{m}$ : a) Bright field TEM micrograph of CoCrMo subsurface b) Close-up image of tribochemical products on surface c) SAED of structure 1 d) SAED of structure 2 e) SAED of CoCrMo bulk.**

EDS map of the third-body product shown in Figure 6-21 reveals that the chemical composition of structure 1 is dominantly Cr, Co and O. Cl can also be seen faintly in the region nearest to structure 2. In structure 2, it is observable that Cr is absent in the region leaving the honeycomb-like structure of mainly Co and Mo. In addition, a layer of Ca with evidence of P can be seen at the uppermost surface of structure 1. This may suggest the formation of Ca-phosphate at the interface as other studies have found for a sliding contact [194].

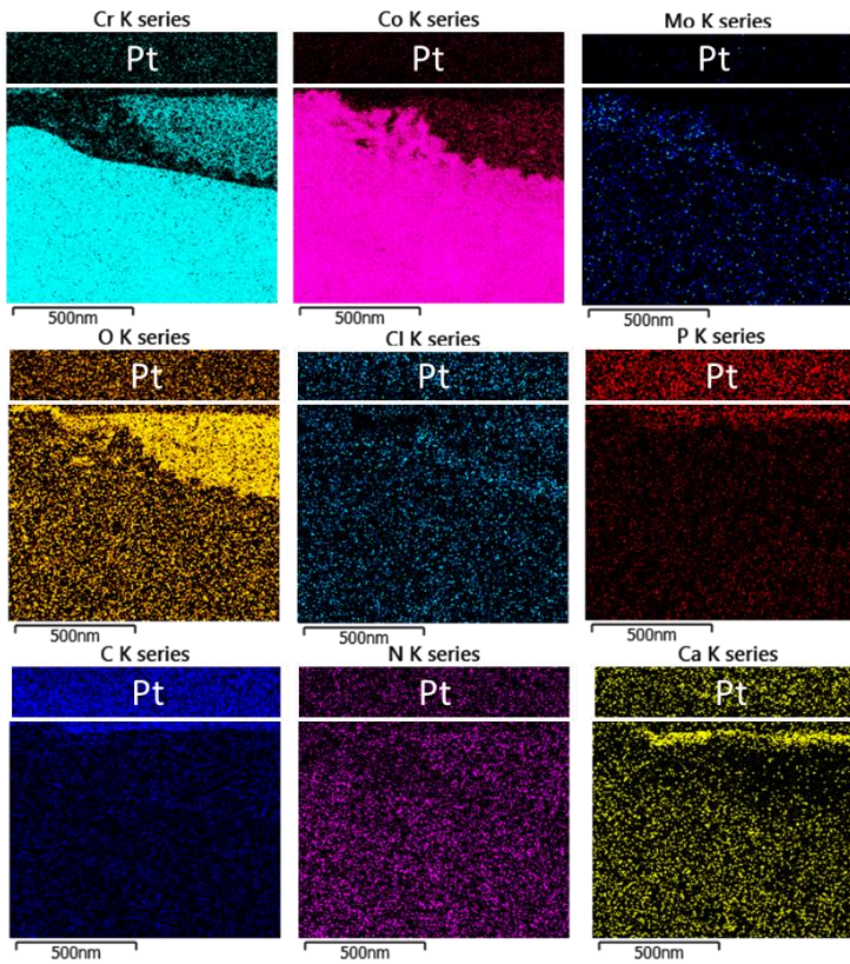
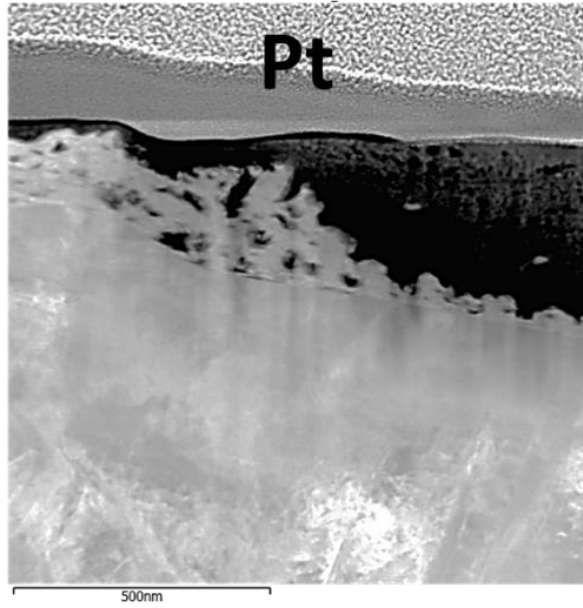
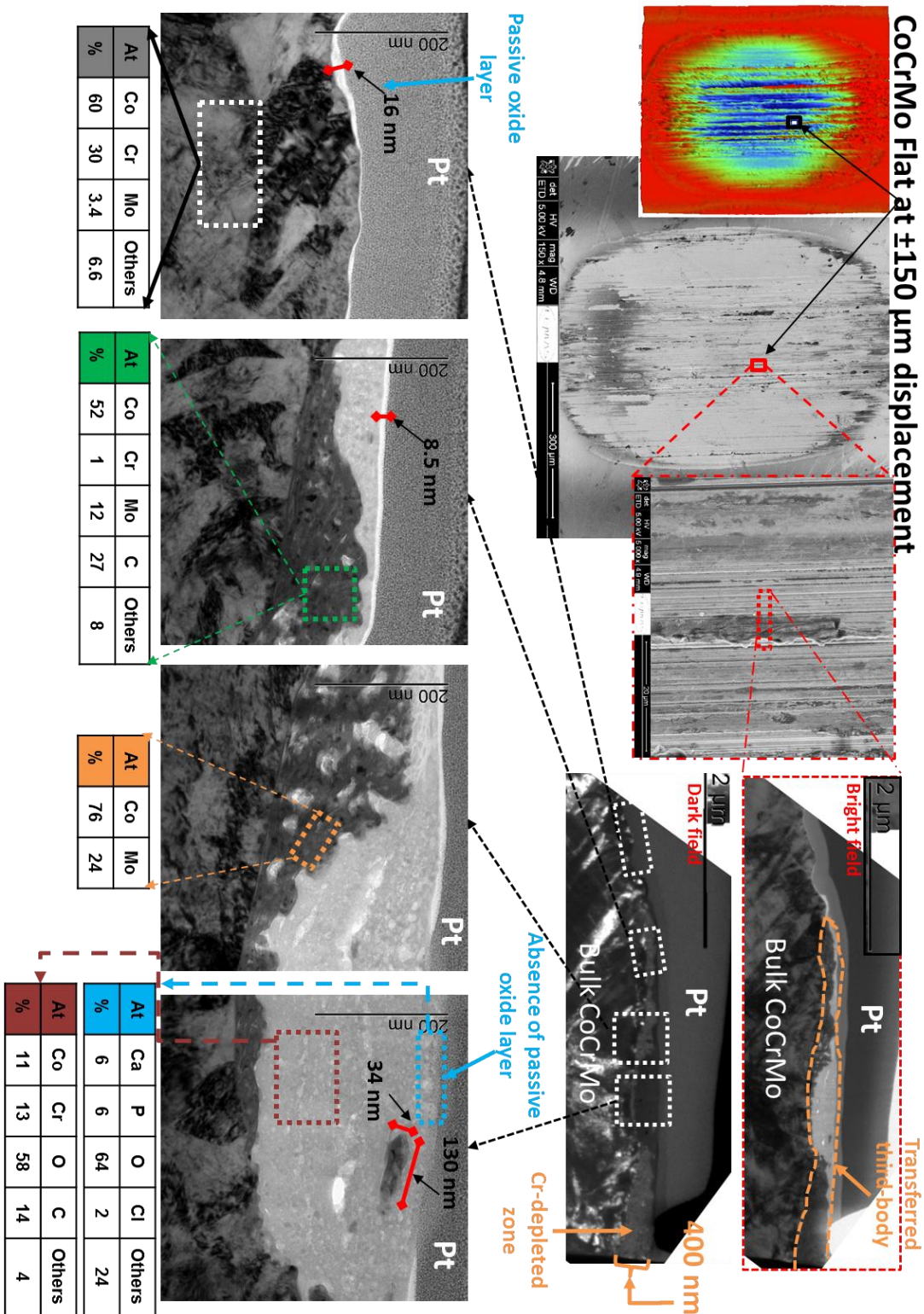


Figure 6-21 – TEM-EDS map of CoCrMo – CoCrMo flat surface at  $\pm 150$   $\mu\text{m}$

In order to better understand the processes involved in the formation of the tribochemical product shown in Figure 6-20, a collage of micrographs from interferometry, SEM, TEM and site-specific EDS analysis is shown in Figure 6-22. From this figure, it is better observed that the honeycomb-like structure from which Cr is depleted, has a maximum thickness of ~400 nm. Interestingly, it can also be seen that a passive layer of maximum thickness 16 nm formed both across the bulk alloy and the crystalline-like mixed Co and Cr-Oxide material (i.e. structure 1). Furthermore, it is also interesting that at the thickest region of structure 1 – specifically the region where the Co and Mo honeycomb-like structure is lacking – the passive oxide layer is not observed. Rather, the uppermost region of the area is abundant in Ca, P, O and Cl. This perhaps highlight the crucial role of Mo in the formation of Cr-rich passive layers.



**Figure 6-22 – TEM and EDS analysis of the transferred third-body at the interface of CoCrMo – CoCrMo, ±150 μm.**

### 6.7.2.2 Analysis of mechanically mixed layers in at the CoCrMo – Ti6Al4V interface

Figure 6-23a shows the micrographs of mechanically mixed layers with varied thicknesses across the surface and subsurface of Ti6Al4V alloy. The uppermost layer (light grey) has a maximum thickness of  $\sim 2.5 \mu\text{m}$  in the thickest region. Beneath this layer is a transformed amorphous-like structure which a darker grey appearance. Directly beneath both layers, a nano-crystalline structure of Ti6Al4V alloy is observed. At the interface where the amorphous-like structure meets the nano-crystalline Ti6Al4V structure, a crack can be seen. The existence of a crack at this point suggests that the mechanical properties of the three structures are likely very different thus causing an internal tension.

Figure 6-23b shows a high resolution micrograph of Figure 6-23a depicting all three layers. Structure 1 appears to have nano-scale sized materials from the amorphous-like structure 2. Similarly, particles from the nano-crystalline Ti6Al4V structure (structure 3) appears to be suspending within structure 2. The diffraction pattern in Figure 6-23c corresponding to structure '1' is confirmed to be a nano-crystalline structure. Although from the TEM micrograph, the nano-scale crystals appear to be suspending within an amorphous-like 'mesh'.

Figure 6-23d shows the diffraction pattern of structure '2'; the micrograph reveals a stronger evidence of an amorphous structure although the presence of distinctive rings likely represents the nano-sized particles of Ti6Al4V. In Figure 6-23e i.e. structure '3', a more definitive nano-crystalline rings of Ti6Al4V polycrystalline structure is observed.

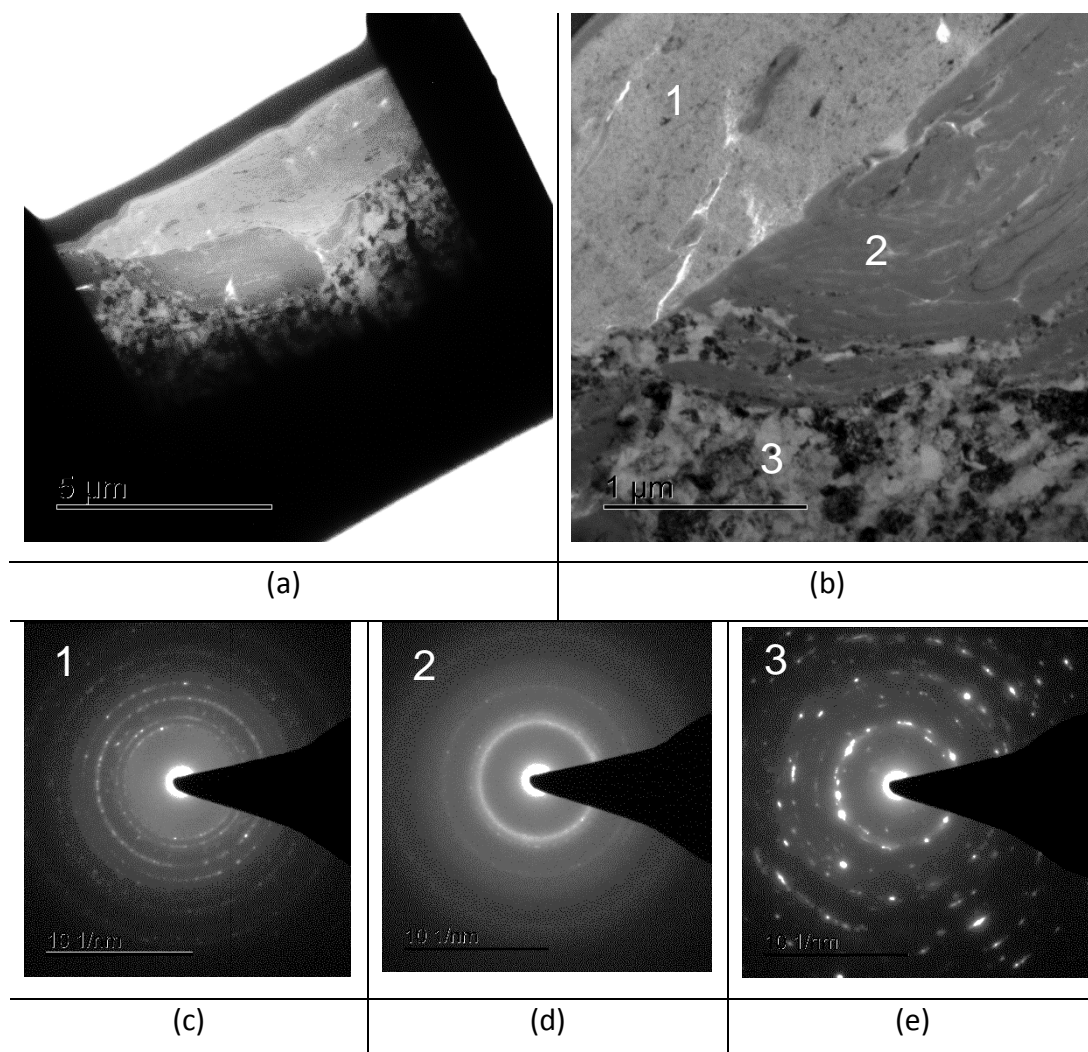


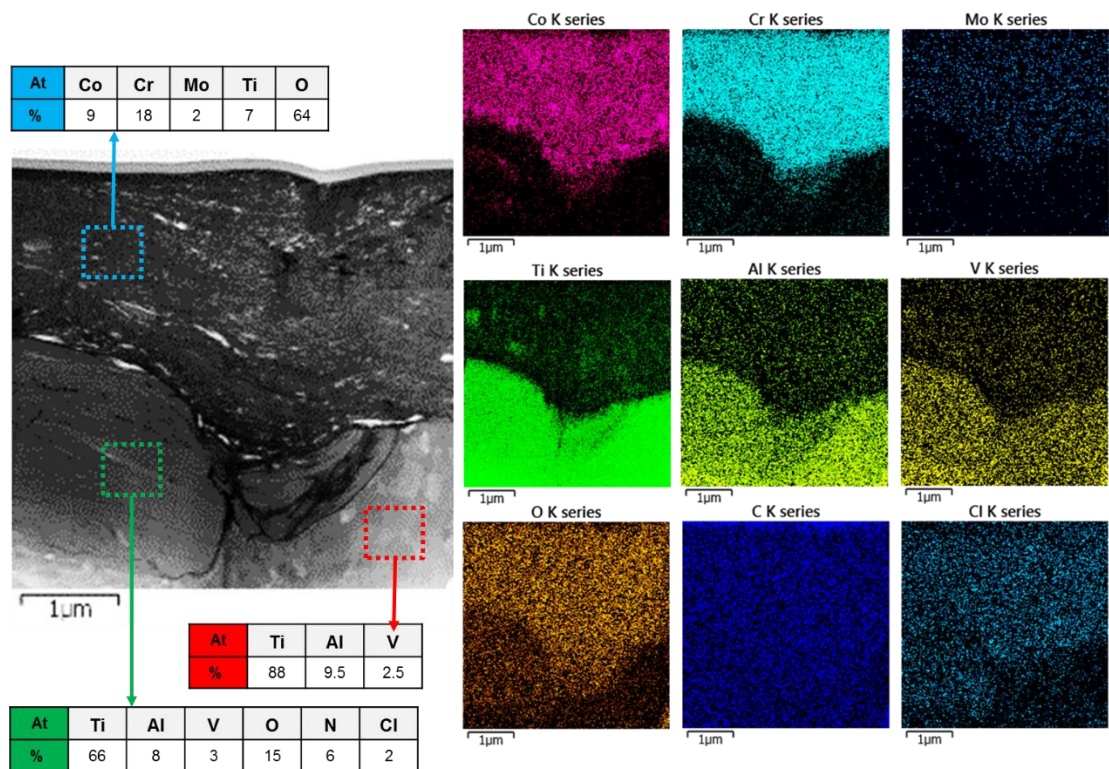
**Figure 6-23 – TEM and SAED of mechanically mixed layers on Ti6Al4V alloy: a) TEM micrograph of Ti6Al4V subsurface b) high-resolution micrographs of the subsurface structures c) SAED of the mechanically mixed layer d) SAED of mechanically mixed Ti6Al4V structures e) SEAD of Ti6Al4V nano-crystalline structure.**

EDS map of the TEM cross-section is presented in Figure 6-24. It can be seen that chemical composition of structure 1 is largely a mix of of Co, Cr, Mo, Ti and high concentration of O. Cl is also evident across the structure. It is thus deducible that structure 1 exists as mixed oxides and chlorides of the above metals where Cr is the dominant metal-oxide. It is worth noting that the elements tabulated as insets in Figure 6-24 are a normalised quantification of the most concentrated elements in the structure. For example, the table does not include Cl, Al and V however, all three are identified in the TEM-EDS map.



The map also clarifies the white appearing particulates suspending in both structures 1 and 2 are Co-rich particles.

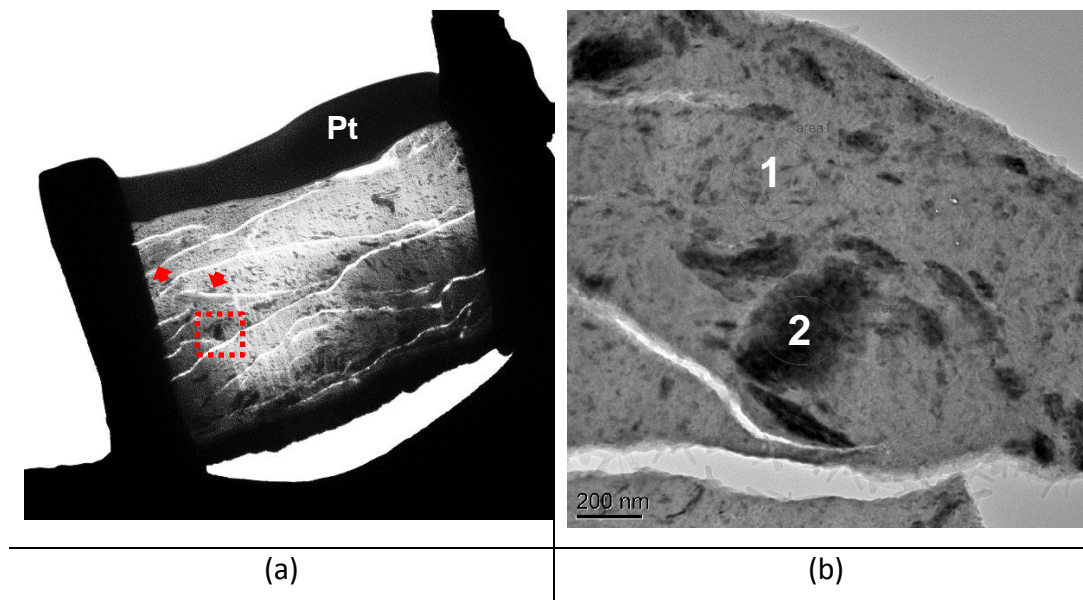
The EDS map also confirms structure 2 as an amorphized Ti6Al4V mixed with the physiological solution as evidenced by the presence of O, N and Cl. EDS also confirms the chemical composition of the nano-crystalline Ti6Al4V structure to be Ti, Al and V as expected. This highlights the role that the physiological solution played in the transformation of nano-crystalline Ti6Al4V. C in the map is mainly from the background signal as it exist uniformly across all three structures.



**Figure 6-24 – TEM-EDS map of the mechanically mixed layer and transformed Ti6Al4V alloy from CoCrMo – Ti6Al4V interface.**

### 6.7.2.3 Analysis of mechanically induced crack at the CoCrMo – Ti6Al4V interface

TEM cross-section from the region in Ti6Al4V flat where surface cracks were identified to be mechanically induced (region D of Figure 6-12) was also analysed. In Figure 6-25a the structure appears much coarse and less cohesive in comparison to the structure 1 observed in Figure 6-23b. Large particulates (appears to be grey and are blending into the coarse structure) are seen to be suspending within the coarse structure as indicated with the red arrows. The micrograph also shows numerous horizontal and diagonal cracks across the coarse structure from the uppermost surface deep down into the alloy. Other particles/structures which appear darker within the structure were also seen dispersed across the micrograph. Figure 6-25b presents a high resolution micrograph of such 'darker' appearing particles. From the micrograph, there are evidence of several of these particles suspending in the coarse structure with sizes ranging from 10s of nm to sizes of over 200 nm. The diffraction patterns in structures '1' and '2' are both indicated in Figure 6-25c and Figure 6-25d respectively. These consists of nano-crystalline ringed patterns of multiple structures.



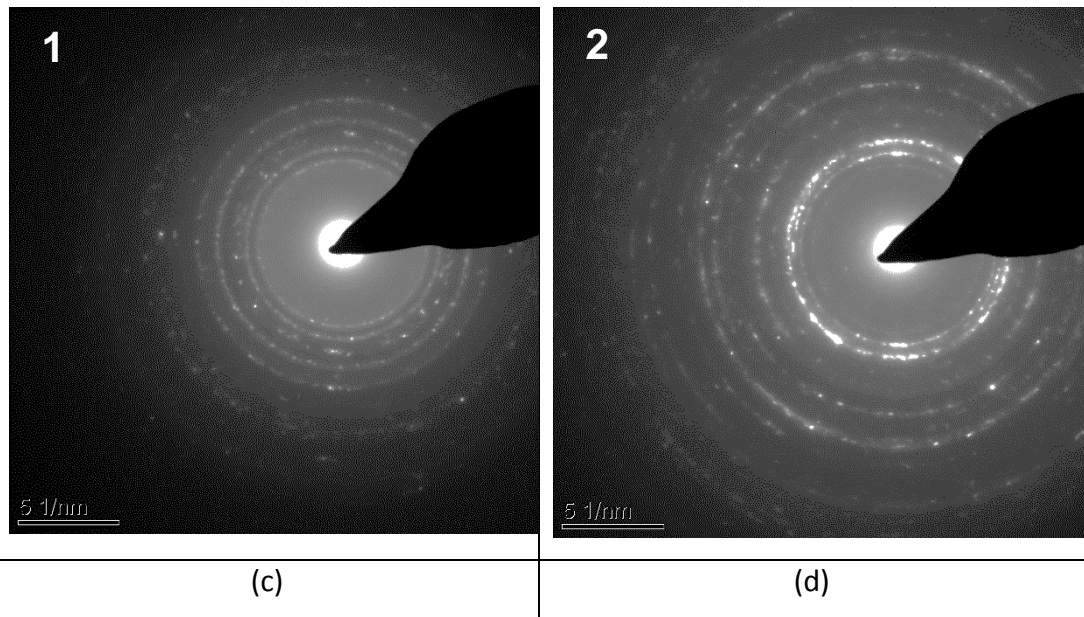


**Figure 6-25 – TEM and SAED of Ti6Al4V surface (mechanically cracked region): a) TEM micrograph of Ti6Al4V subsurface b) high resolution image of the region in red dotted square c) SAED of the nano-crystalline mesh d) SAED of a single large particle.**

EDS map of the TEM cross-section of the coarse structure is shown in Figure 6-26. The map confirms the ‘dark’ particles within the coarse structure, in Figure 6-25b are Co-rich particles. The map also confirms the coarse structure consists mainly of mixed oxides and chlorides of both CoCrMo and Ti6Al4V alloys. A Cr-chloride structure is particularly illustrated with red dashed-circular lines.

It is worth pointing out that, this EDS map, along with others presented previously were unable to distinguish/identify reliably the presence of proteins using EDS. This mainly due to overlapping energies of S and Mo. Reliably detecting S would require other techniques such as electron energy loss spectroscopy (EELS) which was not employed in this study. However, the C map (illustrated with red arrows) in Figure 6-26 identifies a pathways through which physiological solution migrate deeper into the alloy and thus possibly fostering localised corrosion deep inside the alloy.

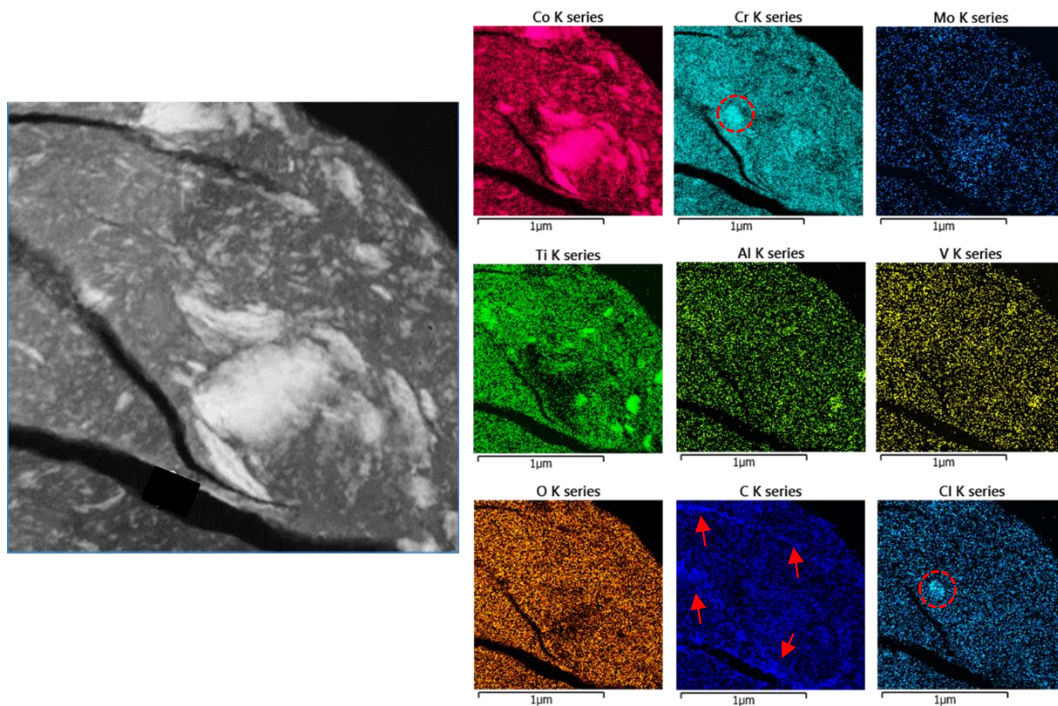
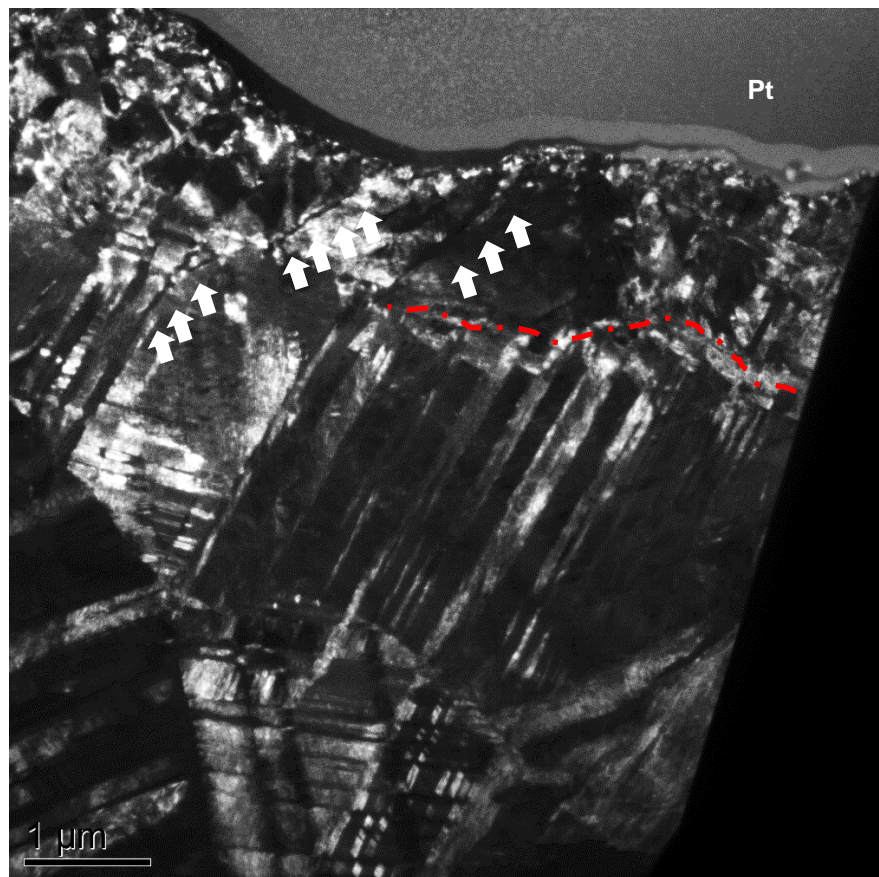


**Figure 6-26 – TEM-EDS map of the Ti6Al4V flat at the mechanically induced crack region of the CoCrMo – Ti6Al4V interface.**

#### **6.7.2.4 Analysis of CoCrMo ball from the CoCrMo – Ti6Al4V interface**

The subsurface transformations of CoCrMo under partial-slip and gross slip regimes have been observed through the TEM micrographs of Figure 6-18. However, considering that a mixed regime was realised at the CoCrMo – Ti6Al4V interface at  $\pm 50 \mu\text{m}$ , TEM and SAED analysis of the CoCrMo ball was analysed. It had been deduced from previous surface analysis in this chapter that the evidence of Co, Cr and Mo – rich structure from Figure 6-12 is indicative of CoCrMo ball separating from the shared interface with Ti6Al4V through a rupture of the interfacial wear and corrosion products formed. This was denoted ‘structure 1’ in Figure 6-23b. Figure 6-27a shows the dark field micrograph of the subsurface structure of the CoCrMo alloy. The image reveal evidence of severe strain-induced twinning of large grains upto depts of  $7 \mu\text{m}$  into the alloy. The red dashed-line in the figure is illustrative of the boundary between a twinned crystal (below) and a nano-crystalline transformed grain (above).

The white arrows are illustrative of cracks which may have propagated along the nano-crystalline structures and cracks formed at the boundary of twinned structures. Figure 6-27b shows the bright field image; evidence of material deposits of ~500 nm thickness was found on the surface; it was denoted structure '1' and the bulk alloy beneath it was denoted structure '2'. In Figure 6-27c, the diffraction pattern shows a nano-crystalline structure for structure '1'. In structure '2', Figure 6-27d, the diffraction pattern appear like a strained single crystal structure as expected.



(a)

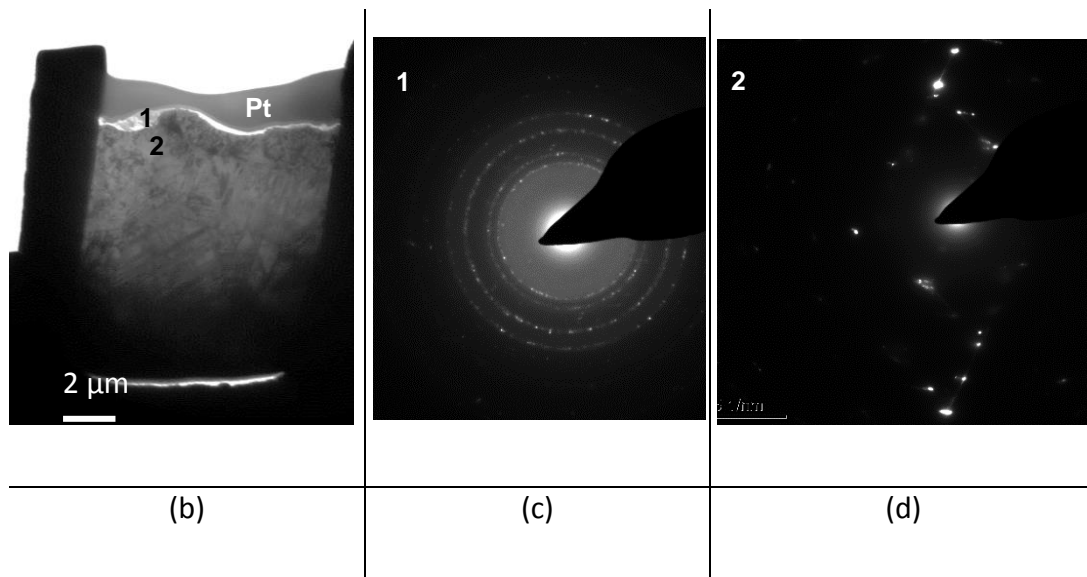


**Figure 6-27 – TEM and SAED of CoCrMo ball surface: a) Dark field TEM micrograph of CoCrMo subsurface b) Bright field image c) SAED of the transferred material d) SAED of near-surface CoCrMo bulk.**

EDS examination of structure '1' from Figure 6-27b is shown below in Figure 6-28. The map shows that the material is a mixture of Co-rich particle, oxides of Cr and Ti, as well as constituents of the physiological solution namely: K and C. S, Cl and Mo are also present.

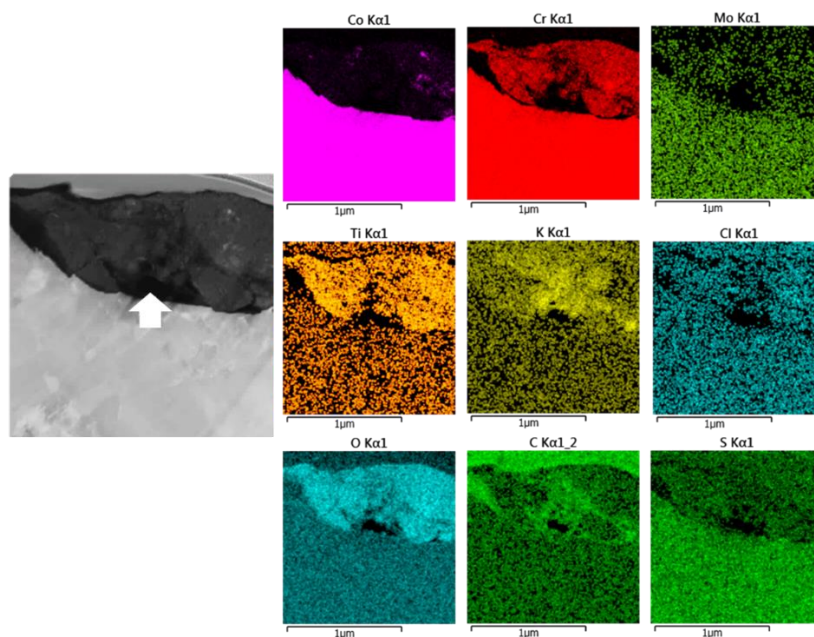


**Figure 6-28 – TEM-EDS analysis of the CoCrMo ball surface from the CoCrMo – Ti6Al4V interface.**

## 6.8 Nano-indentation

Analysis of surface and subsurface chemistry has so far characterised the tribocorrosion products at the interface of both CoCrMo – CoCrMo and CoCrMo – Ti6Al4V material combinations. These were observed to be mixtures of metal-oxides, phosphates, chlorides and hydroxides. However, the layer characterised on the Ti6Al4V flat component from section 6.7.2.2 is sufficiently thick to be characterised using nano-indentation. Figure 6-29a shows the area indented sandwiched between resin and Ti6Al4V alloy. The Figure 6-29b shows the unprocessed P vs. h indentation data. In Figure 6-29c the mean average hardness of the layer is 25.6 GPa. This is more than 3x the bulk hardness of CoCrMo alloy and more than 6x the nano-indentation hardness of Ti6Al4V alloy.

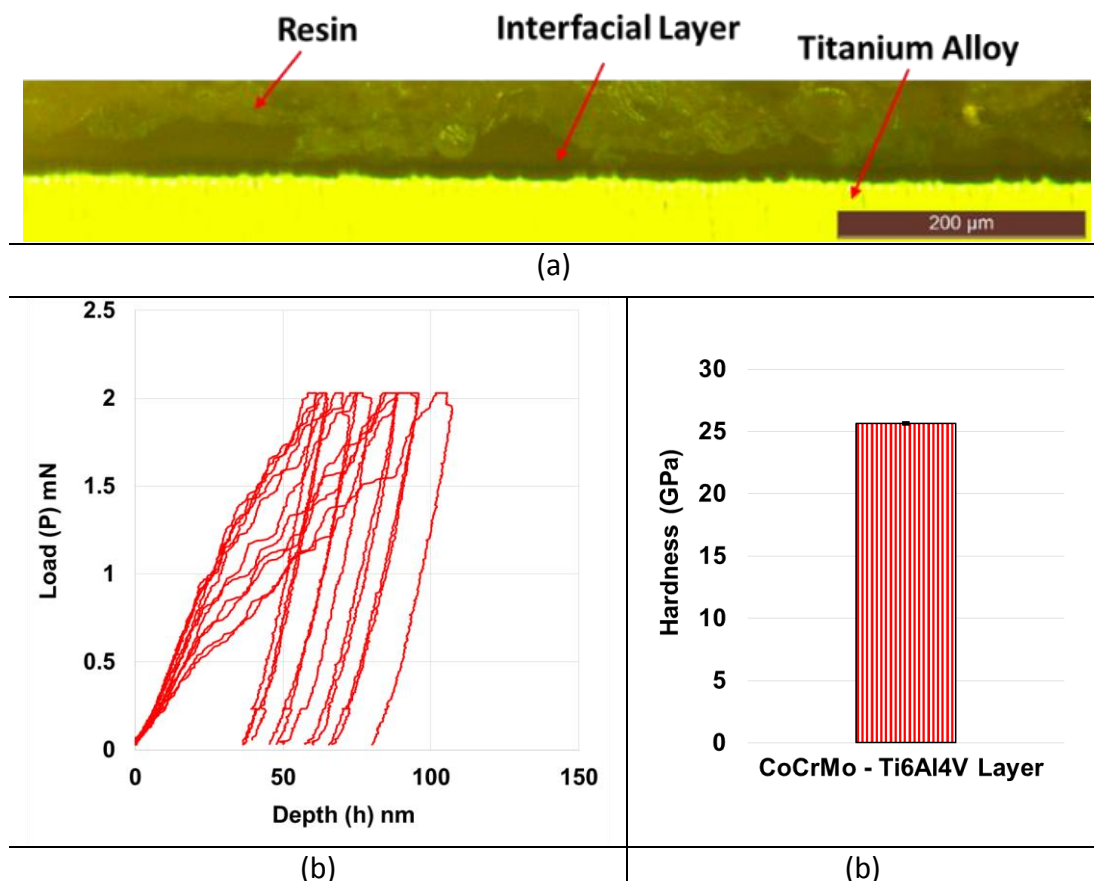


**Figure 6-29 – Nano-indentation of layer formed at the CoCrMo – Ti6Al4V interface: a) image of the indented cross-section b) P vs. h graph of indentations c) average hardness of the layer.**

## 6.9 Discussion and summary

In this chapter, two metal – metal material combinations were assessed under varied fretting displacement amplitudes. The characteristic surface and subsurface damage modes pertaining to each material combination (CoCrMo – CoCrMo and CoCrMo – Ti6Al4V) were assessed. Furthermore, the assessment in chapter has presented in-depth characterisation of tribocorrosion and tribochemical products formed at the interface of each material couple.

For the same initial contact pressure of 1 GPa, the initial Hertzian contact width 'a' for CoCrMo – CoCrMo is calculated to be 60% that of CoCrMo – Ti6Al4V. Thus, the interfacial compliance experienced at the CoCrMo – CoCrMo contact is less than CoCrMo – Ti6Al4V. This explains why self-mated CoCrMo transitions into gross slip at a much lower fretting displacement than CoCrMo – Ti6Al4V. In general, the displacements assessed in this chapter reveal CoCrMo – CoCrMo contact transition from a partial-slip regime to gross slip and to the transition stages of reciprocating sliding condition at  $\pm 150 \mu\text{m}$ .

Examination of the wear pattern at the interface showed the influence of elastic compliance up until reciprocating sliding condition where influence of third-body products at the interface appear to be more prominent. As for the CoCrMo – Ti6Al4V combination, the contact progressed from stick regime to mixed regime then to gross slip regime. Mindlin's description for an elastic contact (see section 2.6.1.5) was observable at the stick regime contacts. The mixed regime was characterised with rupture of what appears to have been a cold-welded interface. Upon transition from mixed regime to a gross slip, a significant increase in the wear volume generated was observed and a large proportion of the wear volume was redistributed at the interface. The main difference in the wearing modes of both material combinations is thus the adhesive wear characteristics of the Ti6Al4V alloy which facilitated redistributed wear at the interface.

*In-situ* OCP measurement in both material combinations highlighted some similarities and differences. As expected, both material combinations



responded to the gross slip regimes with a cathodic shift and subsequent repassivation as soon as fretting stopped. The following are the observed characteristic behaviour of each individual material combinations:

1. The magnitude of cathodic shift at all displacements were much larger for the CoCrMo – Ti6Al4V contact than the CoCrMo – CoCrMo contact as compared in Figure 6-30. This is indicative of a more electrochemically active interface when using a mixed metal combination compared to the self-mated alternative. This may explain why corrosion damage in mixed-metal combination is often more severe than in self-mated material combinations.

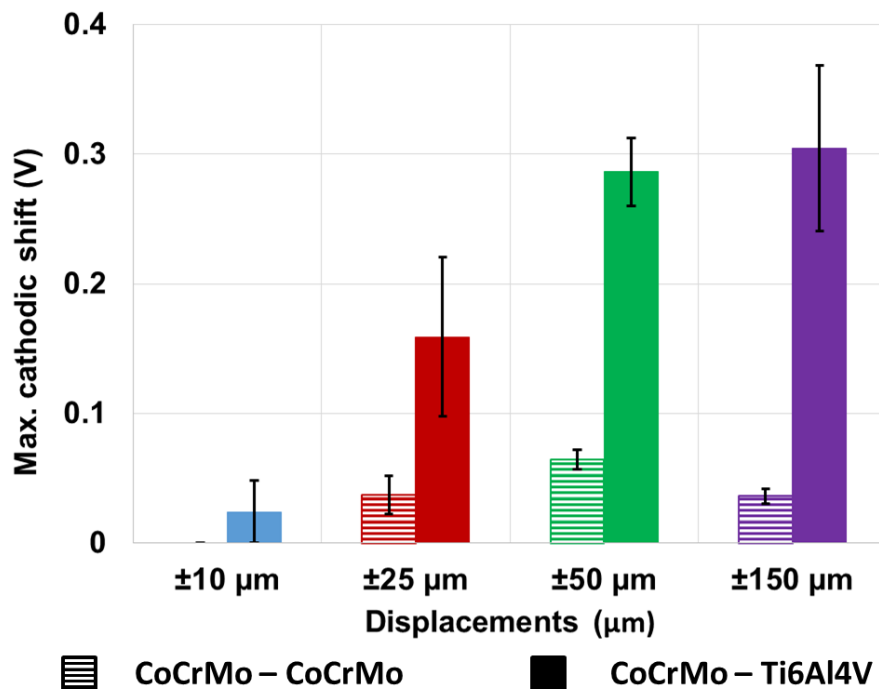


**Figure 6-30 – Comparing Max. cathodic shift of the two metal – metal material combinations.**

2. No cathodic shift was measured at the partial-slip regime ( $\pm 10 \mu\text{m}$ ) of CoCrMo – CoCrMo despite evidence of wear. This suggests that during the partial-slip regime, the reactive (bare) metal was not exposed; likely covered by the wear products. Secondly, the OCP curve was seen to be rising during on-going fretting for the transitioned  $\pm 150 \mu\text{m}$  displacement. This is either indicative of galvanic interaction within the wear interface due to a rearranged contact condition with increase in

third-body influence. Or, the formation of a tribochemical film which acts as a charge barrier thus causing the potential to rise.

3. The depassivation rate and the magnitude of cathodic shift from OCP observations shows that CoCrMo – Ti6Al4V under fretting conditions is more electrochemically responsive to the magnitude of displacement at the interface than the self-mated CoCrMo combination. This behaviour can be attributed to the Ti6Al4V alloy which is known to be more reactive than CoCrMo. A fretting study by Baxmann et al [102] whereby the Ti6Al4V alloy was the only conductive component observed a similarly large cathodic shift upon fretting.
4. The potential during the recovery stages of CoCrMo – Ti6Al4V after gross slip fretting was seen to be partial relative to the potential prior to fretting. This may be due irreversible plastic damage at the fretting interface thus reducing the corrosion resistant properties of the alloys as reported for Ti6Al4V in previous studies. Other possible reasons are the establishment of sites for localised corrosion and substantial changes to the local solution chemistry such that repassivation at the interface is inhibited [195, 196]. Each explanation is equally feasible in this study because there was evidence of cracks within the Ti6Al4V wear surface (see Figure 6-14) thus confirming the establishment of sites for localised corrosion.

Subsurface metallurgical transformations of the CoCrMo alloy at the CoCrMo – CoCrMo interface were observed at various fretting regimes. The partial-slip regime was characterised by material removal (wear) and preservation of nano-crystalline structures at the nearest subsurface. However, with increase in the interfacial slip at the gross slip regimes ( $\pm 25 \mu\text{m}$  and  $\pm 50 \mu\text{m}$ ) loss of the nano-crystalline structures at the nearest subsurface was evident. This observation agrees with the explant analysis performed by Bryant et al [98] who examined TEM images of adjacent unworn (partial-slip) and worn (gross slip) regions of a fretting interface of CoCrMo modular neck.

Furthermore, it was also evident that the severity of subsurface twinning increased with the interfacial energy during the gross slip regimes. However, at the transition gross slip regime of  $\pm 150 \mu\text{m}$ , twinning was observed to be

less severe than at  $\pm 50 \mu\text{m}$ . Loss of nano-crystalline structures were also evident but on the uppermost surface, tribochemical products transferred onto the flat component was observed. This observation also agrees with several *in-vitro* studies and explant analysis of self-mated CoCrMo alloy subjected to a reciprocating sliding condition. It is commonly observed that the wear mechanism at this interface is highly influenced by tribochemical reactions; especially in a proteinaceous media [94, 95, 177, 197, 198].

Electron microscopy and spectroscopy techniques used to analyse third-body products at the self-mated CoCrMo interface observed wear and corrosion products that are chemically identical to the products observed from retrieval studies [85, 199, 200]. Altogether, at the self-mated CoCrMo these were: mixed-metal oxides and chlorides, hydrated Cr-phosphate and possibly Ca-phosphate from the transition gross slip interface. Furthermore, through high resolution imaging, electrochemical mechanisms such as Cr-depletion a nano-crystalline structured wear product was observed. This finding is a novel visual evidence of the electrochemical activity of wear and corrosion products generated from the tribological interfaces of biomedical materials.

Dissipated energy at the interface of a material couple is manifested in several ways as outlined by Fouvry et al [39]. In this study, subsurface metallurgical transformation of Ti6Al4V at the CoCrMo – Ti6Al4V interface was observed to be progressively fatigue oriented unlike the self-mated CoCrMo couple which displayed a preferential damage mode of wear generation. For example, subsurface analysis of the stick regime reveal evidence of strain-induced subsurface transformations which were manifested in directionality and re-orientation of crystallographic planes. Furthermore, it is interesting to note that during the stick regimes of CoCrMo – Ti6Al4V, the Ti6Al4V experienced subsurface transformations and little to no interfacial wear whilst the wear annulus of the CoCrMo increased in size with increasing displacement thus further highlighting the preferential damage modes of the two individual materials.

At the mixed fretting regime of CoCrMo – Ti6Al4V ( $\pm 50 \mu\text{m}$ ) where both partial-slip and gross-slip regimes occurred consecutively, cross-sectional TEM

micrograph showed a material with a 'pseudo-amorphous' structure which until now was described as a 'mechanically mixed layer' on the Ti6Al4V surface. The term 'pseudo-amorphous' is used here because the TEM micrograph shows a material with solid particulates suspending within an amorphous-like 'mesh'. On the other hand, the SAED micrographs describes a nano-crystalline structure which likely corresponds to the crystalline structure of the several particulates of Ti6Al4V wear and Co as revealed in the TEM-EDS (see Figure 6-24). TEM-EDS also revealed that the non-particulate amorphous-like material composes mainly of mixed-metal oxides and chlorides of Cr, Co, Mo and Ti.

From 3D surface analysis, it was clear that the pseudo-amorphous material ruptured away from the CoCrMo counter-body. It was therefore deducible that the rupture corresponded to the regime transition from partial-slip to gross slip as discussed further in the overall discussion chapter (section 10.3.1). This is to say that prior to the sudden rupture, the wear and corrosion products at the interface during the partial-slip regime is likely welding the CoCrMo and Ti6Al4V alloys together through the process of cold-welding. This may also explains why the chemical composition of the corrosion product mainly constituents of CoCrMo and Ti6Al4V alloys both in oxides and particulate forms. Nano-indentation hardness of the corrosion material was found to be more than triple that of CoCrMo alloy and upto six-time that of Ti6Al4V alloy.

It is anticipated that such a hard interfacial material would largely influence the wear phenomena at the interface. From the transition to gross slip, the softer Ti6Al4V is no longer in contact with the CoCrMo counter-body. Rather, the CoCrMo is in direct fretting contact with the interfacial layer several times harder than itself, thus it is expected that CoCrMo would suffer more wear in such condition whilst Ti6Al4V would experience no wear. If such hard phases form *in-vivo*, it proposes a more plausible reason than those given by Moharrami et al [76] as to why CoCrMo wears more than its softer Ti6Al4V counter-part [27].

Underneath the CoCrMo-rich pseudo-amorphous material a Ti6Al4V amorphous material was observed. From this point in the writing, the pseudo-

amorphous 'weld' is called 'pseudo-amorphous CoCrMo or shortened to p-a CoCrMo' while the mechanically transformed amorphous-like Ti6Al4V material will be referred to as 'amorphous Ti6Al4V'. Section 10.3.1 details the mechanism leading to the formation of these two structures. Furthermore, Ti6Al4V alloy in a gross slip regime is mainly characterised with subsurface cracks, mechanically mixing of oxides and deep recrystallization to form nano-crystalline structures.

In general, the corrosion products which are commonly observed in retrieval studies of the mixed-metal couple were also observed at the CoCrMo – Ti6Al4V interface of this study. More so, it was observed that the nature of corrosion products found at the interface was linked to region of the composite contact the product was found. For example, corrosion products located within crevices were abundant in Cl ions whilst those outside of crevices were phosphates and metal-oxides. Figure 6-31 shows a schematic diagram depicting the chemical species observed at specific regions of the fretting interface. SEM micrographs of both CoCrMo and Ti6Al4V is also included in the schematic to show evidence of pitting mechanism on the CoCrMo and the products of pitting deposited on the Ti6Al4V.

The most isolated areas to fresh physiological solution i.e. the most severe crevice of the CoCrMo – Ti6Al4V was located at the centre of the wear surface. The crevice were further isolated because of the pseudo-amorphous CoCrMo (weld) material that was built up within the interface. In this region, evidence of bulk CoCrMo deposits, through a pitting corrosion mechanism was observed. A similarly observation was made by Gilbert et al [27] but the corrosion mechanism was said to be intergranular. In this study, Cr<sup>6+</sup> was also observed in the same region. Cr<sup>6+</sup> is said to be a carcinogenic specie of oxidised Cr. It is a strong indication that a severe crevice such as can facilitate pitting corrosion mechanism can also result to the formation of Cr<sup>6+</sup> *in-vivo* [8].

On the other hand, at the non-creviced region i.e. the region closest to the edges of the Hertzian contact, evidence of physiological solution which penetrated deep down into worn and oxidised structures of the macro-scale cracked region of Ti6Al4V was observed. The implication of this may be the

electrochemical process of oxide-induced stress corrosion cracking as previously observed in a retrieval study of Ti6Al4V [97].

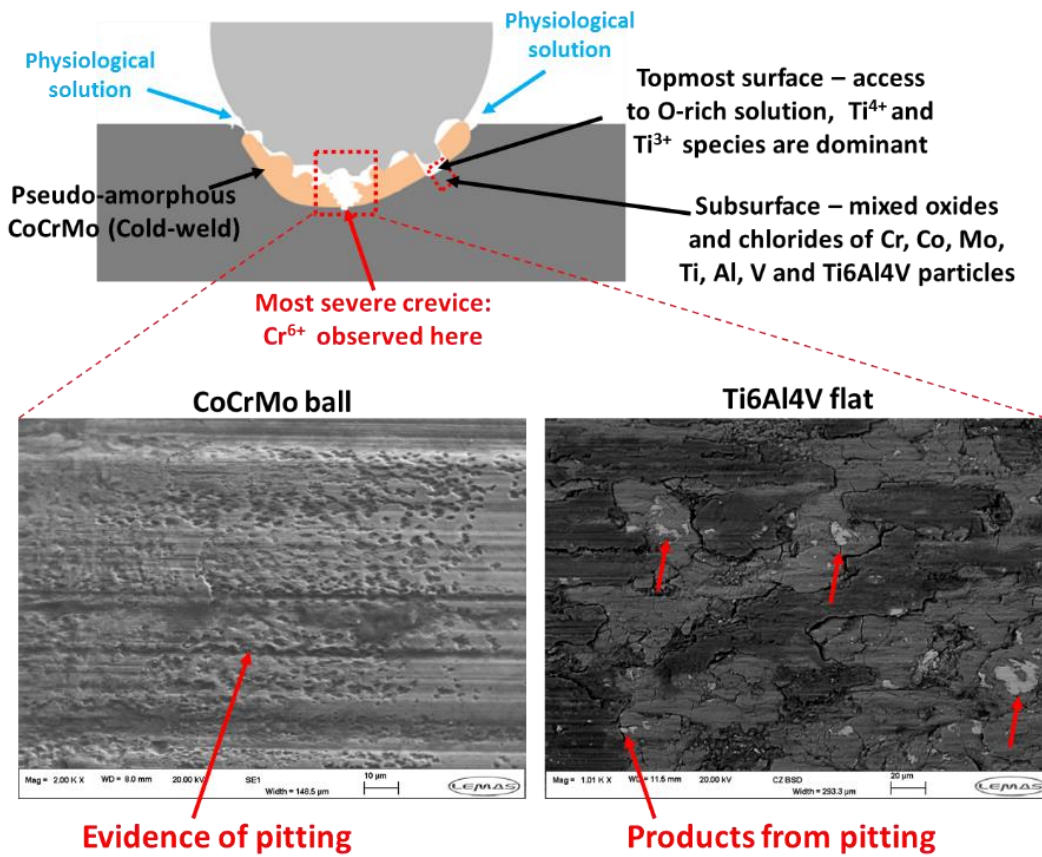


**Figure 6-31 – Schematic diagram of fretting corrosion products and SEM micrographs of CoCrMo and Ti6Al4V from the CoCrMo – Ti6Al4V interface at  $\pm 50 \mu\text{m}$  displacement.**

## Chapter 7 Fretting wear mechanism of ceramic – metal material combinations

### 7.1 Introduction

In the previous chapter, fretting wear mechanism of metal – metal material combinations were assessed. This chapter is focused on the ceramic – metal material combinations with the aim of understanding the fretting wear and corrosion mechanism of the ceramic – metal systems. Ceramic bearings are increasingly being used as an alternative bearing to CoCrMo alloy at the head-neck taper interface. More so, recent studies have shown evidence of reduction in fretting corrosion degradation of the modular taper through the use of ceramic bearings [72, 201].

The fretting test parameter, test conditions and analyses conducted in this chapter are very similar to those conducted in chapter 6.  $\text{Si}_3\text{N}_4$  ceramic was strategically chosen for this study because it is a material increasingly gaining research attention for applications in hip and knee replacements both as bulk material and as a coating[14]. In this vein, characterising the fretting corrosion products and tribochemical interactions at the interface of  $\text{Si}_3\text{N}_4$ – CoCrMo and  $\text{Si}_3\text{N}_4$  – Ti6Al4V combinations is a topical assessment. However, in order to elucidate the role of  $\text{Si}_3\text{N}_4$  in the wear mechanism of a ceramic – metal combination,  $\text{Si}_3\text{N}_4$  –  $\text{Si}_3\text{N}_4$  (a ceramic – ceramic couple) was also assessed.

Biolox ceramic is the most commonly used commercially available ceramic for hip prosthesis. Therefore, fretting wear mechanism of Biolox – CoCrMo and Biolox – Ti6Al4V was also conducted in this chapter. A schematic outline of the experiments and analysis performed in this chapter are shown in Figure 7-1 and Figure 7-2.

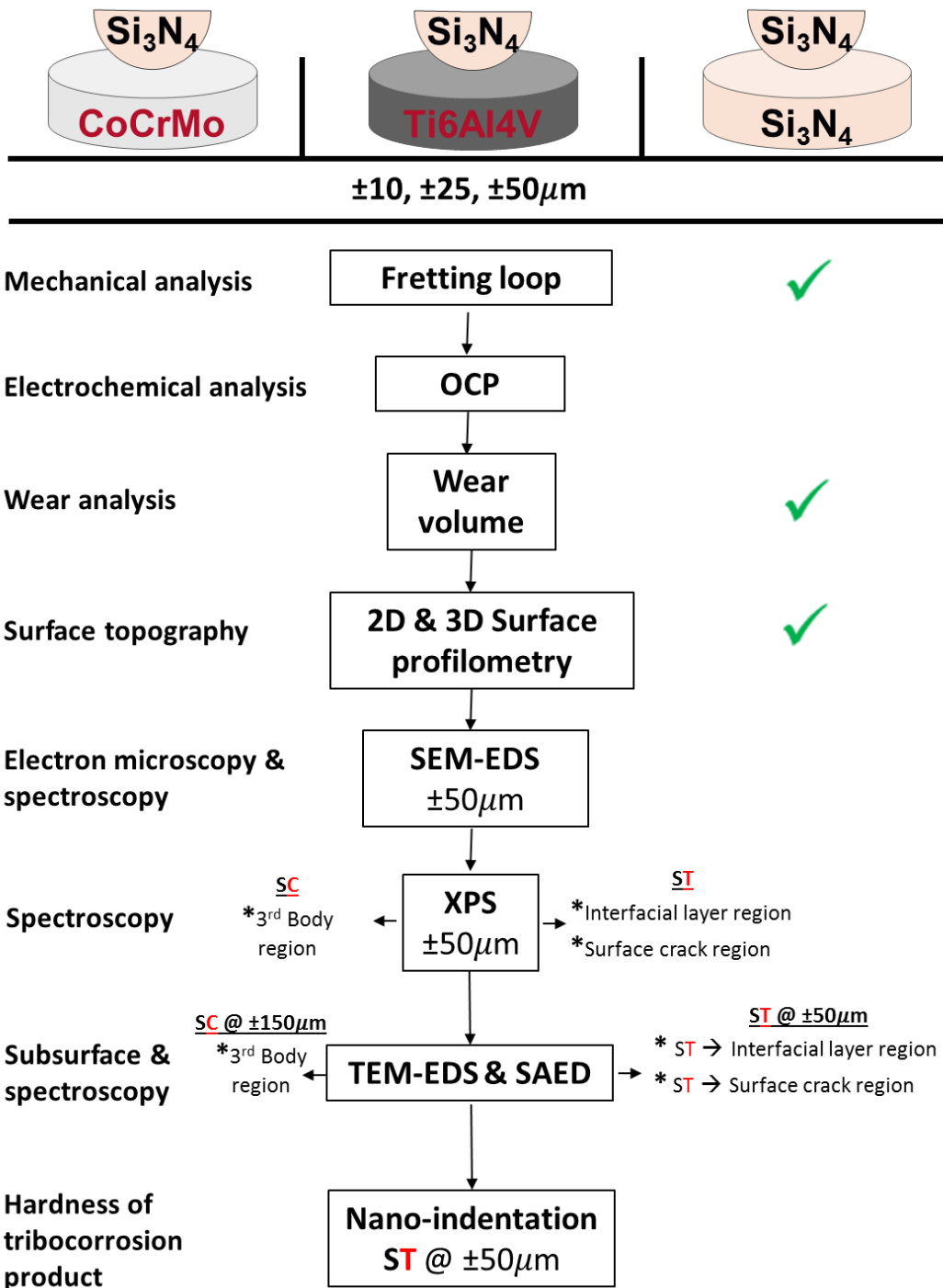


**Figure 7-1 – Outline of the fretting experiments and analyses performed in chapter 7 for  $\text{Si}_3\text{N}_4$  ceramic. C and T represents CoCrMo and Ti6Al4V respectively. The letters that appear in red represent the samples analysed. The green ticks represent the analysis performed on self-mated  $\text{Si}_3\text{N}_4$ .**



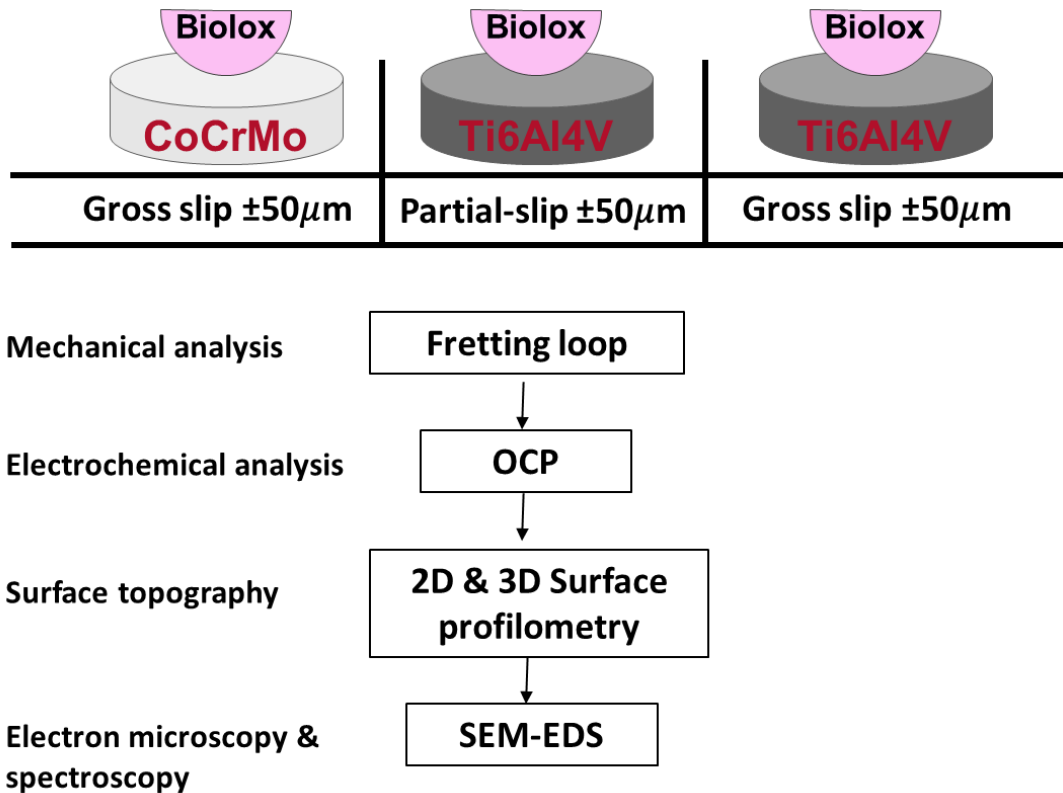
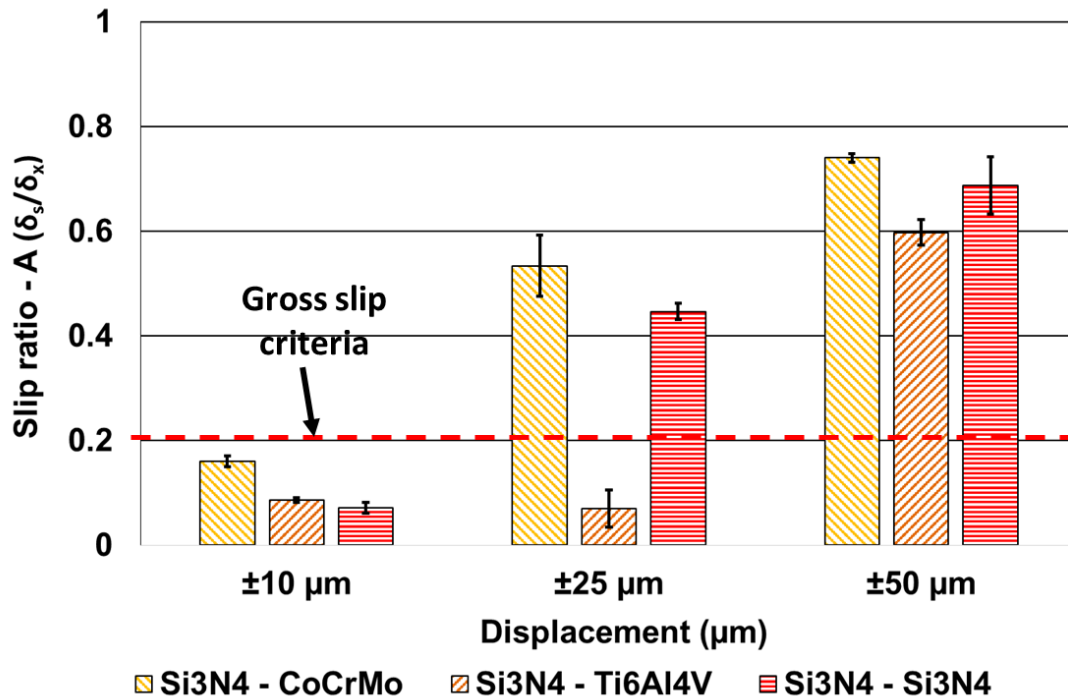


Figure 7-2 – Outline of the fretting experiments and analyses performed in chapter 7 for BioloX ceramic.

## 7.2 Tribological assessment of Ceramic – Metal and Ceramic – Ceramic Fretting Contacts

The fretting displacements assessed for  $\text{Si}_3\text{N}_4$ – CoCrMo,  $\text{Si}_3\text{N}_4$ – Ti6Al4V and  $\text{Si}_3\text{N}_4$ –  $\text{Si}_3\text{N}_4$  were  $\pm 10 \mu\text{m}$ ,  $\pm 25 \mu\text{m}$  and  $\pm 50 \mu\text{m}$ . All the material combination reached a gross-slip fretting regime by  $\pm 50 \mu\text{m}$  as shown in Figure 7-3; although the fretting regime at the  $\text{Si}_3\text{N}_4$ – Ti6Al4V interface was not stable in gross slip regime. At  $\pm 10 \mu\text{m}$  all contacts were in a partial-slip or stick regime and at  $\pm 25 \mu\text{m}$ , only  $\text{Si}_3\text{N}_4$ – Ti6Al4V was still in a stick regime.



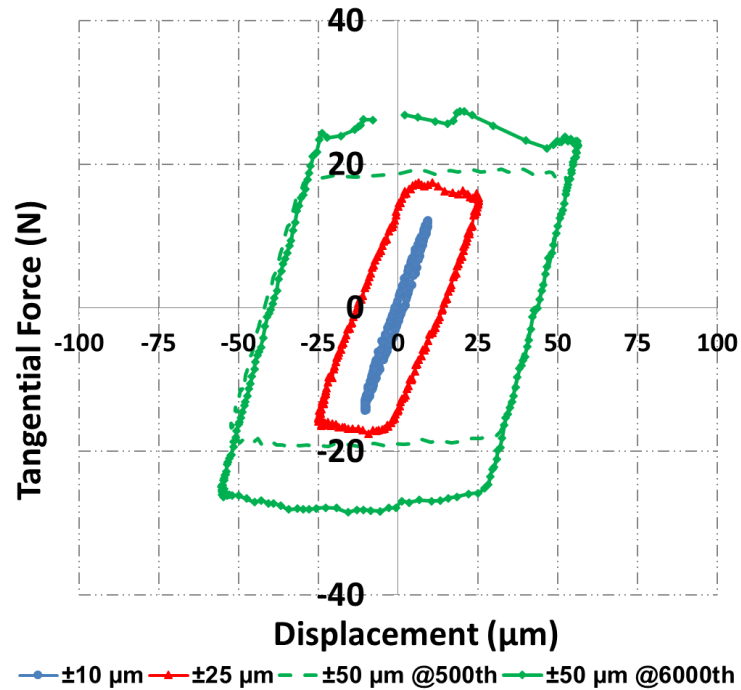
**Figure 7-3 – Slip ratio of Si<sub>3</sub>N<sub>4</sub> – CoCrMo, Si<sub>3</sub>N<sub>4</sub> – Ti6Al4V and Si<sub>3</sub>N<sub>4</sub> – Si<sub>3</sub>N<sub>4</sub> under OCP conditions for ±10, ±25 ±50 μm displacements.**

### 7.2.1 Fretting loop analysis

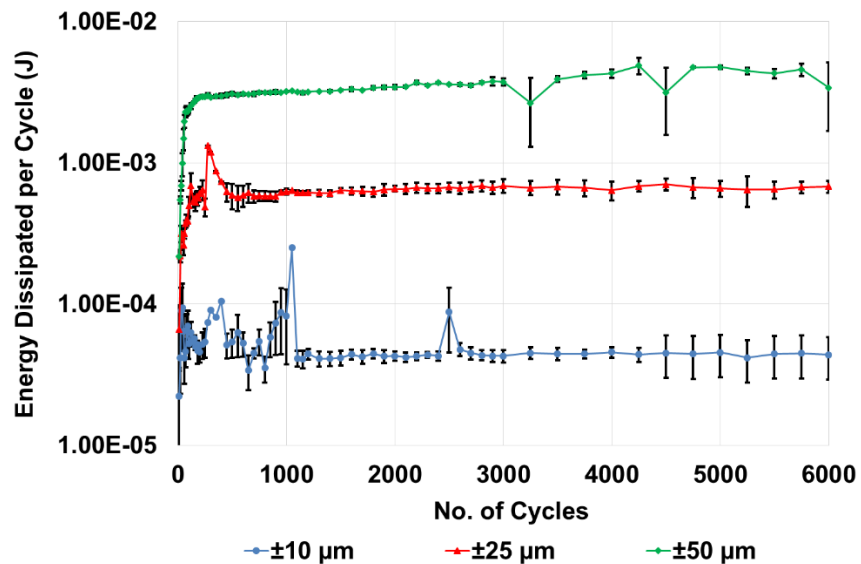
The fretting behaviour of the three Si<sub>3</sub>N<sub>4</sub>-related combinations appeared to be less stable at ±50 μm displacement in comparison to the metal – metal combinations in the previous chapter. For this reason, an additional 2D fretting loop was plotted at ±50 μm displacement in order to portray two extreme in the variation of the contact behaviour. These are presented in green dashed-lines in Figure 7-4a, Figure 7-5a and Figure 7-6a. The green solid-lines represents one of the final few cycles of the fretting contact.

The fretting loop analysis for Si<sub>3</sub>N<sub>4</sub> – CoCrMo is shown in Figure 7-4, Figure 7-4a confirms the regimes at this contact as partial-slip at ±10 μm and gross slip for both ±25 μm and ±50 μm displacements. The energy dissipated per cycle throughout the duration of the fretting tests are shown in Figure 7-4b. These appear to be steady after few 100s of cycles for ±10 μm and ±25 μm. However, at ±50 μm, a steady rise in the energy dissipated can be observed which directly corresponds to a gradual increase in interfacial friction. This is

evidenced in the differences between the tangential forces of the fretting loops at the 500<sup>th</sup> cycle and 6000<sup>th</sup> cycle in Figure 7-4a. The fretting loop at the 6000<sup>th</sup> cycle is also seen to be less stable than at the 500<sup>th</sup> cycle thus indicating a change in the contact condition and wearing mechanism.



(a)



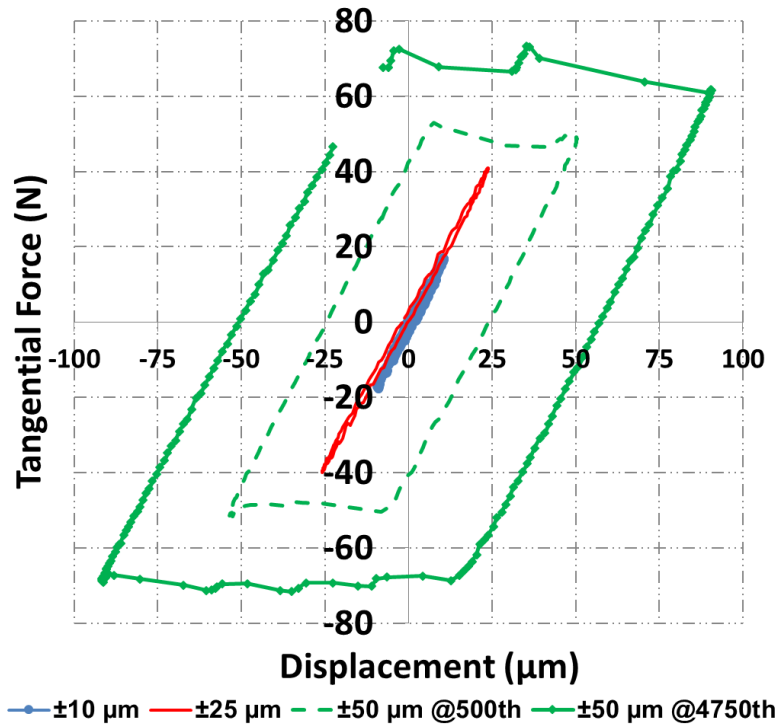
(b)

Figure 7-4 – Fretting contact analysis for  $\text{Si}_3\text{N}_4 - \text{CoCrMo}$ : a) Fretting loop b) Energy dissipated per cycle.

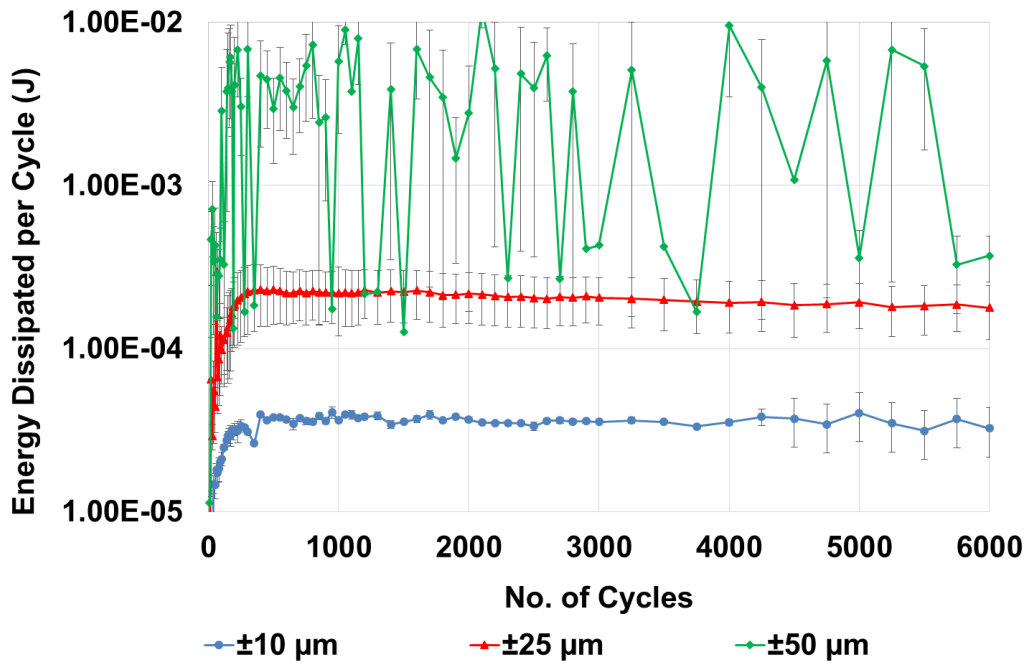
The fretting behaviour at the interface of  $\text{Si}_3\text{N}_4$  – Ti6Al4V is displayed in Figure 7-5. Both  $\pm 10 \mu\text{m}$  and  $\pm 25 \mu\text{m}$  displacements are in a stick regime as shown in the fretting loops of Figure 7-5a. Despite this, there is a clear difference in the magnitude of their energies as shown in Figure 7-5b. This highlights the effect of higher tangential forces in the energy experienced at the contacting interface. From the fretting loop, it is observable that the tangential force at  $\pm 25 \mu\text{m}$  is more than double that of  $\pm 10 \mu\text{m}$  which is in proportion to the magnitude of their displacement amplitudes.

The two fretting loops displayed at  $\pm 50 \mu\text{m}$  displacement appears significantly different, although both displace a gross slip shape. The loop at the 500<sup>th</sup> cycle has a quasi-static feature at its corners. This feature is known as ‘the plunging effect’ and it is commonly observed at the fretting contacts involving Ti6Al4V alloy especially at high contact pressures [202]. For the same fretting loop, the displacement ( $\delta_x$ ) can also be seen to be quite close to the applied  $\pm 50 \mu\text{m}$  displacement whereas, for the fretting loop representing the 4750<sup>th</sup> cycle,  $\delta_x$  is seen to have overshoot to as high as  $\pm 90 \mu\text{m}$  due to the highly unstable fretting interface. The tangential force is also seen to be much higher and unsteady.

The energy dissipated plot of Figure 7-5b show the degree of instability at the fretting interface of  $\pm 50 \mu\text{m}$ . A continuous fluctuation between high tangential force (stick regime energy) to large overshoot (gross slip) fretting displacement energy is observed. This behaviour is better described as an intermittent stiction behaviour.



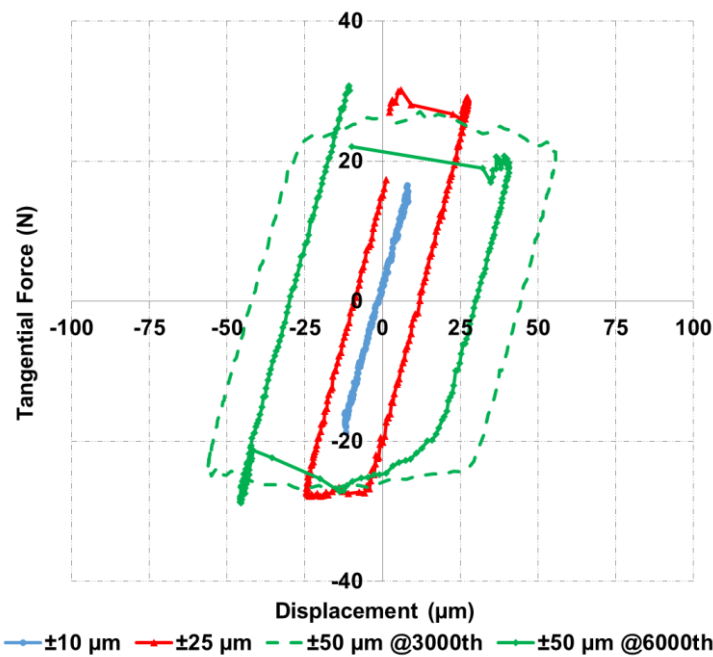
(a)



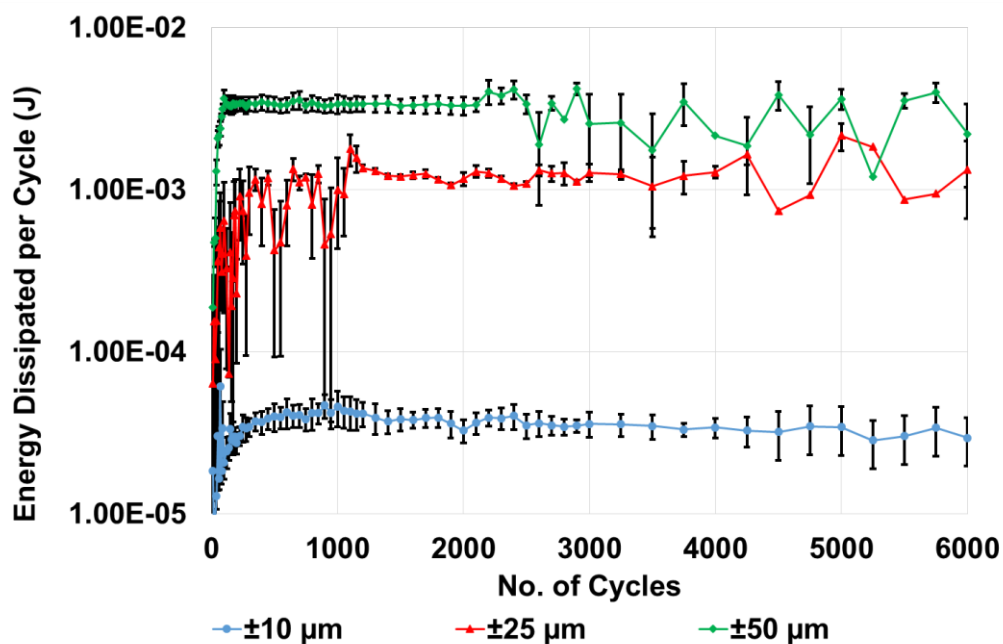
(b)

Figure 7-5 – Fretting contact analysis for  $\text{Si}_3\text{N}_4 - \text{Ti6Al4V}$ : a) Fretting loop b) Energy dissipated per cycle.

In Figure 7-6a, the fretting loop for  $\text{Si}_3\text{N}_4 - \text{Si}_3\text{N}_4$  shows a stick regime at  $\pm 10 \mu\text{m}$  and gross slip regimes for both  $\pm 25 \mu\text{m}$  and  $\pm 50 \mu\text{m}$ . In both gross-slip cases, a distorted, irregular, non-symmetrical loop was observed. This is further illustrated in Figure 7-6b where the energy dissipated per cycle plots appear highly unstable after about 2500 cycles through to the end of the fretting cycles. This is indicative of a change in the wearing mechanism at the interface for both contacts.



(a)



(b)

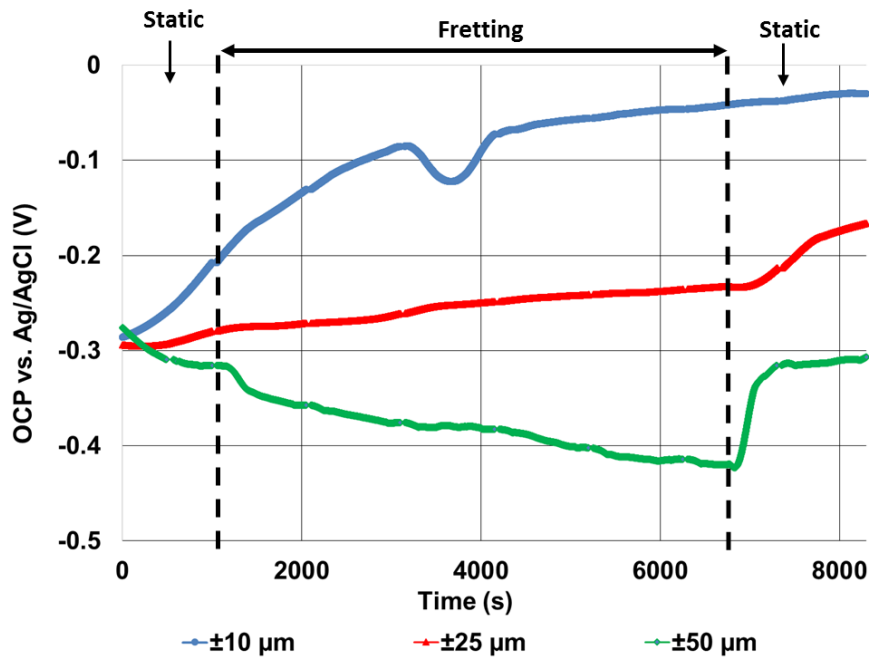
**Figure 7-6 – Fretting contact analysis for Si<sub>3</sub>N<sub>4</sub> – Si<sub>3</sub>N<sub>4</sub>: a) Fretting loop  
b) Energy dissipated per cycle.**

### 7.3 Open circuit potential measurement

The OCP of the ceramic – metal combinations were monitored in the same manner as in the previous chapter. Figure 7-7a shows the OCP behaviour of Si<sub>3</sub>N<sub>4</sub> – CoCrMo combination; it can be observed that depassivation potential i.e. cathodic shift was only observed at ±50 μm. An ennoblement was observed at ±10 μm as similarly seen with the CoCrMo – CoCrMo combination in the previous chapter. For this specific test at ±10 μm, a rapid potential drop followed by an immediate recovery was observed. This may be due to an abrupt change in the fretting surface i.e. a momentary exposure of a depassivated CoCrMo surface to the bulk solution. Interestingly, for the ±25 μm displacement, a general rise in potential with no cathodic shift was observed despite the contact being in a gross slip regime.

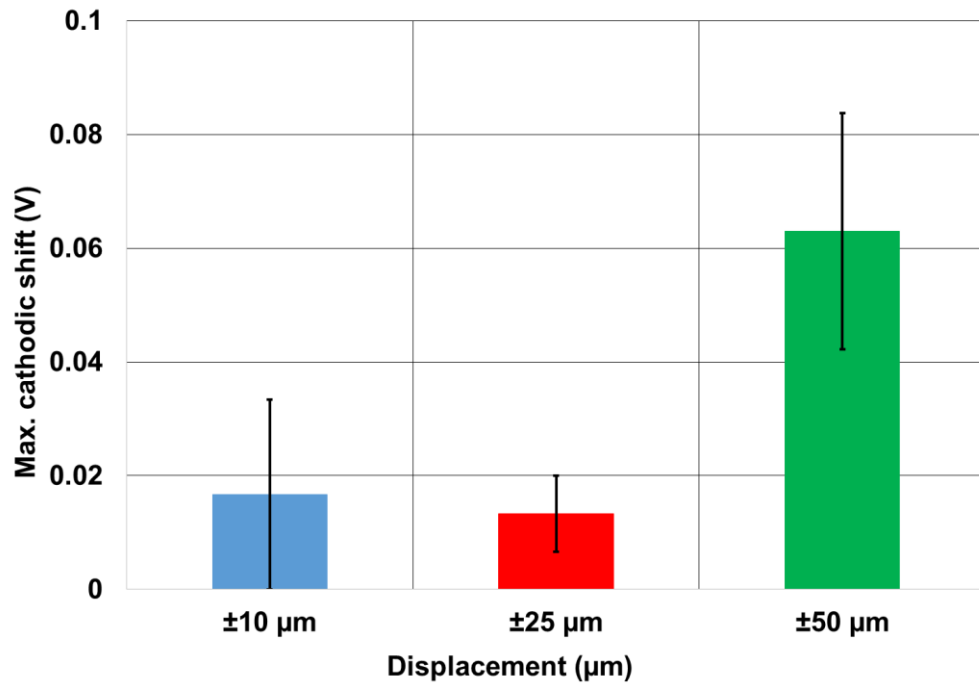
As for the potential at ±50 μm, the cathodic shift continued gradually through to the end of the fretting cycles as was also observed for the CoCrMo – CoCrMo contact at the same displacement. The two gross-slip contacts

displayed a two-stage potential recovery pattern. The potential rises faster in the first stage than in the second thus, in the same manner as observed for the CoCrMo – CoCrMo contact. In addition, the repassivation potential was seen to rise at a faster rate for the  $\pm 50 \mu\text{m}$  than at  $\pm 25 \mu\text{m}$ . This is likely related to the surface area exposed to the bulk solution. Figure 7-7b shows the maximum cathodic shift measured across both static and fretting stages for all the combinations. The errors were large for  $\pm 10 \mu\text{m}$  displacement because the cathodic shift was only observed once and it was due to the transient seen in Figure 7-7a. The maximum cathodic shift at  $\pm 25 \mu\text{m}$  is seen to be minimal relative to  $\pm 50 \mu\text{m}$  despite being in a gross-slip fretting regime. The largest cathodic shift was observed for  $\pm 50 \mu\text{m}$  at an average value of  $\sim 60 \text{ mV}$ .



(a)

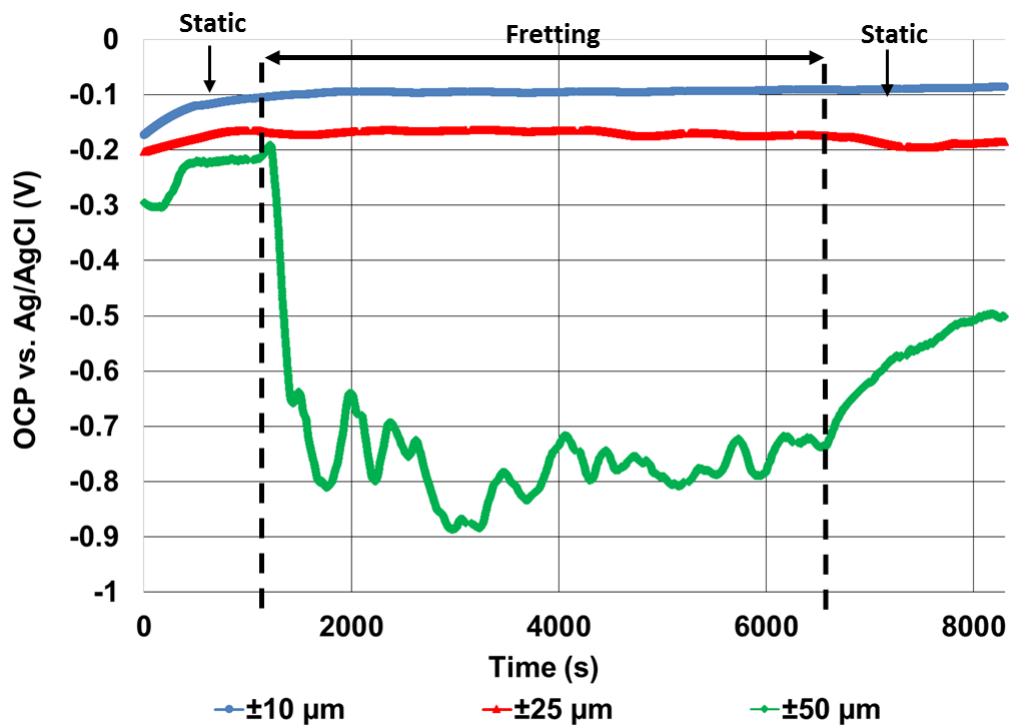




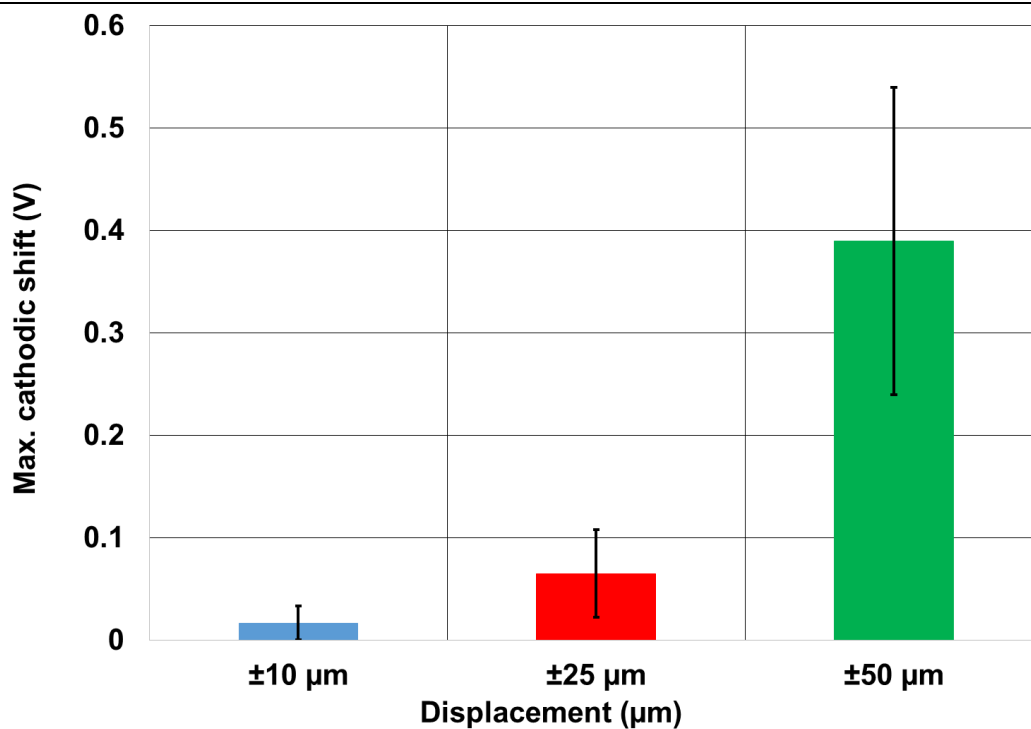
(b)

**Figure 7-7 – Open circuit potential of Si<sub>3</sub>N<sub>4</sub> – CoCrMo: a) OCP plot for ±10 µm, ±25 µm, ±50 µm. b) Max. cathodic shift for all displacements.**

The OCP measurements for the Si<sub>3</sub>N<sub>4</sub> – Ti6Al4V combinations are shown in Figure 7-8a. It is observable that at the stick fretting contacts (±10 µm and ±25 µm) a general rise in potential and no evidence of repassivation at the end of the fretting cycles were observed. However, for the gross slip contact at ±50 µm, an instant cathodic shift to a large negative potential was seen. During fretting, the stiction behaviour identified from the fretting loops was seen to be represented in the OCP plot as a continuous repassivation (sticking) and de-passivation (gross-slip) process. As soon as the fretting ceased, a single recovery stage was identified. In addition, the potential was seen with upto 250 mV of potential difference between the initial potential and at the end of the test – the same observation was made for the CoCrMo – Ti6Al4V interface. In Figure 7-8b, maximum cathodic shift is seen to be minimal at ±10 µm and ±25 µm compared to the cathodic shift measured at ±50 µm.



(a)



(b)

Figure 7-8 – Open circuit potential of Si<sub>3</sub>N<sub>4</sub>– Ti6Al4V: a) OCP plot for ±10 μm, ±25 μm, ±50 μm. b) Max. cathodic shift for all displacements.

## 7.4 Wear volume

The sum of wear volume for ball and flat components of the  $\text{Si}_3\text{N}_4$  – CoCrMo combination are shown in Figure 7-9. The sum of redistributed volume is also shown in the same figure. Across all three displacements, the redistributed volume measured on the surface is minimal. However, while the wear volume at the partial-slip is minimal (as expected), the wear volume for both gross slip displacements are very similar despite the difference in the displacement amplitude by a factor of two. This is an indication of changes to the wearing mechanism at  $\pm 50 \mu\text{m}$  displacement.

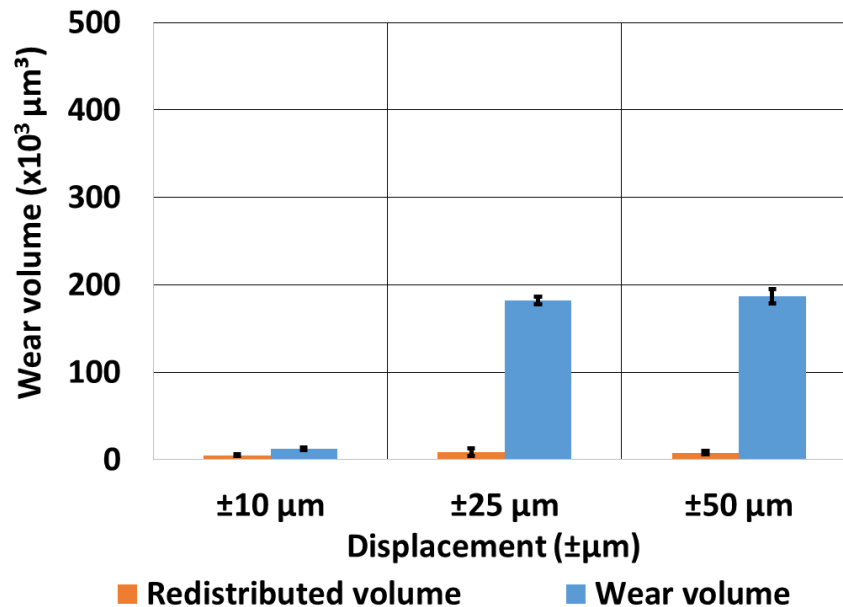


**Figure 7-9 – Wear and redistributed volume from the  $\text{Si}_3\text{N}_4$  – CoCrMo fretting contact. A summation of both ball and flat components.**

The wear volume measured for the  $\text{Si}_3\text{N}_4$  – Ti6Al4V combination is shown in Figure 7-10. The result shows that the wear volume was minimal for the two contacts in a stick regimes ( $\pm 10 \mu\text{m}$  and  $\pm 25 \mu\text{m}$ ) as expected. On the other hand, the redistributed volume at  $\pm 25 \mu\text{m}$  was observed to be higher than the wear volume thus indicating the possibility of material gained at the interface. This may be due to interactions between interfacial wear products and the physiological solution thus resulting in a net material gain. For the mixed fretting regime at  $\pm 50 \mu\text{m}$  displacement of  $\text{Si}_3\text{N}_4$  – Ti6Al4V, the wear volume

is seen to be about three-times higher than those at gross slip regime for Si<sub>3</sub>N<sub>4</sub> – CoCrMo combination. So also is the redistributed volume.

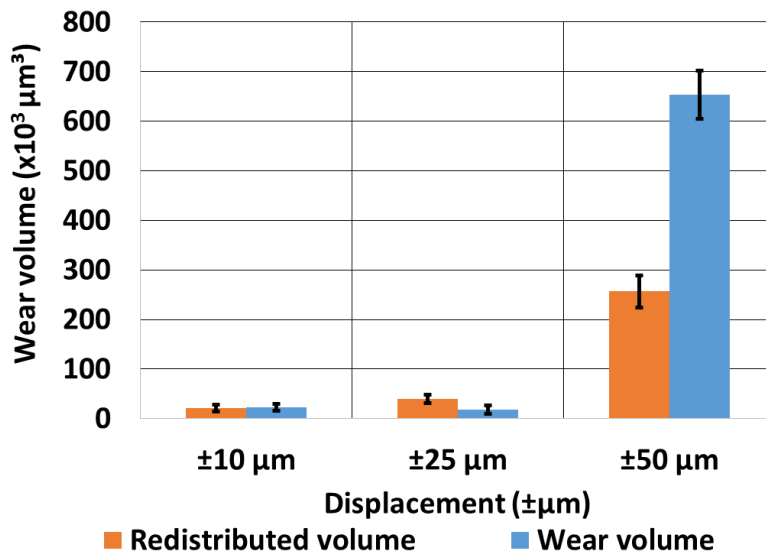


**Figure 7-10 – Wear and redistributed volume from the Si<sub>3</sub>N<sub>4</sub> – Ti6Al4V fretting contact. A summation of both ball and flat components.**

In Figure 7-11, it is observable that for Si<sub>3</sub>N<sub>4</sub> – Si<sub>3</sub>N<sub>4</sub> fretting contact, the measured redistributed volume is negligible and no wear volume was measured at the stick regime. The wear volume measured at the gross slip contacts are seen to be proportional to the displacement amplitude.

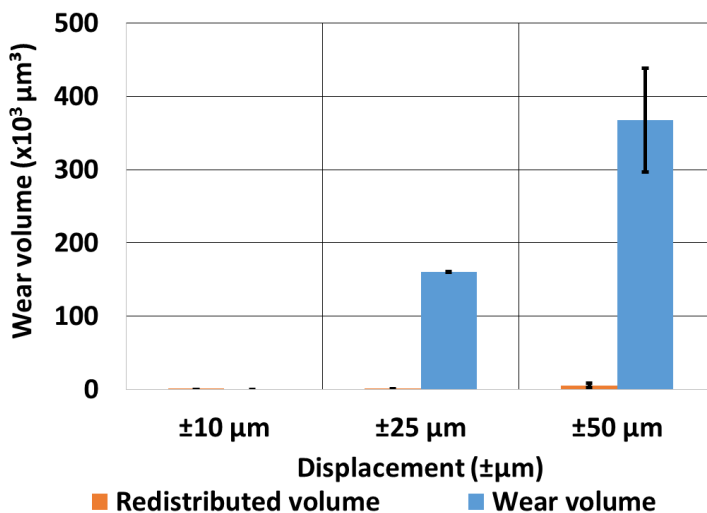


**Figure 7-11 – Wear and redistributed volume from the Si<sub>3</sub>N<sub>4</sub> – Si<sub>3</sub>N<sub>4</sub> fretting contact. A summation of both ball and flat components.**

## 7.5 Surface analysis

In this section, 3D and 2D surface profiles were obtained following a similar outline to the previous chapter. BS-SEM was used to obtain high resolution micrographs of the metallic wear surfaces from the ceramic – metal combinations. The samples assessed are CoCrMo and Ti6Al4V flat components at  $\pm 50 \mu\text{m}$  displacement.

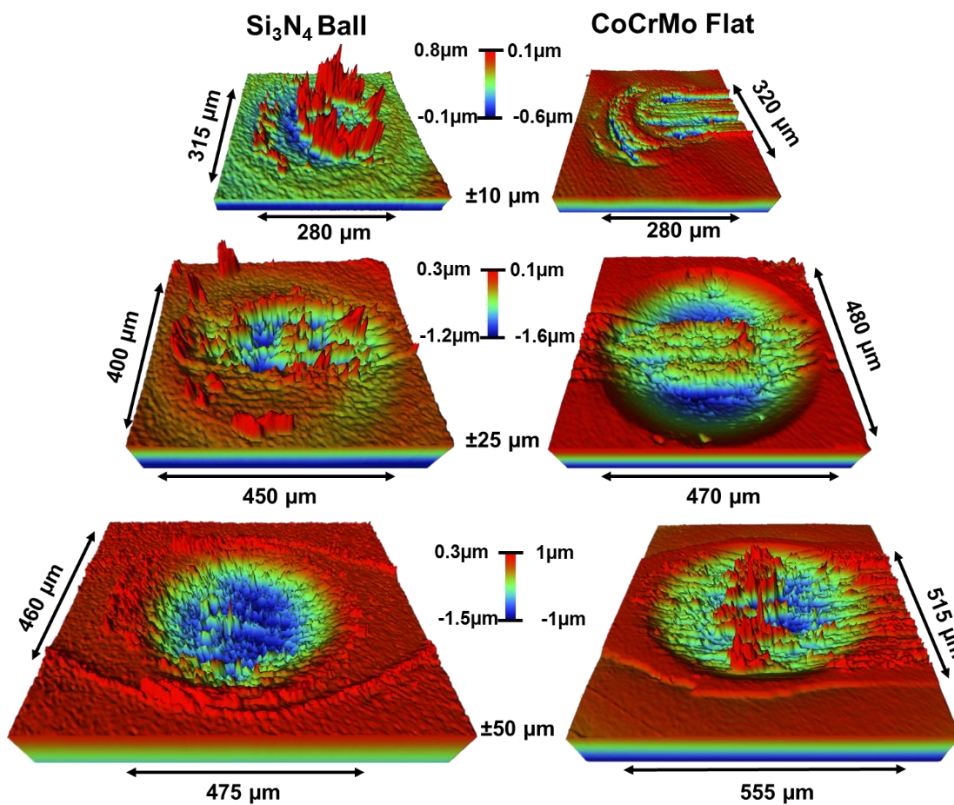
### 7.5.1 3D and 2D surface profilometry of fretted wear surface

Figure 7-12a shows the 3D profile of the wear surface while Figure 7-12b shows the 2D cross-sectional profile of both  $\text{Si}_3\text{N}_4$  ball and CoCrMo flat. The following are the key observations across the displacement amplitudes consecutively:

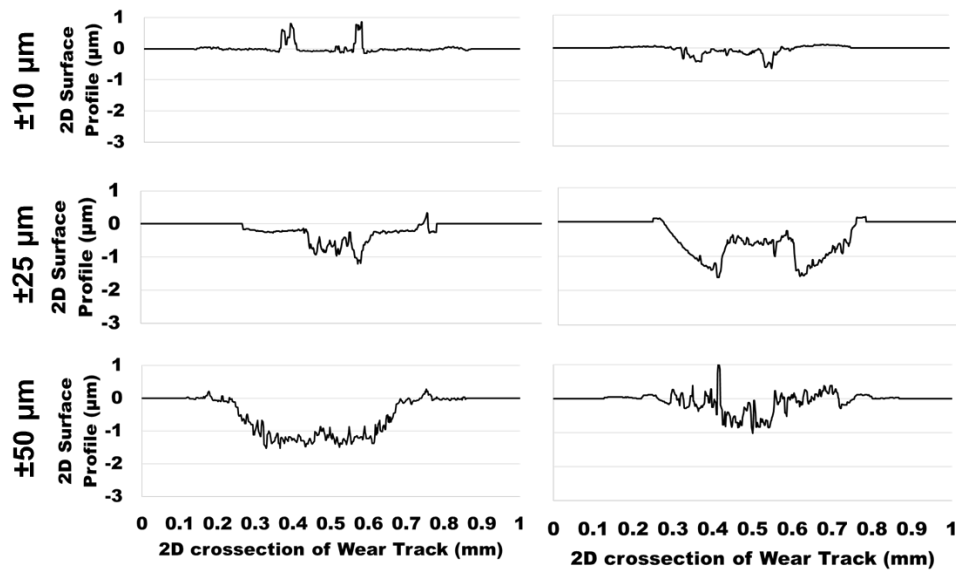
$\pm 10 \mu\text{m}$  – Fretting at this displacement was a partial-slip regime, evidence of a worn annular on the  $\text{Si}_3\text{N}_4$  ball of  $\sim 120 \text{ nm}$  in depth was observed. At the boundary of the worn annulus and the unworn partial-stick region, a heap of third-body material with heights reaching up to  $\sim 850 \text{ nm}$  is can be seen. The 2D surface profile depicts this clearer. From Figure 7-12b, it is also clear that the worn area on the CoCrMo flat corresponds to the third-body product observed on the  $\text{Si}_3\text{N}_4$  ball. Thus, it can be deduced that third-body products at this interface may inflict wear mechanisms such as micro-cutting on to the softer component which in this case was the CoCrMo alloy. The depth of the cut measures up to  $600 \text{ nm}$ .

$\pm 25 \mu\text{m}$  – At the fretting interface of this gross-slip regime, the  $\text{Si}_3\text{N}_4$  ball is seen to have experienced uniform wear of depths  $\sim 260 \text{ nm}$ . However, the centre of the ball experienced the most severe wear with depths reaching up to  $1 \mu\text{m}$ . The CoCrMo flat on the other hand, appear to have worn more than the  $\text{Si}_3\text{N}_4$  ball at the region where  $\text{Si}_3\text{N}_4$  ball experienced the least. And at the centre where the CoCrMo wore the least, the  $\text{Si}_3\text{N}_4$  ball wore more significantly. The phenomena is better depicted in Figure 7-12b.

±50 µm – At this fretting interface, the Si<sub>3</sub>N<sub>4</sub> ball experienced wear of uniform depth of ~1.3 µm with no evidence of a preserved central region. On the other hand, wear depth across the CoCrMo flat component was surprisingly low at a maximum depth of ~1 µm. Third-body material was seen to be agglomerated to the centre of the CoCrMo wear surface. It is anticipated that the third-body material which is later characterised led to the harder Si<sub>3</sub>N<sub>4</sub> ball wear much greater than the softer and less stiff CoCrMo counter-part.



(a)



(b)

**Figure 7-12 – Surface profilometry of Si<sub>3</sub>N<sub>4</sub> ball and CoCrMo flat surfaces: a) 3D surface profile of all displacements, b) 2D cross-section of the vertical axis of the wear surface.**

Figure 7-13a and b shows the 3D and 2D surface profilometry of Si<sub>3</sub>N<sub>4</sub> ball and Ti6Al4V flat.

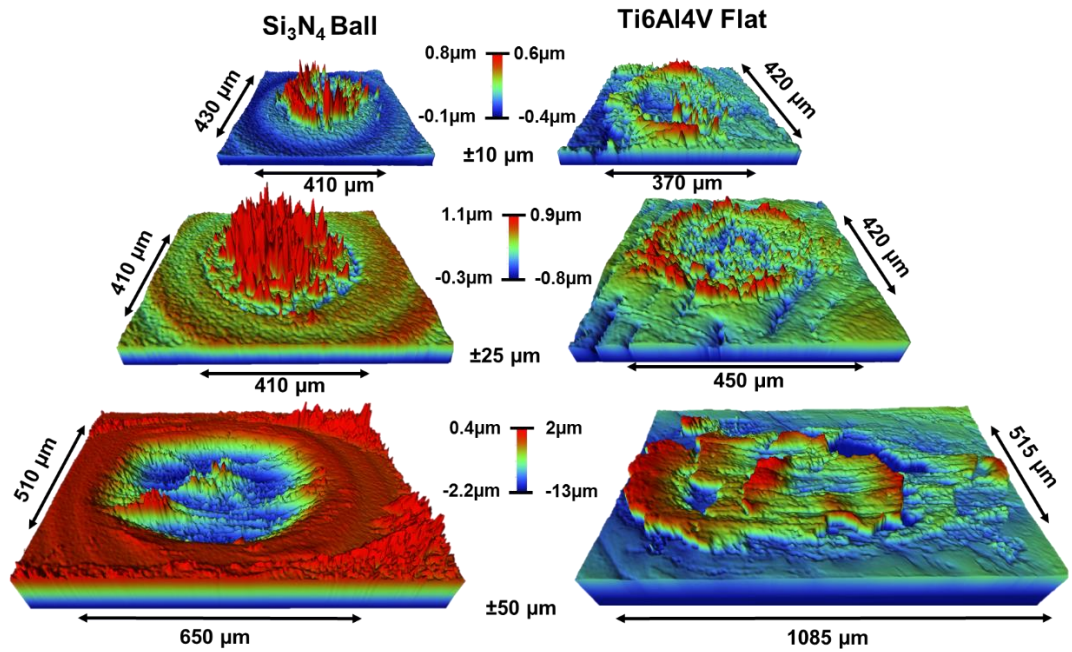
±10 μm – The contact at this fretting displacement experienced a stick regime. The surface profile of the Si<sub>3</sub>N<sub>4</sub> ball shows no evidence of wear but an agglomeration of third-body products which appear ‘needle-like’ and have heights up to ~850 nm. The third-body material mainly originated from the Ti6Al4V surface where evidence of plastic deformation at the edges of the Hertzian contact are visible.

±25 μm – Although the fretting regime at this displacement was also a stick regime, it is observable that a worn annulus of maximum wear depth ~250 nm developed on the Si<sub>3</sub>N<sub>4</sub> ball at the edge of the Hertzian contact. Similarly to the ±10 μm displacement, third-body products populated the central region having the same ‘needle-like’ appearance. At this interface, the height of the needle-like peaks reach up to 1.1 μm. On the Ti6Al4V flat however, a similar feature of dented central region and material pile up around the wear surface is observed.

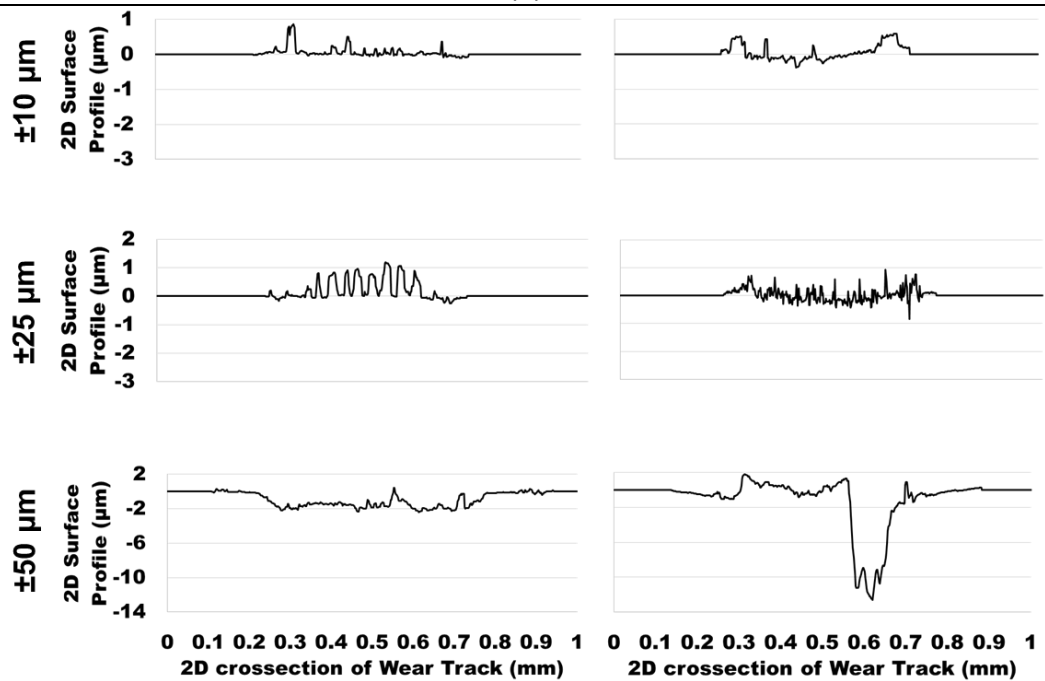
$\pm 50 \mu\text{m}$  – Fretting at this contact is characterised by intermittent sticking and slipping i.e. stiction. The scale of the y-axis in the 2D plot of Figure 7-13b was changed enlarged in order to accommodate the depth of the cracks present within the Ti6Al4V alloy. In addition, the 2D cross-section of Ti6Al4V at this displacement was obtained from the horizontal axis instead of the standard vertical axis. This allowed for both the height of the developed interfacial layer and the crack to be quantified within the same cross-section.

A wear depth of  $\sim 2 \mu\text{m}$  was measured within the  $\text{Si}_3\text{N}_4$  ball, however, some peaks (likely unworn areas) within the wear surface are also visible. This may be indicative of brittle fracture at the interface. The layer present on the wear surface of Ti6Al4V appear similar to that of the ‘mechanically mixed layer’ observed at the CoCrMo – Ti6Al4V interface from the previous chapter. The layer had peaks reaching upto  $2 \mu\text{m}$  above the zero-line. The 3D topography of the surface also depicts evidence of directionality and plastic flow along the axis of the reciprocating fretting displacement at the surface. This phenomenon was repeatable in all  $n = 3$  tests and in other tests, the layer reached up to  $4 \mu\text{m}$ . Furthermore, a relatively wide and deep crack of depths reaching upto  $13 \mu\text{m}$  is observed in the Ti6Al4V alloy.





(a)



(b)

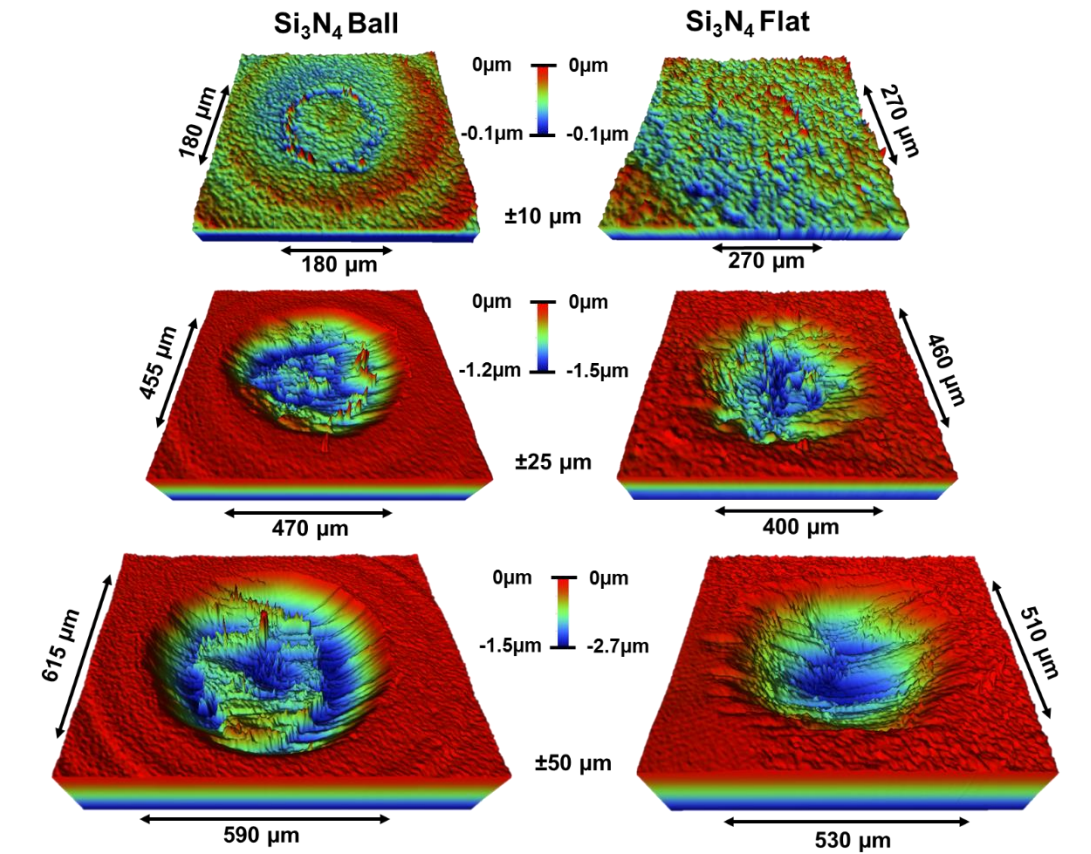
**Figure 7-13 – Surface profilometry of Si<sub>3</sub>N<sub>4</sub> ball and Ti6Al4V flat surfaces:**  
 a) 3D surface profile of all displacements, b) 2D cross-section of the vertical axis of the wear surface.

Figure 7-14 shows the 3D and 2D surface profile of the  $\text{Si}_3\text{N}_4$  ball and flat components.

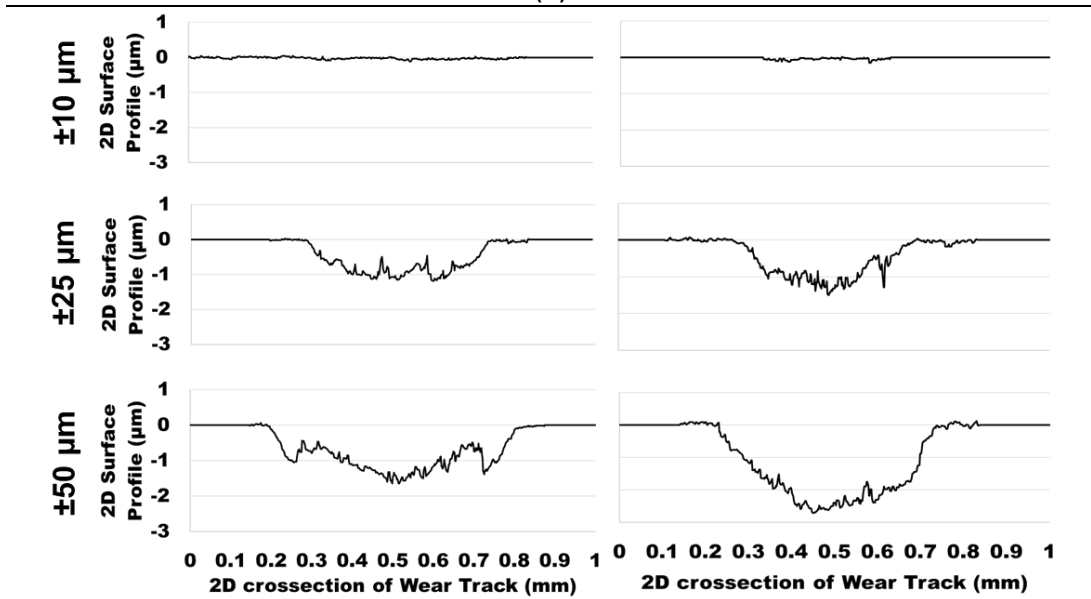
$\pm 10 \mu\text{m}$  – A worn annulus of wear depth  $\sim 100 \text{ nm}$  is visible at the surface of the ball while still in a stick regime. However, no such pattern is observable on the surface of the flat component.

$\pm 25 \mu\text{m}$  – A gross slip regime was realised at this fretting contact. The wear depth for both ball and flat components were  $\sim 1 \mu\text{m}$  and it is observable from the flat component that wear was maximum at the centre. In addition, the 3D topography of the wear surfaces depicts a contact dominated by brittle fracture as would be expected for a self-mated  $\text{Si}_3\text{N}_4$  ceramic couple [203].

$\pm 50 \mu\text{m}$  – At this displacement, the wear depth for the flat component increased to  $\sim 2.5 \mu\text{m}$  while the width of the ball's wear surface increased relative to the width at  $\pm 25 \mu\text{m}$  displacement. Interestingly, the 3D surface profile of the ball shows evidence of brittle fracture at the centre of the wear surface while a uniformly abraded annulus is observed adjacent to the central region. This suggests that as the displacement amplitude increases, the wear mode transitions from a fracture-based wear mechanism to an abrasive wear mechanism. Thus at this displacement, a composite contact of both mechanism was observable.



(a)



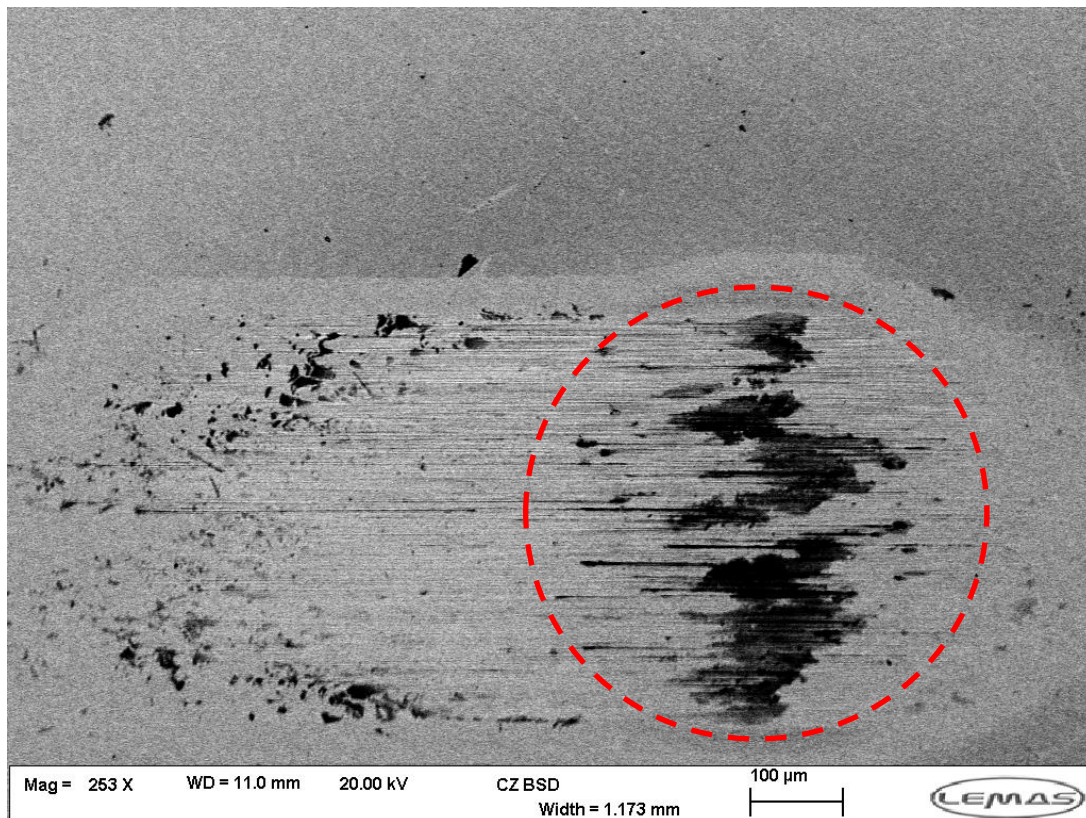
(b)

Figure 7-14 – Surface profilometry of  $\text{Si}_3\text{N}_4$  ball and  $\text{Si}_3\text{N}_4$  flat surfaces: a) 3D surface profile of all displacements, b) 2D cross-section of the vertical axis of the wear surface.

## 7.5.2 BS-SEM analysis

In a similar fashion to the analysis of metal – metal material combinations in the previous chapter, the third-body products at the ceramic – metal interface of this chapter were also assessed on at  $\pm 50 \mu\text{m}$  displacement where it is most prominent. Analyses were only performed on the metallic flat components for all cases.

The BS-SEM micrograph of CoCrMo surface from the  $\text{Si}_3\text{N}_4$  – CoCrMo material combination at  $\pm 50 \mu\text{m}$  displacement is shown in Figure 7-15. As already identified through the 3D surface topography, third-body products can be seen across the centre of the wear surface. The red dashed-line is drawn around the real wear surface so as to make a distinction between the confines of the wear surface and the additional area scratched upon the cessation of fretting.



**Figure 7-15 – Back scatter-SEM micrograph of CoCrMo flat from the fretting against  $\text{Si}_3\text{N}_4$  ball at  $\pm 50 \mu\text{m}$ .**

BS-SEM micrograph of the Ti6Al4V surface from the Si<sub>3</sub>N<sub>4</sub> – Ti6Al4V material combination at ±50 μm displacement is shown in Figure 7-16. This figure identifies four regions of interest. Region 'A' shows the wear tracks on the Ti6Al4V surface. Region 'B' is a material deposited onto the Ti6Al4V surface. The material in region 'C' appears smooth and blended into the Ti6Al4V surface despite being a different material. The material in region C corresponds to the 'mechanically mixed layer' described in the 3D surface profile of Figure 7-13. In region 'D' the surface of the Ti6Al4V looks plastically deformed but no wear tracks could be seen in the region. This is because, region D was once covered with the layer identified in region C however, during the polishing procedure preceding the nano-indentation analysis of the mechanically mixed layer, most of interfacial layer 'flaked' off from the surface, leaving the underlying Ti6Al4V surface, exposed. This proved a positive occurrence as evidence of subsurface plastic deformation occurring in the Ti6Al4V when the Si<sub>3</sub>N<sub>4</sub> ball frets relative to the layer could now be imaged.

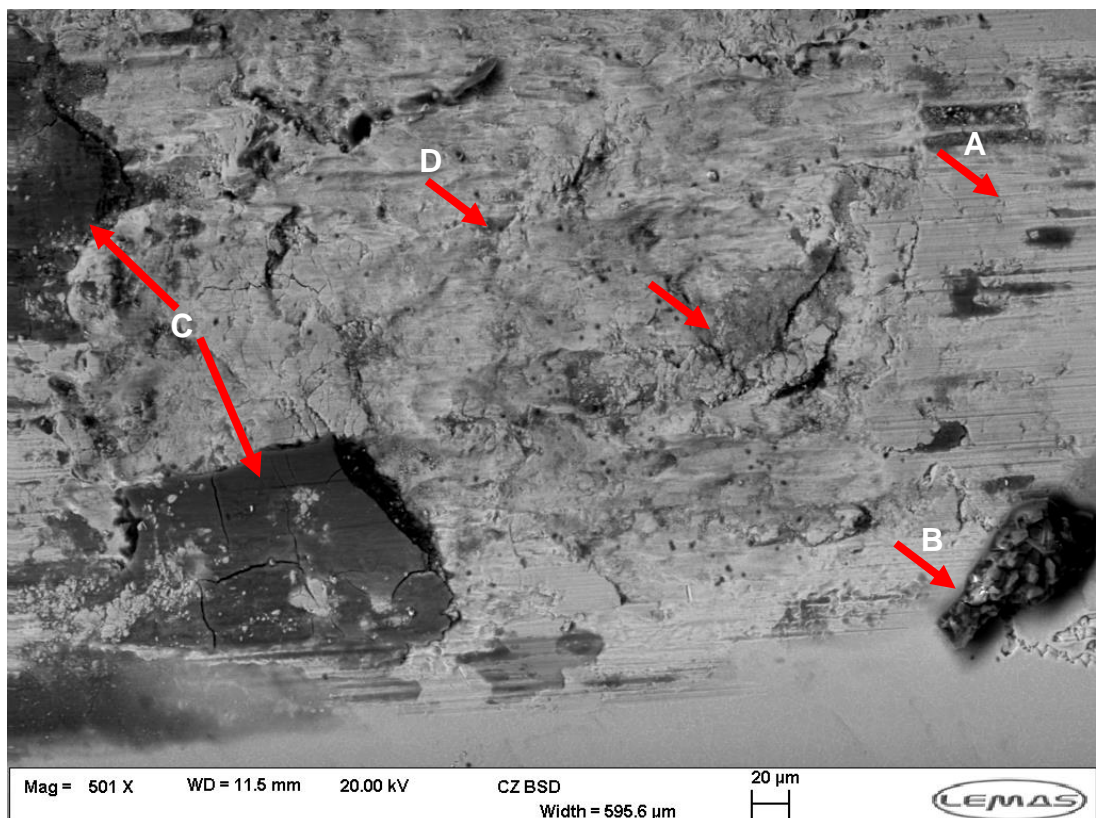


**Figure 7-16 – Back scatter-SEM micrograph of Ti6Al4V flat fretted against Si<sub>3</sub>N<sub>4</sub> ball at ±50 μm.**

## 7.6 Spectroscopy of CoCrMo and Ti6Al4V surface from the ceramic – metal interface

In this section, EDS and XPS spectroscopy techniques is used to further characterise the surfaces imaged with the BS-SEM. High resolution XPS analysis of the third-body products in the centre of the CoCrMo wear surface was scanned for the following key elements: C, O, N, Co, Cr, Mo, P, S and Si. As for the Ti6Al4V surface, high resolution XPS analysis were conducted at two regions namely: regions C and D from Figure 7-13. The key elements scanned in both regions were: C, O, N, Ti, Al, V, P, S and Si. Across all three regions analysed, S was not detected as was the also the case during the analysis of the metal – metal material combinations.

### 7.6.1 EDS analysis of CoCrMo and Ti6Al4V surfaces (ceramic – metal)

The EDS map of the CoCrMo flat surface in Figure 7-17 shows that Co, Cr and Mo were present at the background as expected being the most abundant elements in the bulk alloy. On the other hand, Si and O can be seen to be only highly concentrated across the third-body deposit. C, Cl, S and Ca are present as background signal. This SEM-EDS map strongly indicates that the third-body material present at the  $\text{Si}_3\text{N}_4$  – CoCrMo interface is mainly oxidised Si.

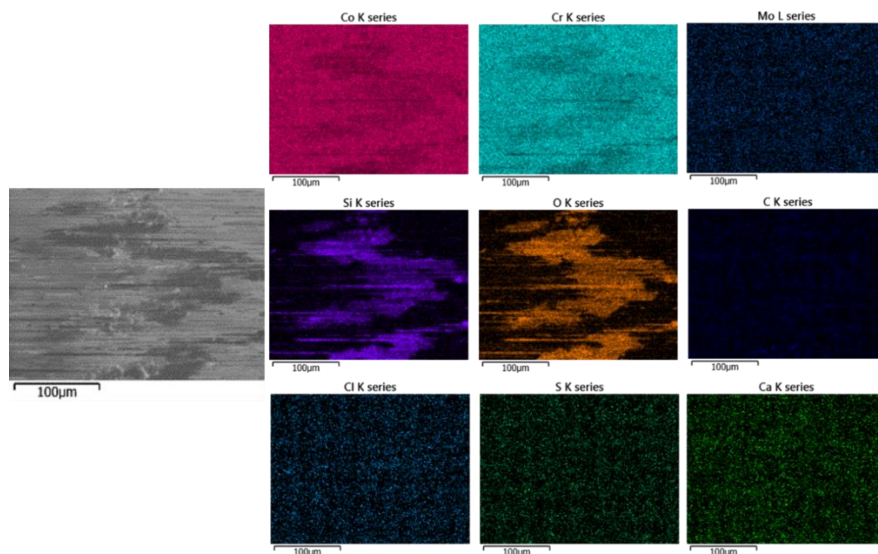
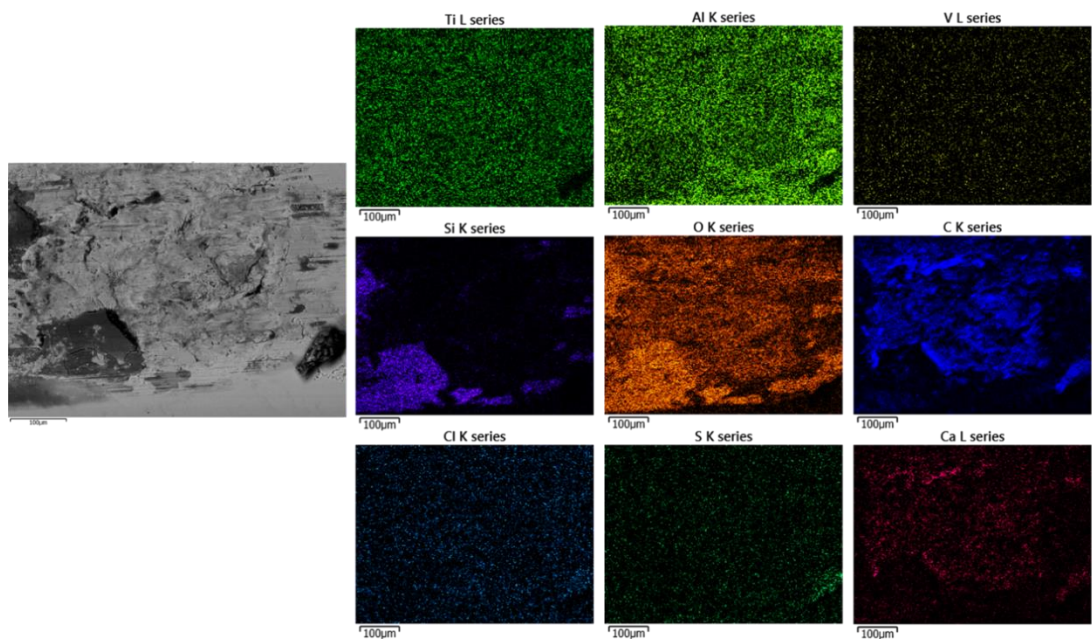


Figure 7-17 – SEM-EDS of CoCrMo flat fretted against  $\text{Si}_3\text{N}_4$  ball at  $\pm 50 \mu\text{m}$ .

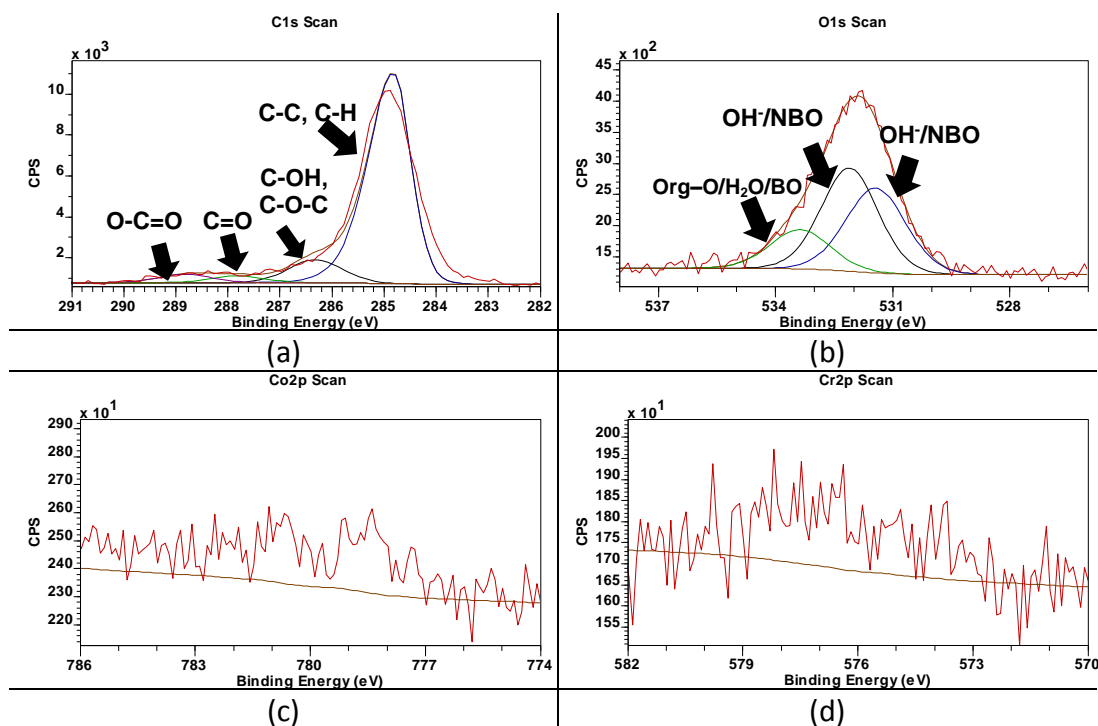
The EDS map of the Ti6Al4V flat surface in Figure 7-18 shows the Ti, Al and V at the background as expected for Ti6Al4V alloy. However, the material deposit in region B of Figure 7-16 is seen to constitute mainly of C, Ca, S and Cl; these elements could only have originated from the physiological solution in which the fretting occurred. The presence of S is also indicative of proteins thus suggesting the deposit is a cluster of denatured protein and other organic species. The ‘mechanically mixed layer’ in region C of Figure 7-16 was identified to constitute mainly of Ti, Si, O and Al. This suggests that the material is made up of mixed oxidised compounds similar to the observation from CoCrMo – Ti6Al4V in the previous chapter. Region D is seen to be covered in C, O and Ca which suggests that the physiological solution migrated beyond the uppermost where fretting occurred and thus might have been trapped at the interface between of the ‘mechanically mixed layer and bulk Ti6Al4V.



**Figure 7-18 – SEM-EDS of Ti6Al4V flat fretted against Si<sub>3</sub>N<sub>4</sub> ball at ±50 µm.**

## 7.6.2 XPS analysis of CoCrMo and Ti6Al4V surface (ceramic – metal)

Analysis of the  $\text{Si}_3\text{N}_4$  – CoCrMo interface is shown in Figure 7-19(a – h). The region scanned is the Si and O-rich third-body product agglomerated onto the CoCrMo flat component. In Figure 7-19a, the series of peaks pertaining to the adventitious C is observed. Three peaks of oxygen was observed in Figure 7-19b however none of these corresponds to the MO specie. Rather, an NBO specie is observed at 531.4 eV followed by a BO specie at 532.1 eV which is attributable to organic species. The other BO specie at 533.4 eV is attributable to  $\text{SiO}_2$  [160]. The main species of interest at this interface are outlined in Table 7-1. From Figure 7-19c – e it can be seen that Co and Cr may be present in the region however, their intensity relative to the background signal appear too low to be computed. As for Mo, there is no evidence it is present within the structure. In Figure 7-19f, evidence of organic N; likely from the serum solution was present. No P peak were identified in Figure 7-19g and both high energy Si (4+) and the organic Si specie were observed for the Si scan in Figure 7-19g. The main product at this interface is therefore  $\text{SiO}_2$  or an hydrated specie of silica generally denoted  $\text{SiO}_x\text{-OH}_y$  as also observed in previous studies [17].





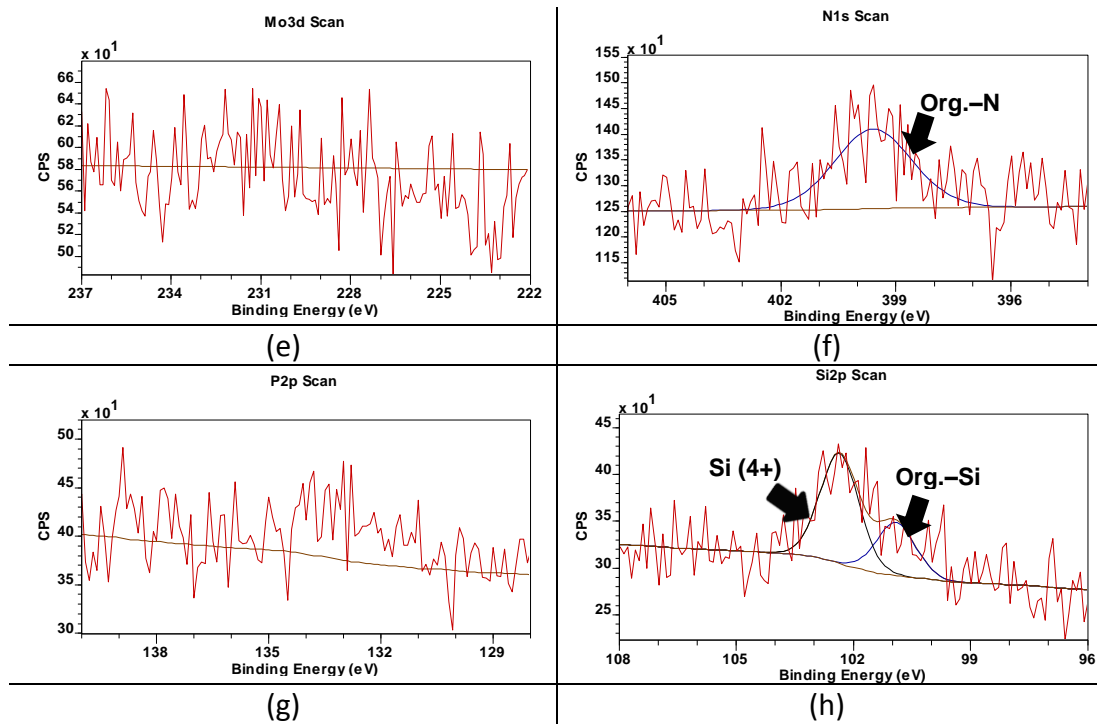


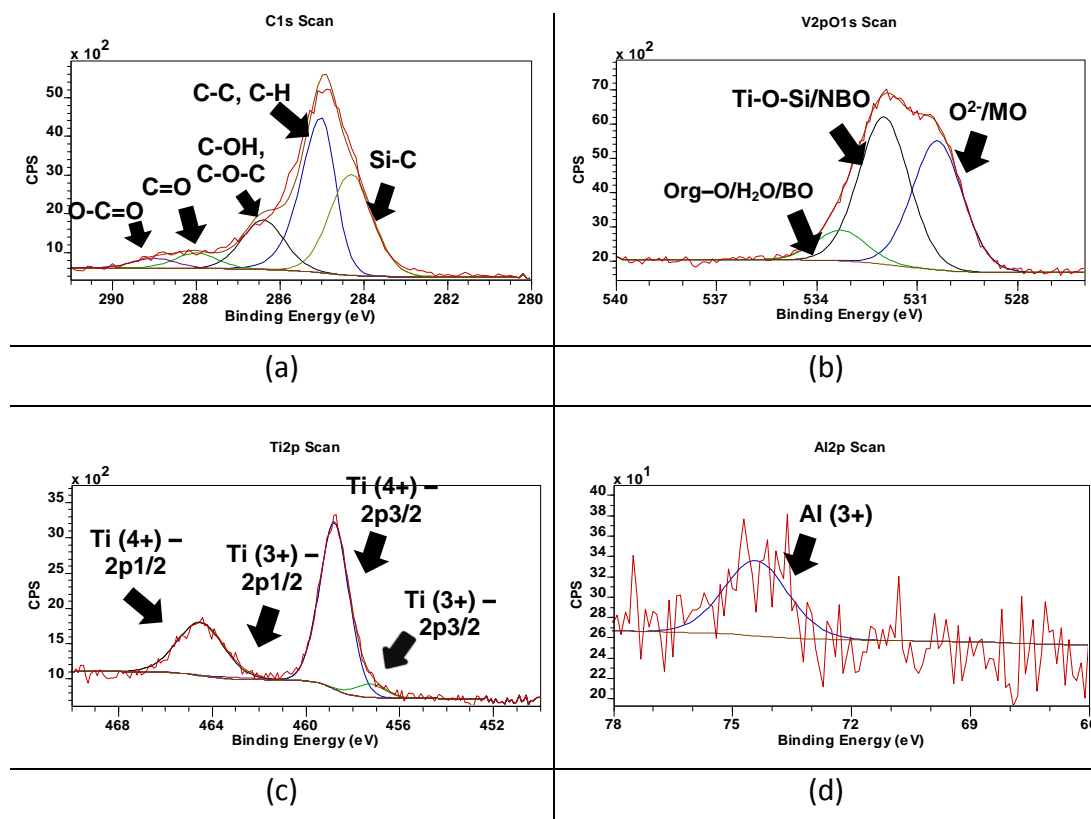
**Figure 7-19 – XPS analysis of wear and corrosion product from the wear surface of Si<sub>3</sub>N<sub>4</sub> – CoCrMo combination at ±50 μm. Si&O-rich third-body product on CoCrMo.**

**Table 7-1 – Attribution of Si, N and O species from Si<sub>3</sub>N<sub>4</sub> – CoCrMo at ±50 μm. Si&O-rich third-body product on CoCrMo.**

Element	Position (eV)	Attributions [17, 160, 161, 204]	(%)	
Si 2p	100.9	Org.-Si: Si-C	33	
	102.4	SiO <sub>2</sub> /SiO <sub>x</sub> -OH <sub>y</sub>	67	
N 1s	399.6	Serum – Organic N	100	
O 1s	531.4	NBO	OH <sup>-</sup>	38
	532.1	BO	H <sub>2</sub> O/Si-O/C-O/N-O	44
	533.4	BO	SiO <sub>2</sub>	18

The curves in Figure 7-20(a – h) are the scans obtained from region C of Figure 7-16 which corresponds to the surface of the Si, Ti, Al and O-rich layer. For the C 1s scan in Figure 7-20a, an extra peak, in addition to the adventitious

C peak was fitted to BE  $\sim 284.3$  eV which corresponds to an organic specie of Si-C [155]. The three O peaks in Figure 7-20b are the standard MO, NBO and BO peaks. From Table 7-2 it can be seen that the MO and NBO species are close in proportion. The MO species corresponds mainly to Ti-oxide whilst the NBO specie corresponds mainly to Ti and Al-silicates. Thus Figure 7-20c and Figure 7-20d show oxidised species of both Ti as Ti (4+) and Ti (3+) and Al as Al (3+) with no indication of their metallic species. No evidence of the V specie was found both in its oxidised and metallic form as shown in Figure 7-20e. Two N species were found in Figure 7-20f: the first corresponds to the N-H bond which is likely ammonia – a by-product of  $\text{Si}_3\text{N}_4$  tribochemical reactions [205] and the other specie corresponds to the organic-N. From Figure 7-20g no specie of P was found on this surface. The Si peaks are of two oxidised Si species: the Si (4+) and the organic-Si.



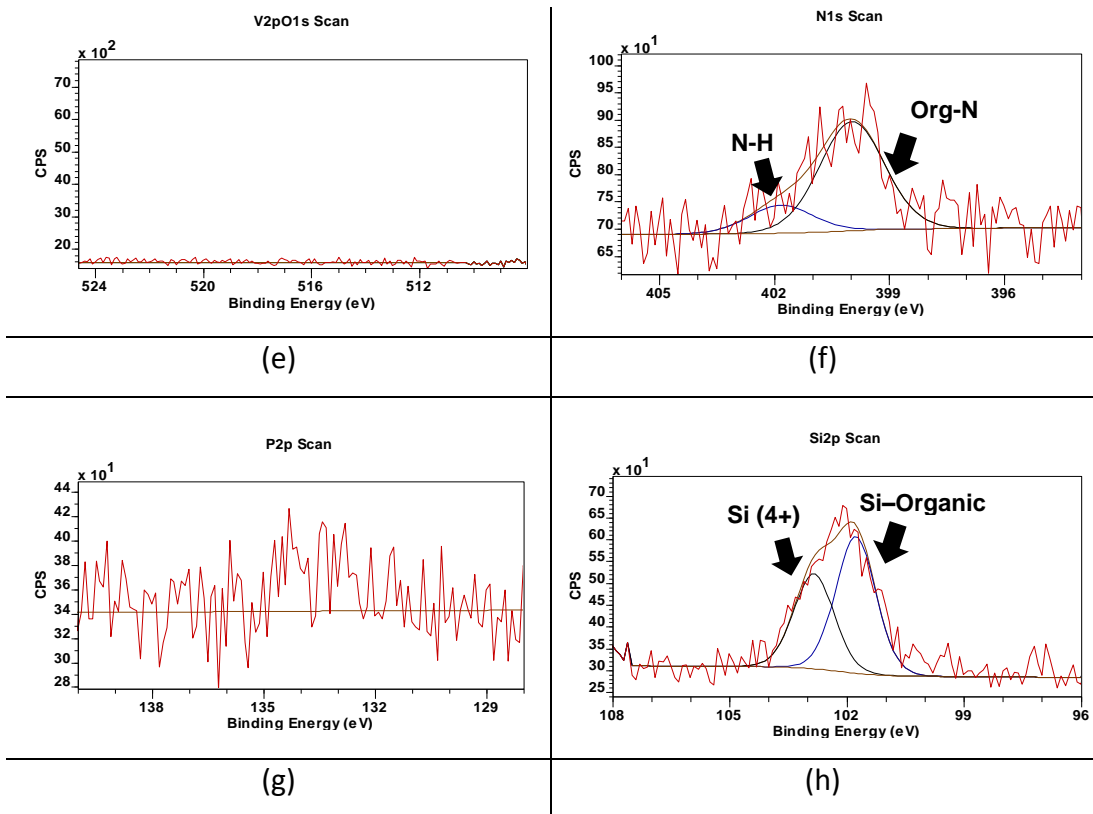


**Figure 7-20 – XPS analysis of wear and corrosion product from the wear surface of  $\text{Si}_3\text{N}_4$  –  $\text{Ti6Al4V}$  combination at  $\pm 50 \mu\text{m}$ . Mechanically mixed layer on  $\text{Ti6Al4V}$  – Region ‘C’.**

**Table 7-2 – Attribution of Si, Ti, Al, N and O species from Si<sub>3</sub>N<sub>4</sub> – Ti6Al4V at ±50 µm. Mechanically mixed layer on Ti6Al4V – Region ‘C’**

Element	Position	Attribution [156, 161, 204]	(%)
Si 2p	102.8	Ti-Si-O/Al-Si-O	41
	101.8	C-Si-O/Si <sub>3</sub> N <sub>4</sub>	59
N 1s	399.9	Serum: Organic N	80
	401.8	Ammonia: N-H	20
Ti 2p	458.8	Ti <sup>4+</sup> : Ti-Si-O/Ti-O	92
	457.3	Ti <sup>3+</sup> : Ti-O	8
Al2p	74.4	Al-Si-O/Al-O	100
O1s	530.4	Ti-O	42
	532.0	Al-Si-O/ Ti-Si-O	48
	533.3	H <sub>2</sub> O/Si-O/C-O/N-O	10

The second surface scanned on the Ti6Al4V flat corresponds to region ‘D’ of Figure 7-16. Figure 7-21a shows that the typical adventitious C peaks were not present in this area as similarly observed in the previous chapter. As aforementioned, the absence of the adventitious C confirms that the region being analysed is located at depth below the uppermost surface. Thus indicative of less surface contamination at surfaces below the uppermost. Similarly to the observations from the previous chapter, the Aliphatic C-C at BE ~284.8 eV and an organic C-O at BE ~ 285.8 eV are both present on the surface. The three standard O species are observed in Figure 7-21b and in Figure 7-21c – e Ti, Al and V were present in their non-oxidised metallic state. From Figure 7-21f – h, N, P and Si species were not detected on the surface. Thus confirming that this region had little to no interactions with the Si<sub>3</sub>N<sub>4</sub> counter-body as expected considering that the surface was unveiled unexpectedly from beneath an interfacial layer.

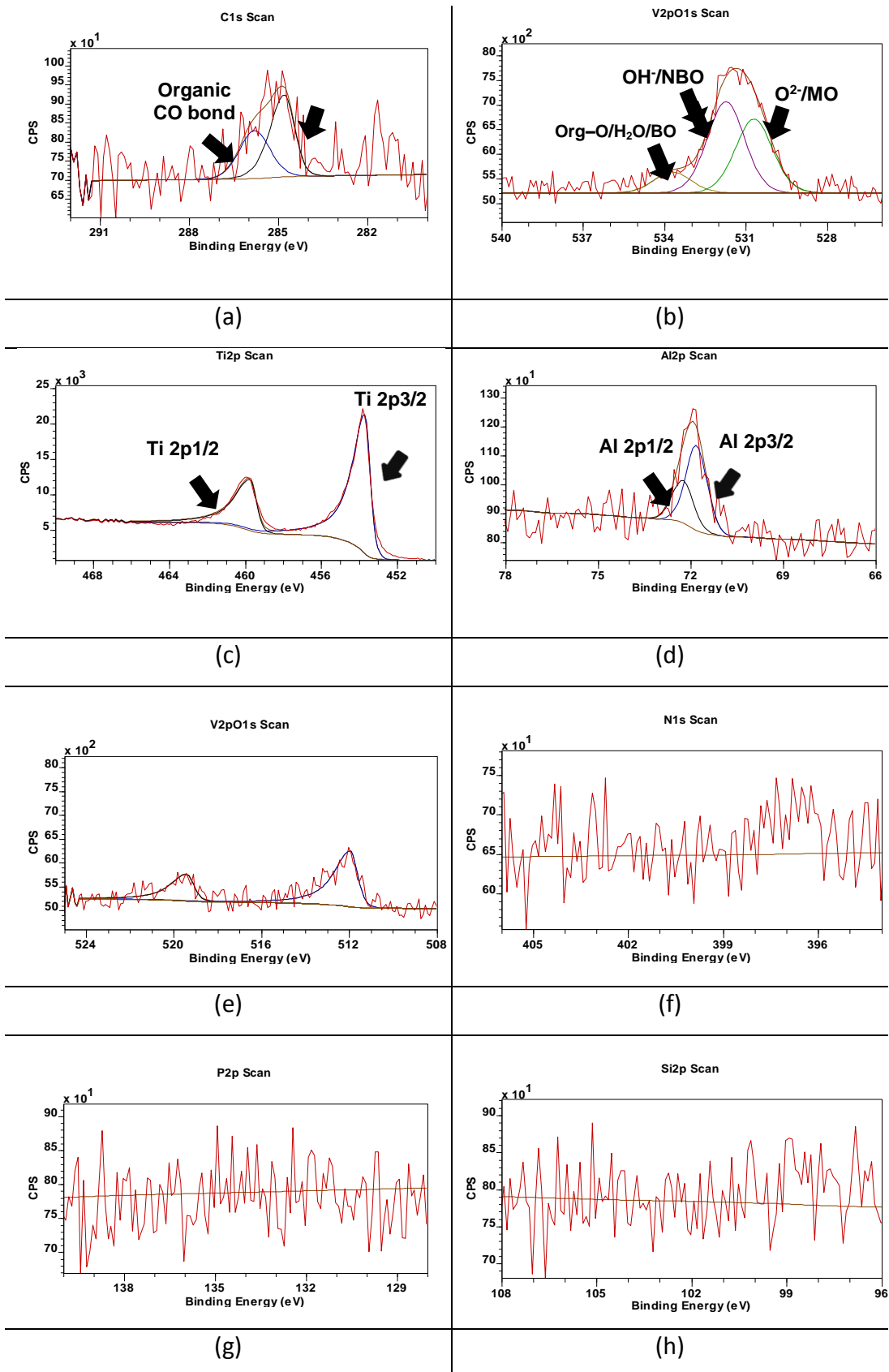


**Figure 7-21 – XPS analysis of wear and corrosion product from the wear surface of  $\text{Si}_3\text{N}_4$  – Ti6Al4V combination at  $\pm 50 \mu\text{m}$ . Ti6Al4V surface which was once covered by the mechanically mixed layer – Region ‘D’**

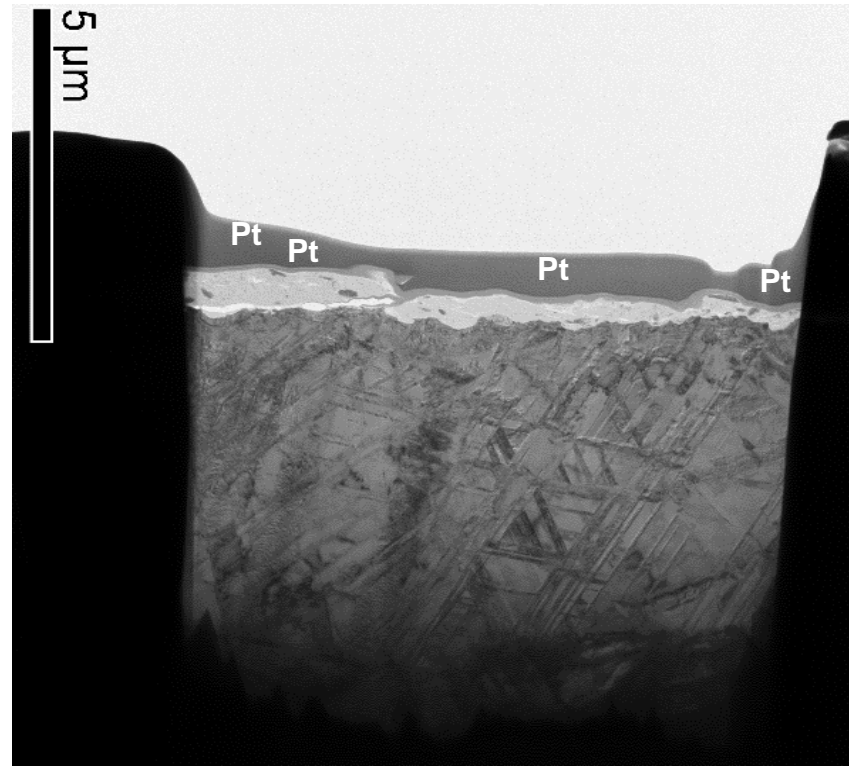
## 7.7 Characterisation of metallurgical transformations (ceramic – metal)

This section employs TEM, SAED and TEM-EDS to characterise the subsurface tribocorrosion and metallurgical transformations of CoCrMo and Ti6Al4V alloys which were fretted against Si<sub>3</sub>N<sub>4</sub> at ±50 µm displacement. The fretting regimes realised at the metal – metal and ceramic – metal interfaces at ±10 µm and ±25 µm fretting displacements were found to be similar although occurring at a higher dissipated energy for the ceramic – metal fretting contacts. For this reason, subsurface analyses of the metal were not conducted at those fretting displacements as they can be expected to be similar to those reported in section 6.7.1. TEM samples in this section were selected mainly from the visual observation of the region of interests using BS-SEM micrographs. The Si and O-rich third-body region was selected from the CoCrMo surface of the Si<sub>3</sub>N<sub>4</sub>–CoCrMo material combination. However for the Ti6Al4V sample, two subsurface samples were obtained: the first was obtained on the region covered with the ‘mechanically mixed layer’ and the second was obtained from the that was not covered with a layer. Both samples were obtained from the same Ti6Al4V surface. As shown in the 3D topography in Figure 7-13a the Ti6Al4V surface has three levels, the top of the mechanically mixed layer, the Ti6Al4V surface and the crack within the Ti6Al4V. Only the first two levels were assessed in study.

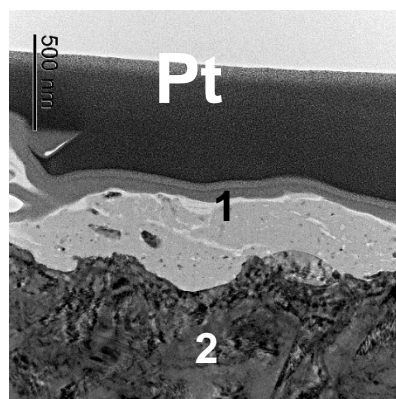
The micrographs in Figure 7-22 shows the subsurface cross-sectional view of the CoCrMo flat component from the Si<sub>3</sub>N<sub>4</sub> – CoCrMo material combination. Figure 7-22a shows the Si and O-rich third-body material on the bulk CoCrMo alloy which has a thickness of ~500 nm in the thickest region. Suspending within the third-body material are fragments of CoCrMo particles as later confirmed with EDS in the following section. The size of the particles range from 10s of nm to as large as ~130 x 250 nm. Figure 7-22b shows a high resolution view of the uppermost region. Figure 7-22a also reveals ~7 µm depth of twinned CoCrMo bulk alloy beneath the Si and O-rich film.

Further analysis of the Si and O-rich product using SAED confirmed the presence of nano-crystalline structures as shown in Figure 7-22c. TEM

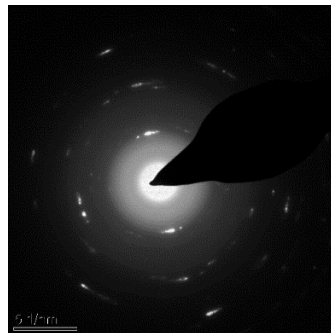
micrograph also indicate that the Si and O-rich material has an amorphous structure although not fully verified. Directly beneath the nano-crystalline region, the SAED structure in Figure 7-22d shows a single crystal structure.



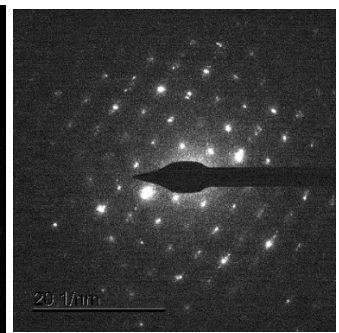
(a)



(b)



(c)



(d)

**Figure 7-22 – TEM and SAED of CoCrMo from the Si<sub>3</sub>N<sub>4</sub> – CoCrMo combination: a) TEM micrograph of CoCrMo subsurface b) high resolution image of the uppermost subsurface c) SAED of Si and O-rich material d) SAED of CoCrMo single-crystal.**

TEM-EDS map of the CoCrMo flat component in Figure 7-23 shows evidence of particles suspending in the Si and O-rich structure which appear to be concentrated in Co and Cr thus confirming the presence of CoCrMo particulates in the layer. The purpose of the white-line drawn is to create a demarcation between the Pt deposits and the Si and O-rich layer. N is also evident in the film as identified also through XPS, although the specie identified was the organic-N specie.

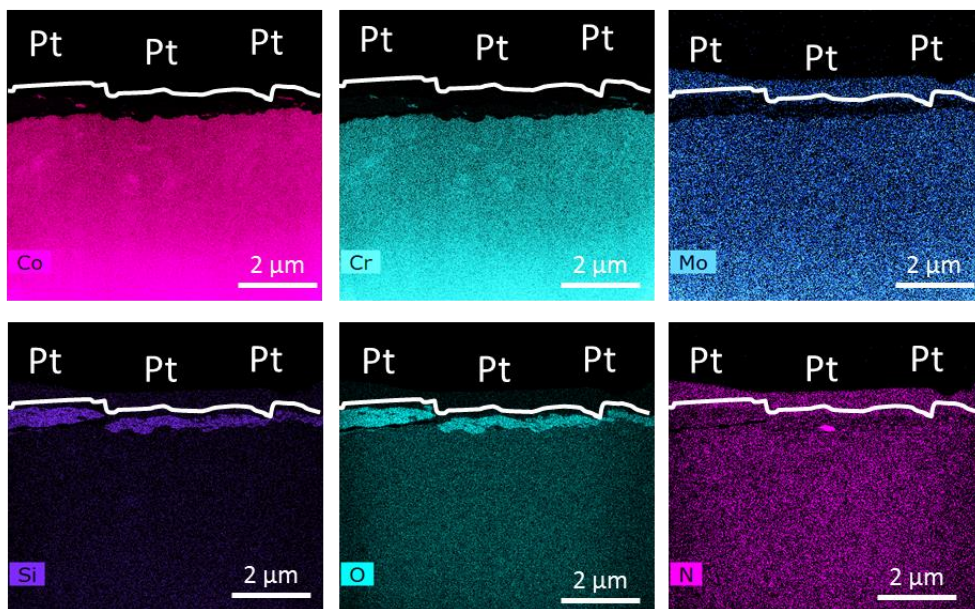
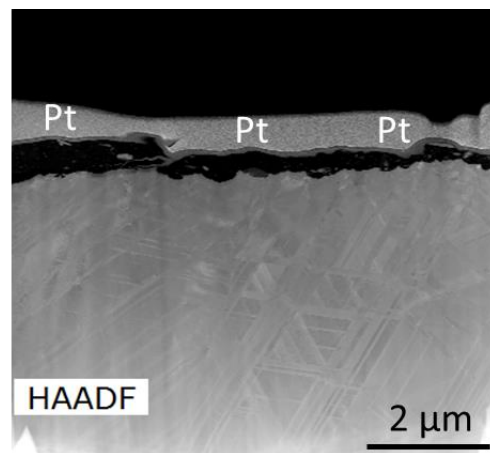


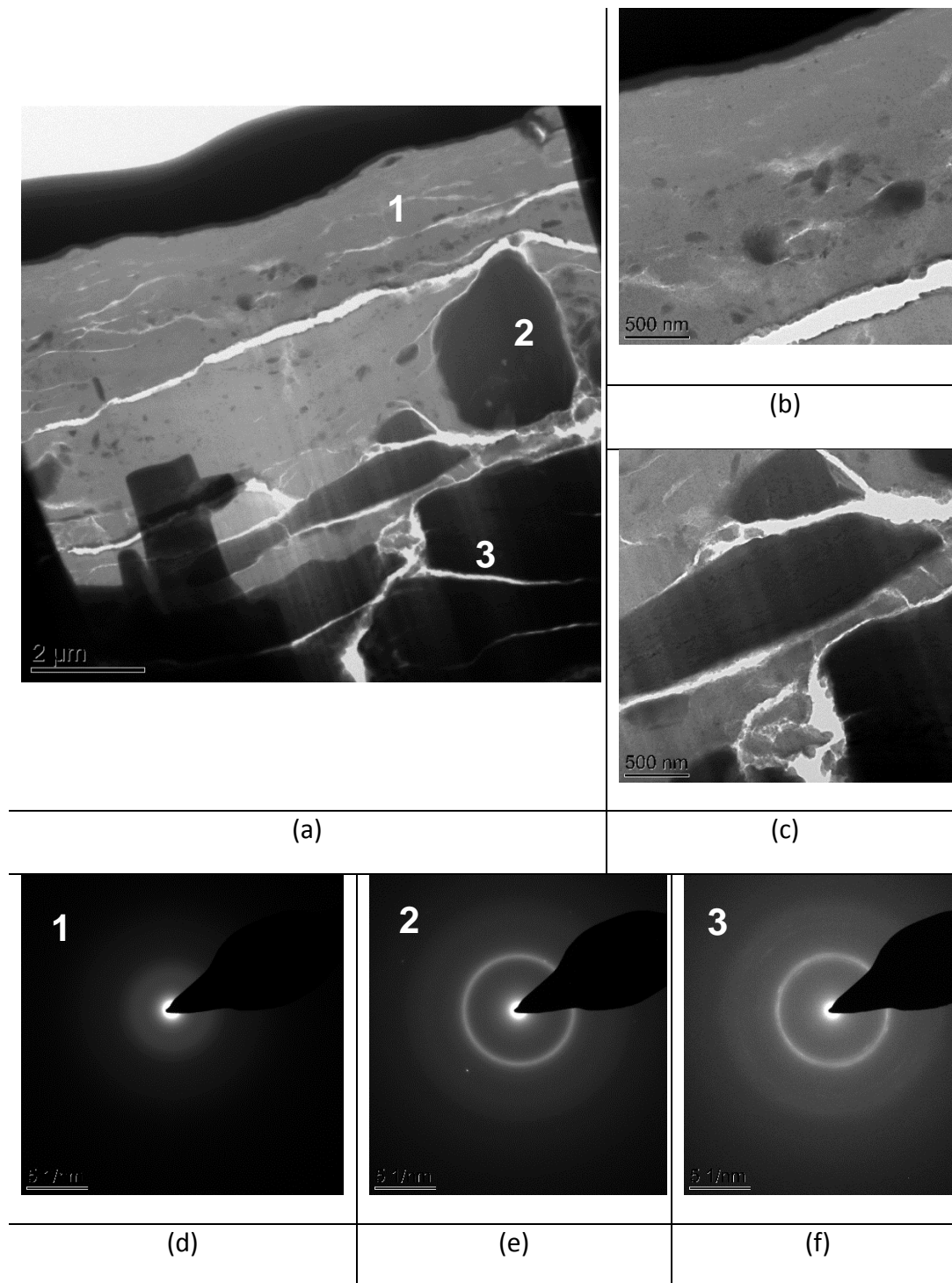
**Figure 7-23 – TEM-EDS map of the CoCrMo subsurface from the Si<sub>3</sub>N<sub>4</sub> – CoCrMo material combination. Above the white-line are deposited Pt and empty space.**



TEM cross-section of the Ti6Al4V alloy from the Si<sub>3</sub>N<sub>4</sub> – Ti6Al4V material combination is shown in Figure 7-24, this figure represents the region covered by the ‘mechanically mixed layer’ denoted region ‘C’ in Figure 7-16. Three regions of interest are identified in the first micrograph in Figure 7-24a. The first, denoted structure ‘1’ represents the ‘mechanically mixed layer’ that exists with heights over 2 μm above the plain Ti6Al4V surface (see Figure 7-13, Ti6Al4V at ±50 μm). The material visually appears highly densified and non-crystalline with some horizontal cracks across it. In addition, nanoscale particles are suspending within the structure.

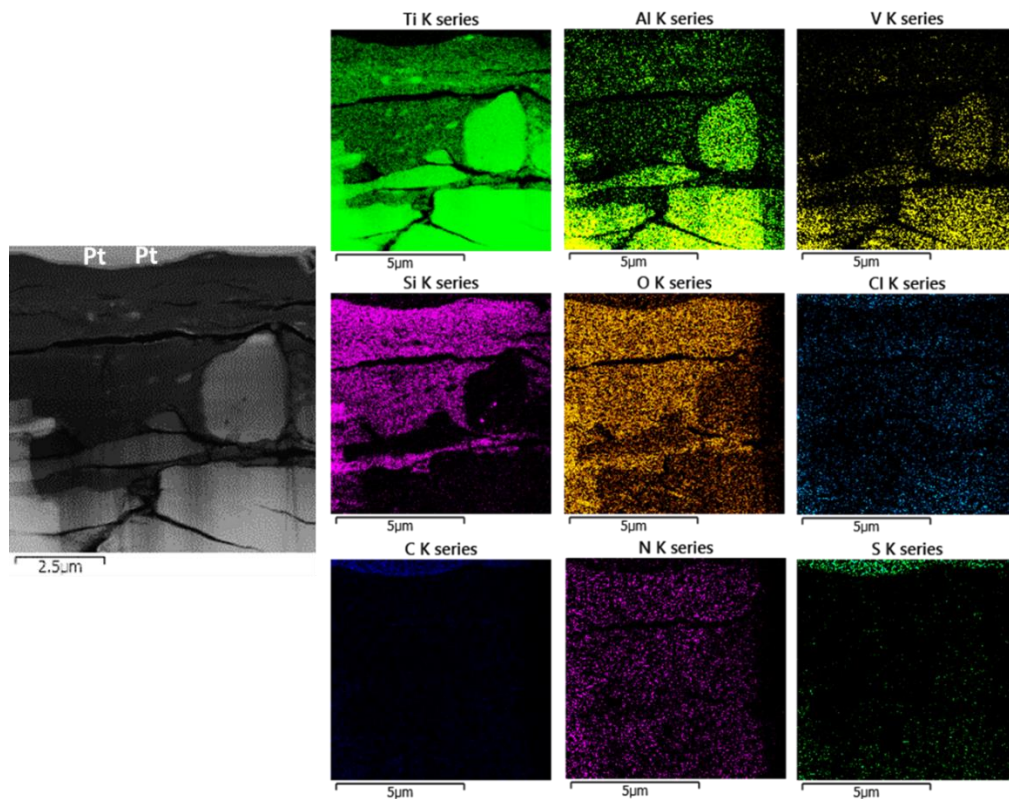
The second, denoted structure ‘2’ is separated by a clear demarcation which indicates that the ‘mechanically mixed layer’ moves relative to the plain surface thus explaining why elements from the physiological solution were present across the surface where the mechanically mixed layer had ‘flaked off’ from in Figure 7-18. It also confirms the evidence of plastic flow and directionality observed in Figure 7-13. Figure 7-24b shows a higher magnification view of the ‘mechanically mixed layer’. In structure 2, a large particle-like material of dimension ~2.5 x 3.0 μm suspending in the non-crystalline, ‘mechanically mixed material’ of similar appearance to that of structure 1 is shown. Further down in the subsurface cross-section, the third, denoted structure ‘3’ is a much larger Ti6Al4V bulk. It can be seen that the structure had suffered fracture into smaller segments due to further ingress of the non-crystalline ‘mechanically mixed layers’ i.e. structures 1 and 2. This is depicted clearer in Figure 7-24c. The fracture is seen to have propagated deeper into the alloy beyond the scope of the TEM micrograph.

SAED analyses were conducted on the three areas and are shown in Figure 7-24d – f consecutively. Quite interestingly, SAED reveals that all three structures are amorphous in structure. This suggests that Ti6Al4V underwent a full transformation to an amorphous structure at this interface as similarly observed with Ti6Al4V at the CoCrMo – Ti6Al4V interface. However, as it is evident that the energy experienced at the ceramic – metal interface is larger than the metal – metal interface, what appears like a brittle fracture of amorphous Ti6Al4V structure is observed under the ceramic – metal condition.



**Figure 7-24 – TEM and SAED of Ti6Al4V from the Si<sub>3</sub>N<sub>4</sub>– Ti6Al4V combination (region of mechanically mixed layer): a) TEM micrograph of the Ti6Al4V subsurface b) high resolution image of the mechanically mixed layer c) high resolution image of the transformed amorphous Ti6Al4V structure d) SAED of the mechanically mixed layer e) SAED of the suspending large particle f) SAED of fractured region.**

The TEM-EDS of the same cross-section shown in Figure 7-25. The observation complements the species observed using XPS. The ‘mechanically mixed layer’ was identified as Ti and Al silicates by the XPS and the map in this figure shows the layer to be mainly Ti, Al, Si and O-rich. It is also evident that the layer migrated deeper beyond the uppermost surface. Si is identifiable in the large particle-like material denoted structure ‘2’ from Figure 7-24a thus further confirming that the particle is no longer a crystalline Ti6Al4V bulk material. Rather, it has undergone a complete transformation from crystalline to nano-crystalline and finally to an amorphous structure. N is equally dispersed across the structure hence it is arguably absent within the structure although XPS identified organic-N species at the uppermost surface. Cl seems to be faintly present specifically in the region where the amorphous Ti6Al4V particle-like materials are. This highlights the possible role of the physiological solution in the full transformation of crystalline bulk Ti6Al4V to an amorphous structure. One cannot confidently say C and S are present in any specific region.

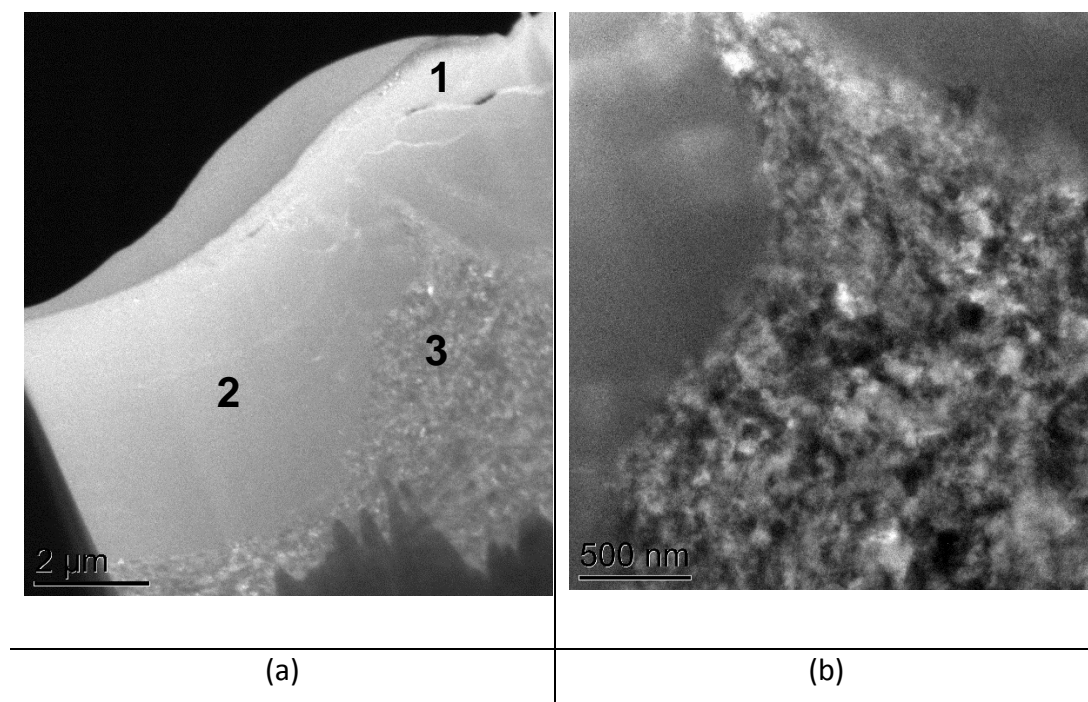


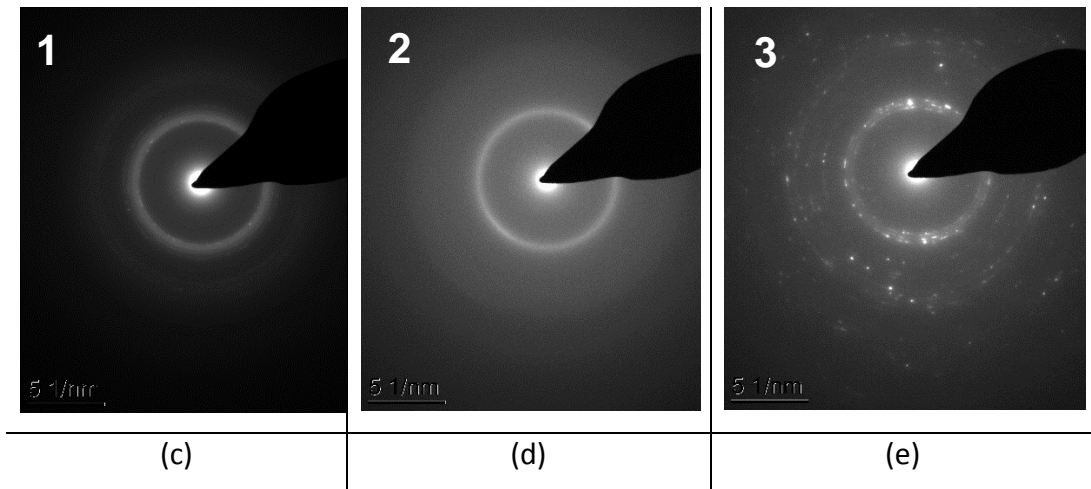
**Figure 7-25 – TEM-EDS map of the Ti6Al4V subsurface from the Si<sub>3</sub>N<sub>4</sub> – Ti6Al4V material combination – region of mechanically mixed layer.**

Figure 7-26 shows the TEM and SAED analysis of the region on Ti6Al4V surface where 'mechanically mixed layers' were not formed. These regions are generally located in-between 'mechanically mixed layers'. Figure 7-26a shows a totally transformed structure and the micrograph also depicts what appears to be subsurface rolling of nano-crystalline Ti6Al4V structures. A significant 'bust' of energy most likely inflicted during the stiction mechanism is attributed to be the cause of such a transformation.

There are three main regions of interest: In structure '1', horizontal cracks run across the uppermost region. Structure '2' appears to be a densely packed amorphous structure of over 4  $\mu\text{m}$  in depth. Structure '3' is a region of densely packed nano-crystalline structures with evidence of directionality. A high resolution image in Figure 7-26b reveals the process through which crystalline structures reach its smallest size in nano-meters closest to the top surface before it gets 'swamped into the sea' of amorphous Ti6Al4V structures.

SAED analyses of the three main area reveal an amorphous structures for structures 1 and 2 as expected and a nano-crystalline structure in structure 3 as expected.





**Figure 7-26 – TEM and SAED of Ti6Al4V from the Si<sub>3</sub>N<sub>4</sub> – Ti6Al4V combination (region absent of mechanically mixed layer): a) TEM micrograph of CoCrMo subsurface b) high resolution image of the nano-crystalline region c) SAED of the uppermost region d) SAED of the totally transformed region e) SAED of nano-crystalline area.**

The TEM-EDS cross-section of Ti6Al4V on which no ‘mechanically mixed layers’ are formed is shown in Figure 7-27. It is observable that Ti and Al are less abundant in the amorphous Ti6Al4V region as compared to the nano-crystalline region. On the other hand, O and Cl can be seen to be more abundant in the amorphous region compared to the nano-crystalline region. V is seen to be equally distributed across both amorphous and nano-crystalline structures however, some V-rich region is seen within the nano-crystalline structure thus indicating the  $\beta$ -phase structure within the nano-crystalline Ti6Al4V alloy. Si, C and S seem to be present as background signal – this is generally attribute to all elements. N may be present in the structure although, only in trace amounts that is generally present in bulk Ti6Al4V alloy.

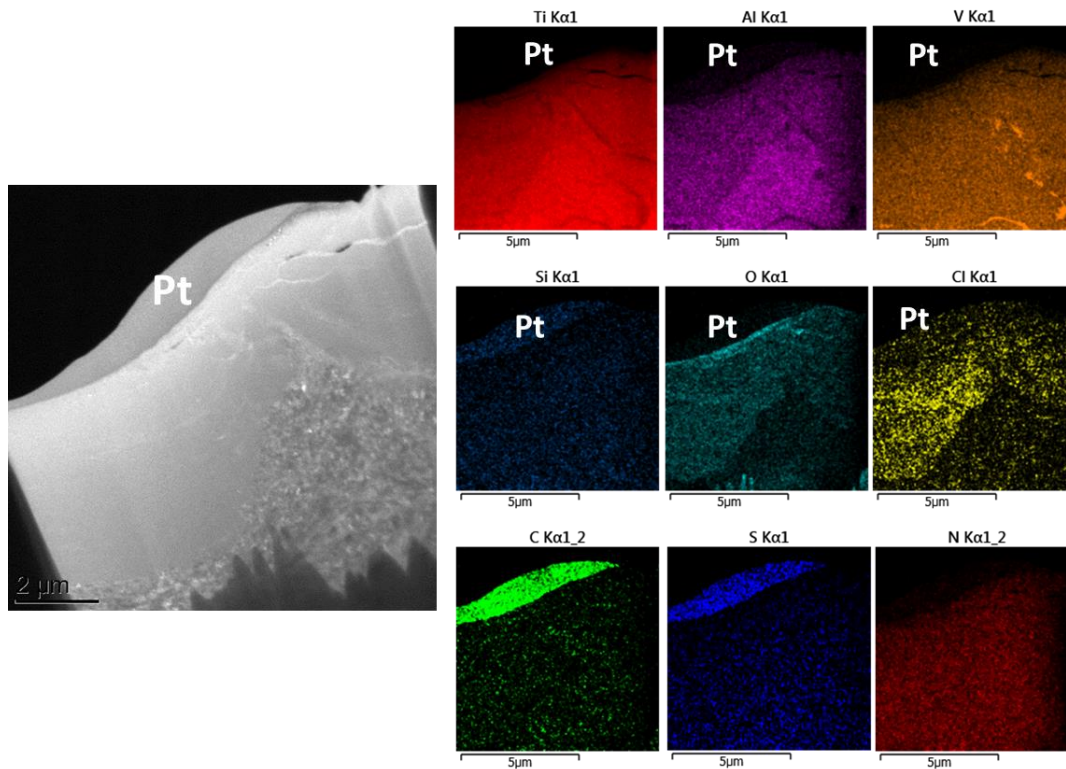


**Figure 7-27 – TEM-EDS map of the Ti6Al4V subsurface from the Si<sub>3</sub>N<sub>4</sub> – Ti6Al4V material combination – region absent of mechanically mixed layer.**

## 7.8 Nano-indentation

Nano-indentation hardness of the Si and O-rich ‘mechanically mixed layer’ was performed following the same procedure outlined in section 4.5.9. Figure 7-28a shows the raw P vs. h data and in Figure 7-28b, the average hardness of the layer is 22.7 GPa. The hardness measured here is a little less than the hardness measured at the CoCrMo – Ti6Al4V interface. Nevertheless, the hardness of the layer is almost double the general bulk hardness of bulk Si<sub>3</sub>N<sub>4</sub> (~13GPa) and about five-times the hardness of Ti6Al4V alloy.

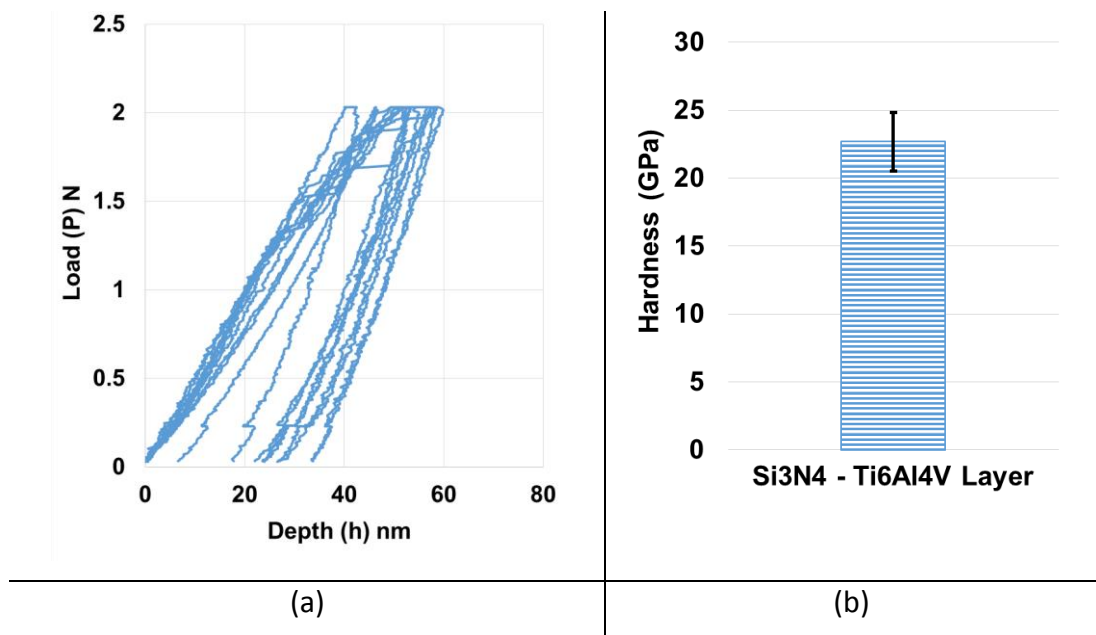


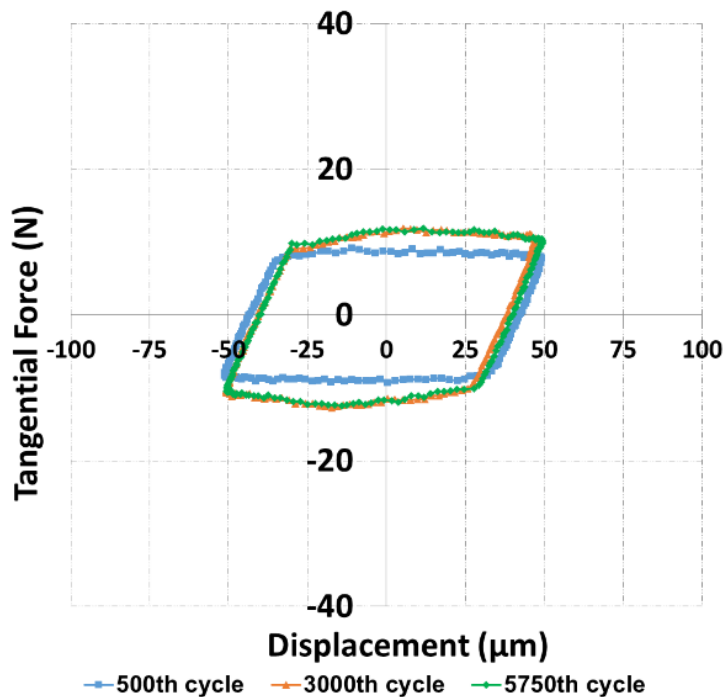
**Figure 7-28 – Nano-indentation of layer formed at the  $\text{Si}_3\text{N}_4$ -  $\text{Ti6Al4V}$  interface: a) P vs. h graph of indentations b) average hardness of the layer.**

## 7.9 Fretting of Biolox Ceramic on CoCrMo and Ti6Al4V alloy

In this section, Biolox was assessed against CoCrMo and Ti6Al4V alloys under the same parameters and conditions as with all other material combinations. However, as it was not the main focus of this study, only the  $\pm 50 \mu\text{m}$  displacement was assessed with a sample size of  $n=1$ . The aim of assessing the ceramic – metal combinations only at this displacement was to observe the third-body interactions that would occur at the Biolox – metal interface during a gross slip regime. It was observed that a gross-slip regime for Biolox – Ti6Al4V was not achievable at the initial contact pressure of 1 GPa, therefore, a second Biolox – Ti6Al4V test was conducted at a lighter load with initial contact pressures of 0.77 GPa. The three tests were complemented with OCP measurement, 3D and 2D surface profilometry and SEM-EDS surface analysis.

### 7.9.1 Fretting wear mechanism of Biolox – CoCrMo

In Figure 7-29a, the fretting loop shows a gross slip fretting regime established at the Biolox – CoCrMo contact. The figure shows three super-imposed fretting loops: one in the early stage of the fretting cycles (500<sup>th</sup>) then another in the middle (3000<sup>th</sup>) and the fretting loop towards the end of the fretting cycle (5750<sup>th</sup>). It can be seen that the tangential force increased from the middle of the fretting cycles through to the end. The slight increase in the tangential force was reflected in the energy dissipated curve of Figure 7-29b. The OCP in Figure 7-29c shows a cathodic shift at the initiation of fretting and the cathodic shift continued gradually during fretting as did CoCrMo – CoCrMo and Si<sub>3</sub>N<sub>4</sub> – CoCrMo at  $\pm 50 \mu\text{m}$  displacement. However after  $\sim 3000$  cycles, a sharp rise in potential was observed during ongoing fretting at the contact. At the end of fretting, a sharp repassivation stage was observed followed by a slower ennoblement stage.



(a)



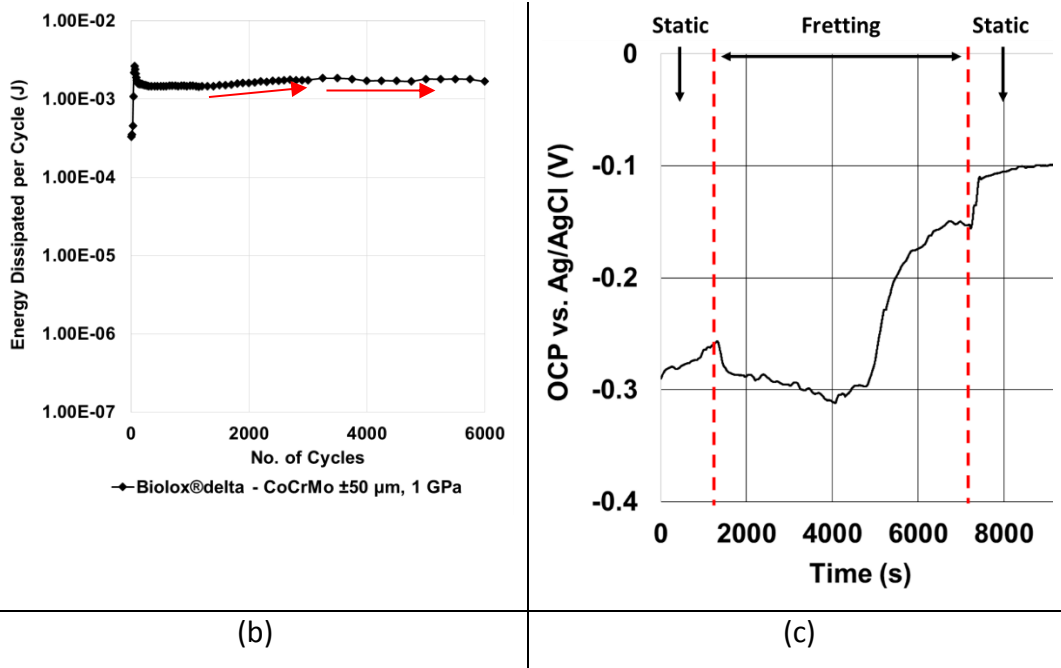


**Figure 7-29 – Fretting of BioloX – CoCrMo material combination at  $\pm 50$   $\mu\text{m}$ ,  $P_{\text{max}} = 1$  GPa: a) 2D fretting loop b) Energy dissipated per cycle c) OCP measurement.**

The 3D and 2D surface profilometry for both ball and flat components are shown in Figure 7-30. No evidence of wear was observed on the BioloX surface, rather, third-body products are observed of heights reaching up to 3  $\mu\text{m}$ . The CoCrMo flat on the other hand has a wear scar with wear depths reaching up to 4  $\mu\text{m}$ . This is more than double the wear depths measured at any of the CoCrMo – CoCrMo/Si<sub>3</sub>N<sub>4</sub> – CoCrMo material combinations. This indicates that the mechanism involved at the BioloX – CoCrMo interface is more degradative than other materials coupled with CoCrCo. Evidence of redistributed third-body products within the CoCrMo wear scar is seen. It is worth noting that the region outside the wear surface of the flat component is a visual effect which depicts material gained outside of the wear surface as though they were material loss.

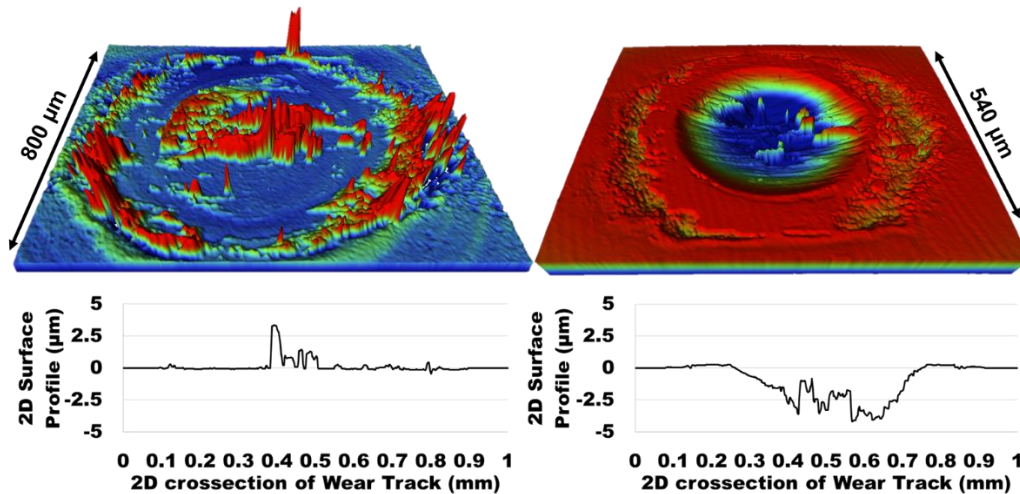
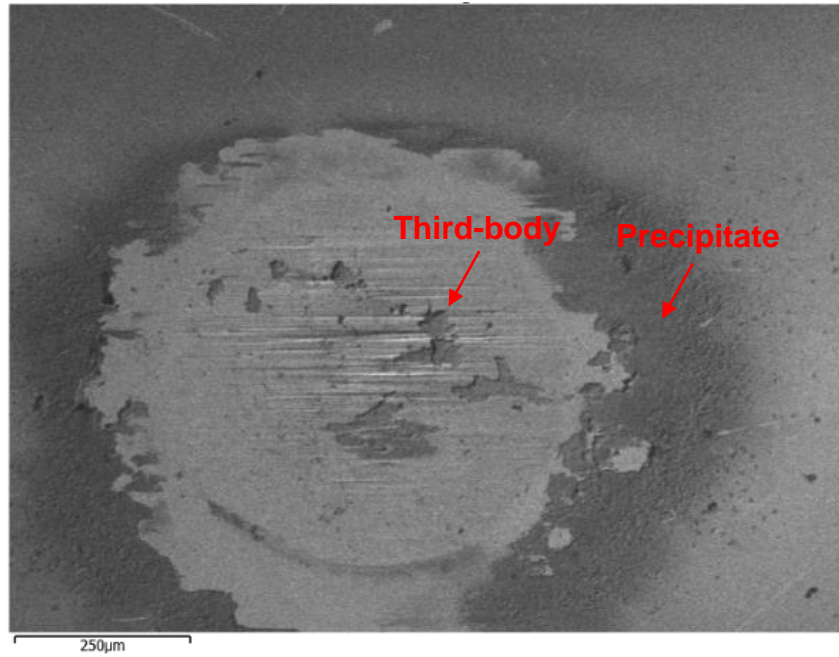


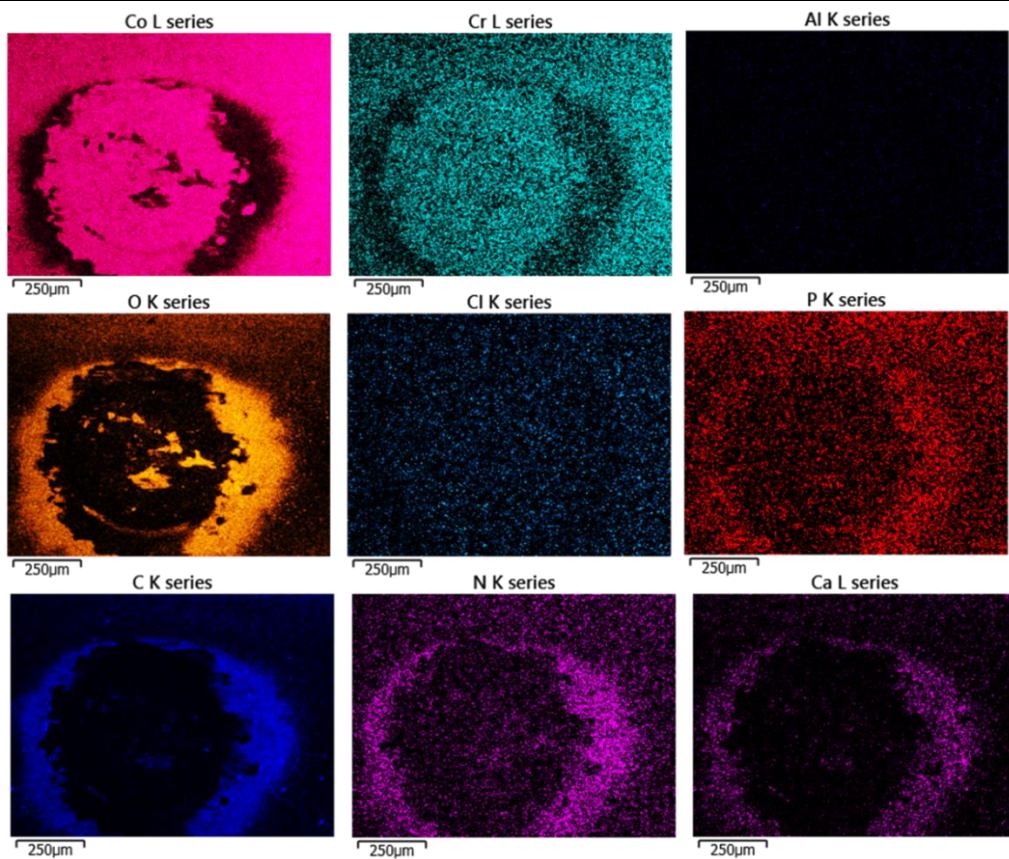
**Figure 7-30 – 3D and 2D surface profilometry of BioloX – CoCrMo at  $\pm 50$   $\mu\text{m}$  displacement.**

BS-SEM micrographs of CoCrMo flat surface in Figure 7-31a depicts a wear surface that takes on the smoothness of the ultra-smooth BioloX counter-body. However, a few wear track marks at the centre of the wear surface is still visible. In the centre of the wear scar also lies third-body products and outside the wear scar are precipitates as indicated in the figure.

SEM-EDS in Figure 7-31b confirms the chemical composition of the third-body products within the wear surface to be mainly of Cr and O as well as C although appearing very faintly. The precipitate outside the wear surface on the other hand is seen to be rich in O, Ca, P, N and C but lacking any of the metallic elements. Therefore, the precipitation outside the wear surface may be electrochemically linked with the oxidation reactions occurring within the fretting contact during on-going fretting. The absence of Al is further evidence that the BioloX ball did not experience wear at this interface.



(a)



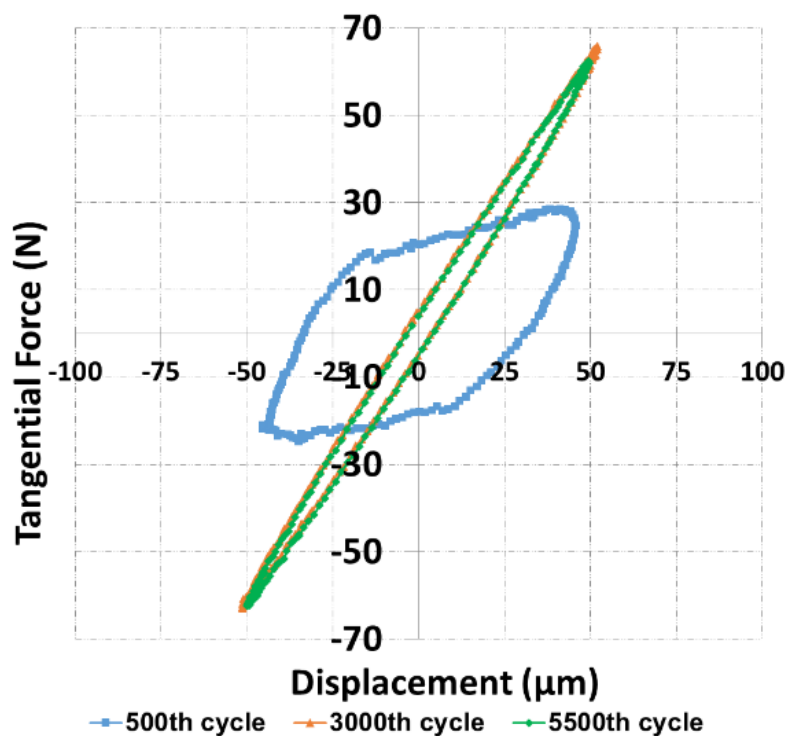
(b)

Figure 7-31 – SEM-EDS map of Biolox – CoCrMo flat surface at  $\pm 50 \mu\text{m}$   
a) BS-SEM micrograph b) SEM – EDS

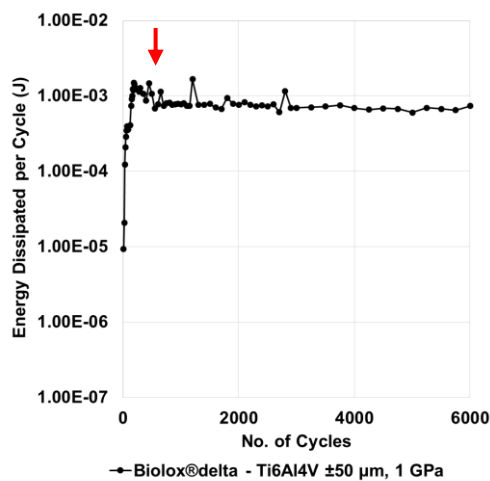
### 7.9.2 Fretting wear mechanism of Biolox – Ti6Al4V (mixed regime)

The Biolox – Ti6Al4V material combination assessed at 1 GPa is shown in Figure 7-32. The fretting loop in Figure 7-32a shows a gross slip behaviour in the initial stages (500<sup>th</sup> cycle) of the fretting cycles. In addition, it is observable that the interfacial slip during this stage was  $\sim 30 \mu\text{m}$  at a relatively low tangential force of  $\sim 20 \text{ N}$ . However by the 3000<sup>th</sup> cycle, the fretting regime had transitioned to quasi-static fretting loop describing a partial-slip behaviour. The point of transition is identified with the red arrow in Figure 7-32b.

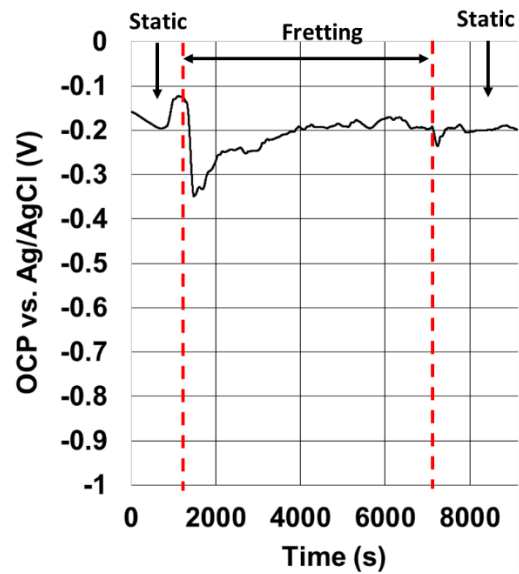
The transition also corresponds to a drop in the energy and surface slip but a significant increase in tangential force reaching up to  $\sim 65 \text{ N}$ . As fretting at the interface began with a gross slip regime, electrochemical response was that of a cathodic shift of  $\sim 200 \text{ mV}$  as expected. In Figure 7-32c the potential is seen to rise gradually to a plateau. Interestingly, as soon as fretting ceased, there was no repassivation stages observed thus indicating that repassivation at the interface may be hindered.



(a)



(b)



(c)

**Figure 7-32 – Fretting of BioloX – Ti6Al4V material combination at  $\pm 50 \mu\text{m}$  ( $P_{\text{max}} = 1 \text{ GPa}$ ): a) 2D fretting loop b) Energy dissipated per cycle c) OCP measurement.**

The 3D and 2D surface profilometry of both ball and flat components show no evidence of wear on the BioloX ceramic. However, its surface is seen to be covered in third – body material as also observed against CoCrMo. These can be seen to reach heights of up to  $\sim 3 \mu\text{m}$ . On the other hand, the Ti6Al4V flat component is seen with third – body products agglomerated on one side of the wear surface with heights reaching up to  $\sim 1 \mu\text{m}$ . Cracks with depths of up to  $\sim 4 \mu\text{m}$  were observable on the Ti6Al4V surface also, particularly in the region where the third – body material agglomerated. This suggests that the heap of third – body material on the BioloX surface, located at the centre is a material pulled out from within the Ti6Al4V considering the surface profilometry indicates a shared interface in both. This is suggestive of a localised corrosion phenomena.

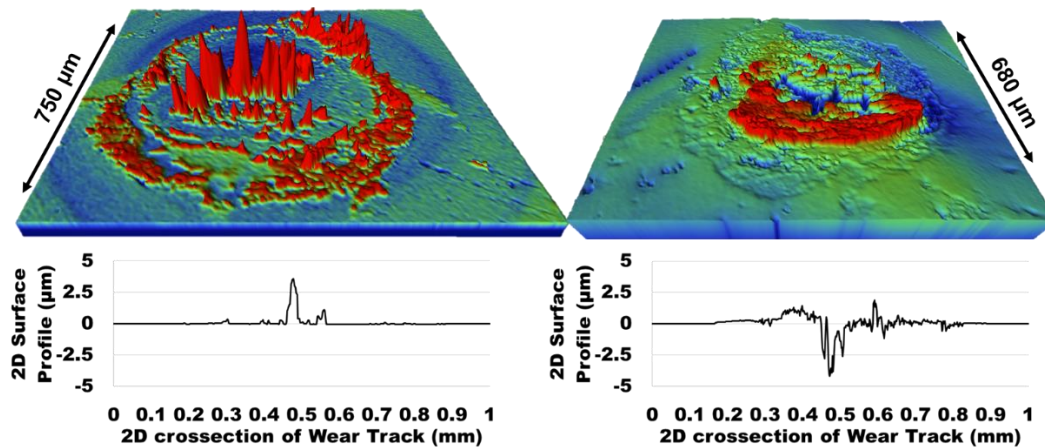
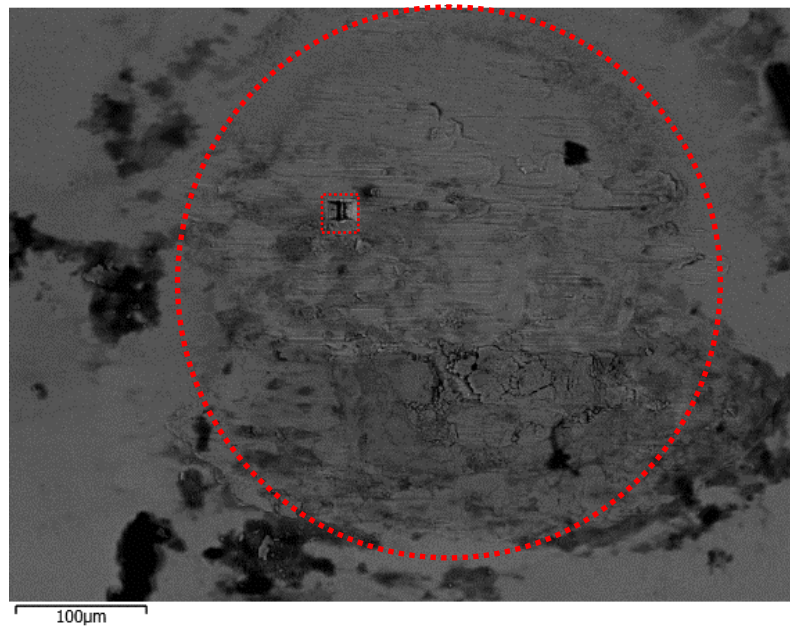


**Figure 7-33 – 3D and 2D surface profilometry of BioloX – Ti6Al4V at  $\pm 50$   $\mu\text{m}$  displacement ( $P_{\text{max}} = 1$  GPa).**

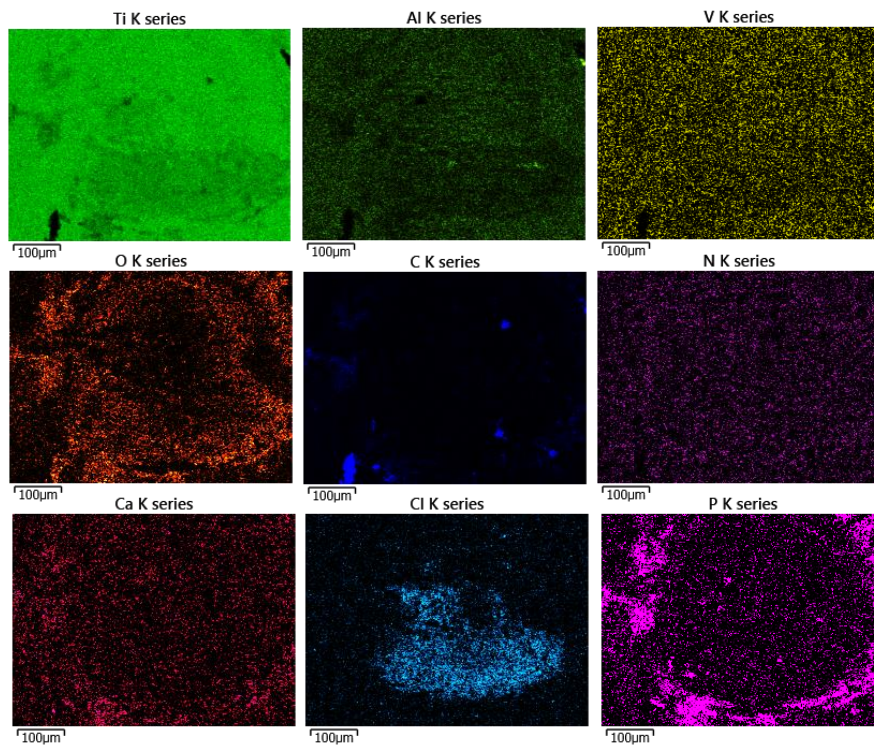
The BS-SEM micrograph of the Ti6Al4V surface is shown in Figure 7-34a. The fretting surface is contained within the red-dotted circle. Outside the dotted red circles are darker appearing material deposits (precipitates) agglomerated around the wear surface. However, within the wear surface are found a region with evidence of galling while in a different region a similar shade of grey with the Ti6Al4V background is observed; 3D surface analysis identified this region as the area with agglomerated third-body product. The region within the red-dotted square indicates the area where TEM sample was obtained using the FIB (the data from this analysis is not presented).

The SEM-EDS maps in Figure 7-34b offers insight into the complexities of this particular mixed fretting contact. Ti, Al and V are observed abundantly across the entire surface as expected for a Ti6Al4V bulk. O appears to present across the wear surface except for the region where evidence of galling in the Ti6Al4V wear surface was identified. C is seen to be highly concentrated in the region outside wear surface. N is seen as background signal thus its presence cannot be verified using EDS. Ca is seen to form outside the wear surface as similarly observed for the BioloX – CoCrMo interface. P is seen in the same region as Ca however it appears with a higher intensity. Cl on the other hand is seen to be highly concentrated within the wear scar, and specifically located within in the region filled with third – body products. Ti is seen to be present across both regions rich in Cl and P while the Al and V were less represented in that

region. This strongly suggests that the tribocorrosion products generated at the Ti6Al4V mixed regime fretting contact can be identified as two main products: the third – body product trapped in the fretting contact is mixed Ti-oxide and Ti-chloride where Ti-chloride is the more dominantly present specie. Outside of the wear surface, compounds of Ca-phosphate or ionic species of Ca and P are precipitated.



(a)



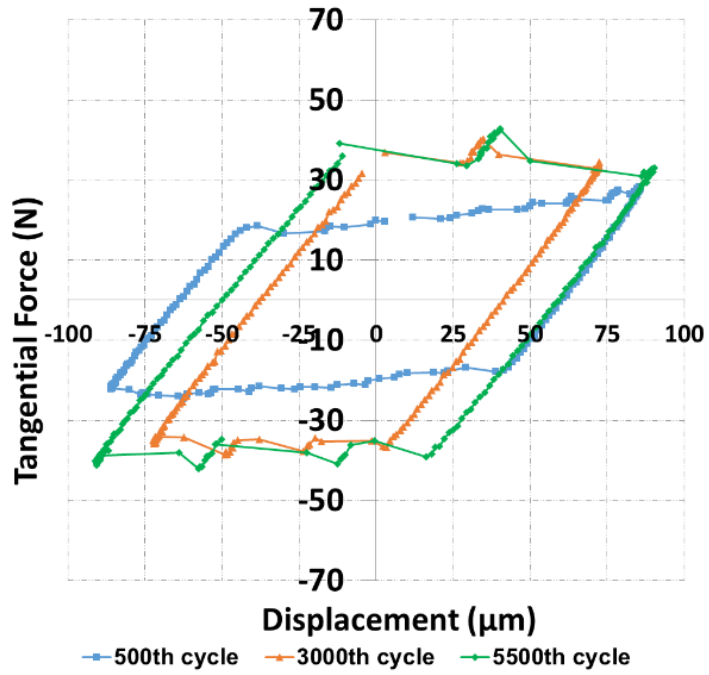
(b)

**Figure 7-34 – SEM-EDS map of BioloX – Ti6Al4V flat surface at  $\pm 50 \mu\text{m}$  (1 GPa) a) BS-SEM micrograph b) SEM – EDS**

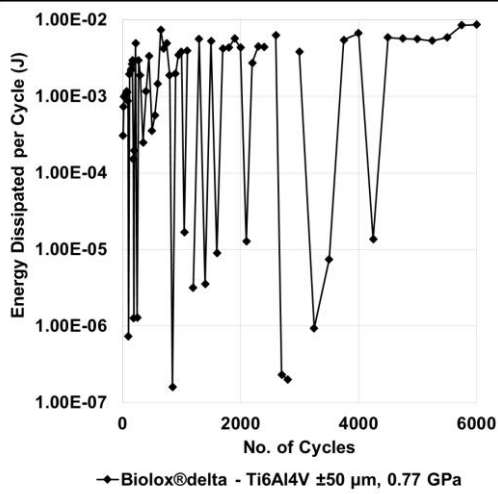
### **7.9.3 Fretting wear mechanism of BioloX – Ti6Al4V (gross slip regime)**

In Figure 7-35a, the fretting loop captured a rather unstable fretting contact; one similar to the observations made at the  $\text{Si}_3\text{N}_4$  - Ti6Al4V contact at  $\pm 50 \mu\text{m}$  displacement. This contact also experienced an overshoot gross slip displacement of  $\delta_x = 85 \mu\text{m}$ . The energy dissipated per cycle in Figure 7-35b describes the instability of the fretting contact; a stiction-like mechanism is also observed at this interface. Stability at the contact was established at 4500<sup>th</sup> cycle till fretting ceased. Figure 7-35c shows how the initial large gross slip at the interface led to a sharp cathodic shift of  $\sim 550 \text{ mV}$  and a maximum cathodic shift of  $630 \text{ mV}$ . At the end of fretting displacements, a single sharp repassivation process occurred. Quite importantly, it was noticeable that the OCP was fully recovered unlike in other cases of mixed/gross slip fretting regimes of CoCrMo – Ti6Al4V and  $\text{Si}_3\text{N}_4$  - Ti6Al4V.

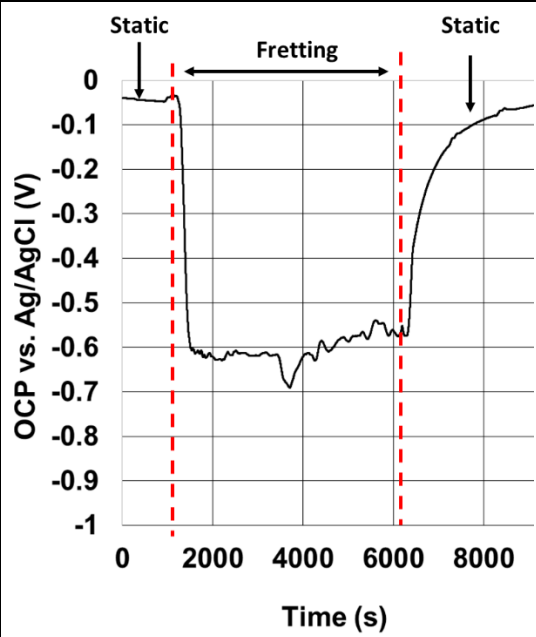




(a)



(b)



(c)

**Figure 7-35 – Fretting of BioloX – Ti6Al4V material combination at  $\pm 50$   $\mu\text{m}$  (0.77 GPa): a) 2D fretting loop b) Energy dissipated per cycle c) OCP measurement.**

Figure 7-36 shows the 3D and 2D analysis of the wear surface. No evidence of wear was observed at the surface of the BioloX, rather, a large heap of third – body material with heights up to  $\sim 4 \mu\text{m}$  was seen at the edge of the fretting contact. The fretting surface of the Ti6Al4V is firstly seen to be elevated above the plain Ti6Al4V surface. Secondly, the wear surface appear to have wear tracks at its edges while the centre of the wear surface appear smooth and at lower depths than its surroundings. The 2D wear depth profile reveals a large crack within the surface of depth  $\sim 7 \mu\text{m}$ . The depth is located where the larger material deposit on the BioloX is also located thereby suggesting that the heap of material was removed directly from the Ti6Al4V bulk subsurface thus it isn't a material transfer.

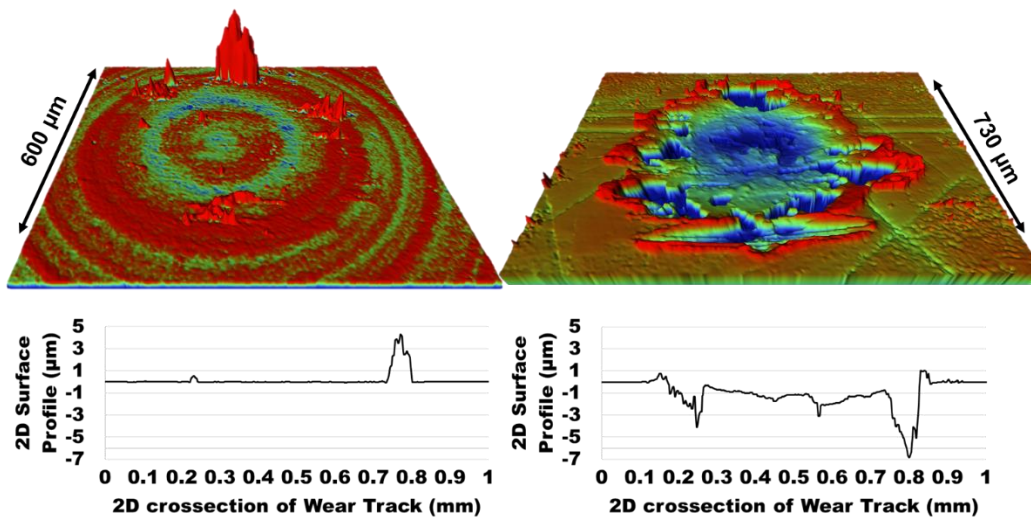
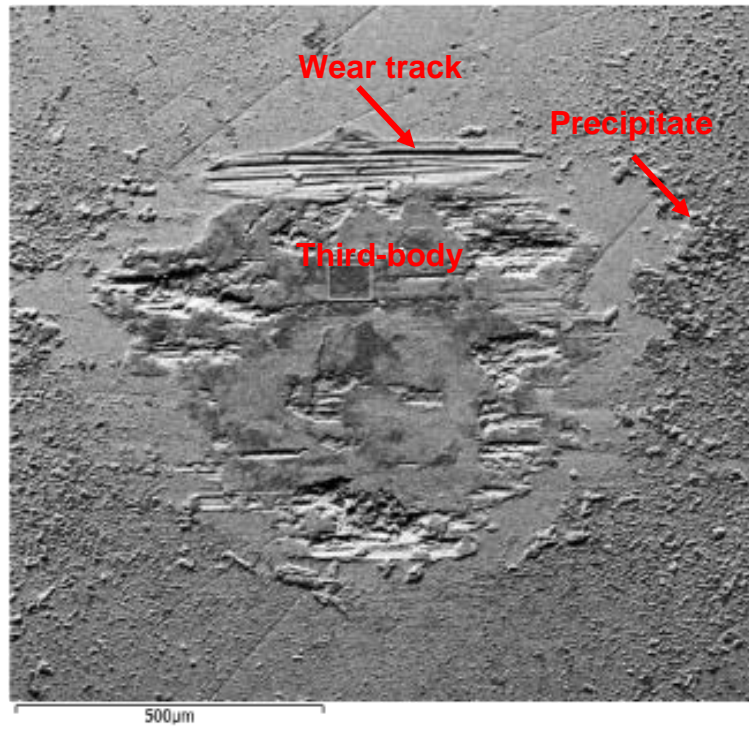


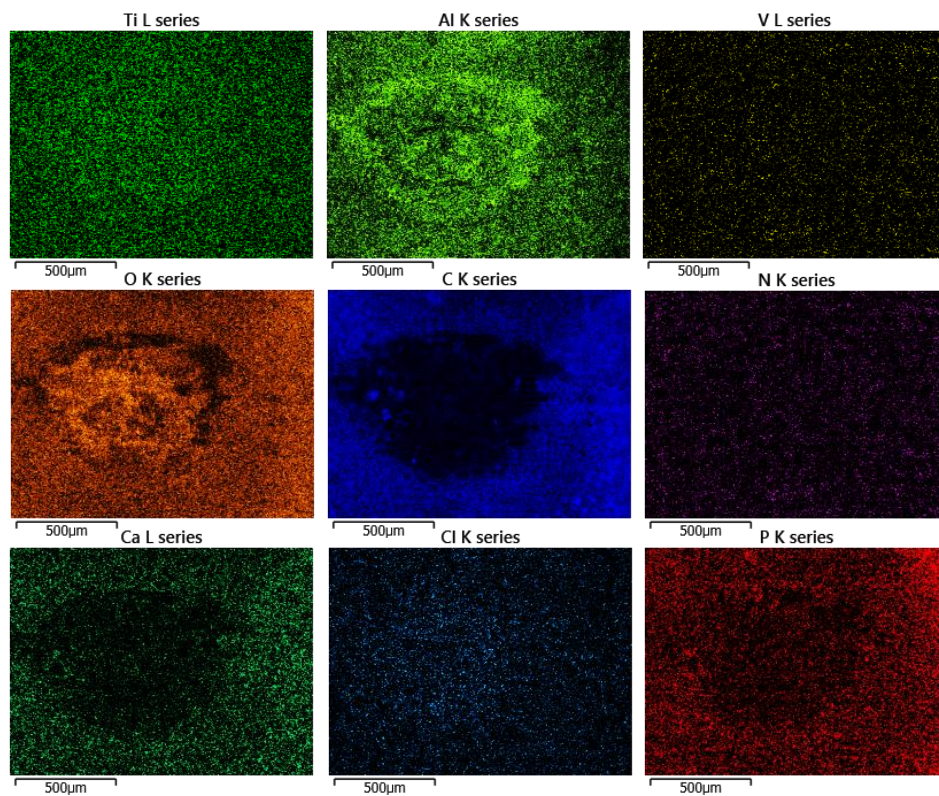
**Figure 7-36 – 3D and 2D surface profilometry of BioloX – Ti6Al4V at  $\pm 50 \mu\text{m}$  displacement ( $P_{\text{max}} = 0.77 \text{ GPa}$ ).**

BS-SEM micrograph of Figure 7-37a shows the wear surface of this gross slip contact. Evidence of wear track is identifiable beneath the smooth third – body material that lies at the centre of the wear surface. The smoothness of the surface confirms that the BioloX counterpart had not experienced wear at this interface. The SEM-EDS of Figure 7-37b shows that Ti is almost equally abundant across the entire wear surface while Al appears to be more concentrated within the wear track which appears to be devoid of O. This suggests that Al is less concentrated in the third-body product. V appears only to be faintly present across the entire surface. O appears to be more

concentrated in the third – body material as expected. C, Ca and P appears to be absent from the wear surface but are precipitated outside the wear surface. Cl appear more concentrated within the third – body region and the presence of N cannot be verified using the EDS map.



(a)



(b)

**Figure 7-37 – SEM-EDS map of BioloX – Ti6Al4V flat surface at  $\pm 50 \mu\text{m}$  (0.77 GPa) a) BS-SEM micrograph b) SEM – EDS**

## 7.10 Discussion and summary

In this chapter, ceramic – metal and ceramic – ceramic material combinations were assessed under varied displacement amplitudes. The two ceramic materials assessed against CoCrMo and Ti6Al4V were  $\text{Si}_3\text{N}_4$  and BioloX. These offered two different perspectives of fretting corrosion mechanisms that can be expected at the ceramic – metal interface of modular taper junction in hip implants. The  $\text{Si}_3\text{N}_4$  ceramic represents the mechanisms involved at the fretting interface whereby the ceramic material is engaged both in wear and oxidation processes. On the other hand, the BioloX ceramic represents the mechanisms involved at the fretting interface whereby the ceramic material is inert both chemically and mechanically. In both cases, an extensive surface and subsurface analysis of the ceramic – metal interfaces were carried out.

Amongst the material combinations assessed in this chapter, the least compliant contact was the self-mated  $\text{Si}_3\text{N}_4$  material combination meaning that there is less elastic contact compliance to overcome before slip is initiated at the interface. However, interestingly, self-mated  $\text{Si}_3\text{N}_4$  was in a stick fretting regime at  $\pm 10 \mu\text{m}$  displacement whilst  $\text{Si}_3\text{N}_4 - \text{CoCrMo}$ ; a combination with more elastic compliance was in a partial-slip regime at the same displacement. This highlights the first fundamental difference between a ceramic – metal and a ceramic – ceramic system. For slip to be initiated at the ceramic – ceramic interface, the traction forces must be sufficient enough to induce fracture at the asperity – asperity level. Whereas, when considering other material combinations such as the self-mated  $\text{CoCrMo}$  and  $\text{Si}_3\text{N}_4 - \text{CoCrMo}$ , less tangential force is required for the transition from static friction to kinetic friction i.e. stick regime to partial-slip regime to occur.

On the opposite extreme, a significant interfacial compliance occurs at the  $\text{Si}_3\text{N}_4 - \text{Ti6Al4V}$  interface hence the contact remains in a stick regime even at  $\pm 25 \mu\text{m}$ . 3D surface topography of the two stick regimes at the  $\text{Si}_3\text{N}_4 - \text{Ti6Al4V}$  interface reveal evidence of a growing worn annulus in the  $\text{Si}_3\text{N}_4$  and a plastically deformed Hertzian contact boundary in the  $\text{Ti6Al4V}$  alloy (Figure 7-13). Thus, it is the case that the multiple times harder  $\text{Si}_3\text{N}_4$  ceramic wears relative to the  $\text{Ti6Al4V}$  which on the other hand experiences plastic deformation at the edges of the Hertzian contact. The wear and corrosion products generated within the stick regime fretting contact are generally trapped at the interface.

In the absence of an *in-situ* imaging technique, the mechanical structure of the third-body products trapped at the interface cannot be characterised. Nevertheless, the examination of 3D surface topography of the third-body products at these regimes after fretting lead us to be that the third-body material displays visco-elastic properties. This is evident by the ‘needle-like’ structures observed in both Figure 7-13 ( $\pm 10 \mu\text{m}$  and  $\pm 25 \mu\text{m}$ ) and Figure 6-10 ( $\pm 10 \mu\text{m}$ ) and by the plastic flow observed in Figure 7-13 ( $\pm 50 \mu\text{m}$ ). Furthermore, assuming the ‘needle-like’ structures form upon separation of the  $\text{Si}_3\text{N}_4$  ball from the  $\text{Ti6Al4V}$  flat after the fretting test is completed; then the 3D surface topography images of the  $\text{Si}_3\text{N}_4 - \text{Ti6Al4V}$  sticking fretting contact

may be offering a depiction of the real (*in-situ*) contact area at the tribological interface. Such an observation may prove useful for computational modelling of real interfacial contacts.

Across all the material combinations, gross slip/mixed regimes were realised at  $\pm 50 \mu\text{m}$  displacement, hence the contact is less governed by elastic interfacial compliance. Therefore, the characteristic fretting wear mechanism for each material combination was described mainly on their characteristic behaviour at  $\pm 50 \mu\text{m}$  displacement. These are outlined as follows:

**Si<sub>3</sub>N<sub>4</sub> – Si<sub>3</sub>N<sub>4</sub>:** This combination was mainly governed by a fracture-induced wear mechanism at low displacement amplitudes while it progressively transitioned towards an abrasive wear mechanism as displacement increases (see Figure 7-14). This observation agrees with a previous study [203].

**Si<sub>3</sub>N<sub>4</sub> – CoCrMo:** The wear mechanism at the interface of this material combination was dominantly governed by tribochemical interactions. This was also the case in a previous study which assessed a Si<sub>3</sub>N<sub>4</sub> – Steel system [206]. Interestingly, in the referenced study, Fe from the steel contributed to the tribochemical material formed at the interface but not Cr. And in the present study, it was observed that Cr-oxide – the natural oxide formed during repassivation in a tribocorrosion process of CoCrMo was suppressed from forming. The tribochemical product observed at this interface was SiO<sub>x</sub>-OH<sub>y</sub>. 3D and 2D surface analytical techniques revealed that the SiO<sub>x</sub>-OH<sub>y</sub> tribochemical product largely influence wear at the interface by inhibiting the severe wearing of CoCrMo. Rather, the Si<sub>3</sub>N<sub>4</sub> counter-body suffered greater wear-depths than CoCrMo at  $\pm 50 \mu\text{m}$  displacement. However, as energy is not consumed, the interfacial energy at the Si<sub>3</sub>N<sub>4</sub> – SiO<sub>x</sub>-OH<sub>y</sub> interface, culminated into subsurface fatigue transformations in the CoCrMo alloy. This was manifested in subsurface twinning up to 7  $\mu\text{m}$  deep into the alloy.

**Si<sub>3</sub>N<sub>4</sub> – Ti6Al4V:** Tribochemical reactions were also highly influential in the manifested wear mechanisms and fretting regime at this interface. Unlike the Si<sub>3</sub>N<sub>4</sub> – CoCrMo interface where only Si was involved in the tribochemical product formed, both material couples were engage in the oxidation processes at this interface. This led to the formation of mixed Ti and Al silicates as well

as oxides of Ti and Si. The material property of the product formed at the interface is suggested to play a significant role in the intermittent stiction mechanism experienced at the contact during fretting at  $\pm 50 \mu\text{m}$  displacement. The proposed mechanism of stiction is addressed in further detail in section 10.3.2. The implication of having a fretting couple with relatively large differences in their hardness and stiffness is that, energy is not easily dissipated through wear. If the fretting interface is not subjected to a large enough displacement amplitude to facilitate gross sliding behaviour, the less stiff material would experience a significant metallurgical transformation which may involve subsurface cracking while the much harder ceramic material experiences fracture-induced wear. This can be catastrophic for a ceramic with low fracture toughness.

TEM-EDS analysis showed no evidence of  $\text{Si}_3\text{N}_4$  wear particle in any of the structures analysed in this chapter. This suggests that particulates of  $\text{Si}_3\text{N}_4$  and  $\text{SiO}_2$  from the bulk material were likely crushed prior to being mechanical mixed into oxides of Ti and Al thus engaging in oxidational process under high contact pressures at the interface to form a new tribochemical product (Ti and Al silicates). A similar process is described in a previous study [207].

**Biolox – CoCrMo and Biolox – Ti6Al4V (gross slip):** 3D surface topography of Figure 7-30, Figure 7-33 and Figure 7-36 all reveal an interfacial mechanism whereby the ultra-smooth Biolox ball remained chemically and mechanically inert throughout the fretting stages. Interestingly, it appears to play the role of using third-body wear and corrosion products of CoCrMo and Ti6Al4V alloys to wear against themselves. For the Biolox – CoCrMo contact, an abrasive mechanism is prevalent and for the Biolox – Ti6Al4V material combination, a galling mechanism is prevalent. The galling mechanism which is generally a result of interfacial adhesion can also be characterised by a highly fluctuant dissipated energy curve as shown in Figure 7-35. This is a typical mechanism observed for contacts where titanium alloy is dominant at the interface [208-210].

Figure 7-38 is a summary plot of the cathodic shift measurement for all the material combinations assessed in this chapter at various fretting

displacements. It can be seen that the cathodic shift experienced at the stick and partial-slip regimes of both  $\text{Si}_3\text{N}_4$  – CoCrMo and  $\text{Si}_3\text{N}_4$  – Ti6Al4V are minimal. This is because at low fretting displacement amplitudes, a relatively small area is depassivated i.e. exposed bare active metal [146]. Furthermore, in most cases, as majority of the fretting contact remain unexposed to the electrolyte, OCP curve displays contact ennoblement despite on-going fretting. However, across the gross slip/mixed regime fretting contacts where large area of depassivation occurs i.e. at  $\pm 50 \mu\text{m}$  displacement, cathodic shifts were observed as expected.

Similarly as observed for metal – metal combinations, the maximum cathodic shift measured at the fretting contacts involving Ti6Al4V are significantly larger than those of CoCrMo. In the case of ceramic – metal combinations involving Ti6Al4V, the magnitude of Max. cathodic shift and the repassivation kinetics (from OCP observation) was observed to be mainly influenced by the fretting regime. As for the BioloX – Ti6Al4V material combination subjected to a partial-slip regime, third-body products accumulated at the interface were unable to escape the contact. Although the magnitude of cathodic shift was relatively small compared to the cathodic shift at BioloX – Ti6Al4V under gross slip regime, the repassivation kinetics at the partial-slip contact was indicative of active localised corrosion mechanisms. This is evidenced by the MACC process identified at the interface. Excess metal ions as O is depleted in the partial-slip contact attracted Cl ions into the region as depicted in the SEM-EDS micrograph of Figure 7-34. This may explain why repassivation process at the interface was inhibited; it is well known that Cl ions play a significant role in the inhibition of passive oxide restoration thus subsequently triggering localised corrosion mechanisms [27, 211].

In the case of  $\text{Si}_3\text{N}_4$  – Ti6Al4V where a stiction mechanism was dominant, repassivation kinetics were largely influenced by the mechanically induced cracks within the Ti6Al4V surface as evidenced in the 3D surface topography of Figure 7-13,  $\pm 50 \mu\text{m}$  displacement. The same observation was made for at the CoCrMo – Ti6Al4V interface in the previous chapter. The BioloX – Ti6Al4V contact at gross slip regime experienced the largest cathodic shift of all the combinations. However, as there was adequate exchange in the physiological



solution during on-going fretting thus restoring access to O at the interface, the third-body product observed was mainly Ti-oxide. In the scarcity of O supply, like in the partial-slip fretting contact, the main corrosion product would be metal-chlorides.

Maximum cathodic shift in both Biolox – CoCrMo and Si<sub>3</sub>N<sub>4</sub> – CoCrMo at ±50 µm were very similar despite forming two different oxidation products at their interfaces. This confirms that the cathodic potential measured at both ceramic – metal interfaces is more representative of the exposed active site in the CoCrMo alloy and less about the reaction kinetics. The main third-body product in the case of the former is Cr-oxide while in the latter was SiO<sub>x</sub>-OH<sub>y</sub> compound.

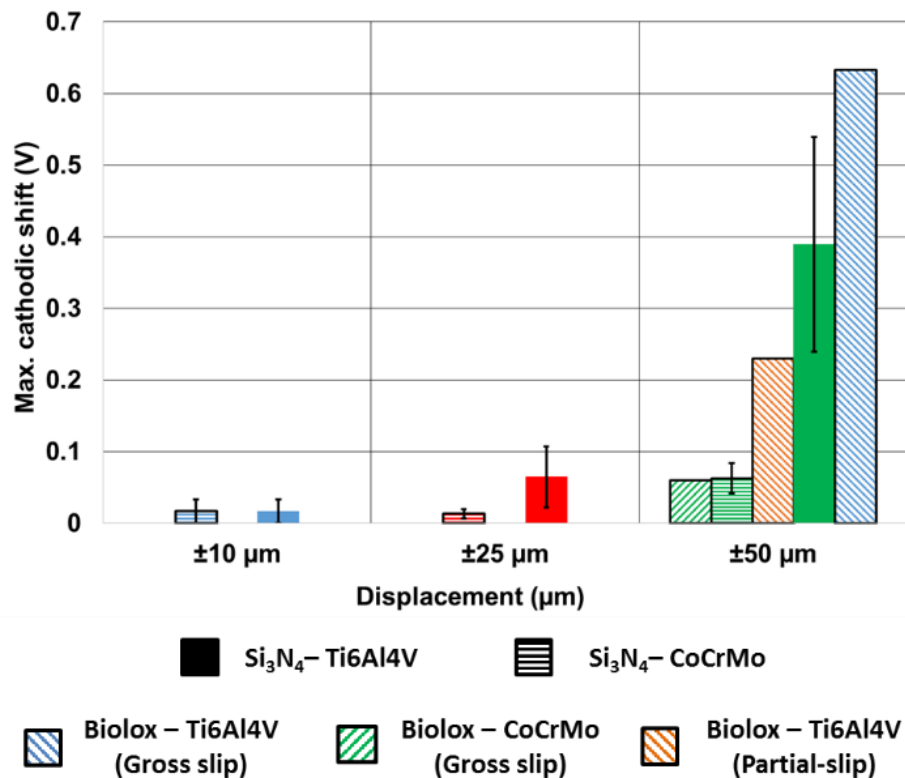


**Figure 7-38 – Comparing Max. cathodic shift in ceramic – metal combinations.**

## Chapter 8 Quantification of fretting corrosion current using self-mated CoCrMo material combination

### 8.1 Introduction

So far, fretting of metal – metal and ceramic – metal combinations have been assessed under OCP conditions. However, the quantification of fretting corrosion current and Faradaic mass loss as a function of displacement amplitude is yet to be addressed. Thus, the purpose of the experiments in this chapter is to quantify corrosion current and assess the effect of surface history on the evolution of fretting current and interfacial energy. By the phrase ‘effect of surface history’ it is anticipated that the fretting interface of the modular taper, experiences diverse forms of oxidation processes and wear mechanisms which may alter the contact conditions and fretting regime *in-vivo* [199]. In the context of tribocorrosion, changes to the contact condition or film formation can strongly influence the synergies of a fretting contact.

The study was carried out on self-mated CoCrMo using three methods schematically outlined in section 4.4.2.2: ‘Method 1’ represents fretting tests conducted for individual displacements; ‘Method 2’ represents fretting tests conducted in series with increasing displacement amplitudes and ‘Method 3’ represents fretting tests conducted in series with decreasing displacement amplitude. A schematic outline of the experiments and analysis performed in this chapter are shown in Figure 8-1.

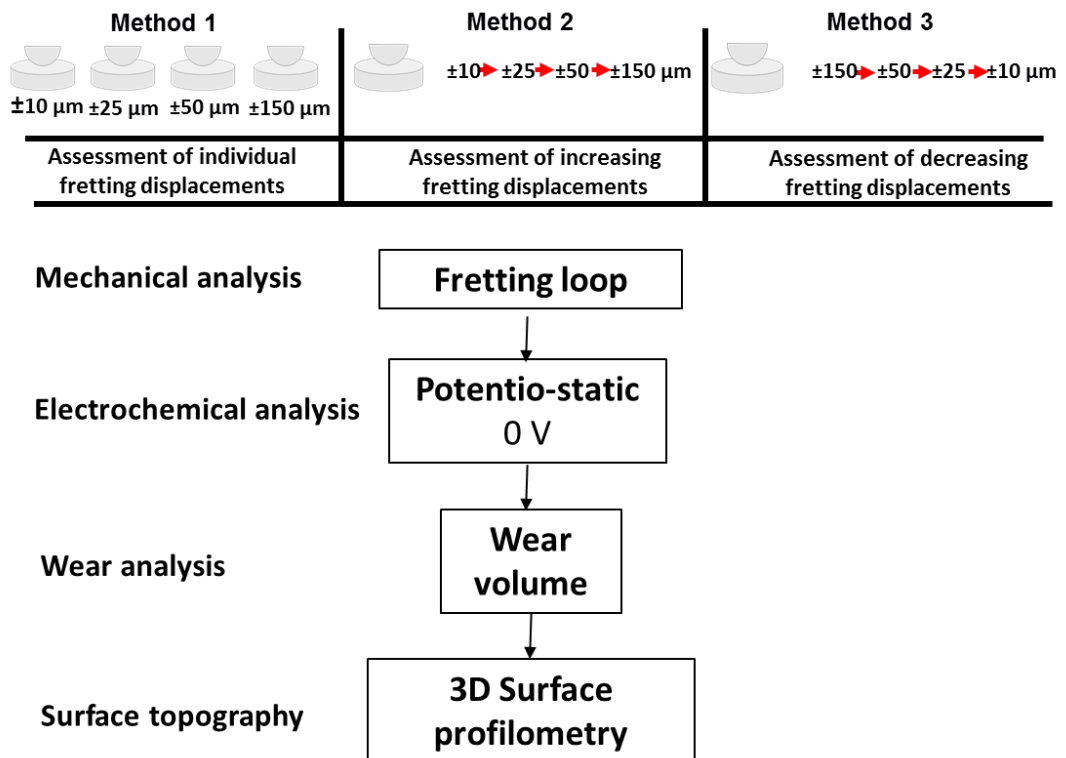


**Figure 8-1 – Outline of the fretting experiments performed in chapter 8**

Figure 8-2 shows the slip ratio for the four displacements assessed across the three methods. In comparison to the gross slip regime criteria, it can be seen that all the displacements amplitudes  $\geq \pm 25 \mu\text{m}$  experienced gross slip fretting regime. Whereas, all displacements at  $\pm 10 \mu\text{m}$  experienced a partial-slip regime except in method 3 where the slip ratio is observed to have exceeded the gross slip criteria.

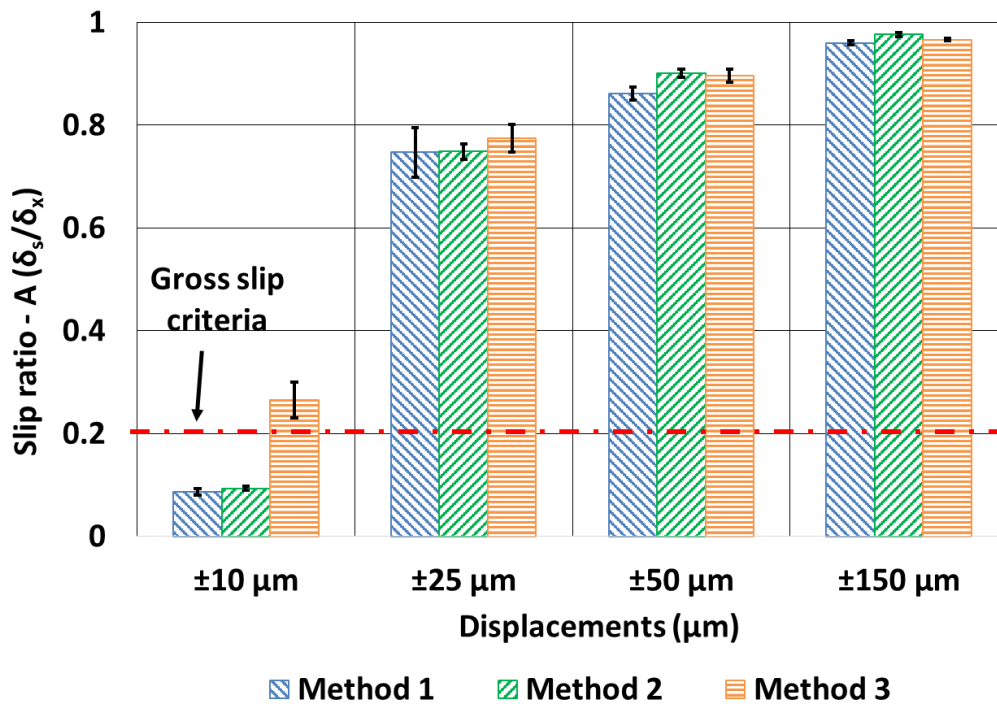


**Figure 8-2 – Slip ratio of CoCrMo – CoCrMo under potentiostatic conditions for  $\pm 10 - \pm 150 \mu\text{m}$  in ‘Methods 1 – 3’.**

## 8.2 Anodic current in static condition

Following the potentiostatic polarisation of the loaded ball-on-flat contact, from OCP to 0V vs. Ag/AgCl, the fretting current dropped exponentially as expected; this is generally indicative of surface coverage of anodic oxide film [212]. The curve follows a power relationship as shown in Figure 8-3. The time ‘t’ = 4000 sec corresponds to an end of the equilibrating stage and the initiation of fretting displacements to the contact. The mean average and standard error of n = 14 samples at this point is  $714 \pm 160 \text{ nA}$ . This value corresponds to the pure corrosion current ‘C’ effective at the contact under static conditions.

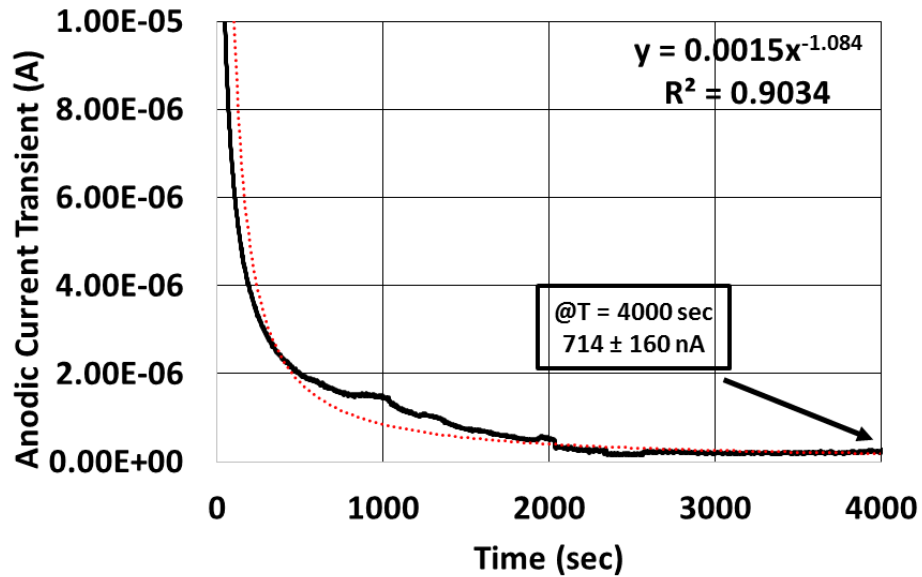


**Figure 8-3 – Anodic current transient of loaded CoCrMo – CoCrMo contact subjected to 0V vs. Ag/AgCl of potenti-static polarisation for 4000 seconds in static conditions.**

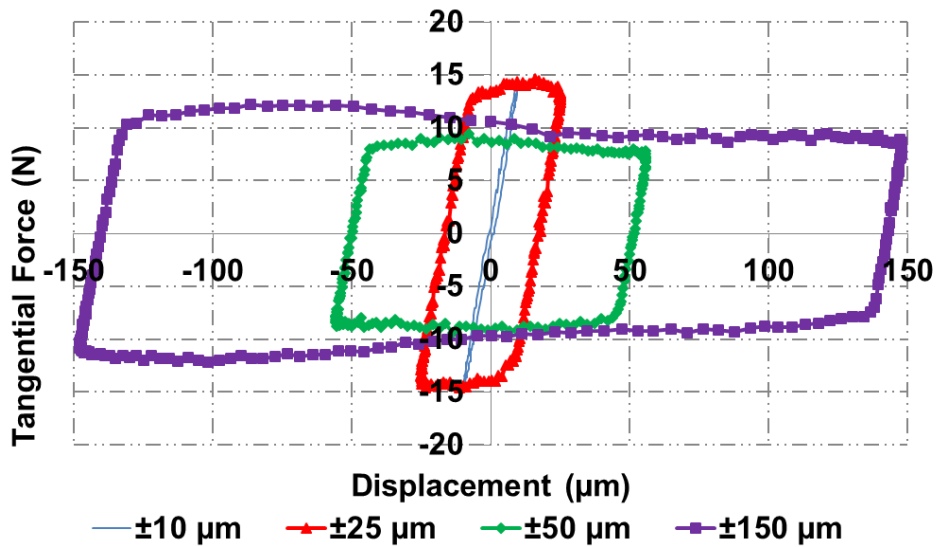
### 8.3 Method 1

#### 8.3.1 Fretting loop analysis

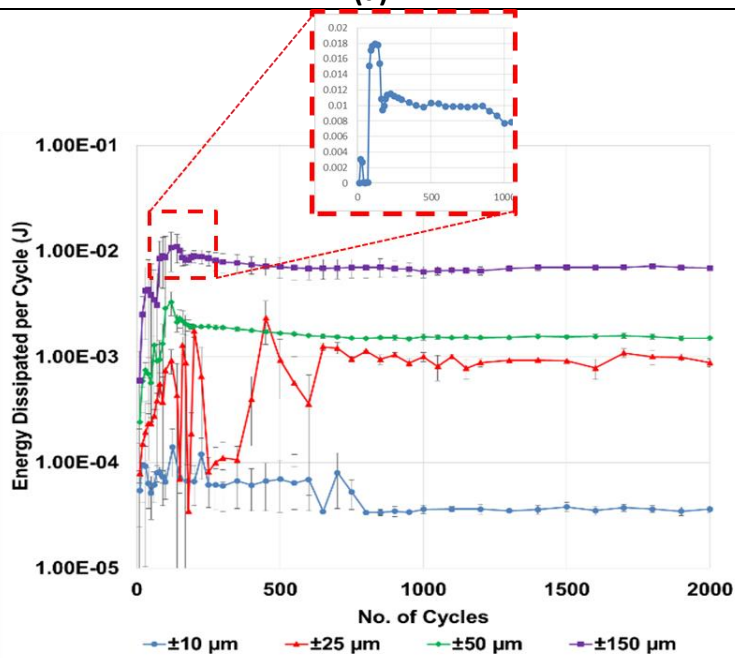
Figure 8-4a shows the fretting loop of the four displacement amplitudes. These are seen to be very similar to the CoCrMo – CoCrMo contact under OCP condition in (section 6.2.1). Each fretting loop represents the fretting contact at the 1000<sup>th</sup> cycle. This cycle corresponds to the fretting loop at middle of the total length of cycle (2000 cycles). The non-symmetrical loop at the  $\pm 150$   $\mu\text{m}$  is indicative of an asymmetric wear surface (see section Figure 10-2 for further details).

Figure 8-4b shows the average plot of energy dissipated per cycle for each displacement variable. The energy dissipated is seen to be higher with higher displacement amplitudes as expected. However, it is observable that the energy drops suddenly at  $\pm 25$   $\mu\text{m}$  to a value close to that of the partial-slip regime at  $\pm 10$   $\mu\text{m}$ . This is indicative of a momentary transition from gross-slip to partial-slip and then back to gross slip again. An inset image is included to

highlight the sudden drop in the energy dissipated at  $\pm 150 \mu\text{m}$  which could not be observed properly in the log plot.



(a)



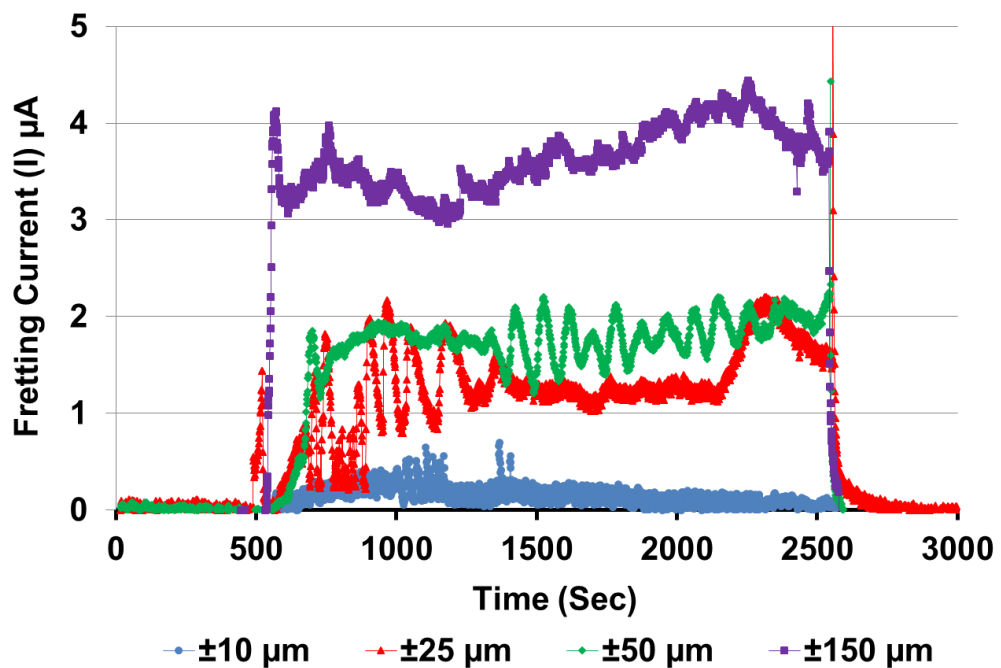
(b)

Figure 8-4 – Method 1: fretting loop analysis of CoCrMo – CoCrMo at  $\pm 10 \mu\text{m}$ ,  $\pm 25 \mu\text{m}$ ,  $\pm 50 \mu\text{m}$ ,  $\pm 150 \mu\text{m}$  displacement in potentiostatic conditions. a) Fretting loop b) Energy dissipated per cycle.

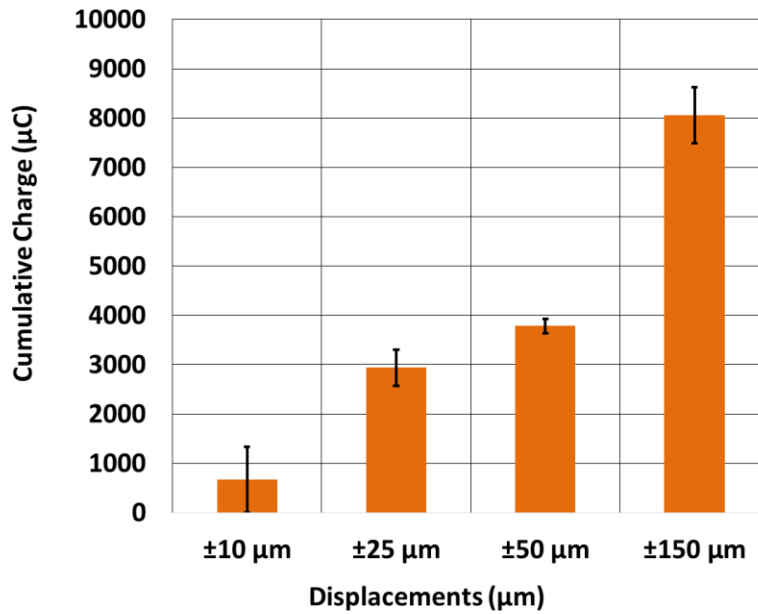
### 8.3.2 Electrochemical results

Figure 8-5a is a representation of the *in-situ* fretting current transient as a result of oxidation processes of each fretting displacement. The result shows that fretting current transient at the partial-slip regime is near zero as expected. However at the gross slip regime, a distinctive fretting corrosion current transient is observed. At  $\pm 25 \mu\text{m}$ , the sudden transition between partial-slip to gross slip regime indicated in the energy dissipated is fully reflected in the fretting current. The fretting current at  $\pm 50 \mu\text{m}$  was not significantly higher than at  $\pm 25 \mu\text{m}$ , however, in comparison to  $\pm 150 \mu\text{m}$ , the magnitude is almost double.

In Figure 8-5b the time-dependent fretting current is represented as cumulative charge which corresponds to the area encompassed within the 'I vs. t' plot of Figure 8-5a. Thus as expected, the difference in magnitude of cumulative charge for the various displacements in Figure 8-5b are seen to be very comparable with that of the fretting current in Figure 8-5a.



(a)



(b)

**Figure 8-5 – Method 1: fretting current from CoCrMo – CoCrMo contact at  $\pm 10 \mu\text{m}$ ,  $\pm 25 \mu\text{m}$ ,  $\pm 50 \mu\text{m}$ ,  $\pm 150 \mu\text{m}$  displacement, a) Fretting current transient b) Cumulative charge**

### 8.3.3 Surface analysis

3D surface profilometry of both CoCrMo ball and flat surfaces are shown in Figure 8-6. The general trends observed are as expected: a) the size of the fretting wear surface increased with increase in fretting displacement; b) the size of central partial-stick region reduced in proportion to the worn annulus as displacement increased. From observation of the ball component at  $\pm 50 \mu\text{m}$  and  $\pm 150 \mu\text{m}$ , it is observable that the main difference between the two is that the central region had worn significantly (although not entirely) in depth at  $\pm 150 \mu\text{m}$ .



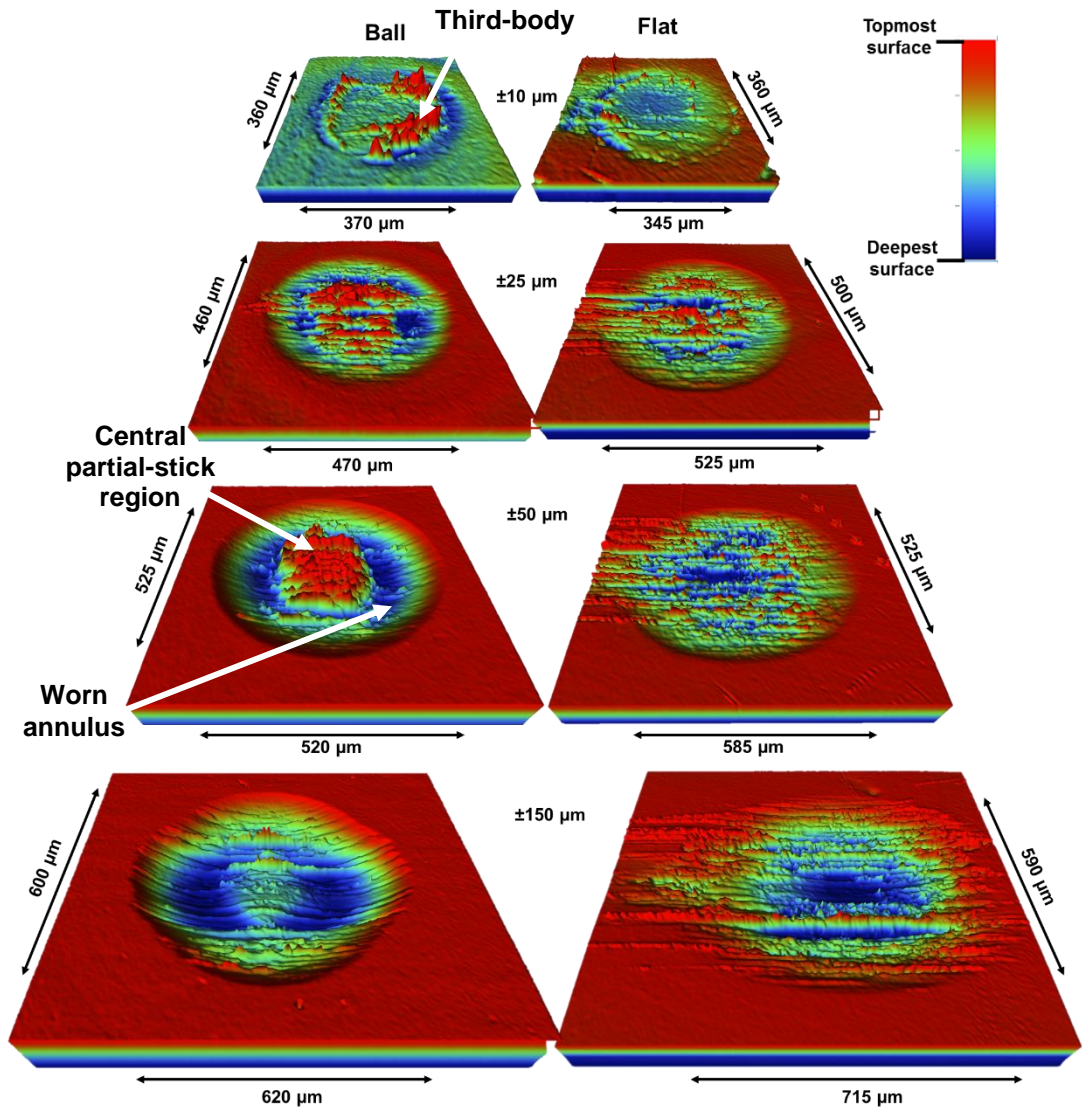


**Figure 8-6 – Method 1: 3D surface profilometry of CoCrMo ball and flat fretting interface assessed under potention-static conditions.**

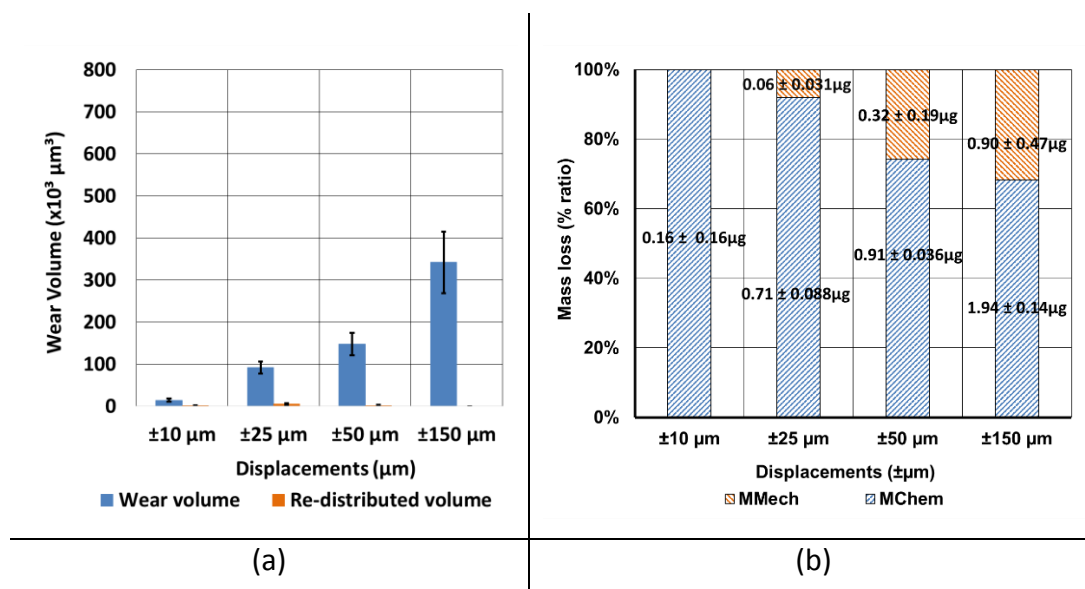
### 8.3.4 Tribocorrosion mass loss

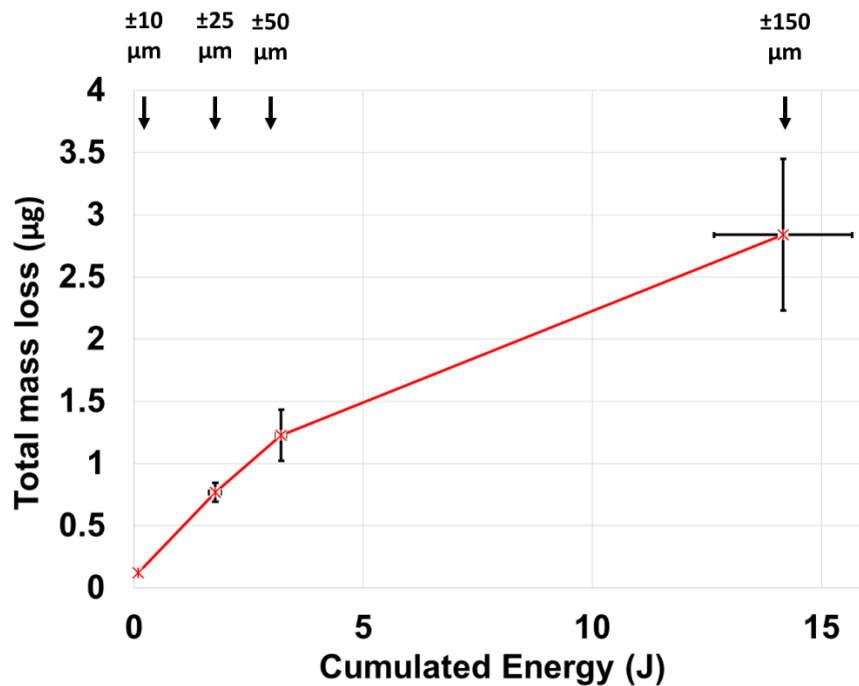
Figure 8-7a shows the wear volume from all the displacements. Interestingly, the pattern of increase from the lowest fretting displacement to the highest corresponds to the cumulative charge increase in Figure 8-5b. In general, the result shows that the wear volume increases with increasing displacement. However, amongst the gross slip fretting displacement increase in wear was not proportional to the increase in displacement amplitude. The wear volume at the gross slip contact of  $\pm 25 \mu\text{m}$  is about 6 times higher than at  $\pm 10 \mu\text{m}$  thus

showing the effect of regime transition from partial-slip to gross slip. The re-distributed volume is considered the volume of material that sits within the wear surface but above the zero-line (see section 4.5.2). These were negligible at all fretting displacements.

In Figure 8-7b, the Faradaic mass loss is reported as a percentage ratio of  $M_{mech}$  and  $M_{chem}$ . The result shows that at the partial-slip regime, the mass loss is completely a result of chemical oxidation and for the gross slip contacts, the ratio of  $M_{mech}$  increased with increasing displacement and so does the overall mass loss. However for all displacements,  $M_{chem}$  is the largest contributor to total mass loss.

In Figure 8-7c, the total tribocorrosion mass loss which incorporates both  $M_{chem}$  and  $M_{mech}$  is plotted against the cumulative energy corresponding to each displacement. The graph shows a linear correlation between  $\pm 10 \mu\text{m}$  and  $\pm 50 \mu\text{m}$  (inclusive). These are the same displacements according to Figure 8-6 where the partial central stick region are still present thus fretting at these displacements are still highly influenced by elastic contact compliance. However, from  $\pm 50 \mu\text{m}$  to  $\pm 150 \mu\text{m}$ , a less steep gradient is observed thus highlighting the influence of third-body interaction at the interface [39].





(c)

**Figure 8-7 – Method 1: the sum of tribocorrosion mass loss from ball and flat components; a) Wear volume (blue) and Re-distributed volume (orange); b) Mass loss as a proportion of  $M_{\text{mech}}$  and  $M_{\text{chem}}$ , c) Total mass loss vs. Cumulative energy.**

The contribution of pure corrosion (C) to the total mass loss for the three methods are shown in Table 8-1. In method 1, the maximum mass loss contribution from pure corrosion was calculated from the sum of the largest worn areas of ball and flat components i.e. the ball and flat surfaces of  $\pm 150 \mu\text{m}$  displacement (see section 4.4.2.3 for the calculation). The total contribution was  $\sim 0.2 \text{ ng}$ . As for methods 2 and 3 whereby all four displacements were performed in series, the contribution of C was estimated to  $0.4 \text{ ng}$ . Thus, in all three methods, the contribution of pure corrosion was found to be negligible compared to the Faradaic mass loss in Figure 8-7b. Nevertheless, these values were included in the calculations of  $M_{\text{chem}}$ .

**Table 8-1 – Breakdown of static current, Faradaic mass loss for both the entire surface sample surface and the fretting surface.**

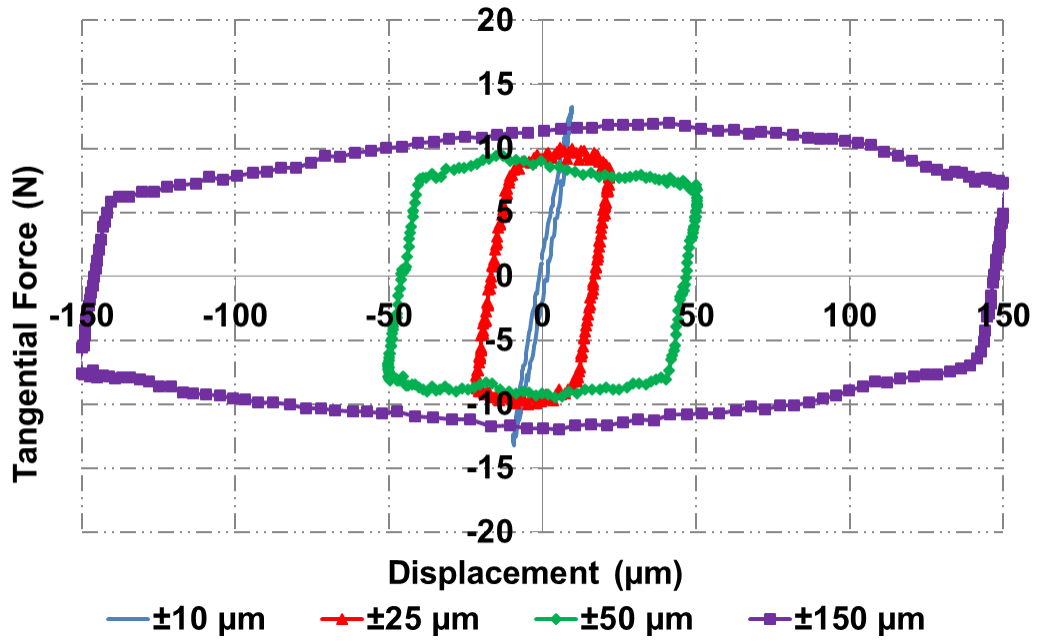
	Static current [Entire surface] @T = 4000 sec (nA)	Faradaic Mass loss [Entire surface] (µg)	Faradaic Mass loss [Fretted surface] (µg)
Method 1  (Max. per displacement)	710.4 ± 160	0.343 ± 0.077	0.0002 ± 0.000045
Methods 2 and 3		0.705 ± 0.167	0.0004 ± 0.000039

## 8.4 Method 2

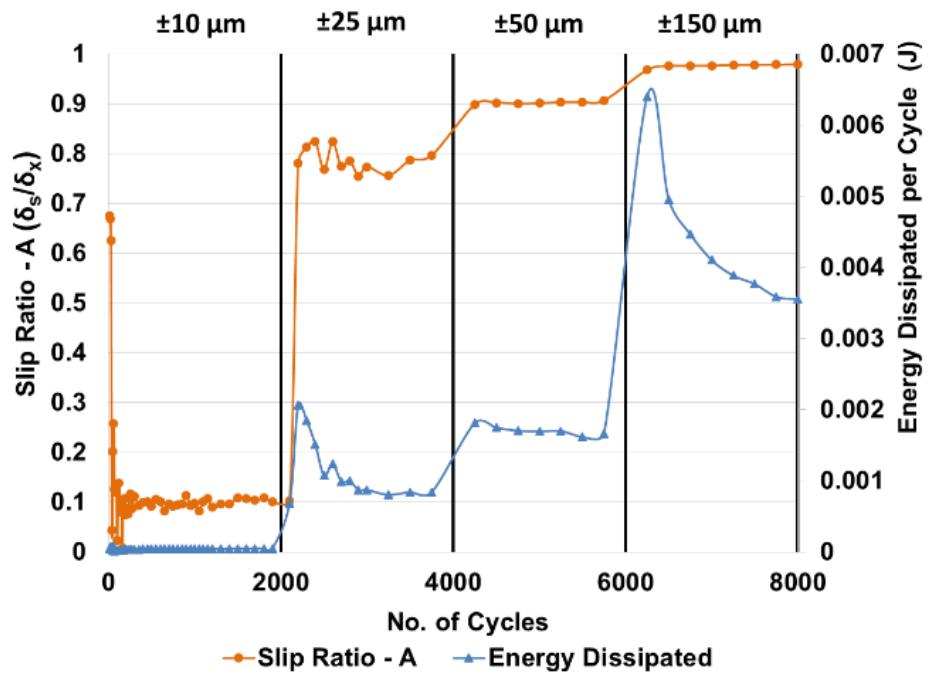
### 8.4.1 Fretting loop analysis

Figure 8-8a shows the fretting loop generated from method 2. The fretting loops observed from this method are the same regimes in every displacement as identified in method 1, although, with subtle differences in the gross slip shapes.

Figure 8-8b shows a super-imposed time-dependent plot of slip ratio and energy dissipated for the four displacements tested in series to each other. The main points of observation are the drop in energy seen at  $\pm 25 \mu\text{m}$  and  $\pm 150 \mu\text{m}$ . When considering the slip ratio corresponding to the  $\pm 25 \mu\text{m}$ , the drop in energy may be correlated with the stabilisation of slip at the interface. However for the  $\pm 150 \mu\text{m}$ , the energy dropped significantly despite the slip ratio remaining constant; this implies the drop in energy is directly correlated to the interfacial friction.



(a)

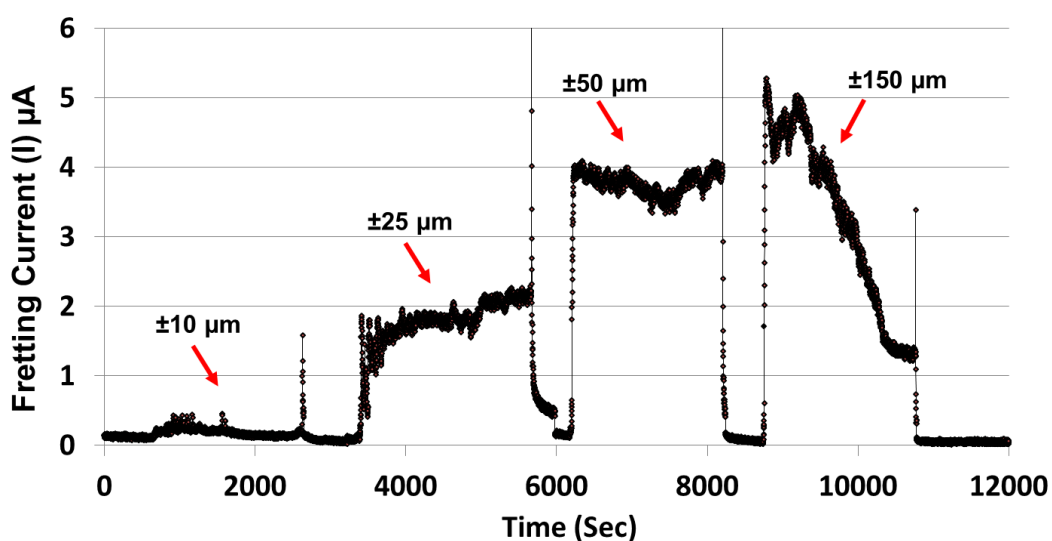


(b)

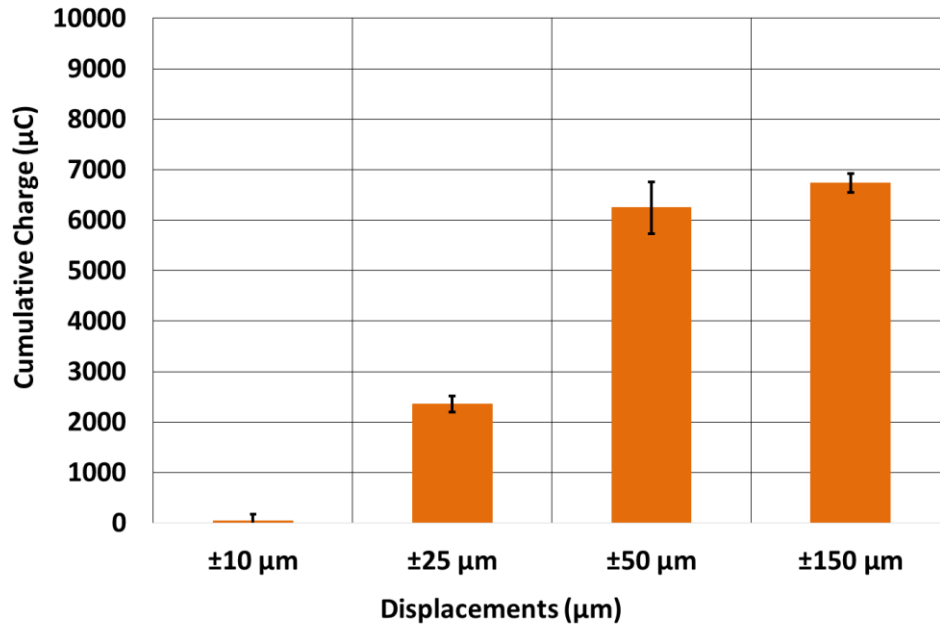
Figure 8-8 – Method 2: fretting loop analysis of CoCrMo – CoCrMo at  $\pm 10 \mu\text{m}$ ,  $\pm 25 \mu\text{m}$ ,  $\pm 50 \mu\text{m}$ ,  $\pm 150 \mu\text{m}$  displacement in potention-static conditions. a) Fretting loop b) Energy dissipated per cycle.

## 8.4.2 Electrochemical results

Figure 8-9a shows the time-dependent fretting current transient for each displacement in an increasing order. As expected, the fretting current at  $\pm 10 \mu\text{m}$  is minimal and as the contact transitions into gross slip regime, the fretting current increased significantly. Unlike in method 1, the fretting current at  $\pm 50 \mu\text{m}$  was almost double the current at  $\pm 25 \mu\text{m}$  which also corresponds to the ratio between the two displacements. Interestingly, the fretting current was not significantly higher at  $\pm 150 \mu\text{m}$  and after just a few hundred cycles, the fretting current dropped rapidly in a manner that corresponds to the drop in the energy dissipated plot in Figure 8-8c. These highlights the effect of surface history as later discussed in the summary section of this chapter. Figure 8-9b shows the cumulative charge from each displacement and as expected, the magnitude of the charge differences from each fretting displacement corresponds with the fretting current transient.



(a)



(b)

**Figure 8-9 – Method 2: fretting current from CoCrMo – CoCrMo contact at  $\pm 10 \mu\text{m}$ ,  $\pm 25 \mu\text{m}$ ,  $50 \mu\text{m}$ ,  $\pm 150 \mu\text{m}$  displacement; a) Fretting current transient b) Cumulative charge**

### 8.4.3 Surface analysis

The wear surface from method 2 is shown in Figure 8-10. Evidence of surface grooving can be seen from the 3D surface profilometry. It appears as though third-body product on the ball had inflicted excessive wear at a localised central region of the flat component. And across the entire flat wear surface evidence of grooving is also noticeable due to the presence of thin grooves which are aligned with those on the ball component.

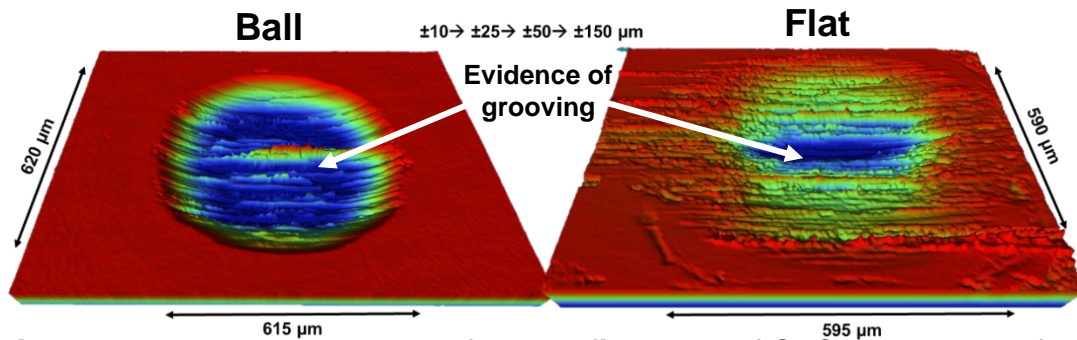


**Figure 8-10 – Method 2: 3D surface profilometry of CoCrMo ball and flat fretting contacts tested in potentiostatic conditions.**

#### 8.4.4 Tribocorrosion mass loss

Figure 8-11a shows that the wear volume for method 2 which totals to  $520000 \pm 43000 \mu\text{m}^3$ . Figure 8-11b shows the mass loss as a ratio of  $M_{\text{mech}}$  and  $M_{\text{chem}}$  for method 2. The magnitude of  $M_{\text{chem}}$  measured in this contact is very similar with method 1; it contributes to 85% of the total mass loss. The total contribution of  $M_{\text{mech}}$  in this method is seen to be roughly half that of the total contribution in method 1.

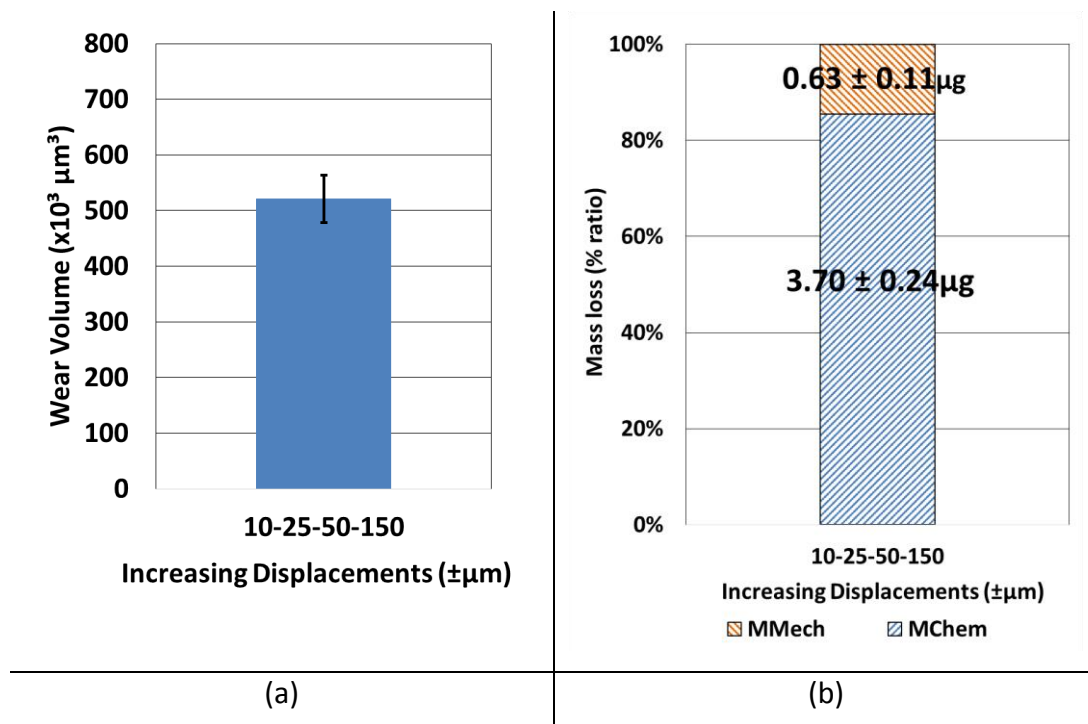


**Figure 8-11 – Method 2: tribocorrosion mass loss; a) Wear volume; b) Mass loss as a proportion of  $M_{\text{mech}}$  and  $M_{\text{chem}}$ .**

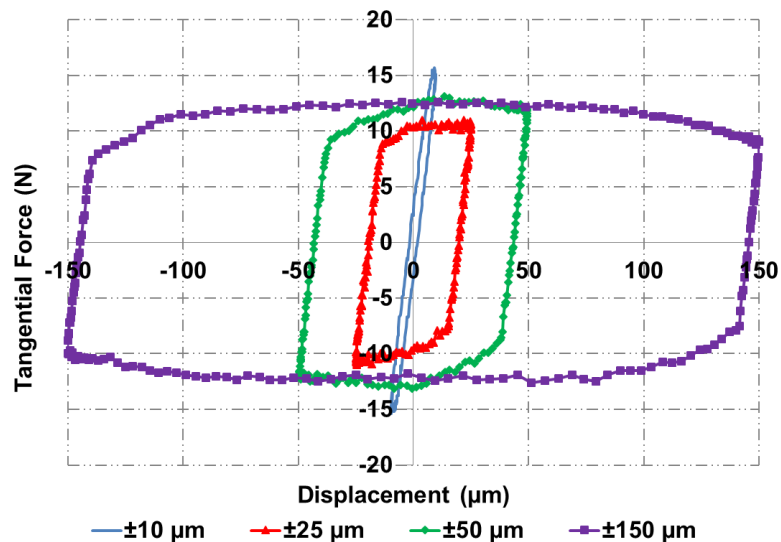


## 8.5 Method 3

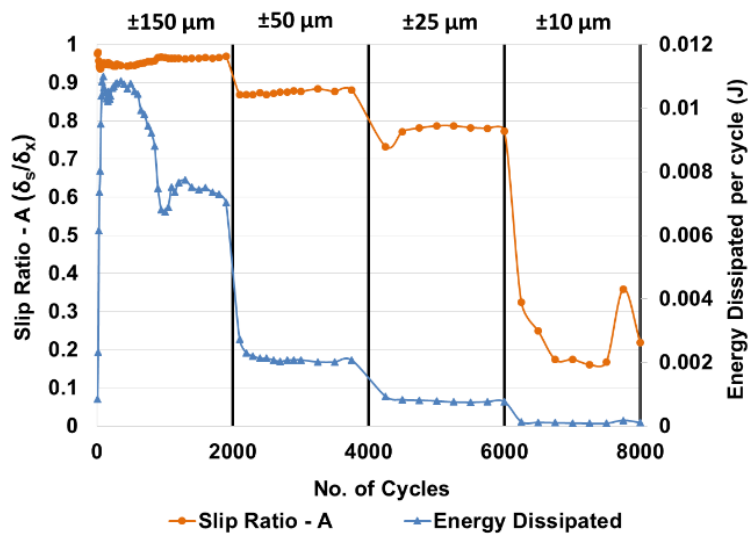
### 8.5.1 Fretting loop analysis

Figure 8-12a shows the fretting loop generated from method 3. It is worth noting that the slip ratio in this method (see Figure 8-2) was similar with the other methods for all displacements except the displacement at  $\pm 10 \mu\text{m}$  where the slip ratio was 3x higher relative to the other methods. Figure 8-12b shows a super-imposed time-dependent plots of both slip ratio and energy dissipated for all displacements, in decreasing order.

It is observable that the energy dropped suddenly and significantly during the initial fretting at  $\pm 150 \mu\text{m}$ . It is also notable that the point where the energy dissipated dropped corresponds to a small increase in the slip ratio, thus indicating that the drop in energy is a direct result of changes to the interfacial friction. Subsequently, the transitions to  $\pm 50 \mu\text{m}$  and  $\pm 25 \mu\text{m}$  resulted a stable slip ratio and energies dissipated, while slip at the partial-slip regime appear less stable.



(a)



(b)

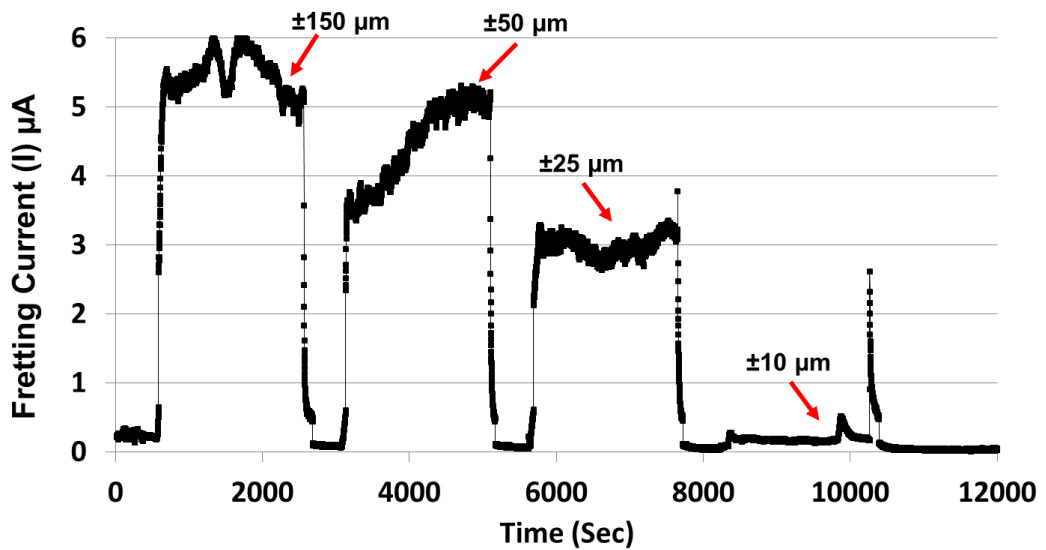
**Figure 8-12 – Method 3: fretting loop analysis of CoCrMo – CoCrMo at  $\pm 150 \mu\text{m}$ ,  $\pm 50 \mu\text{m}$ ,  $\pm 25 \mu\text{m}$ ,  $\pm 10 \mu\text{m}$  displacement in potentiostatic conditions. a) Fretting loop b) Energy dissipated per cycle.**

### 8.5.2 Electrochemical results

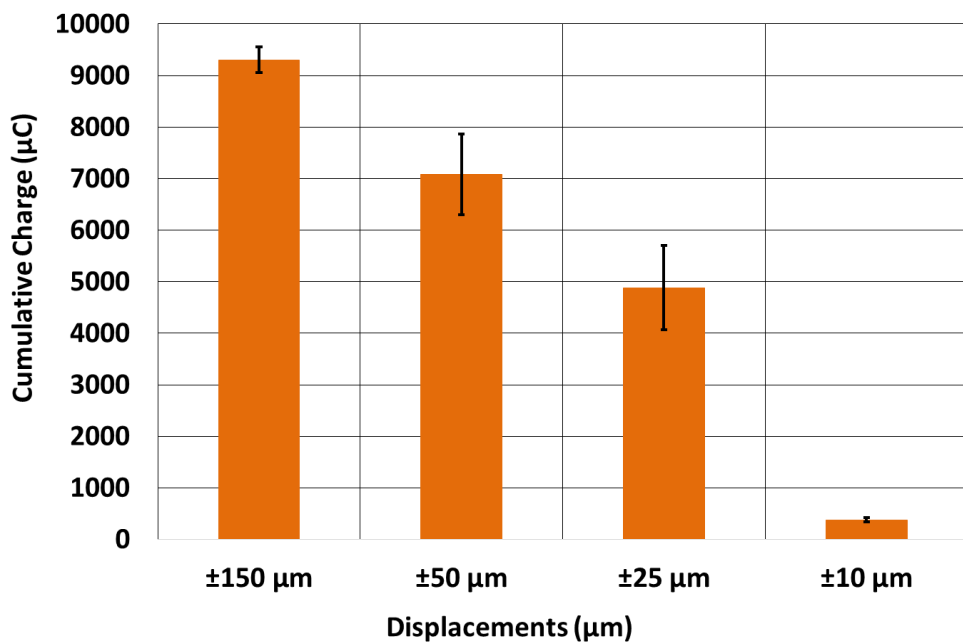
Figure 8-13a shows the corresponding fretting current transient in the decreasing order of the fretting displacements. The point where a significant drop in energy was observed for the  $\pm 150 \mu\text{m}$  is reflected in the fretting current transient as an intermittent reduction in current. Subsequently, while the energy remained low as seen in Figure 8-12b, the fretting current transient was seen to rise to a peak before steadily dropping. This observation was contrary to method 2 in which case, a continuous drop in energy dissipated resulted in a continuous drop in fretting current. The fretting currents transient at  $\pm 50 \mu\text{m}$  and  $\pm 25 \mu\text{m}$  were also relatively higher than in the other methods. The larger slip ratio at the partial-slip regime in this method resulted in a higher fretting current compared to the two previous methods as expected.

The cumulative charge for all the displacements are shown in Figure 8-13b. The values are seen to be higher than all the other methods within the margins

of error and the cumulative charge at  $\pm 25 \mu\text{m}$  in this method is seen to be double the value in method 2.



(a)



(b)

**Figure 8-13 – Method 3: fretting current from CoCrMo – CoCrMo contact at  $\pm 150 \mu\text{m}$ ,  $\pm 50 \mu\text{m}$ ,  $\pm 25 \mu\text{m}$ ,  $\pm 10 \mu\text{m}$  displacement, a) Fretting current transient b) Cumulative charge**

### 8.5.3 Surface analysis

The wear surface from method 3 is shown in Figure 8-14. The wear surface reveal an interesting profile, similar to one already observed at the CoCrMo – CoCrMo,  $\pm 150 \mu\text{m}$  fretting contact, under OCP conditions (section 6.5.1, Figure 6-9). The two heaps of material, present on either side of the central region is a re-distributed third-body product that has become aligned in the reciprocating fretting direction. The material preserved at the centre of the surface is what is left of the central partial-stick region. Evidence of third-body inflicted grooving is observed within the flat wear surface.

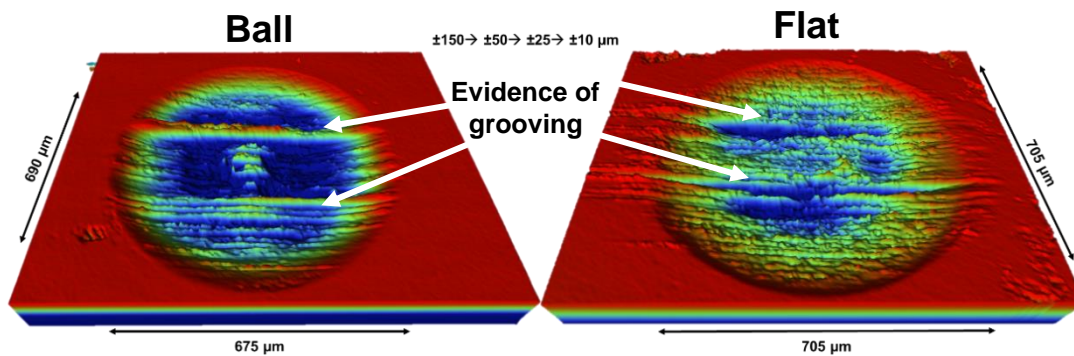


**Figure 8-14 – Method 3: 3D surface profilometry of CoCrMo ball and flat fretting contacts tested in potentiostatic conditions.**

### 8.5.4 Tribocorrosion mass loss

Figure 8-15a shows that the wear volume for method 3 is  $670000 \pm 53000 \mu\text{m}^3$  which is higher than the wear volume of both methods 1 and 2. Figure 8-15b shows the mass loss as a ratio of  $M_{\text{mech}}$  and  $M_{\text{chem}}$  for method 3. The  $M_{\text{chem}}$  measured in this method is much larger than in methods 1 and 2; it contributes to 93% of the total mass loss. Thus the contribution of  $M_{\text{mech}}$  in this method is seen to be much lower than the two previous methods.

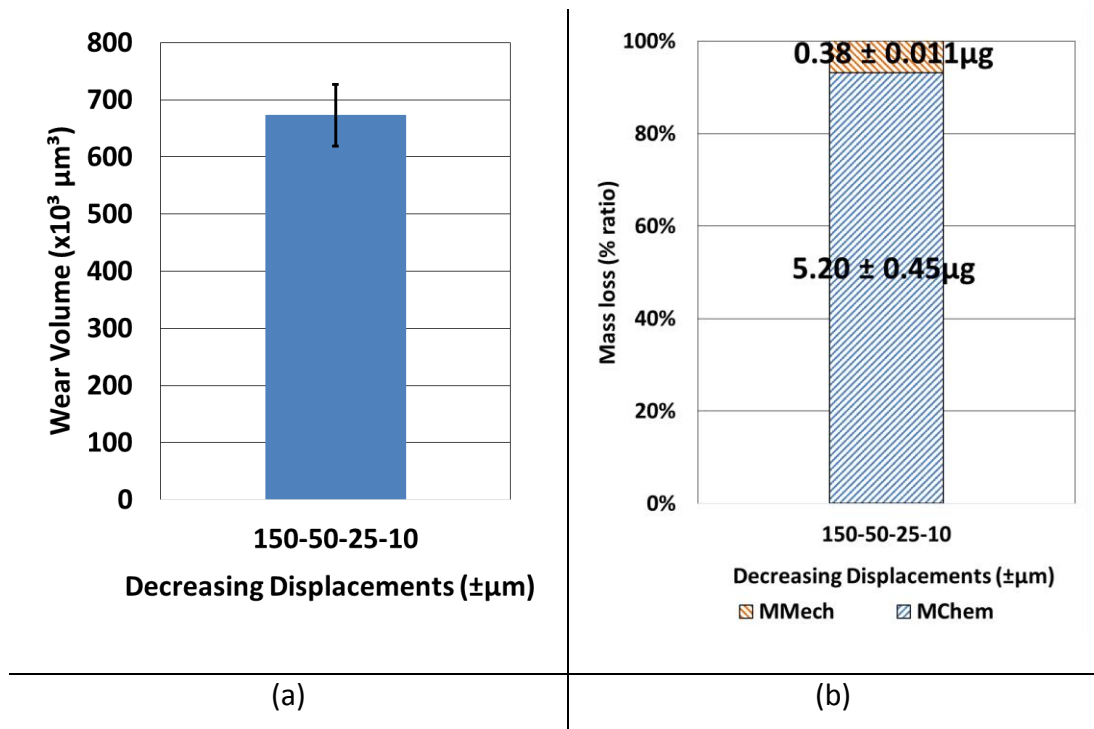


**Figure 8-15 – Method 3: tribocorrosion mass loss; a) Wear volume; b) Mass loss as a proportion of  $M_{mech}$  and  $M_{chem}$ .**

## 8.6 Discussion and summary

In this chapter, self-mated CoCrMo was used to assess fretting corrosion currents for varied fretting displacement amplitudes. Through this study, it was confirmed that fretting corrosion currents at a partial-slip regime is minimal in comparison to the gross slip regime. It is importance to highlight this so that a link can be established between fretting currents and the corresponding fretting regime. Therefore in the subsequent chapter where realistic taper components are subjected to fatigue loads, fretting current can be translated to fretting regimes in the qualitative sense.

The synergistic interactions of wear and corrosion is a topic that has been widely discussed across several decades [136, 139, 145, 213, 214]. Uhlig's mechanistic approach to tribocorrosion mass loss is expressed in Equation 8-1. Equations 8-2 and 8-3 is a widely regarded expression of the contributing mechanical, chemical and synergistic factors contributing to  $M_{mech}$  and  $M_{chem}$ . The study by Bryant and Neville [139] critiqued this expression and highlighted

that the synergistic factor 'C<sub>w</sub>' which is solely placed under the broad umbrella of M<sub>mech</sub> is unfittingly positioned considering that it represents aspects of oxidational processes.

$$M_{total} = M_{chem} + M_{mech} \quad 8-1$$

$$M_{chem} = C + W_c \quad 8-2$$

$$M_{mech} = W + C_w \quad 8-3$$

The general approach for determining C<sub>w</sub> is shown in Equation **8-4**; where 'W' is obtain by suppressing corrosion through cathodic polarisation. W<sub>c</sub> is determined by integrating the area encompassed within the tribocorrosion current transient like those presented in Figure 8-5a. C is determined by integrating the area encompassed within the period of fretting from zero current to the measured current whilst the contact was in static conditions (see Figure 4-1). However, determining C<sub>w</sub> in this manner undermines its magnitude, be it positive (synergistic) or negative (antagonistic). It is meant that, the unknown proportion of electrochemical contributions of C<sub>w</sub> in the tribocorrosion current transient is not considered when Equation **8-4** is used. For this reason, Equations **8-2** and **8-3** are redefined as Equations **8-5** and **8-6** where 'α' and 'β' are unknown proportions of C<sub>w</sub>. Therefore, the area encompassed by the fretting current transients is interpreted as W<sub>c</sub> + αC<sub>w</sub> in this study (see schematic diagram shown in section 4.3.2).

$$C_w = M_{total} - W - W_c - C \quad 8-4$$

$$M_{chem} = C + W_c + \alpha C_w \quad 8-5$$

$$M_{mech} = W + \beta C_w \quad 8-6$$

Positive +αC<sub>w</sub> represents a synergistic contribution to tribocorrosion mass loss through oxidational processed thus, fretting current is increased. Negative -αC<sub>w</sub> represents an antagonistic contribution to tribocorrosion mass loss through oxidational process leading to a reduction in the fretting current.

Positive  $+\beta C_w$  represents a synergistic contribution to tribocorrosion mass loss through mechanical wear processes thus wear is increased at the interface. Negative  $-\beta C_w$  represents an antagonistic contribution to tribocorrosion mass loss through mechanical wear processes leading to a reduction in wear. Several mechanisms such as tribochemical film formation, third-body agglomeration and many more can be occurring simultaneously within a tribocorrosion interface. The unknown (but predictable) summation of these interactions determines whether  $C_w$  in the system is synergistic or antagonistic.

The contribution of pure corrosion (C) to the total mass loss in this study was found to be negligible thus  $M_{\text{chem}}$  was only  $W_c + \alpha C_w$ . Pure wear (W) was not determined in the present study because the ratio of  $M_{\text{chem}}$  and  $M_{\text{wear}}$  was deemed sufficient for determining the degradation mechanisms of the three methods assessed using Stack and Chi's [136] criteria (outlined in section 3.5.1).

It was observed in Method 1 that  $M_{\text{chem}}$  was the main contributor to the total tribocorrosion mass loss for all displacements. This agrees with Bryant and Neville's result which found that  $M_{\text{mech}}$  was more dominant at low initial contact pressures (0.4 GPa) whereas at high initial contact pressures i.e. 1 GPa, the contribution of  $M_{\text{chem}}$  becomes more significant. Stack and Chi's criteria states that for  $1 < M_{\text{chem}}/M_{\text{mech}} \leq 10$ , the degradation mechanism is one of corrosion enhanced wear. Using this criteria, it is observable that the fretting contacts in Method 1 is in a corrosion enhanced wear regime for all the displacements as shown in Figure 8-16. This therefore suggests that, the magnitude of  $+\alpha C_w$  in the expression of  $M_{\text{chem}}$  may exceed  $W_c$  hence making the contact a corrosion enhanced wear dominated. This further highlighting the importance of splitting  $C_w$  into its sub-factors i.e.  $\alpha C_w$  and  $\beta C_w$ . Furthermore, it was observed that with increase in fretting displacement amplitude, the degradation mechanism increasingly transitions towards a wear enhanced corrosion mechanism in which the contribution of  $W_c$  increases relative to  $\alpha C_w$ . This may be linked to reduction in contact pressures with larger fretting displacements.

The purpose of methods 2 and 3 was to identify the effect of surface history on the evolution of fretting corrosion so the displacements were performed in series. One of the key observations from method 2 in which the displacement amplitude increases was the gradual drop in both fretting current and energy dissipated (which represents interfacial friction) at the last displacement  $\pm 150 \mu\text{m}$ . The gradual drop in energy is likely due to tribochemical interactions at the interface which is triggered at a specific charge density as described by Yan et al [194, 215]. In both their studies, they proposed that the tribochemical film forms a physical barrier at the tribological interface thus significantly reducing charge transfer hence the reduction in current. Thus, this behaviour is characterised with an antagonistic interaction whereby  $\alpha C_w$  is negative ( $-\alpha C_w$ ). Assuming the friction modifying film reduced overall wear, the contact would also be characterised with a negative  $-\beta C_w$ .

Contrary to method 2, in method 3 where fretting started at the  $\pm 150 \mu\text{m}$  and decreased, fretting current dropped suddenly in response to a sudden drop in the interfacial friction however, the drop in current was short-lived despite the sharply reduced interfacial friction. This behaviour can be characterised partly by  $+\alpha C_w$  as the fretting current was seen to rapidly rise back up. At the least displacement ( $\pm 10 \mu\text{m}$ ) where both methods 1 and 2 experienced a partial-slip regime, interfacial slip ( $\delta_s$ ) increased 3x higher in method 3 thus rising above the gross slip criteria and generating higher fretting currents.

The transition to gross slip regime for  $\pm 10 \mu\text{m}$  in method 3 is an indication of how the contact conditions of a surface with history of wear and corrosion can significantly change. In this case, the central partial-stick region had been worn away from the initial large gross slip regime of  $\pm 150 \mu\text{m}$  hence there was no elastic compliance at the interface by the time the displacement reached  $\pm 10 \mu\text{m}$ . More so, the 3D surface analysis in Figure 8-14 reveal evidence of a micro-grooved pathway created through third-body re-alignment at the interface.

Furthermore, Figure 8-16 shows the  $M_{\text{chem}}/M_{\text{mech}}$  ratio for the summed up total mass losses of all the displacements assessed using the three methods. Using Stack and Chi's criteria, it is observable that both methods 1 and 2 are



in a corrosion enhanced wear regime whilst method 3 is in a corrosion dominated regime. This observation is clinically relevant in the context of re-using well-fixed implanted stems during a THA revision procedure. In light of this result, it is of utmost importance for surgeons to carefully inspect the stem for signs of wear and corrosion as the effect of such surface history could accelerate the interface into a corrosion degradation mechanism.

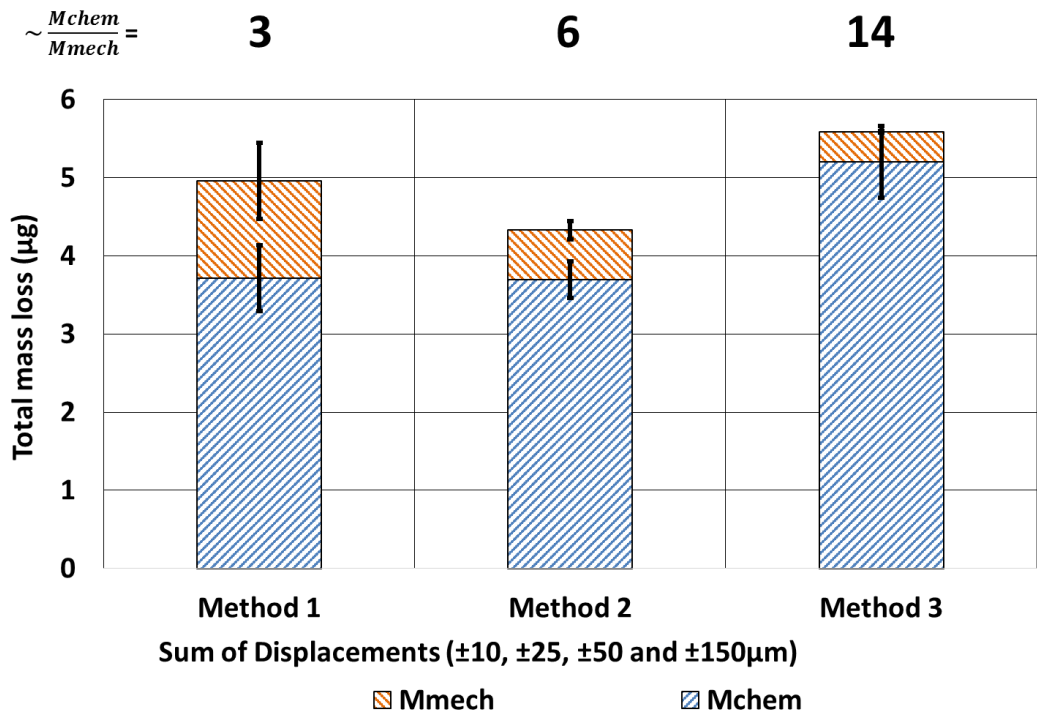


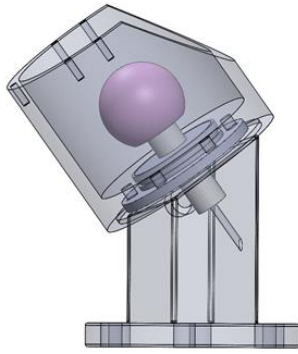
**Figure 8-16 – The sum of  $M_{mech}$  and  $M_{chem}$  for all displacements in the three methods of assessment. The  $M_{chem}/M_{mech}$  ratio for each method is also shown above.**

## Chapter 9 Assessment of fretting current from the head-neck metal-metal and ceramic-metal taper interface

### 9.1 Introduction

The previous three chapters have assessed fretting corrosion mechanisms of metal – metal and ceramic – metal material combinations using a fretting tribometer. However, a rather complex and composite tribological interface is established at the real modular taper junction. This is exemplified through various wear patterns and damage modes which are a result of multi-factorial loading profiles, toggling motion, surface topography and several other factors as described in literature [216].

*In-vitro* fatigue configurations such as described in section 3.3.3 is the standard approach through which short-term and long-term tribocorrosion tests are carried out on modular tapers. Majority of fatigue assessment aim to resolve the role of individual factors or combinations of factors on the evolution of fretting corrosion. The aim of the study presented in this chapter is to assess the effect of frequency variation, mean load variation and cyclic load variation for four relevant material combinations namely: CoCrMo – CoCrMo, CoCrMo – Ti6Al4V, Biolox – CoCrMo and Biolox – Ti6Al4V. A schematic outline of the loading profile and analysis performed in this chapter are shown in Figure 9-1.



	Metal – Metal	Ceramic – Metal
CoCrMo stem	<p>CoCrMo – CoCrMo</p>	<p>BioloX – CoCrMo</p>
Ti6Al4V stem	<p>CoCrMo – Ti6Al4V</p>	<p>BioloX – Ti6Al4V</p>

Loading profile

Effect of frequency variation  
(1 → 2 → 5 Hz)

Effect of mean load variation  
(0.8 → 1.8 → 2.8 kN)

Effect of cyclic load variation  
(±0.5 → ±1.5 → ±2.5 kN)

Electrochemical analysis

OCP & Potentio-static (0 V)

Mechanical analysis

Cross-head migration

Taper separation force

Wear pattern

CMM  
(CC, CT, BC & BT)

Figure 9-1 – Outline of the fatigue experiments and analyses performed in chapter 9. B, C and T represents BioloX, CoCrMo and Ti6Al4V respectively.

Clinically relevant contexts are provided for the fatigue cyclic loading profiles assessed in this chapter. These are outlined below:

**Frequency variation** – ASTM F 1875 – 98 prescribes a frequency of 5 Hz for assessing fretting corrosion damage, and it also recommends 1 Hz and/or 2 Hz for experiments that incorporate electrochemical assessment. Several other studies have conducted fatigue loading experiments using frequencies ranging from 0.66 Hz to 15 Hz [115, 118, 125, 217, 218]. However, to date, only the study by Brown et al [116] had assessed the effect of frequency on fretting corrosion using realistic head-neck taper components and their study was only conducted on CoCrMo – Ti6Al4V combination. Therefore this section aim to assess the effect of frequency variation (1, 2 and 5 Hz) on fretting corrosion current for the four material combinations.

**Mean load variation** – The study by Bergmann et al [122] highlighted the significant role that patient weight plays on the peak loads experienced at the hip. Their study showed that for the DLA of going down the stairs, peaks loads were more than double from 2 kN for a 75 kg patient to 4.2 kN for a 100 kg patient. Thus, a 25 kg weight increase yielded an additional 2 kN to the peak load experienced at the hip. Therefore in this section, the effect of mean load variation (0.8, 1.8 and 2.8 kN) were examined. By ‘mean load variation’ it is meant that, the effect of patients’ weight that yields an additional 1 kN load on an implant is examined for the four material combinations. This was done in isolation of cyclic load as much as possible by keeping the cyclic load at  $\pm 0.5$  kN.

**Cyclic load variation** – Bergmann et al’s study also reported the loading profile of diverse DLAs, all of which occur at various amplitudes of cyclic loading. For example, while standing on one leg may result in amplitudes of  $\sim 1$  kN, stumbling loads can reach amplitudes of up to 9 kN [122]. This section therefore aims to examine the fretting current of the four material combinations whilst subjected to varied cyclic loads of  $\pm 0.5$ ,  $\pm 1.5$  and  $\pm 2.5$  kN.

**Systemic effects** – Fatigue studies like this have previously being conducted in an incremental order where parameters are tested in series to each other

[118]. Similarly, in this study, all three aspects of the study outlined above were conducted in series to each other but not without caution. It was anticipated that systemic effects such as: lengthy anodic polarisation of the components; migration of the trunnion taper into the female bore over time and plastic deformation of the materials may occur. Therefore, a series of checks (partly in accordance with ASTM F 1875 – 98) were implemented after every section. Thus the systemic effect were monitored.

An example of what a full experiment looks like is shown in Figure 9-2. All measurements are an average of  $n = 3$  tests except for BioloX – Ti6Al4V which is an average of  $n = 2$  data. The error bars in this case represent the difference of two tests because observations from CMM surface analysis reveal evidence of misalignment. Therefore the results from the third test are reported separately in section 9.5.

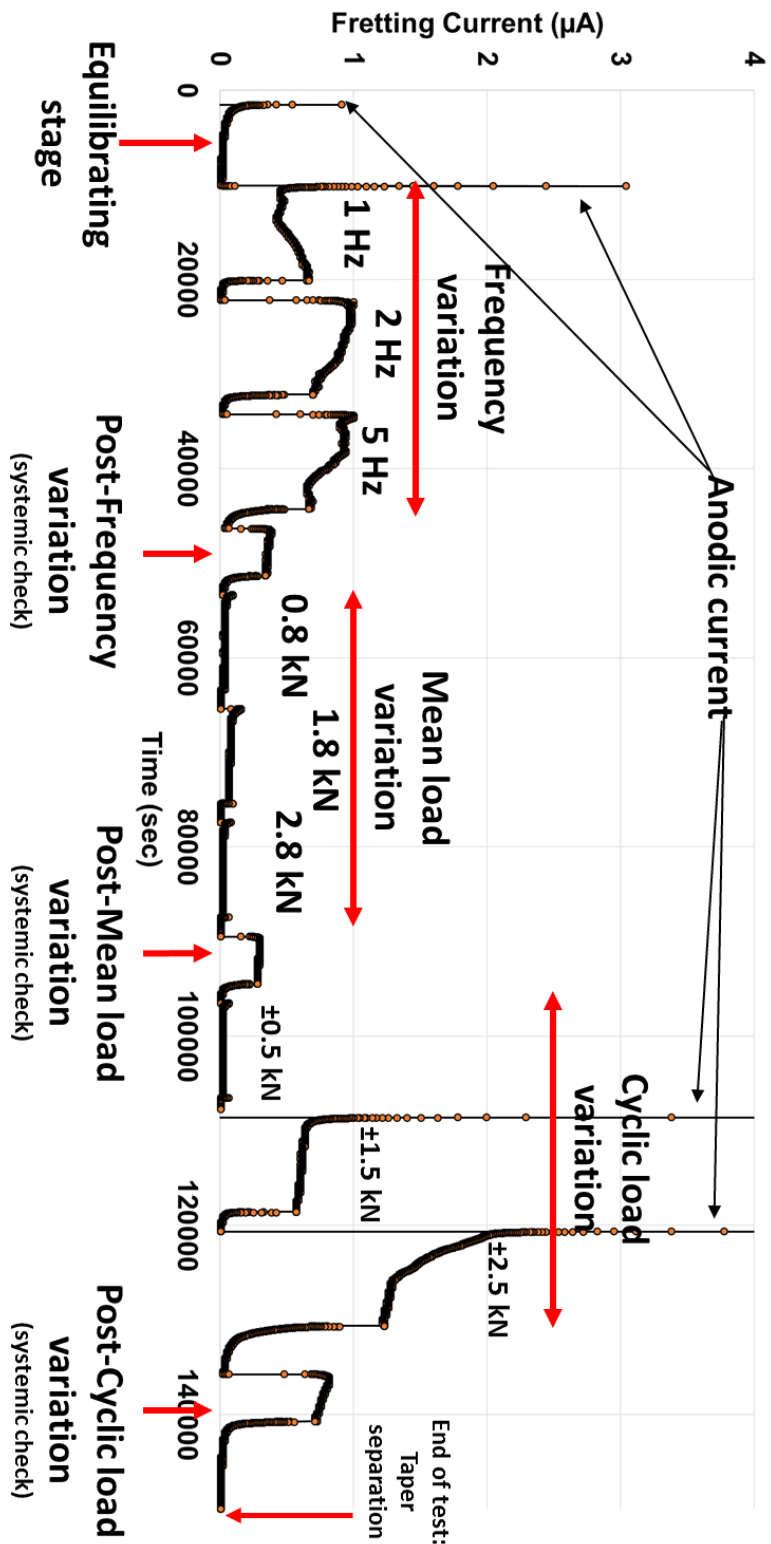


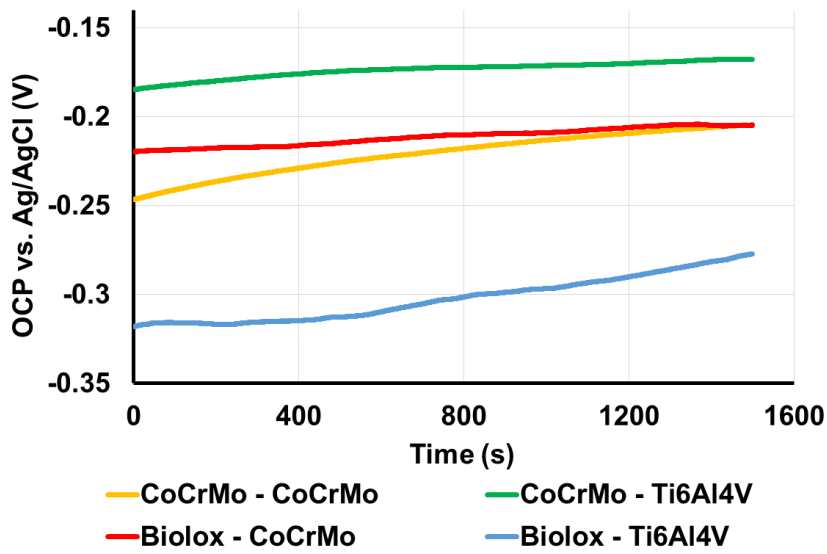
Figure 9-2 – Fretting current vs. time plot for a complete fatigue loading test.

## 9.2 Electrochemical results

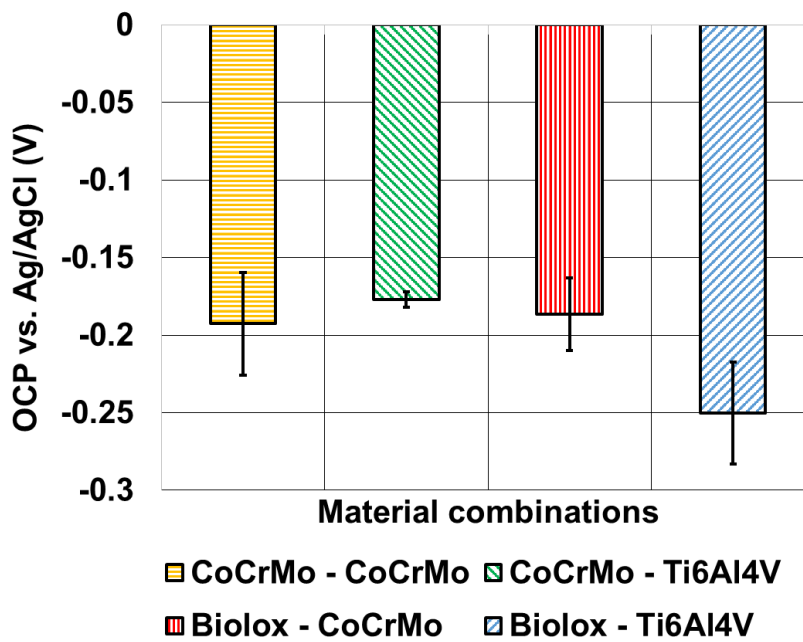
In this section, all electrochemical results pertaining to the static and dynamic stages of the tests are reported. During the static stages, OCP and anodic current transients from the potentiostatic polarisation were monitored respectively. Subsequently, in the dynamic stages, the fretting current and cumulative charge of the variable loading profiles are reported. It is worth noting that in most cases, the scale of the y-axis for both fretting current and cumulative charge of BioloX – Ti6Al4V are much lower than the other combinations. This is because a much smaller fretting current emanated from the contact in comparison to the others.

### 9.2.1 Open circuit potential

The results in Figure 9-3a shows the OCP profile for each material combinations. All combination are seen to ennobles over 1500 seconds after which the anodic polarisation to 0V vs. Ag/AgCl is imposed. Figure 9-3b shows the average potential for each material combination at the point of polarisation. The magnitude of the values in Figure 9-3b also corresponds to the average over-potential applied to each material combination. On average, a similar over-potential of <200 mV is applied for all the material combinations involving CoCrMo. It was only for BioloX –Ti6Al4V combination that an average over-potential of 250 mV was applied.



(a)



(b)

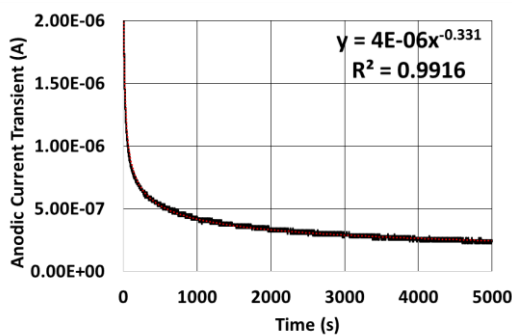
Figure 9-3 – OCP of all combinations prior to potentiostatic polarisation of 0V vs. Ag/AgCl, a) OCP vs. Time plot b) average OCP and applied over-potential.



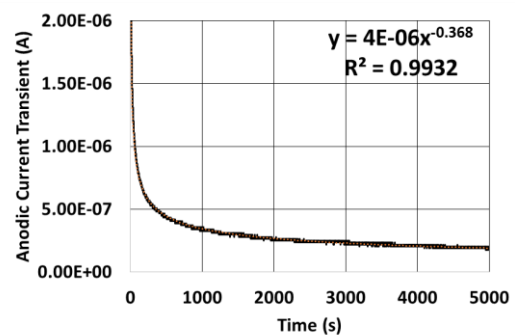
## 9.2.2 Static anodic current transient

Following the anodic polarisation, the anodic current transient was monitored for each material combination. Figure 9-4 (a – d) shows the exponential drop in current for CoCrMo – CoCrMo, CoCrMo – Ti6Al4V, BioloX – CoCrMo and BioloX – Ti6Al4V respectively. The denotation CC, CT, BC and BT are also used sometimes to represent the four material combinations respectively. An exponential curve with the expression  $Y = mX^b$  was fitted to each current transient. As already described in the methodology section (section 4.3.2) ‘m’ represents the peak current ( $I_{\text{peak}}$ ) which is the difference between the maximum current  $I_{\text{max}}$  and the base line current at  $t = \infty$  [175].

The result in Figure 9-4 a & b represents the two metal – metal combination (CC and CT respectively) and the result in Figure 9-4c & d represent the two ceramic – metal combinations (BC and BT respectively). It is observable that the peak current for the metal – metal combination is an order of magnitude higher than the ceramic – metal combination. The same is the case for the average base line current at  $t = 7500$  seconds in Figure 9-4e which corresponds to the current immediately prior to dynamic loading. In order to determine  $I_{\text{max}}$  accurately, a higher resolution data sampling rate at 10 points per sec was used for  $n = 1$  of each combination. As expected,  $I_{\text{max}}$  in Figure 9-4f is also measured to be an order of magnitude different in the currents. These results highlight the effect of having two conductive metal – metal components vs. a single conductive surface in the ceramic – metal combinations.



(a)



(b)

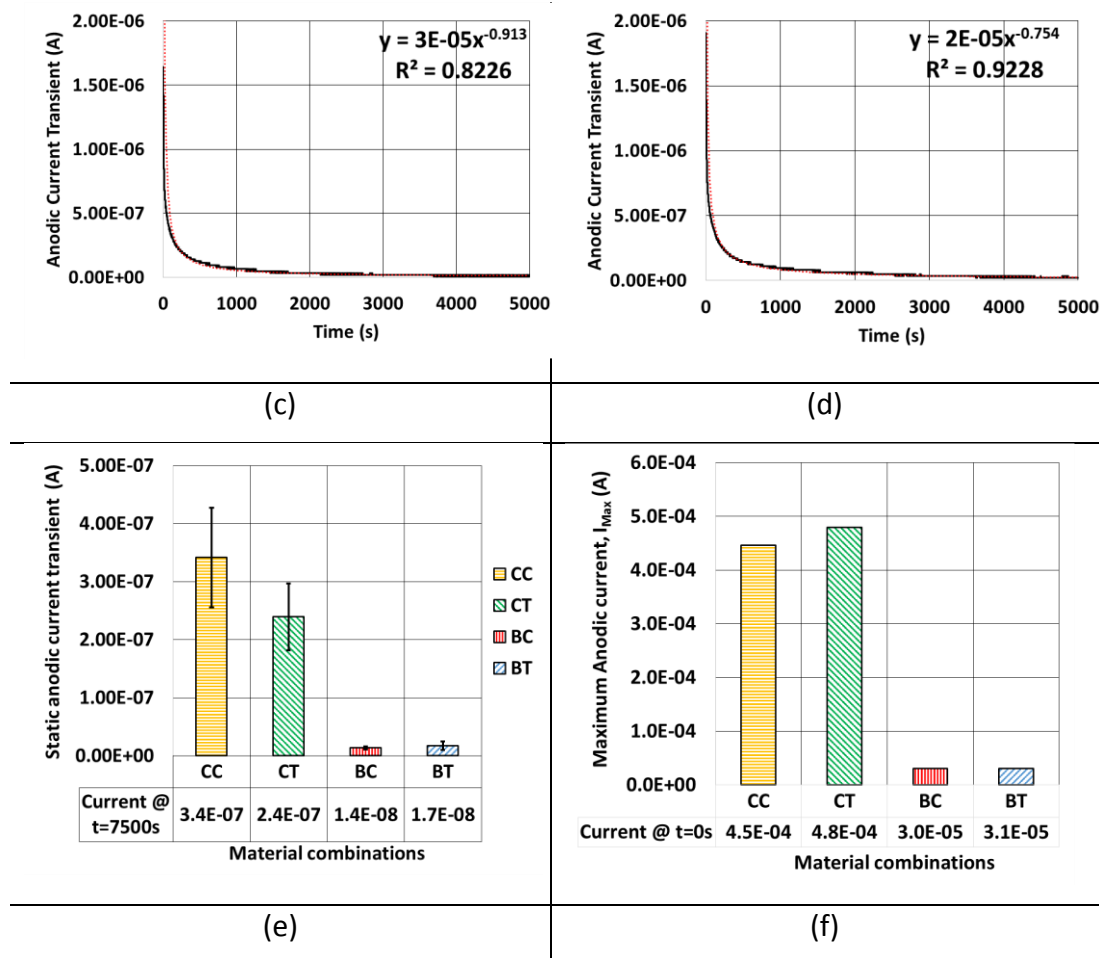
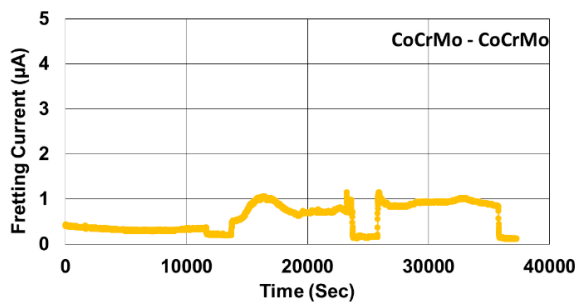


**Figure 9-4 – Anodic current transient of all material combinations under static conditions: a) CoCrMo – CoCrMo; b) CoCrMo – Ti6Al4V; c) Biolox – CoCrMo; d) Biolox – Ti6Al4V; e) average current at the time  $t = 7500$  Sec and f) current at the time  $t = 0$  Sec ( $I_{max}$ ).**

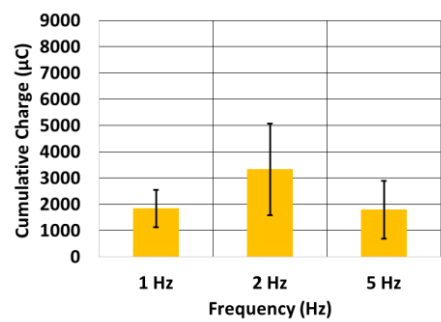
### 9.2.3 Frequency variation

The fretting current vs. time graphs for each frequency (1, 2 and 5 Hz) and all four material combinations are outlined along a single column in Figure 9-5. They appear in the same order (a – d) of CoCrMo – CoCrMo, CoCrMo – Ti6Al4V, Biolox – CoCrMo and Biolox – Ti6Al4V respectively. The column on the right (e – h) corresponds to the average cumulative charge derived from the fretting current transient. Therefore, consider that the cumulative charge represents the quantitative average of the fretting currents emanated over a time period, the cumulative charge (e – h) is used from this point onwards as the main method of describing fretting current of the material combinations.

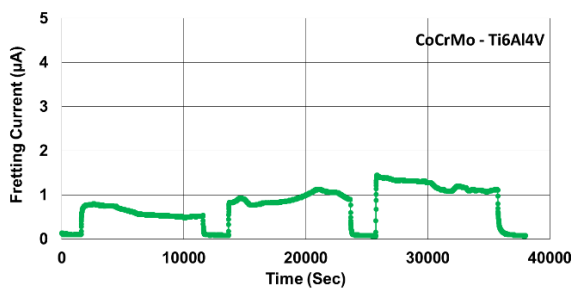
It is observable from Figure 9-5e that within the margins of error, there is no significant difference in the cumulative charge for all three frequencies of CoCrMo – CoCrMo. On the other hand, Figure 9-5f shows a much lower cumulative charge per 10000 cycles at 5 Hz frequency for the CoCrMo – Ti6Al4V combination despite a slightly higher fretting current at 5 Hz than at the other frequencies (Figure 9-5b). This is therefore indicating that the increase in fretting current was not proportional to the number of cycles of fretting per sec. As for both ceramic – metal combinations in Figure 9-5g and h, the cumulative charge decreases as the frequency increases.



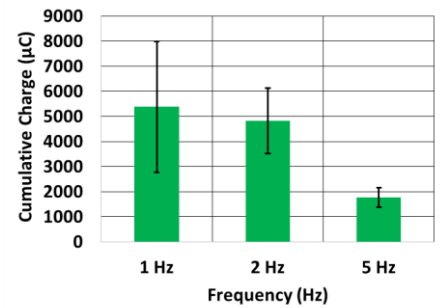
(a)



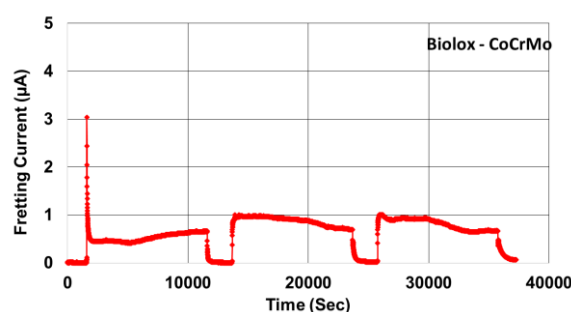
(e)



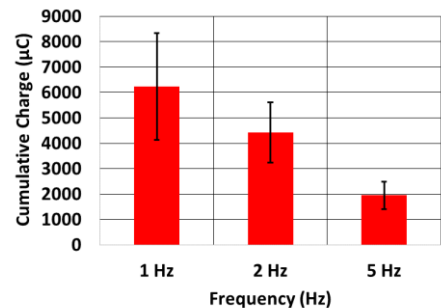
(b)



(f)



(c)



(g)

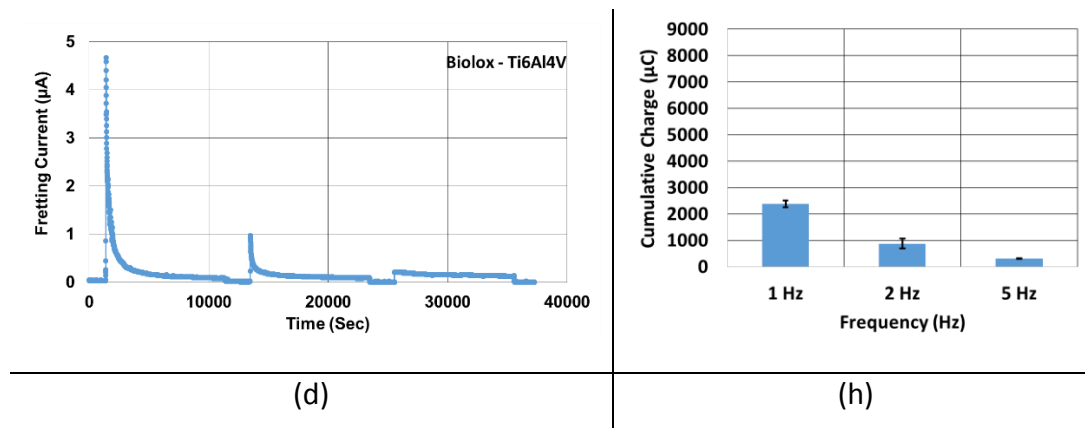


**Figure 9-5 – Fretting current (a, b, c, d) and Cumulative charge per 10000 cycles (e, f, g, h) of the material combinations; these were subjected to  $\pm 1.5$  kN cyclic load and mean load of 1.8 kN with varied frequencies of 1, 2 and 5 Hz.**

#### 9.2.4 Mean load variation

The fretting currents in Figure 9-6a – d are multiple times lower than that of the frequency variation for all material combinations likely due to the low cyclic loads used for the assessment of mean load variation. This is due to the minimal cyclic load used for this assessment. In Figure 9-6e it can be observed that the cumulative charge for CoCrMo – CoCrMo is higher for mean loads above 0.8 kN. A similar pattern is seen for CoCrMo – Ti6Al4V in Figure 9-6f. However, in Figure 9-6g, cumulative charge was about double both the lower and higher mean loads for BioloX – CoCrMo at 1.8 kN. For BioloX – Ti6Al4V in Figure 9-6h it is observable that the cumulative charge at loads lower than 2.8 kN are negligible and considering the fretting current plot in Figure 9-6d, it is observable that the cumulative charge measured at 2.8 kN was not due to fretting current but only a result of the anodic current. It is important to note that the anodic current is main constituted by the current generated through ionic dissolution and the current consumed in the process of film formation.

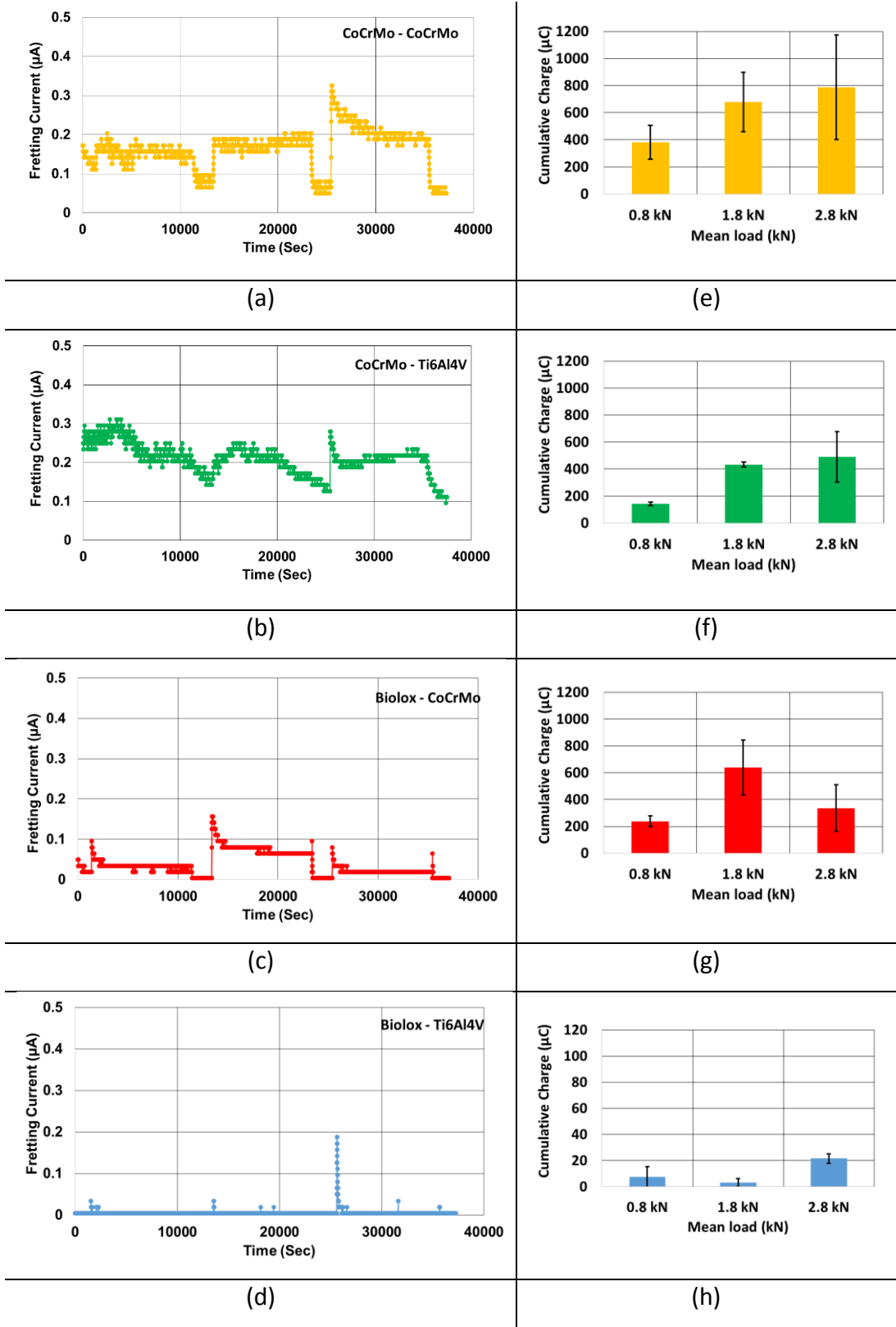
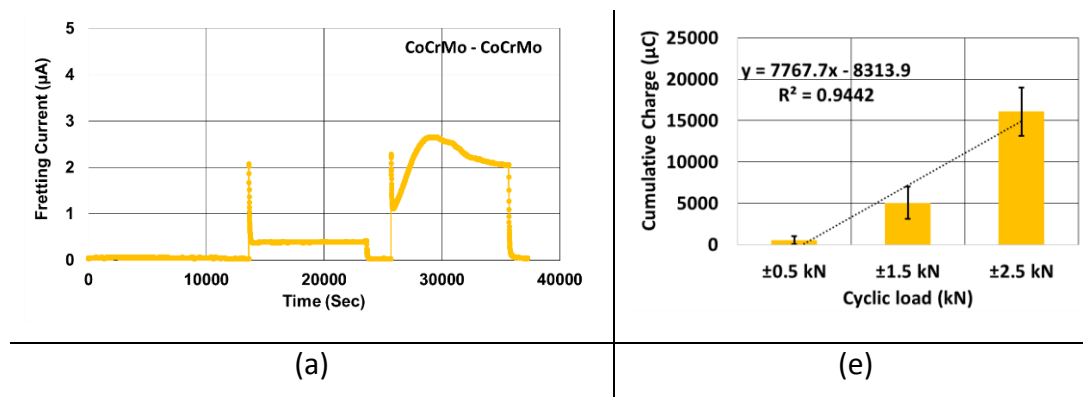


**Figure 9-6 – Fretting current (a, b, c, d) and Cumulative charge (e, f, g, h) of the material combinations; these were subjected to a cyclic load of  $\pm 0.5$  kN at 1 Hz with varied mean load of 0.8, 1.8 and 2.8 kN.**

## 9.2.5 Cyclic load variation

From Figure 9-7 it is observable that all material combinations displayed an increase in fretting current (a – d) and cumulative charge (e – h) as cyclic load amplitude increased. Therefore, a linear correlation was fitted to all of the combinations in e – h. It is observable that the rate of cumulative charge increase for CoCrMo – CoCrMo and Biolox – CoCrMo were similar although the ceramic – metal combination was higher. On the other hand, the rate of cumulative charge increased in CoCrMo – Ti6Al4V and Biolox – Ti6Al4V were much similar. Interestingly, the rate of cumulative charge with increasing cyclic loads was found to be nearly double for the metal – metal and ceramic – metal systems with CoCrMo stem relative to those with Ti6Al4V stems.

When the fretting currents in Figure 9-7 (a – d) is examined, it is observable that for cyclic loads of  $\pm 1.5$  and  $\pm 2.5$  kN in all combinations except CoCrMo – Ti6Al4V at  $\pm 1.5$  kN an anodic current is observed upon initiation of cyclic loads at the contact. The anodic current was quite significant for Biolox – CoCrMo and even more so for Biolox – Ti6Al4V. Interestingly, it was further observed that all combinations involving CoCrMo experienced a quick transition from anodic current to fretting current while Biolox – Ti6Al4V experienced a lengthy transition from anodic current to fretting current. In addition, it appears that the higher the cyclic load, the longer it take for a complete transition to fretting current thus indicating a characteristic mechanism of Ti6Al4V alloy upon abrasion.



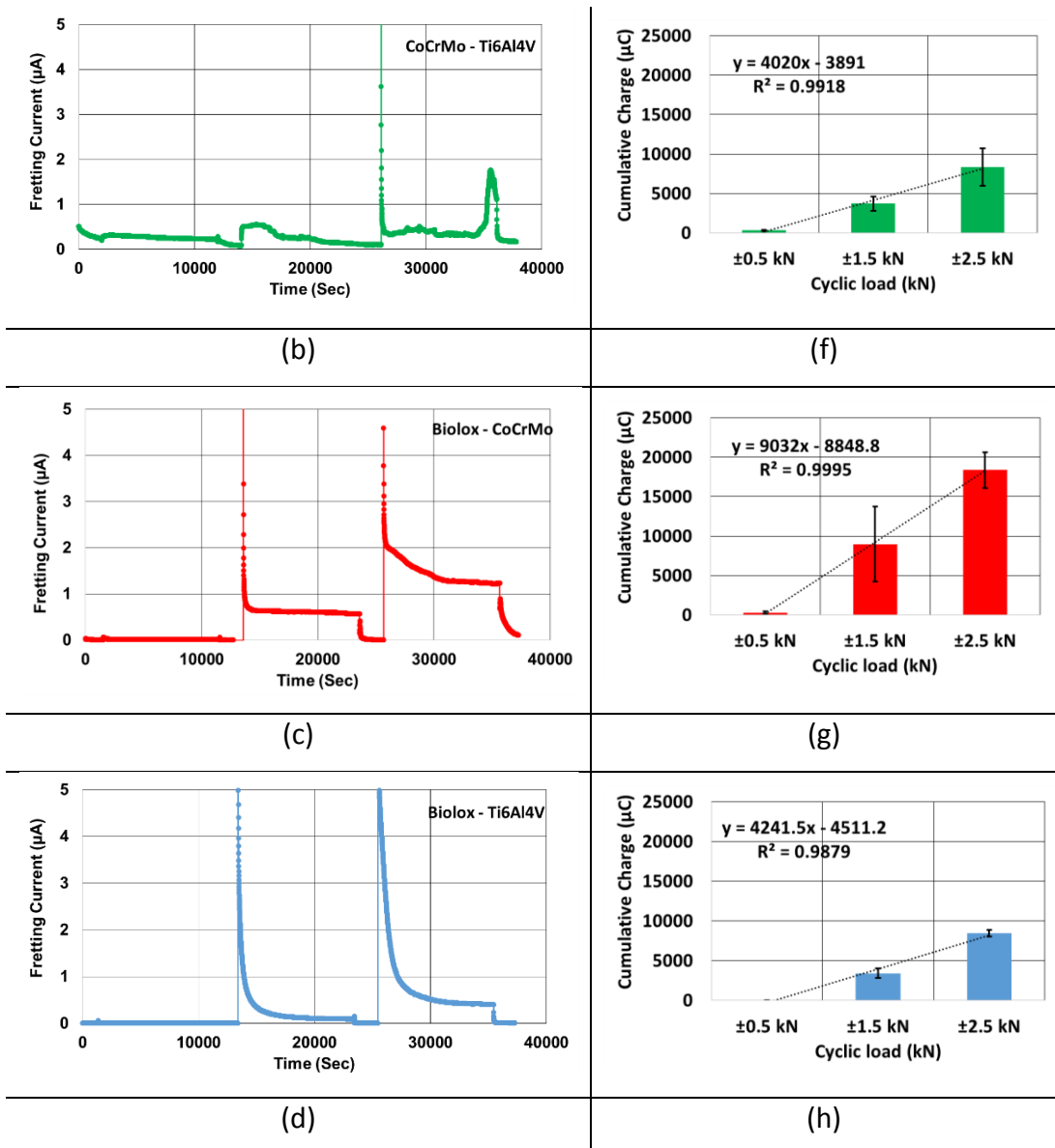
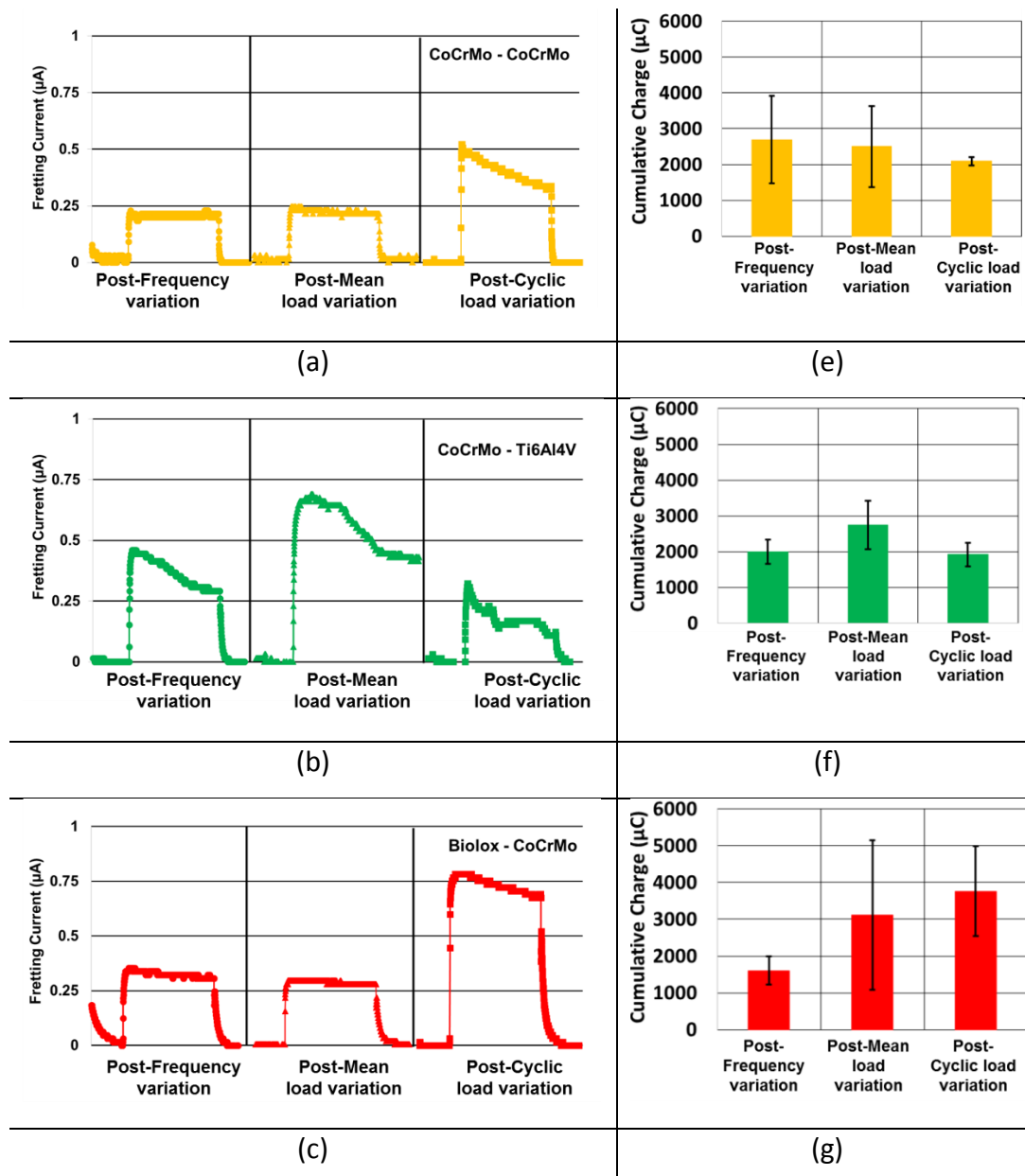


**Figure 9-7 – Fretting current (a, b, c, d) and Cumulative charge (e, f, g, h) of the material combinations; these were subjected to mean load of 2.8 kN at 1 Hz with varied cyclic load of ±0.5, ±1.5 and ±2.5 kN.**

### 9.2.6 Systemic checks

For the systemic checks, Figure 9-8e shows that there are no significant differences in the cumulative charge for CoCrMo – CoCrMo at the end of each loading profiles. Although Figure 9-8a shows an example of one of the test where systemic effects were reflected in the fretting currents after the largest cyclic load of fretting were applied. For the CoCrMo – Ti6Al4V, Figure 9-8f reveals that the cumulative charge is highest post-mean loads. This is

reflected in the magnitude of the fretting current in Figure 9-8b and for this particular test only, it was observed that the fretting current did not return back to zero when load was removed. For both ceramic – metal combinations in Figure 9-8 g and h, the cumulative charge were greatest for the post-cyclic load variation.





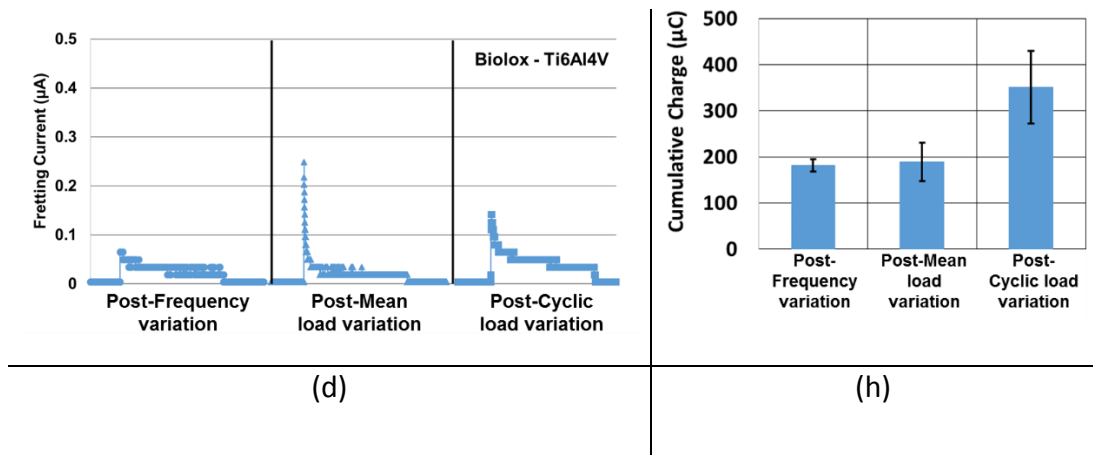


**Figure 9-8 – Fretting current (a, b, c, d) and Cumulative charge (e, f, g, h) of the material combinations; these were subjected to cyclic load of  $\pm 1.5$  kN and mean load of 1.8 kN for 5000 seconds at 1 Hz.**

### 9.3 Mechanical results

It was not possible in this study to obtain information regarding the relative displacement occurring at the taper interface during fatigue loading. However, by tracking the digital position of the cross-head through which the fatigue load is applied, it is possible to obtain information regarding the displacement of the cross head in response to static and dynamic loads. Figure 9-9 shows the graph of cross-head displacement against time from the fatigue test of all material combinations. A schematic image describing the cross-head displacement is also shown as an inset within Figure 9-9.

The schematic diagram represents how femoral head migration can be a contributing factor to the total cross-head displacement measured. The other main factor that may contribute to the cross-head displacement would be the elastic deformation of the spigot during compressive loads. The deformation is expected to be greater for Ti6Al4V spigot being the less stiffer component.

At the beginning of the equilibrating stages, 0.3 kN of static compressive load is applied. From Figure 9-9 it is observable that the load resulted in cross-head displacement for all materials combinations except CoCrMo – CoCrMo. On the other hand, the displacement measured for the Biolox – CoCrMo is seen to be double those of the combinations with Ti6Al4V spigot – both of

which were very similar. Considering that there was no cross-head displacement measured for the CoCrMo – CoCrMo combination, this suggests that no measurable elastic deformation of the CoCrMo spigot occurred during the application of static load. Therefore, the cross-head displacement measured for BioloX – CoCrMo is most likely entirely due to the femoral head migration. On the other hand, it is difficult to know how much of the cross-head displacement for both combinations with Ti6Al4V spigots is due to femoral head migration however, considering the relatively low static load, it is likely that elastic deformation would also be negligible for the Ti6Al4V spigot.

A compressive load of 1.8 kN was applied prior to the initiation of dynamic loading. It was observed that the CoCrMo – CoCrMo combination experienced the least cross-head displacement while the displacement in BioloX – CoCrMo is double that of CoCrMo – CoCrMo. The combinations with Ti6Al4V spigots were both very similar, however, the displacement for CoCrMo – Ti6Al4V was slightly larger than BioloX – Ti6Al4V. More so, throughout the various dynamic loading stages, all the material combinations appear to have a similar rate of increase in cross-head displacement which suggest similar rates of femoral head migration.

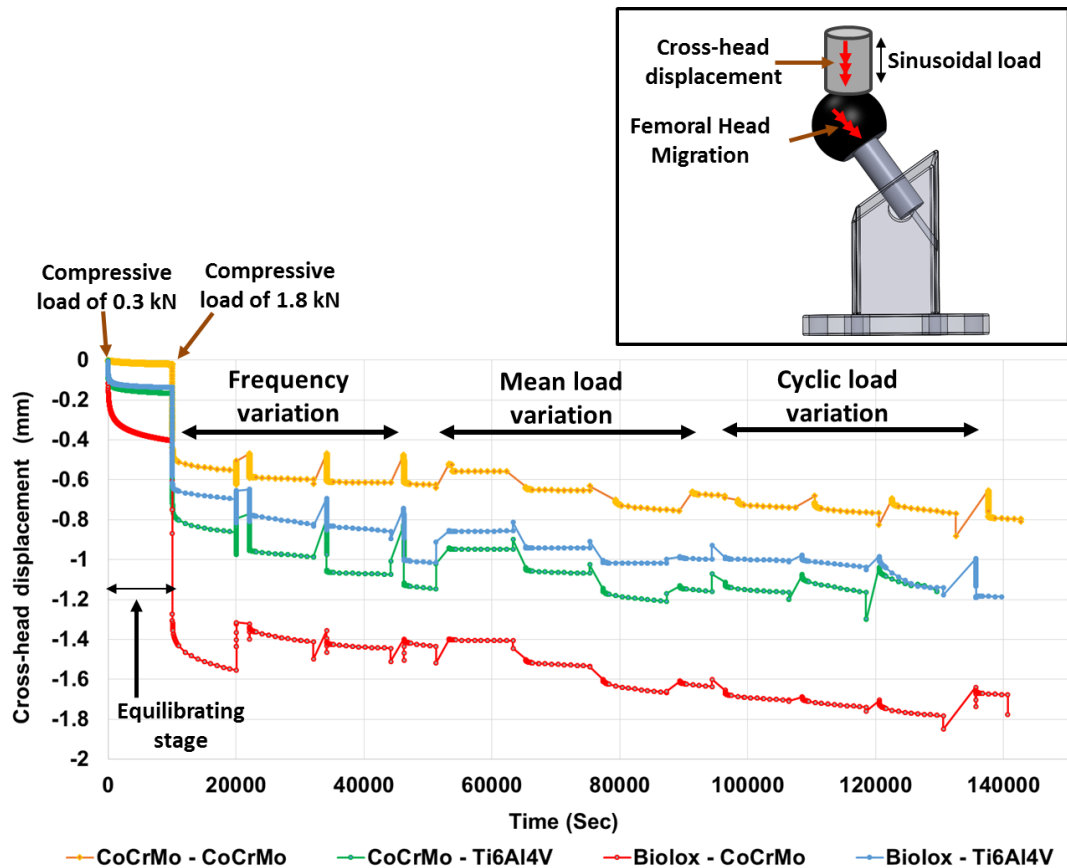


**Figure 9-9 – Cross-head displacement vs. Time graph. Each data point for all material combinations during the dynamic stages represents a point every 1000 seconds of the cross-head position. At the top right corner, a schematic of the cross-head displacement is shown.**

At the end of each test, the force required to separate the femoral head from the male taper is shown in Figure 9-10. The result shows that the separation forces for CoCrMo – Ti6Al4V and BioloX – Ti6Al4V were very similar whereas the BioloX – CoCrMo differs from the CoCrMo – CoCrMo by almost 1 kN. Quite expectedly, the required taper separation force was highest for the BioloX – CoCrMo combination which in Figure 9-9, experienced the largest femoral head migration. Similarly, the CoCrMo – CoCrMo combination which experienced the least femoral head migration required the least separation force. Both CoCrMo –Ti6Al4V and BioloX – Ti6Al4V combinations which were in the middle for femoral head migration, also experienced very similar separation loads that fall in the middle of the greatest and the least taper separation forces.

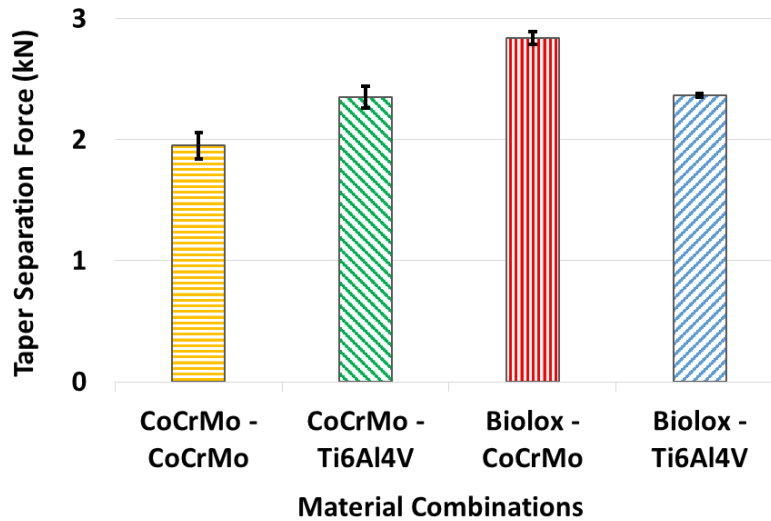


**Figure 9-10 – Taper separation force for all material combinations**

## 9.4 Surface Analysis

The use of CMM in this chapter was solely to identify the wearing pattern and taper engagement pattern for both male and female tapers across the four material combinations. In most cases, between Figure 9-11 to Figure 9-15, a *Customised* 3D reconstruction of the tapers was presented. By ‘Customised’ it is meant that, regions with excessive deviation from the conical reference, either through material gain or material loss appear in bright colour while the other regions are masked and therefore appear in black. Other exceptions to this are described in each specific figure. All material combinations analysed in this study had a positive taper (cone) angle difference. A positive taper angle difference means that the female taper angle is greater than the male taper angle therefore, their initial contact occurs at the proximal-end [219].

### 9.4.1 CoCrMo – CoCrMo

From Figure 9-11a it is observable from the female taper that the taper engagement is circumferential however, from the male taper in Figure 9-11b, the wearing pattern can be described as a coup-countercoup pattern as

described in reference [216]. This wear pattern is generally an indication of a toggling motion.

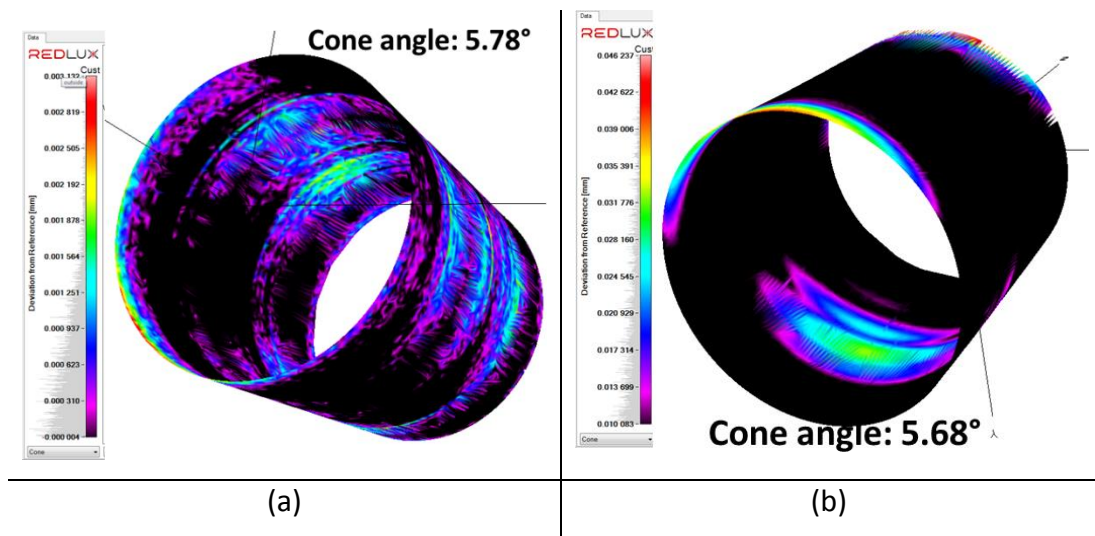


**Figure 9-11 – 3D reconstruction of CoCrMo – CoCrMo taper interface:  
a) CoCrMo female taper, b) CoCrMo male taper.**

#### **9.4.2 CoCrMo – Ti6Al4V**

Figure 9-12a shows that the CoCrMo female taper was engaged on two opposing sides and from Figure 9-12b, the fretted region on the Ti6Al4V male taper is seen to be present on two opposing sides. However, the wear pattern observable shows that fretting was focused at the proximal and near-distal ends of one side as well as distal and near-proximal ends of the opposing side. Thus, a toggling (shimmying) motion is also described at this interface.

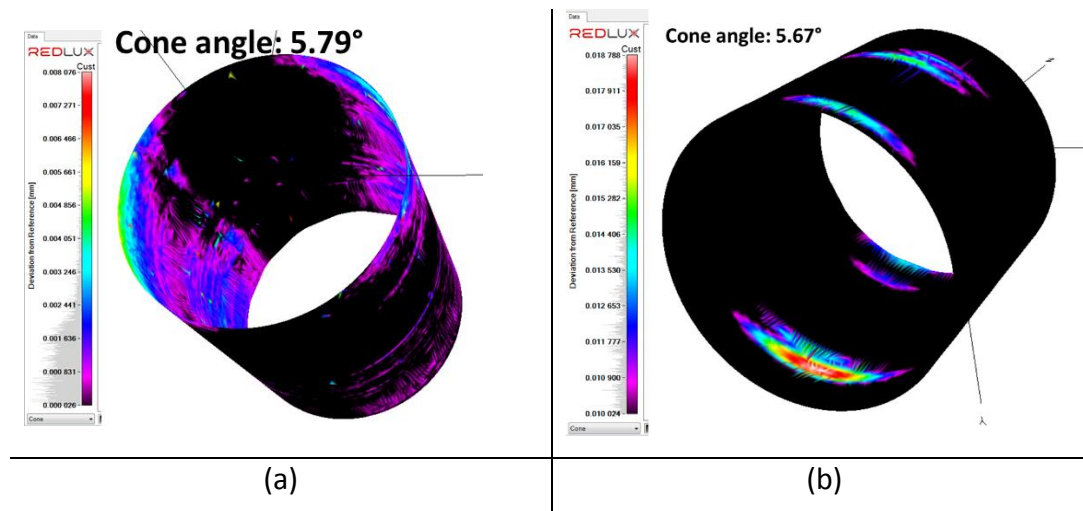


**Figure 9-12 – 3D reconstruction of CoCrMo – Ti6Al4V taper interface: a) CoCrMo female taper, b) Ti6Al4V male taper.**

### 9.4.3 BioloX – CoCrMo

The pattern identified on the BioloX femoral taper in Figure 9-13a appears similar to a coup-counter coup pattern. However, the pink colour of the BioloX head in the image shown in Figure 9-13b helps to physically examine the female taper. The coup-counter coup pattern is seen to be mainly material transfer from the metal component unto the ceramic as often observed at the ceramic – metal taper interface [72, 219].

On the other hand, in Figure 9-13c the unmodified ‘Full’ 3D reconstruction of the CoCrMo male taper displayed an alternating colour effect. This effect is an indication that no preferential wearing pattern was observable across the entire taper surface. The ‘interchanging colour’ which only occurs on grooved male tapers is a result of the interchanging contact of the measuring stylus between the troughs and peaks of the grooved taper. This is to suggest that wearing occurred uniformly across the peaks of the grooved male taper, thus suggesting a circumferential engagement with the female taper. Therefore, the wear from any particular region on the taper surface was not significant enough to create a substantial deviation from the conical reference. This is contrary to the observations made for the metal – metal combinations.

Figure 9-13d shows the attempt to create a 'Customised' reconstruction of the male taper in order to confirm the absence of any preferentially worn region. As expected, no preferentially fretted or worn area was identifiable. However, Figure 9-13a gives an indication that a preferential transfer of material exist hence the displayed coup-counter coup pattern.

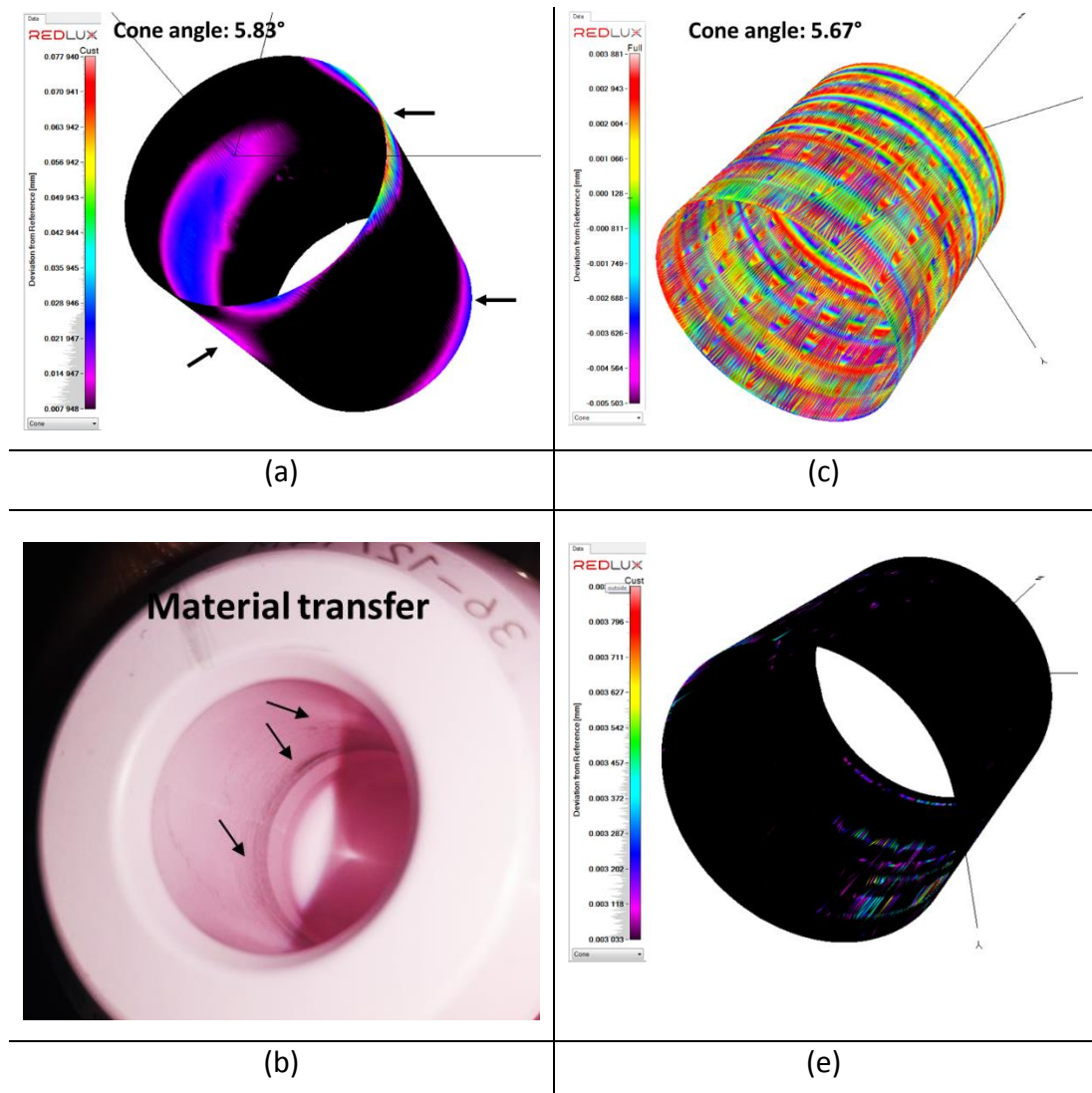


**Figure 9-13 – 3D reconstruction of Biolox – CoCrMo taper interface: a) Biolox female taper, b) Image of the Biolox female taper, c) Full 3D reconstruction of CoCrMo male taper d) Customised reconstruction of CoCrMo male taper.**

### 9.4.4 Biolox – Ti6Al4V

A similar observation to the Biolox – CoCrMo ceramic – metal combination is also seen for the Biolox – Ti6Al4V. Figure 9-14a shows a pattern at the distal and proximal ends of the Biolox female taper. The pattern is confirmed in Figure 9-14b as material transferred from the Ti6Al4V. It appears more prominent at this interface than the Biolox – CoCrMo interface. The same ‘alternating colour’ effect is observed for the Ti6Al4V in Figure 9-14c and Figure 9-14d shows no evidence of preferential wearing pattern. Similarly, this is an indication of uniform engagement of the Ti6Al4V male taper into the ceramic female taper.

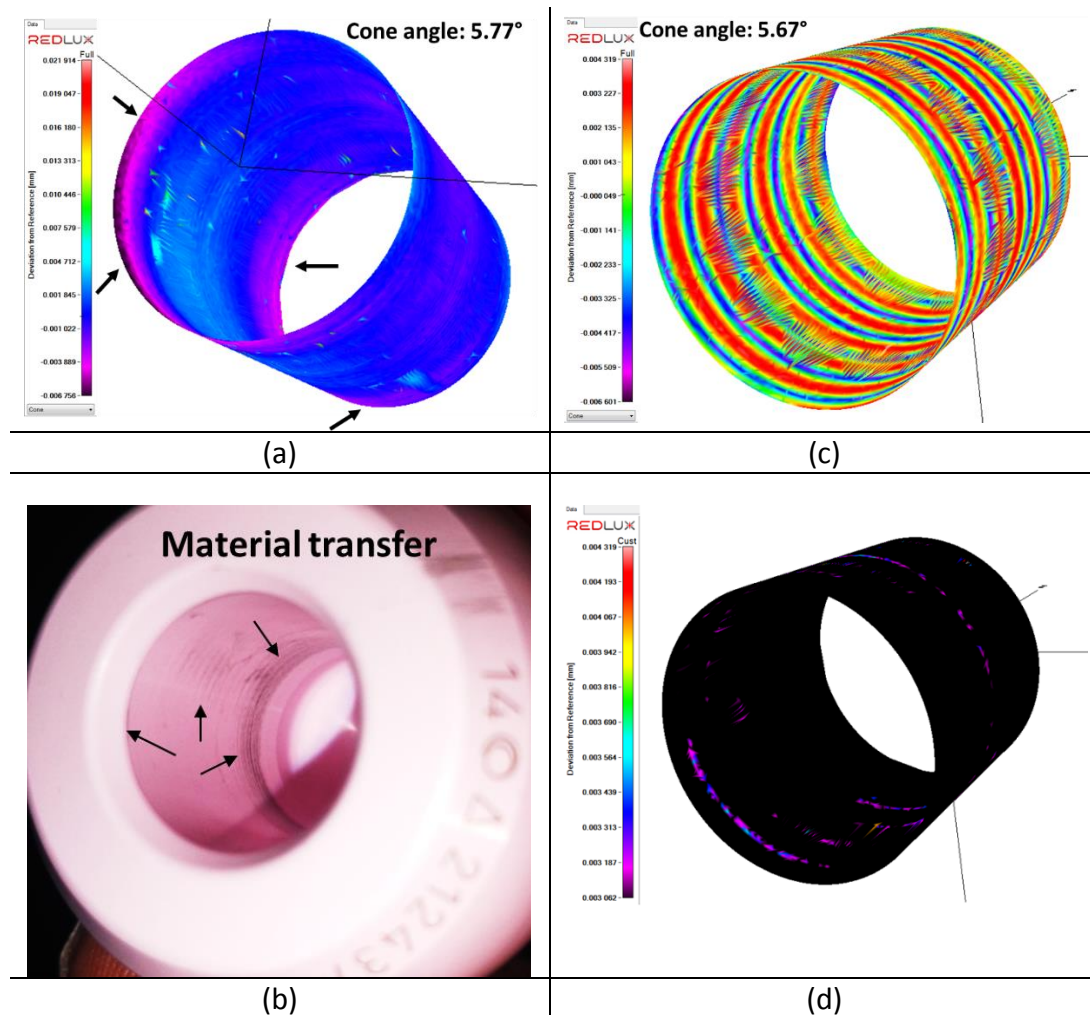


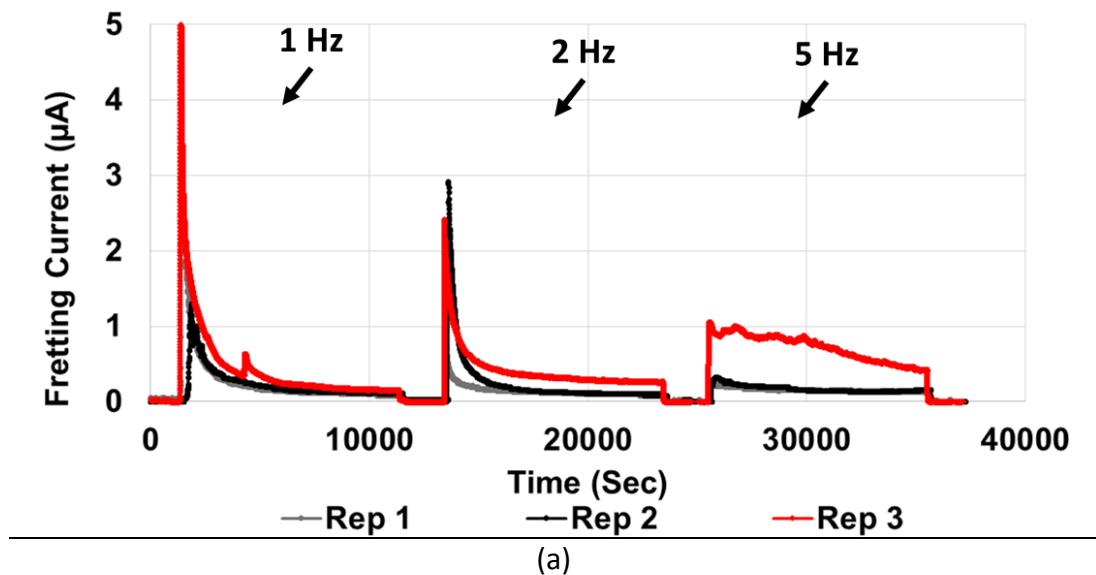
Figure 9-14 – 3D reconstruction of Biolox – Ti6Al4V taper: a) Biolox female taper, b) Image of the Biolox taper c) Full 3D reconstruction of Ti6Al4V male taper, d) Customised reconstruction of Ti6Al4V male taper.

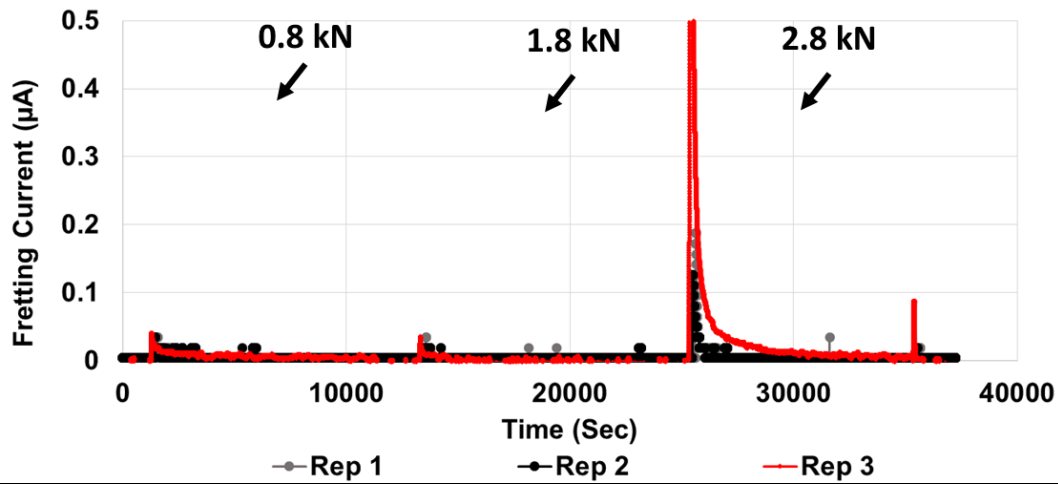


## 9.5 The case of misalignment

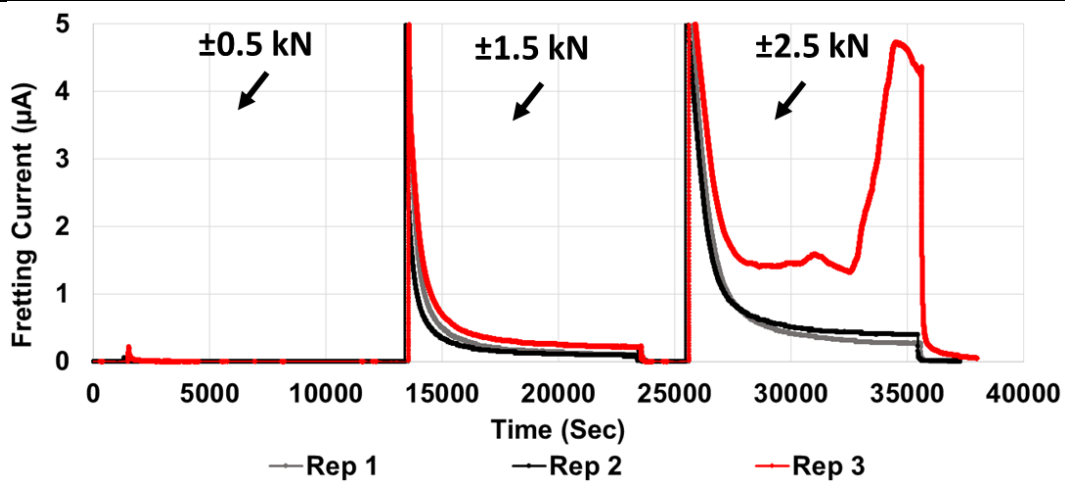
A total of three test were conducted for Biolox – Ti6Al4V combination. For one of the repeats, the fretting current and anodic current was found to be significantly higher than the other repeats. The differences are most substantial at the highest frequency of 5 Hz (see Figure 9-15a); the highest mean load of 2.8 kN (see Figure 9-15b) and the fretting currents peaked at a magnitude ten-times higher for the cyclic load at  $\pm 2.5$  kN in Figure 9-15c.

The 3D reconstruction of both male and female taper was analysed. Figure 9-16a revealed that the Biolox was abraded from the near-distal entrance of the female taper down towards the proximal end by the Ti6Al4V metal. This could only mean that the male taper was misaligned with respect to the Biolox female taper during the application of 2 kN quasi-static load. From Figure 9-16b it is observable that the male Ti6Al4V taper experienced a toggling motion during the fatigue loading stages likely as a result of misalignment. A coup-counter coup wear pattern is identified.





(b)



(c)

Figure 9-15 – Fretting currents of Biolox – Ti6Al4V three repeats, a) frequency variation, b) mean load variation c) cyclic load variation.

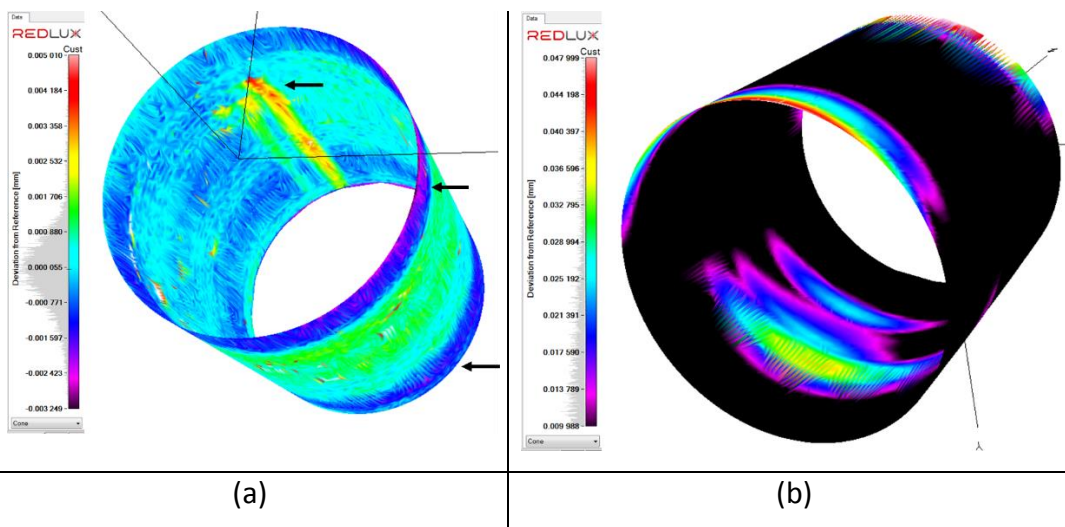


Figure 9-16 – 3D reconstruction of Biolox – Ti6Al4V taper – the case of misalignment: a) BIOLOX female taper, b) Ti6Al4V male taper.

## 9.6 Discussion and summary

In this chapter, the fretting current and wear pattern from four material combinations with realistic modular taper interfaces were assessed under various loading conditions. For the metal – metal combinations, a large metallic surface area (from the bearing) and the taper interface was exposed to the physiological solution during the fatigue loading tests. Thus, a realistic level of exposure comparable to the *in-vivo* condition is established. As a result of this exposure, the peak current was observed to be an order of magnitude higher than the ceramic – metal combinations.

Assessing the effect of frequency across the four material combinations revealed that in most cases, higher frequencies do result in slightly higher fretting currents as observed by Brown et al [116]. However, when the cumulative charge is considered, it is the case that the higher fretting current is not proportional to the increase in fretting cycles. Therefore, fatigue loading 5 Hz frequency was seen to undermine the degree of fretting corrosion quite significantly in most material combinations. For ceramic – metal combinations specifically, a clear declining trend in the cumulative charge with increase in frequency was observed.

As for the mean load variation, increasing the mean load without an keeping a minimal constant cyclic load is synonymous to creating a high contact pressure stick regime at the fretting interface. Therefore the fretting current generated from the mean load assessment was relatively minimal. And from all the material combinations, CoCrMo – CoCrMo generated the most cumulative charge, especially at the higher loads. Interestingly, for the Biolox – CoCrMo, the lowest and highest mean loads generated minimal fretting currents. This suggests that at low mean loads, a large proportion of contacting areas experienced minimal interfacial micromotion that would cause oxide abrasion. Whereas at the highest mean load, interfacial compliance (sticking regime) which also reduces micromotions, limits the areas in contact at the taper interface that could experience oxide abrasion. No fretting current was measured for Biolox – Ti6Al4V which is also a result of minimal interfacial micromotions. However, at the highest mean load,

fracture of the protective oxide led to a transient of anodic current that was immediately restore to zero.

The individual fretting corrosion characteristics of CoCrMo and Ti6Al4V within a metal – metal and ceramic – metal interface was identified during the cyclic load variation assessment. The metal – metal and ceramic – metal combinations that had CoCrMo spigots yielded a higher fretting current than those with Ti6Al4V (except for the case of misalignment). This result could be expected from an electrochemical point of view if one considers Ti6Al4V's ability to repassivate faster than CoCrMo in a non-creviced environment [143]. However, a contrary argument is that the low stiffness of titanium alloy is generally known to cause increase in fretting at the modular taper and thus result in higher fretting corrosion [80, 220]. Therefore, it is worth understanding examining the mechanical influences that could result in larger fretting currents generated for both CoCrMo – CoCrMo and Biolox – CoCrMo fretting contacts.

It was identified that CoCrMo – CoCrMo experienced the least femoral head migration of the four material combinations. This would comparably limit its taper strength because migration of femoral head increases the areas in interference fit within the taper interface [63]. Thus the coup-counter-coup wear pattern observed at the CoCrMo – CoCrMo interface is explained; this is indicative of a toggling form of micromotion. This explains why fretting currents were high at the CoCrMo – CoCrMo interface.

On the other hand, Biolox – CoCrMo is the least compliant contact of all four material combinations (determined from the reduced modulus calculation in Appendix B). Therefore, femoral head migration was found to be the largest at this interface as expected. This also meant that the largest taper separation force was required for disassembly thus indicating that it had the highest taper strength [63]. A greater femoral head migration means a large surface area of CoCrMo in direct contact with the Biolox ceramic as evidenced in the 3D reconstruction of the CoCrMo trunnion. Such a large contacting surface area, against a much harder counter-part would result in abrasion across a larger surface area upon large micromotions at higher cyclic loads. Therefore, it is

deducible that fretting current was at Biolox – CoCrMo contact as a result of greater interference fit between the micro-grooves on CoCrMo and Biolox.

The good balance between taper strength and how Ti6Al4V engages the CoCrMo is suggested to be the reason for its relatively modest fretting current. Although it is expected that the Biolox – Ti6Al4V contact would generate less fretting current than CoCrMo – Ti6Al4V, 3D reconstruction of the Ti6Al4V male taper in Figure 9-14 also reveals an interference fit most Ti6Al4V micro-grooves hence the currents measured are comparable with those of CoCrMo – Ti6Al4V. The large anodic currents observed for the Biolox – Ti6Al4V couple upon the initiation of cyclic loads contributed significantly to the total cumulative charge measured. This suggests that a significant proportion of the current emanated at this fretting interface is a result of film restoration at the interface once depassivation as occurred.

The single case of misalignment in this chapter highlighted how deleterious such cases can be in reality. Unfortunately, misalignment of taper assembly during surgical procedure is not improbable and may result in early revision of the implant. The misalignment observed in this study affected the taper engagement thus creating a coup-counter coup wear pattern at the interface and as a result, a significantly higher fretting corrosion current was generated.

## Chapter 10 Overall discussion

### 10.1 Introduction

Fretting corrosion and tribocorrosion mechanisms of metal – metal and ceramic – metal material combinations have been assessed using both tribometer point-contact configuration and fatigue loading of realistic taper component. Mechanical and electrochemical data were complimented with in-depth surface and sub-surface analyses. Each result chapter in this thesis were summarised with a brief discussion and summary section in order to consolidate the findings from the various material combinations and parameters tested within the chapter. The purpose of this discussion chapter is therefore to discuss the overarching themes and proposed mechanisms. This discussion is split into the following key sections:

- Linking fretting loops with the fretting interface
- Aspects of fretting and corrosion mechanisms
- Characteristics of biomedical materials at the modular taper junction of hip implants
- Relevance to clinical application

### 10.2 Linking fretting loops with the fretting interface

The use of fretting loops to monitor wear regime transformation during fretting tribometer studies is well established in the fretting field. Such fretting loops were presented for all displacement amplitudes and material combinations assessed in this research. The vast number of fretting experiments conducted in this research has made it possible to interpret subtle deviations in the shape of a typical gross slip fretting loop. This deviation is thereby correlated to *in-situ* wear mechanisms. A standard gross slip regime shape has a parallelogram-like shape as depicted in Figure 10-1a. The loop shown was obtained from the gross slip fretting loop of self-mated CoCrMo at  $\pm 25 \mu\text{m}$  displacement. The fretting loop is labelled and correlated to the de-convoluted

graphs of displacement (solid line) and tangential force (dashed line) in Figure 10-1b. The points begin at  $A_1$  and is described in the clockwise direction to end at  $A_2$ .

At  $A_1$ , the tangential force is relatively constant as the ball displaces towards the first corner ( $C_1$ ) of the fretting contact limit. At the side 'B' of the fretting loop, the tangential force transitions from kinetic friction to zero while the cantilever of the tribometer experience few micro-meter of displacement which corresponds to the 'system compliance'. The tangential force increases from zero at the same rate in the opposite direction (negative y-axis) while still at  $C_1$ . This stage represents the static increase in tangential forces (static friction) until a peak value is reached – the value corresponds to the transition force require for the contact to overcome static friction and kinetic friction is introduced. The point of transition is denoted 'corner 1 reverse' ( $C_{1R}$ ).

At side C, the ball displaces from  $C_1$  to the second corner ( $C_2$ ). Subsequently, stage B is repeated at  $C_2$  labelled 'D' and once again, the tangential force generates enough traction to translate into kinetic friction thus the ball slips in the direction of  $C_1$  again; this is denoted  $A_2$ .

There are several interfacial mechanisms at the fretting interface arising from the accumulation of third-body products such as surface ploughing, micro-cutting/grooving, film formation, interfacial layers and so on. Some of these can be identified through the deviations observed in fretting loops. The deviations often appear at specific parts of the fretting loop like the sides  $A_1$  &  $A_2$  and C as well as corners  $C_1$  and  $C_2$ . Some of these mechanisms are outlined in the following subsections:

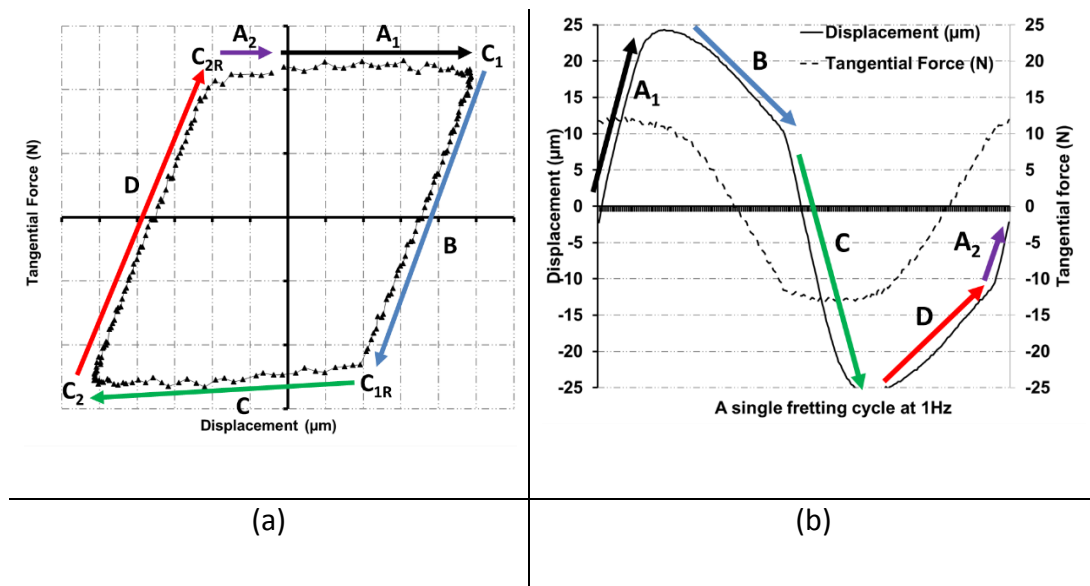


**Figure 10-1 – Fretting loop of gross slip regime; a) labelled fretting loop  
b) de-convoluted fretting loop – displacement (solid-line) and  
tangential force (dashed-line).**

### 10.2.1 Fretting loop deviations at the self-mated CoCrMo interface

The deviation shown in Figure 10-2a was only observed at the self-mated CoCrMo fretting contacts (Figure 6-3a and Figure 8-4a). The red dashed-lines represents the expected gross-slip shape for a symmetrical fretting interface. From the fretting loop shape (plotted in black), it can be seen that the tangential force at the positive x-axis of the fretting loop decreases gradually towards the fretting contact limit i.e.  $C_1$  and increases as it approaches  $C_2$ . This is a result of differences in wear depth about the centre-line of the fretting contact as illustrated in the 3D surface profile of the flat component in Figure 10-2b. The cause of this phenomenon is attributed to possible irregular pressure distribution at the interface due to the presence of third-body products. This is a common process observed at fretting contacts [39, 47]. The fretting loops corresponding to the early cycles of fretting for this interface were verified in order to ensure this phenomenon is not a result of contact misalignment.



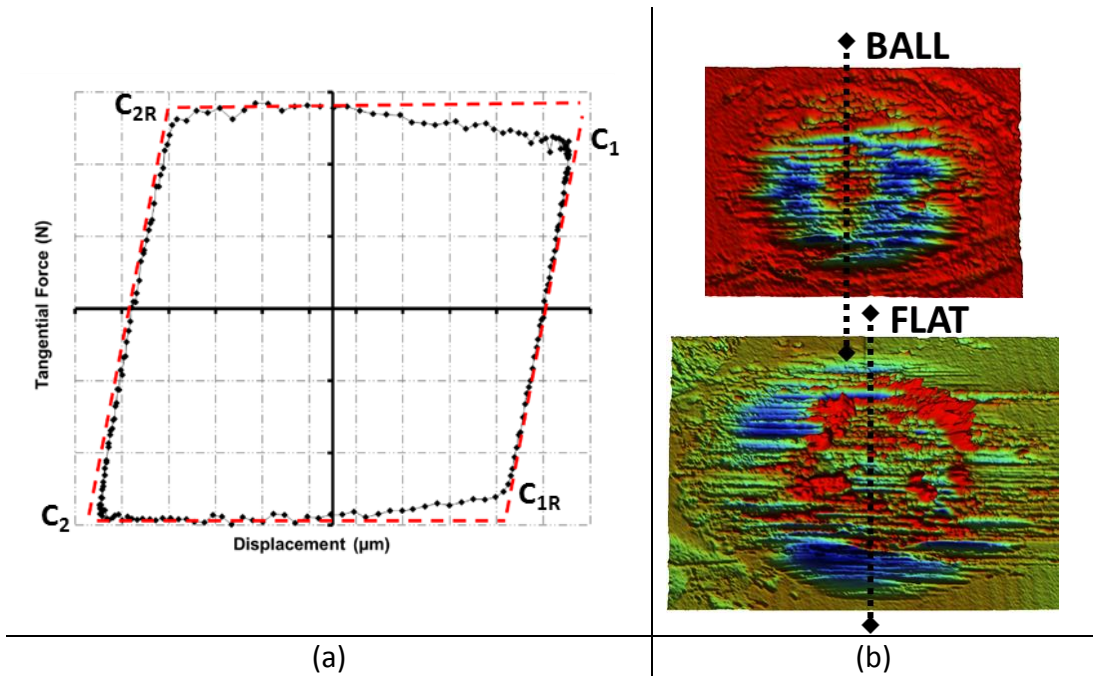


**Figure 10-2 – Non-symmetrical fretting contact a) CoCrMo – CoCrMo  $\pm 50 \mu\text{m}$  fretting loop b) ball and flat wear surface**

Other interesting deviations corresponding to third-body build-up at self-mated CoCrMo interface is presented in Figure 10-3. The behaviour was typically observed at  $\pm 150 \mu\text{m}$  both in OCP and potention-static conditions. In this specific case, maximum tangential force in Figure 10-3a is seen at the centre of the contact which corresponds to the location of a redistributed third-body product at the centre of the moving ball in Figure 10-3b. Correspondingly, the largest micro-cutting/grooved region of the flat component is observed at the centre of the wear surface.

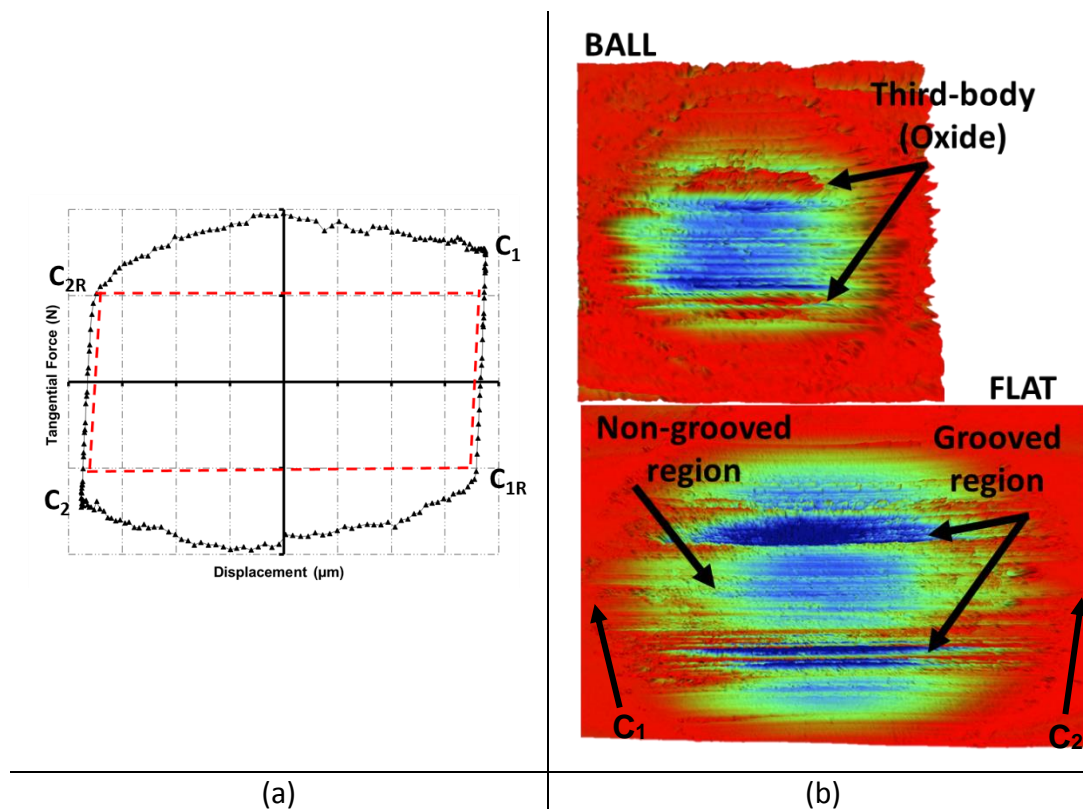


**Figure 10-3 – Third-body grooving a) CoCrMo – CoCrMo,  $\pm 150 \mu\text{m}$  fretting loop b) ball and flat wear surface**

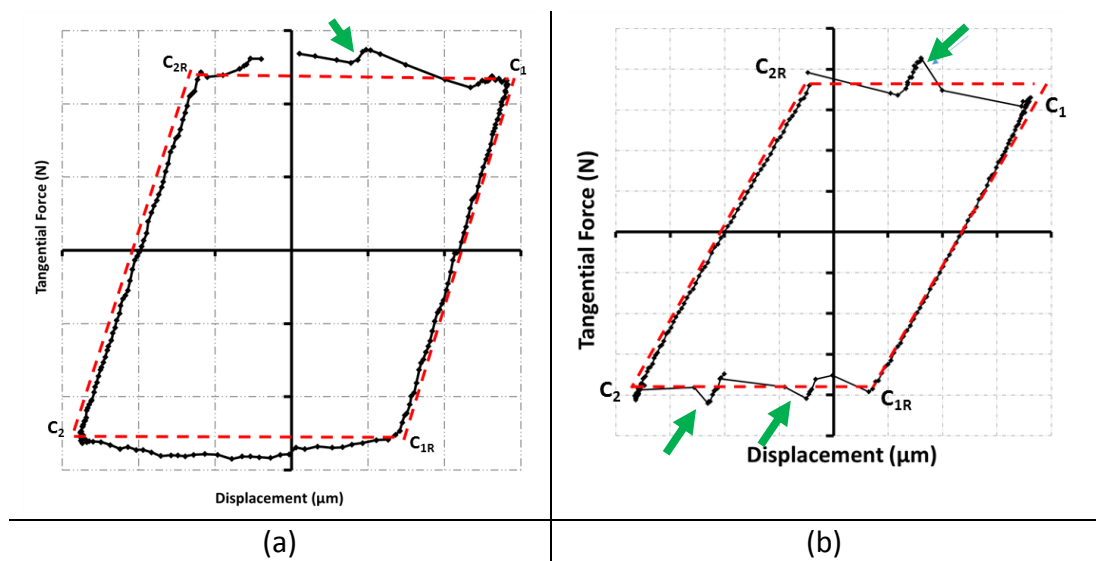
### 10.2.2 Fretting loop deviations at ceramic – metal interface

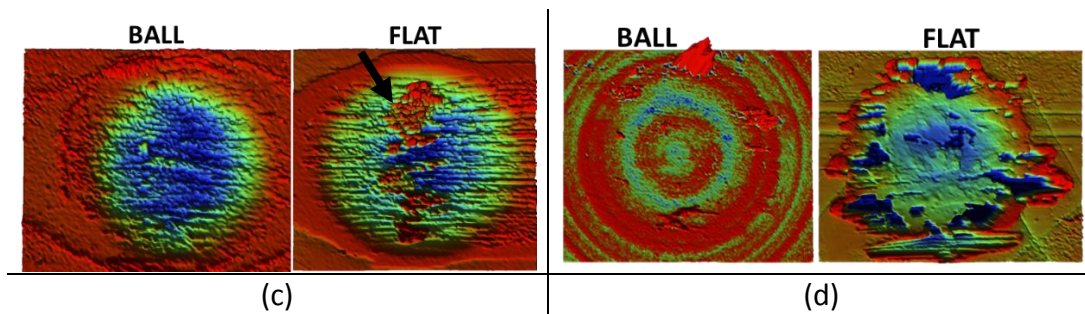
The fretting loops shown in Figure 10-4a and Figure 10-4b includes a feature indicated with the green arrows. This feature corresponds to a quasi-static rise in tangential force during gross slip fretting. Specifically in Figure 10-4a, another deviation from the standard gross slip shape can be seen. The tangential force during kinetic friction is observed with a curved profile. The two figures represent  $\text{Si}_3\text{N}_4$  – CoCrMo and BioloX – Ti6Al4V contacts at  $\pm 50 \mu\text{m}$  respectively.

Figure 10-4c shows the surface profile for both  $\text{Si}_3\text{N}_4$  ball and CoCrMo flat. The agglomerated third-body product on the CoCrMo component is seen at the centre of the fretting contact post-test. However, the fretting loop describes a non-symmetrical fretting behaviour at the interface. As the  $\text{Si}_3\text{N}_4$  ball translates towards  $C_1$  the third-body product builds-up near the centre of the wear contact and thus obstruct relative motion momentarily – this is the cause

for the quasi-static rise in tangential force. However, as the ball translates back from  $C_1$  to  $C_2$ , the quasi-static rise is not present because, the third-body product is redistributed across the CoCrMo surface thus abrading the  $Si_3N_4$  ball rather than obstructing its relative motion. The curved tangential force profile during kinetic friction corresponds to the wear surface of the CoCrMo flat where the centre of the wear surface is the lowest point during fretting.

The same quasi-static feature is observed in Figure 10-4b. However, for this contact, the quasi-static rise in tangential force were also present during the return from  $C_1$  to  $C_2$  and twice in this case. It has already been established through 3D surface profilometry and BS-SEM (Figure 7-36 and Figure 7-37) that the BIOLOX ball experienced no measurable material loss. Rather, wear and corrosion products of Ti6Al4V alloy which became trapped at the interface formed a smooth-appearing third-body material on one side (the side in contact with the Biolox – Figure 10-4d) and on the flip side, the third-body is in direct contact with Ti6Al4V. The wear track identified beneath the third-body product is most likely a result of a galling mechanism which is typical of adhesive contacts and has been well reported for Ti6Al4V – Ti6Al4V contact [208-210] In this contact, the quasi-static rise in tangential force is likely an indication of adhesion at the third-body – Ti6Al4V interface. The feature was also identified at the  $Si_3N_4$  – Ti6Al4V interface in Figure 7-5a.

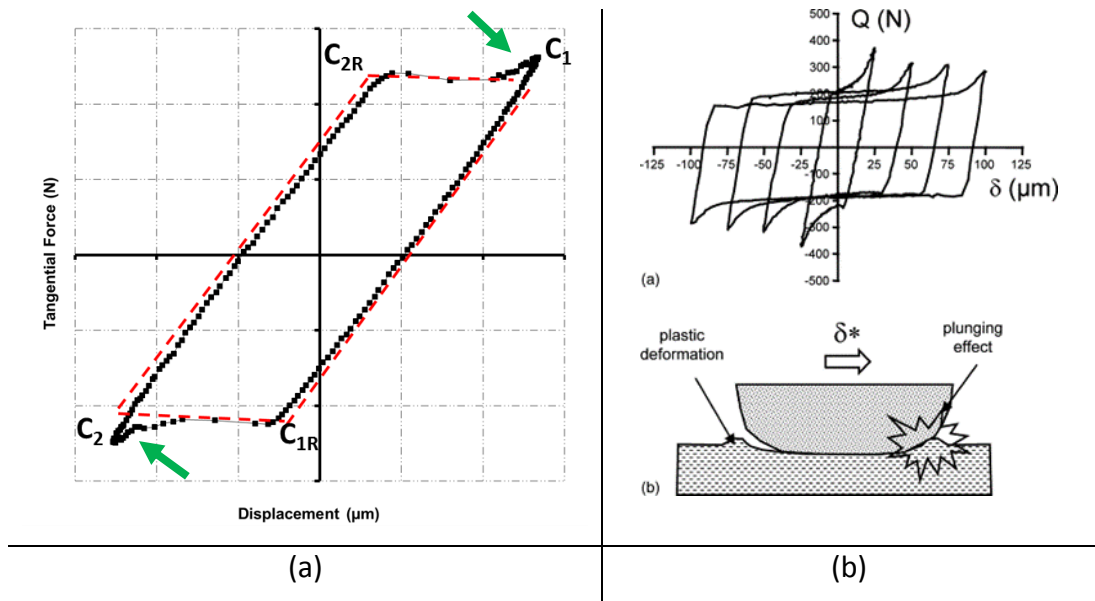




**Figure 10-4 – Influence of third-body a)  $\text{Si}_3\text{N}_4$  – CoCrMo,  $\pm 50 \mu\text{m}$  fretting loop b) BIOLOX – Ti6Al4V,  $\pm 50 \mu\text{m}$  fretting loop c)  $\text{Si}_3\text{N}_4$  – CoCrMo ball and flat wear surface d) BIOLOX – Ti6Al4V ball and flat wear surface.**

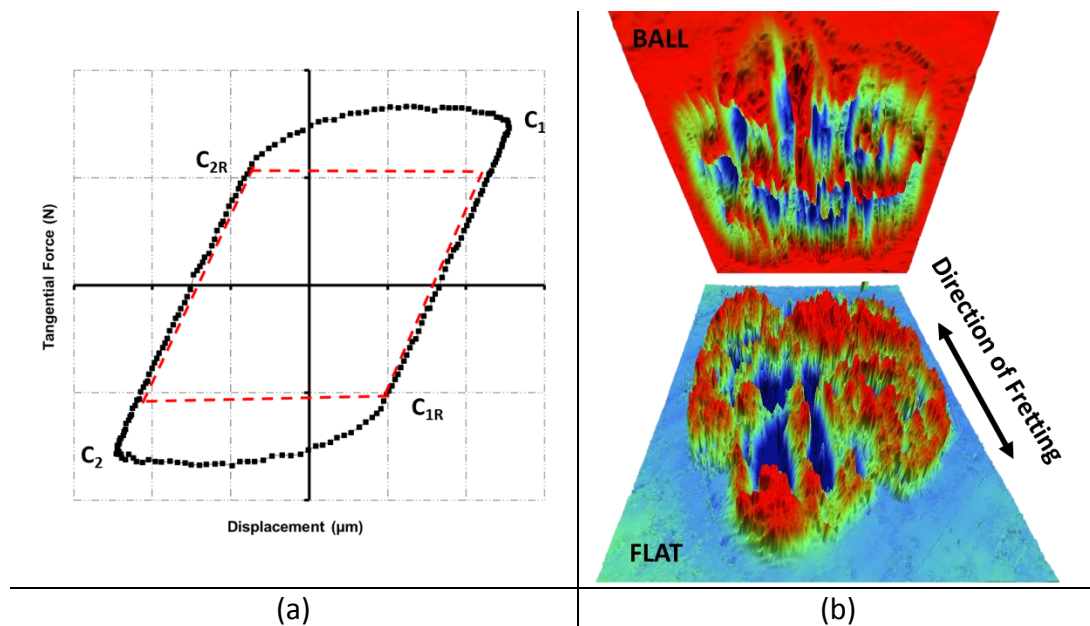
### **10.2.3 Fretting loop deviations at CoCrMo – Ti6Al4V interface**

Figure 10-5a shows the fretting loop of CoCrMo – Ti6Al4V at  $\pm 50 \mu\text{m}$  displacement. For this interface, the quasi-static rise in tangential force was observed at the fretting contact limits ( $C_1$  and  $C_2$ ). This is indicative of some degree of deformation was accommodated at the Ti6Al4V contact edges resulting in the quasi – static rise in tangential force. The phenomenon is commonly observed for Ti6Al4V as shown in the fretting loop of other authors [99, 221]. However, it was termed ‘The plunging effect’ in the study by Fouvry et al [221], Figure 10-5b shows a schematic diagram of the feature obtained from their study.



**Figure 10-5 – The plunging effect (prior to fracture of cold-welded interface): a) CoCrMo – Ti6Al4V,  $\pm 50 \mu\text{m}$  fretting loop, b) schematics of the plunging effect [221].**

Other interesting deviations observed for the CoCrMo – Ti6Al4V at  $\pm 50 \mu\text{m}$  displacement is the fretting loop of the ruptured welded interface during gross slip regime. The fretting loop shown in Figure 10-6a corresponds to the gross slip fretting behaviour subsequent to the fracture of the cold-welded interface. The 3D surface profile in Figure 10-6b shows the interface with well aligned surface cracks and peaks as well as the contact boundary. The main deviation of this fretting loop shape is observable at corners  $C_{1R}$  and  $C_{2R}$  in which case, a curved tangential force profile is observed. The non-definitive transition into kinetic friction and the non-linear increase in tangential force may be indicative of surface adhesion between multiple intertwined grooves established in the ruptured interface. That is, relative slip is no longer just occurring between a point contact, rather, a frictional contact is also established along the sides of the fragmented peaks of the CoCrMo and the surface cracks in the Ti6Al4V.



**Figure 10-6 – Slip within localised fretting grooves (after the fracture of cold-welded interface): a) CoCrMo – Ti6Al4V,  $\pm 50 \mu\text{m}$  fretting loop, b) 3D surface of the ruptured welded interface.**

## 10.2.4 Summary

Deviations in the fretting loop shapes relative to the standard gross slip shape were correlated to their corresponding *in-situ* interfacial mechanisms. Through the identification of these characteristic contact features, *in-situ* wear mechanisms and changes to the contact conditions can be detected in the absence of any *in-situ* surface analytical techniques. It serves as a preliminary stage to characterising *in-situ* wear in a tribological system.

## 10.3 Aspects of fretting and corrosion mechanisms

### 10.3.1 Mechanism of cold-welding and pseudo-amorphous structures at CoCrMo – Ti6Al4V interface

Cold-welding is a solid-state welding process whereby an interfaces adheres together (under high contact pressures) without the use of heat. The cold-welding process involves the oxidation of the two materials in contact. Several cases of cold-welding in modular implants have been reported in literature [80,

84, 222-225]. In all the cases, cold-welding was only prevalent at the self-mated Ti alloy interface. The welding occurs subsequent to thick Ti-oxide build-up resulting from MACC. Consequentially, the welded components are inseparable by the surgeon during a revision procedure, leading to the whole modular stem having to be removed.

To the best of our knowledge, no retrieval study or *in-vitro* study has yet reported the observation of cold-welding at the CoCrMo – Ti6Al4V interface. There are two main reasons that may explain this: either that cold-welding at this interface doesn't occur *in-vivo* (an option deemed unlikely) or it does occur, but it is not as resistant to separation force as the thick, cold-weld formed at the self-mated Ti interface. The latter is considered the more likely reason because while in the present study, the cold-weld (pseudo-amorphous material) observed at the CoCrMo – Ti6Al4V interface had a maximum thickness of 2  $\mu\text{m}$ , the study by Grupp et al [80] reported cold-weld with thickness up to 30  $\mu\text{m}$  at the self-mated Ti interface.

A very recent study by Hall et al [199] described evidence of material transfer at the CoCrMo – Ti6Al4V interface with “related surface break-outs” that is, the two metallic materials were once bonded together. This strengthens the argument that cold-welds do form *in-vivo* of CoCrMo – Ti6Al4V interface but may be susceptible to fracture whilst still assembled or may fracture during surgical revision as a result of low thickness or brittleness. A schematic of the proposed *in-situ* mechanism of how the ‘cold-weld’ with a pseudo-amorphous structure is formed at the CoCrMo – Ti6Al4V interface is shown in Figure 10-7. The 3D fretting loop confirms the point where a regime transition from partial-slip to gross slip occurred. It is believed that this transition stage corresponds to point for which the pseudo-amorphous material ruptured, leaving most of the material still ‘bonded’ to the more ductile of the two alloys – Ti6Al4V.

A proposed mechanism to explain how the pseudo-amorphous structure forms from an initially crystalline structure of the two contributing alloys is shown in Figure 10-8. The mechanism also address the processes involved in the formation of amorphised Ti6Al4V. The interfacial and subsurface

transformations observed from both CoCrMo and Ti6Al4V alloys are categorised into four stages. In this mechanism, 'Stage 1' represents the deepest subsurface of the alloy and 'Stage 4' represents the uppermost subsurface/interface of the alloy.

In stage 1 – the grain sizes of the base alloy are generally few microns in size for both CoCrMo and Ti6Al4V. For stage 2 – smaller grain sizes in the sub-micron range begin to emerge. The low stacking fault energy of CoCrMo leads to strain-induced twinning hence the recrystallization of CoCrMo alloy at this level [6]. Whereas in Ti6Al4V, crystallographic reorientation becomes evident through the presence of directionality (see Figure 6-19d). So also, smaller grain sizes are caused by recrystallization from internal dislocations initiated by plastic straining [226]. In stage 3 – grains are few nano-meters in size and are generally observed near the upper most surface. These nano-crystalline structures in non-lubricated fretting contacts of metallic alloys are known as tribological transformed structures (TTS) [226]. It has also been shown that TTS structures can be multiple times harder than the bulk alloy itself; they are brittle and susceptible to fracture [226].

The CoCrMo and Ti6Al4V interface in this study is both lubricated and subjected to a partial-slip regime prior to fracture of the pseudo-amorphous material, thus 'Stage 4' exist at this interface. Under normal gross slip conditions, the transformation of the alloy would reach 'Stage 3' and the material is subsequently removed from the interface as wear and oxidation product. However, the high contact compliance of the Ti6Al4V alloy relative to the CoCrMo facilitates the detainment of third-body products. And thus, in the presence of physiological solution, mechanical mixing and oxidation processes lead to the formation of 'Stage 4' which is the pseudo-amorphous material (or the cold-weld).

The transformation of bulk crystalline Ti6Al4V into an amorphous structure also follows a similar process to the formation of the pseudo-amorphous structure. However, as shown in Figure 10-8, it is proposed that the stages at which each structure formed differ. Although it cannot be fully verified, it is proposed that subsequent to the rupture of the pseudo-amorphous structure,



gross slip fretting is initiated at the interface of CoCrMo and the pseudo-amorphous structure. Interfacial shear stresses from the interface transmitted through the pseudo-amorphous structure effects subsurface recrystallization in the underlying Ti6Al4V. As the thickness of the pseudo-amorphous structure is not uniform, subsurface mechanical mixing with access to the physiological solution results result in the formation of amorphous Ti6Al4V.

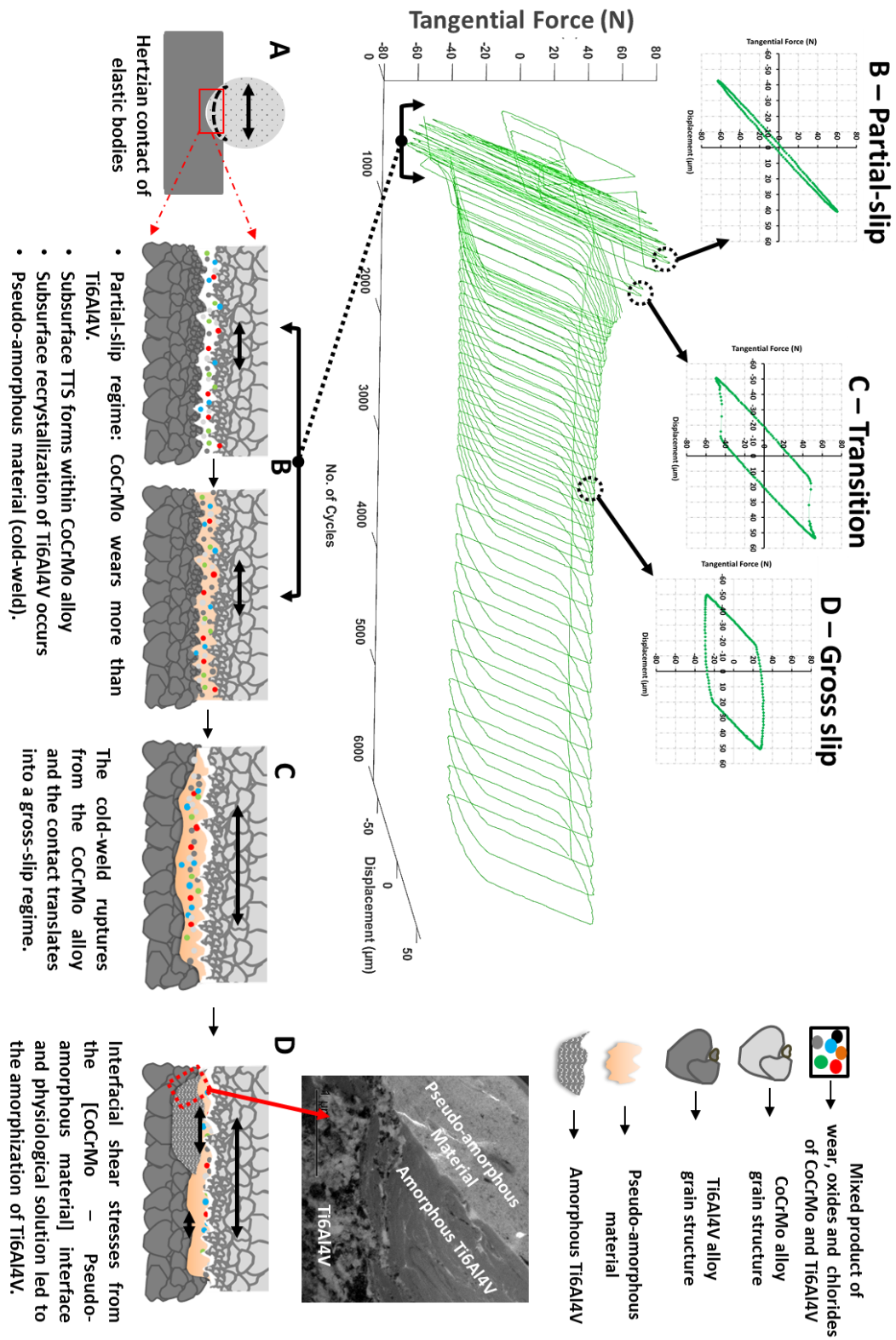


**Figure 10-7 – Mechanism of cold-welding at the CoCrMo – Ti6Al4V interface**

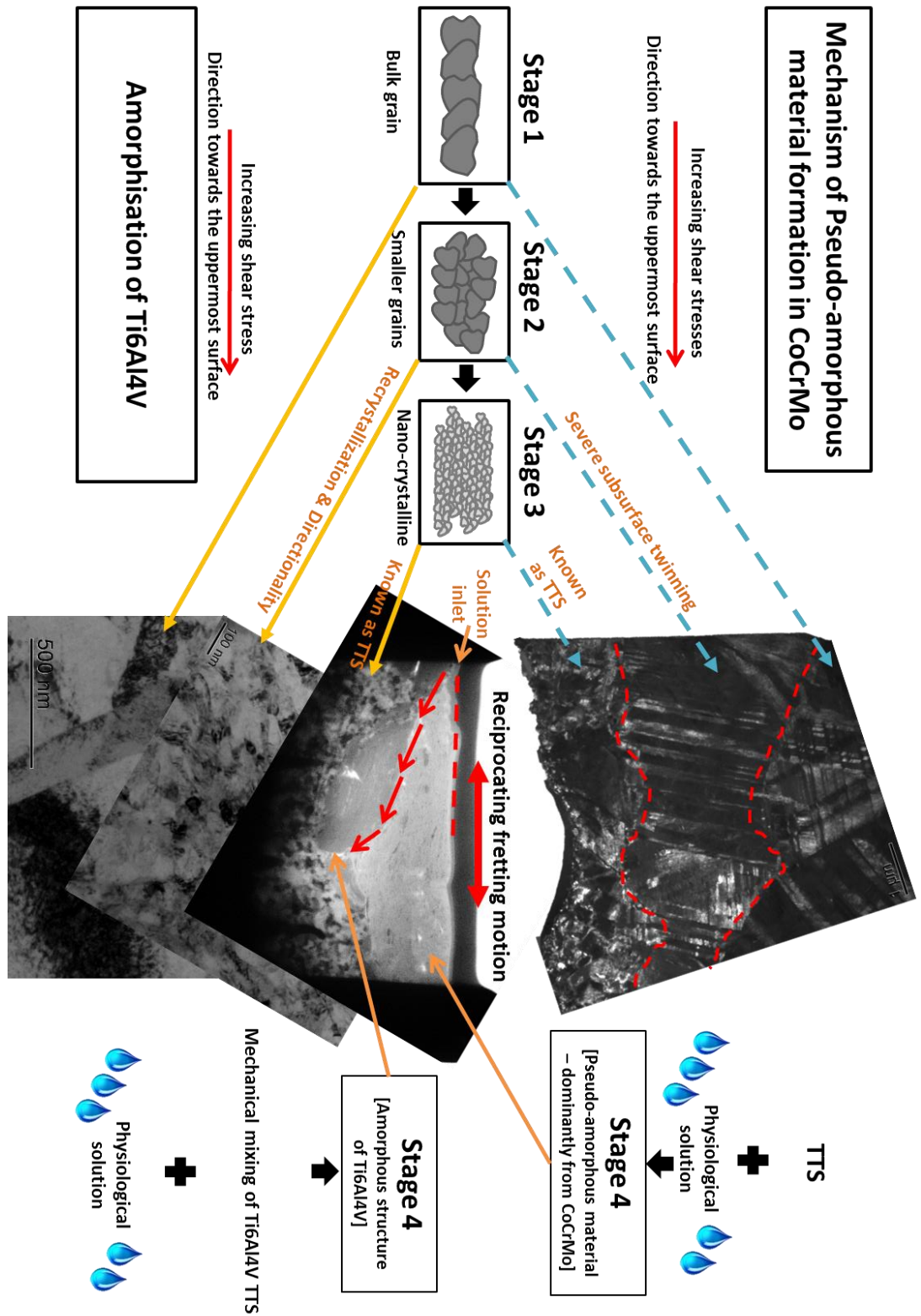


Figure 10-8 – Mechanism of pseudo-amorphous structure of CoCrMo and amorphisation of Ti6Al4V alloys.

### 10.3.2 Mechanism of stiction at the $\text{Si}_3\text{N}_4$ – $\text{Ti6Al4V}$ interface

The word 'stiction' originates from two words 'static' and 'friction'. It is more commonly used to describe the process in diesel engines where static friction is created as a result of build-up of hydrocarbons and is needed to be overcome. The word is used in this context to describe the intermittent alternations between static friction (stick regime) and kinetic friction (gross slip) at the  $\text{Si}_3\text{N}_4$  –  $\text{Ti6Al4V}$  interface.

The mechanism observed at this contact have some similarities with those of  $\text{CoCrMo}$  –  $\text{Ti6Al4V}$  interface in the previous section (10.3.1). The two main similarities are: formation of a pseudo-amorphous structures and formation of amorphous  $\text{Ti6Al4V}$  structure. However, there are several significant differences between the two material combinations. For examples, it had been discussed previously that one of the dominant wear mechanisms for  $\text{Si}_3\text{N}_4$  when in contact with  $\text{Ti6Al4V}$  is fracture-induced wear. The energy dissipated graph (see Figure 7-5) reveal that a significant 'burst' of energy is measured during the intermittent transitions from stick regime to the gross slip regime. It is suggested that this sudden regime translation is always as a consequence of micro-fracture of  $\text{Si}_3\text{N}_4$  at the interface which subsequently leads to interfacial slip. As a consequence of such changes in energy, significant subsurface damage is inflicted to the  $\text{Ti6Al4V}$  alloy beyond those observed in the  $\text{Ti6Al4V}$  of the  $\text{CoCrMo}$  –  $\text{Ti6Al4V}$  couple. Figure 10-9 shows a schematics diagram of the proposed stiction mechanism. While in the previous section, four stages of  $\text{Ti6Al4V}$  was outlined (see Figure 10-8), an additional degradation stage (Stage 5) was introduced for  $\text{Ti6Al4V}$  in this figure.

In a similar manner to the  $\text{CoCrMo}$  –  $\text{Ti6Al4V}$  interface, both  $\text{Si}_3\text{N}_4$  and  $\text{Ti6Al4V}$  contributed to the pseudo-amorphous material. A fusion of both Si-oxide, Ti-oxides and Al-oxide under a stick fretting regime is the proposed mechanism leading to the formation of the pseudo-amorphous structure. TEM-EDS and XPS was used to identify the material as possibly Ti and Al silicates.

The energy involved at this interface is such excessive that the regions that are not covered by the pseudo-amorphous material (as shown in phase 'D' of

Figure 10-9) also experienced a full (Stage 1 – 4) subsurface transformation. On the other hand, the regions that were covered by the pseudo-amorphous material (as shown in phase 'E' of Figure 10-9) experienced the newly introduced 'Stage 5' transformation. Stage 5 transformation in Ti6Al4V occurs likely during the sudden transition process from stick regime to gross slip.

In summary, it can be deduced that the stiction mechanism occurs when the Ti6Al4V becomes more compliant due to subsurface fracture (stage 5) and migration of the Ti and Al silicate pseudo-amorphous material. This compliance leads the fretting contact back into a stick regime. During the stick regime, micro-fractures of  $\text{Si}_3\text{N}_4$  at the interface piles up and oxidises to form a new layer of the pseudo-amorphous material. Once enough traction force is gained at the interface, the contact is translated back to a gross slip regime and the process is repeated.

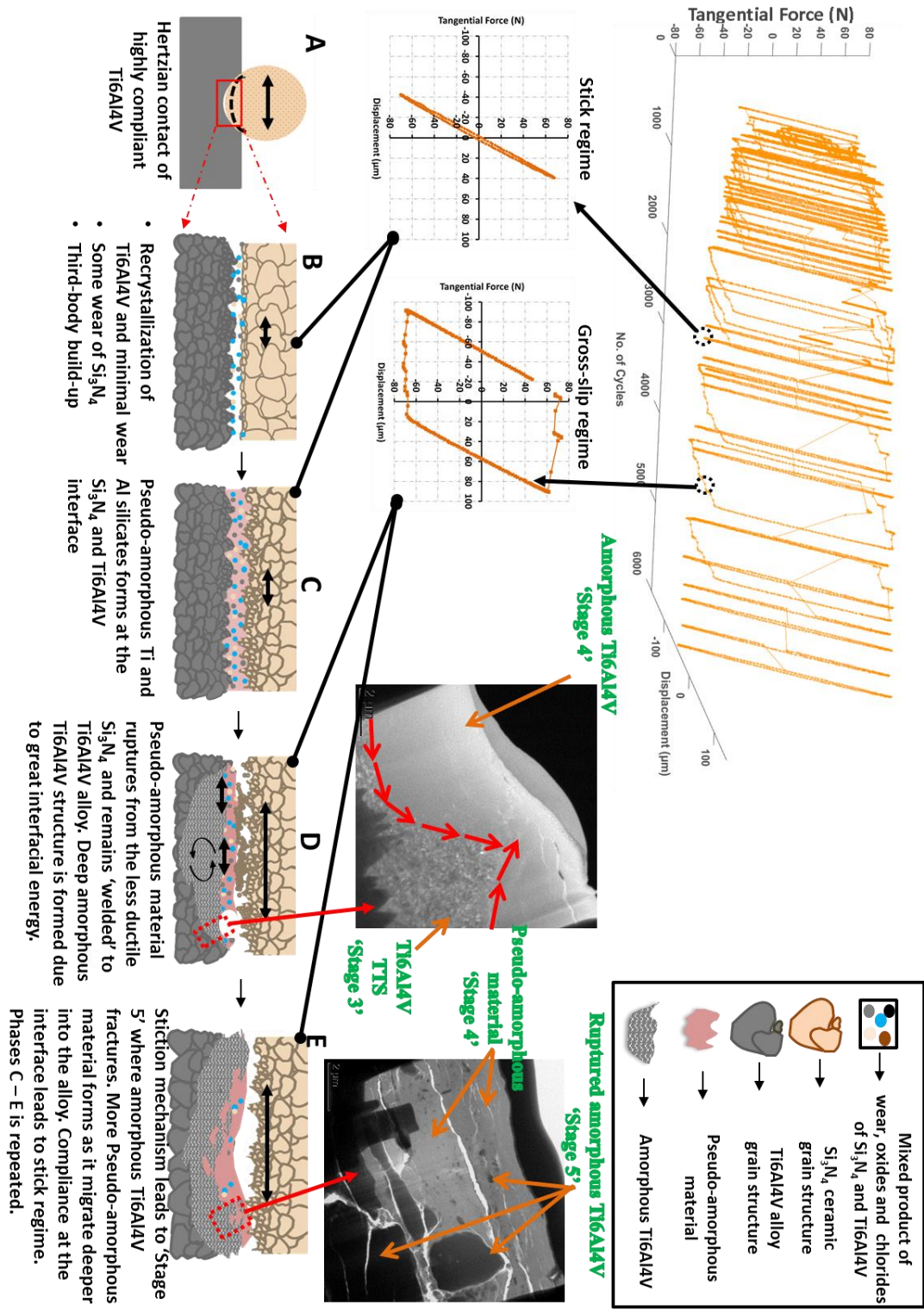


Figure 10-9 – Mechanism of stiction at the Si<sub>3</sub>N<sub>4</sub> – Ti6Al4V interface

## **10.4 Characteristics of biomedical materials at the modular taper junction of hip implants**

This section brings together the key findings from both tribometer and realistic taper component assessment. It further highlights the characteristic role of each biomedical material at the fretting interface of the modular taper junction.

### **10.4.1 CoCrMo at the modular taper interface**

In Chapter 5 the role of Mo in the passivation process of a polished CoCrMo surface was highlighted. This was further emphasised in Chapter 6 (see Figure 6-21 and Figure 6-22) where a thick passive oxide is formed above a Co-Mo structure. In the region absent of the Co-Mo structure, the passive oxide did not form thus highlighting the role of Mo in enhancing surface passivation. Evidence of a Cr-depleted region is generally associated with grain-boundary corrosion or sensitization as its better known in literature [174, 227]. However, the observation from this research found that in the case of micro-cutting or grooving, active wear particles can be generated thus the wear product is not only Cr-oxide and phosphate species. The 'honey-comb' Co-Mo structure was formed as a result of electrochemical process involving preferential depletion of Cr to form oxides. Subsequent fracture of the 'honey-comb' fracture may result in release of tiny Co-rich particles thus increasing the risk of Co-induced toxic effects and other forms of ALTR [93].

Self-mated CoCrMo alloy subjected to fatigue loading had the least taper strength as it was observed to experience the least taper migration. The consequence of this is increase in toggling micromotion which may lead to accelerated fretting corrosion (especially at high cyclic loads). It is such toggling motions that manifest in ploughing or grooving of the modular taper as observed in retrieval analyses [199]. From monitoring the fretting current, it was often the case that the fretting current at the self-mated CoCrMo interface drops after a few thousand cycles. This is attributed to possible electrochemically induced film formation or agglomeration of third-body

products at the interface thus creating a physical barrier against charge transfer [215]. In other words, an antagonistic tribocorrosion reaction.

From Figure 10-10, the presence of a central partial-stick region is indicative of an 'unexposed' region in the gross slip fretting contact. This region is typically poorly aerated hence a type of crevice. The 'unexposed' region in a ball-on-flat configuration is representative of the crevice established at the proximal-end of the modular taper. On the other hand, the slip annulus in the gross slip ball-on-flat configuration represents a well aerated environment and thus representative of the distal-end of the modular taper. As such, the composition of the third-body wear and corrosion products formed in this research are the same with those reported in previous retrieval analyses [85].

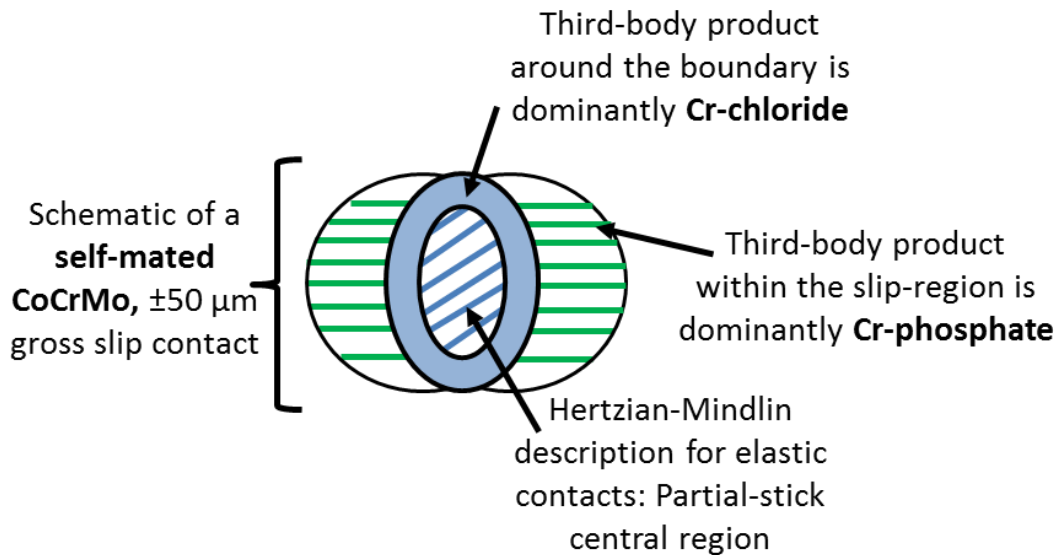


**Figure 10-10 – Schematic diagram of different fretting corrosion products at specific regions within the composite contact of self-mated CoCrMo,  $\pm 50 \mu\text{m}$ .**

The coupling of CoCrMo against Ti6Al4V was observed to have led to the establishment of severe crevice conditions. This is evidenced by pitting corrosion of the CoCrMo; the observation of pitting suggests that the pH of the crevice depicted in Figure 6-31 may be lower than 3.5 – the point where the passive  $\text{Cr}_2\text{O}_3$  layer becomes unstable according to Pourbaix diagram [228].



#### **10.4.2 Ti6Al4V at the modular taper interface**

From retrieval studies, it is common that the mixed-metal combination of CoCrMo – Ti6Al4V experienced greater corrosion damage than the self-mated CoCrMo material combination [27, 67]. While there are several factors contributing to this, it is believed that long-term accumulation of third-body wear and corrosion product at the mixed-metal interface is a key contributing factor. Adhesive wear mechanism of Ti6Al4V at the mixed-metal interface was seen in this study to facilitate a significant volume of redistributed wear at the interface unlike self-mated CoCrMo. From what is known about MACC, significant agglomeration of wear and corrosion product can rapidly change to the local chemistry at the interface which would inevitably accelerate corrosion in both CoCrMo and Ti6Al4V alloy [27].

Titanium alloys have been the most reported material to undergo *in-vivo* fracture all the metallic biomaterials used in THA [54]. Most fractures reportedly occur at the neck-stem interface largely because of the greater moment arm relative to the to the head-neck interface [82]. Fretting and corrosion mechanisms depending on the contact conditions are also major causes of failure and fracture *in-vivo*. The level of metallurgical recrystallization, subsurface oxidation and crevice corrosion mechanisms experienced by Ti6Al4V in this study further emphasises the greater risk of Ti6Al4V failure relative to the other materials. To a large extent, several *in-vivo* failure mechanisms, be it mechanical, corrosion or tribocorrosion have been successfully replicated through the use of a tribometer in this research.

#### **10.4.3 Si<sub>3</sub>N<sub>4</sub> at the modular taper interface**

Si<sub>3</sub>N<sub>4</sub> ceramic was not assessed to the realistic taper component level in this research. However, there are on-going research efforts (led by *Amedica Corporation*) to develop a bulk Si<sub>3</sub>N<sub>4</sub> femoral head component for application in THA. In addition, an EU funded research project – *Life Long Joint* is also actively developing a silicon nitride (SiN<sub>x</sub>) coating for applications in THA. This is to say that, the following material combinations at the modular taper may

be commercially available in the near future:  $\text{Si}_3\text{N}_4$  – CoCrMo,  $\text{Si}_3\text{N}_4$  – Ti6Al4V, CoCrMo –  $\text{SiN}_x$  etc. In this vein, there are a few characteristic of  $\text{Si}_3\text{N}_4$ , observed in this study that should be considered when it is coupled against CoCrMo and Ti6Al4V in a fretting contact:

1.  $\text{Si}_3\text{N}_4$  forms a tribochemical material ( $\text{SiO}_x\text{-OH}_y$ ) against CoCrMo alloy
2. Oxidation processes that forms  $\text{Cr}_2\text{O}_3$  is suppressed by the reactivity of Si in  $\text{Si}_3\text{N}_4$  (see Table 10-1).
3.  $\text{Si}_3\text{N}_4$  forms a tribochemical material with TiAl4V under sticking and slipping (stiction) contact condition. The ‘surge’ of energy involved in this process may only ever be experienced at the modular taper interface during a stumbling load where peak loads can rise up to eleven-times the body weight within a single cycle [122].
4.  $\text{Si}_3\text{N}_4$  when subjected to a partial-slip regime (as commonly realised within the modular taper) or when rubbing against its own oxide, may wear significantly more relative to CoCrMo and Ti6Al4V alloys.
5.  $\text{Si}_3\text{N}_4$  experiences a fracture-induced wear mechanism against Ti6Al4V during a stiction behaviour.

Self-mated  $\text{Si}_3\text{N}_4$  is well known for its ultra-low friction ( $< 0.002$ ) due to tribochemical film that it forms in water-based lubricants [229]. However, the tribochemical material formed against the CoCrMo and Ti6Al4V alloys in this study did not function as a solid lubricant rather, the opposite was the case, thus agreeing with observations of another study [17]. Table 10-1 shows the corresponding electrode potentials for the reduction reactions of several element involved with Si at the tribological interface. The more negative the electrode potential of a reaction is, the higher the tendency for the reaction to occur. It can be seen that Si has a higher tendency to oxidise than Cr whereas most species of Ti and Al have a significantly higher tendency to react than Si. This may explain why there is a preferential formation of  $\text{SiO}_x\text{-OH}_y$  instead of  $\text{Cr}_2\text{O}_3$ . Considering the *in-vivo* toxicity of Cr, the suppression of  $\text{Cr}^{3+}$  formation may prove to be a positive attribute of a  $\text{Si}_3\text{N}_4$  – CoCrMo combination.

**Table 10-1 – Electrode potentials of Si, Cr, Ti and Al vs. SHE [2, 21, 230]. The electrons transferred in the half-cell reaction are omitted from the left column for illustrative purposes.**

Reduction reactions	Electrode potential 'E <sub>o</sub> ' vs. SHE
$\text{Si} \rightleftharpoons \text{Si}^{4+}$	-0.91
$\text{Cr} \rightleftharpoons \text{Cr}^{3+}$	-0.74
$\text{Ti} \rightleftharpoons \text{Ti}^{2+}, \text{Ti}^{3+}, \text{Ti}^{4+}$	-1.63, -1.23, -0.88
$\text{Al} \rightleftharpoons \text{Al}^{3+}$	-1.66

#### **10.4.4 Biolox at the modular taper interface**

It is a reasonable hypothesis that by replacing the metallic head component of hip prosthesis with a ceramic (an inert material) alternative, the fretting current at the fretting interface of the modular taper will be halved. Several recent studies conclude that metal corrosion and wear when coupled against ceramic is less or not different than in metal – metal combinations [72,73, 201]. However, when comparing the fretting currents measured during the cyclic loading from the metal – metal and ceramic – metal combination in this study, it is observable that the ceramic made no difference in reducing fretting corrosion current. Rather, the current was highest in the Biolox – CoCrMo combination thus highlighting that although the ceramic remains inert, fretting corrosion is influenced by how the metallic component engages it.

Other interesting characteristics of the Biolox is that wear and corrosion products are typically attached to it at the taper further preventing it from abrasive wear. The accumulation of these interfacial products may also act as a protective barrier against charge transfer thus reducing fretting corrosion current in the long-term. This may also modify the contact condition at the interface in a manner that reduces wear. Nevertheless, long-term accumulation of third-body products at the ceramic – metal interface may activate localised corrosion dominated mechanisms the kind of which current techniques such as volume loss measurements or the semi-quantitative Goldberg fretting score might not detect.

## 10.5 Relevance to clinical application

The purpose of this section is not to exalt one material or material combination while condemning the other out-rightly; this study is not considered exhaustive enough to take such a stand. However, the stance taken in this study is that, every material and material combination has an advantage it brings to the prostheses used in THA. Having said this, this study hopes to enlighten the orthopaedic community i.e. the clinical practitioners, manufacturers, engineers and regulatory bodies about the possible failure modes and damage mechanisms that each material and material combination is susceptible to. Across all the *in-vitro* assessments conducted in this research, the findings reveal that a heavy and active patient poses the greatest risks to implant failure. And in addition, extreme loading conditions like stumbling and surgical errors such as misalignments and component mismatch equally pose a great risk to implant failure.

Micro-cutting or grooving is one of the wearing mechanism identified at the metal – metal interface of a modular taper junction [199]. The mechanism is expected for a modular taper contact where the trunnion is micro-grooved and the contact pressures are disproportionately distributed across the taper, leading to contact pressures being concentrated at a local region. From the findings of this research, high resolution imaging analysis of wear generated through grooving at a self-mated CoCrMo interface showed evidence of electrochemical activity in the wear product. The implications of such active CoCrMo particles in comparison to oxidised particles i.e. oxides and phosphate species retrieved from the peri-prosthetic tissue are not fully known. Perhaps, it may enhance the formation of complex ionic species and adverse local tissue reactions. On the other hand, for titanium alloys, the adhesive wear mechanism and electrochemical activity of its particles makes it less likely to be released into the tissue in a highly electrochemically active form. Except in the case of implant fracture or severe wearing at the distal-end of the modular taper junction where large volume of particles are expected to be released.

The evidence provided in this study also shows the possible implication of applying new metallic sleeves onto worn and corroded trunnions. Although only the self-mated CoCrMo combination was assessed, it showed how the damage mode may be accelerated to a corrosion dominated mechanism when fretting occurs at an interface that has a history of wear and corrosion. In addition, the possibility of an antagonistic tribocorrosion interaction where interfacial friction and corrosion currents are reduced for self-mated CoCrMo combination suggests it CoCrMo sleeve may be a better option when coupling it against a CoCrMo trunnion. One of the primary aim when using a sleeve is to ensure interference fit at the sleeve – trunnion interface thus preventing any secondary fretting. However, the findings in this research reveal that if a crevice is established at the same interface for a mixed-metal material combination, the contact can rapidly become a severe crevice so much so that repassivation is inhibited thus activating pitting corrosion of the CoCrMo and possibly causing the release  $Cr^{6+}$ . These mechanisms were identified at the fretting interface of CoCrMo – Ti6Al4V in this research and the fretting test lasting just under two hours. Therefore, one can imagine such condition *in-vivo* where the implant is fitted for the longer term.

The selection of ceramic coupled with CoCrMo and Ti6Al4V ought to be done with caution when considering a heavy and active patient. From the fretting corrosion assessment of the ceramic – metal couples in this study, the combination of high mean-load (heavy patient) and large cyclic loads (active patient) resulted in greater fretting currents than the metal – metal couples in some cases. This was a counter-intuitive observation and it was attributed to the fact that a larger metallic surface area of the grooved metallic trunnion is in contact with a much harder ceramic counter-part. Therefore, upon application of large cyclic loads as expected for a heavy and active patient, fretting occurs across a large surface area thus generating a relative higher fretting corrosion current.

On another note, the use of titanium alloy trunnion with ceramic head for an average patient may benefit from the surgeon applying a high assembly loads. This should ensure better load distribution across the taper, it is important because, the excellent toughness and wear resistance of ceramic means that

energy at the ceramic – metal interface is not dissipated through the wearing of both ceramic and metal components. Rather, most of the loads and interfacial shearing at the ceramic – metal interface is absorbed by the less stiff titanium alloy. This makes the titanium alloy more susceptible to high levels of metallurgical recrystallization and risk of crack propagation if load is inadequately distributed.

Ultimately, the application of a durable, corrosion resistant and biocompatible coating at the trunnion may prove highly effective in the mitigation of fretting corrosion of the modular taper junction. Such a coating should serve to increase taper strength while reducing interfacial fretting. And in the case where fretting occurs, the coating should be wear resistant to minimise wear and stiff enough to resist subsurface recrystallization of the underlying metal. And if the coating experiences wear and oxidation, the coating and its product ought to be soluble in physiological media.

## **Chapter 11 Conclusions and Future work**

The thesis has explored the fretting interface of various relevant biomedical material combinations. Numerous findings and novel research themes have been established. Listed below are some key findings which are split into subsections:

### **11.1 Conclusions**

#### **11.1.1 Material characterisation, metal – metal and ceramic – metal systems (Chapters 5 – 7)**

- Metallic species contribute to the protective layers formed on CoCrMo and Ti6Al4V alloys. Cr and Mo were enriched in the transition area of CoCrMo while Ti and V was enriched in the transition area of Ti6Al4V.
- Mo was seen to affect the restoration of a passive oxide layer on CoCrMo worn surface.
- Contact compliance of the material combinations within metal – metal and ceramic – metal systems largely influenced the corresponding fretting regimes realised at the interface. All combinations involving Ti6Al4V experienced greater contact compliance.
- Cathodic shift in both metal – metal and ceramic – metal systems were influenced by the fretting regime. Cathodic shift was minimal for both systems during a stick/partial-slip regime while at gross slip regime, the magnitude of cathodic shift was multiple times higher for contacts involving Ti6Al4V than those without Ti6Al4V.
- The wear mechanism at the CoCrMo – CoCrMo contact becomes increasingly third-body influenced at the gross slip regime. On the other hand, significant proportion of the volume generated at the CoCrMo – Ti6Al4V interface are redistributed within the interface due to an adhesive wear mechanism.

- A cold-weld is formed at the interface of both mixed regime contacts of CoCrMo – Ti6Al4V and Si<sub>3</sub>N<sub>4</sub> – Ti6Al4V. The hardness of the welds were 25.6 GPa and 22.7 GPa respectively. This corresponds to interfacial materials with hardness 3x of CoCrMo and 6x of Ti6Al4V in the metal – metal systems; almost 2x the hardness of Si<sub>3</sub>N<sub>4</sub> and 5x Ti6Al4V in the ceramic – metal system.
- Subsurface degradation of CoCrMo in a CoCrMo – CoCrMo interface was characterised with: formation of nano-crystalline structures during partial-slip regime; loss of nano-crystalline structures and increased severity of strain-induced twinning during gross slip regime; reduced severity of twinning with influence of interfacial tribochemical interactions at the transition to reciprocating sliding.
- Subsurface degradation of Ti6Al4V in a CoCrMo – Ti6Al4V interface was characterised by strain-induced subsurface transformations including directionality and recrystallization at both stick and partial-slip regimes. At the gross-slip regimes, mechanically mixed oxides with nano-crystalline structures. Amorphization of Ti6Al4V was also observed.
- Cold-welds in both metal – metal and ceramic – metal systems had a pseudo-amorphous structure and their main composition was mixed oxides and chlorides where mainly particles of Ti6Al4V were suspending within the amorphous structure.
- At both contacts with cold-weld, amorphization of Ti6Al4V occurred beneath the pseudo-amorphous material.
- The types of corrosion products formed at the interface of the metal – metal system and the Biolox – metal contacts was dependent on the contact conditions. In most cases, metal – oxides/chlorides were formed at the creviced contacts. However, non-creviced regions were characterised with Phosphates and various forms of metal – oxides.
- Cr<sup>6+</sup> specie were detected at the severest region of the CoCrMo – Ti6Al4V contact.



- $\text{Si}_3\text{N}_4$  was engaged both in wear and oxidation at the ceramic – metal interface whereas the Biolox ceramic was inert in both cases.
- $\text{Si}_3\text{N}_4$  suppressed the formation of  $\text{Cr}^{3+}$  at the  $\text{Si}_3\text{N}_4$  – CoCrMo interface by forming a  $\text{SiO}_x$  - $\text{OH}_y$  material whereas, at the  $\text{Si}_3\text{N}_4$  – Ti6Al4V interface, the pseudo-amorphous material composed of Ti and Al silicates.

### **11.1.2 Quantification of fretting corrosion current on self-mated CoCrMo (Chapter 8)**

- The contribution of chemical oxidation to total mass loss was much higher than the mechanical contributions for the fretting displacements assessed.
- Fretting of individual displacements was found to be in corrosion enhanced wear degradation regime. However, the higher the fretting displacement, the more the degradation mechanism transitions to a wear enhanced corrosion mechanism.
- The unknown contribution of corrosion enhanced wear in the fretting current transient could make up a relatively large proportion of fretting current transients during fatigue loading in comparison to the wear enhanced corrosion.
- Effect of surface history when fretting displacement occurs in an incremental order of displacement didn't change the degradation mechanism from corrosion enhanced wear dominated. However, at the transition to reciprocating sliding, tribochemical interactions at the interface led to a significant drop in the interfacial energy and fretting current.
- Effect of surface history when fretting displacement occurs in a decreasing order was found in a corrosion dominated degradation mechanism and the absence of elastic compliance by the least displacement resulted to a transition from partial-slip to gross slip and thus increases fretting current.

### 11.1.3 Component testing of metal – metal and ceramic – metal tapers (Chapter 9)

The term 'fretting current' is used in this summary rather than the cumulative charge as the cumulative charge was the quantitative means through which the fretting current was averaged.

- The use of 5 Hz frequency in component testing undermines the degree of fretting currents for both metal – metal and ceramic – metal systems except in CoCrMo – CoCrMo which showed no significant difference across 1Hz, 2Hz and 5Hz.
- The magnitude of cyclic load had a greater effect on the evolution of fretting current than the increase in mean load for both metal – metal and ceramic – metal systems.
- CoCrMo – CoCrMo was most susceptible to fretting of all four combinations during the mean load assessment. While CoCrMo – Ti6Al4V experienced the most systemic effect after the mean load assessment.
- In general, the Biolox – Ti6Al4V combination generated the least fretting current apart from the cyclic load variation where very similar values were measured with that of CoCrMo – Ti6Al4V. This was found to be a result of larger interference fit at the Biolox – Ti6Al4V contact.
- The single case of misalignment in the Biolox – Ti6Al4V combination resulted in a significant increase in fretting current. Specifically at the 5 Hz frequency, the largest mean load and the largest cyclic load.
- There was a strong correlation between the extent of femoral head migration and taper separation force.
- The metal – metal combinations both experienced a toggling type of motion while the taper strength which is linked to the contacting area at the taper interface was highest for the ceramic – metal combinations.

## 11.2 Future work

**Characterising the surface chemistry of tribofilms during/after fretting** – this begins by characterising a surface that has undergone the process of film formation resulting from fretting a contact that has a history of surface wear and corrosion. XPS analysis of this film can thereby be compared to the chemistry of the films identified by other studies in literature.

**Quantify the hardness of the third-body product formed at the Biolox – Ti6Al4V fretting interface** – this can be done by replicating the smooth third-body product formed at the Biolox – Ti6Al4V surface and subsequently performing nano-indentation hardness to quantify its hardness.

**Employ an *in-situ* technique to observe the formation of amorphous Ti6Al4V** – this may be attempted by *in-situ* imaging and characterisation of a Ti6Al4V alloy rubbing against a transparent counter-body.

**Perform a component level assessment of bulk Si<sub>3</sub>N<sub>4</sub>** – the purpose of this is to see if the findings observed in this study through a 2D fretting contact would apply at a 3D fretting interface.

## References

- [1] NJR. (2016, 29-05-2017). *National Joint Registry for England and Wales: National Joint Registry 13th Annual Reports*. Available: <http://www.njrreports.org.uk/Portals/0/PDFdownloads/NJR%2013th%20Annual%20Report%202016.pdf>
- [2] D. J. T. M J Yaszemski, K Lewandrowski, V Hasirci, D Altobelli, D L Wise, *Biomaterials in Orthopedics* Marcel Dekkar, 2004.
- [3] J. B. Park, Kon Kim, Y. , *Metallic Biomaterials*: Boca Raton: CRC Press LLC, 2000.
- [4] L. Shi, Derek O. Northwood, and Zhengwang Cao, "The properties of a wrought biomedical cobalt-chromium alloy," *Journal of materials science*, vol. 29, pp. 1233-1238, 1994.
- [5] G. K. Smith, "Orthopaedic biomaterials," 1985.
- [6] T. J. Band, "Materials and metallurgy," in *Modern Hip Resurfacing*, ed London: Springer 2009, pp. 43-63.
- [7] Y. Hedberg, and Inger Odnevall Wallinder, "Metal release and speciation of released chromium from a biomedical CoCrMo alloy into simulated physiologically relevant solutions," *Journal of Biomedical Materials Research Part B*, vol. Applied Biomaterials 102, pp. 693-699, 2014.
- [8] B. Scharf, Clement, C.C., Zolla, V., Perino, G., Yan, B., Elci, S.G., Purdue, E., Goldring, S., Macaluso, F., Cobelli, N. and Vachet, R.W., "Molecular analysis of chromium and cobalt-related toxicity," *Scientific reports*, vol. 4, p. 5729, 2014.
- [9] C. Oldani, Alejandro Dominguez, and T. Eli., "Titanium as a Biomaterial for Implants," in *Recent Advances in Arthroplasty*, S. K. Fokter, Ed., ed: InTech, 2012.

- [10] J. V. Bono, *Revision total hip arthroplasty*: Springer Science & Business Media, 1999.
- [11] B. Weisse, Ch Affolter, G. P. Terrasi, G. Piskoty, and S. Köbel, "Failure analysis of in vivo fractured ceramic femoral heads," *Engineering Failure Analysis*, vol. 16, pp. 1188-1194, 2009.
- [12] R. Elke, "Particle disease: status and today's solutions," presented at the 7th international BIOLOX symposium, 2002.
- [13] B. MASSON, "Emergence of the alumina matrix composite in total hip arthroplasty," *International Orthopaedics*, pp. 33, 359-363., 2009.
- [14] B. J. McEntire, B. S. Bal, M. N. Rahaman, J. Chevalier, and G. Pezzotti, "Ceramics and ceramic coatings in orthopaedics," *Journal of the European Ceramic Society* vol. 35, pp. 4327-4369, 2015.
- [15] CeramTec. (2015). *BIOLOX(R)delta*. Available: [http://www.ceramtec.co.uk/files/mt\\_bioloX\\_delta\\_en.pdf](http://www.ceramtec.co.uk/files/mt_bioloX_delta_en.pdf)
- [16] S. Lal, Lisa Allinson, Richard M. Hall, and Joanne L. Tipper, "A comprehensive assessment of biological responses to silicon nitride nanoparticles and cobalt chromium wear debris from total hip replacements," *In Front. Bioeng. Biotechnol.* , vol. 4, 2016.
- [17] J. Olofsson, T. Mikael Grehk, Torun Berling, Cecilia Persson, Staffan Jacobson, and Håkan Engqvist, "Evaluation of silicon nitride as a wear resistant and resorbable alternative for total hip joint replacement," *Biomatter* vol. 2, pp. 94-102, 2012.
- [18] *Arx Spinal System*, US Food and Drug Administration (FDA), 2006.
- [19] B. S. Bal, and Mohamed Rahaman, "The Rationale for Silicon Nitride Bearings in Orthopaedic Applications," *Advances in Ceramics-Electric and Magnetic Ceramics, Bioceramics, Ceramics and Environment, InTech, Bioceramics, Ceramics and Environment*, 2011.

- [20] M. Herrmann, "Corrosion of silicon nitride materials in aqueous solutions," *Journal of the American Ceramic Society*, vol. 96, pp. 3009-3022, 2013.
- [21] P. R. Roberge, *Corrosion engineering: principles and practice*: New York: McGraw-Hill, 2008.
- [22] R. B. E. Stansbury, "Fundamentals of Electrochemical Corrosion," *Ohio: ASM International*, 2000.
- [23] U. o. Cambridge. (2017, 13-06-2017). *The Electrical Double Layer*. Available: <http://www.ceb.cam.ac.uk/research/groups/rg-eme/teaching-notes/the-electrical-double-layer>
- [24] INSA-LYON-LABORATOIRE. (2014, 23-7-14). *The Multimedia Corrosion Guide*. Available: [http://www.cdcorrosion.com/mode\\_corrosion/corrosion\\_uniform.htm](http://www.cdcorrosion.com/mode_corrosion/corrosion_uniform.htm)
- [25] Z. Ahmad, *Principles of corrosion engineering and corrosion control*: Butterworth-Heinemann, 2006.
- [26] J. L. Gilbert, Christine A. Buckley, Joshua J. Jacobs, Kim C. Bertin, and Michael R. Zernich, "Intergranular corrosion-fatigue failure of cobalt-alloy femoral stems. A failure analysis of two implants," *J Bone Joint Surg Am*, vol. 76, pp. 110-115, 1994.
- [27] J. L. Gilbert, Christine A. Buckley, and Joshua J. Jacobs., " In vivo corrosion of modular hip prosthesis components in mixed and similar metal combinations. The effect of crevice, stress, motion, and alloy coupling.," *Journal of biomedical materials research*, vol. 27, pp. 1533-1544, 1993.
- [28] M. G. Fontana, and N. G. Greene, *Corrosion Engineering*: New York: Mc Graw Hill, 1978.
- [29] J. W. Oldfield, and W. H. Sutton, "Crevice Corrosion of Stainless Steel I – A Mathematical Model," *British corrosion journal*, vol. 13, pp. 13-22, 1978.

- [30] J. P. Collier, Surprenant, V. A., Jensen, R. E., & Mayor, M. B., "Corrosion at the interface of cobalt-alloy heads on titanium-alloy stems," *Clinical orthopaedics and related research*, vol. 271, 1991.
- [31] R. W. Revie, and Herbert H. Uhlig, "Thermodynamics: Corrosion Tendency and Electrode Potentials," in *Corrosion and Corrosion Control: An Introduction to Corrosion Science and Engineering*, 4th ed: John Wiley and Sons, New York, 2000, pp. 21-41.
- [32] No-Authors-Listed. (2011, 17/8/2014). *How to explain Potentiodynamic*. Available: <http://srizam-expro.blogspot.co.uk/2011/03/how-to-explain-potentiodynamic.html>
- [33] G. Stachowiak, and Andrew W. Batchelor, *Engineering Tribology*, 3rd ed.: Butterworth-Heinemann, 2005.
- [34] J. Williams, *Engineering Tribology*, 2 ed.: Cambridge University Press, 1994.
- [35] V. Cuffaro, "Prediction Method for the Surface Damage in Splined Couplings," PhD, 2013.
- [36] J. A. Williams, *Engineering Tribology*. Oxford: Oxford University Press, 1998.
- [37] J. T. Burwell, "Survey of possible wear mechanisms," *Wear*, vol. 1, pp. 119-141, 1957.
- [38] O. Vingsbo, and Staffan Söderberg, "On fretting maps," *Wear*, vol. 126, pp. 131–147, 1988.
- [39] S. Fouvry, Philippe Kapsa, and Leo Vincent, "Quantification of fretting damage," *Wear*, vol. 200, pp. 186-205, 1996.
- [40] R.D.Mindlin, "Compliance of elastic bodies in contact," *J. Applied Mechanics*, vol. 16, pp. 259 - 268, 1949.

- [41] B. Tritschler, Bernard Forest, and Jean Rieu., "Fretting corrosion of materials for orthopaedic implants: a study of a metal/polymer contact in an artificial physiological medium.," *Tribology international*, vol. 32, 1999.
- [42] O. Vingsbo, and Joakim Schön, "Gross slip criteria in fretting," *Wear*, vol. 162, pp. 347-356, 1993.
- [43] P. Schaaff, "The role of fretting damage in total hip arthroplasty with modular design hip joints-evaluation of retrieval studies and experimental simulation methods," *Journal of applied biomaterials & biomechanics: JABB*, vol. 2, pp. 121-135, 2003.
- [44] I.-M. Feng, and B. G. Rightmire, "An experimental study of fretting," *Proceedings of the Institution of Mechanical Engineers*, vol. 170, pp. 1055-1064, 1956.
- [45] U. Bryggman, and Staffan Söderberg, "Contact conditions in fretting," *Wear*, vol. 110, pp. 1-17, 1986.
- [46] G. A. Tomlinson, "The rusting of steel surfaces in contact," in *Proceedings of the Royal Society of London*, 1927, pp. 472-483.
- [47] D. Landolt, S. Mischler, M. Stemp, and S. Barril, "Third body effects and material fluxes in tribocorrosion systems involving a sliding contact," *Wear*, vol. 256, pp. 517-524, 2004.
- [48] I. D. Learmonth, C. Young, and C. Rorabeck, "The operation of the century: total hip replacement," *The Lancet*, vol. 370, pp. 1508-1519, 2007.
- [49] S. R. Knight, Randeep Aujla, and Satya Prasad Biswas, "Total Hip Arthroplasty-over 100 years of operative history," *Orthopedic reviews*, vol. 3, 2011.
- [50] H. McKellop, Fu-wen Shen, Bin Lu, Patricia Campbell, and Ronald Salovey, "Development of an extremely wear-resistant ultra high



molecular weight polyethylene for total hip replacements," *Journal of Orthopaedic Research*, vol. 17, pp. 157-167, 1999.

- [51] U. Sentuerk, P. von Roth, and C. Perka, "Ceramic on ceramic arthroplasty of the hip," *Bone Joint J*, vol. 98, pp. 14-17, 2016.
- [52] S. U. Leslie F. Scheuber, Florence Petkow. (2014, 02-06-2017). *The Neck Taper in Hip Arthroplasty - What does the surgeon have to consider?* Available:  
[https://www.ceramtec.com/files/mt\\_taper\\_and\\_compatibility.pdf](https://www.ceramtec.com/files/mt_taper_and_compatibility.pdf)
- [53] T. McTighe, Declan Brazil, Louis Keppler, John Keggi, and Edward McPherson, "Metallic Modular Taper Junctions in Total Hip Arthroplasty," *Reconstructive Review*, vol. 5, 2015.
- [54] A. Srinivasan, Edward Jung, and Brett Russell Levine, "Modularity of the femoral component in total hip arthroplasty," *Journal of the American Academy of Orthopaedic Surgeons*, vol. 20, pp. 214-222, 2012.
- [55] H. Krishnan, S. P. Krishnan, G. Blunn, J. A. Skinner, and A. J. Hart, "Modular neck femoral stems," *Bone Joint J*, vol. 95, pp. 1011-1021, 2013.
- [56] S. Hussenbocus, Kosuge, D., Solomon, L. B., Howie, D. W., & Oskouei, R. H., "Head-neck taper corrosion in hip arthroplasty," *BioMed research international*, 2015.
- [57] M. Morlock, Dennis Bünthe, Julian Gührs, and Nicholas Bishop, "Corrosion of the Head-Stem Taper Junction—Are We on the Verge of an Epidemic?," *HSS Journal®*, pp. 1-8.
- [58] R. Chana, C. Esposito, P. Campbell, W. Walter, and W. Walter, "Mixing and matching causing taper wear," *J Bone Joint Surg Br*, vol. 94, pp. 281-286, 2012.
- [59] S. Y. Jauch-Matt, A. W. Miles, and H. S. Gill, "Effect of trunnion roughness and length on the modular taper junction strength under

- typical intraoperative assembly forces," *Medical Engineering & Physics*, vol. 39, pp. 94-101, 2017.
- [60] N. Bishop, F. Waldow, and M. Morlock, "Friction moments of large metal-on-metal hip joint bearings and other modern designs," *Medical engineering & physics*, vol. 30, pp. 1057-1064, 2008.
- [61] W. H. Wuttke V, Kempf K, Oberbach T, Delfosse D, "Influence of various types of damage on the fracture strength of ceramic femoral heads," *Biomed Tech (Berl)*, vol. 56, pp. 333–9, 2011.
- [62] Zimmer. (2014). *Zimmer M/L Taper Hip Prosthesis with Kinectiv Technology Surgical Technique*. Available: <http://www.zimmer.com/medical-professionals/products/hip/ml-taper-kinectiv-technology.html>
- [63] F. Witt, Julian Gührs, Michael M. Morlock, and Nicholas E. Bishop, "Quantification of the contact area at the head-stem taper interface of modular hip prostheses," *PloS one*, vol. 10, 2015.
- [64] H. Haschke, S. Y. Jauch-Matt, K. Sellenschloh, G. Huber, and M. M. Morlock, "Assembly force and taper angle difference influence the relative motion at the stem–neck interface of bi-modular hip prostheses," *Proceedings of the Institution of Mechanical Engineers, Part H: Journal of Engineering in Medicine*, vol. 230, pp. 690-699, 2016.
- [65] A. Rehmer, N. E. Bishop, and M. M. Morlock, "Influence of assembly procedure and material combination on the strength of the taper connection at the head–neck junction of modular hip endoprotheses," *Clinical Biomechanics*, vol. 27, pp. 77-83, 2012.
- [66] L. C. Lucas, R. A. Buchanan, and J. E. Lemons, "Investigations on the galvanic corrosion of multialloy total hip prostheses," *Journal of Biomedical Materials Research Part A*, vol. 15, pp. 731-747, 1981.
- [67] J. R. Goldberg, Gilbert, J. L., Jacobs, J. J., Bauer, T. W., Paprosky, W., & Leurgans, S., "A multicenter retrieval study of the taper interfaces of

modular hip prostheses," *Clinical orthopaedics and related research*, vol. 401, pp. 149-161, 2002.

- [68] H. J. Higgs G, MacDonald D, Kane W, Day J, Klein G, Parvizi J, Mont M, Kraay M, Martell J, Gilbert J, "In Metal-On-Metal Total Hip Replacement Devices," in *Method of characterizing fretting and corrosion at the various taper connections of retrieved modular components from metal-on-metal total hip arthroplasty*, ed. ASTM International, 2013.
- [69] S. Munir, Michael B. Cross, Christina Esposito, Anna Sokolova, and William L. Walter, "Corrosion in modular total hip replacements: An analysis of the head–neck and stem–sleeve taper connections," *In Seminars in Arthroplasty*, vol. 24, pp. 240-245, 2013.
- [70] R. M. Urban, Joshua J. Jacobs, Jeremy L. Gilbert, Stephen B. Rice, Murali Jasty, Charles R. Bragdon, and Jorge O. Galante, "Characterization of solid products of corrosion generated by modular-head femoral stems of different designs and materials," *In Modularity of Orthopedic Implants, ASTM International*, 1997.
- [71] G. B. Higgs, Josa A. Hanzlik, Daniel W. MacDonald, Jeremy L. Gilbert, Clare M. Rimnac, Steven M. Kurtz, and Implant Research Center Writing Committee. ": a retrieval study.", "Is increased modularity associated with increased fretting and corrosion damage in metal-on-metal total hip arthroplasty devices?," *The Journal of arthroplasty*, vol. 28, pp. 2-6, 2013.
- [72] S. M. Kurtz, Sevi B. Kocagöz, Josa A. Hanzlik, Richard J. Underwood, Jeremy L. Gilbert, Daniel W. MacDonald, Gwo-Chin Lee et al, "Do ceramic femoral heads reduce taper fretting corrosion in hip arthroplasty? A retrieval study.," *Clinical Orthopaedics and Related Research®*, vol. 471, pp. 3270-3282, 2013.
- [73] A. Di Laura, H. Hothi, J. Henckel, I. Swiatkowska, M. H. L. Liow, Y. M. Kwon, J. A. Skinner, and A. J. Hart, "Retrieval analysis of metal and

- ceramic femoral heads on a single CoCr stem design," *Bone and Joint Research*, vol. 6, pp. 345-350, 2017.
- [74] M. M. Morlock, Dennis Bunte, Harmen Ettema, Cees C. Verheyen, Åke Hamberg, and Jeremy Gilbert, "Primary hip replacement stem taper fracture due to corrosion in 3 patients," *Acta orthopaedica*, vol. 87, pp. 189-192, 2016.
- [75] N. Bishop, F. Witt, R. Pourzal, A. Fischer, M. Rutschi, M. Michel, *et al.*, "Wear patterns of taper connections in retrieved large diameter metal-on-metal bearings," *J Orthop Res*, vol. 31, pp. 1116-22, Jul 2013.
- [76] N. Moharrami, D. J. Langton, O. Sayginer, and S. J. Bull, "Why does titanium alloy wear cobalt chrome alloy despite lower bulk hardness: A nanoindentation study?," *Thin Solid Films*, vol. 549 pp. 79-86, 2013.
- [77] B. A. Lanting, Teeter, M. G., Vasarhelyi, E. M., Ivanov, T. G., Howard, J. L., & Naudie, "Correlation of corrosion and biomechanics in the retrieval of a single modular neck total hip arthroplasty design: modular neck total hip arthroplasty system," *The Journal of arthroplasty*, vol. 30, pp. 135-140, 2015.
- [78] D. Buente, Huber, G., Bishop, N., & Morlock, M., "Quantification of material loss from the neck piece taper junctions of a bimodular primary hip prosthesis. A retrieval study from 27 failed Rejuvenate bimodular hip arthroplasties," *Bone Joint J*, vol. 97, pp. 1350-1357, 2015.
- [79] I. P. S. Gill, J. Webb, K. Sloan, and R. J. Beaver, "Corrosion at the neck-stem junction as a cause of metal ion release and pseudotumour formation," *Journal of Bone & Joint Surgery*, vol. British Volume 94, pp. 895-900, 2012.
- [80] T. M. Grupp, Thomas Weik, Wilhelm Bloemer, and Hanns-Peter Knaebel "Modular titanium alloy neck adapter failures in hip replacement - failure mode analysis and influence of implant material," *BMC musculoskeletal disorders* 11, vol. 1, 2010.

- [81] C. J. Dangles and C. J. Altstetter, "Failure of the modular neck in a total hip arthroplasty," *J Arthroplasty*, vol. 25, pp. 1169 e5-7, Oct 2010.
- [82] J. G. Skendzel, J. D. Blaha, and A. G. Urquhart, "Total hip arthroplasty modular neck failure," *J Arthroplasty*, vol. 26, pp. 338 e1-4, Feb 2011.
- [83] M. Nganbe, Usman Khan, Hakim Louati, Andrew Speirs, and Paul E. Beaulé, "In vitro assessment of strength, fatigue durability, and disassembly of Ti6Al4V and CoCrMo necks in modular total hip replacements," *Journal of Biomedical Materials Research Part B: Applied Biomaterials*, vol. 97, pp. 132-138, 2011.
- [84] A. M. Kop, C. Keogh, and E. Swarts, "Proximal component modularity in THA—at what cost?: an implant retrieval study," *Clinical Orthopaedics and Related Research*, vol. 470, pp. 1885-1894, 2012.
- [85] J. J. Jacobs, Robert M. Urban, Jeremy L. Gilbert, Anastasia K. Skipor, Jonathan Black, Murali Jasty, and Jorge O. Galante, "Local and distant products from modularity," *Clinical orthopaedics and related research*, vol. 319, pp. 94-105, 1995.
- [86] M. Oldenburg, Ralf Wegner, and Xaver Baur, "Severe cobalt intoxication due to prosthesis wear in repeated total hip arthroplasty," *The Journal of arthroplasty*, vol. 24, pp. 825-e15, 2009.
- [87] J. J. Jacobs, Jeremy L. Gilbert, and Robert M. Urban, "Current concepts review-corrosion of metal orthopaedic implants," *J Bone Joint Surg Am*, vol. 80, pp. 268-82, 1998.
- [88] R. M. Urban, Joshua J. Jacobs, Jeremy L. Gilbert, and Jorge O. Galante., "Migration of corrosion products from modular hip prostheses. Particle microanalysis and histopathological findings," *J Bone Joint Surg Am*, vol. 76, pp. 1345-1359, 1994.
- [89] H. J. Agins, N. W. Alcock, Manjula Bansal, E. A. Salvati, P. D. Wilson, P. M. Pellicci, and P. G. Bullough, "Metallic wear in failed titanium-alloy

- total hip replacements. A histological and quantitative analysis," *J Bone Joint Surg Am*, vol. 70, pp. 347-356, 1988.
- [90] J. Black, H. Sherk, J. Bonini, W. R. Rostoker, F. Schajowicz, and J. O. Galante, "Metallosis associated with a stable titanium-alloy femoral component in total hip replacement," *JBJS*, vol. 72, pp. 126-130, 1990.
- [91] G. Meachim, and D. F. Williams, "Changes in nonosseous tissue adjacent to titanium implants," *Journal of Biomedical Materials Research Part A*, vol. 7, pp. 555-572, 1973.
- [92] J. J. Jacobs, Anastasia K. Skipor, Leslie M. Patterson, Nadim J. Hallab, Wayne G. Paprosky, Jonathan Black, and Jorge O. Galante, "Metal release in patients who have had a primary total hip arthroplasty. A prospective, controlled, longitudinal study," *J Bone Joint Surg Am*, vol. 80, pp. 1447-58, 1998.
- [93] L. Leysens, Bart Vinck, Catherine Van Der Straeten, Floris Wuyts, and Leen Maes, "Cobalt toxicity in humans. A review of the potential sources and systemic health effects," *Toxicology*, 2017.
- [94] M. A. Wimmer, Alfons Fischer, Robin Büscher, Robin Pourzal, Christoph Sprecher, Roland Hauert, and Joshua J. Jacobs, "Wear mechanisms in metal-on-metal bearings: The importance of tribochemical reaction layers," *Journal of Orthopaedic Research*, vol. 28, pp. 436-443, 2010.
- [95] M. T. Mathew, C. Nagelli, R. Pourzal, A. Fischer, M. P. Laurent, J. J. Jacobs, and M. A. Wimmer, "Tribolayer formation in a metal-on-metal (MoM) hip joint: an electrochemical investigation," *Journal of the mechanical behavior of biomedical materials*, vol. 29, pp. 199-212, 2014.
- [96] P. Zeng, W. M. Rainforth, and R. B. Cook, "Characterisation of the oxide film on the taper interface from retrieved large diameter metal on polymer modular total hip replacements," *Tribology International*, vol. 89, pp. 86-96, 2015.

- [97] J. L. Gilbert, Mali, S., Urban, R. M., Silverton, C. D., & Jacobs, J. J., "In vivo oxide-induced stress corrosion cracking of Ti-6Al-4V in a neck–stem modular taper: Emergent behavior in a new mechanism of in vivo corrosion," *Journal of Biomedical Materials Research Part B: Applied Biomaterials*, vol. 100, pp. 584-594, 2012.
- [98] M. G. Bryant, D. Buente, A. Oladokun, M. Ward, G. Huber, M. Morlock, and A. Neville, "Surface and subsurface changes as a result of tribocorrosion at the stem-neck interface of bi-modular prosthesis," *Biotribology*, 2017.
- [99] V. Swaminathan, and Jeremy L. Gilbert, "Fretting corrosion of CoCrMo and Ti6Al4V interfaces," *Biomaterials*, vol. 33, pp. 5487-5503, 2012.
- [100] "ASTM F1875-98(2014), Standard Practice for Fretting Corrosion Testing of Modular Implant Interfaces: Hip Femoral Head-Bore and Cone Taper Interface," ed. West Conshohocken, PA: ASTM International, 2014.
- [101] A. Panagiotidou, J. Meswania, K. Osman, B. Bolland, J. Latham, J. Skinner, F. S. Haddad, A. Hart, and G. Blunn, "The effect of frictional torque and bending moment on corrosion at the taper interface," *Bone Joint J*, vol. 97, pp. 463-472, 2015.
- [102] M. J. Baxmann, S. Y. Schilling, C. Blomer, W. Grupp, T. M. Morlock, M. M., "The influence of contact conditions and micromotions on the fretting behavior of modular titanium alloy taper connections," *Med Eng Phys*, vol. 35, pp. 676-83; discussion 676, May 2013.
- [103] D. Royhman, Patel, M., Runa, M. J., Wimmer, M. A., Jacobs, J. J., Hallab, N. J., & Mathew, M. T., "Fretting-Corrosion Behavior in Hip Implant Modular Junctions: The Influence of Friction Energy and pH Variation. ," *Journal of the Mechanical Behavior of Biomedical Materials*, 2016.

- [104] S. Barril, S. Mischler, and D. Landolt, "Influence of fretting regimes on the tribocorrosion behaviour of Ti6Al4V in 0.9 wt.% sodium chloride solution," *Wear*, vol. 256, pp. 963-972, 2004.
- [105] A. Bazzoni, S. Mischler, and N. Espallargas, "Tribocorrosion of pulsed plasma-nitrided CoCrMo implant alloy," *Tribology Letters*, vol. 49, pp. 157-167, 2013.
- [106] F. E. Donaldson, James C. Coburn, and Karen Lohmann Siegel, "Total hip arthroplasty head–neck contact mechanics: A stochastic investigation of key parameters," *Journal of biomechanics*, vol. 47, pp. 1634-1641, 2014.
- [107] T. Zhang, N. M. Harrison, P. F. McDonnell, P. E. McHugh, and S. B. Leen, "A finite element methodology for wear–fatigue analysis for modular hip implants," *Tribology International*, vol. 65, pp. 113-127, 2013.
- [108] V. Swaminathan, and Jeremy L. Gilbert, "Potential and frequency effects on fretting corrosion of Ti6Al4V and CoCrMo surfaces," *Journal of Biomedical Materials Research Part A*, vol. 101, pp. 2602-2612, 2013.
- [109] A. Oladokun, M. Pettersson, M. Bryant, H. Engqvist, C. Persson, R. Hall, and A. Neville, "Fretting of CoCrMo and Ti6Al4V alloys in modular prostheses," *Tribology - Materials, Surfaces & Interfaces*, vol. 9, pp. 165 - 173, 2015.
- [110] J. Dufils, Markus A. Wimmer, Joachim Kunze, Mathew T. Mathew, and Michel P. Laurent, "Influence of molybdate ion and pH on the fretting corrosion of a CoCrMo–Titanium alloy couple," *Biotribology*, 2017.
- [111] M. Wimmer, Mathew Mathew, Michel Laurent, Christopher Nagelli, Yifeng Liao, Laurence Marks, Robin Pourzal, Alfons Fischer, and Joshua Jacobs, "Tribochemical reactions in metal-on-metal hip joints influence wear and corrosion," *In Metal-On-Metal Total Hip Replacement Devices. ASTM International.*, pp. 1–18, 2013.



- [112] M. A. Wimmer, C. Sprecher, R. Hauert, G. Täger, and A. Fischer, "Tribocorrosion reaction on metal-on-metal hip joint bearings: a comparison between in-vitro and in-vivo results," *Wear*, vol. 255, pp. 1007-1014, 2003.
- [113] E. J. Martin, Robin Pourzal, Mathew T. Mathew, and Kenneth R. Shull, "Dominant role of molybdenum in the electrochemical deposition of biological macromolecules on metallic surfaces," *Langmuir*, vol. 29, pp. 4813-4822, 2013.
- [114] S. D. Cook, Robert L. Barrack, Gregory C. Baffes, Alastair JT Clemow, Paul Serekian, Nick Dong, and Mark A. Kester, "Wear and corrosion of modular interfaces in total hip replacements," *Clinical orthopaedics and related research* vol. 298, pp. 80-88, 1994.
- [115] J. L. Gilbert, M. Mehta, and B. Pinder, "Fretting crevice corrosion of stainless steel stem-CoCr femoral head connections: comparisons of materials, initial moisture, and offset length," *J Biomed Mater Res B Appl Biomater*, vol. 88, pp. 162-73, Jan 2009.
- [116] S. A. Brown, Alula Abera, Mark D'Onofrio, and Curt Flemming, "Effects of neck extension, coverage, and frequency on the fretting corrosion of modular THR bore and cone interface," in *Modularity of Orthopedic Implants*, ed: ASTM International, 1997.
- [117] A. Traynor, Amy Kinbrum, Jonathan Housden, and Simon Collins. ". " , no. SUPP (): . "Fretting and Corrosion of Tapered Head-Neck Junctions of Modular Hip Components," *Bone Joint J*, vol. 95, pp. 270-270, 2013.
- [118] M. L. Mroczkowski, J. S. Hertzler, S. M. Humphrey, T. Johnson, and C. R. Blanchard, "Effect of impact assembly on the fretting corrosion of modular hip tapers," *J Orthop Res*, vol. 24, pp. 271-9, Feb 2006.
- [119] A. Panagiotidou, Timothy Cobb, Jay Meswania, John Skinner, Alister Hart, Fares Haddad, and Gordon Blunn, "The Effect Of Impact Assembly On The Interface Deformation And Fretting Corrosion Of

- Modular Hip Tapers: An In Vitro Study," *Journal of Orthopaedic Research*, 2017.
- [120] M. M. Morlock, Nick Bishop, Jozef Zustin, Michael Hahn, Wolfgang R  ther, and Michael Amling, "Modes of implant failure after hip resurfacing: morphological and wear analysis of 267 retrieval specimens," *The Journal of Bone & Joint Surgery*, vol. 90., pp. 89-95, 2008.
- [121] M. Lavigne, Etienne L. Belzile, Alain Roy, Fran  ois Morin, Traian Amzica, and Pascal-Andr   Vendittoli, "Comparison of whole-blood metal ion levels in four types of metal-on-metal large-diameter femoral head total hip arthroplasty: the potential influence of the adapter sleeve," *J Bone Joint Surg Am*, vol. 93, pp. 128-136, 2011.
- [122] G. Bergmann, F. Graichen, A. Rohlmann, A. Bender, B. Heinlein, G. N. Duda, *et al.*, "Realistic loads for testing hip implants," *Biomed Mater Eng*, vol. 20, pp. 65-75, 2010.
- [123] H. Farhoudi, Reza H. Oskouei, Ali A. Pasha Zanoosi, Claire F. Jones, and Mark Taylor, "An Analytical Calculation of Frictional and Bending Moments at the Head-Neck Interface of Hip Joint Implants during Different Physiological Activities," *Materials*, vol. 9, 2016.
- [124] S. Jauch, L. Coles, L. Ng, A. Miles, and H. Gill, "Low torque levels can initiate a removal of the passivation layer and cause fretting in modular hip stems," *Medical engineering & physics*, vol. 36, pp. 1140-1146, 2014.
- [125] A. Panagiotidou, J. Meswania, J. Hua, S. Muirhead-Allwood, A. Hart, and G. Blunn, "Enhanced wear and corrosion in modular tapers in total hip replacement is associated with the contact area and surface topography," *Journal of orthopaedic research*, vol. 31, pp. 2032-2039, 2013.
- [126] A. Panagiotidou, Jay Meswania, Jia Hua, Sarah K. Muirhead-Allwood, John A. Skinner, Alister Hart, and Gordon Blunn, "Do Surface

Topography and Contact Area Effect Fretting Corrosion Behaviour of the Modular Taper Interface in Total Hip Replacements?," *Bone Joint J*, vol. 95, pp. 474-474, 2013.

- [127] R. M. R. Dyrkacz, J. M. Brandt, J. B. Morrison, S. T. O'Brien, O. A. Ojo, T. R. Turgeon, and U. P. Wyss, "Finite element analysis of the head-neck taper interface of modular hip prostheses.," *Tribology International*, vol. 91, pp. 206-213, 2015.
- [128] S. Y. Jauch, G. Huber, H. Haschke, K. Sellenschloh, and M. M. Morlock, "Design parameters and the material coupling are decisive for the micromotion magnitude at the stem-neck interface of bi-modular hip implants," *Med Eng Phys*, Dec 11 2013.
- [129] S. Y. Jauch, G. Huber, K. Sellenschloh, H. Haschke, M. Baxmann, T. M. Grupp, *et al.*, "Micromotions at the taper interface between stem and neck adapter of a bimodular hip prosthesis during activities of daily living," *Journal of Orthopaedic Research*, vol. 31, pp. 1165-1171, 2013.
- [130] B. L. Brandt JM, Marr J, MacDonald SJ, Bourne RB, Medley JB, "Biochemical Comparisons of Osteoarthritic Human Synovial Fluid with Calf Sera Used in Knee Simulator Wear Testing," *Journal of Biomedical Materials Research Part A*, vol. 94A, pp. 961-971, 2010.
- [131] S. A. Brown, Paula J. Hughes, and Katharine Merritt, "In vitro studies of fretting corrosion of orthopaedic materials," *Journal of orthopaedic research*, vol. 6, pp. 572-579, 1988.
- [132] A. C. Lewis, M. R. Kilburn, I. Papageorgiou, G. C. Allen, and C. P. Case, "Effect of synovial fluid, phosphate-buffered saline solution, and water on the dissolution and corrosion properties of CoCrMo alloys as used in orthopedic implants," *Journal of Biomedical Materials Research*, vol. Part A 73, pp. 456-467, 2005.
- [133] T. Hanawa and S. Hiromoto, " Surface Modification of metals and Alloys in a Human Body Environment," *Corrosion Engineering*, pp. 895-907, 1998.

- [134] J. P. Glusker, "Structural aspects of metal liganding to functional groups of proteins," *Advances in protein* 1991.
- [135] Y. Yan., "Corrosion and Tribo-corrosion behaviour of metallic orthopaedic implant material," PhD: , University of Leeds, 2006.
- [136] M. M. Stack, and K. Chi, "Mapping sliding wear of steels in aqueous conditions," *Wear*, vol. 255, pp. 456-465, 2003.
- [137] M. T. Mathew, P. Srinivasa Pai, R. Pourzal, A. Fischer, and M. A. Wimmer, "Significance of tribocorrosion in biomedical applications: overview and current status," *Advances in tribology* 2009, 2010.
- [138] N. E. Stefano Mischler, Anna Igual Muñoz, "Bio-Tribocorrosion Fundamentals to Orthopaedic Surgeon and Researcher," presented at the ORS Annual Meeting, 2014.
- [139] M. Bryant, and Anne Neville, "Fretting corrosion of CoCr alloy: Effect of load and displacement on the degradation mechanisms," *Proceedings of the Institution of Mechanical Engineers, Part H: Journal of Engineering in Medicine*, 2016.
- [140] B. J. Smith, and Paul Ducheyne, "Transitional Behavior in Ti-6AL-4V fretting corrosion," in *In Medical Applications of Titanium and Its Alloys: The Material and Biological Issues*, ed. ASTM International, 1996.
- [141] J. L. Gilbert, Christine A. Buckley, and Eugene P. Lautenschlager, "Titanium oxide film fracture and repassivation: the effect of potential, pH and aeration," in *Medical applications of titanium and its alloys*, ed. The material and biological issues: ASTM International, 1996.
- [142] G. J. Goldberg JR, "Electrochemical Response of Cocrmo to High-Speed Fracture of Its Metal Oxide Using an Electrochemical Scratch Test Method. ," *John Wiley & Sons*, pp. 421-431., 1997.
- [143] T. Hanawa, "Metal ion release from metal implants," *Materials Science and Engineering: C*, vol. 24, pp. 745-752, 2004.

- [144] N. N. M. Morita, Y. Tsukamoto, T. Sasada, *Japanese Society for Biomaterials*, vol. 10, p. 209, 1992.
- [145] S. Mischler, "Triboelectrochemical techniques and interpretation methods in tribocorrosion: a comparative evaluation," *Tribology International*, vol. 41, pp. 573-583, 2008.
- [146] F. W. P. Ponthiaux, D. Drees, J. P. Celis "Electrochemical techniques for studying tribocorrosion processes," *Wear*, vol. 256, pp. 459-468, 2004.
- [147] R. W.-W. Hsu, Chun-Chen Yang, Ching-An Huang, and Yi-Sui Chen, "Electrochemical corrosion properties of Ti-6Al-4V implant alloy in the biological environment," *Materials Science and Engineering*, vol. 380, pp. 100-109, 2004.
- [148] B. Alemón, M. Flores, W. Ramírez, J. C. Huegel, and Esteban Broitman, "Tribocorrosion behavior and ions release of CoCrMo alloy coated with a TiAlVCN/CNx multilayer in simulated body fluid plus bovine serum albumin," *Tribology International*, vol. 81, pp. 159-168, 2015.
- [149] S. Fouvry, Ph. Kapsa, and L. Vincent., "Analysis of sliding behaviour for fretting loadings: determination of transition criteria," *Wear*, vol. 185, pp. 35-46, 1995.
- [150] M. Bryant, "Fretting-crevice corrosion of cemented metal on metal total hip replacements," PhD Thesis, University of Leeds, 2013.
- [151] K. Elleuch, and S. Fouvry, "Wear analysis of A357 aluminium alloy under fretting," *Wear*, vol. 253, pp. 662-672, 2002.
- [152] C. Hammond, *Basics of crystallography and diffraction* vol. 214: Oxford University Press, 2009.
- [153] M. C. Biesinger, Brad P. Payne, Andrew P. Grosvenor, Leo WM Lau, Andrea R. Gerson, and Roger St. C. Smart, "Resolving surface chemical states in XPS analysis of first row transition metals, oxides

- and hydroxides: Sc, Ti, V, Cu and Zn," *Applied Surface Science*, vol. 257, pp. 887-898, 2010.
- [154] M. C. Biesinger, Brad P. Payne, Andrew P. Grosvenor, Leo WM Lau, Andrea R. Gerson, and Roger St C. Smart, "Resolving surface chemical states in XPS analysis of first row transition metals, oxides and hydroxides: Cr, Mn, Fe, Co and Ni," *Applied Surface Science*, vol. 257, pp. 2717-2730, 2011.
- [155] A. K.-V. Alexander V. Naumkin, Stephen W. Gaarenstroom, and Cedric J. Powell NIST X-ray Photoelectron Spectroscopy Database [Online]. Available: <https://srdata.nist.gov/xps/Default.aspx>
- [156] G. Beamson, and David Briggs, "High resolution XPS of organic polymers," 1992.
- [157] G. D. Silversmit, Diederik Poelman Hilde, Marin Guy B. De Gryse, Roger, "Determination of the V2p XPS binding energies for different vanadium oxidation states (V5+ to V0+)," *Journal of Electron Spectroscopy and Related Phenomena*, vol. 135, pp. 167-175, 4// 2004.
- [158] I. Milošev, and Maja Remškar, "In vivo production of nanosized metal wear debris formed by tribochemical reaction as confirmed by high-resolution TEM and XPS analyses," *Journal of Biomedical Materials Research Part A* vol. 91.4, pp. 1100-1110, 2009.
- [159] M. Biesinger. ([27-06-2017]). *X-ray photoelectron spectroscopy*. Available: <http://www.xpsfitting.com>
- [160] W. F. S. John F. Moulder, Peter E. Sobol, Kenneth D. Bomben, *Handbook of X-ray Photoelectron Spectroscopy*: Perkin-Elmer Corporation, Physical Electronics Division, 6509 Flying Cloud Drive, Eden Prairie, Minnesota 55344, United States of America, 1992.
- [161] No-Authors-Listed. (2017, [27-06-17]). *XPS Knowledge Base*. Available: <http://xpssimplified.com/periodictable.php>

- [162] L. V. Duong, Barry J. Wood, and J. Theo Kloprogge, "XPS study of basic aluminum sulphate and basic aluminium nitrate," *Materials Letters*, vol. 59, pp. 1932-1936, 2005.
- [163] A. I. Muñoz, and S. Mischler, "Interactive effects of albumin and phosphate ions on the corrosion of CoCrMo implant alloy," *Journal of the Electrochemical Society*, vol. 154, pp. C562-C570, 2007.
- [164] Y. Fu, Hejun Du, Sam Zhang, and Weimin Huang, "XPS characterization of surface and interfacial structure of sputtered TiNi films on Si substrate," *Materials Science and Engineering: C*, vol. A 403, pp. 25-31, 2005.
- [165] F. Cordier, and E. Ollivier, "X-ray photoelectron spectroscopy study of aluminium surfaces prepared by anodizing processes," *Surface and interface analysis*, vol. 23, pp. 601-608, 1995.
- [166] W. C. Oliver, and George Mathews Pharr, "An improved technique for determining hardness and elastic modulus using load and displacement sensing indentation experiments," *Journal of materials research*, vol. 7, pp. 1564-1583, 1992.
- [167] Z. Guo, Xiaolu Pang, Yu Yan, Kewei Gao, Alex A. Volinsky, and Tong-Yi Zhang, "CoCrMo alloy for orthopedic implant application enhanced corrosion and tribocorrosion properties by nitrogen ion implantation," *Applied surface science*, vol. 347, pp. 23-34, 2015.
- [168] M. Bryant, R. Farrar, R. Freeman, K. Brummitt, and A. Neville, "The role of surface pre-treatment on the microstructure, corrosion and fretting corrosion of cemented femoral stems," *Biotribology*, vol. 5, pp. 1-15, 2016.
- [169] S. Kurosu, Naoyuki Nomura, and Akihiko Chiba, "Effect of sigma phase in Co-29Cr-6Mo alloy on corrosion behavior in saline solution," *Materials transactions*, vol. 47, pp. 1961-1964, 2006.

- [170] T. Zhu, and Miaoquan Li, "Effect of 0.770 wt% H addition on the microstructure of Ti-6Al-4V alloy and mechanism of  $\delta$  hydride formation," *Journal of Alloys and Compounds*, vol. 481, pp. 480-485, 2009.
- [171] A. S. E. J. McHargue C.J., Hammond J.P, "Aluminum Titanium - ICS Database," *Trans. Am. Inst. Min. Metall. Pet. Eng.*, vol. 197, 1953.
- [172] R. J. Wasilewski, "Titanium - ICS Database," *Trans. Met. Soc. AIME*, vol. 221,, 1961.
- [173] S. Suwarno, Solberg, J.K., Maehlen, J.P., Krogh, B., Yartys, V.A., "Titanium Vanadium - ICS Database," *Int. J. Hydrogen Energy*, vol. 37, 2012.
- [174] M. Jenko, Matevž Gorenšek, Matjaž Godec, Maxinne Hodnik, Barbara Šetina Batič, Črtomir Donik, John T. Grant, and Drago Dolinar, "Surface chemistry and microstructure of metallic biomaterials for hip and knee endoprotheses," *Applied Surface Science*, 2017.
- [175] J. R. Goldberg, and Jeremy L. Gilbert, "Electrochemical response of CoCrMo to high-speed fracture of its metal oxide using an electrochemical scratch test method," *Journal of biomedical materials research*, vol. 37, 1997.
- [176] G. Manivasagam, Durgalakshmi Dhinasekaran, and Asokamani Rajamanickam, "Biomedical implants: Corrosion and its prevention-a review," *Recent patents on corrosion science*, vol. 2, pp. 40-54, 2010.
- [177] R. Büscher, and A. Fischer "The pathways of dynamic recrystallization in all-metal hip joints," *Wear* vol. 259, pp. 887-897, 2005.
- [178] M. Textor, Caroline Sittig, Vinzenz Frauchiger, Samuele Tosatti, and Donald M. Brunette, "Properties and biological significance of natural oxide films on titanium and its alloys," in *Titanium in medicine*, ed. Berlin Heidelberg: Springer 2001, pp. 171-230.



- [179] J. Vaithilingam, Elisabetta Prina, Ruth D. Goodridge, Richard JM Hague, Steve Edmondson, Felicity RAJ Rose, and Steven DR Christie, "Surface chemistry of Ti6Al4V components fabricated using selective laser melting for biomedical applications," *Materials Science and Engineering*, vol. C 67, pp. 294-303, 2016.
- [180] I. Milošev, and H-H. Strehblow, "The composition of the surface passive film formed on CoCrMo alloy in simulated physiological solution," *Electrochimica Acta*, vol. 48, pp. 2767-2774, 2003.
- [181] M. Metikoš-Huković, and Mihajlo Ceraj-Cerić, "p-Type and n-Type Behavior of Chromium Oxide as a Function of the Applied Potential," *Journal of the Electrochemical Society*, vol. 134, pp. 2193-2197, 1987.
- [182] N. McIntyre, D. Johnston, L. Coatsworth, R. Davidson, and J. Brown, "X-ray photoelectron spectroscopic studies of thin film oxides of cobalt and molybdenum," *Surface and interface analysis*, vol. 15, pp. 265-272, 1990.
- [183] T. R. Beck, "Electrochemistry of freshly-generated titanium surfaces—I. Scraped-rotating-disk experiments," *Electrochimica Acta*, vol. 18, pp. 807-814, 1973.
- [184] J. R. Tavera, DY Peña Ballesteros, and HA Estupiñán Duran, "Evaluation of the stiffness and friction of Ti6Al4V ELI treated by glow discharge nitriding," *In Journal of Physics: Conference Series*, vol. 687, p. 012021, 2016.
- [185] R. Liu, Xiaoying Li, Xiao Hu, and Hanshan Dong, "Surface modification of a medical grade Co-Cr-Mo alloy by low-temperature plasma surface alloying with nitrogen and carbon," *Surface and Coatings Technology*, vol. 232, pp. 906-911, 2013.
- [186] D. L. Roll, "Passivation and the Passive Layer," ASTRO PAK.

- [187] K. Hashimoto, K. Asami, M. Naka, and T. Masumoto, "The role of alloying elements in improving the corrosion resistance of amorphous iron base alloys," *Corrosion Science*, vol. 19, pp. 857-867, 1979.
- [188] M. Metikos-Huković, Ana Kwokal, and Jasenka Piljac, "The influence of niobium and vanadium on passivity of titanium-based implants in physiological solution," *Biomaterials*, vol. 24, pp. 3765-3775, 2003.
- [189] S. M. Bholá, and Brajendra Mishra, "Effect of pH on the Electrochemical Properties of Oxides formed over  $\beta$ -Ti-15Mo and Mixed Ti-6Al-4V Alloys," *Int. J. Electrochem Sci*, vol. 8, pp. 7075-7087, 2013.
- [190] D. Mareci, Daniel Sutiman, Adrian Cailean, and Igor Crețescu, "EFFECT OF VANADIUM REPLACEMENT BY ZIRCONIUM ON THE ELECTROCHEMICAL BEHAVIOR OF Ti6Al4V ALLOY IN RINGERS SOLUTION," *Environmental Engineering and Management Journal*, vol. 7, pp. 701-706, 2008.
- [191] N. J. Hallab, Shelley Anderson, Marco Caicedo, Ameer Brasher, Katalin Mikecz, and Joshua J. Jacobs, "Effects of soluble metals on human peri-implant cells," *Journal of Biomedical Materials Research Part A*, vol. 74, pp. 124-140, 2005.
- [192] S. Fouvry, C. Paulin, and T. Liskiewicz, "Application of an energy wear approach to quantify fretting contact durability: Introduction of a wear energy capacity concept," *Tribology International*, vol. 40, pp. 1428-1440, 2007.
- [193] M. Bryant, R. Farrar, K. Brummitt, R. Freeman, and A. Neville, "Fretting corrosion of fully cemented polished collarless tapered stems: The influence of PMMA bone cement," *Wear*, vol. 301, pp. 290-299, 2013.
- [194] Y. Yan, A. Neville, and D. Dowson, "Biotribocorrosion—an appraisal of the time dependence of wear and corrosion interactions: II. Surface analysis," *Journal of Physics D: applied physics*, vol. 39, p. 3206, 2006.

- [195] A. C. Fernandes, F. Vaz, E. Ariza, L. A. Rocha, A. R. L. Ribeiro, A. C. Vieira, J. P. Rivière, and L. Pichon. , "Tribocorrosion behaviour of plasma nitrided and plasma nitrided+ oxidised Ti6Al4V alloy," *Surface and Coatings Technology*, vol. 200, pp. 6218-6224, 2006.
- [196] M. T. Mathew, Valentim A. Barão, Judy Chia-Chun Yuan, Wirley G. Assunção, Cortino Sukotjo, and Markus A. Wimmer, "What is the role of lipopolysaccharide on the tribocorrosive behavior of titanium?," *Journal of the mechanical behavior of biomedical materials*, vol. 8, pp. 71-85, 2012.
- [197] P. Zeng, J. Sharp, A. Rana, R. Thompson, W. M. Rainforth, and R. B. Cook, "Sub-surface characterisation of tribological contact zone of metal hip prostheses," *In Journal of Physics: Conference Series*, vol. 644, p. 012029, 2015.
- [198] R. Pourzal, R. Theissmann, M. Morlock, and A. Fischer, "Micro-structural alterations within different areas of articulating surfaces of a metal-on-metal hip resurfacing system," *267*, vol. *Wear*, pp. 689-694, 2009.
- [199] D. J. Hall, Robin Pourzal, Hannah J. Lundberg, Mathew T. Mathew, Joshua J. Jacobs, and Robert M. Urban, "Mechanical, chemical and biological damage modes within head-neck tapers of CoCrMo and Ti6Al4V contemporary hip replacements," *Journal of Biomedical Materials Research Part B*, vol. *Applied Biomaterials*, 2017.
- [200] A. Di Laura, Quinn, P. D., Panagiotopoulou, V. C., Hothi, H. S., Henckel, J., Powell, J. J., ... Hart, A. J. , "The Chemical Form of Metal Species Released from Corroded Taper Junctions of Hip Implants: Synchrotron Analysis of Patient Tissue," *Scientific Reports*, vol. 7, 2017.
- [201] S. B. Kocagoz, Underwood, R. J., MacDonald, D. W., Gilbert, J. L., & Kurtz, S. M., "Ceramic Heads Decrease Metal Release Caused by

- Head-taper Fretting and Corrosion," *Clinical Orthopaedics and Related Research*, vol. 474, pp. 985-994, 2016.
- [202] S. R. Pearson, P. H. Shipway, J. O. Abere, and R. A. A. Hewitt, "The effect of temperature on wear and friction of a high strength steel in fretting," *Wear*, vol. 303, pp. 622-631, 2013.
- [203] J. Vižintin, M. Kalin, S. Novak, G. Dražič, L. K. Ives, and M. B. Peterson, "Effect of slip amplitude on the fretting wear of silicon nitride against silicon nitride," *Wear*, vol. 192, pp. 11-20, 1996.
- [204] M. R. Alexander, R. D. Short, F. R. Jones, W. Michaeli, and C. J. Blomfield, "A study of HMDSO/O<sub>2</sub> plasma deposits using a high-sensitivity and-energy resolution XPS instrument: curve fitting of the Si 2p core level," *Applied Surface Science*, vol. 137, pp. 179-183, 1999.
- [205] B. J. McEntire, Ramaswamy Lakshminarayanan, Darin A. Ray, Ian C. Clarke, Leonardo Puppulin, and Giuseppe Pezzotti, "Silicon Nitride Bearings for Total Joint Arthroplasty," *Lubricants*, vol. 4, p. 35, 2016.
- [206] S. Novak, G. Dražič, M. Kalin, and J. Vižintin, "Interactions in silicon nitride ceramics vs. steel contact under fretting conditions," *Wear*, vol. 225, pp. 1276-1283, 1999.
- [207] J. Qu, Peter J. Blau, Thomas R. Watkins, Odis B. Cavin, and Nagraj S. Kulkarni, "Friction and wear of titanium alloys sliding against metal, polymer, and ceramic counterfaces," *Wear*, vol. 258, pp. 1348-1356, 2005.
- [208] C. H. Hager Jr, J. H. Sanders, and S. Sharma, "Characterization of mixed and gross slip fretting wear regimes in Ti6Al4V interfaces at room temperature," *Wear*, vol. 257, pp. 167-180, 2004.
- [209] K. G. Budinski, "Tribological properties of titanium alloys," *Wear*, vol. 151, pp. 203-217, 1991.
- [210] J. S. Kawalec, Stanley A. Brown, Joe H. Payer, and Katharine Merritt, "Mixed-metal fretting corrosion of Ti6Al4V and wrought cobalt alloy,"

*Journal of Biomedical Materials Research Part A*, vol. 29, pp. 867-873, 1995.

- [211] *Titanium in medicine: material science, surface science, engineering, biological responses and medical applications*: Springer Science & Business Media, 2012.
- [212] J. C. Scully, Ed., *Corrosion: Aqueous Processes and Passive Films* (Treatise on Materials Science and Technology. 1983, p.^pp. Pages.
- [213] S. W. Watson, F. J. Friedersdorf, B. W. Madsen, and S. D. Cramer, "Methods of measuring wear-corrosion synergism," *Wear*, vol. 181, pp. 476-484, 1995.
- [214] H. Uhlig, "Mechanism of fretting corrosion," *J Appl Mech*, vol. 21, pp. 401–7, 1954.
- [215] Y. Yan, Anne Neville, and Duncan Dowson, "Tribo-corrosion properties of cobalt-based medical implant alloys in simulated biological environments," *Wear*, vol. 263, pp. 1105-1111, 2007.
- [216] H. S. Hothi, Andreas C. Panagiotopoulos, Robert K. Whittaker, Paul J. Bills, Rebecca A. McMillan, John A. Skinner, and Alister J. Hart, "Damage patterns at the head-stem taper junction helps understand the mechanisms of material loss," *The Journal of arthroplasty*, vol. 32, pp. 291-295, 2017.
- [217] J. M. M. Anna Panagiotidou, Osman Khabab, Alister Hart, John Skinner, Fares Haddad and Gordon Blunn, "The effect of diamond like carbon coating on fretting corrosion and wear at the modular head-stem junction of metal on metal total hip replacements," presented at the 10th World Biomaterials Congress, Montréal, Canada, 2016.
- [218] J. P. Kretzer, Eike Jakubowitz, Michael Krachler, Marc Thomsen, and Christian Heisel, "Metal release and corrosion effects of modular neck total hip arthroplasty," *International orthopaedics*, vol. 33, p. 1531, Dec 2009.

- [219] S. B. Kocagöz, Richard J. Underwood, Shiril Sivan, Jeremy L. Gilbert, Daniel W. MacDonald, Judd S. Day, and Steven M. Kurtz, "Does taper angle clearance influence fretting and corrosion damage at the head–stem interface? A matched cohort retrieval study," *Seminars in arthroplasty*, vol. 24, pp. 246-254, 2013.
- [220] S. Y. Jauch, G. Huber, E. Hoenig, M. Baxmann, T. M. Grupp, and M. M. Morlock, "Influence of material coupling and assembly condition on the magnitude of micromotion at the stem–neck interface of a modular hip endoprosthesis," *Journal of biomechanics*, vol. 44, pp. 1747-1751, 2011.
- [221] S. Fouvry, P. Duo, and Ph Perruchaut, "A quantitative approach of Ti–6Al–4V fretting damage: friction, wear and crack nucleation," *Wear*, vol. 257, pp. 916-929, 2004.
- [222] M. Kiran, & Boscainos, "Adverse reactions to metal debris in metal-on-polyethylene total hip arthroplasty using a titanium-molybdenum-zirconium-iron alloy stem," *The Journal of arthroplasty*, vol. 30, pp. 277-281, 2015.
- [223] R. K. Whittaker, Ahmed M. Zaghoul, Harry S. Hothi, Imran A. Siddiqui, Gordon W. Blunn, John A. Skinner, and Alister J. Hart, "Clinical Cold Welding of the Modular Total Hip Arthroplasty Prosthesis," *The Journal of arthroplasty*, vol. 32, pp. 610-615, 2017.
- [224] C. R. Fritzl, Luis E. Moya, Lorenzo Castellani, Timothy M. Wright, and Robert L. Buly, "Corrosion at the stem-sleeve interface of a modular titanium alloy femoral component as a reason for impaired disengagement," *The Journal of arthroplasty*, vol. 26, pp. 113-119, 2011.
- [225] N. A. Nassif, Danyal H. Nawabi, Kirsten Stoner, Marcella Elpers, Timothy Wright, and Douglas E. Padgett, "Taper design affects failure of large-head metal-on-metal total hip replacements," *Clinical Orthopaedics and Related Research®*, vol. 472, pp. 564-571, 2014.

- [226] E. Sauger, S. Fouvry, L. Ponsonnet, Ph Kapsa, J. M. Martin, and L. Vincent., "Tribologically transformed structure in fretting," *Wear*, vol. 245, pp. 39-52, 2000.
- [227] E. E. Hoffman, Alex Lin, Yifeng Liao, and Laurence D. Marks, "Grain Boundary Assisted Crevice Corrosion in CoCrMo Alloys," *Corrosion*, vol. 72, pp. 1445-1461, 2016.
- [228] J. M. West, "Basic corrosion and oxidation," 1986.
- [229] H. Tomizawa, and T. E. Fischer, "Friction and wear of silicon nitride and silicon carbide in water: hydrodynamic lubrication at low sliding speed obtained by tribochemical wear," *ASLE transactions*, vol. 30, pp. 41-46, 1987.
- [230] G. Milazzo, Sergio Caroli, and Robert D. Braun, "Tables of standard electrode potentials," *Journal of The Electrochemical Society*, vol. 125, pp. 261C-261C, 1978.
- [231] G. Gstraunthaler, and Toni Lindl. Zell-und Gewebekultur, *allgemeine Grundlagen und spezielle Anwendungen*: Springer-Verlag, 2013.

## Appendix A– Composition of FBS and PBS

Component	Average	Range
Endotoxins (ng/ml)	0.35	0.01 - 10.0
Glucose (mg/ml)	1.25	0.85 - 1.81
Protein (mg/ml)	38	32 - 70
Albumin (mg/ml)	23	20 - 36
Hemoglobine (µg/ml)	113	24 - 181
Bilirubin, total (µg/ml)	4	3 - 11
Bilirubin, direct (µg/ml)	2	0 - 5
Urea (µg/ml)	160	140 - 200
Urate (µg/ml)	29	13 - 41
Creatinin (µg/ml)	31	16 - 43
Insulin (µU/ml)	10	6 - 14
Cortisol (ng/ml)	0.5	0.1 - 23
Growth hormone (ng/ml)	39.0	18.7 - 51.6
Parathormone, PTH (ng/ml)	1.72	0.085 - 6.18
Triiodothyronine, T3 (ng/ml)	1.2	0.56 - 2.23
Thyroxine, T4 (ng/ml)	0.12	0.08 - 0.16
Thyroid-stimulating hormone, TSH (ng/ml)	1.22	0.2 - 4.5
Follicle-stimulating hormone, FSH (pg/ml)	95	20 - 338
Testosterone (pg/ml)	400	210 - 990
Progesterone, P4 (pg/ml)	80	3 - 360
Prolactin = Luteotropic hormone, LTH (pg/ml)	176	20 - 500
Luteinizing hormone, LH ?? (pg/ml)	8	1,2 - 18
Prostaglandin E (ng/ml)	5.9	0.5 - 30.5
Prostaglandin F (ng/ml)	12.3	3.8 - 42.0
Vitamine A (ng/ml)	90	10 - 350
Vitamine E (ng/ml)	1.1	1 - 4.2
Cholesterol (µg/ml)	310	120 - 630
Lactate-dehydrogenase, LDH (mU/ml)	864	260 - 1,215
Alkaline Phosphatase (mU/ml)	255	110 - 352
Aspartate-Aminotransferase, ASAT (mU/ml)	130	20 - 200
Sodium, Na <sup>+</sup> (µeq/ml)	137	125 - 143
Potassium, K <sup>+</sup> (µeq/ml)	11.2	10.0 - 14.0
Calcium, Ca <sup>2+</sup> (µeq/ml)	6.75	6.30 - 7.15
Chloride, Cl <sup>-</sup> (µeq/ml)	103	98 - 108
Phosphate, P <sub>i</sub> (µg/ml)	98	43 - 114
Selen (µg/ml)	0.026	0.014 - 0.038
pH	7.40	7.20 - 7.60

**Figures 11-1 – Composition of FBS [231]**



Components	Molecular Weight	Concentration (mg/L)	mM
<b>Inorganic Salts</b>			
Potassium Phosphate monobasic (KH <sub>2</sub> PO <sub>4</sub> )	136.0	210.0	1.5441177
Sodium Chloride (NaCl)	58.0	9000.0	155.17241
Sodium Phosphate dibasic (Na <sub>2</sub> HPO <sub>4</sub> ·7H <sub>2</sub> O)	268.0	726.0	2.7089553

**Figures 11-2 – Composition of PBS**

## Appendix B– Determination of contact compliance

For a fretting displacement amplitude  $\delta x$  imposed upon a tribo-couple, a proportion of this displacement is not translated into slip at the contact, rather, some of the displacement is expended in two main form of compliances namely: Contact compliance ( $C_c$ ) and System compliance ( $C_s$ ). While  $C_c$  may differ with varying material combinations,  $C_s$  varies in depending on the value of  $C_c$  as both parameters together make up the total recorded compliance ( $C_r$ ). For example,  $C_c$  is a function of the contact stiffness 'K' and the Hertzian contact radius 'a' of the tribo-couple as expressed by Fouvry et al [149] and shown in Equation 11-1.

$$C_c(F_t) = \frac{2K}{3a} \quad 11-1$$

$C_s$  on the other hand is a parameter related to the cantilever deformation of the fretting tribometer. It is determined only by firstly measuring the recorded compliance  $C_r$  which is obtainable directly from the quasi-stick fretting loops of the material combinations in subject. Figures 11-3a and b are the fretting loops at  $\delta_x = \pm 10 \mu\text{m}$  for CoCrMo – CoCrMo and CoCrMo – Ti6Al4V respectively. Errors in the determination of  $C_r$  can be minimised by using quasi-stick fretting loop because the maximum tangential force ' $F_t$ ' occurs at the maximum displacement  $\delta_x$ . In addition,  $\delta_x \cong \delta_e$  where  $\delta_e$  is the elastic (reversible) part of the displacement and  $\delta_s$  is the irreversible, dissipative slip incurred at the tribo-couple interface.  $C_r$  is determined using Equation 11-2.

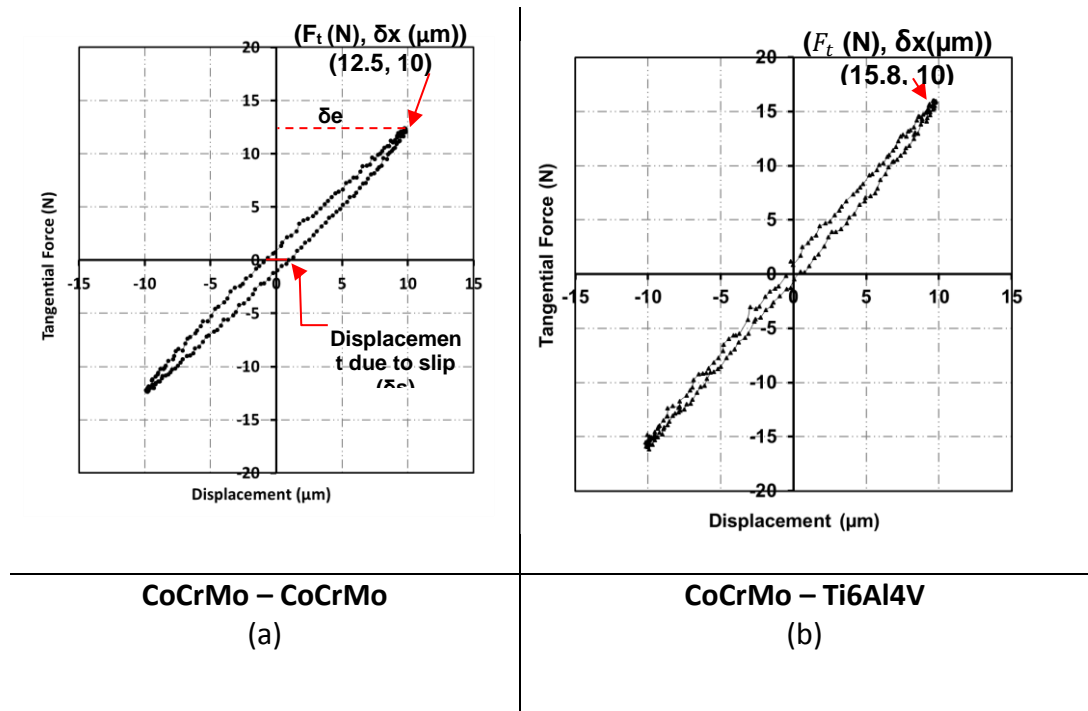
$$C_r(F_t) = \frac{\Delta \delta_x}{\Delta Q} \quad 11-2$$

$C_s$  is determined from the difference between  $C_r$  and  $C_c$  as expressed in Equation 11-3.

$$C_s = C_r(F_t) - C_c(F_t) \quad 11-3$$

The calculated values are outlined in Table 4-1 along with the Hertzian contact radius and the reduced modulus. The results show that Hertzian contact

radius of CoCrMo – Ti6Al4V is ~ 36% larger than it is for CoCrMo – CoCrMo while the reduced modulus values also differ by ~32%, and CoCrMo – CoCrMo is the larger value. The contact compliance at the contact of both combinations were ~ 30 nm/N and relatively similar system compliances with values of 96.1% and 97.6% for CoCrMo – CoCrMo and CoCrMo – Ti6Al4V respectively. The system compliance, reported as a percentage ratio of the total compliance was measured at the quasi-stick fretting loop of both material combinations.



**Figures 11-3 – Quasi-stick fretting loop of (a) CoCrMo – CoCrMo and (b) CoCrMo – Ti6Al4V tribo-couples**

**Table B 1 – Tribological parameters of the Metal – Metal fretting contact**

	CoCrMo – CoCrMo	CoCrMo – Ti6Al4V
Hertzian Contact Radius 'a' ( $\mu\text{m}$ )	160	250
Reduced Modulus (GPa)	123	84
Contact Compliance 'Cc' ( $\mu\text{m}/\text{N}$ )	0.0315	0.0293
System Compliance 'Cs' (%)	96.1	97.6

**Table B 2– Tribological parameters of the Ceramic ( $\text{Si}_3\text{N}_4$ ) – Metal and Ceramic ( $\text{Si}_3\text{N}_4$ ) – Ceramic ( $\text{Si}_3\text{N}_4$ ) fretting contact**

	$\text{Si}_3\text{N}_4$ – CoCrMo	$\text{Si}_3\text{N}_4$ – Ti6Al4V	$\text{Si}_3\text{N}_4$ – $\text{Si}_3\text{N}_4$
Hertzian Contact Radius 'a' ( $\mu\text{m}$ )	130	200	120
Reduced Modulus (GPa)	143	94	171
Contact Compliance 'Cc' ( $\mu\text{m}/\text{N}$ )	0.0325	0.0325	0.0285
System Compliance 'Cs' (%)	96.6	95.0	95.0

**Table B 3 – Tribological parameters of the Ceramic (Biolox) – Metal fretting contact**

	<b>Biolox – CoCrMo  (1 GPa)</b>	<b>Biolox – Ti6Al4V  (1 GPa)</b>	<b>Biolox – Ti6Al4V  (0.77 GPa)</b>
<b>Hertzian Contact Radius 'a' (μm)</b>	140	230	180
<b>Reduced Modulus (GPa)</b>	147	97	97
<b>Contact Compliance 'Cc' (μm/N)</b>	0.0291	0.0276	0.0353
<b>System Compliance 'Cs' (%)</b>	97.0	96.5	93.7

## Appendix C – Interactions between energy and wear

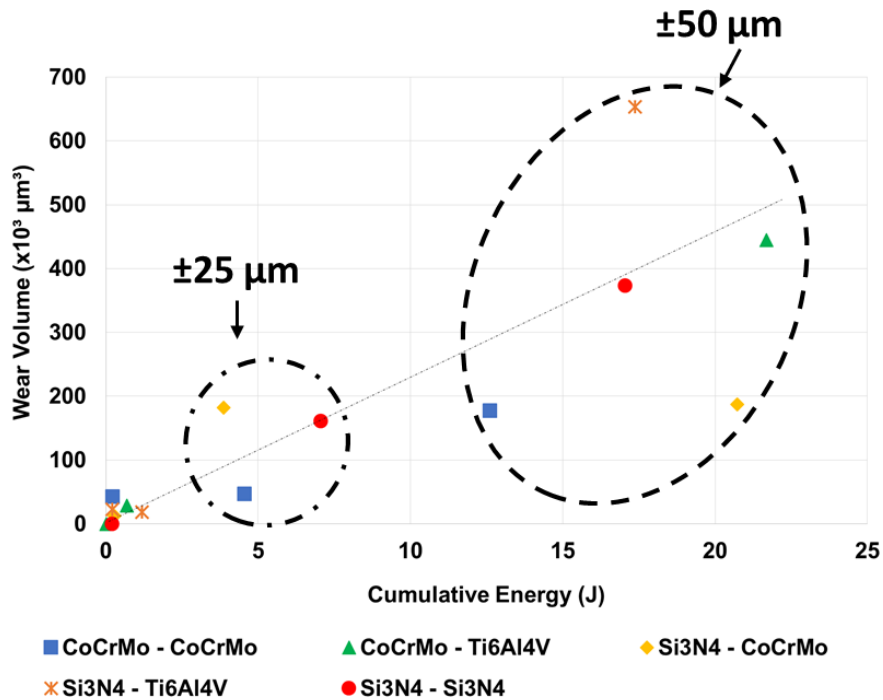


Figure 11-4– Wear-Energy plot of metal – metal and ceramic – metal material combinations.

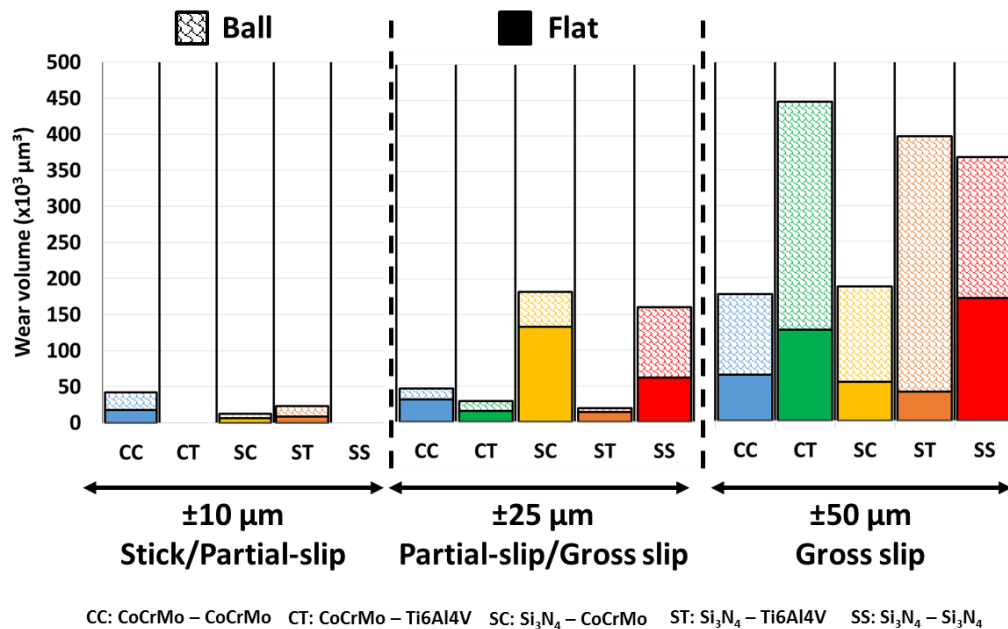


Figure 11-5 – Average wear volume of metal – metal and ceramic metal material combinations. The contribution of the ball component is shown above and the contribution of the flat component beneath.

## Appendix D – List of oral presentations

1. Fretting corrosion regime and wear mechanism of CoCrMo and Ti6Al4V
  - **{Leeds – Lyon Tribology Conference, Leeds, UK} 2014**
2. *In-vitro* studies of fretting corrosion at the modular THR taper junction: The effect of mixed metal couples **1<sup>st</sup> Prize (poster) Award!**
  - **{Corrosion Science Symposium, Manchester, UK} 2014**
3. Fretting of CoCrMo and Ti6Al4V alloys in modular prostheses
  - **{Micro-tribology Symposium, Warsaw, Poland} 2014**
4. Subsurface investigation of fretted CoCrMo and Ti6Al4V alloys **1<sup>st</sup> Prize (oral) Award!**
  - **{International Society of Technology and Arthroplasty, Vienna, Austria} 2015**
  - **{Tribology Conference, Leeds, UK} 2016**
5. Effect of tribocorrosion products in metal – metal modular fretting interfaces
  - **{Leeds – Lyon Tribology Conference, Leeds, UK} 2016**
6. The effect of cyclic load on the evolution of fretting current at the interface of metal-metal and ceramic – metal taper junction of hip prosthesis
  - **{International Society of Technology and Arthroplasty, Boston, USA} 2016**
7. The influence of surface history on the evolution of fretting corrosion current
  - **{International Conference on Biotribology, London, UK} 2016**
8. Subsurface transformation of Ti6Al4V alloy under fretting conditions **IMechE Research Prize!**
  - **{Mission of Tribology, London, UK} 2017**